Experimental evaluation of biaxial out-of-phase fatigue life failure criteria

AF Brown



orcid.org/0000-0002-7464-4007

Dissertation accepted in fulfilment of the requirements for the degree *Master of Engineering in Mechanical* Engineering at the North-West University

Supervisor: Mr AJK van der Walt

Graduation: June 2023

Student number: 26998459

ACKNOWLEDGEMENTS

I want to express my deepest gratitude to the following persons for their part in completing this research product.

Family and friends

To my parents, Andrew and Suneria, for your moral and financial support throughout two difficult and uncertain years. My significant other, Esre, for your support, love, understanding and, most of all, patience throughout the years. Words will fail to describe how much I appreciate you. My friends, in all areas of my life, for your continuous motivation and support.

Study leader and university personnel

Andre van der Walt, for being my mentor. Your knowledge, time and guidance are indeed recognized and appreciated.

Sarel Naudé, Thabo Diobe and Willem van Tonder, for your assistance and availability in the laboratory. Christo van der Merwe, for your electronic know-how and assistance with the test benches. Tiaan Lombaard (SPS) and Roland Wahler (Dantec Dynamics), for your continuous assistance and valued inputs for the DIC measurement system. Bartlo van der Merwe, for manufacturing multiple specimens and test bench components. Lourencia Augustinho, Rojanette Coetzee and Jana Von Moltke, for all the assistance with purchases, study funding and administrative work.

ABSTRACT

Complex multiaxial fatigue loading conditions often arise in mechanical components like crankshafts, propeller blades and gas turbines. The loading conditions are often out-of-phase, and the out-of-phase fatigue limit of the material is also unknown. Designing a component for fatigue resistance under these loading conditions using conventional in-phase fatigue failure criteria is considered less appropriate and requires cautious and conservative assumptions.

In the existing literature, several multiaxial fatigue criteria are proposed and reviewed. The criteria are evaluated using fatigue data of metals under complex multiaxial loading. However, the available data sets are argued to be old and insufficient, which makes the data sets questionable. The criteria, with reported differences in fatigue limit estimation and material applicability, are consequently also questioned based on the reliability of the data sets with which the criteria are validated.

This research study aimed to generate new fatigue data for a single ferrous metal under uniaxial and out-of-phase biaxial loading conditions. The required experimental verification measurements and considerations were made for these data sets. Supplemented and compared with the available literature data, these material and fatigue strength data were used to evaluate three critical plane fatigue criteria.

It was shown from experimental testing for 90 [°] out-of-phase bending-torsion loading with λ = 0.5 [-] on EN19 (T-condition) that the dominant Von Mises stress component (bending) seemingly determined the material's fatigue failure instead of the combination of the components. It was also observed for the 90 [°] phase difference that the biaxial stress components can be considered independent of each other. The experimental uncertainties were shown to be sufficiently low. A comparison between the literature and experimental investigation data showed that the validity of the multiaxial fatigue literature data set is questionable. It was shown that all three fatigue criteria made conservative predictions of the experimental data, and one of them is considered more appropriate for the tested material and loading. However, for the literature data set, it was shown that only one of the criteria made a comparative prediction, whilst the others overestimated the fatigue limit. The criteria validity was, therefore, also questionable. Consequently, it is suggested that more experimental test data is required on the same or different loading and material to investigate further the criteria evaluation differences observed.

***Keywords**: multiaxial fatigue criteria, multiaxial fatigue data, hard ferrous metal, out-of-phase bending-torsion, high-cycle fatigue testing*

OPSOMMING

Komplekse meer-assige vermoeidheid beladingskondisies kom dikwels voor in meganiese komponente soos krukasse, skroefblaaie en gasturbines. Die beladingskondisies is dikwels uit-fase, en die uit-fase vermoeidheidsgrens van die materiaal is ook onbekend. Die ontwerp van ‘n komponent vir vermoeidheids-sterkte met konvensionele in-fase vermoeidheidskriteria, word as minder toepaslik beskou onder die kondisies en vereis omsigtige en konserwatiewe aannames.

In die bestaande literatuur word verskeie meer-assige vermoeidheidskriteria voorgestel en hersien. Die kriteria word geëvalueer met vermoeidheidsdata van metale onder komplekse meer-assige belading. In die literatuur word egter aangevoer dat die beskikbare datastelle oud en onvoldoende is en word dus bevraagteken. Die kriteria, met gerapporteerde verskille in vermoeidheidsberaming en materiaal-toepasbaarheid, word gevolglik ook bevraagteken op grond van die betroubaarheid van die datastelle waarmee die kriteria gevalideer word.

Hierdie navorsingstudie het ten doel gehad om nuwe vermoeidheidsdata vir ‘n enkel ysterhoudende metaal onder enkel-assige en uit-fase twee-assige beladingskondisies te genereer. Die vereiste eksperimentele verifikasie-metings en oorwegings is vir hierdie datastelle gemaak. Dié materiaal en vermoeidheids-sterktedata is met die beskikbare datastelle van die literatuur vergelyk en aangevul, en daarna gebruik om drie vermoeidheidskriteria te evalueer.

Dit is getoon, uit eksperimentele toetsing met 90 [°] uit-fase buig-torsie belading en λ = 0.5 [-] op EN19 (T-kondisie) staal, dat die dominante Von Mises spanningskomponent (buiging) skynbaar die vermoeidheidsfaling van die materiaal bepaal het, in plaas van die kombinasie van komponente. Daar is ook vir die 90 [°] fase-verskil waargeneem dat die spanningskomponente as onafhanklik van mekaar beskou kan word. Die eksperimentele onsekerhede is getoon om laag te wees. ‘n Vergelyking tussen die data uit die literatuur en eksperimentele ondersoek het getoon dat die meer-assige vermoeidheidsdatastel van die literatuur se geldigheid bevraagteken kan word. Daar is gewys dat al drie vermoeidheidskriteria konserwatiewe voorspellings gemaak het van die eksperimentele data, en dat een van hulle as meer toepaslik beskou word vir die getoetste materiaal en beladingskondisie. Daar is egter vir die literatuur datastel gewys dat slegs een van die kriteria ‘n vergelykende voorspelling gemaak het, terwyl die ander die vermoeidheidsgrens oorskat het. Die kriteriageldigheid word dus ook bevraagteken. Gevolglik word daar voorgestel dat meer eksperimentele toetsdata benodig word op dieselfde of ander beladingskondisies en materiaal om die waargenome kriteria evaluasie verskille verder te ondersoek.

***Sleutelterme**: meer-assige vermoeidheidskriteria, meer-assige vermoeidheidsdata, harde ysterhoudende metaal, uit-fase buig-torsie, hoë-siklus vermoeidheidstoetse*

TABLE OF CONTENTS

ACKNOWLEDGEMENTS ..... **I**

ABSTRACT ..... **II**

OPSOMMING ..... **III**

LIST OF FIGURES ..... **X**

LIST OF TABLES ..... **XVIII**

ABBREVIATIONS ..... **XXI**

NOMENCLATURE ..... **XXVI**

CHAPTER 1 – INTRODUCTION **1**

1.1 Background and Rationale **1**

1.2 Research Problem **4**

1.3 Research Questions **4**

1.3.1 Main Research Question 4

1.3.2 Secondary Research Questions 4

1.4 Research Objectives **5**

1.4.1 Main Research Objective 5

1.4.2 Secondary Research Objectives 5

1.5 Contribution of the research **5**

1.6 Scope of Study **5**

1.6.1 Study Limitations 6

1.7 Chapter Outline **7**

CHAPTER 2 – LITERATURE REVIEW **8**

2.1 Introduction **8**

2.2 General Overview **9**

2.3 Multiaxial Fatigue Loading **12**

2.4 Multiaxial Fatigue Criteria 16
2.4.1 Reported Multiaxial Fatigue Criteria 17
2.4.2 Considered Multiaxial Fatigue Criteria 20
2.4.3 Fatigue Criteria Evaluation 23
2.5 Materials Data 25
2.6 Multiaxial Fatigue Data 33
2.7 Fatigue Test Equipment 38
2.8 Issues and Shortcomings 41
2.9 Conclusion 42
CHAPTER 3 – THEORY 43
3.1 Introduction 43
3.2 Multiaxial Non-proportional Loading 43
3.3 Multiaxial Fatigue Criteria Models 46
3.4 Critical Plane Theory 52
3.5 Conclusion 59
CHAPTER 4 – EXPERIMENTAL METHODOLOGY 60
4.1 Introduction 60
4.2 Specific Experimental Selections and Motivations 61
4.2.1 Experimental Biaxial Fatigue Loading Condition 62
4.2.2 Multiaxial Fatigue Criteria 62
4.2.3 Experimental Test Material 63
4.2.4 Serviceable Fatigue Data 65
4.3 Experimental Test and Measurement Equipment 67
4.3.1 Test Equipment 67
4.3.1.1 Monotonic Tensile / Uniaxial Axial Fatigue 68
4.3.1.2 Uniaxial Bending Fatigue 69
4.3.1.3 Uniaxial Torsion Fatigue 69
4.3.1.4 Out-of-phase Biaxial Bending-Torsion Fatigue 70
4.3.2 Measurement and Evaluation Equipment 71
4.3.2.1 General Measurement Equipment 71
4.3.2.2 Principal Measurement Instrument 74

4.4 Experimental Considerations 81
4.4.1 Test Specimens 81
4.4.1.1 Specimen Material, Machining and Management 81
4.4.1.2 Specimen Geometry 83
4.4.1.3 Specimen Surface Condition 85
4.4.2 Experimental Loading 87
4.4.2.1 General Considerations 88
4.4.2.2 Resonance Frequency and Loading Gain 89
4.4.2.3 Test Specimen Measurement Processing 92
4.4.2.4 Test Bench Verification Measurements and Characterisation 96
4.4.3 Experimental Fatigue Limit and Failure Definition 104
4.5 Experimental Biaxial Fatigue Testing and Measurement 105
4.5.1 Testing Methodology 106
4.5.2 Specimen Measurement 107
4.6 Experimental Data Processing 110
4.6.1 Experimental Stresses 110
4.6.2 Fatigue Limit Strength Estimation 113
4.6.3 Uncertainty Analysis 114
4.7 Multiaxial Fatigue Data and Criteria Evaluation 121
4.8 Conclusion 123
CHAPTER 5 – EXPERIMENTAL RESULTS 124
5.1 Introduction 124
5.2 Results and Discussion 124
5.2.1 Monotonic Tensile Tests 124
5.2.2 Uniaxial Fatigue Tests 125
5.2.2.1 Torsion Fatigue Test Bench – Experimental Measurement Results 125
5.2.2.2 Uniaxial Fatigue Test Results 127
5.2.3 Biaxial Fatigue Tests 131
5.2.3.1 Bending-Torsion Fatigue Test Bench – Experimental Measurement Results 132
5.2.3.2 Biaxial Fatigue Test Results 135
5.2.4 Multiaxial Fatigue Criteria Evaluations 139
5.3 Conclusion 146
CHAPTER 6 – CONCLUSIONS AND RECOMMENDATIONS 149

6.1 Introduction 149

6.2 Study Overview and Main Findings 149

6.3 Critique and Recommendations 154

6.3.1 Areas of Further Research 155

6.4 Contribution of the research 156

6.5 Conclusion 157

BIBLIOGRAPHY 158

APPENDICES 166

A. EXPERIMENTAL TEST EQUIPMENT 166

A1. MTS Landmark Tensile Test Machine 166

A2. TERCO MT 205G Rotating Cantilever Bending Fatigue Test Bench 169

A3. Torsion Fatigue Test Bench 172

A4. Biaxial Fatigue Test Bench M1 Bending-Torsion 174

B. EXPERIMENTAL MEASUREMENT EQUIPMENT 176

B1. Mitutoyo Absolute Digital Vernier and SMIEC Micrometre 176

B2. SARTORIUS BP110S and PRW30++ Microscale 178

B3. FLUKE 52 K/J Thermocouple Thermometer 179

B4. MTS Extensometer 634.31F-24 180

B5. Lutron DT-2234BL Digital Tachometer 182

B6. DANTEC Dynamics Q400 DIC System 183

B7. RS Pro EZM-3735 Digital Timer Controller and WEG CFW100 VSD 187

B8. Aptina CMOS Digital Camera Microscope 187

C. SPECIMEN DETAIL AND PREPARATION 188

C1. Monotonic Tensile Test Specimens 188

C2. Axial Fatigue Test Specimens 189

C3. Bending Fatigue Test Specimens 190

C4. Torsion Fatigue Test Specimens 191

C5. Bending-Torsion Fatigue Test Specimens 192

C6. Specimen Manufacturing, Management and Polishing 193

D. SPECIMEN DIAMETER MEASUREMENTS 195

D1. Monotonic Tensile Test Specimen Diameters 195

D2. Axial Fatigue Test Specimen Diameters 195

D3. Bending Fatigue Test Specimen Diameters 196

D4. Torsion Fatigue Test Specimen Diameters 196

D5. Bending-Torsion Fatigue Test Specimen Diameters 197

E. MASS MEASUREMENTS 198

E1. Calibration Mass Pieces 198

E2. Centrifugal Mass Pieces 199

E3. Bending-Torsion Fatigue Test Bench Head Mass 203

F. RESONANCE FREQUENCY AND GAIN CONSIDERATIONS 205

F1. Methodology for Theoretical Resonance Frequencies and Gain 205

F2. Torsion Fatigue Test Bench – Resonance Frequencies and Gain 213

F3. Bending-Torsion Fatigue Test Bench – Resonance Frequencies and Gain 215

G. EXPERIMENTAL TEST PROCEDURES 218

G1. Monotonic Tensile Test Procedure 218

G2. Axial Fatigue Test Procedure 221

G3. Bending Fatigue Test Procedure 225

G4. Torsion Fatigue Test Procedure 227

G5. Bending-Torsion Fatigue Test Procedure 229

H. EXPERIMENTAL TEST MEASUREMENTS AND CALCULATIONS 232

H1. Monotonic Tensile Test Measurements and Calculations 232

H2. Axial Fatigue Test Measurements and Calculations 254

H3. Bending Fatigue Test Measurements and Calculations 260

H4. Torsion Fatigue Test Measurements and Calculations 263

H5. Bending-Torsion Fatigue Test Measurements and Calculations 287

I. EXPERIMENTAL TEST SIMULATIONS 308

I1. Theoretical Torsional Displacement Measurement 308

I2. Theoretical Bending and Torsion Displacement Measurement 310

J. EXPERIMENTAL TEST RESULTS 313
J1. Monotonic Tensile Test Results 313
J2. Axial Fatigue Test Results 315
J3. Bending Fatigue Test Results 316
J4. Torsion Fatigue Test Results 317
J5. Bending-Torsion Fatigue Test Results 318
K. EXPERIMENTAL TEST UNCERTAINTIES 319
K1. Monotonic Tensile Test Uncertainties 319
K2. Axial Fatigue Test Uncertainties 321
K3. Bending Fatigue Test Uncertainties 323
K4. Torsion Fatigue Test Uncertainties 325
K5. Biaxial Bending-Torsion Test Uncertainties 329
L. MULTIAXIAL FATIGUE CRITERIA EVALUATION RESULTS 333
L1. Papadopoulos 1994/1997 – Critical Plane Criterion 333
L2. Carpinteri and Spagnoli 2001 – Critical Plane Criterion 334
L3. Liu and Mahadevan 2005 – Critical Plane Criterion 335
M. MATERIAL AND HEAT TREATMENT CERTIFICATE(S) 336

LIST OF FIGURES

Figure 1-1: In-service fatigue failure of an EN19 steel propeller shaft due to unforeseen multiaxial cyclic loading and surface indentation [6] 2

Figure 1-2: Fundamental uniaxial loading: (a) tension-compression (axial), (b) bending and (c) torsion [3, 17] 3

Figure 2-1: Proportional (in-phase) multiaxial loading – Mohr stress circle illustration [27] .. 13

Figure 2-2: Non-proportional (out-of-phase) multiaxial loading – Mohr stress circle illustration [27] 14

Figure 2-3: Schematic biaxial load combination illustrations for (a) axial-torsion [56], (b) axial-bending [3] and (c) bending-torsion [61] loading 15

Figure 2-4: Schematic illustration of general multiaxial fatigue criteria classification 17

Figure 2-5: Summary of reported multiaxial fatigue criteria in the literature 18

Figure 2-6: Generalised multiaxial fatigue failure criteria evaluation process and inputs 24

Figure 2-7: S-N curve – reported uniaxial bending, torsion and axial fatigue strength and limit data 31

Figure 2-8: Comparative S-N curve (normalised) – reported uniaxial bending, torsion and axial fatigue limit data 33

Figure 2-9: S-N curve – reported biaxial in-phase and out-of-phase bending-torsion fatigue strength and limit data 36

Figure 2-10: Comparative S-N curve (normalised) – reported biaxial in-phase and out-of-phase bending-torsion fatigue limit data 37

Figure 2-11: Bending-torsion test bench and specimen(s) of: (a) MZGS-100Ph in-phase loading machine [43] and (b) MZGS-200E out-of-phase loading machine [14, 55, 78] 39

Figure 2-12: Electromechanical bending-torsion fatigue test bench and specimen geometry [64] 40

Figure 2-13: Uniaxial (a) axial, (b) bending [80] and (c) torsion [79] fatigue test benches proposed or referenced in the literature 41

Figure 3-1: Out-of-phase (non-proportional) biaxial bending-torsion loading – Mohr stress circles 44

Figure 3-2: Biaxial bending-torsion stresses – (a) out-of-phase and (b) in-phase VM stress calculation 46

Figure 3-3: Theoretical critical plane methodology [10] – (a) material volume element and (b) arbitrary material plane and stress definition 55

Figure 3-4: Theoretical critical plane methodology [10] – stress paths and cyclic behaviour during loading on the material plane 56

Figure 3-5: Theoretical critical plane methodology [10] – critical plane stresses and paths due to bending and torsion loading 57

Figure 4-1: Comparative S-N curve (normalised) – usable uniaxial bending, torsion and axial fatigue limit data from the literature 65

Figure 4-2: Comparative S-N curve (normalised) – usable biaxial in-phase and out-of-phase bending-torsion fatigue limit data from the literature 66

Figure 4-3: MTS Landmark servo-hydraulic tensile test system 68

Figure 4-4: TERCO MT205G rotating cantilever bending fatigue test bench 69

Figure 4-5: Torsion fatigue test bench 70

Figure 4-6: Biaxial Fatigue Test Bench M1 – Bending-Torsion 71

Figure 4-7: DANTEC Dynamics Q400 DIC System [83] (a) cameras and setup, (b) specimen speckle pattern and (c) correlation mesh and displacement measurement 75

Figure 4-8: Secondary verification measurement – DANTEC line gauge positioning 77

Figure 4-9: TEN test Spec6 strain measurements – DANTEC (strain-step) and Extensometer (strain-time) overlay curves 79

Figure 4-10: Bending-torsion (BT) fatigue test specimen 85

Figure 4-11: Surface polishing result – bending-torsion (BT) fatigue test specimen 87

Figure 4-12: T and BT fatigue test bench – theoretical bending and torsion loading gain curves 91

Figure 4-13: T and BT fatigue test bench – DANTEC bending and torsion displacement measurement 93

Figure 4-14: T and BT fatigue test bench – static FEM models and inputs 94

Figure 4-15: T and BT fatigue test bench – static FEM torsion and bending displacement 95

Figure 4-16: T fatigue test bench verification – experimental and theoretical gain response curves 99

Figure 4-17: BT fatigue test bench loading characterisation – experimental and theoretical gain response curves 102

Figure 4-18: Illustrative S-N curve of fatigue tests on medium-strength steel [62] 104

Figure 4-19: BT fatigue test specimen measurement – DANTEC DIC System setup for biaxial bending-torsion displacement measurement 108

Figure 5-1: T fatigue experimental measurement results – experimental vs theoretical torsion gain and assumed experimental gains 126

Figure 5-2: T fatigue experimental measurement – sinusoidal torsion displacement curve of Spec9 127

Figure 5-3: Experimental uniaxial fatigue S-N curves and fatigue limits – (a) AX fatigue, (b) B fatigue and (c) T fatigue 129

Figure 5-4: Experimental uniaxial fatigue limits (callouts) compared with literature fatigue limit data 130

Figure 5-5: Comparative S-N curve (normalised) – experimental AX, B and T fatigue strength and limit data comparison with literature uniaxial fatigue limit data 131

Figure 5-6: BT fatigue experimental measurements – sinusoidal bending and torsion displacement curves 133

Figure 5-7: BT fatigue experimental measurements – DANTEC rotating true principal strain vectors 134

Figure 5-8: Experimental biaxial fatigue S-N curves – (a) bending (and axial) fatigue strength and (b) torsion fatigue strength 136

Figure 5-9: Comparative S-N curve (normalised) – experimental BT fatigue strength data comparison with literature biaxial fatigue limit data 138

Figure 5-10: Biaxial BT fatigue S-N curve – experimental BT equivalent fatigue strength comparison with uniaxial T fatigue limit (PPD) 139

Figure 5-11: Biaxial BT fatigue stress data – experimental nominal bending-torsion fatigue strengths vs PPD ellipse arc model: (a) no fail tests and (b) failed tests 140

Figure 5-12: Biaxial BT fatigue S-N curve – experimental BT equivalent fatigue strength comparison with uniaxial B fatigue limit (C&S) 141

Figure 5-13: Biaxial BT fatigue stress data – experimental critical plane fatigue stresses vs C&S elliptic model: (a) no fail tests and (b) failed tests 142

Figure 5-14: Biaxial BT fatigue S-N curve – experimental BT equivalent fatigue strength comparison with uniaxial fatigue limit parameter (L&M) 143

Figure 5-15: Biaxial BT fatigue stress data – experimental critical plane fatigue stresses vs L&M elliptic model: (a) no fail tests and (b) failed tests 144

Figure 5-16: Multiaxial BT fatigue failure criteria – experimental BT fatigue limit estimate comparison with criteria proposed uniaxial fatigue limit 145

Figure A-1: MTS Landmark – test system and components 166

Figure A-2: MTS Landmark – compression calibration certificate 167

Figure A-3: MTS Landmark – tension calibration certificate 168

Figure A-4: TERCO MT 205G – bending fatigue test bench and components 169

Figure A-5: Bending fatigue test bench – calibration process 170

Figure A-6: Bending fatigue test bench – calibration curves 171

Figure A-7: Torsion Fatigue Test Bench 172

Figure A-8: Torsion Fatigue Test Bench – components 172

Figure A-9: Torsion Fatigue Test Bench – working principle 173

Figure A-10: Biaxial Fatigue Test Bench M1 Bending-Torsion 174

Figure A-11: Biaxial Fatigue Test Bench M1 Bending-Torsion – components 174

Figure A-12: Biaxial Fatigue Test Bench M1 Bending-Torsion – working principle 175

Figure B-1: Mitutoyo Absolute Digital Vernier and SMIEC Micrometre 176

Figure B-2: Mitutoyo Absolute Digital Vernier – vernier size measurement results 177

Figure B-3: Microscales – (a) SARTORIUS BP110S and (b) PRW30++ 178

Figure B-4: FLUKE 52 K/J Thermocouple Thermometer 179

Figure B-5: MTS Extensometer 634.31F-24 – components 180

Figure B-6: MTS Extensometer 634.31F-24 – 25 [mm] calibration certificate 181

Figure B-7: Lutron DT-2234BL Digital Tachometer 182

Figure B-8: DANTEC Dynamics Q400 DIC System – components and setup 183

Figure B-9: DANTEC Dynamics Q400 DIC System – measurement illustration 184

Figure B-10: DANTEC Dynamics Q400 DIC System – speckle pattern preparation 185
Figure B-11: DANTEC Dynamics Q400 DIC System – measurement and guide [83] 186
Figure B-12: (a) WEG CFW100 Mini Drive VSD and (b) RS Pro EZM-3735 Digital Timer Controller 187
Figure B-13: Aptina CMOS Digital Camera Microscope 187
Figure C-1: Tensile (TEN) specimen – geometry and surface finish 188
Figure C-2: Axial (AX) fatigue specimen – geometry and surface finish 189
Figure C-3: Bending (B) fatigue specimen – geometry and surface finish 190
Figure C-4: Torsion (T) fatigue specimen – geometry and surface finish 191
Figure C-5: Bending-Torsion (BT) fatigue specimen – geometry and surface finish 192
Figure C-6: Test Specimens – manufacturing, management and polishing 193
Figure E-1: Calibration weights 198
Figure E-2: Centrifugal mass pieces 200
Figure E-3: Centrifugal mass pieces – general nut geometry and radial position options on bilateral wheels 201
Figure E-4: Centrifugal mass pieces – COM distance measurements in (a) T fatigue and (b) BT fatigue test bench CAD model 202
Figure E-5: BT fatigue test bench – lever-head theoretical COM position 204
Figure F-1: (a) T fatigue and (b) BT fatigue test bench – polar mass moments of inertia measurement 206
Figure F-2: Torsional angular displacement – (a) inferring linear x-displacement measurement from (b) static FEM model 207
Figure F-3: Linear dependency of torsion and bending resonance frequencies on specimen diameter 209
Figure F-4: BT specimen modal analysis FEM model – (a) CTETRA10 meshed body and fixed constraint with (b) CONM2 element and RBE2 connector 211
Figure F-5: BT specimen modal analysis results – (a) theoretical mode 1 to 8 resonance frequencies, (b) bending resonance mode 1 and 2 specimen shapes, and (c) additional mode 3 and 4 shapes 211
Figure F-6: T fatigue test bench - theoretical torsion loading gain curves 214

Figure F-7: BT fatigue test bench - theoretical bending and torsion loading gain curves.... 217

Figure G-1: B fatigue test specimen mounting and loading schematic [17] 225

Figure G-2: BT fatigue test procedure – flow diagram 231

Figure H-1: TEN test Spec1 to Spec5 – pre and post-test images 233

Figure H-2: TEN test Spec1 to Spec5 – (a) load vs extension curves and (b) yield load estimation method..... 234

Figure H-3: TEN test Spec6 to Spec10 (Extensometer and DANTEC) – pre and post-test images 236

Figure H-4: TEN test Spec6 to Spec10 measurements – extensometer strain vs time curves 238

Figure H-5: TEN test Spec6 to Spec10 – load vs displacement curves 239

Figure H-6: TEN test Spec6 to Spec10 measurements – DANTEC DIC System setup schematic (top view) 245

Figure H-7: TEN test Spec6 (Extensometer and DANTEC) – DANTEC (a) mask and start point definition, (b) evaluation grid, (c) displacement grid and (d) measurement (user) coordinate system definition 248

Figure H-8: TEN test Spec6 (Extensometer and DANTEC) – DANTEC (a) line gauge element definition and positioning, (b) specimen extension measurement 249

Figure H-9: TEN test Spec6 to Spec10 measurements – DANTEC digital line gauge strain curves..... 251

Figure H-10: TEN test Spec6 to Spec10 measurements – DANTEC (strain-step) and Extensometer (strain-time) overlay curves 253

Figure H-11: AX fatigue test Spec1 to Spec8 – pre and post-test images..... 255

Figure H-12: AX fatigue test Spec1 – cyclic axial fatigue load vs time curve from (a) exported DAQ data and (b) MTS display (in-test)..... 258

Figure H-13: AX fatigue test Spec1 to Spec8 results – experimental vs theoretical loading . 259

Figure H-14: B fatigue test specimen – cantilever loading schematic 261

Figure H-15: B fatigue test specimen – sinusoidal loading vs rotation angle curve..... 261

Figure H-16: B fatigue test Spec1 to Spec7 – pre and post-test images 262

Figure H-17: Torsion fatigue test bench – working principle (repeat) 264

Figure H-18: T fatigue test Spec1 to Spec9 – pre and post-test images 265

Figure H-19: T fatigue test specimen measurement – DANTEC DIC System setup schematic (side and top view)..... 266

Figure H-20: T fatigue test bench – (a) experimental displacement stabilisation weights and (b) pre and post-displacement measurements 267

Figure H-21: T fatigue test specimen – DANTEC (a) prepared specimen speckle pattern and markings, (b) evaluation grid and (c) measurement (user) coordinate system definition 270

Figure H-22: T fatigue test specimen – DANTEC point gauge elements definition and positioning within best fit sphere area..... 271

Figure H-23: Hang scale test #1 to #3 – hang scale loading on wheel..... 272

Figure H-24: Hang scale test #1 – DANTEC and static FEM displacement measurement ... 273

Figure H-25: T specimen measurements – DANTEC digital point gauge P1 and P2 y-displacement curves at 40 [Hz] test speed 278

Figure H-26: T specimen measurements – (a) experimental and theoretical gain comparison and (b) gain response curves..... 280

Figure H-27: T fatigue test Spec8 measurements – DANTEC digital point gauge P1 and P2 y-displacement curves at 40 [Hz] test speed..... 284

Figure H-28: T fatigue test Spec1, 5, 8 and 9 measurements – DANTEC sinusoidal displacement curves (collapsed)..... 285

Figure H-29: T fatigue test Spec1, 5, 8 and 9 measurements – experimental and theoretical torsional gain at tested speeds..... 286

Figure H-30: Bending-Torsion fatigue test bench – working principle (repeat)..... 288

Figure H-31: BT fatigue test Spec1 to Spec17 – pre and post-test images..... 290

Figure H-32: BT fatigue test specimen measurement – DANTEC DIC System setup schematic (top and front view)..... 291

Figure H-33: BT fatigue test specimen – DANTEC (a) prepared specimen speckle pattern and markings, (b) evaluation grid and (c) measurement (user) coordinate system definition 294

Figure H-34: BT fatigue test specimen – DANTEC point gauge elements definition and positioning within best fit sphere area..... 295

Figure H-35: BT Spec18 measurement – DANTEC digital point gauge P1 and P2 y (torsion) and z (bending) displacement curves at 48 [Hz] with NUT 5 300

Figure H-36: BT Spec18 measurement – experimental and theoretical gain response curves 302

Figure H-37: BT fatigue test Spec9 measurements – DANTEC digital point gauge P1 and P2 y and z-displacement curves at 38 [Hz] test speed 305

Figure H-38: BT fatigue test Spec3, 9 and 15 measurements – DANTEC sinusoidal displacement curves (collapsed) 306

Figure I-1: Theoretical torsional displacement measurement – (a) NX FEM model y-displacement measurement and (b) static FEM model 309

Figure I-2: Theoretical bending-torsion displacement vs FEM Elasticity Modulus 310

Figure I-3: Theoretical bending-torsion displacement measurement – (a) NX FEM model y and z-displacement measurement and (b) static FEM model 312

Figure J-1: Tensile (TEN) specimen fracture zone 313

Figure J-2: Tensile (TEN) testing results – monotonic ultimate tensile and yield strengths 314

Figure J-3: Axial (AX) fatigue specimen fracture plane 315

Figure J-4: Bending (B) fatigue specimen fracture plane 316

Figure J-5: Torsion (T) fatigue specimen fracture plane 317

Figure J-6: Bending-Torsion (BT) fatigue specimen fracture plane 318

Figure K-1: Tensile (TEN) test result uncertainties – partial derivatives 320

Figure K-2: Axial (AX) fatigue test result uncertainties – partial derivatives 322

Figure K-3: Bending (B) fatigue test result uncertainties – partial derivatives 324

Figure K-4: Torsion (T) fatigue test result uncertainties – partial derivatives 328

Figure K-5: Bending-Torsion (BT) fatigue test result uncertainties – partial derivatives 332

Figure M-1: EN19 (T-condition) alloy steel – material test certificate 336

Figure M-2: EN19 (T-condition) alloy steel – mechanical test certificate 337

Figure M-3: EN19 (T-condition) alloy steel – heat treatment certificate 338

LIST OF TABLES

Table 2-1: Considered stress-based out-of-phase multiaxial fatigue criteria 20

Table 2-2: Metals and simple material strength properties reported in the literature 27

Table 4-1: Selected multiaxial fatigue failure criteria 63

Table 4-2: Summary of usable monotonic tensile and fatigue data for EN19 steels from the literature 67

Table 4-3: Experimental material strength tests performed in this study 67

Table 4-4: Secondary verification measurement results – DANTEC vs Extensometer 76

Table 4-5: EN19 (T-condition) alloy steel – material chemical element composition 82

Table 4-6: T fatigue test bench verification – DANTEC vs static FEM simulation displacements 97

Table 4-7: T fatigue test bench verification – experimental vs theoretical torsion gain 98

Table 4-8: BT fatigue test specimen measurement – measured and inferred tests 109

Table 5-1: EN19 (T-condition) alloy steel – monotonic tensile test results 124

Table 5-2: T fatigue experimental measurement results – experimental vs theoretical torsion gain 126

Table 5-3: EN19 (T-condition) alloy steel – uniaxial fatigue limit test results 128

Table 5-4: BT fatigue experimental measurement results – experimental bending and torsion gain comparison 132

Table A-1: Bending fatigue test bench – load cell force measurements 171

Table B-1: Mitutoyo Absolute Digital Vernier – vernier size measurements 177

Table D-1: Tensile (TEN) specimens – diameter measurements 195

Table D-2: Axial (AX) fatigue specimens – diameter measurements 195

Table D-3: Bending (B) fatigue specimens – diameter measurements 196

Table D-4: Torsion (T) fatigue specimens – diameter measurements 196

Table D-5: Bending-Torsion (BT) fatigue specimens – diameter (and length) measurements 197

Table E-1: Calibration mass pieces – mass measurements 198

Table E-2: Centrifugal mass pieces – mass measurements 199

Table E-3: BT fatigue test bench – lever-head mass measurements 203

Table F-1: T fatigue test bench – theoretical polar mass moments of inertia and torsional resonance frequencies 213

Table F-2: BT fatigue test bench – theoretical polar mass moments of inertia and torsional resonance frequencies 215

Table F-3: BT fatigue test bench – theoretical bending resonance frequencies 216

Table G-1: Monotonic tensile test procedure 218

Table G-2: Axial fatigue test procedure 221

Table H-1: TEN test Spec1 to Spec5 measurements – DAQ data exports 234

Table H-2: TEN test Spec1 to Spec5 measurements – DAQ data tables (peak loads) 234

Table H-3: TEN test Spec6 to Spec10 measurements (Extensometer) – DAQ data exports 237

Table H-4: TEN test Spec6 to Spec10 measurements (Extensometer) – DAQ data tables (peak and yield loads, E Modulus) 237

Table H-5: Monotonic tensile test (Extensometer) procedure 240

Table H-6: TEN test Spec6 to Spec10 measurements – DANTEC DAQ data exports from ISTRA 4D measurements 250

Table H-7: TEN test Spec6 to Spec10 verification measurement results – Extensometer vs DANTEC 252

Table H-8: AX fatigue test Spec1 to Spec8 measurements – DAQ data exports 256

Table H-9: AX fatigue test Spec1 to Spec3 measurements – DAQ data tables (post-test results for fatigue cycle count) 257

Table H-10: AX fatigue test Spec1 to Spec8 results – experimental loading 259

Table H-11: Hang scale test #1 to #3 – measurement comparison 274

Table H-12: T specimen measurements – DANTEC DAQ data exports from ISTRA 4D measurements 277

Table H-13: T specimen measurements – experimental and theoretical gain 279

Table H-14: T fatigue test Spec1, 5, 8 and 9 measurements – DANTEC DAQ data exports from ISTRA 4D measurements 283

Table H-15: T fatigue test Spec1, 5, 8 and 9 measurements – experimental and theoretical gain 286
Table H-16: BT Spec18 measurement – DANTEC DAQ data exports from ISTRA 4D measurements 299
Table H-17: BT Spec18 measurement – experimental and theoretical gain 301
Table H-18: BT fatigue test Spec3, 9 and 15 measurements – DANTEC DAQ data exports from ISTRA 4D measurements 305
Table H-19: BT fatigue test Spec3, 9 and 15 measurement – experimental gain comparison 307
Table J-1: Tensile (TEN) testing results 313
Table J-2: Axial (AX) fatigue testing results 315
Table J-3: Bending (B) fatigue testing results 316
Table J-4: Torsion (T) fatigue testing results 317
Table J-5: Bending-Torsion (BT) fatigue testing results 318
Table K-1: Tensile (TEN) test result uncertainties 319
Table K-2: Axial (AX) fatigue test result uncertainties 321
Table K-3: Bending (B) fatigue test result uncertainties 323
Table K-4: Torsion (T) fatigue test result uncertainties 325
Table K-5: Bending-Torsion (BT) fatigue test result uncertainties 329
Table L-1: Papadopoulos 1994/1997 criterion – equivalent multiaxial fatigue stress predictions 333
Table L-2: Carpinteri and Spagnoli 2001 criterion – equivalent multiaxial fatigue stress predictions 334
Table L-3: Liu and Mahadevan 2005 criterion – equivalent multiaxial fatigue stress predictions 335

ABBREVIATIONS

#	
0D	Zero-dimensional
1D	One- dimensional
2D	Two-dimensional
3D	Three-dimensional
A	
AISI	American Iron and Steel Institute
ASTM	American Society for Testing and Materials
AVG/avg	Average
AX	Axial Fatigue (loading or specimen)
AZA	Aluminium Zinc Alloy
B	
B	Bending Fatigue (loading or specimen)
BSI	British Standards Institution
BT	Bending-Torsion Fatigue (loading or specimen)
B&T	Bending and Torsion
C	
CAD	Computer-Aided Design
CAS	Chrome Alloy Steel
CMAS	Chrome Molybdenum Alloy Steel
CMOS	Complementary Metal-Oxide-Semiconductor (camera sensor)
CNC	Computer Numerically Controlled
COM	Centre Of Mass
CONM	Concentrated Mass Element
CTETRA	Tetrahedral Element
C&S	Carpinteri and Spagnoli

D		
	DAQ	Data Acquisition (control system or box or data set)
	DE	Distortion Energy
	DIC	Digital Image Correlation
	DIN	German Institute for Standardisation / Deutsches Institut für Normung (Werkstoff Number)
E		
	EN	European Norm
F		
	F	Findley
	FEA	Finite Element Analysis
	FEM	Finite Element Method (numerical technique)
	FST	Froustey
	F&L	Froustey and Lasserre
G		
	G	Gough
H		
	HCF	High Cycle Fatigue (10^5 - $2x10^6$ or 10^7 cycles)
	HCS	High Carbon Steel
	HMI	Human Machine Interface
	HPU	High-Pressure Unit
	HS	Hard Steel
I		
	IP	In-Phase
	ISO	International Organisation for Standardisation
J		
	JL	Li *et al.*
K		

L	
LCF	Low Cycle Fatigue (10^1 – 10^5 cycles)
LCS	Low Carbon Steel
LHS	Left-Hand Side
LRS	Limiting Ruling Section (material effective heat treatment depth)
LSB	Lee Son-Book
L&M	Liu and Mahadevan
L&Y	Luo *et al.*
L&Z	Lasserre and Zenner
M	
MCS	Medium Carbon Steel
MOR	Morettini *et al.*
MRL	Morel
MS	Mild Steel
N	
N-N	Life-Life
NCAS	Nickel Chrome Alloy Steel
NCMA	Nickel Chrome Molybdenum Alloy
NCMAS	Nickel Chrome Molybdenum Alloy Steel
NK	Nishihara and Kawamoto
O	
OG	Ogawa *et al.*
OP	Out-Of-Phase
P	
PCD	Pitch Circle Diameter
PPD	Papadopoulos
PPG	Papuga *et al.*
Q	

R	
RBE	Rigid Body Element
RHS	Right-Hand Side
S	
S-N	Stress-Life
SAE	Society of Automotive Engineers
SG	Stanfield
SHS	Swedish Hard Steel
Spec	Specimen
SS	Stainless Steel
STDEV/stdev	Standard Deviation
SUS	Susmel
T	
T	Torsion Fatigue (loading or specimen)
TAVA	Titanium Aluminium Vanadium Alloy
TEN	Tensile (loading or specimen)
U	
UTS	Ultimate Tensile Strength
V	
VA	Variable Amplitude (loading or criteria)
VHCF	Very High Cycle Fatigue (10^7 - 10^{10} cycles) or Giga Cycle Fatigue (GCF)
VM	Von Mises Stress
VSD	Variable Speed Drive / Variable Frequency Drive (VFD)
W	
X	
XW	Aluminium Cross Wheel Configuration (test bench)
XWS	Aluminium Cross Wheel and Shaft Configuration (test bench)
Y	

Z

Z	Zenner *et al.*
ZR	Zenner

NOMENCLATURE

A	
α	Loading Cycle Angle (of test bench wheel rotation) [rad] or [°]
A	Cross Sectional Area [mm^2]
B	
β	Phase Angle [rad] or [°]
C	
C	Shear Stress On The Critical Plane [MPa]
D	
δ	Phase Angle (alternatively use in literature) [rad] or [°]
d	Specimen Diameter (test zone) [m]
E	
ε	Strain [-]
ε_{eng}	Engineering Strain [-]
η	Material Parameter [-]
E	Young's Modulus of Elasticity [GPa]
F	
F	Force [N]
$F_{centrifugal}$	Centrifugal Force [N]
$F_{0.2\%;yield}$	Yield-offset Load [N]
F_{UTS}	Ultimate Tensile Force [N]
F_Y	Yield Force [N]
F_{offset}	Offset Force [N]
$F_{axial;a}$	Axial Fatigue Loading Force [N]
$F_{load\ cell}$	Load Cell Force [N]
$F_{cantilever}$	Cantilever Force [N]
f_{-1}	Fully Reversed Bending Fatigue Limit [MPa]

G	
G	Gain [-]
G_B	Bending Gain [-]
G_T	Torsion Gain [-]
G_{th}	Theoretical Gain [-]
H	
H_a	Hydrostatic Stress [MPa]
I	
I	Error Index [%]
$I_{x/y/z}$	Polar Mass Moment of Inertia (NX or SolidWorks) [kg.m^2]
J	
J_0	Polar Mass Moment of Inertia [kg.m^2]
K	
k	Constant [-]
k_t	Torsional Stiffness [N.m/rad]
L	
λ	Biaxial Nominal Stress Amplitude Ratio [-]
L_{lever}	Test Bench Moment Lever Length [m]
$L_{cantilever}$	Test Bench Cantilever Moment Arm Length [m]
M	
M_B	Bending Moment [N.m]
M_T	Torsion Moment [N.m]
m_{centr}	Centrifugal Mass [kg]
N	
N	Normal Stress On The Critical Plane [MPa]
N	Test Speed / Frequency [Hz]

N_f	Fatigue Cycles To Failure [-]
N_c	Natural/Resonance Frequency [Hz]
O	
ω	Rotational Speed [rad/s]
P	
φ	Arbitrary Critical Plane Orientation [rad] or [°]
φ_c	Critical Plane Orientation [rad] or [°]
φ_f	Fracture Plane Orientation [rad] or [°]
Q	
R	
R	Stress Ratio [-]
R_a	Surface Roughness [μm]
r_{wheel}	Test Bench Wheel Radius Position [m]
r	Radial position [m]
S	
σ	Normal Stress [MPa]
σ'	Von Mises (VM Stress [MPa]
σ_a	Normal / Axial / Bending Stress Amplitude [MPa]
σ_m	Normal / Axial Bending Stress Midrange [MPa]
σ_{axial}	Axial Stress [MPa]
$\sigma_{bending}$	Bending Stress [MPa]
$\sigma_{1/2}$	Principle Stress [MPa]
σ_{eq}	Uniaxial Equivalent Stress [MPa]
S_y	Yield Strength [MPa]
S_{ut}	Ultimate Tensile Strength [MPa]
S_e	Endurance Limit [MPa]
S'_e	Unmodified Endurance Limit [MPa]

s_{-1}	Fully Reversed Axial Fatigue Limit [MPa]
s	Fully Reversed Torsion/Bending Fatigue Limit Ratio [-]
T	
τ	Shear Stress [MPa]
τ_a	Shear Stress Amplitude [MPa]
τ_m	Shear Stress Midrange [MPa]
θ	Torsional Angular Displacement [rad]
T	Temperature [°]
t	Time [s]
t_{-1}	Fully Reversed Torsion Fatigue Limit [MPa]
U	
$u(P)$	Uncertainty on Stress / Force / Geometry Parameter [-]
V	
V	Volume
W	
X	
x_{break}	Cantilever Test Zone Position [m]
x	Linear (x-direction) Displacement [m]
Y	
y	Linear (y-direction) Displacement [m]
Z	
ζ	Damping Ratio [-]
z	Linear (z-direction) Displacement [m]

CHAPTER 1 – INTRODUCTION

1.1 Background and Rationale

The first chapter aims to provide a background on multiaxial fatigue. After this, the research problem and questions are stated, followed by the research objectives. A short discussion of the proposed research contribution is also provided, and the research scope and limitations are then identified. The chapter is ultimately concluded with a chapter outline.

Metal fatigue is a unique failure condition induced by repeated loading and cumulative damage in a mechanical part or structural component. Fatigue failure most commonly originates from the surface of a part, where cyclic stresses are most severe [1, 2]. These stresses are often much lower than the yield strength of the material [3]. In most cases, fatigue failure is initiated or accelerated by stress concentrations like manufacturing defects, surface discontinuities (grooves and slots) or indentations. However, where stress levels permit, failure could also initiate around internal stress concentrations like metallic or alloying inclusions or imperfections in the material. Failure here is dangerously concealed, and the initiation or propagation of a fatigue crack (start of failure) is not as proactively observed or prevented [4]. These fatigue cracks grow for most of the fatigue life [5].

Fatigue damage is reported to be responsible for most registered failures of metal components and structures [1, 5, 6]. It is caused by simple or complex loading conditions that often only manifest during a part's service life [6]. These in-service loading conditions are often multiaxial and seldom considered during the design of a component [6]. Figure 1-1 below illustrates an example of the in-service multiaxial fatigue failure of a large EN19 (42CrMo4 / AISI 4140) steel propeller shaft initially designed for moderate fluctuating torsional loads but also experienced unforeseen rotative bending (due to misaligned bearings). Fatigue failure was initiated by a surface indentation introduced during fabrication or routine maintenance activities.

Complex multiaxial fatigue loading is experienced by mechanical components in everyday machinery, automobiles, aircraft, railroad, marine and civil vessels or structures. Such components include crankshafts, connecting rods, axles, suspension components, press shafts, propeller shafts, propeller blades, wind turbine hubs, train wheels, gas turbine blades, welded joints and pipelines [7-9]. The multiaxial cyclic load components can either occur in-phase (proportional) or out-of-phase (non-proportional) with each other. The latter ultimately contributes to the complexity of characterising and analysing an already complex metallic failure condition.

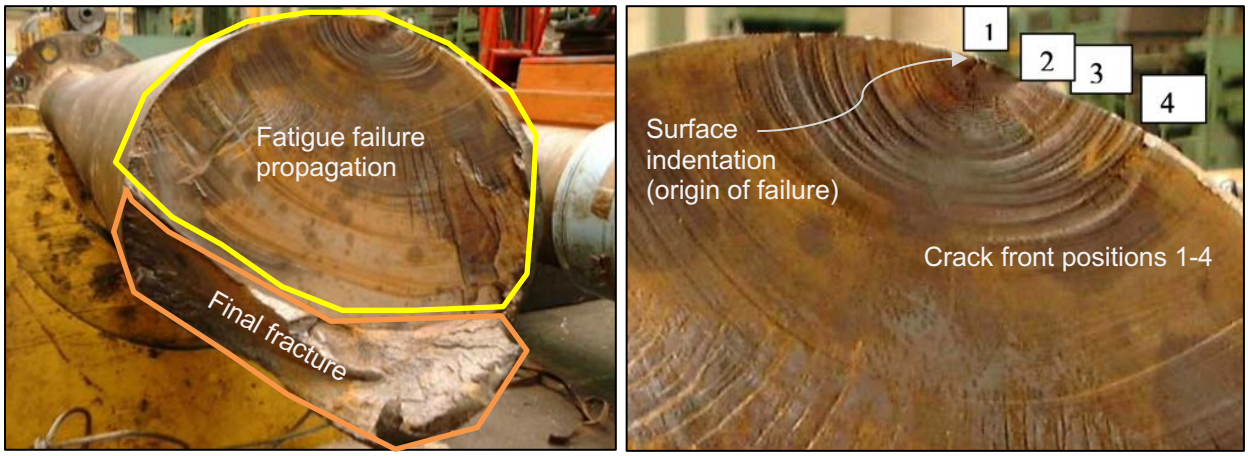


Figure 1-1: In-service fatigue failure of an EN19 steel propeller shaft due to unforeseen multiaxial cyclic loading and surface indentation [6]

The successful design of mechanical components that may experience such complex loading conditions depends on using validated and verified material and fatigue strength properties under the different types of loading. This is especially the case when a design is done for fatigue resistance, which is typically performed so that a component can withstand an infinite number of stress cycles (>10^6 and sometimes >10^7) [1]. These cyclic stresses are very often multiaxial and out-of-phase. Knowing the fatigue limit of the material under these complex stress conditions and implementing a suitable, well-defined, and accurate fatigue failure criterion becomes imperative, especially during the design phase of a component [5]. Such a criterion should have an analytical solution under basic loading conditions [10]. It must also be universal for high-cycle and low-cycle fatigue strength estimation under both uniaxial and multiaxial loading [11].

Fatigue limit data for typical engineering materials, particularly ferrous metals, are generally reported in the relevant textbooks, articles, and literature data sources. Fatigue limit tests for these materials are usually performed using the various standards (see Abbreviations on pg.XXI), including but not limited to the ISO12106:2017 standard (for metallic materials), the ISO/DS 22407 standard (for axial-plane bending fatigue), the ASTM E606/E606M standard (for strain-controlled axial fatigue), the ISO 1099 standard (for force-controlled axial fatigue), the ASTM E466 standard (for axial fatigue) and the ASTM E2207-15(2017) standard (for axial-torsional fatigue). However, these fatigue limits are usually reported for specific loading conditions (e.g., in-phase or irregular multiaxial loads) and, most often, only for uniaxial loading (e.g., axial, plane or rotative bending, and torsion) [1, 10, 12-16]. These uniaxial loads are illustrated in Figure 1-2 below.

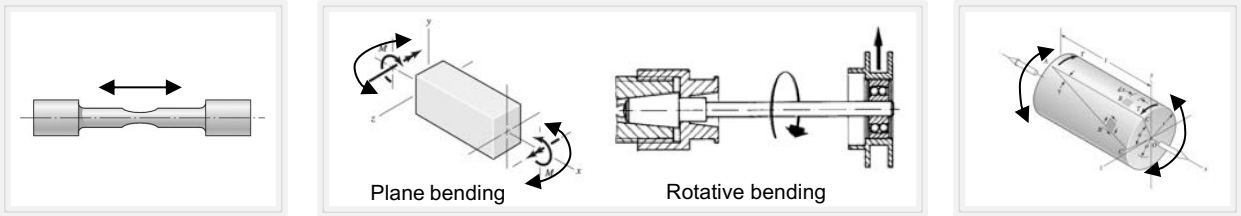


Figure 1-2: Fundamental uniaxial loading: (a) tension-compression (axial), (b) bending and (c) torsion [3, 17]

In many engineering applications, these uniaxial loads can occur independently (rarely in the pure uniaxial form) or as in-phase multiaxial combinations with each other [1]. Under these simpler loading conditions, the conventional fatigue failure theories permit a designer to predict the allowable stresses in a component with reasonable accuracy by using a known fatigue limit of the material. Fatigue failure theories like these typically include uniaxial or in-phase multiaxial fatigue criteria (e.g., Soderberg and Goodman) [3]. These criteria are often based on the Von Mises or Tresca static failure theories [18]. For the fatigue limits typically used with these criteria, new theoretical estimation methods that combine a material's experimental tensile and hardness properties have been recently proposed in the literature [16].

When the multiaxial fatigue load components are out-of-phase, and the material's fatigue limit under these loading conditions is unknown (as is often the case), estimating the allowable stress with an in-phase fatigue criterion becomes problematic. Cautious and conservative design assumptions are then required, and if incorrectly done, it can lead to non-optimal, costly, and over-designed components or even failure. These in-phase criteria are, therefore, not considered applicable for these types of loading. Under these complex fatigue loading conditions, using an appropriate out-of-phase multiaxial fatigue failure criterion from the literature is considered better for estimating the allowable stresses in a component.

However, these criteria themself have restricted fatigue failure prediction capabilities and do not apply to all materials, loading conditions and fatigue life regimes. The reported multiaxial fatigue data sets in the literature used to derive, test, and validate these criteria are also argued to be scarce, incorrect, and incomplete [14, 19]. It is also reflected in these data sets that simple material tensile and uniaxial fatigue strength properties are often not reported in full. These uniaxial fatigue properties are consistently used in formulating the criteria. These criteria, therefore, come under question due to the often-repeated use of these available (and old) fatigue data sets.

1.2 Research Problem

Dependable and accurate out-of-phase multiaxial fatigue failure criteria are required for performing complex modern-day high-cycle fatigue designs and analyses. In the existing research, several approaches and criteria exist to estimate the allowable fatigue stresses in a component. However, differences and inconsistencies exist between the various criteria and the fatigue strength or limit predictions they make for metals under out-of-phase multiaxial fatigue loading. These discrepancies remain unresolved due to the limited multiaxial fatigue data sets that are repeatedly used. Unreliable predictions or assessments and the eventual use of large safety factors can often result from this.

Very little data on multiaxial out-of-phase experimental fatigue testing exists in the literature. These data sets are considered incomplete, old and incorrect in the literature. They are often also reported for more specific and less applicable loading (e.g., uniaxial or in-phase multiaxial), which are inappropriate for use in specific real-world design scenarios. The data sets in the literature are also not reported with any experimental uncertainty, which casts doubt on their correctness, applicability and reliability for multiaxial fatigue criteria verifications and evaluations.

1.3 Research Questions

1.3.1 Main Research Question

The main research question is, can the multiaxial fatigue criteria in the literature be trusted based on the uniaxial and multiaxial fatigue data used to validate them that may be untrustworthy?

1.3.2 Secondary Research Questions

- Are the fatigue limit data sets from the literature comparable to the verified experimental fatigue limit test data?
- Are the fatigue limit strength evaluations of the multiaxial fatigue criteria with these data sets comparable with the presumed fatigue limits of the criteria?
- Are the presumed fatigue limits of the criteria comparable with verified experimental out-of-phase multiaxial fatigue limit estimates?

1.4 Research Objectives

1.4.1 Main Research Objective

The main objective is to generate new fatigue data and perform a complete evaluation for a single ferrous metal under uniaxial and out-of-phase biaxial loading and have enough data points to enable meaningful trends. The experimental and literature fatigue limit data will then be evaluated with the appropriate multiaxial fatigue failure criteria from the literature.

1.4.2 Secondary Research Objectives

The secondary objective is to make the required verification measurements and considerations for the different fatigue test loading conditions and stresses. The experimental fatigue test data will then be compared with the applicable literature data. The experimental fatigue test data and the literature data will then be used to evaluate and compare each criterion based on the fatigue limit and strength predictions.

1.5 Contribution of the research

This research study will contribute to the available ferrous metal uniaxial and multiaxial fatigue test data. It will also provide insight into the chosen multiaxial fatigue criteria when comparing experimental and predicted multiaxial fatigue strengths. The out-of-phase effect on the fatigue strength of ferrous metals may also become evident. The research will provide an understanding of the applicability of selected criteria to a particular material and loading condition in the high-cycle fatigue regime. The additional and verified experimental test data may contribute to more conclusive validations, testing, analyses and better understanding and implementation of the existing multiaxial fatigue criteria.

1.6 Scope of Study

The scope of study entails the following:

- A comprehensive literature review on multiaxial fatigue to obtain
    - the various multiaxial fatigue criteria proposed and studied in the literature
    - the fatigue data sets used to derive, test and verify these criteria and
    - the typical materials tested under multiaxial fatigue loading

with which a summary, categorisation, and appropriate selection from the above could be made for experimental and theoretical comparison purposes.

- Performing extensive experimental testing on a single ferrous metal to generate monotonic tensile, uniaxial, and biaxial fatigue measurements and data sets to compare with the literature data.
    - The relevant calibration, measurement and verification tasks will be done for these experimental tests to ensure correct and trustworthy data is obtained.
    - Uncertainty analyses will also be done on all experimental data.
- Performing fatigue criteria evaluations and comparisons using the experimental results to devise proper discussions and conclusions for the criteria and their multiaxial fatigue strength prediction and evaluation capability based on verified experimental test data results.

1.6.1 Study Limitations

For this research study, the following limitations are applicable:

- Only one multiaxial fatigue loading combination (bending-torsion) is considered.
- Only one out-of-phase loading angle is used for experimental multiaxial fatigue testing.
- No midrange or variable amplitude (VA) fatigue loading or effects are investigated, and only fully reversed loading is considered in this study.
- Only ferrous metal data is used from the literature.
- Only a single ferrous metal is experimentally tested.
- Only a selected number of tests are performed for each experimental test type due to time and stock material constraints.
- Only high-cycle and infinite fatigue life experimental tests are performed.
- No heat treatment, surface roughness and specimen geometry effects on material strength are investigated in this study.
- Only multiaxial fatigue failure criteria that apply to the loading condition in this study are considered from the literature for experimental and literature data evaluations.
- Only uniaxial and multiaxial fatigue data sets reported as valid and for the required loading and material type is used from the literature for comparison with experimental data.

1.7 Chapter Outline

Chapter 1 provided the appropriate background on the multiaxial fatigue studied in the literature. The research problem, questions and objectives were identified for this study after this. The research scope of study and limitations were also provided.

Chapter 2 elaborates on the relevant multiaxial fatigue literature concerning the fatigue loading conditions, materials and the uniaxial and multiaxial fatigue data that are generally considered during the study, verification and comparison of the existing fatigue failure criteria. The fatigue criteria and data sets applicable to this study are also identified from this literature. The chapter is concluded with the identified issues from the literature review.

Chapter 3 discusses the theoretical considerations for the applicable multiaxial loading condition. The fatigue criteria chosen for experimental data evaluations are further discussed, and their models are provided. A general theoretical overview of the critical plane approach taken by many fatigue criteria is also provided.

Chapter 4 outlines and discusses the experimental methodology for obtaining the required experimental material and fatigue strength data. The chapter also discusses the methods, equipment and considerations used to ensure valid test data was generated during experimental testing. These include the principal measurement system verifications, test bench loading verification, and characterisation measurements. The chapter is concluded with the provision of the data processing and fatigue criteria evaluation methodologies.

Chapter 5 provides the results and discussions of each experimental material and fatigue strength test performed in this study. For these results, the appropriate experimental uncertainties are also reported. The fatigue criteria evaluation results for the experimental and literature data sets are also provided and discussed for each criterion.

Chapter 6 ultimately provides the overview of this research study and the relevant experimental conclusions. The appropriate critique and recommendations are provided after that.

CHAPTER 2 – LITERATURE REVIEW

2.1 Introduction

Chapter one previously identified the need for dependable and accurate multiaxial fatigue failure criteria. However, the metal fatigue data sets that derive and test such fatigue criteria are considered insufficient and incomplete. This chapter discusses some of the typical challenges continuously revealed and discussed for multiaxial fatigue in the literature. The discussion revolves around the roleplaying factors considered during complex multiaxial fatigue loading, the criteria used for analyses and the data (or lack thereof) on which these criteria are based.

The typical weight reduction and lifespan improvement requirements for components in the industry demand new, more relevant and validated fatigue limit data to enable proper designs and analyses under various complex fatigue loading conditions [1]. Such loading conditions include the commonly occurring out-of-phase multiaxial loading condition. However, for new data to be valid, it is required that the testing procedures and failure criteria applicable to these loading conditions be very well understood. In an enquiry of 100 engineering companies (in 1999), it was found that 70 of them encountered considerable problems and uncertainties regarding long-life complex fatigue design [20]. More recently (in 2018), Lu *et al.* [4] argued that multiaxial fatigue damage is still a common engineering concern. They argue that the fatigue life associated with multiaxial fatigue loading is difficult to predict and assess since, unlike uniaxial fatigue, many more factors play a critical role. These factors include load proportionality (phase difference), principal stress rotation, cyclic hardening (or softening), and unseen fatigue crack initiation, propagation and direction changes [4, 5].

This chapter aims to provide insight and definitions of the loading conditions, criteria, materials and data reported in the multiaxial fatigue literature. Firstly, a general overview of the typical challenges and arguments associated with multiaxial fatigue is provided. This is followed by a discussion on the multiaxial fatigue loading conditions reported in the literature. The multiaxial fatigue criteria evaluated for these loading conditions are then discussed. The criteria are identified and discussed based on their applicability and relevance. After this, a short overview of the general fatigue criteria evaluation process and the typically required material data is provided. The materials and fatigue data sets reported in the relevant literature are then provided for both uniaxial and multiaxial loading conditions. A brief overview of the fatigue test benches used in the literature to generate these data sets follows. The chapter concludes with the identified issues and shortcomings from the literature review.

2.2 General Overview

Concerning the nature and inherent attributes of out-of-phase multiaxial loading, Papuga *et al.* [21] argue that it is not the phase difference that makes life predictions difficult. It is, however, the effect of the rotating principal stresses with respect to the component axes resulting from this phase difference between the loads. This argument is also agreed upon and reported on by others in the literature [4, 12, 19, 22-26]. This principal stress rotation phenomenon is typically illustrated using Mohr's circle theory and, for example, out-of-phase bending and torsion loading [27, 28]. Examples of this are later shown with the formal definitions used to classify the proportionality of multiaxial fatigue loading. Due to this principal stress rotation, the components of an arbitrary stress tensor at any point of the fatigue load cycle are not simple multiples of the same components at another point of the load cycle [21]. This phenomenon is argued to cause increased fatigue stress amplitudes on material planes with a particular orientation to the component axis of loading, decreasing fatigue life (especially of ductile metals) [12, 18, 23]. The increased stresses are attributed to a second phenomenon known as the additional cyclic hardening of the material, and its only evident in ferrous metals [23]. This cyclic hardening of the material is caused by metallic grain dislocations (known as slip behaviour) in the material microstructure due to the phase difference between multiaxial loading components [26, 29].

Luo *et al.* [19] state that this hardening effect of multiaxial fatigue loading on steels makes designing against fatigue difficult. They add that this effect should be better considered so crack initiation process modelling, accumulated fatigue damage assessment, and fatigue lifetime predictions could be adequately performed. Firat [30] proposed to do this by incorporating the material's yield strength in a fatigue criterion. Several other studies found that the cyclic hardening effect is only of genuine concern in the low-cycle fatigue (LCF) regime [12, 13, 19, 31, 32]. That is because material fatigue strengths in this regime show a more significant influence of the load non-proportionality (at typically higher stress levels) than in the high-cycle fatigue (HCF) regime (at typically lower than yield stress levels).

In formulating his HCF criterion, Papadopoulos [8] maintains the importance of considering the cyclic hardening of metal under out-of-phase loading. However, the phase difference effect (specifically for cyclic bending-torsion) on the HCF strength predictions of a hard metal (Swedish hard steel) was argued not to be of concern. The HCF strength of a hard metal is reported to be completely independent of the phase difference between bending and torsion according to the fatigue limit criteria of Papadopoulos, Galtier and Seguret, and Froustey and Lasserre (see [8, 33]) in the comparative studies of Pereira *et al.* [9] and Papadopoulos *et al.* [10]. Other criteria considered in the latter study predicted a pronounced effect of the phase difference on the HCF strength of hard metals. It is argued that this is incorrect under bending-torsion loading [8, 10].

Ambiguity, therefore, exists on the importance and influence of cyclic hardening (and phase difference) on the HCF strength of hard metals.

Mielke, in Morel [31], and Papadopoulos [34] reported the detrimental effect of the phase difference on the fatigue strength of AISI 4130 / 25CrMo4 steel (a hard metal) but under a biaxial axial loading condition. A marked influence of the phase difference between bending and torsion was shown to exist on the fatigue strengths of other metal types like ductile and brittle steels [10, 29]. Especially for ductile metals, a severe detrimental influence was reported on the experimental fatigue strengths tested under 90 [°] out-of-phase bending-torsion with a fully reversed stress amplitude ratio of 0.5 (shear/bending) [29]. McDiarmid [2] reported a 25 [%] fatigue limit reduction on ductile materials for this loading condition. His follow-up study showed that this is due to all material planes experiencing the same (and constant) amount of maximum shear stress during a loading cycle [35]. This constant maximum shear stress is argued to promote a greater statistical chance of fatigue crack (failure) initiation [36]. Therefore, this specific loading condition is deemed one of the most damaging out-of-phase multiaxial loading conditions [12]. It is therefore observed that only ductile metal fatigue strengths are influenced by out-of-phase loading (e.g., bending-torsion). For other biaxial load combinations (e.g., axial-axial), an effect of the phase difference on a hard metal's fatigue strength is, however, shown to exist. New methods for characterising the effect of a phase difference between loads are required since no well-accepted method currently exists [4]. For the fatigue criteria in the literature, disagreement exists on whether fatigue damage on a specifically oriented material plane is dictated by the combined effect of the normal and shear stress, the maximum shear stress or the maximum principal stress or if it is equivalent for all loading conditions [4].

The disagreements and arguments on cyclic hardening, phase difference and most damaging stress effects mentioned above are what many researchers have been studying over the years. As a result, many multiaxial fatigue criteria and life prediction methods have been proposed [5, 9, 10, 25, 37-40]. Between 1930 and 1950, some of the first in-phase and out-of-phase bending-torsion fatigue tests were conducted by Stanfield [41], Nishihara and Kawamoto [42] (mild and hard steel), Gough [43] (12 steel's) and Findley [44] (aluminium). Only later in the 1980s did several other researchers make their first fatigue test data contributions which include Zenner *et al.* [45], Froustey and Lasserre [14], and Lempp [45]. Whilst these multiaxial fatigue tests were conducted, several researchers also started to generate their fatigue criteria proposals, reviews and comparisons, with very little new data being further generated. These include the early in-phase criteria proposals of Gough [43], Stulen and Cummings [46], Marin [47], Crossland [10], Findley [48], Sines-Waisman [10], Smith-Watson-Topper [49] and McDiarmid [2]. These mainly were empirical-based criteria often deduced from static stress failure theories. These criteria were

later supplemented by the out-of-phase criteria proposals of McDiarmid [7, 35, 50], Kandil-Brown-Miller [4, 40], Socie [22], Dang Van and Papadopoulos [36], Fatemi and Socie [12], Fatemi and Kurath [13], and Papadopoulos [8, 20, 34, 51-53]. These out-of-phase criteria take a critical plane approach to fatigue strength or failure assessment. Other more recent criteria proposed include Morel [31], Gupta *et al.* [25], Yu *et al.* [54], and Lu *et al.* [4]. A more in-depth discussion on the multiaxial fatigue criteria and the reasons for excluding several of them is provided in Section 2.4.

With all the decades of research and effort on in-phase and out-of-phase multiaxial fatigue for metals, it is unclear (apart from the differences mentioned above) why no universally accepted and applicable criterion or method has been established [11, 19, 20, 40]. Additional studies with more precise and complete evaluations under multiaxial fatigue loading are still required [54]. Wang and Yao [40] also argue this requirement due to the specific applicability of the various available criteria to certain materials and loading conditions, even if multiple data sets are used during their testing and validation. The different approaches and formulations used for the existing criteria (e.g., critical plane, empirical, invariant and energy) also make it difficult to accept or standardise a single criterion, even if some show more promise than others.

Lu *et al.* [4] argued that the fatigue criteria proposed in the last century have specific drawbacks that require further investigation. Wang and Yao [40] maintain that too few critiques and analyses are done on multiaxial fatigue criteria, which prevents solving these differences due to insufficient data in the literature. They add that such studies rely heavily on good experimental multiaxial fatigue tests. Due to the time requirements, complexity and cost of such tests and equipment, very few (especially new) data sets are available [16, 55]. The lack of good data is also emphasised by Papuga *et al.* [21]. They argue that the available data sets are old, incomplete, and insufficient, and not enough materials are considered in testing. Many researchers use the widely referenced multiaxial fatigue data set of Nishihara and Kawamoto for their criterion formulations, testing and validation [2, 7, 8, 10, 20, 24, 29, 35, 36, 38, 44]. Papuga *et al.* [21] and Morettini *et al.* [56] boldly critique this data set and argue that it should be disregarded entirely due to experimental errors, incompleteness, and insufficient data points. Its usefulness in quantitatively investigating different phase angles (as in the data set) and the effect on a material's fatigue limit is also questioned. However, this data set was still included in the collection of multiaxial fatigue data due to its prevalence in the literature [56]. The data set of Lempp (for AISI 4140 / 42CrMo4 steel) reported by Zenner *et al.* [45] and Papadopoulos *et al.* [10] is also critiqued and argued to only be of use for comparing different loading combinations and not in quantifying a phase difference effect [21].

Yu *et al.* [54] also argue that multiaxial fatigue data on different materials are very scarce. This makes it challenging to attempt all-inclusive and methodical comparisons of the existing criteria

[40]. Also, to determine and set the relevant fatigue and material constants often associated with them [54]. Luo *et al.* [19] also support the notion of testing more materials because many of the criteria considered in their study show inconsistent fatigue life predictions for certain metals. They add that considering more fatigue data and materials during the derivation will allow researchers to generate more inclusive and accurate fatigue limit criteria. The correlation of fatigue limit results between literature sources is also troublesome since different definitions of fatigue failure, limits and specimen geometry are reported for the data sets. Such definitions, for example, include complete fracture or crack initiation, 10^6 or 10^7 cycles and solid or hollow specimen shapes. These definitions are not always explicitly communicated. It is also observed in the literature that the testing and measurement methods and equipment used to generate multiaxial fatigue data are not always reported. The ones that provide this information for the test data range from the very old [11-14, 22, 33, 43, 45] to somewhat recent test data articles [1, 39, 54, 55, 57, 58]. However, these data sources are repeatedly referenced and re-used throughout the literature. Uncertainties on experimental fatigue and material strength data in the literature are not reported, and possible data transcription and omission errors between respective sources are also observed. The following section discusses the loading conditions typically reported for multiaxial fatigue testing of metals in the literature.

2.3 Multiaxial Fatigue Loading

The less distinctive 'multiaxial fatigue' term is generally used to describe the type of fatigue loading, and it can refer to either biaxial (2 loads) or triaxial (3 loads) type loading. Triaxial loading conditions are rarely studied in the literature [34, 45]. This term is used in this form in most of the literature and will therefore be maintained. Unless stated otherwise, it specifically refers to 'biaxial' loading, as this is the fatigue loading type considered in this study. The phrase 'load condition' will serve as a collective term for the load combination (e.g., bending-torsion), the phase angle (β) and the nominal stress amplitude ratio (λ) under consideration. These loading condition elements are all discussed next.

Mechanical components mentioned in Section 1.1 can experience different forms of multiaxial fatigue loading. For many in-service components, multiaxial loading conditions can arise due to several uniaxial loads that work on a component. These include the fundamental axial, bending and torsion loads previously shown in Figure 1-2 on pg.3. Fatigue strength and limit testing of metals are customarily performed with these uniaxial loads and then often utilised during more complex loading condition analyses. Recently methods for estimating these uniaxial fatigue limits from the monotonic tensile and hardness data of a material have been proposed in the literature

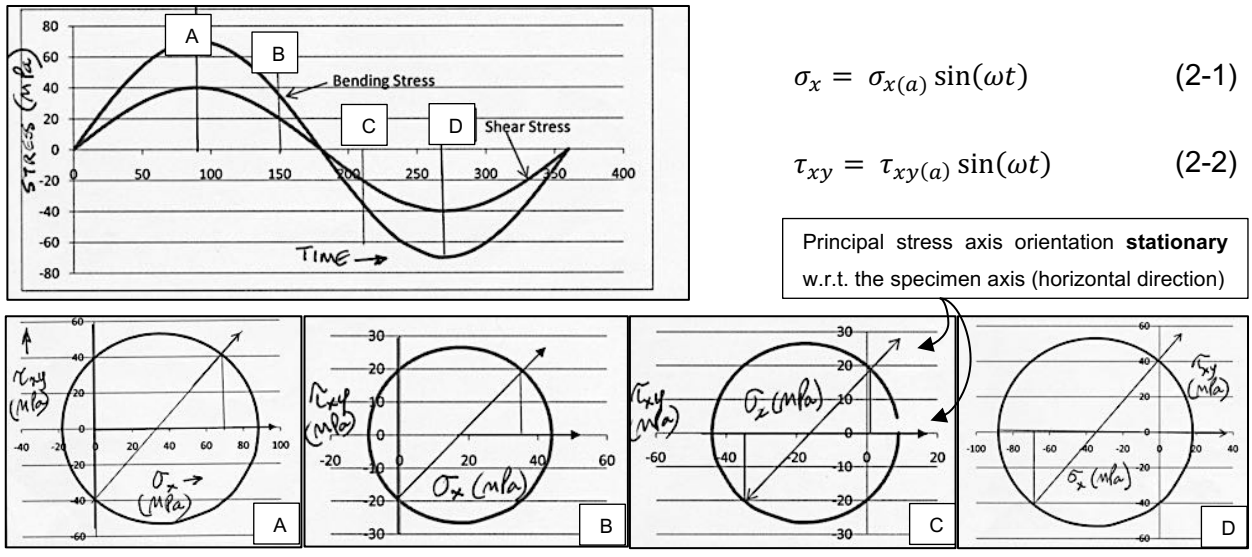
[16]. When these uniaxial loads occur in combination, they can be in-phase (proportionally) or out-of-phase (non-proportionally) with each other. These out-of-phase loading combinations do not receive as much attention in modern experimental fatigue test programmes due to the expense, complexity and time required, especially for HCF. The phase angle β between two cyclic load components can range from 0 to 180 [°]. The phase angles used for multiaxial fatigue testing of metals in the literature include 0, 30, 60 and 90 [°].

The formal definition(s) for the two types of loading proportionality used in the literature are provided below, along with two alternatively worded versions from different sources. These terms are equivalent to describing or distinguishing between in-phase and out-of-phase loading.

- **Proportional loading is –** any state of time-varying stress where the orientation of the principal stress axis does not change with respect to the component axis [1].
  Or *the multiaxial loading paths that result in a stationary principal stress axis or maximum shear stress axis* [26].
  Or *the principal stress directions remain fixed in time, and the principal stress ratio (σ_2 / σ_1) remains constant* [59].

- **Non-proportional loading is –** any state of time-varying stress where the orientation of the principal stress axis changes with respect to the component axis [1].
  Or the multiaxial loading paths that cause a local element's principal stress axis or maximum shear stress axis to rotate with time and with respect to a local coordinate system [26].
  Or *the principal stress directions rotate, and the principal stress ratio varies in time (-1 < σ_2 / σ_1<0)* [59].

Figure 2-1 and Figure 2-2 below illustrate these definitions graphically using Mohr stress circles.

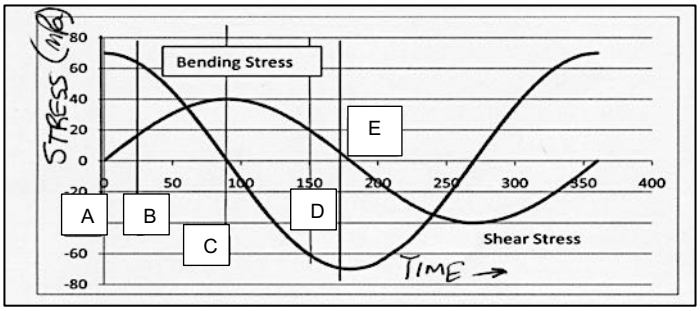


$$\sigma_x = \sigma_{x(a)} \sin(\omega t) \qquad (2\text{-}1)$$

$$\tau_{xy} = \tau_{xy(a)} \sin(\omega t) \qquad (2\text{-}2)$$

Figure 2-1: Proportional (in-phase) multiaxial loading – Mohr stress circle illustration [27]

These Mohr circles are for an arbitrary biaxial bending (σ_x [MPa]) and torsion (τ_{xy} [MPa]) loading condition. Equations (2-1) and (2-2) define the in-phase cyclic stresses, and Equations (2-3) and (2-4) define the 90 [°] out-of-phase cyclic stresses, respectively. The cyclic bending stress amplitude is denoted by $\sigma_{x(a)}$ and the shear stress amplitude by $\tau_{xy(a)}$.



$$\sigma_x = \sigma_{x(a)} \sin(\omega t - 90°) \qquad (2\text{-}3)$$

$$\tau_{xy} = \tau_{xy(a)} \sin(\omega t) \qquad (2\text{-}4)$$

Principal stress axis orientation **changing** w.r.t. the specimen axis (horizontal direction)

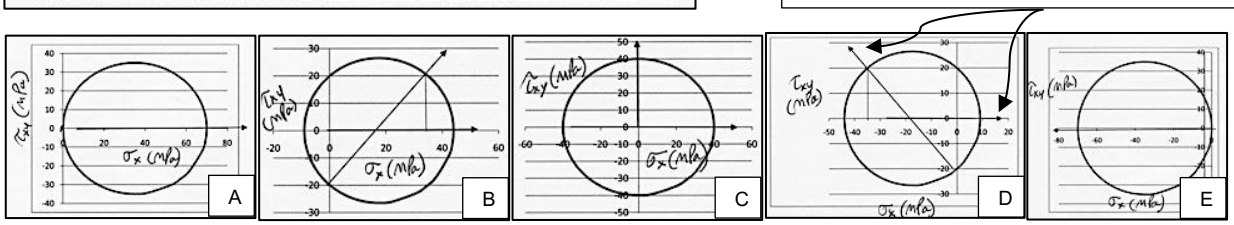
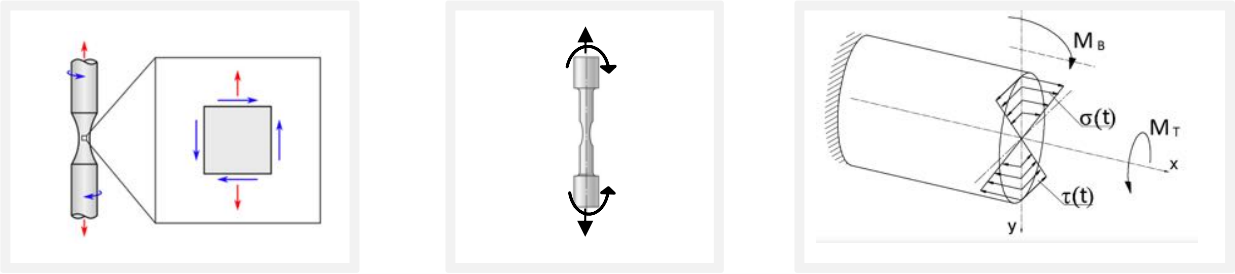


Figure 2-2: Non-proportional (out-of-phase) multiaxial loading – Mohr stress circle illustration [27]

Different combinations of multiaxial load components are also reported in the literature. The combinations most used in experimental fatigue testing of cylindrical specimens include axial-torsion, axial-bending, and bending-torsion. Figure 2-3 below shows schematic examples of these typical biaxial load combinations, of which the last (bending-torsion) is the one considered in this research study (see limitations in Section 1.6.1). For these biaxial load combinations, the two loads can be synchronous or asynchronous, sinusoidal or non-sinusoidal (blocked or triangular). The load components are also often considered with or without a midrange load. To this end, it has been reported that midrange tensile stress is detrimental, and midrange compressive stress benefits the fully reversed bending fatigue limit of a ferrous metal [23, 24, 38, 43]. For this, the bending load is either plane or rotative bending.

Interestingly, it has been reported that no significant influence of a midrange shear stress exists on the fully reversed torsion fatigue limit of a hard and ductile ferrous metal. That is, as long as the static yield shear strength (according to distortion energy DE theory, $S_{sy} = 0.577 S_y$) is not exceeded by the maximum shear stress ($\tau_{max} = \tau_a + \tau_m$) [24, 39, 43, 48]. This unique phenomenon under shear loading is well argued and supported in the literature. For a metal such as Aluminium, a severely detrimental effect of midrange fatigue stress exists under both bending

and torsion loading [44, 60]. However, these midrange fatigue stress effects on the fatigue limit of metal are not investigated in this study (see Section 1.6.1).



(a) (b) (c)

Figure 2-3: Schematic biaxial load combination illustrations for (a) axial-torsion [56], (b) axial-bending [3] and (c) bending-torsion [61] loading

Another loading factor that plays an essential role in multiaxial fatigue is the biaxial nominal stress amplitude ratio λ [-] given in Equation (2-5) below. This ratio indicates the difference in magnitude between the two constituting nominal stresses exerted on a component. The stress ratio R [-] in Equation (2-6) is mainly used to indicate if loading is fully reversed (also known as symmetrical loading, no midrange loads). This is often placed as a subscript on symbols (e.g., t_{-1}).

$$\lambda = \tau_a / \sigma_a \tag{2-5}$$

$$R = \text{maximum stress/minimum stress} \tag{2-6}$$

where: τ_a : is the cyclic shear stress amplitude (e.g., torsion) [MPa]

σ_a : is the cyclic normal stress amplitude (e.g., bending) [MPa]

Typical values reported for the stress amplitude ratio in the literature include 1.21, 1, 0.5 and 0.21 (e.g., for fully reversed biaxial bending-torsion loading) [7]. This ratio is varied (in large test programs) to test the effect of the biaxial stress amplitude intensity combinations on the multiaxial fatigue strength of a metal. The stress ratio R is reported as -1 (fully reversed) for most of the uniaxial fatigue and relevant biaxial fatigue data in the literature.

2.4 Multiaxial Fatigue Criteria

The previous section discussed the multiaxial fatigue loading conditions for which data is typically reported in the literature. This section discusses the multiaxial fatigue criteria reported, evaluated and tested in the literature for these bending-torsion loading conditions and data sets.

Due to the complexity of out-of-phase multiaxial fatigue and its effects, it is extensively revealed throughout the literature that there are no definitive and universally applicable multiaxial fatigue criteria or methods for fatigue life and failure analysis. Some criteria proposed during the last century and considered the most accurate are used in modern-day fatigue design activities. Occasionally more than one criterion is required to perform suitable yet still conservative fatigue life or failure assessments. These criteria do not always accommodate all the loading conditions, materials or fatigue regimes (HCF or LCF), which impedes proper fatigue analyses and designs [4, 21, 52]. The known multiaxial fatigue criteria have varying applicability and constraints and are discussed next in this section. Before this, the general classification of the different criteria types/methods, models/approaches, and scales of assessment reported in the literature is required. Fatigue criteria can, yet seldomly, belong to more than one sub-category. A schematic for these classifications is provided in Figure 2-4 below.

Fatigue criteria are generally classified into *three main types* [3, 9]:

- Stress-based or Stress-life criteria (typically for HCF and elastic stress conditions)
- Strain-based or Strain-life criteria (typically for LCF and plastic stress conditions)
- Energy-based or Linear-elastic fracture mechanics criteria (stress-strain criteria mainly used for fatigue crack initiation and growth studies)

Furthermore, they can be classified using one or more of the *four approaches* [9, 10, 31]:

- Critical plane approach (derived from critically stressed or strained material planes)
- Invariant approach (derived using stress or strain tensor deviatoric or hydrostatic values)
- Integral or energy approach (derived using average quantities in elementary material volume)
- Empirical equivalent approach (derived using quantitative experimental data)

Fatigue life estimation and analysis can also be explored on different scales [10]. However, this is rarely specified for criteria in the literature. These include the following:

- Macroscopic or continuous medium scale (e.g., used in engineering)
- Mesoscopic scale (intermediate and metallurgic grain aggregate level)
- Microscopic scale (e.g., used in physics)

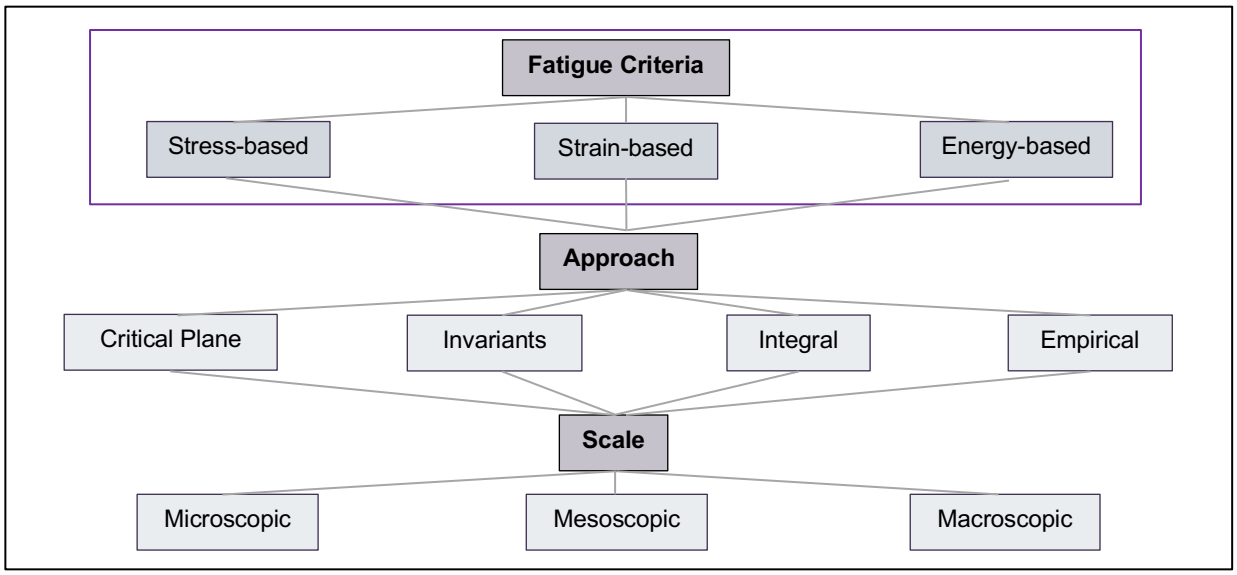


Figure 2-4: Schematic illustration of general multiaxial fatigue criteria classification

2.4.1 Reported Multiaxial Fatigue Criteria

Several multiaxial fatigue criteria are reported in the literature, where reviews and comparisons between criteria are performed. In total, 67 criteria were identified, and the most applicable to bending-torsion loading [5, 9, 10, 25, 37-40]. The literature articles that considered the most criteria (for both in and out-of-phase loading) include that of Beaver [37], Lasserre and Froustey [33], Socie [23], Papadopoulos *et al.* [10, 51], Carpinteri and Spagnoli [38], Davoli *et al.* [39], Wang and Yao [40], Gupta *et al.* [25], Santecchia *et al.* [5], Luo *et al.* [19] and Pereira *et al.* [9]. These criteria are summarised in Figure 2-5 below, under the above general classifications. A complete summary of all the criteria and models from the literature would be far too extensive to provide here. For compactness of the figure, the criteria are only identified by the primary author(s) and the year of the proposal. The reference numbers are only provided next to the stress-based criteria (sources of the criterion), with the reason in the discussion after Figure 2-5 below.

The earliest and most widely referenced multiaxial fatigue criteria were proposed by Gough [43], Stulen and Cummings [46], Marin [47], Findley [48], Crossland [10], Sines-Waisman [10], Smith-Watson-Topper [49] and McDiarmid [2]. The well-known Crossland and Sines-Waisman criteria are stress-invariant based in-phase models that are deemed easy to implement and have been widely used for engineering design [5]. Most of the above are empirical and in-phase criteria based on the conventional static failure theories (e.g., Rankine, Von Mises and Tresca) consisting of nominal or local stresses and strains [18]. The Smith-Watson-Topper and McDiarmid criteria were strain-invariant and critical plane-based criteria, respectively. The out-of-phase and critical

plane-based criteria proposals of McDiarmid [7, 35, 50], Kandil-Brown-Miller [4, 40], Socie [22], Dang Van and Papadopoulos [36], Fatemi and Socie [12], Fatemi and Kurath [13], and Papadopoulos [8, 20, 34, 51-53] were generated soon after the above in-phase models. Some of the most recent strain and energy-based criteria proposals include those of Morel [31] (in-phase bending-torsion loading), Gupta *et al.* [25] (for axial-torsion loading), and Yu *et al.* [54] and Lu *et al.* [4] (for out-of-phase bending-torsion loading).

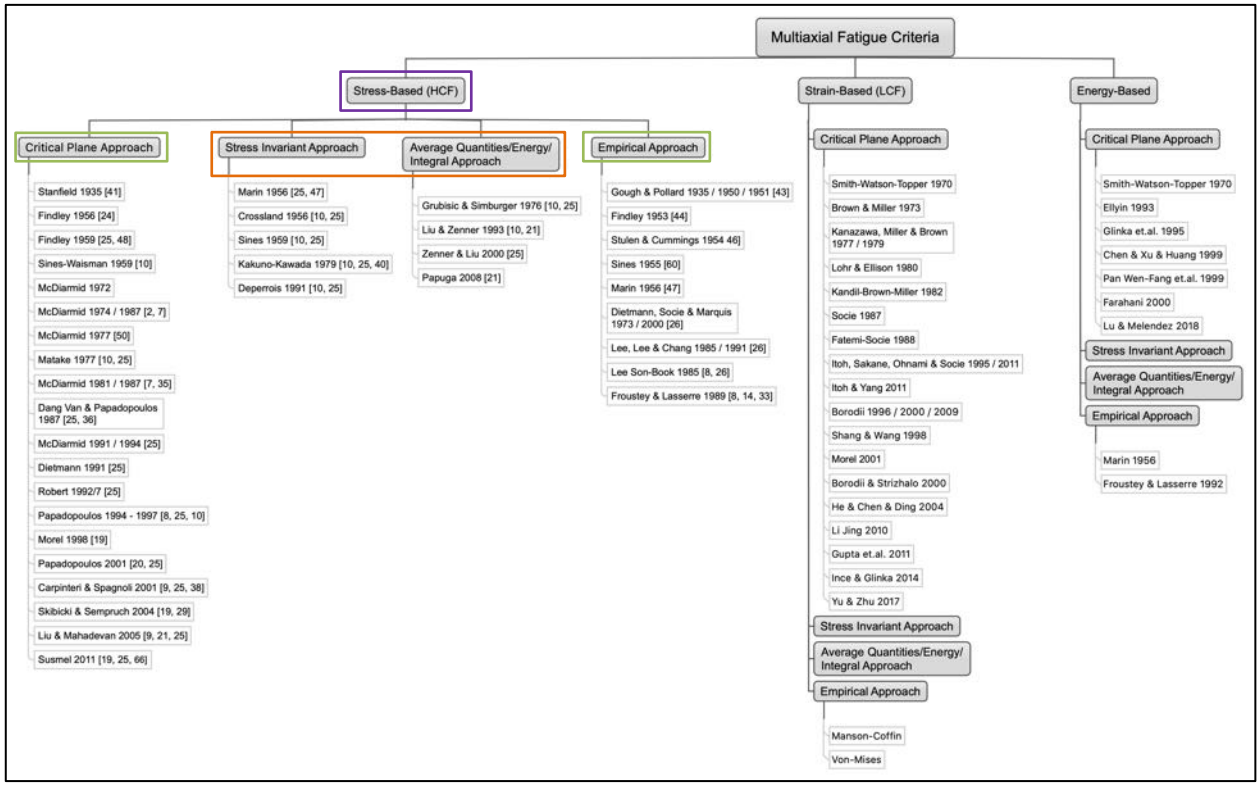


Figure 2-5: Summary of reported multiaxial fatigue criteria in the literature

As seen from the summarised fatigue criteria in Figure 2-5 above, the stress-based criteria are the most prevalent in the literature. They are reported to have better applicability and capability, especially in the HCF regime (most considered) [1, 9, 20]. This is due to the assumptions that stresses are relatively low and that primarily elastic material behaviour is observed in this fatigue regime (10^5 – 10^8 cycles) [1, 5, 25, 60, 62]. The LCF regime is much less considered in the literature on multiaxial fatigue. Therefore, the strain-based and energy-based LCF criteria are not considered and are only provided for completeness.

The stress-based criteria take different approaches to evaluate the fatigue stress condition under multiaxial loading. It can be seen from Figure 2-5 that most of the criteria either take a critical plane or an empirical approach. The empirical fatigue criteria are regarded as very useful and easy to use in conventional and simple mechanical designs and are suitable for most general

metals. These criteria are some of the oldest and most referenced in the literature. They are also primarily derived for and from in-phase multiaxial loading corresponding to the dominant loading condition tested during that time. Therefore, these criteria are argued to have limited applicability in multiaxial fatigue design because they can only be applied to similar loading conditions [8]. This inherently limits most of them from applying to out-of-phase loading conditions since they overestimate the fatigue limit [18]. However, some reported empirical fatigue criteria allow for use under out-of-phase loading or are derived as out-of-phase models. These include the in-phase criterion of Stulen and Cummings [46] and the out-of-phase criteria of Lee Son-Book [20] and Froustey and Lasserre [14].

The critical plane fatigue criteria (as referred to in the literature) also comprise some of the oldest criteria (e.g., the Stanfield and Findley criteria). These criteria were proposed soon after out-of-phase fatigue loading and its effects on metal components became a recurring phenomenon. Some of the most classical critical plane criteria were proposed by Matake and Dang Van [10]. As seen from Figure 2-5, the critical plane criteria represent most of the stress-based criteria in the relevant literature. These criteria are generally considered to have better capability and utility under multiaxial and especially out-of-phase fatigue loading conditions. Many of these criteria consider the unique material state under fatigue by utilising the material and uniaxial fatigue strength properties as inputs in their models [4].

Not all the critical plane criteria are, however, easily implemented. This is due to the calculation of the critical plane of failure assessment and often of unknown criterion coefficients (usually determined from additional experimental tests). These criteria are also more specific with the material types they apply. This is mainly due to the use mentioned above of uniaxial fatigue strength properties in the criteria. Some of the criteria are reported only to apply to ductile metals (e.g., Lee Son-Book in [20, 26] and McDiarmid [35]) and others to hard metals (e.g., Papadopoulos [8, 10]). Other critical plane criteria apply to both these metal types or just polycrystalline steels in general (e.g., Matake in [10], Morel [19, 63], Carpinteri and Spagnoli [38], Stulen and Cummings [46] and Froustey and Lasserre [14]). Different definitions or classifications identify a material as ductile or hard. For many of these criteria, the suitable material type is therefore specified differently or not at all. However, all the above criteria are generally derived explicitly for or reported applicable to bending-torsion loading.

The stress-based fatigue criteria that take an invariant or energy approach to fatigue life or failure assessment are mainly formulated and tested on in-phase multiaxial loading data (e.g., Crossland and Sines-Waisman). Those reported applicable to out-of-phase loading conditions (e.g., Kakuno-Kawada) are scarce, and the required stress values for their evaluation are not as easily measured or experimentally obtained. These criteria are, however, regarded as very easy to use

[5]. However, they have less diverse material applicability (if at all specified) and do not receive as much attention in the relevant literature as empirical or critical plane criteria do. This is clearly illustrated by the lower number of these criteria in Figure 2-5 (orange square). They also often require numerous material parameters or equation constants from additional experimental tests and curve fittings for evaluation.

2.4.2 Considered Multiaxial Fatigue Criteria

As previously identified in the limitations of this study (see Section 1.6.1), only HCF and infinite fatigue life experimental testing will be performed. Inherently this limits the applicable fatigue criteria to the stress-based HCF criteria (purple square in Figure 2-5). Based on the previous discussion, the criteria taking a critical plane and empirical approach (green squares in Figure 2-5) are argued to have applicability for the relevant bending-torsion fatigue loading conditions. Of the total 67 multiaxial fatigue criteria identified in the preceding part, only 32 stress-based criteria are appropriate. With this study's experimental fatigue loading condition being limited to out-of-phase loading, it further eliminated 20 of these criteria. This elimination is either because it was explicitly reported that a criterion only applies to in-phase loading or was not specified at all. Others are eliminated due to their complexity and lack of criterion description in the literature. The remaining 12 criteria (9 critical plane and 3 empirical) that are considered for this study are provided in Table 2-1 below.

Table 2-1: Considered stress-based out-of-phase multiaxial fatigue criteria

Criterion		Year	References
Critical Plane Criteria	Matake	1977	[10, 21, 38, 40]
	McDiarmid	1981	[7, 35, 36, 50]
	DangVan and Papadopoulos	1987	[10, 36]
	Papadopoulos	1994/1997	[4, 8, 9, 10, 21, 25]
	Morel	1998	[19]
	Papadopoulos	2001	[4, 20, 40]
	Carpinteri and Spagnoli	2001	[4, 9, 19, 38, 40]
	Skibicki and Sempruch	2004	[19, 29]
	Liu and Mahadevan	2005	[4, 9, 21]
Emprical Criteria	Stulen and Cummings	1954	[2, 23, 46, 48]
	Lee Son-Book	1985	[8, 16, 19, 20, 26]
	Froustey and Lasserre	1989	[8, 10, 14, 33]

The Morel, Stulen and Cummings, and the Froustey and Lasserre criteria in Table 2-1 are the only ones that are not tested or evaluated in the literature using the Nishihara and Kawamoto bending-torsion fatigue data set that is argued to be insufficient [21, 56].

The Matake criterion is referred to as one of the first and most classical critical plane criteria [10]. It is reported that this criterion appropriately predicts the distinct uniaxial torsion fatigue limit and its independence of a midrange shear stress. It also correctly predicts the dependence and the influence of a midrange bending stress on the uniaxial bending fatigue limit [10]. For this criterion, the critical plane is defined as the plane on which the shear stress amplitude reaches a maximum. It also had a mean fatigue failure prediction error closest to Papadopoulos' 1994/1997 criterion on various hard metals under 90 [°] out-of-phase bending-torsion loading [10]. However, though this criterion has promising capability, it is still very unclear in the reported literature how the critical plane and resolved shear stresses are determined and then evaluated in the criterion.

McDiarmid's criterion is reported to apply to any phase angle between bending and torsion. This is after his in-phase model was extended to apply to out-of-phase bending-torsion loading [2, 35, 50]. This criterion applies to only ductile metals classified according to the fully reversed bending f_{-1} and torsion t_{-1} fatigue limit ratio range of $1 < f_{-1}/t_{-1} < 2$. The criterion also correctly considers the normal (bending) and shear (torsion) stress on the critical plane since it adheres to the general stress summation rule at points in a load cycle [29]. The critical plane is defined for this criterion as the plane on which the shear stress amplitude reaches a maximum. The maximum shear stress amplitude point on this plane is where the corresponding normal stress is obtained to evaluate the criterion. The critical plane is not explicitly determined or required since the criterion is expressed in terms of the macro (applied) nominal stresses. This criterion is regarded as easy to implement on biaxial data. However, ambiguity exists on which shear stresses are referred to (lacking explanation) and which should be used in its evaluation. It is also warned that this criterion can overestimate a ductile metal's out-of-phase bending-torsion fatigue limit if the loading's correct, true shear stress (on the critical plane) is not used [35].

The Dang Van and Papadopoulos criterion is considered one of the first critical plane fatigue criteria. It is based on a microscopic shake-down stress cycle that presented slightly better predictions than McDiarmid's criterion [10, 36]. This criterion is evaluated with microscopic stress quantities that are not as clearly provided or discussed, and elaboration on the critical plane determination is also not provided. The criterion is reported to have significant prediction errors specifically for the relevant out-of-phase bending-torsion loading condition [36].

Papadopoulos's 1994/1997 critical plane criterion is an ellipse arc equation. This fatigue failure criterion of Papadopoulos could be derived from the Crossland ellipse arc criterion (in-phase

tension-torsion) [8, 10]. However, under out-of-phase bending-torsion loading [24]. It has been shown to closely resemble Gough's ellipse arc equation (derived for hard/brittle metals under in-phase bending-torsion) [43]. This criterion is reported to apply only to out-of-phase bending-torsion and hard metals classified within the range of $1.2 \leq f_{-1}/t_{-1} \leq 1.732$ (smaller than McDiarmid's ductile metal classification above). The criterion is written in terms of the applied macroscopic (nominal) stresses, whilst its derivation was done on the mesoscopic scale considering microscopic stresses and their interaction and behaviour on the critical plane. The determination of the critical plane itself is not required to apply the criterion. This criterion is argued to be independent of the phase difference between bending-torsion loading on a hard metal [8, 10]. Application of the criterion is easy, and no additional material constants or parameters are required to solve its model.

Morel's criterion is reported as a 'life prediction model' based on the Papadopoulos 1994/1997 criterion and the methods he used to calculate the resolved shear stresses on the critical plane. The criterion has three unknown material constants that must be obtained experimentally before application. The Papadopoulos 2001 criterion is also reported as a 'life prediction model' but for ferritic steels only (containing less than 0.1 [%] Carbon, e.g., stainless steels). It is considered easier to apply than Morel's criterion [5, 20, 40]. These criteria are fatigue life prediction methods and not fatigue failure models. Therefore, they are not used for this study due to the interest in obtaining fatigue limit strength predictions rather than life counts.

The Carpinteri and Spagnoli and the Lee Son-Book criteria are both reported as an adaptation of the Gough ellipse quadrant equation (for ductile materials and in-phase loading) to apply to out-of-phase loading. These criteria are also mentioned and studied by many others [5, 8, 9, 19, 38, 40]. Carpinteri and Spagnoli's criterion applies to mild and hard steels but primarily to hard metals in general [5]. The critical plane is determined empirically for this and the Liu and Mahadevan criterion [9]. The Carpinteri and Spagnoli criterion is reported to have less predictive capability than Papadopoulos's 1994/1997 criterion [9]. Liu and Mahadevan's criterion is reported to have a slightly more conservative predictive capability than Carpinteri and Spagnoli's criterion under fully reversed loading [9]. The Liu and Mahadevan criterion only applies to hard metals under both in-phase or out-of-phase bending-torsion [5]. These two criteria (excluding Lee Son-Book discussed below) have relatively long but easy-to-apply solution methods.

Skibicki and Sempruch proposed an adaptation of McDiarmid's [2] earliest in-phase criterion by incorporating a so-called 'load non-proportionality parameter' to the criterion so that it could be applied for out-of-phase bending-torsion loading. This adaptation was proposed to predict especially better the 90 [°] out-of-phase and λ = 0.5 bending-torsion fatigue limits of metals which are often incorrectly predicted by fatigue criteria. The applicability of the adapted criterion to hard

or ductile metals is unspecified. The quantities used in this parameter are not as clearly described or easily calculated.

Stulen and Cummings' empirical criterion is one of the oldest multiaxial empirical-based criteria initially derived as an in-phase model using Gough and Findley's data on steels and Aluminium. However, it applies to out-of-phase bending-torsion loading [43, 44, 46]. However, this criterion has some unclearly defined parameters and linearly combined stresses, and the application method is not clearly reported.

The Lee Son-Book empirical criterion is reported to have applicability to various metals under fully reversed out-of-phase bending-torsion. However, many unknown parameters are required for applying the criterion to fatigue limit data.

Lastly, there is the Froustey and Lasserre empirical criterion that is reported to have applicability to both ductile and hard metals for which f_{-1}/t_{-1} > 1.732 (harder than what Papadopoulos applies to). It applies to in-phase or out-of-phase bending-torsion [8, 10]. This criterion also has a claimed independence of the phase angle between bending and torsion (like Papadopoulos) on a hard metal; however, no theoretical justification could be reported in the original criterion article [14]. The above ratio is often smaller than 1.732 for the metals to which other criteria above are considered applicable (like the Zenner *et al.* [45] AISI 4140 alloy steel).

In the following part of this section, the typical evaluation process is discussed for the criteria in Table 2-1 above. It also identifies what test data is typically required for these criteria evaluations.

2.4.3 Fatigue Criteria Evaluation

Multiaxial fatigue criteria evaluations typically require multiple material and fatigue strength data to allow for their evaluation. The diagram in Figure 2-6 below outlines the general process and the material properties often required to perform these evaluations. The diagram is in no way a whole procedure for evaluating multiaxial fatigue criteria.

The monotonic tensile properties of metals are often reported supplementary to the fatigue limit data. They typically include Young's Modulus of Elasticity E, the ultimate tensile strength S_{ut} and the yield strength S_y. These material tensile strength properties are not usually required for the evaluations of stress-based (HCF) multiaxial fatigue criteria. They are, however, often used in strain- and energy-based LCF criteria evaluations (not considered). It is regarded as good practice to report these tensile properties as they can be used to normalize fatigue limit data and differentiate between different materials when compared.

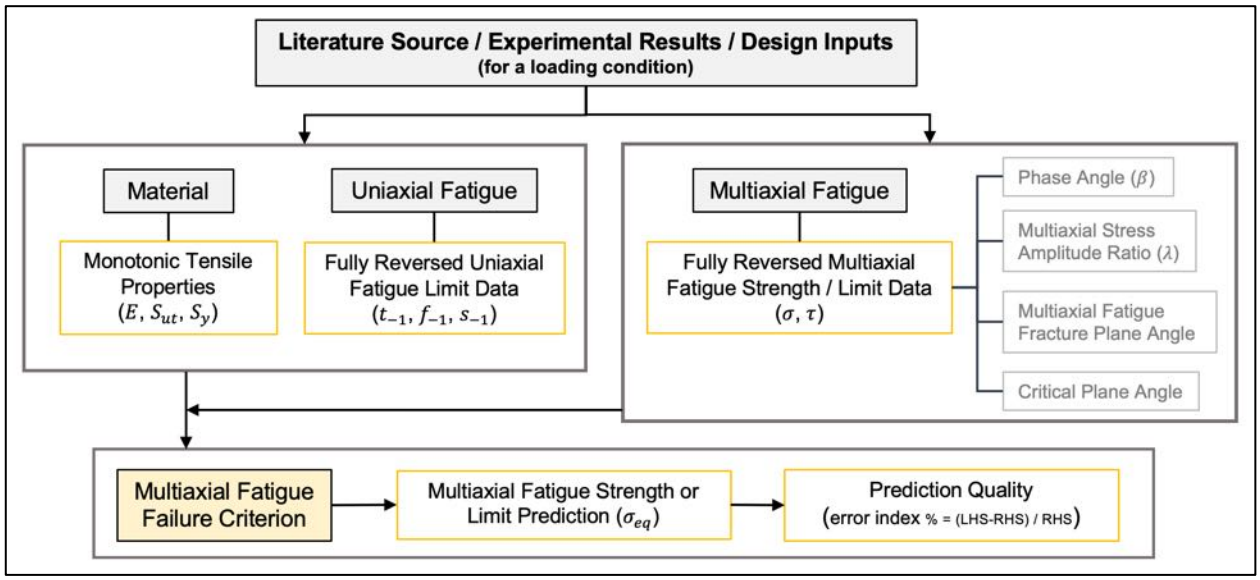


Figure 2-6: Generalised multiaxial fatigue failure criteria evaluation process and inputs

Stress-based criteria (especially critical plane criteria) are often formulated with a material's fully reversed uniaxial torsion t_{-1}, bending f_{-1} or axial s_{-1} fatigue limits as part of their models. The criteria, therefore, require these fatigue limits as inputs to allow assessment of the model that predicts the fatigue limit or strength of a metal at a specific multiaxial stress state. Many fatigue failure criteria also use these uniaxial fatigue limits as the multiaxial fatigue limit for failure. In this way, material specificity and applicability are inherently incorporated into the criteria and thus limit the materials for which they are valid. Unreported tensile and uniaxial fatigue properties, therefore, hinder the prediction and evaluation of a metal's multiaxial fatigue strength or limit under a specific loading condition using a criterion from the literature. The simple tensile and uniaxial fatigue strength properties (left top block in Figure 2-6 above) and the various metals reported in the literature are discussed in Section 2.5 hereafter.

Multiaxial fatigue criteria evaluations inherently require the relevant multiaxial fatigue stresses (σ and τ) in a component under in or out-of-phase (β) bending-torsion loading (λ) as inputs for a fatigue limit assessment. The multiaxial fatigue limit data sets (right top block in Figure 2-6) that are reported for the relevant metals and loading conditions in the literature are discussed in Section 2.6. After this, a brief overview of the experimental test equipment typically used to generate these data sets in the literature is also provided in Section 2.7.

A criterion's fatigue strength or limit prediction quality (bottom block in Figure 2-6) is often quantified by an 'error-index' value (later defined in Section 3.3). Fatigue criteria models in the literature are often an inequality that has to be satisfied. The error-index value is used to demonstrate the percentage difference between the predicted 'left-hand side' equivalent

multiaxial stress condition (σ_{eq}) and the presumed 'right-hand side' multiaxial fatigue limit of a criterion. The relevant fatigue criteria were discussed in the previous parts of this section. To summarise the above, the following data is therefore typically required (for ductile and hard metals) to allow evaluation and comparison of any of the fatigue criteria in Table 2-1:

- Monotonic tensile strength data (E, S_{ut} and S_y)
- Fully reversed uniaxial fatigue limit data (t_{-1}, f_{-1} and s_{-1}), and ultimately
- Data on in or out-of-phase bending-torsion fatigue limit tests (σ and τ)

2.5 Materials Data

Section 2.4 discussed the multiaxial fatigue criteria considered for this research study, and the typically required data for their evaluation were identified. This section discusses the materials and monotonic tensile and uniaxial fatigue limit data reported in the literature with the multiaxial fatigue data sets and criteria.

The metals most commonly used for multiaxial fatigue testing in the literature (mainly on out-of-phase bending-torsion loading) are provided in Table 2-2 to follow. These metals range from low carbon to high alloy special and stainless steel. Non-ferrous metals like Aluminium and superalloys like Inconel are also reported in the literature. These metals are known not to have inherently clear or definite fatigue limits when tested for fatigue (e.g., Aluminium). The fatigue limit during their testing is often defined at 10^8 cycles, and multiple experimental tests are performed [44]. These non-ferrous metals are only included in Table 2-2 for completeness and to reflect their occasional use (as relevant ductile or hard metals) in the literature and criteria.

For the above metals, the monotonic tensile and uniaxial fatigue limit properties are often reported (as in Table 2-2) supplementary to the multiaxial fatigue test data (Section 2.6 hereafter). For Table 2-2, some additional uniaxial fatigue data sets, applicable to similar materials and loading, were identified from Li *et al.* [16], Ogawa *et al.* [64] and Lee [65] in [20]. These basic material strength properties are often only reported according to their necessity for the relevant fatigue criteria in a study. To this end, the properties are not always reported in full or referenced from a primary source. Sometimes a material and its properties are reported from the same primary source but with different values in the respective secondary studies that consider it. Data transcription errors or omissions can occur with this cross-reporting of the basic strength properties (and the accompanying multiaxial fatigue data) between criteria review and assessment studies [56]. For example, a 2 and 40 [%] difference was observed between the

fatigue limit and material ultimate tensile strength values reported for AISI4330V between [10] and [66], both supposedly from [14].

The difference between cross-reported values for materials is occasionally elucidated by the different material designations or descriptions in the sources that consider it (e.g., AISI 1045 and 1040). These designations vary significantly in the literature and are not always clearly stated. It is often left to the reader to deduce from the data sets. This makes it challenging to identify or confirm the use of materials and their properties between different sources. The utility of the reported values and materials in multiaxial fatigue criteria evaluations then becomes questionable. Material conditions (e.g., heat treatment, hot rolled or cold rolled) are also rarely specified for the relevant data sets in the literature. These conditions are occasionally fully specified for a test material [11-13, 23, 42, 43, 57, 64, 66]. Alternatively, it is provided implicitly through the material designation (with postfix numbering and lettering) as generally done for Aluminium alloys like 24S-T3 [49], 6061-T6 [40, 60] and 6082-T6 [67].

For the materials provided in Table 2-2, identification is primarily made according to their American Iron and Steel Institute (AISI) designation. Other standards and alternative designations reported in the literature are also provided, and where possible additional designations (e.g., BSI/EN and DIN) were identified for each material type. It should be noted that the materials in Table 2-2 are not always reported with an AISI designation. Most of them are reported with the designations provided in columns four and five of the table. All the relevant abbreviations are defined in the Abbreviations list on pg. XXI and in the notes at the end of Table 2-2. These material designations are provided in the table's first five columns. The source(s) where a material was used or tested are listed in the rows below the designations. Column six provides the source(s) from which the corresponding material's monotonic tensile and uniaxial fatigue strength properties are reported. These material properties are given in columns seven through twelve. The monotonic tensile property (E, S_{ut}, S_y) and the uniaxial fatigue limit (t_{-1}, f_{-1}, s_{-1}) symbols were previously defined below Figure 2-6. Note that axial fatigue limit s_{-1} data is included in Table 2-2 (where reported) as a reference for the corresponding or unreported bending fatigue limit data f_{-1} of a material.

The AISI number subscript next to a source number in column six is used to distinguish between the similar material types that were grouped in the table. This grouping was done due to the similar and different material identifications or property values reported between respective sources. The † symbol indicates that the source next to it is the original (primary) source and that data was obtained from it (if found) or from a secondary article explicitly referencing the primary article for the data. The Li *et al.* [16] data set is reported in the literature with multiple uniaxial axial fatigue limit values and materials from three different sources. These materials have the same (or

similar) AISI designations and are too many to include in Table 2-2. For this data set's entries in the table, the ‡ symbol is only used to indicate that the corresponding material (subscript next to reference) is considered, with it the tensile and uniaxial axial fatigue data. The axial fatigue limits in the [16] data set are later wholly illustrated in Figure 2-7 and Figure 2-8.

Despite it being reported that not enough materials are considered for multiaxial fatigue testing in the literature, it is seen in Table 2-2 that a good variety of general and special engineering metals (especially steels) have been previously tested [19, 54]. However, for these metals and the reported data, the following problems are identified from Table 2-2 and the literature:

- Inconsistent and often incomplete material designation standards and descriptions are used.
- Generally, a lack of reported material tensile and uniaxial fatigue limit data is observed.
- Of these, specific key values required for criteria evaluations are also unreported.
- The repeated use of some data sources and the differences between reported values is also observed, and some values are reported as two different properties.

Table 2-2: Metals and simple material strength properties reported in the literature

Standard Designation					Values from ref.	Monotonic Tensile Properties			Uniaxial Fatigue Properties		
AISI & SAE	**BSI & EN**	**DIN** (Werkstoff)	**Other**			E [GPa]	S_{ut} [MPa]	S_y [MPa]	t_{-1} [MPa]	f_{-1} [MPa]	s_{-1} [MPa]
1010 **(12)**	BS 045M10	1.0301	-	LCS	[41] †$_{1010}$	-	-	-	137.9	241.33	-
Used in ref.: [41, 43] †,					[43] †$_{1012}$	204.2	384.7	228.9	132.4	234.4	-
1015 **(16/17/ 18)**	BS 080M15	1.0401	-	LCS	[49]$_{1015}$	207	415	228	-	-	-
					[33] in [56]$_{1018}$	210	520	350	179	310	273
Used in ref.: [43, 49, 66], and [33] in [56]					[66]$_{1018}$	-	520	-	186	332	-
1020 **(22/25)**	BS 070M20 EN 3(A)	1.0402	-	LCS	[16] ‡$_{1020}$	207	502.2	294.9	-	-	194.3
Used in ref.: [16, 24]					[16] ‡$_{1025}$	207	547	306	-	-	197.8
-	-	-	-	**MS** (LCS)	[7, 20, 35, 36]	-	-	-	137 / 137.3	230 / 235.4	-
					[66]	-	375	-	137.3	235.4	-
Used in ref.: [7, 9, 20, 29, 35, 40, 66, 68] from [42] †					[9, 38, 40]	-	518.8	-	137.3	235.4	-
1035 **(38)**	EN 5	1.0516	-	MCS	[66]$_{1035}$	-	559	-	142	216	-
Used in ref.: [19, 24, 66]					-	-	-	-	-	-	-
1045 **(40/43)**	BS 080M40 EN 8	1.0503	-	MCS	[43] †$_{1040}$	212.7	579.2	322.7	186.2	286.8	-
					[12, 13]$_{1045}$	204	-	380	-	-	-
					[34]$_{1045}$	-	-	-	287	-	423
					[65] in [20]$_{1045}$	-	-	-	311	442	-

AISI & SAE	BSI & EN	DIN	Other		Values from ref.	E	S_{ut}	S_y	t_{-1}	f_{-1}	s_{-1}
					[30]$_{1045}$	202	-	200	-	-	-
					[19]$_{1045}$	202	-	382	175	303	-
					[16] ‡$_{1045}$	207	752	517	-	-	291.1
Used in ref.: [4, 12, 13, 16, 19-23, 30, 34, 40, 43, 49, 65, 68]					[21]$_{1045}$	-	850	-	286.2	-	419.6
1090	BS C92D	1.0618	-	HCS (HS)	[43] †	207.8	757.1	-	224.8	517.1	-
Used in ref.: [43] †					-	-	-	-	-	-	-
-	-	-	-	SHS (982FA) (**HS**)	[7, 8, 10, 24, 35, 36]	-	680	-	196.2	313.9 / 314	-
					[38, 40]	-	704.1	-	196.2	313.9	-
					[66]	-	680	-	196.2	313.9	-
					[9]	-	708.1 / 608	-	196.2	313.9	-
Used in ref.: [7-10, 15, 29, 35, 36, 40, 66] from [42] †					[42] † in [56]	215	681.1	401.3	196.1	313.8	-
5132	BS 530A32 EN 18B	1.7033	34Cr4	CAS (HS)	[45] †	-	710 / 795 / 858	550 / 657 / 700	204 / 256 / 259	410 / 415	343
					[9, 10, 24]	-	795	-	256	410	-
					[66]	-	795 / 710	-	256 / 204	410	343
Used in ref.: [16, 31], and [8-10, 15, 24, 45, 66] from [45] †, and [14, 69, 70] in [56]					[14, 69, 70] in [56]	218 / 192	-	657 / 550 / 700	256 / 204	-	410 / 343 / 415
4130	BS 708A30 EN 16	1.7218	25CrMo4 (25CD4)	CMAS (HS)	[33, 45]	-	-	660	228	361	-
					[34]	-	-	-	228	-	361
					[66]	-	-	-	228	340 / 361	-
Used in ref.: [16, 31, 33, 34, 45, 52, 66], and [71, 72] in [56]					[71, 72] in [56]	220 / 217	-	660 / 672	228	-	361 / 340
4140 **(42)**	BS 709M40 EN 19	1.7225	42CrMo4	CMAS (HS)	[45] †$_{4140}$	-	1025	888	260	398	-
					[10, 40]	-	1025	-	260	398	-
					[66]	-	996	-	336.3	525.7	-
					[6]	-	800	700	-	-	-
					[16] ‡$_{4140}$	207	1042.9	928.9	-	-	437.4
Used in ref: [6, 16, 31, 66], and [1, 9, 10, 39, 40, 66] from [45] †					[9]	-	1025	-	260	398	-
-	EN 39NiCrMo3	1.6510	**39NiCrMo3**	NCMAS (HS)	[39]	206	856	625	-	-	-
					[57]	-	-	-	265	-	367.5
Used in ref: [39, 57, 66]					[66]	-	856	-	265	-	367.5
4340 **(20)**	BS 816M40 EN 24	1.6582	34CrNiMo6	NCMAS (HS)	[43] †	206.4	893.6	845.3	296.5	517.1	-
					[44] in [24]$_{4340}$	-	-	-	285	470	-
					[66]$_{4340}$	-	-	-	286	462	-
Used in ref.: [16, 24, 43, 44, 47-49, 66]					[16] ‡$_{4340}$	190	1048	834	-	-	429.8
4330 V	BS 835M30 EN 30B	1.6747	30NCD16 or (30NiCrMo16)	NCMAS AIR 9160 (HS)	[14, 33] †	-	1880	1020	410	660	-
					[33]	195	1880	1020	-	-	-
					[10]	-	1880	-	426	660	-
					[31]	-	1177	1090	426	680	-

AISI & SAE	BSI & EN	DIN	Other		Values from ref.	E	S_{ut}	S_y	t_{-1}	f_{-1}	s_{-1}
					[66]	-	1160	-	410	660	-
					[9]	-	1880	-	410	660	-
Used in ref.: [31], [8-10, 33, 52, 66] from [14, 33] †, and [73-76] in [56]					[73-76] in [56]	195 / 200	-	1020 / 1090 / 950	450 / 410 / 428	710 / 660 / 690	560
3310	BS 655M13 EN 36A	1.5752	14NiCr14 or 15NiCr13 or 12NC15	NCAS	[41] †	-	-	-	314.4	482.7	-
Used in ref.: [41] † and [43] †					-	-	-	-	-	-	-
304	BS 304S15	1.4301	X5CrNi18	SS	[22, 23]	183	650	325	-	-	-
Used in ref.: [19, 22, 23, 40, 64]					[19]	185	-	325	83	-	138
-	-	2.4668	**Inconel 718**	NCMA (GH 4169)	[13, 23]	209	-	1160	-	-	-
Used in ref.: [4, 13, 22, 23, 39, 54]					[54]	182	-	626.4	-	-	-
-	-	3.7164	**Ti-6Al-4V** Ti64 or TC4 **(Alpha-Beta Titanium Alloy)**	TAVA	[66]	-	1090	-	411	652	-
Used in ref.: [54, 66]					[54]	108.4	-	942.5	-	-	-
-	-	-	**76S-T61**	AZA	[66]	-	419.3	-	143 / 119 / 109	217 / 188 / 170	-
Used in ref.: [44, 46, 48, 49, 66]					-	-	-	-	-	-	-

Notes:

† = The original data source or repeatedly referenced as a data source

‡ = Has multiple materials (with similar designation) and material strength data entries. Only reported here, with the symbol, to reflect the use and availability of each material and the data for it in the literature (Li *et al.* [16], all axial fatigue limits are later shown in Figure 2-8).

The standard material designations (first three columns) are defined in the Abbreviations list on page XXI.

Column five abbreviations: **LCS** = low Carbon steel | **MS** = mild steel | **MCS** = medium Carbon steel | **HCS** = high Carbon steel | **HS** = Hard Steel | **SHS** = Swedish Hard Steel | **CAS** = Chrome alloy steel | **CMAS** = Chrome Molybdenum alloy steel | **NCMAS** = Nickel Chrome Molybdenum alloy steel | **NCAS** = Nickel Chrome alloy steel | **SS** = stainless steel | **NCMA** = Nickel Chrome Molybdenum alloy | **TAVA** = Titanium Aluminium Vanadium alloy | **AZA** = Aluminium Zinc alloy

As stated, many of the materials are not re-tested in the literature. The same data sets are often used in successive fatigue criteria reviews and assessments by different authors. For example, the data for MS and HS of [42] †, AISI 5132 and AISI 4140/42 steel of [45] † and AISI 4330V steel of [14, 33] †. These repeatedly used data sets are criticised by other authors concerning their validity and correctness for evaluating fatigue criteria [21, 56]. A recent study generated a collection of original experimental material property and fatigue strength data sets from all the known multiaxial fatigue literature for various materials and loading conditions [56]. Many of the same data set (above) discrepancies are also identified and discussed in this collection. Many of the materials (e.g., cast irons) and loading conditions (e.g., axial-torsion) reported in that data collection do not apply to this study.

Little new mechanical properties and fatigue strength tests (uniaxial or multiaxial) are reported for materials like those in Table 2-2. Where such new tests are done, it is mainly done to study the effects of midrange stress, specimen geometry and specimen size on the fatigue limits under uniaxial loading [14, 33, 39, 58, 64]. Alternatively, the tests are done on less general materials (e.g., AISI 4330V or 39NiCrMo3) and loading (e.g., non-sinusoidal or asynchronous). The lack of new test data is specifically observed for materials like mild steel (MS), Hard Steel (HS), AISI 5132, AISI 4140 and AISI 4330V in Table 2-2. For these materials, the primary sources (†) are specifically used and referenced in the literature, and the reported values are similar for respective entries at each material. Lack of new material data is also observed from the more considerable amount of literature references where a material used ('*Used in ref.'* rows) versus the number of references in which the relevant material data is obtained or reported from ('*Values from ref.'* column six).

It is seen in Table 2-2 that ferrous metals are used more for multiaxial and uniaxial fatigue testing in the literature. Specifically, medium carbon steel also referred to as ductile metals, where 0.1 < t_{-1}/f_{-1} < 0.58 [19]. And low to high alloy steel, also referred to as hard metals, where 0.577 < t_{-1}/f_{-1} < 0.833 [10]. This may be due to their broad applicability in general and specialised engineering activities and their workability, availability, cost, and fatigue strength. The alloyed steels have the most reported tensile and uniaxial fatigue strength properties. Corrosion-resistant metals (typically nonferrous and special alloys) like stainless steel, Inconel and Aluminium are much less considered in the literature, and very little data is reported.

Different definitions of fatigue failure and the fatigue limit are often reported for the values of t_{-1}, f_{-1}, and s_{-1} in Table 2-2 [56]. These definitions are not always explicitly provided with the data and often have to be assumed from the multiaxial data set. Therefore, direct comparison or use of the fatigue limit values is not always possible. These uniaxial fatigue limits are required in almost all the multiaxial fatigue failure criteria for fatigue life assessment and fatigue limit estimation with experimental multiaxial fatigue data. For the fatigue data sets of Stanfield [41], Findley in [24] and others [19, 21, 34, 66], the fatigue limit definitions are not reported. For the rest of the fatigue data sets, the limit definitions are used as reported [8, 10, 14, 33, 43, 56].

Figure 2-7 below provides a Stress-Life (S-N) graph that illustrates the uniaxial bending, torsion, and axial fatigue strength (B, T and AX) and fatigue limit (f_{-1}, t_{-1} and s_{-1}) data from Table 2-2. For this graph, only the ferrous metals in Table 2-2 that are classified as ductile or hard metals are used (see Section 1.6.1). Therefore, the three non-ferrous metals are excluded (see reasons on pg.25). The reason for only considering ductile and hard metals is due to the general applicability of the considered fatigue criteria (in Table 2-1 pg.20). For each data set used, the uniaxial loading condition is reported as being fully reversed.

The data values for each material (in Figure 2-7 and onwards) are identified with the abbreviation of the author's name(s) (of the primary or appropriate secondary source). These are Lee (LSB), Ogawa *et al.* (OG), Li *et al.* (JL), Stanfield (SG), Nishihara and Kawamoto (NK), Gough (G), Findley (F), Zenner *et al.* (Z), Froustey and Lasserre (F&L), Susmel (SUS), Luo *et al.* (L&Y), Papuga *et al.* (PPG), Papadopoulos (PPD), Zenner (ZR), Lasserre and Zenner (L&Z), Froustey (FST), Morel (MRL) and Morettini *et al.* (MOR). The reference number corresponding to each material, data value and the author is provided next to them in the legend. These numbers can reference the relevant material data entries in Table 2-2 (column six).

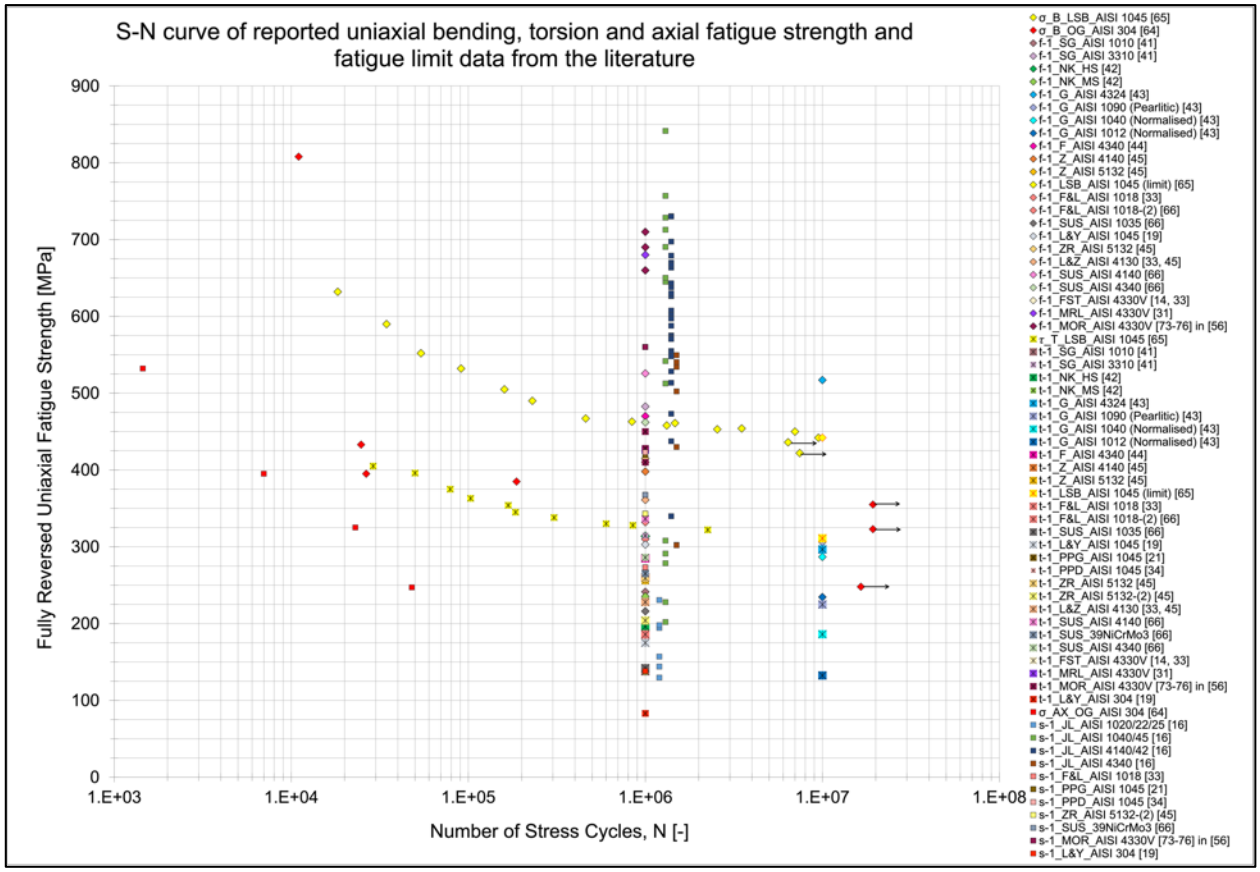


Figure 2-7: S-N curve – reported uniaxial bending, torsion and axial fatigue strength and limit data

The test specimen conditions (e.g., surface finish and geometry) are sometimes reported for the data sets mentioned above (for uniaxial or multiaxial specimens). However, this is often done cryptically and primarily only for the multiaxial fatigue specimens. For example, the OG multiaxial fatigue specimens are reported as solid cylindrical hourglass-shaped and the JL axial fatigue specimens as smooth unnotched and highly polished. The rest of the test specimen conditions

are not reported, or evident from the data set sources. Therefore, an assumption that an ASTM standard or other standard uniaxial fatigue test specimens are used is incorrect.

The arrows on some data points in Figure 2-7 (and Figure 2-9 later) are used to show, what the literature refers to, the 'run-out' of a test (if reported as such). The arrows indicate the experimental tests that did not fail according to the fatigue failure and limit definitions of the relevant data set.

Figure 2-8 below provides the normalised uniaxial fatigue data values from Figure 2-7 above. Normalisation was done by dividing the respective fatigue data point stresses with the associated material's reported ultimate tensile strength S_{ut}. The normalisation is done so that the different fatigue data sets and materials can be compared using a single graph. The normalised stress ratio (<1) represents the fully modified fatigue strength or limit for each material and loading condition. The materials for which the ultimate tensile strength is not reported with the corresponding fatigue data are consequently omitted. In this case, it applies to the data of LSB, OG, SG, F, L&Y, PPD and L&Z and some of the SUS and MOR data from Figure 2-7. The different fatigue limit definitions used in the literature are observed in both Figure 2-7 and Figure 2-8, where all but the G, LSB and OG data sets are defined at 10^6 cycles (or very close to it). The fatigue limit for these three data sets is reported as 10^7 cycles. For the JL axial fatigue limit data set, the definition of the fatigue limit is also 10^6 cycles for all four materials. The data points were spaced a few thousand cycles apart for clarity between the multiple material entries since they overlap with each other and the other data.

It is observed in Figure 2-8 that the general bending (B) fatigue limit data spread is similar to the axial (AX) fatigue limit spread and more prominent than the torsion (T) fatigue limit spread. The spread in the normalised data points of each uniaxial fatigue type is attributed to the fact that various steels are considered, each with its own reported S_{ut}. It is also attributed to the fact that for an arbitrary material from this Figure 2-8, all three uniaxial fatigue limits are often not reported, as seen in Table 2-2. The spread is also expected due to the inherent nature of metal fatigue testing under different uniaxial loading conditions. There are much fewer uniaxial fatigue limits after normalising the data sets. It is also shown in general that the bending fatigue limits are higher than the axial ones, which is expected and a well-known phenomenon. The bending fatigue limit strength of steel is generally higher than axial fatigue limit strengths due to less material volume being stressed (with a gradient profile) in bending than in axial loading (uniform stress profile). In turn, the torsion fatigue limit data is generally lower than the axial fatigue data, which is also expected due to the severity of torsion loading (also a gradient profile) relative to axial loading.

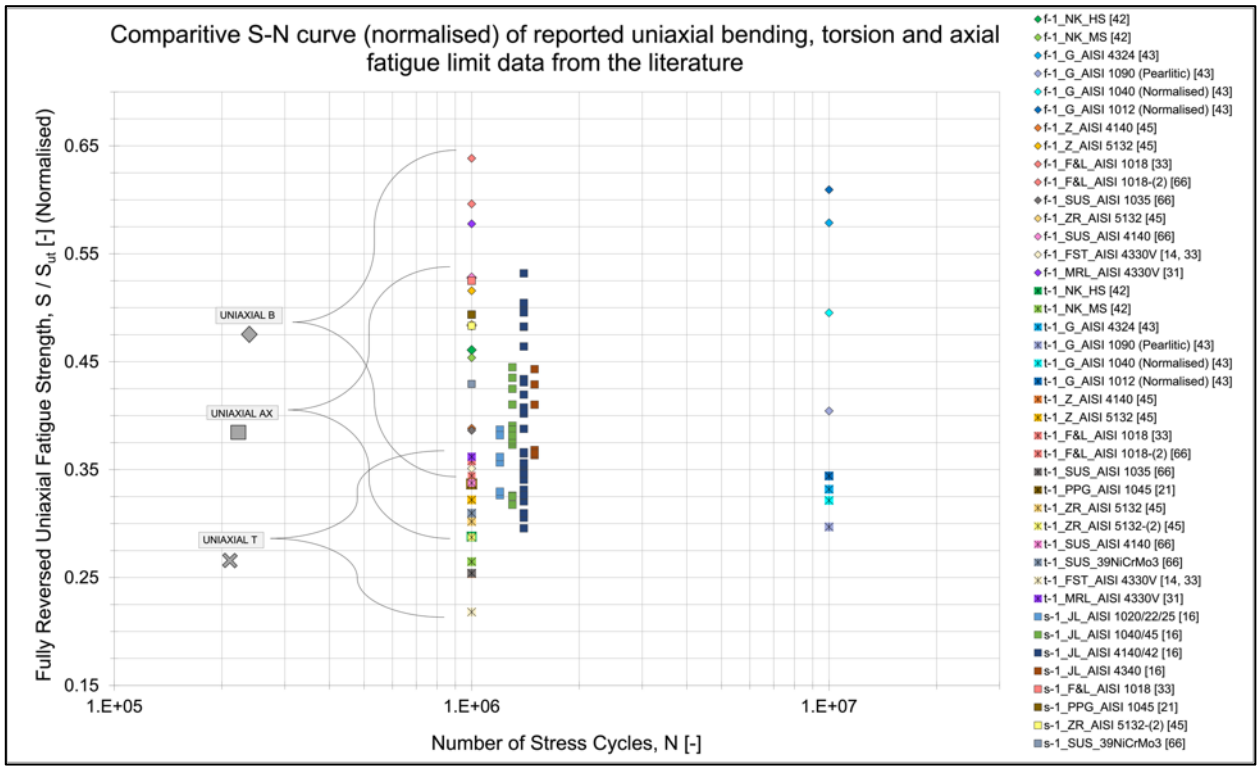


Figure 2-8: Comparative S-N curve (normalised) – reported uniaxial bending, torsion and axial fatigue limit data

2.6 Multiaxial Fatigue Data

The previous section identified and discussed the materials and basic material strength data reported with the relevant multiaxial fatigue data and criteria. This section discusses these multiaxial fatigue data sets from the same literature regarding the applicable:

- biaxial loading condition (for out-of-phase as well as in-phase bending-torsion) and the
- hard and ductile ferrous metals (applicable to the fatigue criteria)

To further limit the focus of the data discussed in this section, it was required that more specificity to the multiaxial fatigue loading limitations be added (see Section 1.6.1). This is because the multiaxial fatigue limit data in the literature are often reported for tests conducted with multiple phase angles (β), loading combinations and biaxial stress amplitude ratios (λ), as discussed earlier in Section 2.3. Performing an experimental investigation (as in this study) for all the generally reported bending-torsion loading conditions in the literature would be too comprehensive and beyond the scope of this study. Considering the effect of a specific loading

condition on the multiaxial fatigue strength of a single material, which is also applicable to the criteria, was considered more appropriate. This way, a specific and complete investigation could be performed, instead of a generalised one, as is typically done and reported in the relevant literature.

The specific limitation was made based on the previously mentioned literature observations for different biaxial loading conditions and metal types (on pg.10). It was reported that a 90 [°] phase angle difference between bending-torsion with a λ value of 0.5 [-] is deemed one of the most damaging multiaxial fatigue loading conditions, especially on ductile metals [2, 12, 35, 36]. Adopting this presumed 'worst-case' bending-torsion loading as the preferred fatigue loading condition on an appropriate metal was considered suitable. Motivation is later provided in Sections 4.2.1 and 4.2.3 for both this loading condition and the eventual test material. It should be noted that in-phase bending-torsion data with a λ value of 0.5 [-] is also considered from the relevant data sets, primarily for comparison and completeness.

From the literature, it misleadingly appears that a large number and variety of multiaxial fatigue data sets are available for evaluating multiaxial fatigue criteria. This is due to the general consideration of as many materials as possible, loading conditions, and data sets in respective criteria review and evaluation articles. As shown and discussed in the previous data section, many of the original fatigue data sets are repeatedly used and referenced for criteria evaluations. The data set expressly referred to includes those of Nishihara and Kawamoto [42] (NK) in [2, 7-10, 20, 24, 35, 36, 38, 56], Gough [43] (G), Zenner *et al.* [45] (Z) and Froustey and Lasserre [14, 33] (F&L). The NK data set is one of the first and most referenced in-phase and out-of-phase bending-torsion fatigue data sets for steels in the literature [56]. The G data set is one of the most comprehensive in-phase bending-torsion fatigue data sets considering twelve steels. The four data sets above are also referenced in the fatigue data collection of Morettini *et al.* [56]. These data sets are also used and referenced in the review and comparative study articles of McDiarmid [7, 35], Papadopoulos [8, 10, 24, 52, 77], Luo *et al.* [19] and Susmel [66]. A limited number of other applicable multiaxial fatigue data sets were also found in the literature. These are less used and referenced but still applicable to the relevant loading and materials. They include the in-phase data sets of Stanfield [41] (SG) and Findley [24] (F) and the out-of-phase data set of Ogawa *et al.* [64] (OG).

It was previously mentioned that the literature's multiaxial (and uniaxial) fatigue data sets had reported drawbacks or concerns surrounding their utility for fatigue limit estimation and failure criteria evaluation. The NK data set is especially criticised by Papuga *et al.* [21] and Morettini *et al.* [56] as incomplete, experimentally erroneous and lacking sufficient data points. They argue that this data set should be omitted because of this. However, it is still considered in this section

for the completeness of the reported literature data. Other data sets (for the considered and other loading conditions) are argued to be scarce, old and also incomplete [14, 19, 21, 40, 54]. The number of experimental fatigue test data points needed to adequately describe a metal's fatigue limit is suggested to be between 10 and 15 [56]. This is not the case for most, if not all, of the fatigue data sets, as merely a single data point is reported for each claimed fatigue limit entry in the literature. This data point typically only consists of the uniaxial or biaxial stress amplitude and midrange stresses σ_a, σ_m, τ_a and τ_m and supplementary to that the nominal stress amplitude ratio λ, the stress ratio R and the phase angle β (sometimes also designated as δ). Where applicable, the t_{-1}, f_{-1} and s_{-1} values are reported along with S_{ut} of the material (S_y is rarely reported). Experimental uncertainties on the fatigue data sets are also not reported in the literature. The method and equipment with which the multiaxial fatigue tests are conducted are only provided for the data sets of G, Z and F&L.

Different definitions for the *fatigue limit* are also reported throughout the literature, which is rarely explicitly reported [1, 24]. The different definitions (infinite life) vary between the data sources as $1x10^6$ (conventional theoretical definition, and most used), $1.5x10^6$ and $2x10^6$ (both common) and $1x10^7$ (very scarce) [56]. Two of the main definitions used in the literature to define the *fatigue failure condition* of an experimental test specimen (or full-scale component) include complete fracture or crack initiation [49, 60]. The complete fracture definition is primarily used and applies to stress-based (or fatigue failure) criteria which merely estimate the cyclic stresses that will cause the complete failure of a component. The crack initiation definition is mainly used for strain-based (or fatigue damage) criteria concerned with the crack formation and growth mechanisms and the associated characteristics (not considered for this study). These fatigue limit and failure definitions will later be explicitly outlined for this research study and the experimental testing that will be performed.

The multiaxial fatigue data sets from the literature are not all usable for this study, based on the loading limitation discussed on pg.33 previously. Some consider a relevant material (e.g., ductile or hard steel). However, under loading conditions that are very different (e.g., $\lambda \neq 0.5$) as in F&L and L&Z. Others consider different phase angles (e.g., 30, 45, and 60 [°]) as in NK, Z, F&L and L&Z, or with biaxial loads that are not bending and torsion (e.g., axial-torsion, axial-bending or axial-axial) [11, 22, 25, 34, 39, 49, 54, 57]. Others consider materials that are not as applicable or easily obtainable (e.g., cast irons and superalloys). For these reasons, many of the data sets have even less usable data for verification with this study's experimental data or for evaluating the multiaxial fatigue criteria. The multiaxial fatigue data sets that apply to the loading condition, criteria and ferrous metal types are illustrated in Figure 2-9 and Figure 2-10.

Figure 2-9 provides an S-N curve with the reported multiaxial fatigue strength and limit data of Nishihara and Kawamoto (NK), Zenner *et al.* (Z), Ogawa *et al.* (OG), Stanfield (SG), Gough (G) and Findley (F). The loading of these data sets is reported as fully reversed in-phase (IP) and out-of-phase (OP) bending-torsion (BT). These data sets' specimen conditions (e.g., surface finish and geometry) are not always reported. For the NK data, it is only reported that smooth specimens were used. The Z specimens are reported to be solid and hollow, the OG specimens are reported as solid cylindrical hourglass-shaped specimens, and the G specimens are reported only as solid specimens. Lastly, the conditions of the SG and F specimens are not reported.

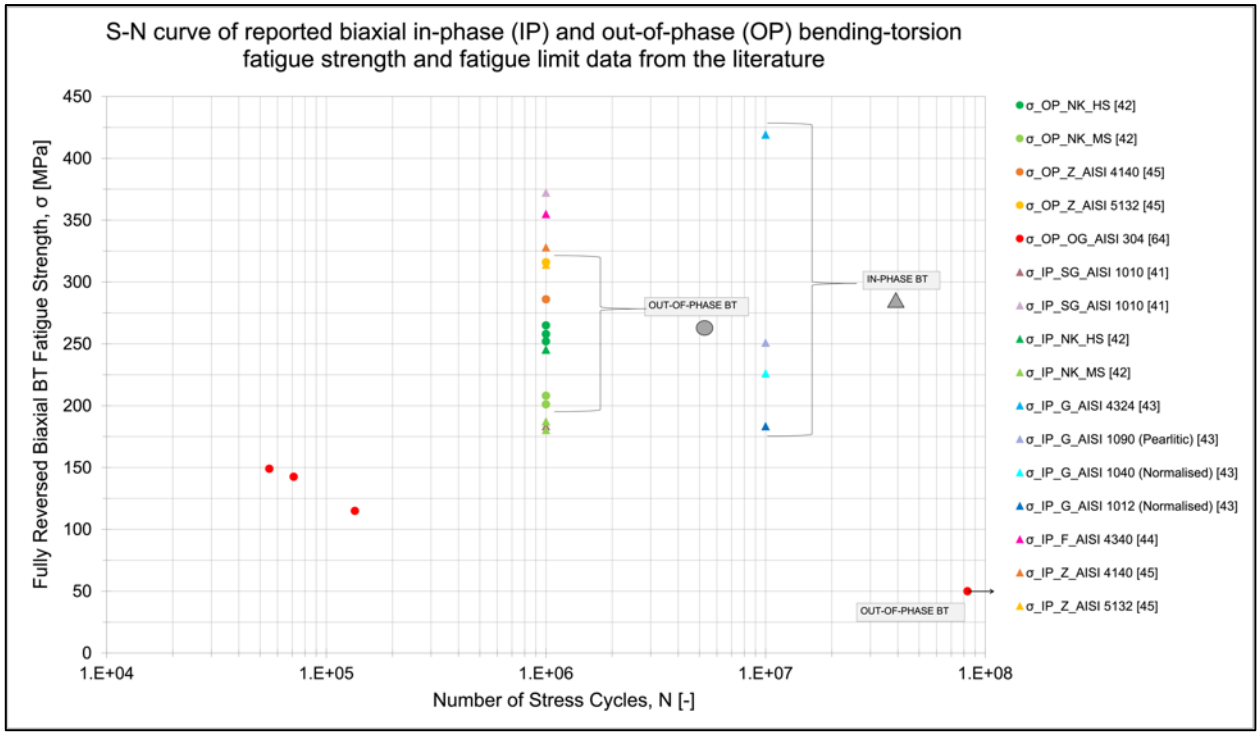


Figure 2-9: S-N curve – reported biaxial in-phase and out-of-phase bending-torsion fatigue strength and limit data

Specifically, for Figure 2-9 above, only the data for steels classified as ductile or hard steels were used (similar to the previous uniaxial data section). Other metals like cast irons [7, 41, 42, 48], AISI 4330V / EN30B [14, 31, 33], AISI 4130 / EN16 [33, 45, 71, 72], Aluminium [40, 42, 44, 46, 48, 49, 60, 66, 67] and tube or plate steels [11, 19, 45, 55, 61, 64, 66] are also reported in some of the above data sources (with the materials from Table 2-2). However, these metals (often designated as brittle or very hard) or the loading conditions used in testing them did not apply to this study.

Both in-phase and 90 [°] out-of-phase bending-torsion with λ = 0.5 [-] were considered for the loading of the above data. The bending component of the biaxial loading condition in the data

sets is reported as plane bending, and the materials in the graph are previously defined in Table 2-2. The in-phase BT data points are indicated using only the bending stress σ_{IP} component so that they can be plotted on the same graph as the out-of-phase data (σ for the y-axis). As specified, for both in-phase and out-of-phase data, it is thus known that the torsion stress is half that of the bending stress according to λ. The out-of-phase BT data points are also indicated with only the bending stress, using the symbol σ_{OP}. As with the uniaxial data graphs of the previous section, the author(s) initials, material AISI designation and source number are used to identify each data set (see Table 2-2). The reasoning for not simply using the Von Mises (VM) stress for both in-phase and out-of-phase loading data points is discussed in Section 3.2.

The multiaxial fatigue data values from Figure 2-9 were normalised by dividing the respective bending stress σ values with the associated material's S_{ut} value, as done for the uniaxial fatigue data in the previous section (see Figure 2-8). It should be noted for both in-phase and out-of-phase data values that $\lambda = 0.5$ [-] is maintained if both the stresses of the biaxial B&T condition are divided by S_{ut}. The normalised data is depicted in Figure 2-10 below. Again, if no S_{ut} of a material is reported with the fatigue data (in this case, OG, SG and F), it is omitted from the normalised graph. This results in even less usable multiaxial fatigue data.

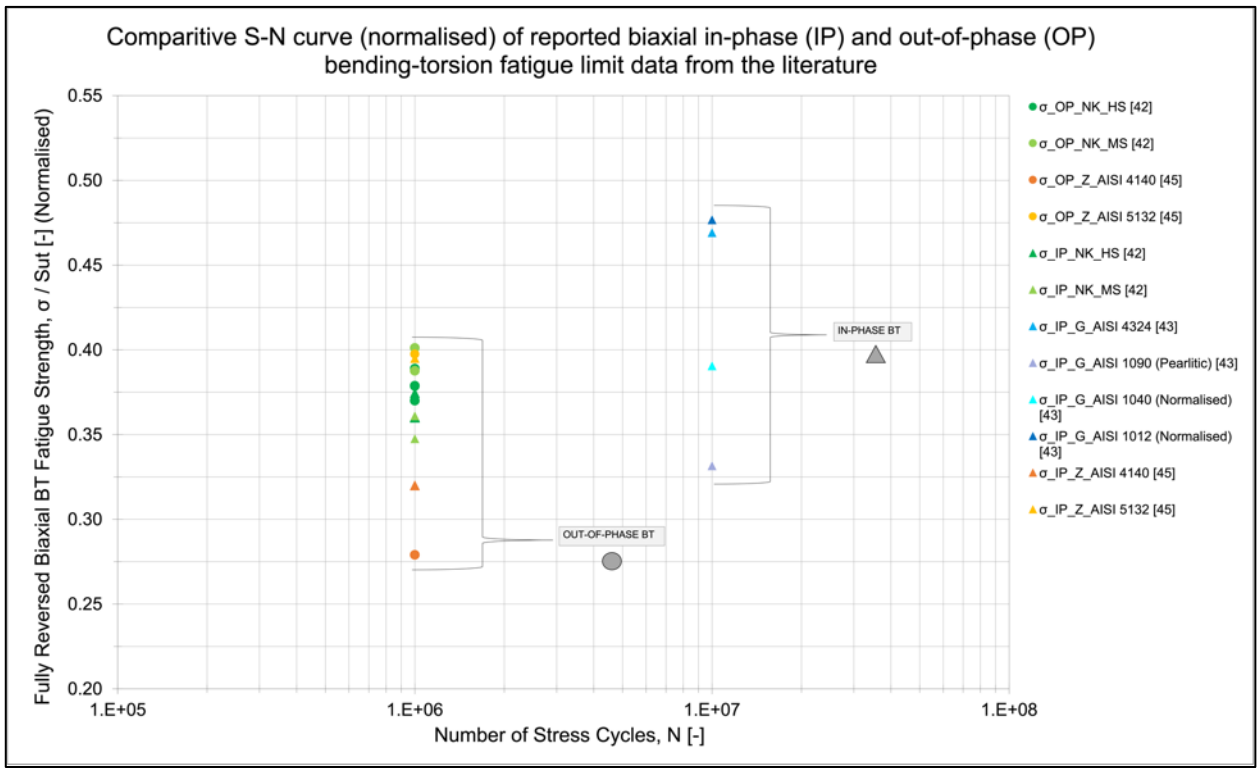


Figure 2-10: Comparative S-N curve (normalised) – reported biaxial in-phase and out-of-phase bending-torsion fatigue limit data

From both Figure 2-9 and Figure 2-10, the different fatigue limit definitions used are observed, where all but the G and OG data sets are defined at 10^6 cycles (or very close to it). Their fatigue limits are reported or illustrated in the literature as 10^7 cycles. For the hard and mild steel of NK, the S_{ut} values were obtained from [56] and [38], as the original NK article was directly referenced for the data values. Other literature sources using the NK data also reportedly used the original NK article [2, 7-10, 20, 24, 29, 35, 36, 38]. However, the reported material and fatigue strength values differ between the respective sources (see Table 2-2 for MS – mild steel and SHS – Swedish hard steel). The difference is seen in the S_{ut} values of these two NK materials.

It is shown for the multiaxial fatigue data sets in the literature that very little difference exists between the reported in-phase and out-of-phase bending-torsion fatigue limits of hard and ductile metals (see NK and Z data). The spread observed after normalisation for the in-phase data of G is attributed to the fact that the four materials are very different based on tensile strength.

Figure 2-7 (previous section, pg.31) and Figure 2-9 above show the insufficient fatigue limit data of the ductile and hard ferrous metals. It is seen for most of the reported literature data sets (e.g., NK, Z, G, F and JL) as only single data point values are reported in most cases. Where there is more than one fatigue strength data point (e.g., fatigue strength curves for OG and LSB in Figure 2-7 and OG in Figure 2-9), the lack of sufficient HCF test points and the required material S_{ut} values are also evident. It is mainly seen when translating the data to the normalised graphs in Figure 2-8 (previous section, pg.33) and Figure 2-10 above. The absence of S_{ut} values for many of the applicable data sets results in a significant loss of comparable uniaxial and multiaxial fatigue data from the literature. The following section discusses the fatigue test equipment typically reported for generating these above (and previous) fatigue data sets.

2.7 Fatigue Test Equipment

The fatigue data sets reported and discussed in the previous sections are generated using different experimental fatigue test benches and measurement equipment. These can be mechanical, hydraulic, servo-hydraulic or electromagnetic actuated test benches. As reported in the literature, these test machines are often scarce, complex and expensive, especially in the case of multiaxial fatigue testing [16, 55]. Some of the more modern machines have accelerated testing capability (50[Hz] or more), whereas the older machines have limited loading and test speed capability (up to 5[Hz]) [14, 43, 62]. This section provides a short overview of the fatigue test benches and machines reported and referenced in the multiaxial fatigue literature. The measurement equipment used during fatigue testing is referenced where reported.

Fatigue testing machines typically consist of three main parts. These include a drive or loading system, a control system and a monitor system [62]. The four most common fatigue test machine types are axial fatigue machines (electromechanical, servo-hydraulic and electromagnetic), bending fatigue machines (cantilever beam or rotating beam), torsional fatigue machines (often electromechanical or servo-hydraulic) and multiaxial fatigue machines (designed to induce combinations of the three fundamental uniaxial type machines) [62].

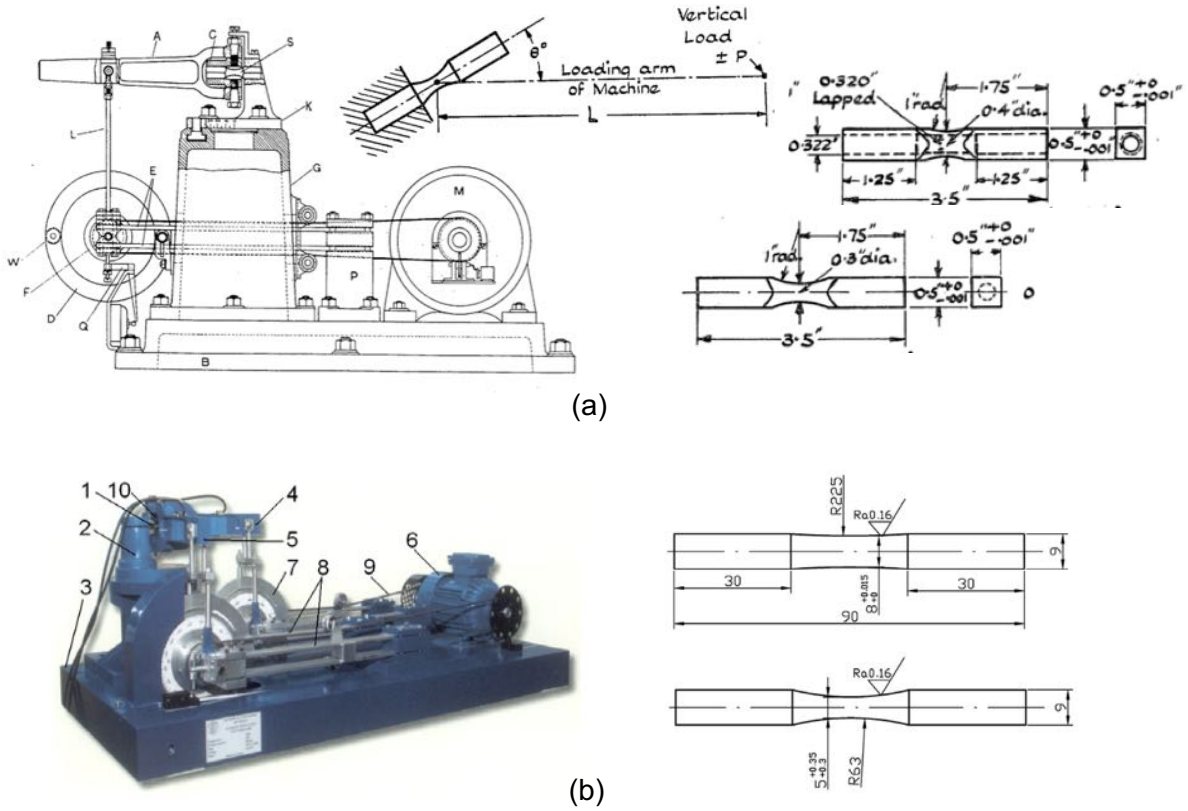


Figure 2-11: Bending-torsion test bench and specimen(s) of: (a) MZGS-100Ph in-phase loading machine [43] and (b) MZGS-200E out-of-phase loading machine [14, 55, 78]

Multiaxial fatigue tests (for in and out-of-phase bending-torsion) are typically done on electro-mechanically actuated machines like those shown in Figure 2-11 above [14, 33, 43, 55]. These tests are primarily done on solid or hollow cylindrical hourglass-shaped test specimens, as is customary for bending-torsion loading in the literature. These machines can test from 5-50 [Hz] at loads of 120 [N.m] torsion and 100 [N.m] bending, in-phase or out-of-phase. The machine's working principle is based on an imbalance mass piece attached to a rotating wheel (mounted on leaf springs) which connects with a moment lever arm that exerts bending and torsion loading on the attached specimen. This machine exerts cyclic fatigue loading on the specimen and stops when displacement sensors detect excessive displacement due to crack formation, or the programmed cycle count is reached [14].

Another biaxial bending-torsion fatigue test bench recently proposed by Ogawa *et al.* [64] induces and measures the loading on the specimen similarly to those machines above, with the addition of a mechanical switch (for failure) and a direct strain gauge measurement on the specimen (for loading). This test bench is illustrated in Figure 2-12 below.

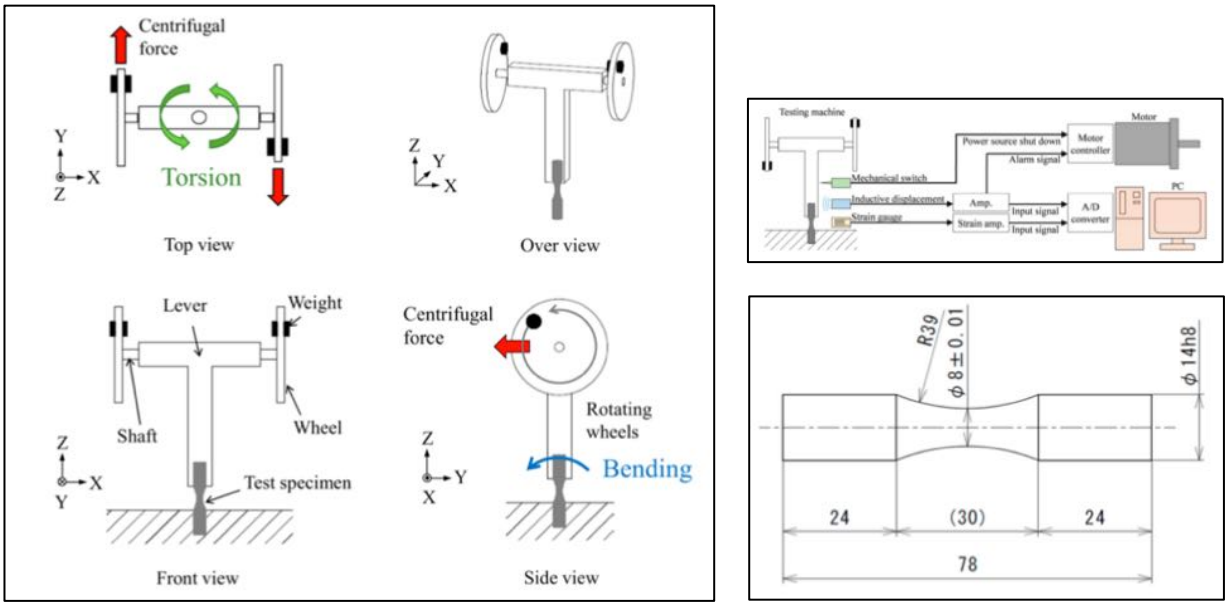


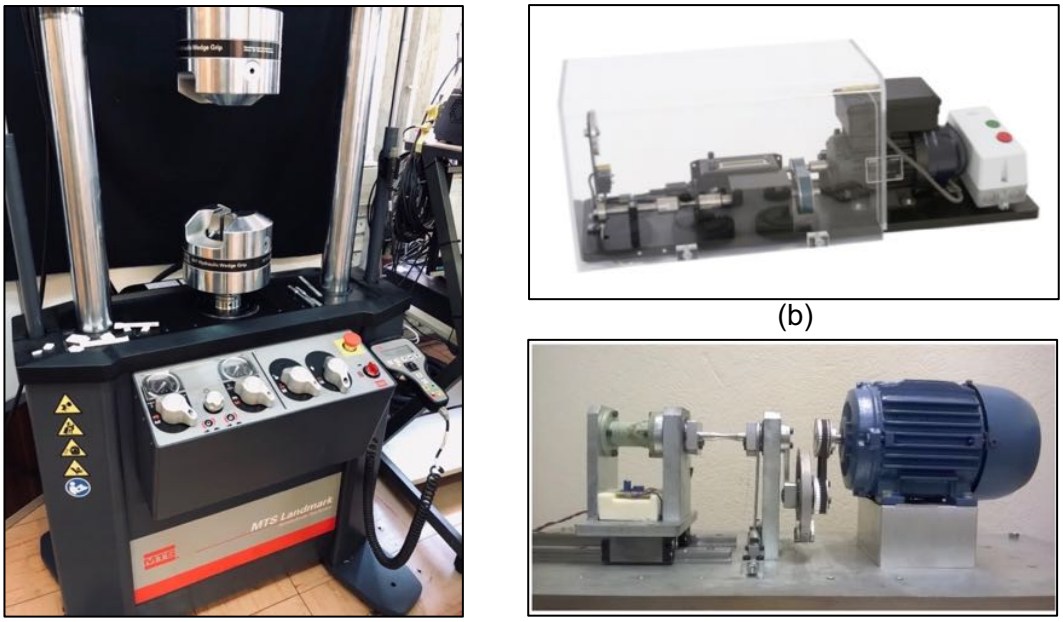
Figure 2-12: Electromechanical bending-torsion fatigue test bench and specimen geometry [64]

An electro-magnetically actuated machine was also recently used to study in-phase bending-torsion fatigue [67]. In-plane biaxial fatigue test machines (electromagnetic or servo-hydraulic) are also used to test biaxial cruciform specimens. These tests supposedly allow complete characterization of a material's behaviour under any biaxial loading condition when results are combined with tension-torsion test measurements [1]. Modern servo-hydraulic fatigue test machines allow loading to be adapted or designed to induce biaxial tension-torsion (in or out-of-phase, synchronous or not) multiaxial loading on cylindrical specimens [1, 62].

The machine types used for uniaxial fatigue testing are very similar to those previously discussed. These often induce fatigue forces through electromechanical or servo-hydraulic action and are also 'simpler' concerning the induced loading condition.

The most well-known uniaxial fatigue test machine is the R.R. Moore fatigue test bench (rotating or cantilever bending), shown in Figure 2-13 (b). Uniaxial axial fatigue testing is usually performed on servo-hydraulic test machines like the MTS Landmark in Figure 2-13 (a) due to the better control of test parameters, procedures and failure. This machine commonly performs monotonic

tensile and compressive tests on various materials. Some uniaxial torsion machines (Figure 2-13 (c)) have been proposed in the literature [79]. However, these tests are often performed on servo-hydraulic or electromagnetic machines.



(a) (b) (c)

Figure 2-13: Uniaxial (a) axial, (b) bending [80] and (c) torsion [79] fatigue test benches proposed or referenced in the literature

2.8 Issues and Shortcomings

Concerning the general overview of multiaxial fatigue, it was shown from the literature discussion that differences exist between what is considered to play a role in multiaxial fatigue damage. For the loading, it was shown that multiple multiaxial fatigue loading conditions (and subsequent loading factors) are reported in the relevant literature for fatigue data sets. Based on this, the loading condition had to be restricted for the applicable data sets (generated with all these loading conditions).

Of the numerous multiaxial fatigue criteria reported in the literature for bending-torsion loading, only a small number of the stress-based critical plane and empirical fatigue criteria are applicable based on the loading condition, material and fatigue regime limitations set for this study. These criteria apply only to certain metal types (ductile or hard). Most criteria are also not deemed appropriate for this study's experimental test data evaluations because they have unknown variables requiring additional material-specific property tests or calculations. An inadequate description of some criteria and their variables is also evident for some of these criteria. Some

criteria are regarded as too complicated and cumbersome based on their reported (or lack thereof) evaluation procedures.

Various discrepancies were identified for the reported tensile, uniaxial and multiaxial fatigue data sets. A general lack of reported ferrous metal tensile and fatigue strength data exists for the data sets and materials from the literature. Very little new data is reported in the literature, and many key material strength values required for criteria evaluations are not reported. Many relevant material and fatigue strength data sets are continuously re-used and cross-reported, and transcription and omission errors are evident for some data sets. These include values reported in separate sources as two different uniaxial fatigue properties. The data set of Nishihara and Kawamoto is especially criticised by other authors and deemed inappropriate for this study.

2.9 Conclusion

This literature review chapter consisted of three main parts. The first part discussed the general knowledge, challenges and arguments associated with multiaxial fatigue in the literature.

The second part discussed the typical multiaxial fatigue loading conditions and their subsequent variability as tested and reported in the literature. After this, the relevant multiaxial fatigue criteria that apply to these loading conditions were discussed. The twelve most applicable fatigue criteria were identified and discussed based on their relevance and material and loading applicability. The completeness with which these criteria and their required material strength parameters are reported was also discussed.

The third part discussed the relevant materials, tensile and fatigue strength data reported and required for evaluating these criteria. The reported problems for multiaxial and uniaxial fatigue data sets were also illustrated using the various comparative S-N curves. From these discrepancies and an evident lack of appropriate fatigue data, it was evident that more specific and complete experimental fatigue testing (uniaxial and multiaxial) is required to investigate the stated problem of this research study. The next chapter will discuss the theory of the multiaxial fatigue loading condition and criteria.

CHAPTER 3 – THEORY

3.1 Introduction

The previous chapter discussed the relevant multiaxial fatigue loading condition, fatigue criteria and materials from the literature. The reported multiaxial fatigue data sets were also discussed, and for this study, the appropriate ones were identified. This chapter aims to provide a discussion of the relevant theory associated with these criteria and the loading condition. The multiaxial fatigue failure criteria models that are evaluated with the experimental test data of this study are also provided. The chapter is concluded with a general theoretical discussion of the critical plane approach taken by many of the criteria in the relevant literature.

3.2 Multiaxial Non-proportional Loading

As previously mentioned in Section 2.2, it is argued in the literature that the principal stress axis rotation phenomenon resulting from out-of-phase multiaxial loading causes decreased fatigue strength of ferrous metals due to what is referred to as additional cyclic material hardening [4, 12, 19, 21-26]. The formal definitions used to identify the type of multiaxial fatigue loading condition utilise this principal axis phenomenon to describe the difference between in-phase (proportional) and out-of-phase (non-proportional) loading (see pg.13) [1, 26, 59]. The principal stress (or strain) axis rotation phenomenon and these definitions are illustrated using Mohr circles that are applied to an arbitrary fully reversed sinusoidal loading condition (see Figure 2-1 and Figure 2-2) [27].

The principal stress axis orientation remains constant throughout a loading cycle for in-phase multiaxial loading (not tested in this study). However, as expected, due to cyclic stress magnitudes changing (positive to negative), the Mohr circle size and position on the σ and τ stress plane vary during this in-phase loading cycle (see Figure 2-1). Conversely, for out-of-phase multiaxial loading (as tested in this study), the principal stress axis orientation changes throughout a loading cycle, as illustrated in Figure 3-1 below. The Mohr circle size also often changes along with its position on the σ stress axis (see Figure 2-2). However, this size change can vary based on the loading condition. The Mohr circle size change depends on the out-of-phase angle (e.g., β = 90 [°]) between loading components and the stress amplitude ratios (e.g., λ = 0.5).

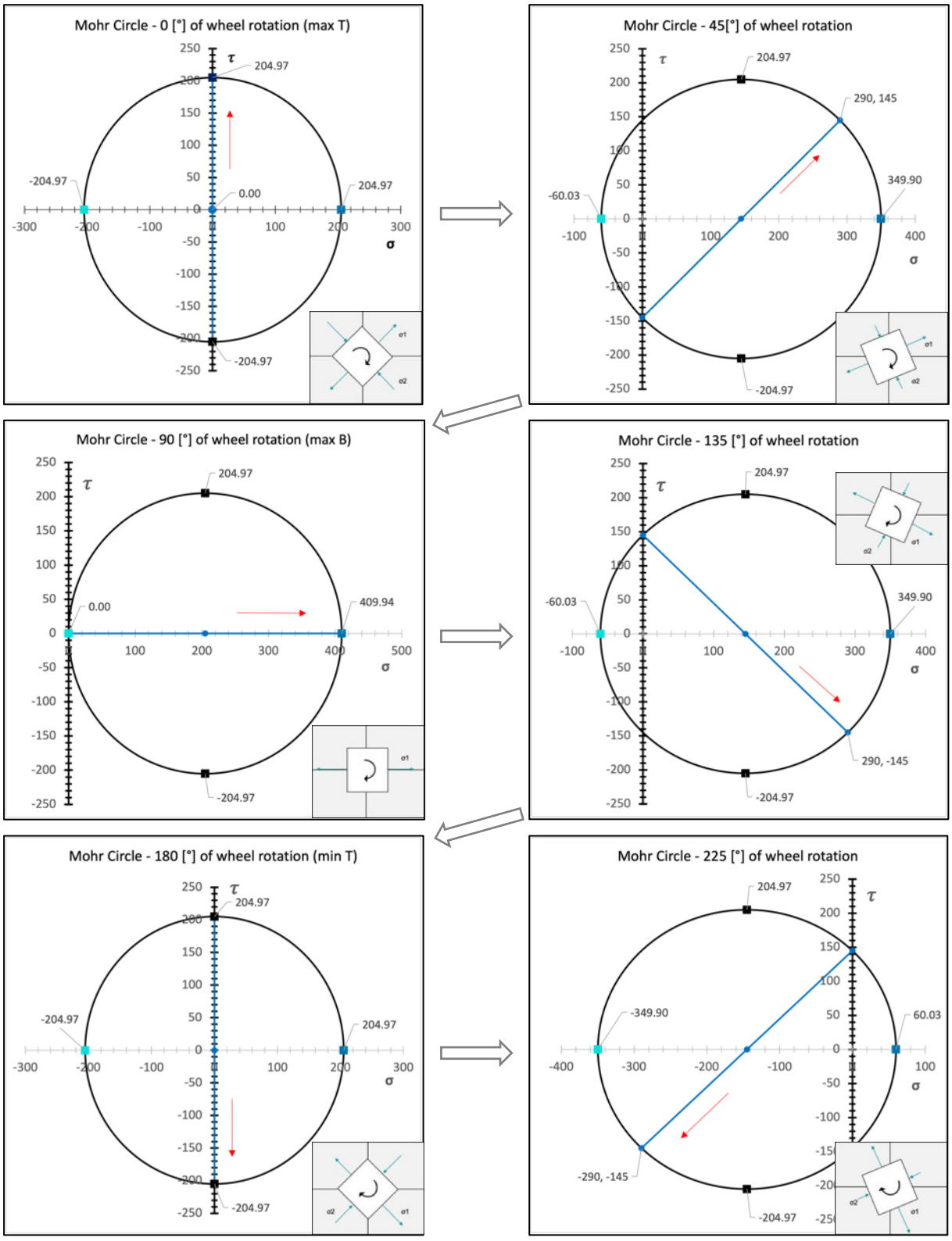
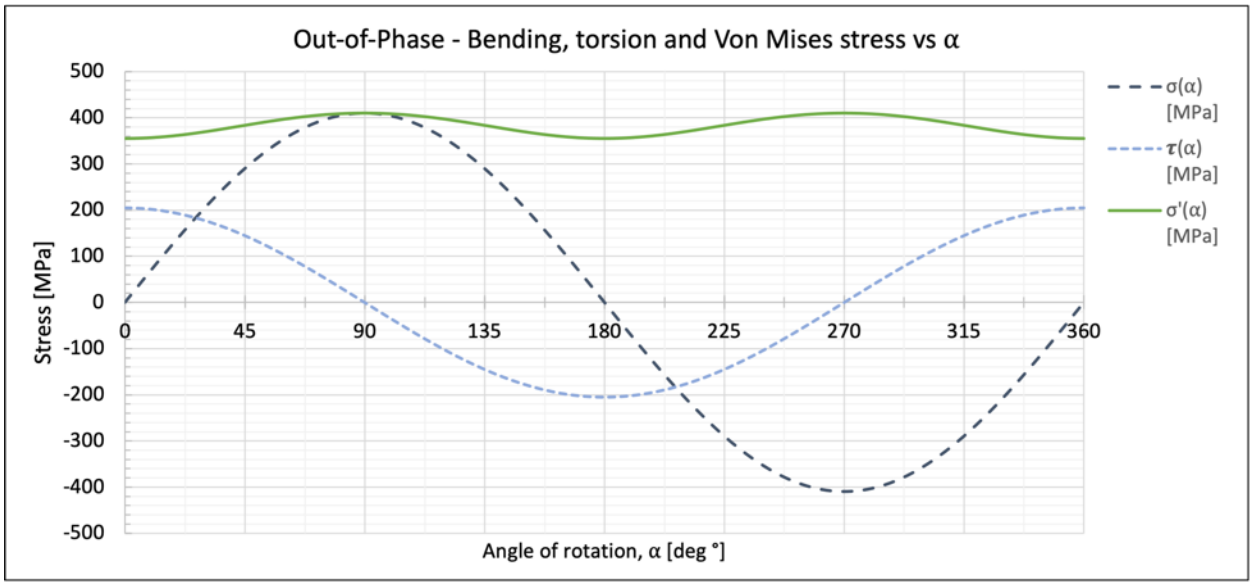


Figure 3-1: Out-of-phase (non-proportional) biaxial bending-torsion loading – Mohr stress circles

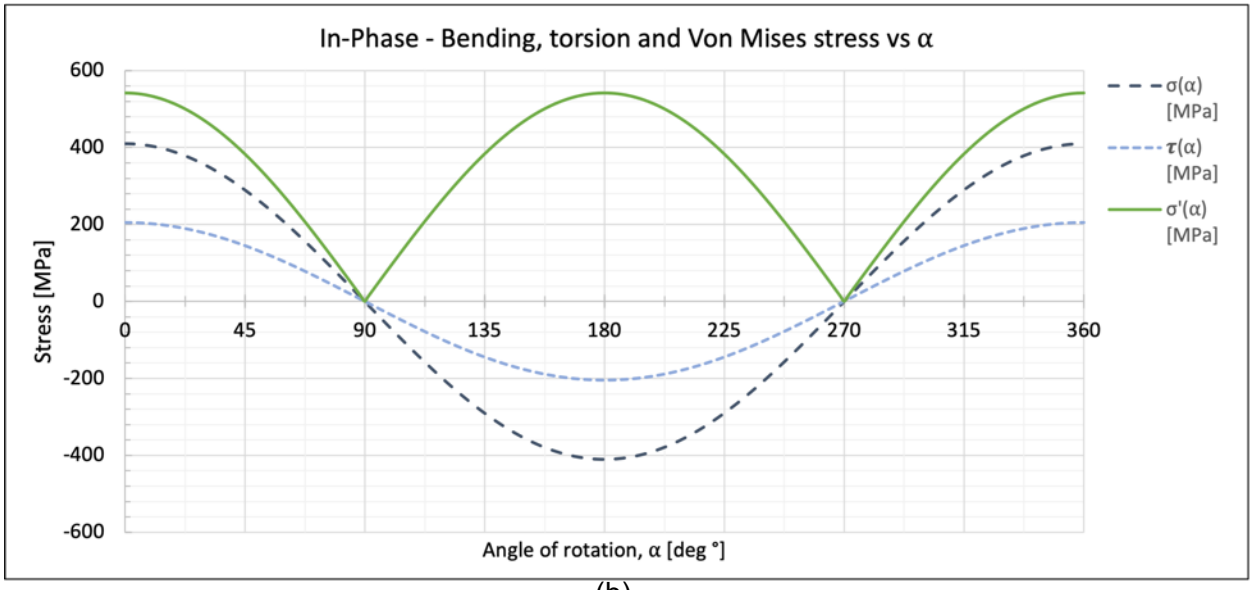
For the biaxial fatigue loading condition in this study (90 [°] out-of-phase bending and torsion with λ = 0.5 [-]), the rotating principal stress phenomenon was also shown to be relevant (Figure 3-1 above). These Mohr circles were generated for an arbitrary specimen diameter and loading moment value that would be tested on the bending-torsion fatigue test bench (identified in Section 4.3.1.4). The Mohr circles were generated at each 45 [°] angle increment of the loading cycle (or wheel rotation). The relevant biaxial bending-torsion stress quantities were calculated using the Mohr circle theory and equations from Budynas and Nisbett [3].

Figure 3-1 above shows that the principal stress axis is oriented in another direction at each point in the biaxial loading cycle. The principal stress values vary throughout the loading cycle due to the shifting Mohr circle (blue σ_1 and turquoise σ_2 squares on the σ-axis). For it, the principal stress ratio varies between -1 $\leq \sigma_2/\sigma_1 \leq$ 0 [59]. It is also shown for the chosen loading condition that the Mohr circle size remains constant, with radius = $(\sigma^2 + \tau^2)^{0.5}$, whilst it shifts position along the σ-axis during the loading cycle. This seemed to agree with the observations made in the literature that all material planes experience a constant maximum amount of shear stress [2, 12, 35]. Because of this, the loading condition is regarded as one of the most damaging in the literature.

Because the bending and torsion loading components of the chosen loading condition are 90 [°] out of phase, either the bending or the torsion is always a maximum when the other is zero, as shown in Figure 3-2 (a) (for the same loading as with Mohr circles above). The in-phase version of the above loading condition is shown in Figure 3-2 (b). These theoretical stress curves are fully reversed sinusoidal functions of the loading cycle angle α (or test bench wheel angle). Due to the above observation for the out-of-phase loading, it is deemed unfitting to calculate the combined biaxial stress amplitude value (maximum value) as a Von Mises (VM) stress σ'. For it, the bending stress σ and torsion stress τ maxima are assumed to be in-phase (as in Figure 3-2 (b)). It, therefore, results in a maximum VM stress value that is much larger (as in-phase loads) than calculated when the loads are out of phase with each other. When the biaxial loads are out-of-phase (as in Figure 3-2 (a)), the VM stress seemingly represents a sinusoidal stress with an offset (midrange stress) and a small amplitude value. This, in turn, would lead to an underestimation of the biaxial condition maximum stress amplitude value when using regular amplitude and midrange stress definitions. Figure 3-2 (a) shows that the bending stress maximum is equal to the VM stress maximum if the VM stress were calculated at each incremental angle α of the loading cycle (using σ and τ at those angles). This suggests that the more dominant bending stress may cause fatigue failure for the chosen out-of-phase bending-torsion loading condition. Not by both bending and torsion as would be assumed for in-phase loading (VM stress calculated only with maxima values, irrespective of the phase difference).



(a)



(b)

Figure 3-2: Biaxial bending-torsion stresses – (a) out-of-phase and (b) in-phase VM stress calculation

3.3 Multiaxial Fatigue Criteria Models

As reported in the relevant literature, the multiaxial fatigue criteria models are provided in this section for the selected three critical plane stress-based criteria regarded most applicable for the loading condition. These criteria were discussed in Section 2.4 and are summarised in Table 4-1. The criteria evaluation methodology using the experimental fatigue test data generated for the chosen EN19 (T-condition) steel is discussed in Section 4.7.

Fatigue Criteria Evaluation Quality and Comparison

The three multiaxial fatigue criteria that will be evaluated in this study are elliptic models (expressed as inequalities). Satisfaction of each criterion (no fatigue failure) is achieved when the left-hand side (LHS) of the inequality, termed the 'uniaxial equivalent stress' σ_{eq}, is less than (or equal to) the right-hand side (RHS). This side represents the material's uniaxial fatigue limit (or fatigue limit parameter). The LHS of a criterion effectively represents the 'combined biaxial fatigue stress condition' of the loading condition (bending-torsion in this case), and the RHS is the presumed 'biaxial fatigue limit' for the criterion.

For an arbitrary biaxial fatigue strength or limit test value (at 10^6 cycles or higher) evaluated with a criterion, the difference between the LHS and the RHS is calculated as an 'error-index' I value with Equation (3-1) below (RHS as reference). As in the literature, this value represents the prediction or evaluation quality of a criterion for the fatigue strength or limit condition (LHS) with respect to the proposed fatigue limit (RHS).

$$I\,[\%] = \left(\frac{\sigma_{eq} - \mathrm{A}}{\mathrm{A}}\right) 100 \; = \left(\frac{Left\text{–}Hand\ Side - \mathrm{Right\text{–}Hand\ Side}}{\mathrm{Right\text{–}Hand\ Side}}\right) 100 \qquad (3\text{-}1)$$

where: A : is the uniaxial fatigue limit or fatigue limit parameter

As stated above, this error-index value only applies to fatigue limit stress conditions with theoretical or experimental fatigue lives > 10^6 cycles (infinite life test data points). A criterion is considered 'conservative' in its fatigue strength evaluation if the value of I is positive (e.g., LHS > RHS at the fatigue limit). That is if the criterion predicts fatigue failure for a stress condition where failure did not occur. Conversely, a criterion is considered 'non-conservative' if the value of I is negative (e.g., LHS < RHS at the fatigue limit). That is if the criterion predicts no fatigue failure for a stress condition where failure has occurred. The criterion, therefore, overestimates the fatigue strength of the material for a given stress condition and assumed fatigue limit (RHS) and could lead to a risk of increasing applied loading.

The average I value can be calculated over infinite life or fatigue limit tests for each criterion. With this value, the criteria can be compared based on their average prediction quality for a fatigue data set. However, it is deemed appropriate to calculate a 'fatigue limit difference' value, using Equation (3-2), between the proposed biaxial fatigue limit value (RHS) of a criterion and the experimental fatigue limit estimated for the evaluated test data (to be generated). The three fatigue limit difference values are then compared (discussed later in Section 4.7) to illustrate how well each criterion evaluation agrees with this study's experimental out-of-phase biaxial bending-

torsion fatigue strength data. The experimental fatigue limit estimation method is discussed later in Section 4.6.2.

$$Fatigue\ Limit\ Difference\ [\%] = \left(\frac{Limit\ Estimate - \text{Criterion Limit}}{\text{Criterion Limit}}\right) 100 \tag{3-2}$$

Papadopoulos 1994/1997 – Critical Plane Criterion

The PPD multiaxial fatigue failure criterion (ellipse arc model) is provided in Equation (3-3) below [8, 10]. Reference can be made to Section 2.4.2 for a discussion of this criterion and its applicability under out-of-phase biaxial bending-torsion fatigue loading.

PPD

$$\sqrt{\frac{\sigma_a^2}{3} + \tau_a^2} + \alpha \frac{\sigma_a + \sigma_m}{3} \leq \beta \tag{3-3}$$

where: σ_a : is the bending stress amplitude [MPa]

σ_m : is the midrange bending stress (0 for R = -1, fully reversed loading)

τ_a : is the torsion stress amplitude [MPa]

α : is the uniaxial bending/torsion fatigue limit coefficient $(3t_{-1}/\ f_{-1}) - \sqrt{3}$ [-]

β : is the uniaxial torsion fatigue limit t_{-1} [MPa]

For this criterion to be valid, the value of α has to be positive and in the range of $0 \leq \alpha \leq 0.666$ (preserves the compressive normal stress benefit on the bending fatigue strength of the material) [10]. Also, for this criterion to apply to a metal, the uniaxial bending and torsion fatigue limit ratio of that metal has to be $1.2 < f_{-1}/t_{-1} < 1.732$ (a hard metal) or equivalently $0.577 \leq t_{-1}/f_{-1} \leq 0.833$. The PPD criterion is reported as independent of the phase difference between the bending and torsion loading on a hard metal (since it does not appear in the criterion or after the derivation) [8, 10]. It is also deemed applicable to the general nominal stress amplitude loading conditions (e.g., λ = 0.21, 0.5, 1 or 1.21, see pg.16).

The left-hand side (LHS) of the criterion is designated with the equivalent stress symbol $\sigma_{eq;PPD}$. This stress is calculated from the applied (macroscale) bending and torsion stress amplitudes and the α coefficient. The right-hand side (RHS) of the criterion is the uniaxial torsion fatigue limit t_{-1} of the material. It should be noted that the β symbol used in the PPD criterion is merely done here

for completeness (as reported in the literature). It should not be confused with the previously mentioned out-of-phase angle (also β) between the bending and torsion loading components.

Carpinteri and Spagnoli 2001 – Critical Plane Criterion

The C&S multiaxial fatigue failure criterion (ellipse quadrant model adaptation) is provided in Equation (3-4) below [9, 19, 38, 40]. Reference can also be made to Section 2.4.2 for discussing this criterion and its applicability under out-of-phase biaxial bending-torsion fatigue loading. The complete empirical method for determining the critical plane on which this criterion evaluates the biaxial fatigue strength of a hard metal can be referenced in Pereira *et al.* [9].

C&S

$$\sqrt{N_{max}^2 + \left(\frac{f_{-1}}{t_{-1}}\right) C_a^2} \leq f_{-1} \tag{3-4}$$

where: N_{max} : is the maximum critical plane normal stress equal to $N_a + N_m$ [MPa]

N_a : is the normal stress amplitude on the critical plane [MPa]

N_m : is the midrange bending stress on the critical plane [MPa]

C_a : is the shear stress amplitude on the critical plane [MPa]

Since the biaxial loading condition is fully reversed, the value $N_m = 0$ leads to $N_{max} = N_a$, calculated with Equation (3-5) below. The value of C_a is calculated with Equation (3-6) below.

$$N_a = \sqrt{[\sigma_a \sin^2(\varphi_c) + \tau_a \cos(\beta) \sin(2\varphi_c)]^2 + [-\tau_a \sin(\beta) \sin(2\varphi_c)]^2} \tag{3-5}$$

$$C_a = \sqrt{[\,0.5\sigma_a \, sin(\varphi_c) + \tau_a \cos(\beta) \cos(2\varphi_c)]^2 + [-\tau_a \sin(\beta) \cos(2\varphi_c)]^2} \tag{3-6}$$

where: φ_c : is the critical plane orientation [°]

β : is the biaxial loading phase difference (90 [°])

The C&S criterion is reported to apply to primarily hard metals, and for this, it was assumed that the same f_{-1}/t_{-1} fatigue limit ratio range of PPD applies [5]. The assumption is based on PPD's criterion being evaluated on similar metals with the C&S criterion in the literature [9]. In the derivation of the C&S criterion (and L&M criterion), the C_a stress is derived with the 'minimum circumscribed circle' method [38]. PPD proposed this method for determining resolved shear

stresses on the critical plane during his criterion derivation [8, 10]. There are no claims in the literature that the C&S criterion (or L&M criterion) is either dependent or independent of the β between the bending and torsion loading on said hard metals. However, the β value is used as part of the criterion evaluation in the above equations (unlike with PPD). This criterion is also deemed applicable to the general nominal stress amplitude loading conditions previously discussed in the literature (e.g., λ = 0.21, 0.5, 1 or 1.21).

The critical plane φ_c angle value (in N_a and C_a above) is calculated empirically for the C&S criterion (and the L&M criterion below). This plane angle is deduced from the fatigue fracture plane (φ_f). It has been shown in the literature that the critical and fracture planes correlate well with each other, with only a small angle value difference calculated from a material parameter (designated as angle δ). The fatigue fracture plane is estimated by maximising the value of the normal stress N through an iterative incrementation of an arbitrary critical plane angle (initially designated as φ) in the above equations.

The left-hand side (LHS) of the criterion is designated the equivalent stress symbol $\sigma_{eq;C\&S}$. This stress is calculated from the critical plane normal and shear stress amplitudes and the uniaxial fatigue limit ratio f_{-1}/t_{-1} . The right-hand side (RHS) of the criterion considers the uniaxial bending fatigue limit f_{-1} of the material.

Liu and Mahadevan 2005 – Critical Plane Criterion

The L&M multiaxial fatigue failure criterion (elliptic model) is provided in Equation (3-7) below [5, 9]. Reference can be made to Section 2.4.2 for a discussion of this criterion and its applicability to in and out-of-phase biaxial bending-torsion fatigue loading. The complete empirical method for determining the critical plane on which this criterion evaluates the biaxial fatigue strength of a hard metal is also referenced from Pereira *et al.* [9].

L&M

$$\sqrt{\left[\frac{N_a\left(1+\eta\frac{N_m}{f_{-1}}\right)}{f_{-1}}\right]^2+\left(\frac{C_a}{t_{-1}}\right)^2+k\left(\frac{H_a}{f_{-1}}\right)^2}\ \leq\ \lambda \qquad (3\text{-}7)$$

where: η : is a material parameter dependent on f_{-1} and t_{-1} [-]

k : is a constant that is 0 for $t_{-1} \leq f_{-1}$ (most metals), or $9((t_{-1}/f_{-1})^2 - 1)$ [-]

H_a : is the hydrostatic stress amplitude on the critical plane [MPa]

λ : is a material parameter dependent on f_{-1} and t_{-1} [-]

The values of N_a, N_m and C_a are defined and calculated the same way as previously with the C&S criterion (using Equations (3-5) and (3-6)). For this criterion, N_m is also 0.

The material of this study is an alloy (hard) metal, and for similar hard metals in Table 2-2, the value of k is 0 based on the values reported for t_{-1} and f_{-1} in the literature. Therefore, the terms with η, N_m and k in the L&M criterion become zero, reducing it to Equation (3-8) below. The λ value of the L&M criterion RHS is calculated using Equation (3-9). It should be noted that this λ value is a uniaxial fatigue limit material parameter which is different from the biaxial nominal stress amplitude ratio (Equation (2-5) previously, and later Equation (4-6)).

$$\sqrt{\left[\frac{N_a}{f_{-1}}\right]^2 + \left(\frac{C_a}{t_{-1}}\right)^2} \leq \lambda \tag{3-8}$$

$$\lambda = [\cos^2(2\delta)\, s^2 + \sin^2(2\delta)]^{0.5} \tag{3-9}$$

$$\delta = 0.5 \cos^{-1}\left[\frac{-2 + \sqrt{4 - 4(1/s^2 - 3)(5 - 1/s^2 - 4s^2)}}{2(5 - 1/s^2 - 4s^2)}\right] \tag{3-10}$$

where: δ : is the angle difference between the critical and fracture planes [°]

s : is the fully reversed torsion/bending fatigue limit ratio t_{-1}/f_{-1} [-]

The value of δ is calculated differently for L&M than for C&S. The above δ angle value (Equation (3-10)) is used in calculating λ (biaxial fatigue limit - parameter) for the L&M criterion. The value of the critical plane angle φ_c for the L&M criterion (for N_a and C_a calculation) is also calculated empirically. For this criterion, the angle δ is used to determine the critical plane angle φ_c from the fatigue fracture plane (φ_f). In contrast, the C&S criterion uses the angle δ calculated with Equation (3-11) below. This is because the C&S and L&M criteria consider similar critical plane methods. However, different correlations were observed between the critical and fracture planes of metals and consequently used to derive the δ equation for each criterion [9].

$$\delta = \left[1 - \left(\frac{t_{-1}}{f_{-1}}\right)^2\right] 3\pi/8 \tag{3-11}$$

The L&M criterion is reported to apply to hard metals, for which the same f_{-1}/t_{-1} fatigue limit ratio range of PPD is assumed. This assumption is also made based on the L&M criterion evaluated in the literature using similar hard metal data sets as the PPD criterion. This criterion applies to the same typical λ values (amplitude ratio) as the other two criteria. The left-hand side

(LHS) of the criterion is designated the equivalent stress symbol $\sigma_{eq;L\&M}$. This stress is also calculated from the critical plane normal and shear stress amplitudes and uniaxial fatigue limits f_{-1} and t_{-1}. The criterion's right-hand side (RHS) considers the material parameter λ for the material.

As can be seen from the three fatigue failure criteria chosen for this study, both uniaxial and biaxial fatigue strength properties are required for their evaluation. Specifically, the fully reversed bending fatigue limit f_{-1}, torsion fatigue limit t_{-1} and the out-of-phase bending-torsion fatigue strength σ_a and τ_a of the test material are required. It is, therefore, best to obtain these material fatigue properties through experimental testing to allow for proper evaluation of the chosen fatigue criteria. These tests are identified and discussed further in Chapter 4.

3.4 Critical Plane Theory

It was previously mentioned in Section 2.4.1 that critical plane fatigue criteria are often preferred over others due to the common use of unique material or uniaxial fatigue strength properties in their models [4]. This way, the material fatigue strength under different uniaxial fatigue conditions is incorporated into a criterion. These criteria are generally reported to have better capability and utility than other criteria types (see Figure 2-5 on pg.18) under multiaxial and specifically out-of-phase fatigue loading conditions.

Some critical plane criteria can provide information on the physical orientation angle of the critical plane itself (e.g., C&S and L&M in the previous section). These models have been reported to correlate this critical plane direction with the macroscopic fatigue fracture plane or crack initiation and growth directions [9, 19, 23]. These criteria, therefore, allow one to consider more appropriate stress quantities (on a micro- or macroscale) with the magnitudes that cause fatigue damage and obtain the orientation of some physical phenomenon like these fatigue failure planes and crack directions.

The argument for the above is that these fatigue criteria have a better physical interpretation of the fatigue damage on a material plane, termed the 'critical plane' [10, 25]. The critical plane is the plane in the three-dimensional stress space where the fatigue damage reaches a maximum. The damage referred to is the combined effect of the shear stress amplitude and the normal stress that acts on the grains and grain boundaries of the material on an arbitrary material plane (see Figure 3-3 to follow). This shear stress amplitude is often termed and calculated (geometrically) as a 'resolved shear stress' of the 'shear stress' that acts parallel to the material plane (oriented at an angle to the component axis and loading axes). The normal stress that acts perpendicular

to this plane is calculated (also geometrically) from the stresses induced in the component due to the external complex multiaxial loading.

For critical plane criteria, the critical plane (where 'damage' is a maximum) is determined by maximising one (or both) of the above stress parameters (shear amplitude and normal). This is done through the 'rotation' of a material plane (with arbitrary initial orientation) in three-dimensional spherical coordinate directions [25]. In most criteria, the shear stress amplitude is the parameter that is maximised, and the corresponding normal stress at that maximum is then used for the damage calculation on the then-identified critical plane. Some criteria from the literature consider the principal stress as the parameter to maximise [5].

The multiaxial fatigue loading condition of this research study (90 [°] out-of-phase bending and torsion with λ = 0.5 [-]) is regarded in the literature to be the most damaging. This is because all material planes (in a component) experience a constant maximum amount of shear stress during the loading cycle (see discussion on previous Figure 3-1 pg.44). Therefore, the identification of the critical plane also requires maximising the normal stress parameter. This normal stress maximisation is partly how the identified criteria in Section 3.3 determine and consider the critical plane that experiences the most damage [8-10]. Their models are accordingly formulated (as inequalities) to, on the LHS, calculate the 'combined effect' of the multiaxial fatigue loading condition on a component, which should be below the 'allowable fatigue limit' on the RHS. That is if no fatigue failure should occur under complex loading. As previously shown for the three criteria, this fatigue limit can be the uniaxial torsion limit, the uniaxial bending limit or a parameter based on both these limits and the fracture plane angle. As a general summary of all the above, the following is therefore evident for the critical plane criteria:

[combined effect ~ damage ~ uniaxial equivalent stress] $\leq$ [fatigue limit ~ uniaxial material fatigue limit]

$\therefore$ [stress condition on the critical plane (LHS)] $\leq$ [presumed multiaxial fatigue limit (RHS)]

The three chosen fatigue criteria (PPD, C&S and L&M) differ mainly in how they define the fatigue damage on the critical plane (LHS) and, secondly, what the fatigue limit is (RHS). Note that they 'determine' the critical plane similarly (maximising stresses). However, they 'define' the combined effect of stresses on it differently.

These multiaxial fatigue criteria differ from other conventional fatigue criteria (e.g., Soderberg or Goodman) in that they physically interpret the maximum fatigue damage on a critically oriented material plane and not only consider the maximum stresses induced in a component (from external loading). Conventional fatigue criteria are also not considered applicable to out-of-phase multiaxial fatigue loading since they assume, using only stress maxima, that the combined stress

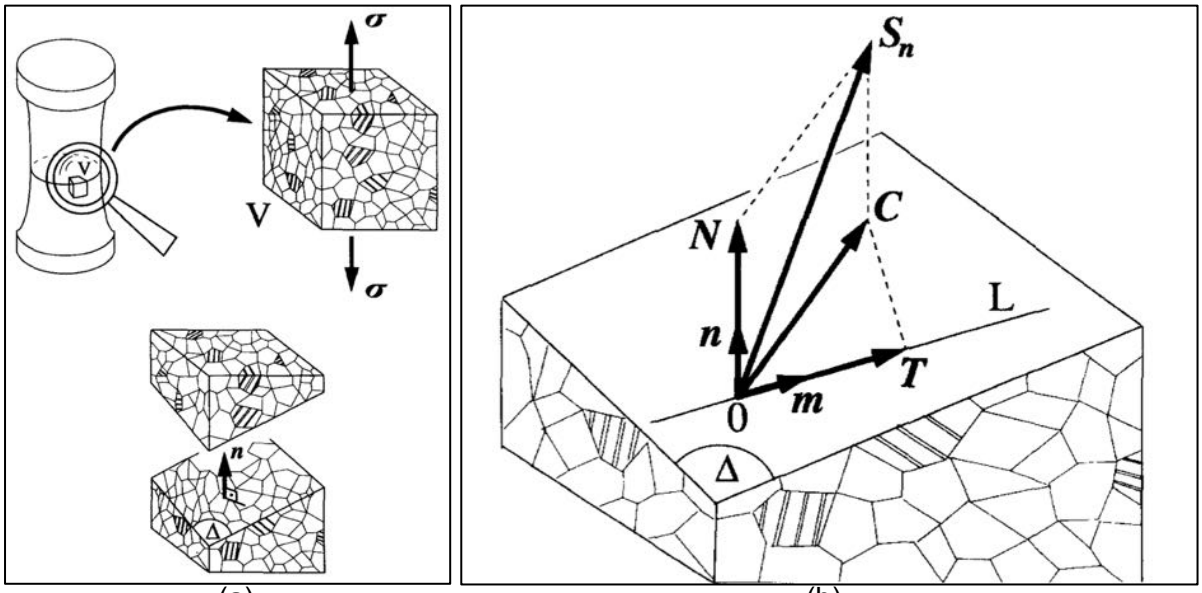
effect in a component is 'in-phase'. Another significant difference between multiaxial fatigue criteria (e.g., PPD) and conventional fatigue criteria is that uniaxial fatigue limit properties (e.g., t_{-1}) are used with the induced multiaxial fatigue stresses (σ, τ). In this way, they consider the different uniaxial fatigue strengths of the material with the multiaxial loading condition. In conventional fatigue criteria (based on VM and Tresca static failure theory), the fatigue evaluation is done for a multiaxial fatigue stress condition (σ, τ), but concerning static tensile material properties (e.g., S_y and S_{ut}). Conventional fatigue criteria, therefore, overestimate the fatigue strength of a material under a complex multiaxial fatigue loading condition. This is because the 'uniaxial equivalent' or 'combined effect' stress they calculate is often higher than the fatigue limit of the material. Fatigue strengths of metals are inherently lower than static tensile strengths.

Example of Critical Plane Approach

The general methodology associated with the derivation or evaluation of a critical plane criterion and the critical plane is discussed next. This discussion uses the Papadopoulos *et al.* [10] criterion derivation and illustrations for the critical plane. Note that the symbols used are restricted to this discussion and for illustration purposes only. The symbols are used within round brackets '()' to emphasise this and not to indicate that they are end-references or notes within the text. The discussion also references how the C&S and L&M fatigue criteria typically consider the critical plane and its relevant stresses. For this, reference can be made to the literature where these criteria were reported [5, 9, 38]. For these criteria, the general notion is to find the material plane (the critical plane) that experiences the maximum normal stress (perpendicular to the plane) and shear stress (parallel to the plane) by varying an arbitrary material plane orientation until the maxima values are obtained. These maximum stresses on the critical plane are functions of the plane angle and the externally applied loading (e.g., σ and τ). For the C&S and L&M criteria, this process (considering geometric plane orientations) is performed empirically using the material uniaxial fatigue limits and the estimation of the fatigue fracture plane angle (based on these limits). For the PPD criterion, the critical plane is considered only during the mathematical derivation of the model (on the mesoscopic scale). The criterion is ultimately expressed in terms of the applied (macroscale) stresses and material uniaxial fatigue limits, specifically for out-of-phase bending-torsion loading.

Regarding Figure 3-3 (a) below, an elementary material volume (V) of dimension 1 [mm^3] is chosen. The volume element size is chosen to be the smallest homogeneous material sample for which all the metal elements and properties are evenly represented. The element is intersected by an arbitrary plane (Δ), through the point (O) of consideration, with orientation defined by a unit-

normal vector ($\boldsymbol{n}$) on it. Later, the maximisation of the normal stress on this plane through the varying orientation of the plane angle (with integration) will result in this plane being designated as the 'critical plane'. Regarding Figure 3-3 (b), the arbitrary stress vector ($\boldsymbol{S}$) is defined on this plane. Along with it, the normal stress vector ($\boldsymbol{N}$) is projected onto ($\boldsymbol{n}$), and its shear stress vector ($\boldsymbol{C}$) is projected onto the plane (Δ). A slip line (L) is defined in the unit normal vector ($\boldsymbol{m}$) direction on the material plane for the material crystals intersected by the plane. The shear stress vector projection onto this slip line is defined as the 'resolved' shear stress vector ($\boldsymbol{T}$). Vector ($\boldsymbol{N}$) is normal to the plane (Δ), and vectors ($\boldsymbol{C}$) and ($\boldsymbol{T}$) parallel to the plane (Δ) are the main concern for further discussion.



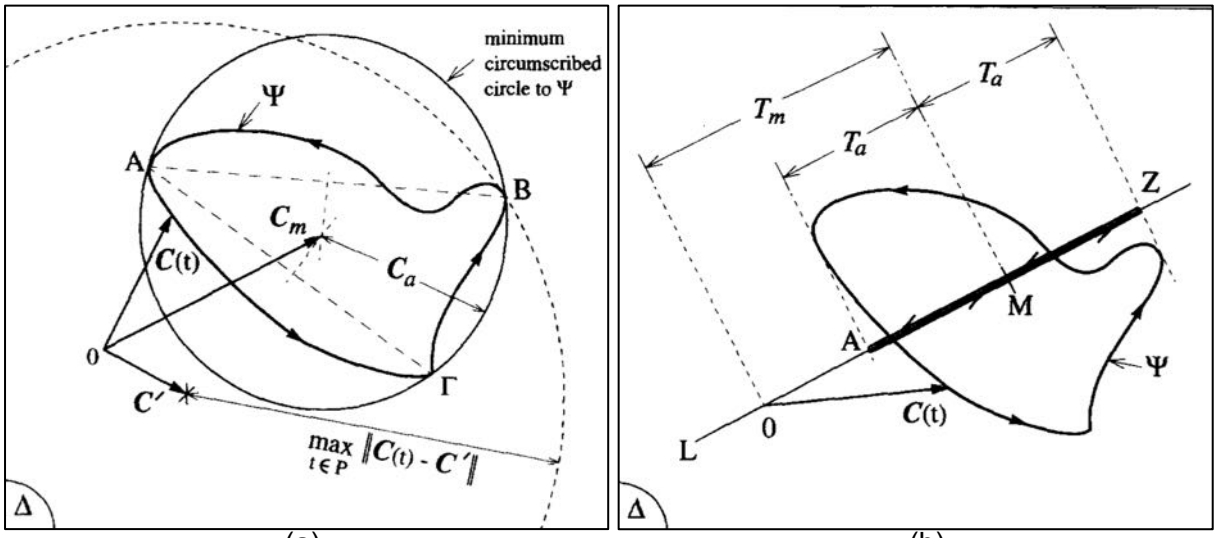
(a) (b)

Figure 3-3: Theoretical critical plane methodology [10] – (a) material volume element and (b) arbitrary material plane and stress definition

During a loading cycle, the shear stress vector in Figure 3-3 (b) varies in both magnitude and direction on the material plane (Δ) as a function of time, as shown in Figure 3-4 (a) below. During this, the tip of the vector ($\boldsymbol{C}(t)$) traces a closed loop (Ψ) which is then circumscribed by a circle intersecting all the maxima points of this loop. The length of the vector ($\boldsymbol{C}$) to the middle point (calculated and described in [10]) of this circle is then uniquely defined as the midrange shear stress (C_m), and the radius of the circle is the shear stress amplitude (C_a). The latter amplitude value is considered the same for the C&S and L&M criteria, but it is geometrically calculated using the previous Equation (3-6) for their evaluations.

During the same loading cycle, the shear stress vector's projection ($\boldsymbol{T}$) on the slip line oscillates between the maxima (A and Z) of the closed loop, as shown in Figure 3-4 (b) below. The resolved

shear stress amplitude value (T_a) and midrange value (T_m) are calculated as half this oscillation and the midpoint length from (O) on the slip line. All the stress values discussed up to this point form the basis of critical plane stress analysis. The specific bending-torsion loading condition stresses are calculated with them, as discussed in Figure 3-5 hereafter.



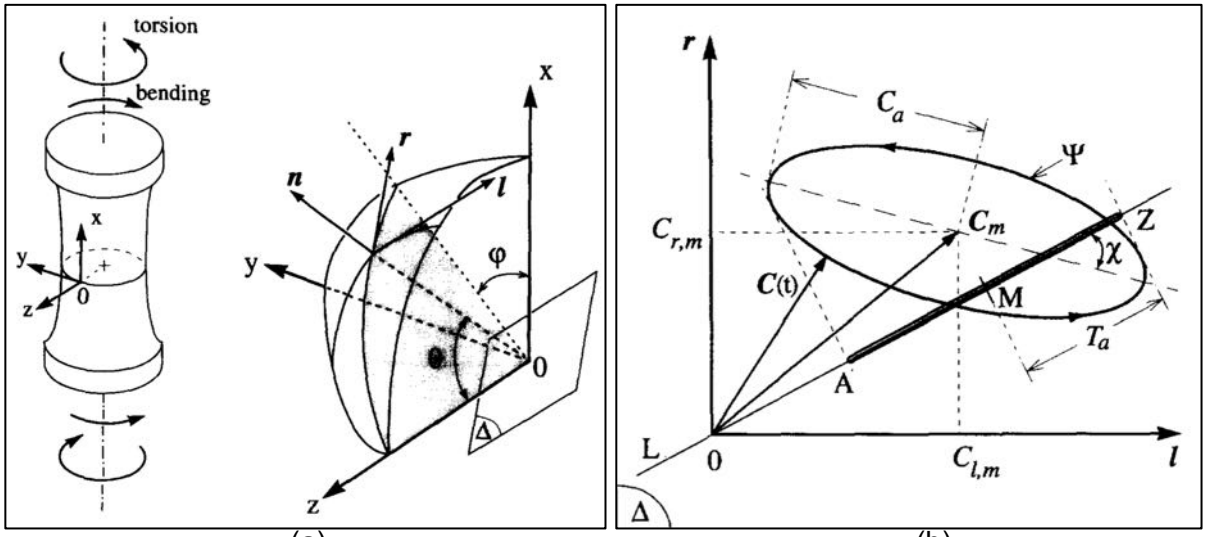
(a) (b)

Figure 3-4: Theoretical critical plane methodology [10] – stress paths and cyclic behaviour during loading on the material plane

For an arbitrary out-of-phase bending-torsion loading specimen and condition shown in Figure 3-5 (a) below, a cartesian coordinate system is defined at the arbitrary point (O) of consideration. This coordinate system intersects the arbitrary material plane (also Δ) with a unit-normal vector ($\boldsymbol{n}$). The stress state relative to this coordinate system (bending around the z-axis and torsion around the x-axis) is then defined by a three-dimensional stress tensor that utilises the applied loading stress values (σ_a, σ_m, τ_a and τ_m), as well as the phase difference (δ). The stresses are then translated into their normal stress (N) counterpart, which acts on the material plane. It is done by applying the spherical coordinate projections of the normal vector onto the xy-plane (forming angle φ with the torsional x-axis) and the z-axis (forming angle θ, for the bending). The (N_a) normal stress amplitude value perpendicular to this plane is similarly determined for the C&S and L&M criteria, but for evaluations, it is also geometrically calculated using Equation (3-5).

A second n, l, r coordinate system is adopted through (O), as shown in Figure 3-5 (a) below. This coordinate system is oriented such that the l and r axes are parallel to the material plane (Δ) and the n-axis in the direction of ($\boldsymbol{n}$). With this second coordinate system, the shear stress ($\boldsymbol{C}$) movement on the material plane is better represented, as shown in Figure 3-5 (b) below. Therefore, the shear stress components are only considered in this frame (existing only along the

l and r axes). However, they also similarly exist in the x, y, and z coordinates frame along all three axes. The shear stress state relative to the new coordinate system is then defined using the orthogonal normal vector to the l and r axes and the same stress tensor above in terms of the applied loading stress values (σ_a, σ_m, τ_a and τ_m), as well as the phase difference (δ). The shear stress vector ($\boldsymbol{C}$) follows an elliptic path for the loading condition under consideration. The eventual translation of this path in terms of the above-applied stresses leads to the shear stress amplitude and midrange value (C_a and C_m) counterparts that act on the material plane. The shear stress amplitude is shown to be the same as the ellipse major-axis length, also designated C_a but a function of φ and θ. The cyclic resolved shear stress on the slip line for this ellipse loading path forms an angle (χ) with this major-axis, and its value is calculated as half the length of the ellipse path projection onto the slip line (L) passing through (O).



(a) (b)

Figure 3-5: Theoretical critical plane methodology [10] – critical plane stresses and paths due to bending and torsion loading

For the eventual PPD criterion derivation, an average value ($< N >$) of the normal stress ($N(\varphi, \theta)$) is calculated in the material volume (V) through integration over (φ and θ, for the $N(\varphi, \theta)$). Where (N) only depends on the orientation of (Δ, identified by φ and θ). The average value is reported as a mean spatial value of (N) over all orientations of the material plane in the volume. Integration and consequent maximisation of this average normal stress (over the loading cycle) on the material plane eventually leads to the second term (after α) in the PPD criterion provided previously in Equation (3-3).

For the eventual PPD criterion derivation, the root means squared value (T_n) of the previously resolved shear stress amplitude value ($T_a(C_a(\varphi, \theta), \chi)$) on the material plane (Δ) is calculated

through integration over (χ). This is done first since the PPD criterion considers the average value of (T_a) in the material volume (V), and for it, (T_a) not only depends on the orientation of (Δ, identified by φ and θ) but also the direction of (L) on (Δ). The slip line is angled at (χ) from the material plane shear stress vector's elliptic path major-axis ($C_a(\varphi,\theta)$) as in Figure 3-5 (b), also known as the shear stress amplitude (C_a) on the plane. After this, the root mean square value ($\sqrt{< T_n^2 >}$) is then calculated through integration over (φ and θ, for the $C_a(\varphi,\theta)$ and $C_b(\varphi,\theta)$ ellipse axes) in the material volume by varying the orientation of the material plane in the volume. Integration eventually leads to the first square root term in the PPD criterion, provided previously in Equation (3-3). Through this analytical integration (to φ and θ) of the last n, l, r-coordinate system stress components in $C_a(\varphi,\theta)$ and $C_b(\varphi,\theta)$, which are also functions of the phase difference (δ), the phase difference (δ) ultimately disappears from the criterion. From this, the claimed independence of the phase difference between bending and torsion of the PPD fatigue criterion.

Due to the PPD criterion's derivation on the critical plane (on the mesoscopic scale), it is therefore evident, as in Equation (3-3), that it is not required to explicitly determine the critical plane to allow evaluation of the criterion. The criterion is expressed directly in terms of the applied biaxial out-of-phase stresses after considering the critical material plane and its stresses. On the other hand, the C&S and L&M criteria are expressed directly in terms of critical plane stresses as in Equations (3-4) and (3-8). To determine these stresses, the criteria both determine the orientation of the critical plane through an empirical method that considers the material fracture plane angle. This angle is determined as a material parameter (dependent on the uniaxial fatigue limits of the material) and the maximisation of the normal stress amplitude value on the material plane by varying its orientation throughout a loading cycle.

All three criteria, therefore, maximise the normal stress component to obtain the critical plane. On this plane, the (N_a) and (C_a) stresses that would cause microscopic grain plastic strain are then utilised. Due to the resolved shear stresses acting along the grain slip directions (e.g., slip line (L)) and boundaries on the plane, fatigue crack initiation and, thus, failure is then appropriately taken into account [10].

3.5 Conclusion

This theory chapter consisted of three main parts. The first section discussed the theory associated with in and out-of-phase multiaxial fatigue loading. For this, Mohr stress circles were used for an arbitrary 90 [°] out-of-phase bending and torsion (λ = 0.5 [-]) fatigue loading condition to show the rotating principal stress phenomenon that is caused by a phase difference between the biaxial loading components. This phenomenon is also typically used to define and illustrate the difference between the proportionality of the two main types of multiaxial fatigue loading. A short discussion was also provided on why a conventional VM stress calculation cannot be used to describe the equivalent biaxial stress condition or effect of the chosen loading condition.

The second part provided and discussed the multiaxial critical plane stress-based fatigue failure criteria that were selected for evaluation of the experimental fatigue data in this study (as discussed in the experimental methodology in the next chapter). For this, the criteria models, their applicability and overall calculation procedures were discussed specific to the loading condition and material in this study. From these models, the required uniaxial fatigue limits for evaluation of the criteria were also identified. This, in turn, dictated which additional experimental tests had to be performed with the out-of-phase biaxial fatigue tests.

The chapter concluded with a discussion of the relevant critical plane theory (applicable to the above criteria) and an example using the derivation of PPD's criterion. The general methodology in the literature to obtain the critical plane and the multiaxial fatigue stresses on it was also discussed. The next chapter discusses the experimental methodology for all the material strength and fatigue strength tests and criteria evaluations performed in this research study.

CHAPTER 4 – EXPERIMENTAL METHODOLOGY

4.1 Introduction

In Chapter 1, it was discussed that complex multiaxial fatigue loading conditions often cause difficulty in the design of metal mechanical components. Under these loading conditions (often out-of-phase), it is required to implement an appropriate fatigue failure theory to assess and predict the component's fatigue strength or resistance. Conventional (in-phase) fatigue theories are often deemed less appropriate for these purposes, and multiaxial fatigue failure criteria are therefore required. The literature reports many of the available fatigue failure criteria typically used for these evaluations (Section 2.4.1). These criteria are derived, tested and validated using the multiaxial fatigue data of metals (Section 2.5) under various loading conditions (Section 2.3) reported in the literature. However, based on this study's loading and material limitations, it was shown that these fatigue data sets often have very little useable data (Sections 2.5 and 2.6). The literature also argues that many of these data sets are insufficient and sometimes incorrect. Therefore, the fatigue criteria based on these data sets are questioned regarding their fatigue limit evaluation correctness and accuracy.

To use or test the applicable multiaxial fatigue criteria (Section 2.4.2) requires a complete and verified material and fatigue strength data set. That is, the criteria require both uniaxial and multiaxial fatigue strength properties to allow for the evaluation of the models under a relevant multiaxial fatigue loading condition on a specific material. The uniaxial fatigue strength properties are required due to the criteria formulated with these properties as part of their models. Supplementary to these properties, fatigue criteria often use basic tensile material properties as part of their evaluations or post-processing of their fatigue strength predictions (Section 2.4.3). Since the fatigue data sets from the literature have little data for proper and meaningful fatigue criteria evaluations in this study, it was required to perform new and comprehensive experimental material strength tests. These tests included monotonic tensile, uniaxial and out-of-phase biaxial fatigue tests on a single ferrous metal.

Section 4.2 identifies and discusses the chosen experimental biaxial fatigue loading condition and test material for these tests. This material choice was based on the chosen fatigue criteria most applicable to this study, and their models can be referenced in Section 3.3. Based on these selections, only usable fatigue data sets from the literature are provided. The experimental testing and measurement equipment required for the above material tests are then identified and discussed in Section 4.3. With this, the required secondary verification of the principal measurement instrument, the DANTEC Dynamics Q400 Digital Image Correlation (DIC) system,

is also discussed in Section 4.3.2.2. This verification of the DANTEC ensured that the required measurements with it on the relevant fatigue test benches could be trusted. These DANTEC verification measurements were made during the monotonic tensile tests that were performed with the MTS Extensometer.

In Section 4.4, the additional experimental considerations are discussed for the tests performed. In the first part, Section 4.4.1 discusses all the tensile, uniaxial and biaxial fatigue specimen considerations for material, geometry and surface finish. Section 4.4.2 discusses all the experimental loading considerations made for each test bench. These considerations merely involved loading calibrations and referencing the relevant calibration certificates for most test benches. The verification and loading characterisation measurements with the DANTEC system are specifically discussed for the uniaxial torsion and the biaxial bending-torsion fatigue test bench. For these displacement measurements, it was also required to perform the necessary static finite element method (FEM) simulations for the theoretical displacements of the specimens under the relevant loading conditions. These measured and simulated displacements were then appropriately utilised to obtain the induced fatigue stresses in a specimen. Section 4.4.3 after this discusses the experimental fatigue failure and limit definitions used for the tests.

Section 4.5 discusses the specific experimental test and measurement (with the DANTEC) methodology of the biaxial bending-torsion fatigue test bench. Section 4.6 then discusses the data processing methodology. This discussion involves the experimental stress calculations (Section 4.6.1), the fatigue limit strength estimations (Section 4.6.2), and the uncertainty analyses (Section 4.6.3). Section 4.7, which follows, ultimately discusses the methodology for fatigue data and failure criteria evaluations and comparisons. For this, the chosen fatigue criteria (Section 4.2.2) and the usable literature data (Section 4.2.4) are utilised along with the experimental material strength data obtained from testing in this study.

4.2 Specific Experimental Selections and Motivations

Chapter 2 previously identified and discussed the multiaxial fatigue loading (Section 2.3), fatigue criteria (Section 2.4) and the materials (Section 2.5) that are reported in the literature. This section aims to identify and motivate the chosen multiaxial fatigue loading condition, criteria and test material for this study. As part of this, the eventual usable literature data is also identified based on the criteria and material choices. Identifying the required material strength properties for the chosen criteria contributed to the choice of test and measurement equipment in Section 4.3 hereafter.

4.2.1 Experimental Biaxial Fatigue Loading Condition

The loading condition chosen for multiaxial fatigue testing in this study is 90 [°] out-of-phase bending-torsion with a nominal stress amplitude ratio λ = 0.5 [-]. This loading condition was explicitly limited to β = 90 [°] and λ = 0.5 [-] during the multiaxial fatigue data discussion in Section 2.6, based on literature observations and the study limitations. The reasons for this demarcation of the loading are provided on pg.33. The motivation for considering this loading condition is, however, discussed here.

The chosen biaxial load condition is regarded as one of the literature's most damaging normal-shear fatigue loading combinations. This is because all the material planes in a component experience a constant maximum amount of shear stress [2, 12, 35]. Cyclic out-of-phase bending-torsion is a general loading condition experienced by machine components like crankshafts and axles. This loading condition is generally reported in the multiaxial fatigue literature, where experimental tests and fatigue failure criteria are considered for analyses, reviews, and comparisons. A biaxial load condition is deemed complex enough to differentiate between and classify multiaxial fatigue criteria based on their prediction accuracy [10]. Therefore, experimental testing using this loading condition was satisfactory. It should be noted that in-phase biaxial bending-torsion 'testing' (β = 0 [°] and λ = 0.5 [-]) was not performed in this study. Only in-phase literature fatigue 'data' was considered for completeness purposes with the relevant out-of-phase data (as later in Table 4-2).

For the identified loading, it is recommended in the literature that fully reversed, sinusoidal and synchronous biaxial load components are considered for experimental testing. Synchronous sinusoidal loading is easier to induce and analyse experimentally. Fully reversed loading also allows the exclusive consideration of the biaxial loading condition's effect (e.g., single phase difference and stress amplitude ratio) on the material fatigue strength without, for example, requiring consideration of the reported influences of a midrange load [10, 81]. The chosen loading condition ultimately assisted in selecting the most applicable fatigue failure criteria, as discussed in the next part of this section.

4.2.2 Multiaxial Fatigue Criteria

The multiaxial fatigue failure criteria applicable to the specific bending-torsion loading condition motivated above (e.g., β = 90 [°] and λ = 0.5) were selected from the literature in Section 2.4.2 (see Table 2-1 on pg.20). The three (3) critical plane criteria most applicable for evaluation with this study's experimental fatigue test data are provided in Table 4-1 below. These criteria were

selected based on the discussions in Section 2.4.2 (below Table 2-1). In this, ease of use and completeness of criteria reporting in the literature were determining factors.

Table 4-1: Selected multiaxial fatigue failure criteria

Criterion		Year	References
Critical Plane Criteria	Papadopoulos (PPD)	1994/1997	[4, 8, 9, 10, 21, 25]
	Carpinteri and Spagnoli (C&S)	2001	[4, 9, 19, 38, 40]
	Liu and Mahadevan (L&M)	2005	[4, 9, 21]

The three criteria above do not apply to all the multiaxial fatigue loading conditions or materials generally reported in the literature. However, they are derived for and evaluated with out-of-phase (and in-phase) biaxial bending-torsion loading and are predominantly used for hard metals. The criteria also do not require any determination of 'additional' or 'unknown' material strength parameters or model coefficients to allow for their evaluation. The equations and models of these criteria are provided and discussed in the theory Section 3.3.

As identified from the criteria models in that section, both the uniaxial and biaxial fatigue strength properties of a hard metal are required for their evaluation. Specifically, the fully reversed bending fatigue limit f_{-1}, torsion fatigue limit t_{-1} and the out-of-phase bending-torsion fatigue strength (σ_a and τ_a) properties of the material. It was, therefore, best to obtain all these material fatigue properties through experimental testing to allow for proper evaluation of the chosen criteria. As part of the experimental fatigue testing on an appropriate material (identified in the next part), it was also required to perform monotonic tensile testing. Additionally, it was decided to include the fully reversed axial fatigue limit s_{-1} testing on this material for completeness and to serve as a secondary reference for the experimental bending fatigue limit. These tests and the equipment used for them are identified and discussed in Section 4.3.

The reason for performing these experimental tests was not only because an appropriate evaluation of the criteria was required. It was also because the available fatigue data from the literature, based on the above-chosen loading condition, was shown to be limited for hard metals to which the chosen criteria apply. This lack of usable literature data is shown in the last part of this section, based on the test material selected in the next part.

4.2.3 Experimental Test Material

This research study focussed on ferrous metals since they are more commonly used in the industry and have the highest presence in the relevant multiaxial fatigue literature. Specifically,

only ductile and hard steels were considered due to the general applicability of fatigue criteria to these metal types (see Table 2-1 and discussion) and corresponding data sets in the literature. Steels that are ‘typed’ as ‘very hard’ metals (e.g., AISI 4330V) and ‘brittle’ metals (e.g., cast irons) often have much less consideration and applicability to criteria and were therefore excluded along with the non-ferrous metals that were identified in the literature. Some of the applicable steels identified (see Table 2-2 on pg.27) are referenced more than others, reflecting the interest and importance of considering them for experimental testing. However, these steels are not always classified as ‘hard metals’ applicable to or typically evaluated with the chosen criteria (in the last part, Table 4-1).

Since the purpose of this study was not to perform an experimental fatigue strength investigation using multiple metals or metal types, it was deemed appropriate to focus on a single steel (as in limitations). A complete experimental evaluation of this steel would be more appropriate than a generic evaluation of many, which is often what review and comparative studies do in the literature. Time constraints and the requirement for this complete investigation also contributed to this material limitation. Therefore, it became evident that an appropriate hard steel had to be selected for the required experimental testing.

For this, the choice was made to test AISI 4140 / EN19 steel, which is typically classified as a hard metal. EN19 steel is one of the generally considered steels in the literature [9, 10, 40, 45]. This steel had adequate literature data for reference for mechanical and uniaxial fatigue strength properties. However, new and complete tensile and fatigue strength tests were required for the chosen material because of transcription errors, omissions, unreported experimental uncertainty, and tensile properties in the data sets. The tests were done to ensure accurate, valid and reliable material properties are obtained and used for criteria evaluations and comparisons.

EN19 steel is a general choice of material for most moderate to heavy engineering applications. It is typically used for crankshafts, axles and presses due to its high strength (under fatigue and torsional loading), hardenability (for punches and dies), ductility and shock resistance under severe loading conditions. A specific material condition (e.g., heat treatment) was not preferred for the test material due to it not being typically reported in the literature. However, the material was ultimately purchased in the T-condition of heat treatment (commercial condition) and adhered to the limitation mentioned above on maximum strength (see Figure M-2). Any other specific material condition effects on the strength were presumed to be accounted for by the performed monotonic tensile and uniaxial fatigue tests.

4.2.4 Serviceable Fatigue Data

The fatigue data reported in the literature was discussed in Sections 2.5 and 2.6 (see Figure 2-7 pg.31 and Figure 2-9 pg.36). From this, the most applicable data sets were identified (see Figure 2-8 on pg.33 and Figure 2-10 on pg.37) based on the loading condition and material limitations of this study, as well as the data set applicability for the fatigue criteria from the literature (Table 2-1 on pg.20). Since only EN19 (T-condition) alloy steel was chosen for this study's experimental testing, the correspondingly applicable data from the literature reduced to that shown in the normalised S-N data graphs of Figure 4-1 and Figure 4-2 below. Therefore, the usable literature data for comparison and criteria evaluations were less than initially obtained from the literature.

That is, of the original eighteen (18) uniaxial and six (6) multiaxial fatigue data sets, only three (3) and one (1), respectively, remained. Some of the EN19 axial fatigue limit data of JL (from Figure 2-8) was also eliminated for Figure 4-1 below. This was due to the material S_{ut} values being larger than what was deemed applicable (>1300 [MPa]) for comparison with the chosen test material, which was not as tough (as from the material certificate in Figure M-2). For the S-N graphs shown below, the Nishihara and Kawamoto (NK) data (for MS and HS materials) was finally disregarded from the uniaxial and multiaxial data sets due to the reasons provided and discussed earlier in Section 2.6 (see pg. 33) from [21, 56]. As stated in that section, the NK data was only considered in the first place for completeness and its frequent reference in the relevant literature.

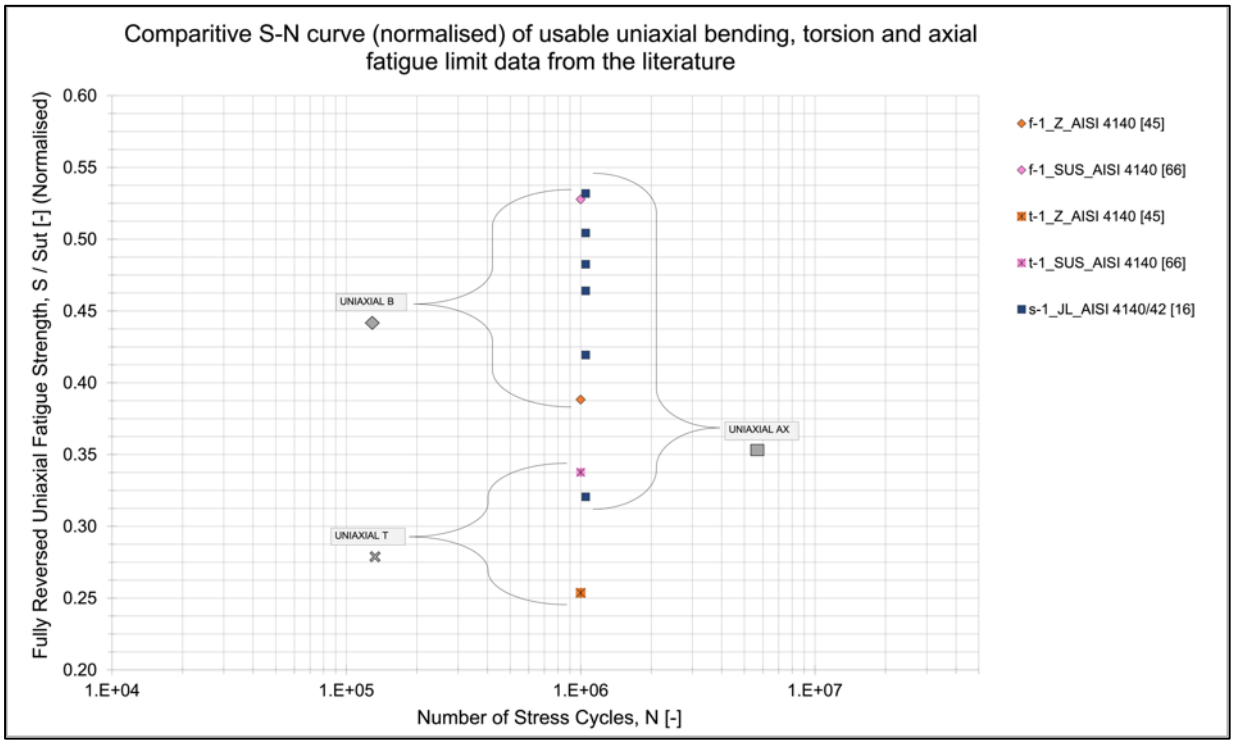


Figure 4-1: Comparative S-N curve (normalised) – usable uniaxial bending, torsion and axial fatigue limit data from the literature

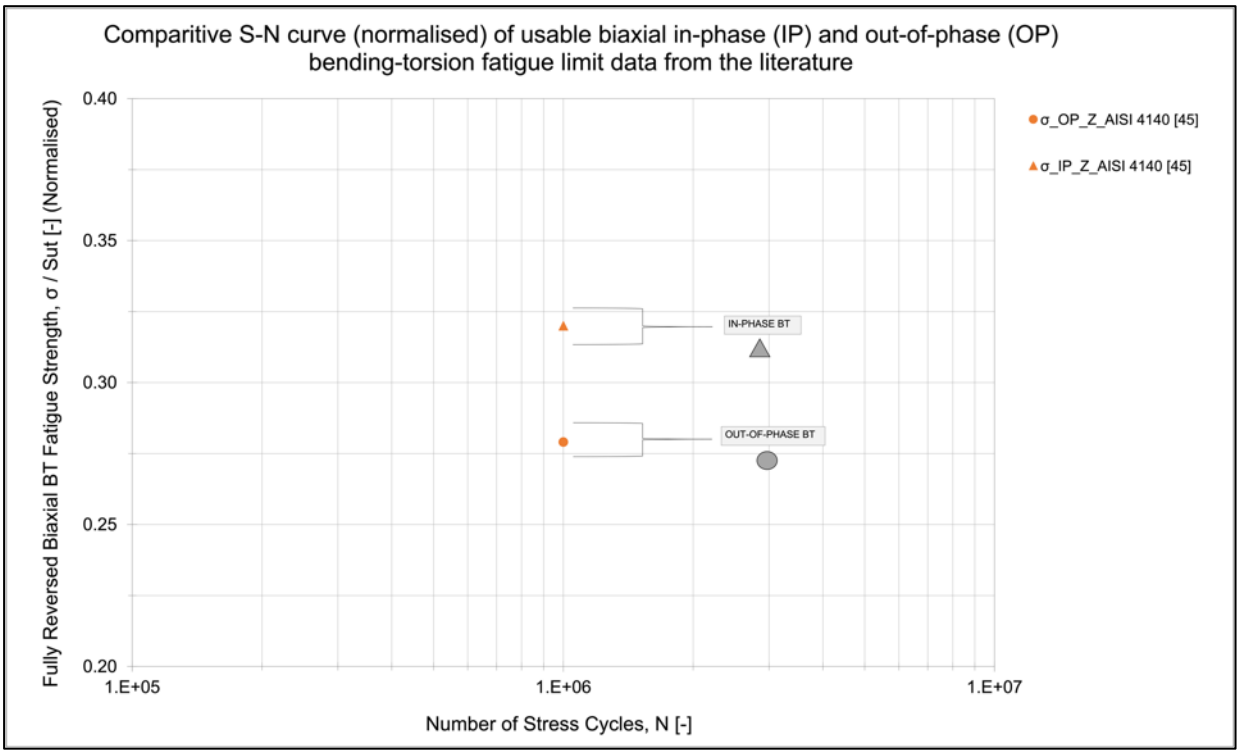


Figure 4-2: Comparative S-N curve (normalised) – usable biaxial in-phase and out-of-phase bending-torsion fatigue limit data from the literature

The Susmel (SUS) and Li *et al.* (JL) uniaxial fatigue data and the Zenner *et al.* (Z) multiaxial fatigue data (and tensile properties where available) that were ultimately used for comparison with the experimental test results obtained in this study are summarised from the S-N graphs above, in Table 4-2 on the next page. The Z data was the only relevant multiaxial fatigue data from the literature, and it was also used for evaluations with the chosen fatigue criteria for comparison purposes. For all three data sources in Table 4-2, the defined fatigue limit is reported as 10^6 cycles for both the uniaxial and biaxial fatigue limit values (also seen in the graphs above). The data and criteria comparisons mentioned are ultimately provided and discussed in the results (Section 5.2).

Table 4-2: Summary of usable monotonic tensile and fatigue data for EN19 steels from the literature

AISI & SAE: 4140/42 BSI & EN: BS709M40 EN19		Used in ref: [6, 16, 31, 66], and [1, 9, 10, 39, 40, 66] from [45] †									
		Monotonic Tensile Properties			Uniaxial Fatigue Limit Properties			Biaxial Fatigue Limit Properties			
Ref. for values Fatigue limit def: 10^6		E [GPa]	S_{ut} [MPa]	S_y [MPa]	t_{-1} [MPa]	f_{-1} [MPa]	s_{-1} [MPa]	σ_a [MPa]	τ_a [MPa]	β [°]	λ [-]
(Z) Zenner *et al.* [45] †	4140	-	1025	888	260	398	-	328	157	0°	0.48
								286	137	90°	0.48
(SUS) Susmel [66]	4140	-	996	-	336.3	525.7	-				
(JL) Li *et al.* [16]	4140	207	1042.9	928.9	-	-	437.4				
	4140	203	1247.3	1157.5	-	-	601.9				
	4140	207	1239.5	1167.1	-	-	575.2				
	4140	200	1075	-	-	-	571.7				
	4142	200	1060	-	-	-	339.8				
	4140	207	938	848	-	-	473.1				

4.3 Experimental Test and Measurement Equipment

4.3.1 Test Equipment

Tests had to be performed on four different test benches to obtain the required experimental material tensile and fatigue strength properties of EN19 (T-condition) alloy steel. Table 4-3 summarises the tests, the required result (property) and the relevant test benches used for testing. These test benches are discussed in this section, and reference can be made to Appendix A for elaboration. All experimental fatigue tests were performed with fully reversed loading (R = -1).

Table 4-3: Experimental material strength tests performed in this study

Identifier	Test	Required Result(s)	Test Bench
TEN	Monotonic tensile	S_{ut}, S_y, E	MTS Landmark
AX	Uniaxial axial fatigue (reference for B)	s_{-1}	MTS Landmark
B	Uniaxial bending fatigue	f_{-1}	TERCO MT205G
T	Uniaxial torsion fatigue	t_{-1}	Torsion fatigue test bench (new)
BT	Out-of-phase biaxial bending-torsion fatigue	σ_a, τ_a	Biaxial Fatigue Test Bench M1 – Bending-Torsion (new)

4.3.1.1 Monotonic Tensile / Uniaxial Axial Fatigue

The *MTS Landmark tensile test system* was used to perform monotonic tensile (TEN) tests and fully reversed axial (AX) fatigue tests to obtain S_{ut}, S_y, E and s_{-1}. This machine, shown in Figure 4-3 below, has a 90 [kN] axial tension-compression load rating, an 85 [mm] actuator displacement ability and a cyclic loading frequency capability of up to 100 [Hz]. Specimens are gripped with the 647.10 vee-serrated clamping wedges (5.8-11.9 [mm]) in the 647 hydraulic wedge grip heads. The machine is controlled by the dedicated MTS FlexTest® 4.0 controller and the relevant MTS TestSuite® software in both experimental test types. The calibration status of the MTS test system was confirmed before testing. These calibration certificates are provided in Figure A-2 and Figure A-3, with the detail on the MTS in Appendix A1.



Figure 4-3: MTS Landmark servo-hydraulic tensile test system

Although this s_{-1} is not explicitly required for evaluating the chosen fatigue criteria; it was incorporated into the test program. That is, to serve as a secondary reference for the bending fatigue limit f_{-1} test results because of the age and associated loading uncertainty on the bending fatigue test bench, shown next.

4.3.1.2 Uniaxial Bending Fatigue

The fully reversed bending (B) fatigue tests for f_{-1} were done on a *rotating cantilever bending fatigue test bench*. This machine, shown in Figure 4-4 below, has a 300 [N] maximum load cell capacity and 50 [Hz] maximum test speed. The cantilever force is exerted on the tip of the specimen through a linear spring load cell (see Figure H-14) with an analogue force scale engraved on it with a 5 [N] maximum resolution. A microswitch maintains contact with the load cell mount (black bearing holder) during a test, and when the specimen fails, the load cell pulls up and away from this switch, stopping the motor. The motor shaft is connected to a mechanical cycle counter with a plastic tube which records the direct cycle count (1:1 ratio) for each test. For this bench, it was required to perform a load cell calibration to ensure the correct cantilever force was applied to each tested specimen. This calibration is discussed later in Section 4.4.2 and provided with more elaboration on the test bench in Appendix A2.

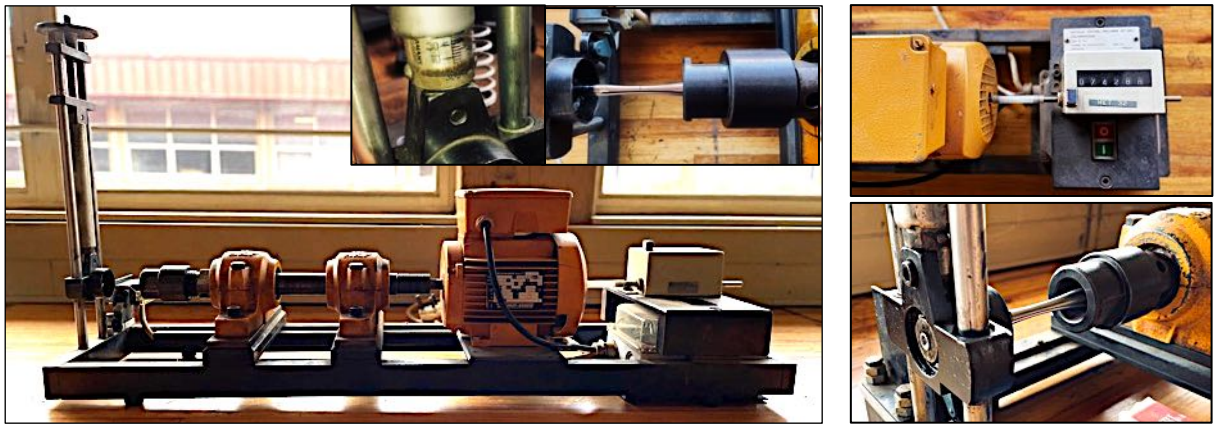


Figure 4-4: TERCO MT205G rotating cantilever bending fatigue test bench

4.3.1.3 Uniaxial Torsion Fatigue

The fully reversed torsion (T) fatigue tests for t_{-1} were done on a newly developed *torsion fatigue test bench* in the laboratory [82]. This machine, shown in Figure 4-5 below, exerts a fully reversed torsional moment around the specimen's longitudinal axis through centrifugal imbalance forces. These imbalance forces are induced by the rotating bilateral wheels, which have machined mass pieces fastened to them (180° apart) at a specific radial distance from the shaft rotation axis. These forces act at a set perpendicular distance (moment lever) from the specimen's longitudinal axis, which translates to the sinusoidal twisting of the specimen attached to the bottom of the head stem. The magnitude of the centrifugal forces can be altered by changing the mass pieces or radial positions on the rotating wheels. The test speed (maximum 50 [Hz]) can also be adjusted.

However, it is dictated by the specimen diameter and material strength. An electric motor drives the wheel shaft with a timing belt, and the motor speed is controlled by the connected variable speed drive (VSD). A relay timer connected to the VSD records the elapsed time of each test (cycle count), and it is stopped when the microswitch (under the wheel shaft, beside the head) is triggered upon specimen failure. Verification measurements of the induced torsional loading on a specimen were required for this test bench. These are discussed in Section 4.4.2 and also provided in Appendix H4. Elaboration on this fatigue test bench is provided in Appendix A3.



Figure 4-5: Torsion fatigue test bench

4.3.1.4 Out-of-phase Biaxial Bending-Torsion Fatigue

The fully reversed bending-torsion (BT) fatigue tests for σ_a and τ_a (out-of-phase biaxial fatigue strengths) were done on a newly developed *biaxial fatigue test bench* in the laboratory [28]. This machine, shown in Figure 4-6 below, induces fully reversed 90° out-of-phase bending and torsion moments on the specimen through centrifugal imbalance forces acting at respective moments in time. These imbalance forces are generated by mass pieces fastened to the rotating bilateral wheels at a specific radial position (180° apart). The forces act at a set distance (moment lever) around the specimen's longitudinal axis (torsion) and around the axis perpendicular to the test zone (bending) at different positions of the mass pieces during wheel rotation. The magnitude of the induced centrifugal force can be altered by changing the mass pieces or their radial positions on the rotating wheels. Adaptation of the test speed (maximum 50 [Hz]) can also be made. However, it is dictated by the specimen diameter and material strength. An electric motor drives the wheel shaft with a timing belt from the bottom shaft below the specimen mount, and the VSD controls the motor speed. A relay timer connected to the VSD records the elapsed time of each

test (cycle count), and it is stopped by the wheel shaft triggering either of the microswitches (besides the head) upon specimen failure. This bench was also required to make verification measurements for the induced biaxial loading on a specimen. These measurements are discussed further in Section 4.4.2 and also provided in Appendix H5. More detail on the biaxial fatigue test bench is provided in Appendix A4.

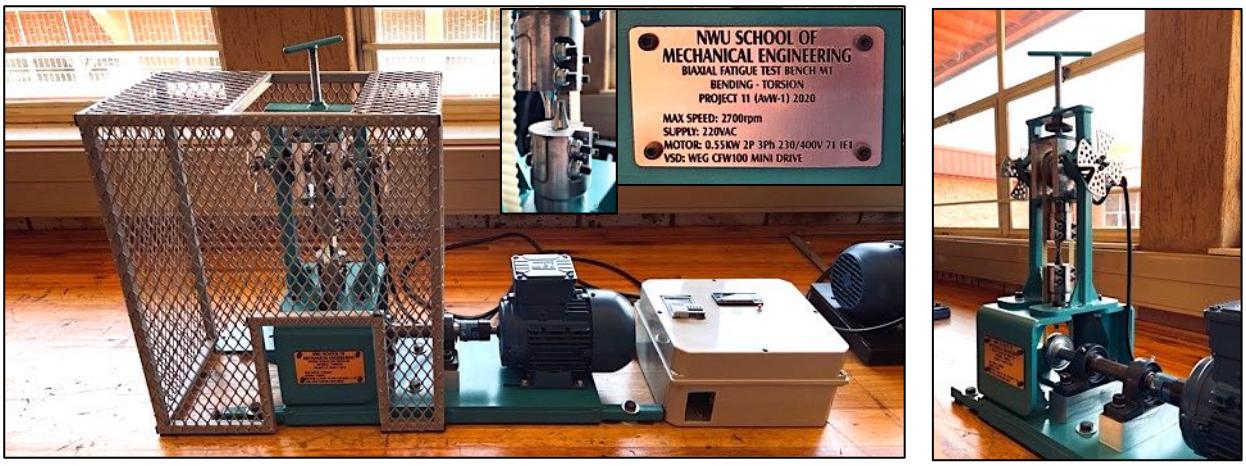


Figure 4-6: Biaxial Fatigue Test Bench M1 – Bending-Torsion

4.3.2 Measurement and Evaluation Equipment

For the above-mentioned experimental test benches, it was subsequently required to perform the necessary test measurements to ensure the correctness and accuracy of test data. It included the measurement of specimen diameters, load-inducing components and specimen displacements. The measurement equipment utilised for these purposes is identified below concerning their place of use. Reference can be made to Appendix B for further discussion, description and illustration of these measurement instruments.

4.3.2.1 General Measurement Equipment

Pre-Test Measurements

All experimental test specimen diameters were measured after surface polishing with the ***Mitutoyo Absolute digital vernier*** (see Appendix B1). The vernier was used due to some complex specimen geometry (hourglass test zones). The thin vernier jaws allow for more localised measurement of diameters at marked test zone centre positions. The vernier was used to measure these test zone centre positions (expected break lines), the cantilever maximum stress

positions and other experimental measurement positions (for cameras) on the relevant specimens. The digital vernier measurement accuracy was verified against a SMIEC micrometre, as discussed in Appendix B1. The measured test specimen diameters are reported in Appendix D1 through D5.

Mass measurements were made using the ***Sartorius BP110S and PRW30++ microscales*** (see Appendix B2). These measurements were made for the calibration mass pieces (B bench), the centrifugal mass pieces (T and BT benches) and the lever-head mass (BT bench). Secondary calibration mass pieces were used to confirm the microscale measurement accuracies informally. Because the scales were 'zeroed' before each measurement, a full calibration for each scale was deemed unnecessary. All measured masses are reported in Appendix E1 through E3.

The ***Aptina CMOS digital camera microscope*** (see Appendix B8) was used to take illustrative images of some arbitrarily chosen test specimens and their prepared surfaces and test zone conditions. These images were taken for each of the specimen types. These images are provided in Appendix C1 through C5 for the experimental test specimen types.

In-Test Measurements

At the start and end of each monotonic tensile (TEN) test, room temperature measurements were made using the ***Fluke 52 K/J thermocouple thermometer*** (see Appendix B3) with a K-type thermocouple probe. These measurements were made since tensile properties are customarily reported at an average temperature [14]. They are also often on material certificates (see Appendix M). Temperature measurements were not primarily required. However, they were recorded for completeness of the tensile test results. The thermometer was recently calibrated for other high- and low-temperature applications in the laboratory. It was therefore considered accurate enough for use in the general room temperature ranges. These measurements are reported in Appendix J1, and the procedure for them is discussed in Appendix B3. This thermometer was also used to measure the room temperature during the digital vernier measurement verification mentioned above. For this, it was shown at an average room temperature of 26.85 [°C] that the digital vernier accurately measures the size of a micrometre calibration cylinder. A negligible 0.12 [%] difference between the vernier and micrometre measurements was obtained (see Table B-1).

Tensile specimen gauge extension measurements were made using the ***MTS – 634.31F-24 extensometer*** (see Appendix B4) on the *MTS Landmark tensile test machine* (Figure 4-3). The extensometer gauge length was extended to a 25 [mm] gauge length setting to cover the

recommended 70-80 [%] of the 32.8 [mm] tensile test specimen gauge length. The extensometer calibration status was confirmed before testing and measurement, and the certificate can be referenced in Appendix B4. Measurements made with the extensometer had a two-fold purpose. One was to obtain the experimental Elasticity Modulus E of EN19 (T-condition) alloy steel using the procedure discussed in Appendix H1.2. The results for E are reported in Appendix J1. The second purpose of these measurements was to compare the extensometer (contact measurement) and the DANTEC (identified in Section 4.3.2.2 to follow) based on the measured specimen extensions. This comparison was made as the secondary verification for the DANTEC system (non-contact measurement), also used in other (T and BT) test measurements. The measurement procedure for the tensile specimens with this camera system is discussed in Appendix H1.3.

Bending (B) fatigue test bench speed measurements were taken at the start of each test using the ***Lutron DT-2234BL digital tachometer*** (see Appendix B5). These measurements were primarily used to confirm the test speed and estimate each test's duration, and the testing speed did not influence the B test loading conditions. A short description of the tachometer measurement procedure is provided in Appendix B5, and the measured speeds are reported in Appendix J3 for each specimen. The experimental fatigue cycle count measurements of each B fatigue specimen were made with the mechanical cycle counter on the test bench.

Fatigue life cycle counts for the torsion (T) and bending-torsion (BT) fatigue tests were obtained with the ***RS Pro EZM-3735 Digital Timer Controller*** and the ***WEG CFW100 Mini Drive (VSD)*** (see Appendix B7) connected to each test bench, respectively. The timer recorded the elapsed test time from the start to the end of each test. The speed for each test was set and maintained by the VSD, which was also connected to the timer. The total elapsed time and the test speed were then utilised for each fatigue cycle count calculation (until failure or fatigue limit was reached).

Post-Test Measurements

The axial (AX) fatigue and bending (B) fatigue specimen fracture-zone diameters and positions were measured after testing by again using the ***Mitutoyo Absolute digital vernier***. The measurement was done for the axial fatigue specimens since fatigue failure was not confined to a specific area (e.g., with the hourglass-shaped B, T or BT specimens) due to the somewhat lengthy and cylindrical-shaped gauge areas. The fatigue failure position was measured for the bending fatigue specimens due to some specimens that failed at an offset position along the cantilever length other than that marked in the hourglass test zone before testing (see Figure

H-14). The diameters of these B specimens were also measured at this failure position. Re-measuring the failure point diameters and cantilever failure positions of the AX and B specimens that failed in fatigue ensured accurate fatigue stress calculations. The specimens this was done for are marked in orange in the measured diameter tables provided in Appendix D2 and D3.

It should be noted that post-test fracture-zone diameter measurements of the failed tensile (TEN) specimens, the torsion (T) and the bending-torsion (BT) fatigue specimens were not measured. That is because the tensile specimens inherently experienced ductile failure deformation at the failure location (sometimes measured for other material studies). Therefore, the diameter at these locations was smaller and would result in incorrect tensile strength calculations. The torsion and bending-torsion specimen fracture zone diameters were also not measured due to the localised failure under fatigue because of their hourglass-shaped test zone geometry. Therefore, the measured specimen diameter tables provided in Appendix D1, D4 and D5 contain only the pre-test diameter measurements with the vernier.

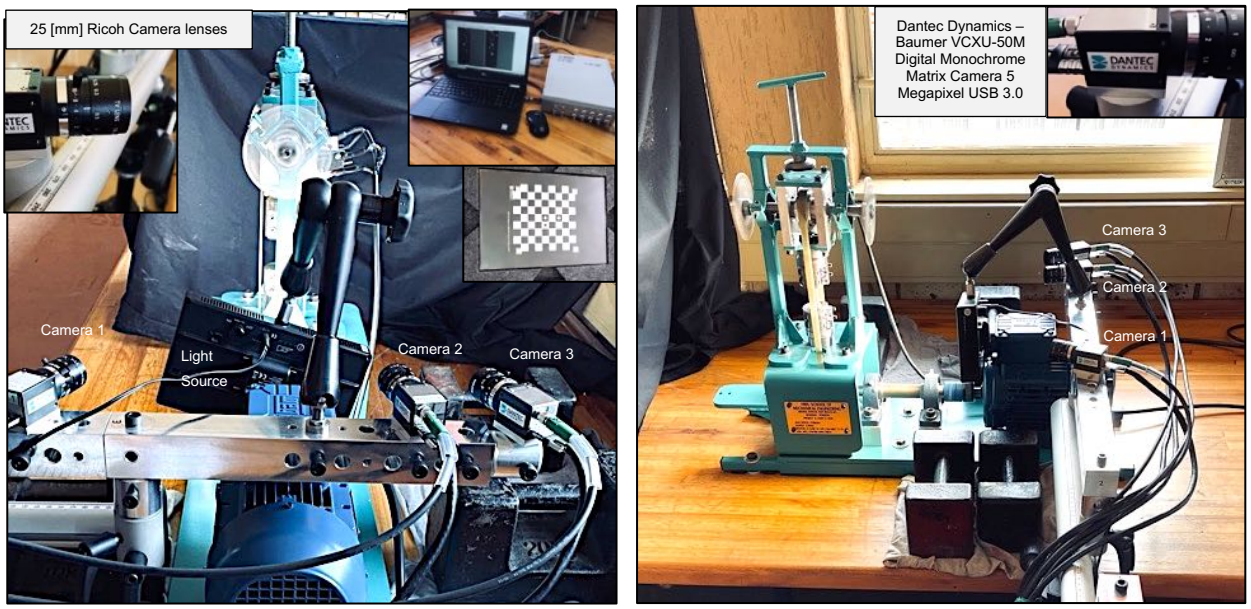
The previously identified ***Aptina CMOS digital camera microscope*** was again used to take illustrative images of similar arbitrarily chosen test specimens and their fracture or failure surfaces. These images are reported in Appendix J1 through J5 for the experimental test specimens.

4.3.2.2 Principal Measurement Instrument

This research study's principal measurement system is the ***DANTEC Dynamics Q400 DIC system*** (also discussed in Appendix B6). It measured the experimental torsion (T) and bending-torsion (BT) test specimen displacements under fatigue loading. Figure 4-7 on the next page illustrates the system cameras and general setup, the required speckle pattern on a specimen surface, the image correlation mesh formed and the evaluation results (displacements) obtained from measurement processing in the ISTRA 4D software. Displacement measurements with this system and the necessary static FEM simulations were used to obtain the experimentally induced specimen stresses on the T and BT fatigue test benches, as discussed further in Section 4.4.2.3. The detailed measurement procedures and results of the experimental T and BT specimen measurements with this camera system can be referenced in Appendix H4.2 and H5.2. Moreover, in Appendix B6, reference can be made to the general procedure(s) associated with a DIC measurement and the required speckle pattern preparation.

The DANTEC measurement system was the most advanced instrument available for this study. This system was considered the most appropriate instrument for the above experimental test measurements due to the relatively high test speeds, multi-directional specimen displacements,

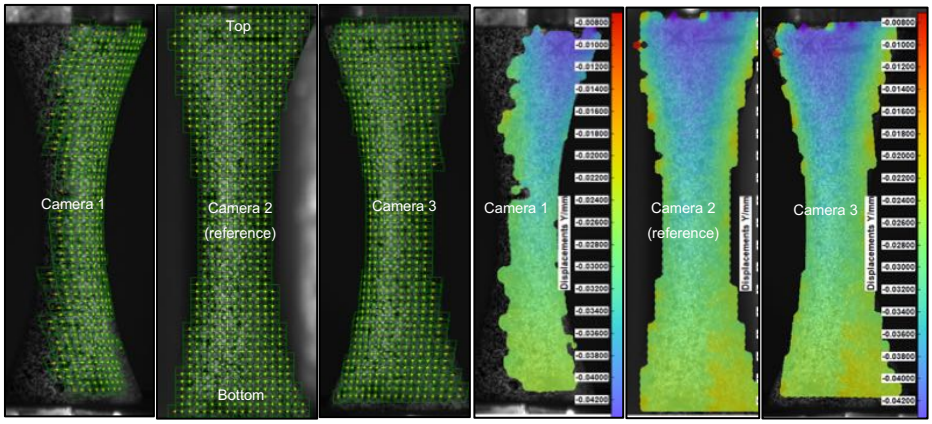
and physical test bench constraints. These constraints inhibited mounting other sensors (e.g., strain gauges, optical or inductive sensors). Secondary vibrations of the test benches could influence these sensors or manifest in their readings during test measurement. The non-contact and free-standing high-speed DANTEC system was not subject to these constraints as long as the general measurement and specimen preparation procedures (mentioned above) were used.



(a)



(b)



(c)

Figure 4-7: DANTEC Dynamics Q400 DIC System [83] (a) cameras and setup, (b) specimen speckle pattern and (c) correlation mesh and displacement measurement

DANTEC DIC System – Secondary Verification

Since the DANTEC DIC System was considered the primary measurement instrument, it was required to perform a secondary verification of the system measurements. This verification was done to ensure that the system is appropriately understood and utilised and that all subsequent measurements will be correct. For this, specimen gauge extension measurements were made during the last five experimental tensile (TEN) tests (Spec6-Spec10), where the MTS Extensometer was used to obtain the test material's experimental Elasticity Modulus. The relevant specimen gauge extensions measured with the extensometer (contact measurement, with the procedure and results in Appendix H1.2) were compared with those measured with the DANTEC (non-contact measurement, with the procedure and results in Appendix H1.3). The results of the verification measurements are summarised in Table 4-4 below. The difference between the DANTEC engineering strain ε_{eng} measurement and the extensometer engineering strain measurement $\varepsilon_{eng;ref}$ (reference) was calculated as a percentage difference value for each test specimen, using Equation (H-6) in Appendix H1.3.

Table 4-4: Secondary verification measurement results – DANTEC vs Extensometer

Specimen #	Diameter	Engineering Strain - ε_{eng}			
		Extensometer $\varepsilon_{eng;ref}$	Uncertainty +- 0.04 [%] $\varepsilon_{eng;ref}$	DANTEC ε_{eng}	Difference
	[mm]	[-]	[-]	[-]	[%]
EN19T-TEN-Spec-6	6.144	0.01032	0.00000413	0.01023	-0.89
EN19T-TEN-Spec-7	6.162	0.00994	0.00000398	0.01053	5.95
EN19T-TEN-Spec-8	6.279	0.01029	0.00000411	0.00975	-5.19
EN19T-TEN-Spec-9	6.310	0.01029	0.00000411	0.01008	-2.02
EN19T-TEN-Spec-10	6.352	0.01028	0.00000411	0.00943	-8.25

It is evident that all the measurement differences were low and the DANTEC DIC system measurements (using only two cameras) appeared to be satisfactory. The strain measurement differences higher than 5 [%] were all attributed mainly to the positioning of the digital line gauge ends (front) relative to the extensometer knife edge positions (back). Refer to Figure 4-8 below for Spec10. This was due to the attachment springs (front) not being ideally positioned (above or below) with regards to the same knife edges (e.g., digital line gauge length ≠ 25 [mm] nominal extensometer gauge length). These line gauge ends (DANTEC) could, therefore, not be better positioned (in-line with the knife edges) in the post-processed image views since the attachment spring positioning (shown in images) did not allow it. Placement of the line gauge ends on the metallic attachment springs themselves could not be done to accommodate for this since they had un-speckled surfaces and were thus unmeasured by the DANTEC. The DANTEC line gauge ends were therefore positioned (within measured colour fields) slightly inside (shorter length) the

knife edge positions on the back. Thus, measuring a maximum of 0.00065 [-] strain (or 21.19 [μm]) less extension than the extensometer (for Spec10). Positive (+) strain difference values were indicative that the DANTEC measured a larger specimen strain (extension) than the extensometer and vice versa.

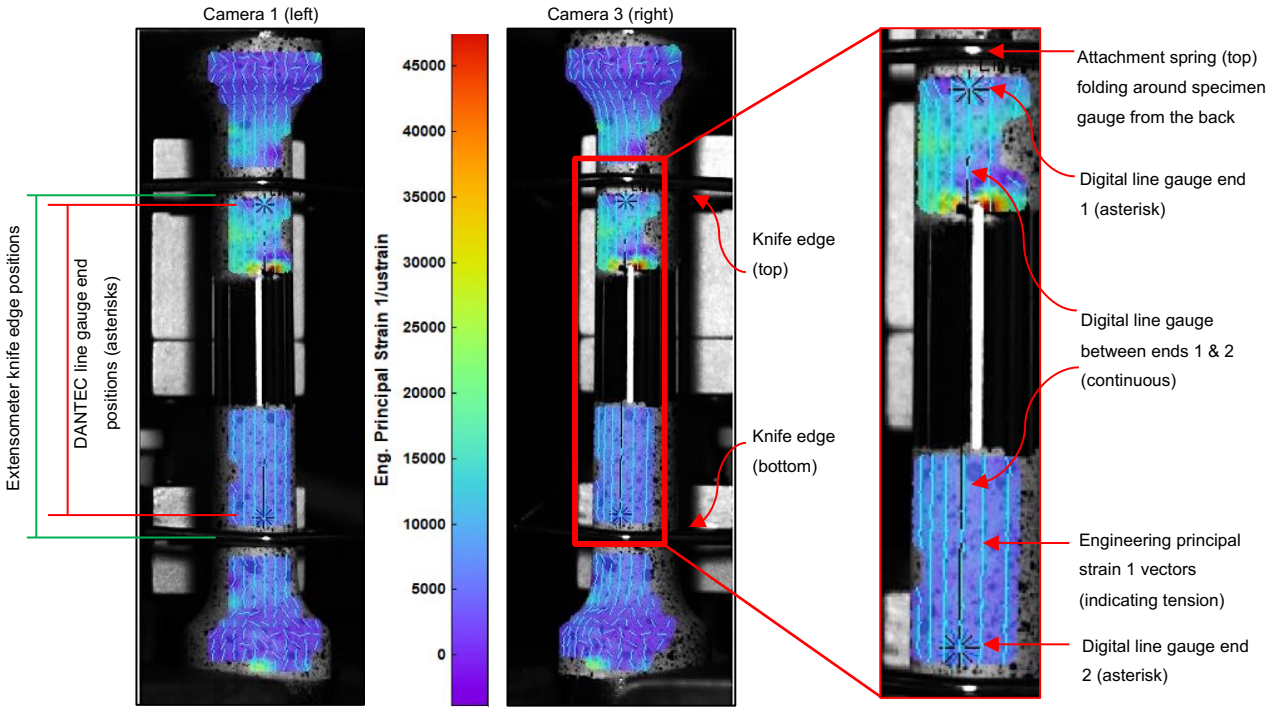


Figure 4-8: Secondary verification measurement – DANTEC line gauge positioning

The measurement differences were also attributed to the fact that the extensometer had to measure specimen extension on the 'back' of the tensile specimen to allow for the DANTEC optical measurement on the 'front'. The strain measurements were therefore made at very similar longitudinal cylindrical levels on the specimen gauge surface (top and bottom knives/line gauge ends). However, they were not on the same side of the specimen. The measurement differences may also be attributed to the spray paint layer on the specimen back gauge surface where the extensometer knife edges are pressed against the specimen cylinder. A small amount of spray paint may have been 'pinched' between the knife edges and the test specimen's metallic surface at the measurement points. During the tensioning of the specimen, this could have caused small and unforeseen (but influential enough on strain measurements) knife edge movements, which may also have occurred separately from the specimen extension.

Splitting the speckle pattern into an independent top and bottom part on the surface of Spec9 and Spec10 (control measurements) showed no notable influence on either the DANTEC or extensometer strain measurements. That is because no secondary or mutually influential spray

paint layer deformations or strains were observed in the measurements between the top and bottom parts of the specimens. Spec9 had a lower measurement difference than Spec7 and Spec8 prior to it (which had continuous speckle patterns, see Table H-6 in Appendix H1.3).

The strain measurement differences in Table 4-4 can be attributed to the extensometer and the DANTEC measuring specimen gauge strains up to (or slightly past) the point of extensometer removal (see Figure H-9). This removal point was an internally calculated MTS parameter within the extensometer test-procedure software program. It indicated the point during the first part of each tensile test where the extensometer measurement limit was reached and had to be removed (whilst the test was paused, see Table H-3 data). For each tensile test strain measurement performed, this removal point was unavoidably past the experimental yield loading point (as indicated in Figure H-5 tensile test curves). Due to this, the tensile test specimens went well past the approximate experimental elastic limit of the material (linear material response). Poisson's effect and the specimen experiencing plastic strain (material response) may have caused a cylindrical diameter reduction in the tensile specimen gauge area.

Since the extensometer is a contact measurement device, this gauge area diameter reduction seemingly did not influence the measured strain. This was because the knife edges maintained contact with the specimen gauge surface throughout each test due to moderate pressure being applied by the attachment springs pulling the extensometer towards the front of a specimen (pressing knife edges through the speckle pattern paint layer). Inherent to how the speckle pattern is prepared for the DANTEC measurements, this gauge area size reduction (and polished specimen surface) may have caused the dry and slightly brittle spray paint layer to detach from the gauge area surface at the line gauge end locations. Lack of the spray paint adhesion to the elongating tensile specimen may have caused the lower DANTEC strain measurement values due to specimen material extension (although very small) underneath this spray paint layer. This is reflected in Table 4-4, where most of the measurement difference values are negative (-), irrespective of the line gauge end positions being slightly inside the extensometer knife edges. It is also clearly evident from the strain curve overlays of Spec8, Spec9 and Spec10 in Figure H-10, where the DANTEC maximum strain measurements were lower than that of the extensometer. Spec6 (overlay curves in Figure 4-9 below) and Spec7 may not have experienced this spray paint layer detachment since their maximum line gauge strain values were either on or slightly above those of the extensometer (at the removal point).

A more general reason for the reported strain measurement differences could be attributed to how the DANTEC digital line gauge strain measurements were obtained from the exported data and graphs. In this, the DANTEC measured the specimen gauge strain before, during and after the actual tensile tests to 'overlap' the extensometer gauge strain measurement made during

each test (see line gauge strain curves and notes in Figure H-9). The point (or step) where the maximum line gauge strain value was obtained from (to compare with the extensometer measured strain value) could therefore have been improperly identified as a step too early (e.g., 36 instead of 37) or too late with respect to the corresponding moment at which the extensometer measurement ended (removal point). Nevertheless, for all the tests, this maximum line strain point was identified as the last data point where the line gauge strain curve started flattening out (TEN test paused, DANTEC measurement concluding after that). Therefore, this maximum DANTEC strain measurement point was subject to the visual inspection of each line strain graph (and data set). In contrast, the extensometer maximum strain value (reference value, in Table 4-4) was calculated using Equations (H-4) and (H-5) as the difference between final and initial strain values in the exported measurement data.

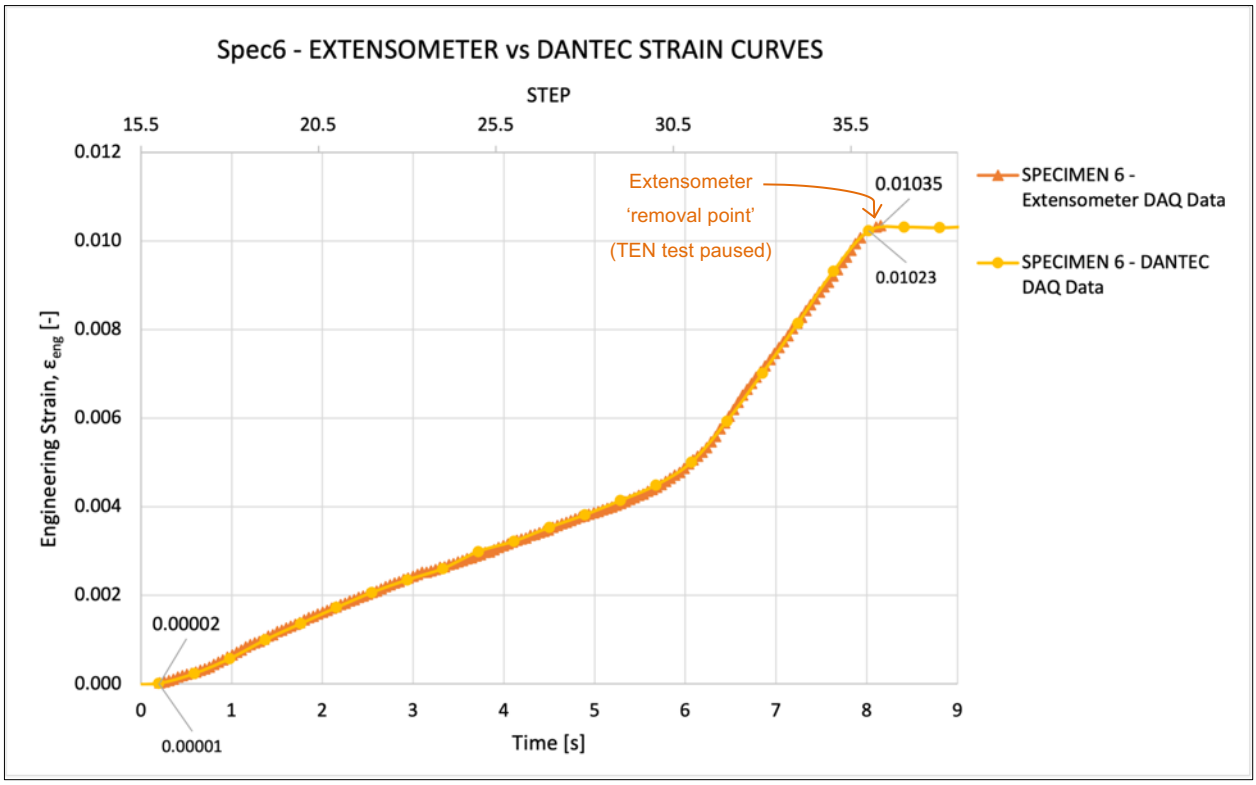


Figure 4-9: TEN test Spec6 strain measurements – DANTEC (strain-step) and Extensometer (strain-time) overlay curves

From the strain curve overlay graph of Spec6 shown in Figure 4-9 above (and others in Figure H-10), it is seen that both measurement instruments measured very similar specimen strain responses. These overlay graphs were prepared by matching the appropriately identified strain measurement data points and measurement intervals of the DANTEC (converted from μstrain to strain) onto those of the extensometer.

Another possible reason for the strain measurement differences is the fact that the extensometer recorded measurement data at a much higher rate (20 [Hz]) than what the DANTEC did (about 2-2.5 [Hz]). The moment of each respective data point's measurement for the two instruments was therefore not precisely synchronised with each other during test measurement. It is thus seen from Figure 4-9 above that the DANTEC did not measure as 'complete' a strain response as the extensometer did. This resulted in 'lost' data points, which may have allowed more accurate identification of the maximum DANTEC line strain values as seen above at the removal point. The DANTEC measurement procedure of recording the specimen extension before, during and after the extensometer measurement could have been done better.

The DANTEC measurement procedure was not necessarily incorrect. However, allowing the MTS system to digitally 'trigger' (start and stop) the DANTEC camera recording sequence simultaneously with the tensile test (with extensometer) would have provided more precise measurement matching. This triggering could be done by connecting the DANTEC's data acquisition (DAQ) box with the available 'analogue input' cable and port on the MTS machine and defining the correct image recording sequence on the ISTRA 4D software programme. However, what would have certainly improved the reported measurements and comparison differences (in Table 4-4) for the overlapping measurement sequence used, would have been to increase the DANTEC image acquisition rate (to about 20 [Hz] or higher). An increased image rate would have allowed the DANTEC strain measurement data-point count to be at least that of the extensometer (or more). Because the extensometer data acquisition rate of 20 [Hz] is fixed (based on the tensile test rate) within the pre-programmed TW Elite MTS test procedure.

Using only two (of the three available) cameras for the extension measurements with the DANTEC (middle camera 2 had digital setting faults at the time) also influenced the non-contact measurement accuracy due to one less camera image set (overlapping the other camera images) being available for correlation and evaluation of the specimen measurements in the ISTRA 4D software.

The verification measurements for the DANTEC (also discussed in Appendix H1.2 and H1.3) showed that the measured strain curves had very similar forms and values for each tensile test specimen. This implied that the DANTEC strain measurements (regarding the extensometer) appropriately measured each specimen's extension during testing, considering all the above experimental interpretations, observations and recommended improvements. The measurements with the DANTEC provided sufficient confidence in the system's measurement capability and correctness since the strain measurement differences were thoroughly interpreted, sufficiently small and possible to address where necessary in any subsequent measurements with the system. The low difference values and the full-field measurements obtained on each specimen

(see Table H-6 images) also confirmed that the surface speckle patterns were appropriately applied (regarding Figure B-10 general application). There were also no discernible image evaluation or correlation problems encountered during image processing in the ISTRA 4D software. The secondary verification of the principal measurement instrument ultimately provided the necessary measurement certainty. This certainty allowed the use of the system in the relevant torsion (T) and bending-torsion (BT) fatigue test specimen displacement measurements, as long as the general DANTEC measurement and specimen preparation methods were followed.

4.4 Experimental Considerations

The previous section identified and discussed all the experimental testing and measurement equipment used for testing the EN19 (T-condition) alloy steel. This section will discuss all the experimental test considerations made for the test specimens and the induced loading from each test bench. The experimental fatigue limit and fatigue failure definitions used for experimental fatigue testing will also be discussed. The relevant literature that provided insight or support for the test specimens, their preparation and their experimental testing was referenced in the following section [3, 21, 26, 39, 55, 57, 62].

4.4.1 Test Specimens

For the test specimens used in this study, it was required to consider several important factors that typically play a role during metal tensile and fatigue testing. These include the material properties, specimen type, quantity, machining, geometry and preparation.

4.4.1.1 Specimen Material, Machining and Management

The EN19 (T-condition) alloy steel chosen for experimental testing in this study was purchased in the T-condition of heat treatment from a local supplier as a 25 [mm] diameter 6 [m] length round bar. Monotonic tensile tests were done to obtain the actual mechanical strength properties, and are provided later in Section 5.2.1. No additional heat treatment was done on this material, and it was utilised as-is for test specimen machining.

The material chemical composition was also not re-analysed in this study, and it is therefore reported in Table 4-5 below as from the accompanying material certificate of the material. It should be noted that these chemical element composition values are provided for the original as-rolled stock bar material (see Figure M-1 of Appendix M). Standard elemental periodic table symbols are used to identify each comprising material element.

Table 4-5: EN19 (T-condition) alloy steel – material chemical element composition

Chemical Element Composition [%]														
	C	Si	Mn	S	P	Cr	Ni	Mo	Cu	V	Al	Ti	Sn	Hppm
Cast Analysis	0.37	0.2	0.81	0.015	0.011	1.03	0.11	0.272	0.1	0.025	0.005	0.002	0.014	2.2

Manufacturer steel making method: Fine grain practice and vacuum degassed

The material's mechanical properties after manufacturer heat treatment to the T-condition can be referenced in Figure M-2. The limiting ruling section (LRS) of the stock material (effective isotropic heat treatment depth) is reported according to the specification limit maximum as 100 [mm] on this heat treatment mechanical test certificate. Therefore, based on the small 25 [mm] stock bar diameter, it was assumed that consistent heat treatment conditions were achieved to the full depth of the material. To further consider this, all the test specimens were machined from the core part of the stock bar material. This general method is also recommended in the literature as it mitigates the possibility of macro anisotropic material distribution in each specimen [39].

Each experimental test specimen type was machined along the longitudinal length of the stock bar material on a conventional 3-jaw lathe to obtain the maximum diameter blanks. These blanks were then machined on a 3-jaw computer numerically controlled (CNC) lathe to obtain the specimen drawing dimensions and geometry (as discussed in Section 4.4.1.2). The specimens were each provisionally sanded (200 grit emery paper) for uniform surface conditions after machining (further finishing is discussed in Section 4.4.1.3).

The literature-recommended number of experimental fatigue test specimens is reported as 10 – 15 to adequately describe, identify and estimate the fatigue limit of a material [56, 84]. Because of the multiple material property tests performed in this study, the respective specimen lengths and only one 6 [m] stock material bar being available, this was not possible for all the tests. The number of experimental specimens tested in each test type was therefore chosen as follows:

- x10 monotonic tensile (TEN) test specimens
- x8 uniaxial axial (AX) fatigue test specimens
- x8 uniaxial bending (B) fatigue test specimens
- x9 uniaxial torsion (T) fatigue test specimens
- x18 biaxial bending-torsion (BT) fatigue test specimens

The monotonic tensile (TEN) test specimen quantity was chosen such that an appropriate number of tests could be conducted to obtain accurate material properties that could be used with reasonable confidence for subsequent calculations. The uniaxial fatigue test specimen quantities

(for AX, B and T) were limited to 8 or 9 specimens each. This limitation was made so that only a sufficient amount of experimental data points were obtained to estimate the uniaxial fatigue limits (method in Section 4.6.2) instead of estimating them from the literature data for similar materials. Therefore, most of the stock material was allocated to the BT test specimens since these were the primary required fatigue tests for this study. The number of test specimens for the BT tests consequently exceeded the literature-recommended amount, which allowed for accommodating possible experimental testing errors and omissions if needed.

With the variety and quantity of experimental test specimens in this study, it was required to implement a methodical specimen numbering and management system to ensure that the correct specimens were tested and measured in respective tests. For this, each experimental test specimen type was colour coded as green – TEN, yellow – AX, turquoise – B, pink – T and blue – BT. Along with this, a unique identification was awarded to each specimen using the material, the test type and the specimen number (e.g., EN19T-AX-Spec1). Each test specimen was further packaged into a small sealable bag with a label on which the identification and colour code were marked. This label was also used to note pre-, in- and post-test parameters, recordings and measurements when required. A small piece of tissue paper was also included inside each bag to prevent the polished specimen surfaces from scratching before and after each test. Appendix C6 can be referenced for examples of the above-mentioned specimen management methods. Specific specimen markings (e.g., with specimen designation) were not defined or implemented since these markings often rub off before, during or after a test.

4.4.1.2 Specimen Geometry

Since different material and fatigue strength tests were performed in this study, it was required to consider the standard practices and the recommendations made in the literature for specimen geometry in each test type [14, 39, 43, 62, 64, 85-87].

For the monotonic tensile (TEN) tests, the standard ASTM E8/E8M – 13a (dog-bone) specimen was considered. This specimen is a solid cylindrical specimen with geometry, as referenced from the relevant standard [86]. The specific specimen dimensions were selected based on the material ultimate tensile strength (from material certificates) and the test bench (MTS Landmark) load capability and limitations. This specimen is illustrated in the drawing shown in Appendix C1.

The axial (AX) fatigue test specimens were designed to the geometry and dimensions specified in the ASTM E606 - 92 standard [85, 87]. However, due to the test bench (MTS Landmark) load capability and specimen clamp dimension constraints, it was required to reduce the size of this

specimen. This size reduction was made by scaling down all the recommended dimensions whilst maintaining the constant geometric ratios between respective dimensions from the standard. This solid cylindrical specimen is illustrated in the drawing shown in Appendix C2.

For the bending (B) fatigue test specimens, the typical and standard bending fatigue specimen geometry could not be used since these specimens for the existing test bench in the laboratory had specific geometric and dimensional requirements. It was also required to implement specific geometric design changes so that the initially provided sample specimen from the laboratory (designed for stress concentration effects under bending fatigue loading) would have a more appropriate geometry. That is the rotating cantilever bending (Wöhler type) specimens mentioned in the literature [43, 62]. These specimens typically included ‘dog-bone’ and hourglass-shaped test zone geometries, which were considered and integrated into the existing specimen geometry by using an hourglass geometry for a section of the specimen cantilever length so that failure could be concentrated in a specific area. This solid cylindrical specimen is illustrated in the drawing shown in Appendix C3.

The torsion (T) and bending-torsion (BT) fatigue test specimens were designed to have the same geometry specifically for the test benches. No explicit design guidelines or standards could be found, especially for the BT specimens. The recommended and standard-practice specimen geometries and dimensions referenced in the literature were used for this design. The specimen geometries are illustrated in Figure 4-10 below (and the drawings shown in Appendix C4 and C5). Flattened specimen ends were not required to transfer torsional loading between the two halves of the specimens (as is typically done) since a sufficient clamping torque was applied to specimen ends in each test bench.

Based on the stresses induced in each of these specimens, it is usually preferred to use solid cylindrical hourglass-shaped specimens. This preference is because the geometrical shape inherently provides sufficient stiffness for testing at the desired loading frequencies, and it confines failure to a specific area of the specimen [39]. It is also argued that this specimen shape is best suited as a transitional geometry between those commonly used for simultaneously accommodating both bending and torsion (or just torsion) loads [43, 62, 64, 88].

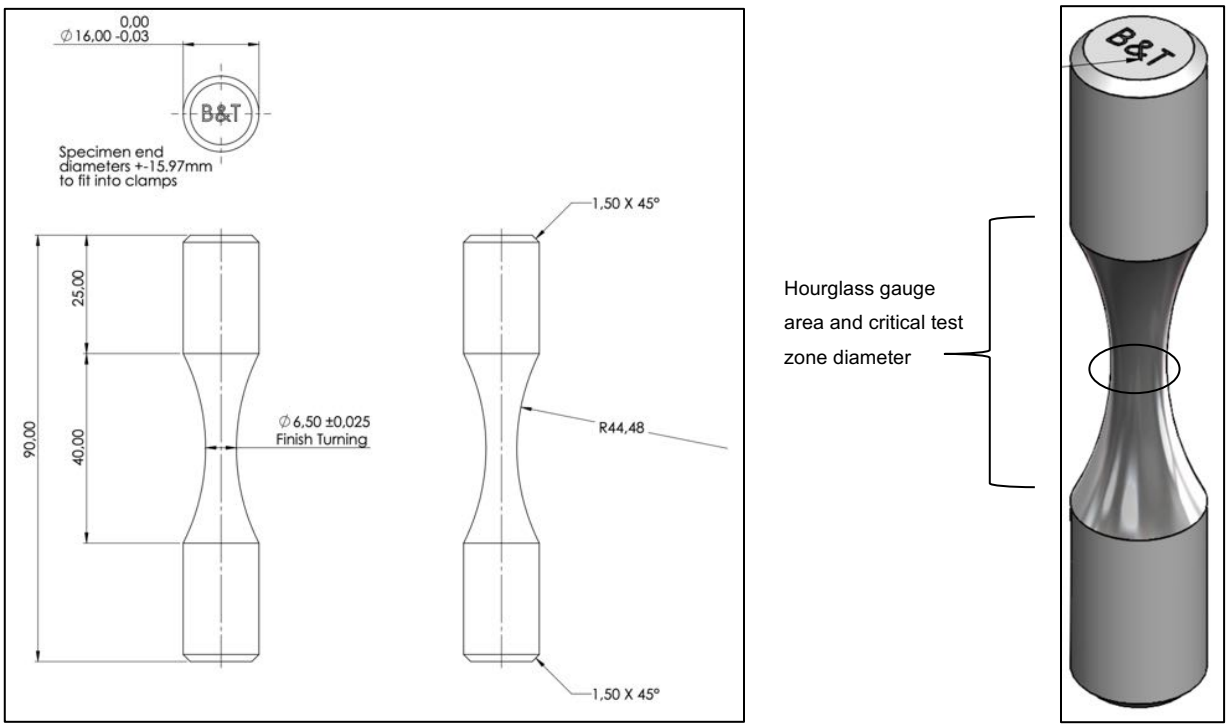


Figure 4-10: Bending-torsion (BT) fatigue test specimen

4.4.1.3 Specimen Surface Condition

For the identified experimental test specimens and their respective geometry, it was also required to consider the surface finish condition during material strength and fatigue strength tests. This was done to the usual methods used and reported in the relevant literature [39, 44, 55, 60, 62, 89]. It has been shown in the literature that the surface finish or roughness of a fatigue test specimen directly influences the HCF strength of a ferrous metal [90]. It is because machining grooves, scratches or indentations inherently cause higher and undesirable localised stress conditions on the surface of a specimen, especially under bending and torsion loading conditions, which is also where fatigue failure originates.

The surface finish, often regarded as sufficient for fatigue testing specimens, is reported as a smooth metallographic or mirror-like finish free from visible grooves and scratches [62]. The conventional circumferential polishing of specimen test surfaces on a lathe with successively finer grit sandpaper and water or lubricant is reported as an appropriate method to achieve this for metals [39, 44, 55, 60]. Other polishing methods like longitudinal (axial) polishing, also with sandpaper, are mentioned and can be implemented as an additional step of improving specimen surface finish. Modern surface polishing of fatigue specimens includes dry electrochemical

polishing methods and advanced surface grinding methods. These are, however, much less common and carry great expense, despite saving time.

The surface polishing method used in this study was chosen according to the conventional method reported in the literature. That is circumferential polishing on a lathe with successively fine grit sandpaper and a cutting fluid-water mixture as a lubricant. Specifically, the sandpaper grits used included P150, P320, P400, P600, P800, P1200, P1500 and P2000. The Tapmatic (cutting fluid) and water lubrication mixture continuously washed away material and sandpaper residue. These can be viewed in Appendix C6, along with the general surface polishing procedure steps. The reasons for considering eight incrementally finer sandpaper grits include the following:

- Faster polishing of the specimens could be achieved because each successive grit only removes the material from the surface with greater roughness from the preceding grit. That is, instead of a P1200-grit taking much longer to polish off the roughness (material peaks and grooves) that, for example, the P320-grit sandpaper left behind, it was faster for a P400-grit to follow the P320-grit.
- Step-wise finer grit sandpaper polishing also allowed for better visual inspection and control of the hand polishing technique to ensure a constant surface finish with each grit used on a specimen. This technique consisted of medium to light pressure and various longitudinal movements and rates of movement relative to the rotating specimen (providing cross-hatched lines instead of concentric ones from the original machining).
- Polishing (or machining grooves) from preceding sandpaper grit steps was also visually easier to observe during the subsequent finer grit sandpaper step. This allowed reverting to a previous grit to polish out grooves or lines too big for the current grit to remove effectively. This helped ensure a more uniform surface polishing result for each specimen and no machining grooves remaining after the last grit was used.

A finished specimen after polishing was conservatively assumed to have a two-dimensional surface roughness factor close to R_a = 0.021 [μm], as reported for similarly polished stainless steel specimens using P2000-grit sandpaper and lubrication [89].

One of the primary steps to ensure correct experimental stress calculation for each test included the careful multiple test zone measurements (ten (10) times with the vernier) for each specimen to obtain the appropriate average diameter. These measurements were performed after each specimen was polished. Appendix B1 and D1 through D5 can be referenced for the procedure used and the measured diameters of all test specimens.

Figure 4-11 below illustrates the polished specimen surface finish of an arbitrarily photographed bending-torsion (BT) test specimen. For the other test specimen types, this is illustrated in

Appendix C1 through C5. Some residual microscopic polishing grooves were still observed on the specimen surface, as shown below. However, these were unavoidable and inevitable considering the chosen polishing procedure, the test specimens and the finest grit sandpaper that could be obtained (P2000). However, these minute grooves or lines were only visible in the camera microscope images, not with a regular visual inspection. Also, from the resultant surface finish illustrated in Figure 4-11 and those for other specimens (in Appendix C), it can be said that a consistent surface polish was obtained for all individual specimens. Further, this confirmed that an appropriate polishing method was used, and any surface condition effects were mitigated as far as possible and negligibly small.

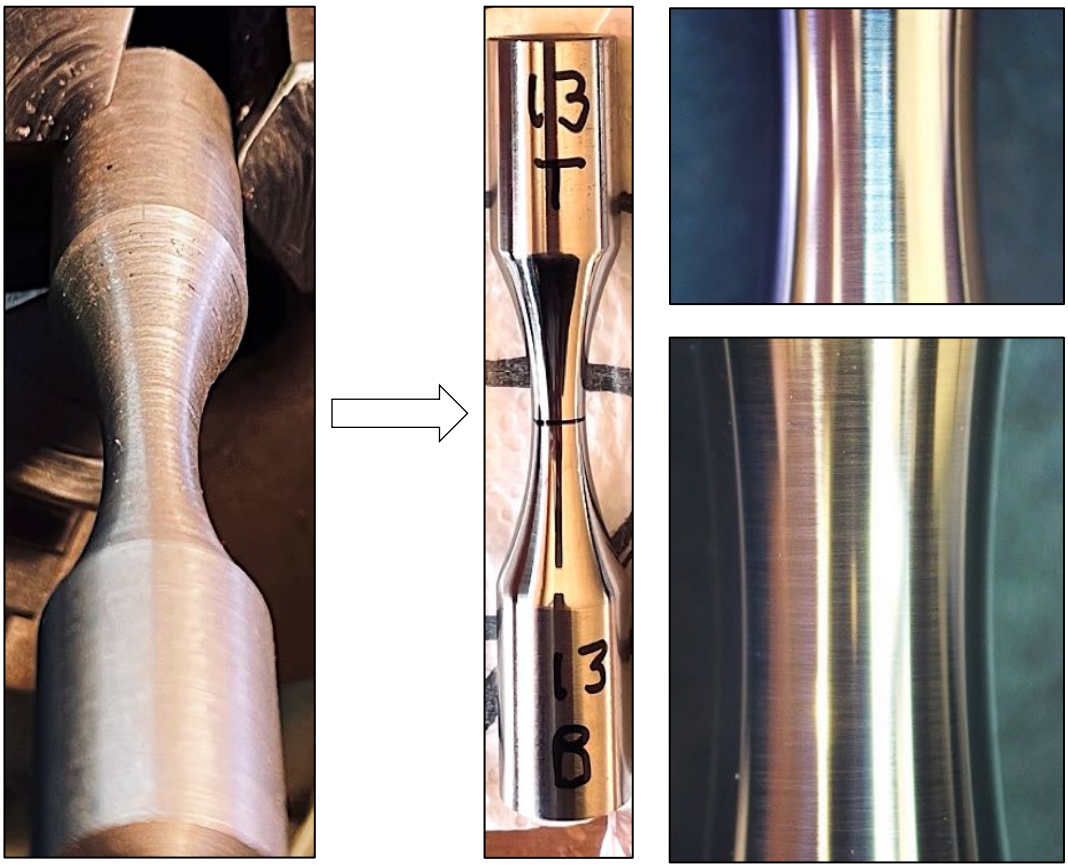


Figure 4-11: Surface polishing result – bending-torsion (BT) fatigue test specimen

4.4.2 Experimental Loading

It was necessary to ensure the correct specimen loading during each test to obtain valid and thorough experimental test results. For some of the test benches used in testing (e.g., the T and BT), this necessitated verification measurements for the induced loading on a specimen. For other

test benches, it was required to calibrate the load-inducing components (e.g., the B) or implement the correct procedural steps during a test (e.g., for TEN and AX). These loading considerations, therefore, ensured that subsequent stress calculations (as discussed in Appendix H) were correct for each test type and specimen. The sub-sections to follow discuss these considerations regarding the previously discussed test benches (in Section 4.3.1), measurement equipment (in Section 4.3.2) and the test specimens (in Section 4.4.1).

4.4.2.1 General Considerations

For the tests performed on the MTS Landmark machine (e.g., TEN and AX), it was considered, regarding the relevant calibration certificates and loading ranges (see Figure A-2 and Figure A-3), that the experimental tensile or axial fatigue loading was induced accurately for each test specimen. For this, the experimental loading values in both test types were obtained from the exported test data of each test specimen. These data files were then processed (see Appendix H1.1, H1.2 and H2) to obtain the correct experimental yield load, ultimate tensile load and axial fatigue load amplitude values for calculating the experimental tensile strengths and fatigue stresses. Reference can be made to Appendix J1 and J2 for the experimental loading values obtained for each test.

One of the procedural steps for the tensile (TEN) and axial (AX) fatigue tests also incorporated the correct ‘zeroing’ of the test bench load-cell measurement after clamping a specimen before conducting a test. However, secondary tensile or axial fatigue load offsets still manifested in the recorded load cell force measurements due to inherent specimen slippage in the wedge grips, residual clamping forces and possible axial-misalignment of the wedge grips. The exported test data made it possible to identify and accommodate any of these offset force measurements. It was done by subtracting or adding the offset values (vertical axes of tensile and axial fatigue loading graphs) from the relevant tensile test or axial fatigue amplitude loading values (see Equation (H-1), (H-2) and (H-7)). Concerning only the tensile tests performed on the MTS Landmark machine, all specimens were tested at a tensile extension rate of 3 [mm/min] (or 0.05 [mm/s]) as recommended and customarily implemented for steel on this machine in the laboratory.

A load cell calibration was required for the tests performed on the rotating cantilever bending (B) fatigue test bench in the laboratory. This calibration was required due to the age of the test bench (and components) and no recent tests on it being done. The load-inducing linear spring load cell was calibrated with weighed mass pieces according to the procedure discussed in Appendix A2. The result from the calibration showed a consistently lower load cell reading than the actual applied weight. The induced load on a B fatigue test specimen was 10.2 [%] higher than what the

inscribed scale on the load cell reflected. The cantilever bending forces (and resultant stresses) were calculated for each test using this calibration curve illustrated in Figure A-6. The cantilever bending moment and stress calculation procedure are provided in Appendix H3.

Apart from the more specific experimental loading considerations (and corresponding measurements) to be discussed in the following two sections for the torsion (T) fatigue and bending-torsion (BT) fatigue test bench, two more general loading factors had to be considered. These regarded the centrifugal force-inducing mass pieces and moment lever lengths on each test bench. The machined centrifugal mass pieces (used in both test benches) were weighed ten (10) times. The average masses were then used to calculate the experimentally induced centrifugal forces at a specific test speed and mass-radius position on the bilateral wheels. The moment lever lengths or distances at which these centrifugal forces acted from the lever-head central axis were also obtained, for each mass piece, to assist in calculating the experimentally induced torsion and bending moments as accurately as possible. This was done using the respective test bench assembly models (in Siemens NX12). The general mass measurement procedure is provided in Appendix B2, and the mass piece mass measurements (with steps for measurement) are reported in Appendix E2, along with a discussion and illustration of how the moment lever length for each of them was measured from the relevant bench models.

4.4.2.2 Resonance Frequency and Loading Gain

Both the bending-torsion (BT) and torsion (T) fatigue test benches (identified in Section 4.3.1) were newly designed and built fatigue test benches used for experimental fatigue testing in this study. Their construction and working principle are based on imbalance forces that induce either torsional or out-of-phase bending-torsion moments as the fully reversed experimental fatigue loading on a test specimen (as discussed in Appendix A3 and A4).

For these BT and T fatigue test benches, it was identified that the first bending and torsion vibration modes of a test specimen influence the induced stress in the specimen [28, 82]. This influence is due to an experimental loading gain G, a function of the test frequency and vibration mode frequency. This gain manifests in the bending and torsion components of the relevant loading conditions induced on each test bench. It was therefore required to consider these bending and torsion loading gains further to provide a theoretical understanding of the phenomenon on each test bench. The illustrative T and BT loading gain curves of an arbitrary specimen in each test bench are shown in Figure 4-12 below.

From these preliminary theoretical calculations for each test bench, it was identified that specific test bench lever-head design changes had to be implemented. This was due to the respective theoretical loading gain responses showing undesirable (high gain) specimen loading conditions at the relevant test speeds initially used on each test bench (40-50 [Hz]). That is, passing through or testing near the relevant specimen resonance frequencies. The required design changes for the lever-heads involved the substitution of the original 5 (BT) and 6 (T) [mm] thick steel lever-head wheels with smaller, thinner and lighter Aluminium wheels (XW configurations) for each test bench. These changes resulted in the appropriate bending and torsion loading gain responses to higher frequencies for which the induced loading gains also decreased, as shown in Figure 4-12 below. That is, for BT – a lower equivalent gain point (test point) at a higher test speed, and for T – lower gains at higher test speeds.

The system design was therefore done for the T fatigue test bench so that higher test speeds can be considered, with lower loading gain values. The system design for the BT fatigue test bench was done so that an equivalent bending-torsion loading gain test point is obtained (between the first vibration modes). Also, with lower loading component gain values, but at a higher test speed. The above theoretical torsional and bending resonance and loading gain considerations and calculations can be referenced in Appendix F1 through F3 for each test bench's chosen lever-head configuration ('XW'). The original ('orig') and third ('XWS') configurations are also illustrated there for comparative and completeness purposes only. As a summary from these appendices, the T fatigue test bench was only required to consider the torsional resonance frequency and the resultant torsional loading gain for a specimen. For the BT fatigue test bench, it was required to consider the torsional and the bending resonance and gain for a specimen based on the new lever-head configurations (smaller, lighter and thinner wheels). In the BT fatigue test bench, the torsional resonance and gain were obtained similarly to the T fatigue test bench. The bending resonance and gain were obtained using specimen modal analyses in NX12 FEM.

From the above theoretical gain considerations made for each test bench, it was ultimately made evident which experimental test speeds would be appropriate. For the T fatigue test bench, measuring the experimental torsional displacement of an arbitrary specimen at the appropriate speed below the test bench maximum was required. For the BT fatigue test bench, it was required to measure the experimental bending and torsion displacement of an arbitrary specimen at the theoretical equivalent gain point (between the first vibration modes). Therefore, this operating point for the BT fatigue test bench had to be determined. The experimental loading gains are obtained from these direct measurements for both test benches.

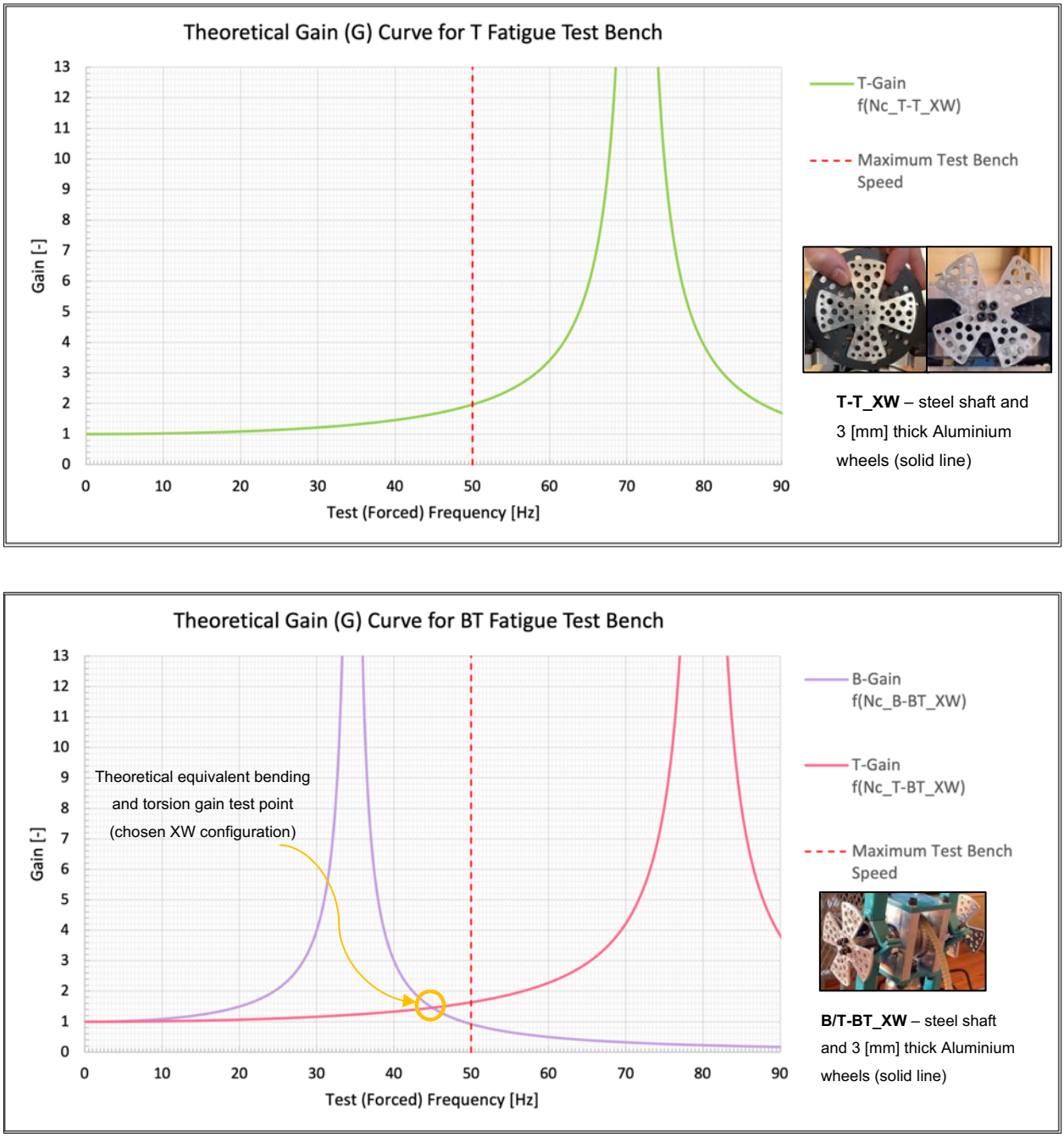


Figure 4-12: T and BT fatigue test bench – theoretical bending and torsion loading gain curves

The direct measurements were performed using the previously identified and verified DANTEC system (see Section 4.3.2.2). From these experimental 'gained' displacement measurements and the appropriate static FEM simulation displacements (under nominal 'ungained' loading, as if G = 1), it was then possible to obtain the relevant experimental loading gains. The displacement measurement and gain calculation methods are discussed in Section 4.4.2.3 next. The reason(s) for the direct experimental measurement approach was primarily due to the following:

- Damping coefficients would play an important role, and in the theoretically considered loading gains (Equation (F-4)), the damping ratio ζ [-] was assumed to be zero.
- Verifying damping on the test benches would be difficult.
- Full test bench modal analyses were not performed (e.g., more appropriate theoretical gain and possible complex damping considerations) since certain assumptions would have to be made (e.g., for damping) and would require further validation of the analyses.

4.4.2.3 Test Specimen Measurement Processing

For the torsion (T) and bending-torsion (BT) test bench loading gain previously referred to, this part discusses the methodology for obtaining the loading gain G from the direct DANTEC displacement measurements and the appropriate static FEM displacements of a specimen. This methodology applies to the test bench verification measurements discussed hereafter (Section 4.4.2.4) and the official experimental measurements performed while testing the relevant T and BT fatigue specimens. These official test measurements are discussed for T fatigue testing in Appendix H4.2 part 2c and BT fatigue testing in Section 4.5.2 later. The results of these official measurements are provided in Sections 5.2.2 and 5.2.3. Equation (4-1) below shows the calculation of an arbitrary torsion or bending loading gain value from the relevant displacements.

$$G\ [-] = DANTEC\ [mm]\ /\ NX\ FEM\ [mm] \tag{4-1}$$

where $DANTEC$: is the experimentally measured test specimen displacement

$NX\ FEM$: is the theoretical (ungained) test specimen displacement

DANTEC Displacement Measurements

The DANTEC system measured the displacement of two pre-marked specimen positions (small crosses) during loading on each test bench. These markings were made on the prepared speckle pattern of the relevant specimens, 2 [mm] from the top and bottom edges of the gauge area, as shown in Figure 4-13 (a) below. For the T fatigue test bench (measured from above, see Figure H-19) and the BT test bench (measured from the right side, see Figure 4-19 or Figure H-32), these specimen markings were oriented perpendicular towards the three DANTEC cameras.

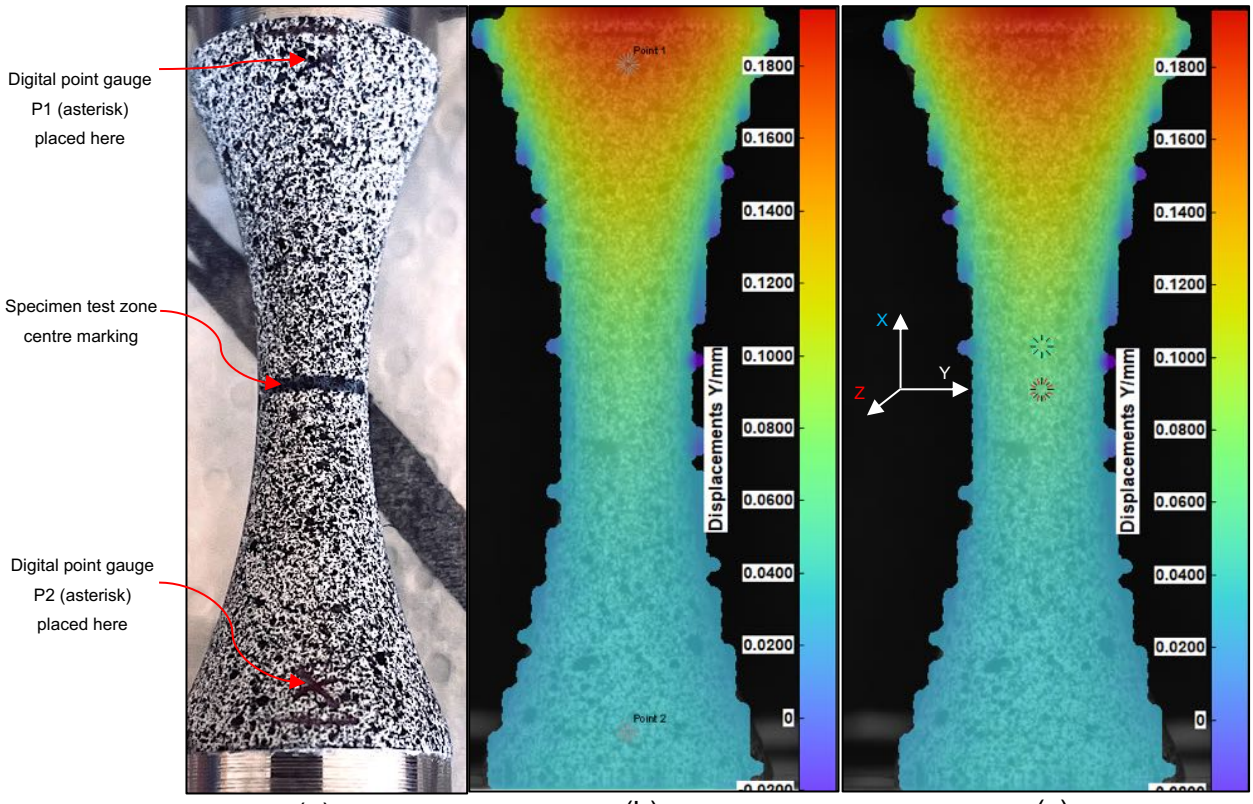


Figure 4-13: T and BT fatigue test bench – DANTEC bending and torsion displacement measurement

The appropriate evaluated measurement coordinate system could be defined with this orientation, as shown in Figure 4-13 (c) above. Within this coordinate system, and with the placement of two 'digital point gauges' (P1 and P2, in Figure 4-13 (b)) on the small surface crosses, the required experimental specimen displacements (bending (z-direction) and torsion (y-direction)) could then be obtained for each relevant test. The P1 and P2 gauge point displacement data was exported from the ISTRA 4D software. After processing, the relevant displacement values were appropriately calculated (as reported for each test measurement, e.g., Table 4-6 to follow). For the T and BT fatigue test benches, the displacement measurement procedures can be referenced in Appendix H4.2 and H5.2 for each experimental measurement (e.g., verifications and official tests).

Static FEM Displacements

After the experimental displacement measurements of the relevant T and BT specimens were obtained with the DANTEC (above), the next step was to obtain the theoretical (ungained) displacements. These displacements were obtained from the appropriate static FEM simulations

performed in Siemens NX12 Nastran (see Appendix I1 and I2). The reason for using FEM (instead of analytical methods) to obtain the specimen displacements was due to the complex (hourglass) geometry of the T and BT fatigue test specimens. The discretisation of the specimen gauge area for displacement calculations was considered more tedious and less appropriate than FEM.

The appropriate test specimen geometry (hourglass) was used for each simulation to generate the specimen FEM models. This was done such that the model represents the specimen and the attached test bench lever-head geometry (assumed rigid) as illustrated for an arbitrary torsion and bending loading, respectively, in Figure 4-14 below. The model was then assigned with the appropriate material properties and then meshed with a 2 [mm] 3D tetrahedral mesh (CTETRA10 elements) and a 1 [mm] mesh refinement in the specimen gauge area (similar results were observed for finer mesh refinements). The bottom of each specimen model was constrained using a fixed constraint representing the ideal experimental clamping conditions for each test bench. The nominal (ungained) centrifugal forces calculated for each measured test specimen were then applied to the tips of the lever arms in the directions that would produce a torsion or bending moment. These lever arms had the lengths associated with the relevant centrifugal mass piece used on the test bench wheels (e.g., lever lengths), as previously mentioned in Section 4.4.2.1.

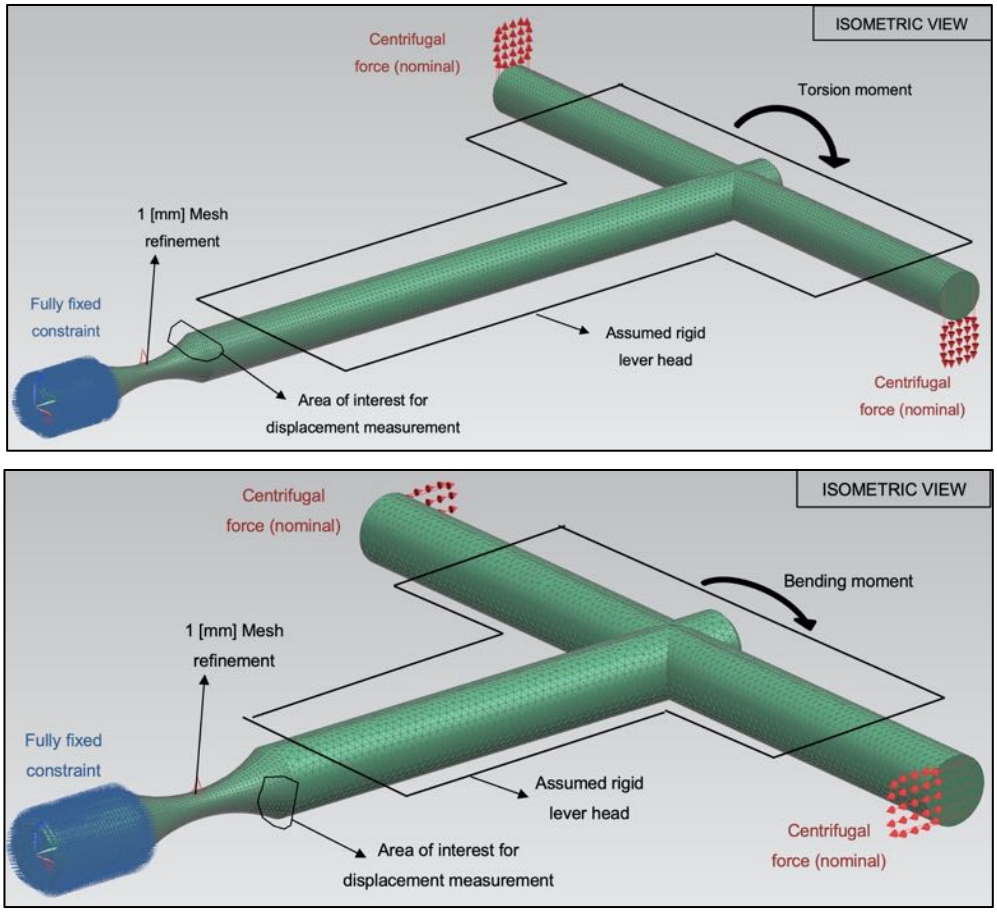


Figure 4-14: T and BT fatigue test bench – static FEM models and inputs

Once the static FEM model was solved, it was possible to probe the theoretical specimen displacement at the position corresponding to the DANTEC ISTRA 4D software P1 gauge point position (shown previously in Figure 4-13). The 1 [mm] mesh refinement on the specimen model gauges at the top was utilised. The displacement result probe process is illustrated for an arbitrary T and BT specimen on the front and the right side, respectively, in Figure 4-15 below.

It should be noted that only the P1 gauge point position (of DANTEC measurement) was measured at the relevant position in the FEM simulations. This was due to the ideal fixed constraint applied to the bottom of the specimen FEM model. For this, it was assumed that no 'rigid body' motion (accounted for by P2 in DANTEC measurements) was of concern in the simulations. Negligibly small displacements (torsion or bending) were observed from the NX result probes at the bottom of the relevant specimen models.

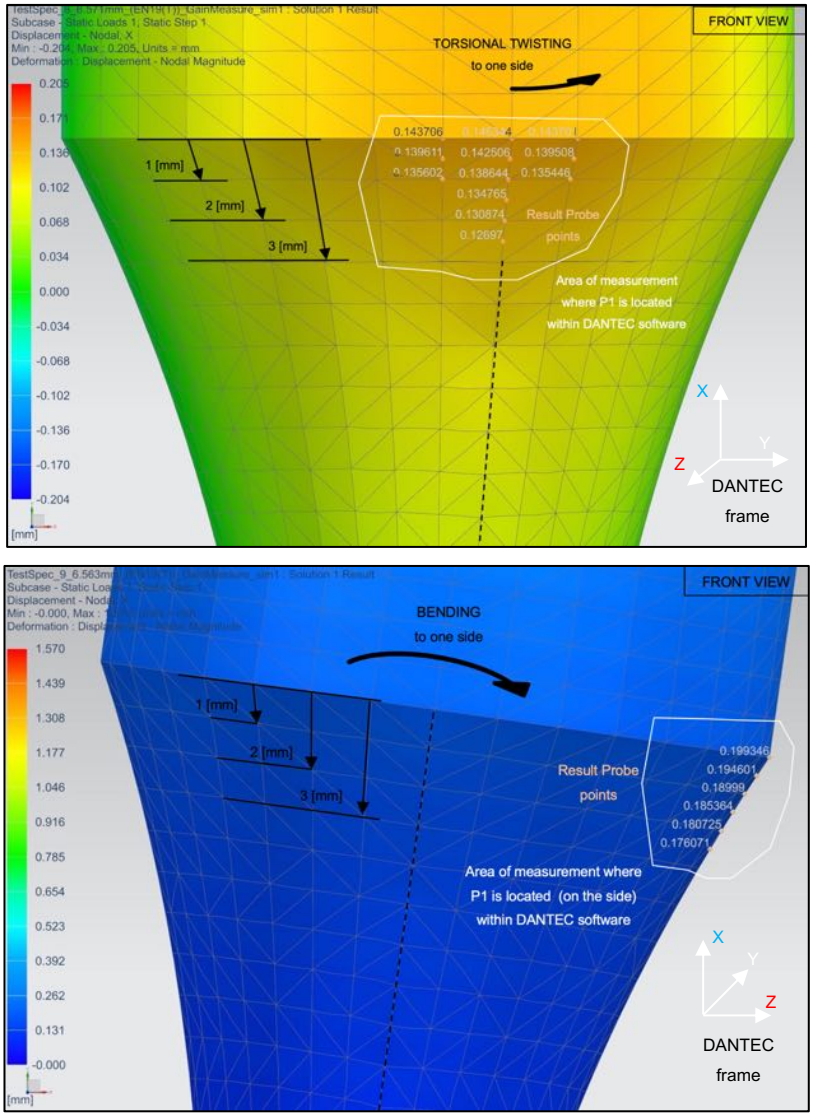


Figure 4-15: T and BT fatigue test bench – static FEM torsion and bending displacement

Experimental Stress Calculation

The loading gain values calculated with Equation (4-1) from the above displacements were then utilised for each specimen's stress calculation. The nominal stress calculated for each T or BT test specimen was multiplied by this gain value. As an example, a torsion stress τ calculation for an arbitrary torsion moment T and loading gain G is shown in Equation (4-2) below. The 'gained' stress (τ in this example) was then considered the appropriate experimental stress induced in a specimen during T or BT fatigue testing. The torsion and bending stress calculations for the experimental tests performed are further discussed in Section 4.6.1.

$$\tau\,[MPa] = \left\{\left[\frac{16T\,[N.m]}{\pi d_{spec}^{3}\,[m^{3}]}\right] / 10^{6}\right\} G \qquad (4\text{-}2)$$

where d_{spec} : is the fatigue specimen test zone diameter

The next part of this section discusses the required T and BT test bench verification measurements performed. The above method for calculating the loading gain was similarly used to obtain the relevant loading gain responses and values for comparison and discussion in these measurements.

4.4.2.4 Test Bench Verification Measurements and Characterisation

Before the required experimental torsion (T) and bending-torsion (BT) fatigue test measurements were performed, it was essential first to perform verification measurements. For this, the DANTEC measurement system was used. With this system, the appropriate specimen displacement measurements were made under the loading conditions of each test bench. For the T fatigue test bench, the purpose of the measurements was to verify the test bench setup and the measurement procedure used for it. For the BT fatigue test bench, the purpose of the measurements was to characterise the test bench load system based on the experimentally measured loading gain responses. The verification measurements performed for each test bench are discussed in the following parts below. Reference can be made to Appendix H4 and H5 for each test bench's measurement, setup and calculation methodology.

TORSION Fatigue Test Bench – Test Bench, Loading and Measurement Verification

With the DANTEC system being the most suitable instrument for the experimental torsion fatigue test measurements (see Section 4.3.2.2), it was deemed appropriate to perform the necessary verification measurements for the test bench. These measurements were done to determine if

the DANTEC system measures correctly in the test bench measurement set-up and if these measurements are comparable to those expected for the induced loading on the test bench.

The first verification measurements made on this test bench involved the measurement of an EN19 (R-condition) steel specimen loaded in torsion with a hanging scale (with force reading) pulling upwards on one of the bilateral wheels. With the hanging scale, it was attempted to apply three different loads so that comparisons could be performed based on the results. The DANTEC was used to measure the torsional displacement (procedure and camera setup in Appendix H4.2 part 1) of the specimen to compare it with the theoretical displacement from a static FEM model simulation (discussed in Appendix I1). These inspection displacement measurements and the method for them on the T fatigue test bench can be referenced in Appendix H4.2 part 2a. The results are summarised in Table 4-6 below.

Table 4-6: T fatigue test bench verification – DANTEC vs static FEM simulation displacements

Specimen #	Diameter	Hang Scale Test #	Hang Scale Maximum Load			S_y / T_{VM}	NX FEM	DANTEC	Difference
	[mm]		[kg]	[N]	[N.m]	[MPa]	[mm]	[mm]	[%]
EN19R-T-Spec-1	6.364	1	8.92	87.51	9.63	1.99	0.07957	0.07603	4.45

The results showed that only the first hang scale test (#1) was valid. It was because the induced VM stress τ_{VM} in the specimen exceeded the yield strength of the EN19 (R-condition) metal during test #2 (S_y reported as 657 [MPa] in [28]). Consequently, test #3 was also assumed invalid (even if $\tau_{VM} < S_y$) due to the plastic deformation the specimen experienced beforehand. Inherently no torsional displacement measurement comparisons could be made for tests #2 and #3 since the relevant static FEM simulations do not account for plastic deformation. For hang scale test #1, a suitably low difference between the theoretical (FEM) and experimental (DANTEC) displacements were obtained (using Equation (H-12)).

After the above measurements were performed, an additional test was performed to show further that the measurement and calculation process for the DANTEC on this test bench is correct. For these measurements, and due to the single vibration mode experienced by the T fatigue test bench, it was presumed that the experimental torsion gain of a specimen (also EN19 (R-condition) material) would be comparable with those calculated theoretically. The loading on this specimen was induced with the centrifugal mass pieces on the test bench bilateral wheels, rotating at speed.

These measurements were also made with the DANTEC over a chosen range of test speeds N [Hz] whilst keeping the centrifugal mass piece and the radial position on the wheels constant. The purpose of these measurements was to compare the experimentally measured torsional gain (G_T)

response of the specimen (under fully reversed torsional loading) with the theoretically calculated gain response (the reference, see Appendix F1 and F2). The measurements made with the DANTEC and the method and the equations used to obtain the specimen's experimental loading gain response can be referenced in Appendix H4.2, part 2b. The results of these measurements and the corresponding experimental gain calculations (using methodology in previous Section 4.4.2.3) are summarised in Table 4-7 below.

Table 4-7: T fatigue test bench verification – experimental vs theoretical torsion gain

			V ref point	Gauge P1-P2 Displacement - @ E = E_{NX} = 206.9GPa			
Specimen #	**Diameter**	**N**	**Theoretical G_T**	**NX FEM**	**DANTEC**	**Experimental G_T**	**Difference G_T**
	[mm]	**[Hz]**	**[-]**	**[mm]**	**[mm]**	**[-]**	**[%]**
EN19R-T-Spec-1	6.364	-	-	-	-	-	-
EN19R-T-Spec-2	6.368	25	1.134	0.02044	0.02221	1.086	-4.21
	6.368	30	1.205	0.02943	0.03363	1.142	-5.23
	6.368	35	1.302	0.04006	0.05086	1.269	-2.50
	6.368	40	1.435	0.05233	0.07608	1.454	1.35
	6.368	45	1.622	0.06623	0.11522	1.740	7.28

From the results reported and illustrated in the table above and Figure 4-16 below, it was shown that the experimental torsional gain response (from the DANTEC and FEM simulation displacements) was very similar to the theoretically calculated gain response of the specimen (yellow curve) over the five test speeds considered with the relevant centrifugal mass piece (NUT 8). Reference can also be made to Figure H-26. The calculated difference values between the theoretical and experimental gains (using Equation (H-15)) at each test speed were sufficiently low, with only the 30 [Hz] and 45 [Hz] test speeds showing differences more significant than 5 [%].

The assumption of little to no damping on the torsional loading gain for the T fatigue test bench (see Appendix F1), therefore, is appropriate over the considered test speed range. That is since the theoretically calculated gain response (without damping, Equation (F-4)) was very similar to that measured experimentally (see Equation (H-14)). The test speeds that showed the lowest gain difference values for this were 25 [Hz], 35 [Hz] and 40 [Hz]. It is possible that for test speeds lower or higher than the range considered (in Figure 4-16), the experimental gain response may become less similar to the theoretical gain response under this assumption for damping.

The variations between the results might be attributed to the DANTEC digital gauge point placement on the specimens for displacement measurement (P1 & P2, see Figure H-25). A separate evaluation of the DANTEC data in the ISTRA 4D software had to be performed for each test speed measurement. For these evaluations, the gauge points had to be placed (with consistency) on the specimen surface markings. These markings were adapted after the hanging

scale measurement specimen markings were deemed too large relative to the speckle pattern. It was also postulated that the T fatigue test bench may have experienced rigid body displacements (within DANTEC coordinate system). This rigid body motion may have influenced the displacement measurements of the specimen and, thus, the calculated experimental gain value. These rigid body displacements of the test bench were initially accommodated by considering the second digital gauge point (P2) displacement at the bottom of the specimen (see Equation (H-13)). However, as only later observed during the first official torsion displacement measurement with the DANTEC (discussed in Appendix H4.2 part 2c), the rigid body motion influence of the test bench may have manifested in the above displacement measurements. This rigid body motion was addressed for all subsequent (official) T fatigue test bench measurements with the DANTEC by placing 50 [kg] mass pieces around the test bench on the laboratory workbench (see Appendix H4.2 part 1, Figure H-20).

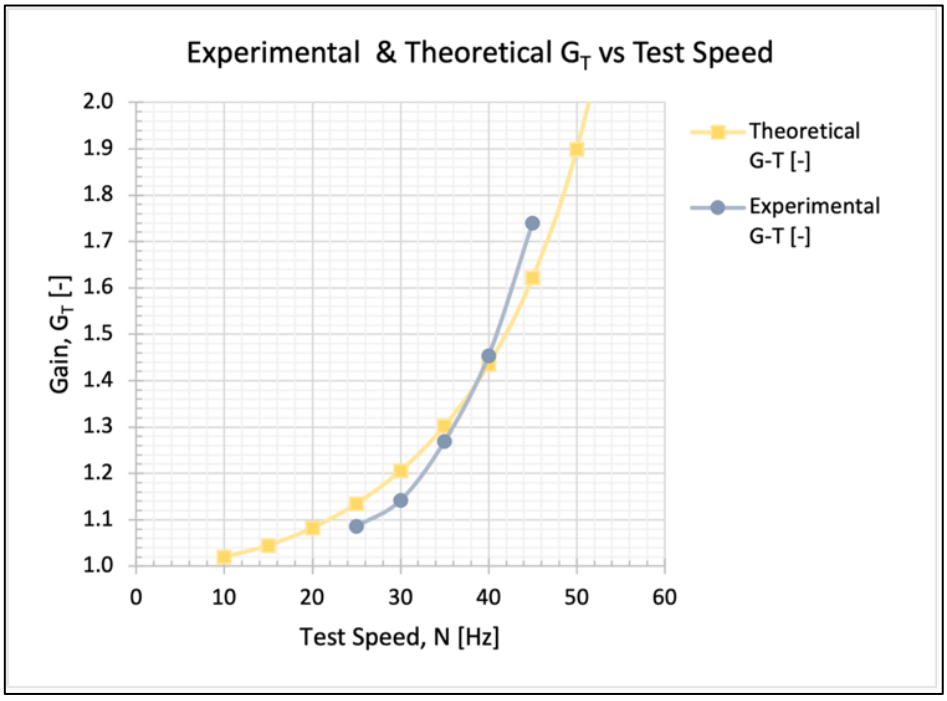


Figure 4-16: T fatigue test bench verification – experimental and theoretical gain response curves

The NX static FEM simulations (Appendix I1) for the theoretical (nominal 'ungained' loading) displacement measurements used to calculate the experimental gain values in Table 4-7 above were performed with the torsion specimen FEM model being assigned with the NX standard 'steel' library material (Elasticity Modulus E_{NX} = 206.9 [GPa]). The same E_{NX} was used for the hang scale FEM specimen in Table 4-6. This was due to the unknown E value of the specimen EN19 (R-condition) steel. It was, however, later shown that not using an experimentally determined E

value would have had a negligibly small influence. That is, on the theoretical FEM simulation displacements (see Figure I-2 of Appendix I2) and thus the experimental gain calculation result. For the official four T fatigue specimen displacement measurements made in NX (discussed in Appendix I1), the appropriate experimentally determined Elasticity Modulus E_{exp} = 211.174 [GPa] of EN19 (T) was, however, used. It was done by applying a user-defined material to the FEM model. Therefore, the most significant gain difference in Table 4-7 was not due to the above simulation approach and material selection.

Another possible reason for the largest differences in gain at the 30 and 45 [Hz] test speeds may be attributed to how the theoretical torsional gain calculation (Equation (F-1) to (F-4)) input values were considered and calculated (e.g., the polar mass moments of inertia and the specimen stiffnesses, in Appendix F). It is also possible that complex damping effects, not considered in the theoretical gain calculation, could be present. However, the sufficiently low difference values in Table 4-7 suggest that the theoretical torsion gain values were satisfactorily calculated with these input values. The low gain difference values also suggested that these theoretical gain values can be useful.

The above-discussed test bench setup and measurement verification with the previously verified DANTEC system provided the necessary results to show that the T fatigue test bench induced the appropriate torsion loading on a specimen. Along with the formerly discussed theoretical torsion gain and general loading considerations (Section 4.4.2.1) for this test bench, these results provided ample confidence that the subsequent experimental torsion fatigue loading on the official test specimens would also be correct. A selected few (4) of these specimens were also measured for the assurance with the DANTEC during experimental testing (Appendix H4.2 part 1 and 2c) to obtain the experimental torsion gain values which the relevant uniaxial torsion fatigue stresses could be calculated. The experimental and theoretical gain comparisons from these measurement results were very good (see Table H-15). A negligible influence of specimen diameter uncertainty on the torsion gain was also taken into account (see Figure K-4). It was ultimately shown to be valid and sufficient to set the remaining experimental T fatigue specimen gain values (not measured) equal to the theoretically calculated values. That is, performing direct measurements for each test specimen was not required. These official experimental torsion gain measurement and calculation results are reported in Table J-4 and will be later discussed in Section 5.2.2. The measured fully reversed torsion fatigue displacement (loading) curves (from the DANTEC) will also be provided, showing that the induced loading was correct on each test specimen.

BENDING-TORSION Fatigue Test Bench – Loading Characterisation

The DANTEC system was also the most suitable instrument for the required experimental fatigue test measurements on the bending-torsion (BT) fatigue test bench. Before these official out-of-phase BT fatigue tests and measurements were performed (Section 4.5), it was first required to determine if the theoretical equivalent gain point (in Figure 4-12) would be comparable to one obtained from experimental displacement measurements of a BT fatigue specimen. These direct bending and torsion displacement measurements were performed with the DANTEC. From these displacements and the appropriate static FEM displacements, the necessary system characterisation could be achieved based on the calculated experimental bending and torsion gain responses. The experimental equivalent gain point could be identified from these gain responses for this test bench.

For the displacement measurements, it was decided to test one of the official BT fatigue test specimens (Spec18) over a selected range of test speeds N [Hz] with two centrifugal mass pieces respectively at the same radial positions on the wheels (NUT 8 – lightest and then NUT 5 – heaviest at the time). The reason for only considering these two nuts was because they were the extremes regarding the mass (see Appendix E2). It was considered that the relevant measurements with these nuts would provide sufficient enough results that may be assumed applicable to the intermediary-sized nuts. In each of these measurements, the DANTEC was used to measure the bending and torsion displacement of Spec18 in the relevant directions (as in Figure H-33 of Appendix H5.2 part 1). The DANTEC measurement procedure and camera setup can be referenced there.

Based on the observations made for the T fatigue test bench measurements (previously below Figure 4-16), the same 50 [kg] mass pieces were placed around the BT test bench during displacement measurements (both for Spec18 here and official specimen measurements later). That is, to suppress excessive laboratory workbench and test bench rigid body displacements that might manifest on the DANTEC measurements (as shown in Figure H-20). The negligible influence (see Figure I-2) of using the NX standard 'steel' library material with an E_{NX} = 206.9 [GPa] for the relevant static FEM model displacements was again taken into account for the experimental gain calculations. The experimental E value of EN19 (T-condition) was undetermined at the time of the FEM simulations of Spec18.

The purpose of these measurements was to obtain the experimental equivalent loading gain values (and the test speed) for which the biaxial nominal stress amplitude ratio of λ = 0.5 [-] is maintained. That is, between the out-of-phase bending and torsion fatigue stresses of the chosen loading condition (see Equation (H-17) to (H-19)). This equivalent gain or 'test' point would be

obtained from the experimental gain response characterisation following the experimental displacement measurements. With this test point (a speed value), all subsequent official specimens could be tested to ensure the appropriate loading is induced. In addition, the experimentally measured bending and torsion gain response (G_B and G_T for Spec18) were compared with the corresponding theoretically calculated gain responses. This comparison was made to determine if like with the T fatigue test bench (previous sub-section above), the theoretical and experimental gain responses were comparable and if the theory could be used to identify this equivalent gain test point.

The measurements made with the DANTEC, the method and the equations used to obtain the experimental bending and torsion loading gain values of Spec18 can be referenced in Appendix H5.2 part 2a. The results of these measurements and corresponding experimental gain calculations are provided in Table H-17 and are graphically illustrated in Figure 4-17 below. These experimental gains were obtained using the method discussed in previous Section 4.4.2.3.

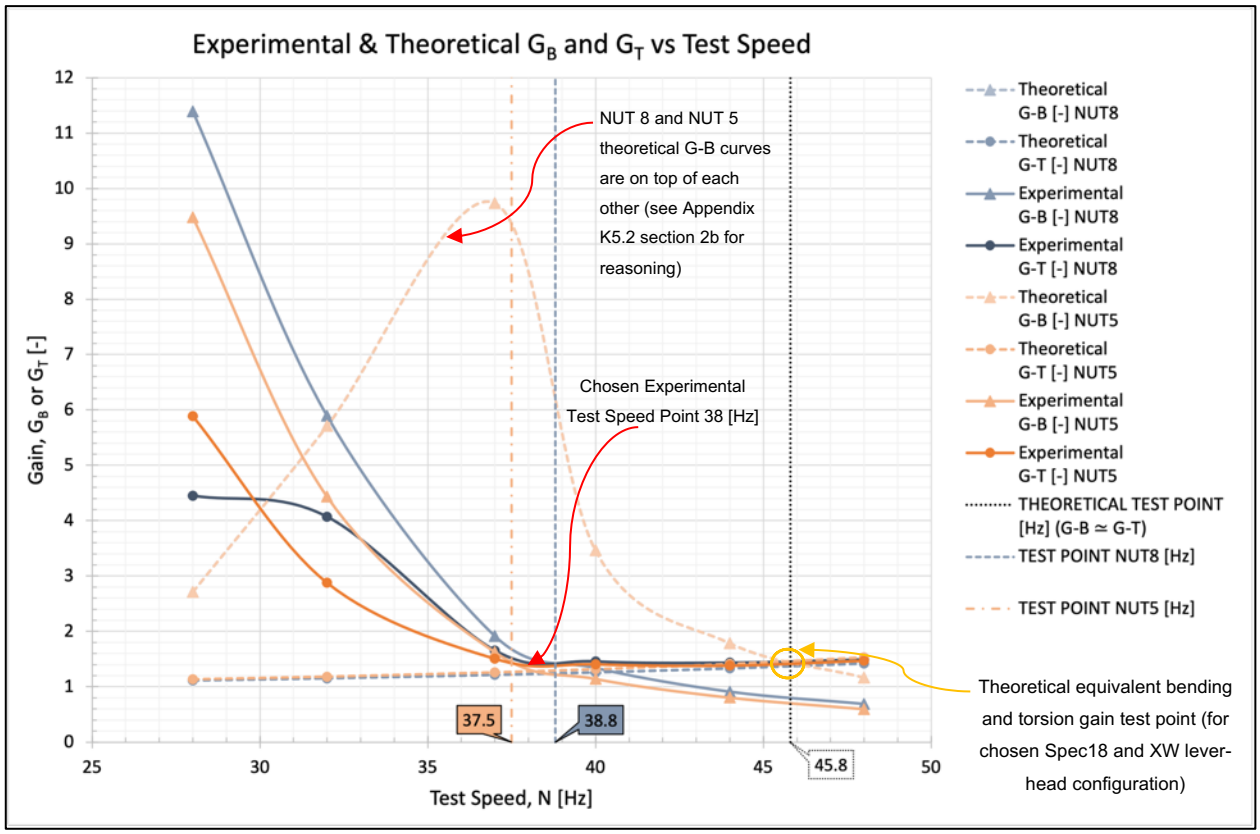


Figure 4-17: BT fatigue test bench loading characterisation – experimental and theoretical gain response curves

These results showed that the experimental bending and torsion gain responses (from the DANTEC and FEM displacements) were different from the theoretically calculated gain responses

(dashed lines) of Spec18. Over the six test speeds, that is, for both centrifugal mass pieces (NUT 8 and NUT5). This difference was unlike what was shown for the T fatigue tests bench (in the previous measurements). The theoretical loading gain considerations made for the BT fatigue test bench in Section 4.4.2.2 were therefore shown to be insufficient. It was also shown that the bending and torsion vibration modes severely influenced each other over the 28-40 [Hz] speed range (near bending resonance). This unexpected phenomenon showed that considering these modes separately (as theoretically done for dashed line curves) is not appropriate for this test bench. The bending resonance of the specimen was also visually observed during the above measurements on the BT test bench.

There was a test speed range (from 37-40 [Hz]) where the vibration mode influence appeared to diminish, and the bending gain decreased to below the torsion gain. It was in this speed range where the experimental gains also reached a point of equivalence for which the required out-of-phase biaxial loading conditions would be achieved. Based on the results, it was decided that these experimental bending and torsion gain response curves of Spec18 would serve as a reference. It also characterised the experimental gain response that could be expected for the official specimens tested and measured on the BT fatigue test bench.

From the experimental gain curves (solid lines in Figure 4-17 above), it was shown that 38 [Hz] would be the most appropriate test speed for obtaining the required experimentally equivalent loading gains of bending and torsion (for λ = 0.5). This was irrespective of the nut used on the wheels. Based on this and the above observations and measurement results of Spec18, 38 [Hz] was chosen as the official experimental BT fatigue test speed for subsequent tests on this test bench (later substantiated). For these tests, it was also assumed, based on very similar average specimen diameter measurements (see Table D-5, the maximum deviation of 0.03 [mm]), that this test speed would be suitable for all the BT fatigue specimens.

Regarding the experimental gain curves, smaller test speed increments (over the same range) for respective displacement measurements would have provided more detailed gain responses. A more precise identification of the equivalent test point might have been possible. However, due to the previously mentioned bending resonance visually observed during the Spec18 measurements (at low speeds), it was not considered appropriate since the specimen experienced substantial displacements and, thus, stresses at these lower test speeds. Specimen failure was, therefore, a concern. For the results shown in Figure 4-17 above, the displacement measurements were first performed at the higher test speeds (lower gains) and then at the lower test speeds.

The above-discussed DANTEC measurement results of Spec18, in conjunction with the torsion measurement verification (previous part), provided sufficient confidence that the official BT fatigue tests and measurements that followed would also be correct if performed at the identified equivalent gain test speed of 38 [Hz]. The resultant bending and torsion gain values obtained from these official and direct experimental displacement measurements at 38 [Hz] (for three (3) specimens only) were utilised in the subsequent bending and torsion stress amplitude calculations of all the official test specimens. The experimental test and measurement methodology used for the official BT fatigue tests are discussed in Section 4.5 to follow.

4.4.3 Experimental Fatigue Limit and Failure Definition

The last experimental consideration that had to be made was for the experimental fatigue failure and fatigue limit definition implemented on the uniaxial and biaxial fatigue tests. The fatigue limit (or endurance limit) for ferrous metal fatigue testing and data in the literature is generally defined around the theoretically infinite fatigue life cycle count of 10^6 cycles, where the life curve starts to flatten out at a certain fatigue failure stress level [3, 16, 45, 62, 66]. This is typically shown on an S-N curve (stress-life), as in Figure 4-18 below.

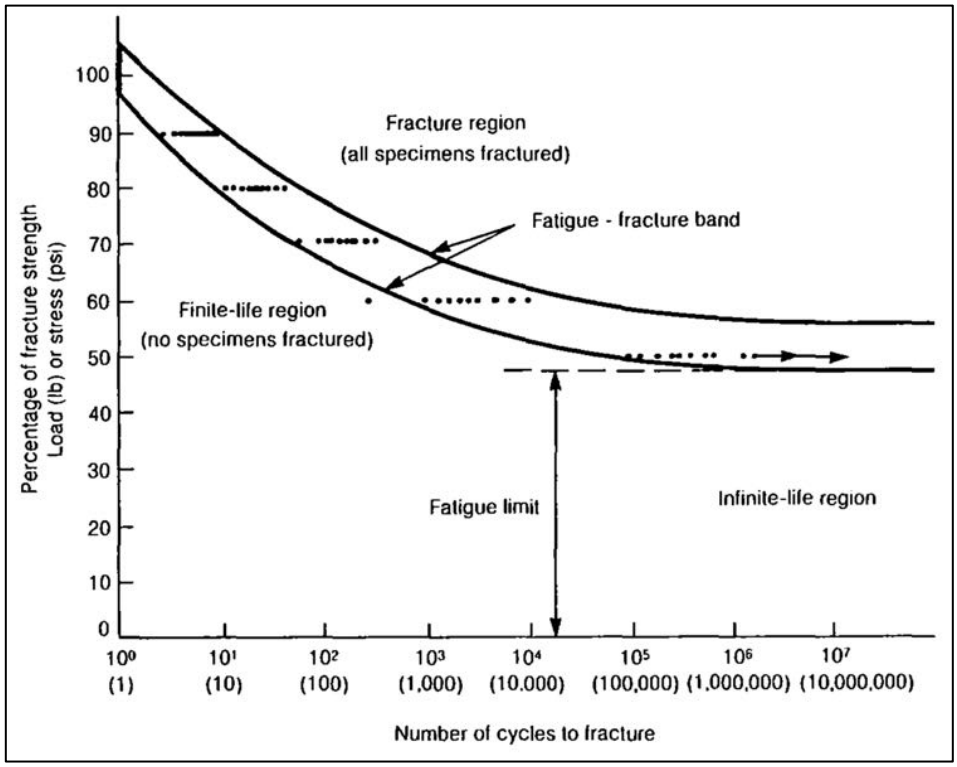


Figure 4-18: Illustrative S-N curve of fatigue tests on medium-strength steel [62]

However, there are other experimental fatigue limit definitions reported for different fatigue limit data sets in the literature (see Section 2.5 and 2.6), and these include $1.5x10^6$ and $2x10^6$ (both common) and $1x10^7$ (scarce) [43, 64]. The higher $1x10^8$ definition is primarily used for non-ferrous metal fatigue testing [1, 24, 56]. A new fatigue limit regime has recently become a topic of study in the literature. It is referred to as the 'giga-cycle fatigue' (GCF) or 'very high cycle fatigue' (VHCF) regime, where especially uniaxial fatigue testing is done for lives of 10^7 - 10^{10} cycles to investigate mechanical behaviour, fatigue life and fatigue failure mechanisms of materials [1].

For this study, the *experimental fatigue limit* was conservatively chosen as $1.5x10^6$ cycles (for both uniaxial and biaxial fatigue tests). The reason for choosing this fatigue limit was time constraints since various types, and quantities of fatigue tests had to be performed (see Section 4.4.1.1). More and longer fatigue life tests were therefore not feasible. Some non-failed specimens (in biaxial BT fatigue tests) were allowed to run up to $3x10^6$ cycles to ensure that no failure would occur at the experimentally evident fatigue limit stress level.

The two primary definitions reported in the literature for the fatigue failure of a specimen include *complete fracture* (easiest to test and observe and most used) or *fatigue crack initiation* (less common) [49, 60]. The former is typically used for stress-based fatigue criteria (failure criteria), which estimate the cyclic stresses that would cause complete failure of a component. These are the criteria considered in this study. Therefore, the *experimental fatigue failure definition* assumed was *a complete fracture* of a fatigue test specimen. The experimental *fatigue life* or *failure cycles* N_f [-] reported for each test specimen (Sections 5.2.2 to 5.2.3) was the *number of fatigue stress cycles* until the *complete fracture*.

4.5 Experimental Biaxial Fatigue Testing and Measurement

The previous sections of this chapter identified the experimental test and measurement equipment (Section 4.3) and the testing and loading considerations (Section 4.4) for all the relevant tests performed. This section considers the experimental out-of-phase biaxial bending-torsion (BT) fatigue test and measurement methods used to generate the necessary multiaxial (biaxial) fatigue data.

Only BT fatigue testing is discussed in this section because it was the primary fatigue test data set required for evaluating the chosen three multiaxial fatigue criteria (see Section 3.3 and Table 4-1). These evaluations are discussed later in Section 4.7. It was also for the compactness and brevity of this test and measurement section. For the supplementary and required experimental tests performed (TEN, AX, B and T), the test, measurement and calculation procedures would

have been too comprehensive to include here. For these tests, references can be made to Appendix G1 to G4 and Appendix H1 to H4, respectively. These tests are again included in the data processing discussion in Section 4.6.

4.5.1 Testing Methodology

The main experimental BT fatigue test objective was to obtain the bending and torsion stresses and the fatigue life cycle counts. With these, the relevant S-N curves could be established to represent the out-of-phase biaxial BT fatigue strength behaviour of the EN19 (T-condition) alloy steel. The experimental stresses could also be utilised to evaluate the three fatigue criteria. The fatigue cycle counts (to failure or fatigue limit) were calculated from the test speed (set in [Hz] on the test bench VSD) and the elapsed time recorded for each test on the dedicated relay timer (in [hr], see Appendix B7). This timer was set on an hour-minute setting to allow for longer test time recordings, resulting in an unavoidable 1 [min] (or average 2387) cycle count uncertainty on each of the calculated experimental fatigue cycle counts. Reference can be made to Appendix H5.1 for further discussion on the BT fatigue test and calculation methodology and Appendix J5 for the individual test results obtained. All the BT fatigue tests were performed at room temperature conditions (isothermal fatigue), as typically done for fatigue tests in the literature [14].

For the out-of-phase biaxial BT fatigue tests, seventeen (17) specimens were available (see Figure H-31). These specimens were machined and polished, after which their test zone diameters were measured (as in Section 4.4.1) to obtain the appropriate average values (see Appendix B1 and D5) required for calculating the experimental stresses in each test.

All the BT fatigue tests were performed on the Biaxial Fatigue Test Bench M1 - Bending-Torsion (see Figure 4-6) according to the test procedure provided in Appendix G5. These tests were performed at the previously identified experimental test speed of 38 [Hz]. At this speed, the biaxial bending and torsion gain values were supposed to be equivalent (see verification measurements in Section 4.4.2.4). The relevant specimen displacement measurements (with the DANTEC and static FEM simulations for three tests) and the calculations to obtain and confirm these equivalent experimental gain values are discussed in Section 4.5.2 hereafter.

For each BT fatigue test performed, an appropriate centrifugal mass piece and radial position were chosen (from Appendix E2) to produce the centrifugal forces and the bending and torsion moments, as illustrated in Figure H-30. Initially, the approach was to arbitrarily choose these such that a specimen would either experience fatigue failure at a relatively low cycle count ($\sim 10^5$ cycles) or not fail at all. This approach aimed to obtain the ‘end points’ (or boundaries) of the experimental bending-torsion fatigue S-N curve (based on the bending stress). All subsequent

specimens could then be tested between these boundaries to obtain the fatigue strength of the material at the intermediate biaxial out-of-phase loading levels (around the expected S-N curve inflexion point, see previous Figure 4-18). This initial 'end point' testing approach was similarly taken for the other experimental uniaxial fatigue tests (AX, B and T).

Once it was known which centrifugal mass pieces (and radiuses) would provide the necessary intermediate fatigue loading conditions (for HCF data points), more tests were performed with the remaining specimens. These specimens were all tested until either failure occurred or the defined fatigue limit cycle count (1.5×10^6) was reached. After sufficient trend-forming data points were obtained over the 10^4 to 10^6 cycle count range (HCF), repeating the tests that failed close to 106 cycles was deemed appropriate. These tests were repeated using the same centrifugal mass pieces and radial positions on the wheels (specifically of the Spec5, Spec6 and Spec7 tests). This repetition was done for the last ten (10) test specimens (Spec8 to Spec17) to obtain the expected fatigue life spread inherent to fatigue testing. This spread is later illustrated with the experimental results in Section 5.2.3.

Apart from repeating tests, it was also decided to allow three tests (Spec13, Spec14 and Spec17, respectively) to run up to $2.8 – 3.5 \times 10^6$ cycles. This extended life testing was done to ensure that no failure would occur at the related stress levels at cycle counts far beyond the defined fatigue limit cycle count. These extended tests further contributed to the experimental fatigue data spread around the theoretical fatigue limit of 10^6 cycles (also illustrated in Figure 4-18). The repeating or extended run-time of tests was not implemented for the experimental uniaxial fatigue tests (AX, B and T) due to the much fewer test specimen being available.

4.5.2 Specimen Measurement

It was previously shown for the BT fatigue test bench (in Section 4.4.2.4) that the theoretical and experimental bending and torsion gain response differences were significant. It resulted in no allowance for using theoretically calculated gain values in the above-mentioned experimental stress calculations (see Figure 4-17). Therefore, unlike with the T fatigue test bench, the experimental loading gain values (of un-measured test specimens) could not be set equal to the theoretically calculated values. Instead, the unmeasured specimen gains had to be estimated from the three (3) official experimental bending and torsion displacement measurements. The methodology for these direct experimental measurements of the specimens is discussed in this section.

The experimental displacement measurements were performed using the DANTEC system setup illustrated in Figure 4-19 below and the procedure discussed in Appendix H5.2, part 1. In each of these measurements, the DANTEC system measured the bending (z-direction) and torsion (y-direction) displacement of the specimen gauge surface markings (as shown in Figure 4-13) at a frame rate of 195 [Hz]. These specimen markings were positioned perpendicular to the 'mount bar' as far as possible (through specimen clamping) and the cameras measured from the right-hand side of the test bench.

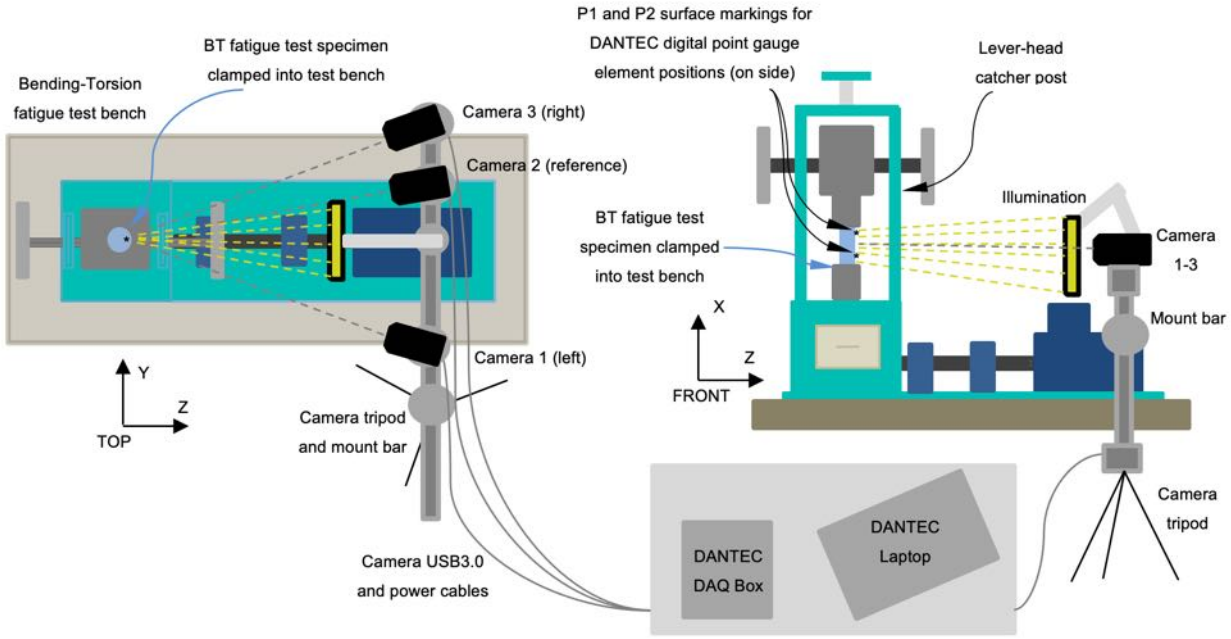


Figure 4-19: BT fatigue test specimen measurement – DANTEC DIC System setup for biaxial bending-torsion displacement measurement

The approach to measuring from the side was deemed most appropriate for obtaining direct linear bending and torsion displacement measurements (to compare with the relevant static FEM displacements). It also allowed the use of all three high-speed cameras (1 left, 2 middle as reference and 3 right), which inherently increases the DANTEC's measurement quality, accuracy and 3D specimen displacement portrayal under biaxial loading. The reasons linear (translational) displacement measurements were used for each loading component (and direction) are discussed in Appendix H5.2, part 1. These measurements were, therefore, performed similarly to the previously discussed measurements of the BT fatigue test bench. Now, only for three (3) of the official experimental BT test specimens to obtain and confirm the experimental loading gain values (to be very similar) at the identified experimental test speed of 38 [Hz].

These three specimens (Spec3, Spec9 and Spec15) were tested with different centrifugal mass pieces (NUT 9, NUT 5 and NUT 4), as shown in Table 4-8 below. These nuts were fastened at the selected wheel radius position for each test. The relevant image correlation and evaluation were performed for each specimen in the ISTRA 4D software of the DANTEC. The evaluated displacement measurements were exported and further processed as discussed in Appendix H5.2, part 2b. The necessary static FEM simulations were also performed using the experimental EN19 (T-condition) tensile properties for the FEM model material. With these, the nominal 'ungained' bending and torsion displacements (as discussed in Appendix I2) were obtained to calculate the respective experimental loading gain values (using the method discussed in Section 4.4.2.3).

Table 4-8: BT fatigue test specimen measurement – measured and inferred tests

Measured Spec3

Specimen #	Diameter [mm]	Nut #	Radius [mm]	N [Hz]	Experimental G_B [-]	Experimental G_T [-]
EN19T-BT-Spec-1	6.527	NUT 1	35	38.0	1.359	1.269
EN19T-BT-Spec-2	6.534	NUT 3	35	38.0	1.364	1.274
EN19T-BT-Spec-3	6.560	**NUT 9**	30	38.0	**1.428**	**1.486**
EN19T-BT-Spec-4	6.548	NUT 9	40	38.0	1.425	1.482
EN19T-BT-Spec-5	6.552	NUT 9	35	38.0	1.428	1.485
EN19T-BT-Spec-6	6.554	NUT 5	35	38.0	1.367	1.357
EN19T-BT-Spec-7	6.563	NUT 4	40	38.0	1.384	1.293
EN19T-BT-Spec-8	6.539	NUT 4	40	38.0	1.367	1.277
EN19T-BT-Spec-9	6.563	**NUT 5**	35	38.0	**1.372**	**1.365**
EN19T-BT-Spec-10	6.653	NUT 9	35	38.0	1.500	1.558
EN19T-BT-Spec-11	6.568	NUT 9	35	38.0	1.439	1.496
EN19T-BT-Spec-12	6.571	NUT 5	35	38.0	1.379	1.369
EN19T-BT-Spec-13	6.539	NUT 4	40	38.0	1.367	1.277
EN19T-BT-Spec-14	6.577	NUT 4	40	38.0	1.394	1.302
EN19T-BT-Spec-15	6.571	**NUT 4**	40	38.0	**1.389**	**1.299**
EN19T-BT-Spec-16	6.574	NUT 5	35	38.0	1.381	1.371
EN19T-BT-Spec-17	6.589	NUT 5	35	38.0	1.392	1.382

Considering only three specimens for experimental measurement (bold Nut # and $G_{B/T}$ values) was based on the assumption that repeating these tests with the other specimens would result in very similar experimental bending and torsion gain values (at 38 [Hz]), as is shown in Table 4-8 above. The effect of specimen diameter uncertainty on the experimental bending and torsion gains of the three specimens was obtained for this. For all the unmeasured BT fatigue test specimens (light green/blue/orange), the gains were subsequently estimated from the three measured specimens using the applicable gain sensitivity trendline equations from Figure K-5 (c), (e) and (g), respectively, in Appendix K5.

The experimental displacement measurement and calculated gain results of the three relevant BT fatigue specimens can be referenced in Table H-19. The measured and estimated (unmeasured) specimen experimental gains (as above) can also be collectively referenced in

Table J-5 (test results table). These official loading gain measurement results will be discussed along with the measured bending-torsion fatigue loading displacement curves in Section 5.2.3. These fully reversed out-of-phase sinusoidal displacement curves further reflected that the expected biaxial loading was, in fact, appropriately induced on each test specimen in this test bench. The unique phenomenon of rotating principal stresses (due to out-of-phase bending-torsion loading condition), as previously identified in Section 2.3 and discussed in Section 3.2, was also observed in all these experimental measurements with the DANTEC system.

4.6 Experimental Data Processing

The preceding sections in this chapter identified and discussed the relevant experimental methodology followed to generate the material and fatigue strength data for EN19 (T-condition) steel. This section will discuss the methods considered for experimental stress calculation, uniaxial fatigue limit strength estimation and uncertainty analysis for each of the five test types performed.

4.6.1 Experimental Stresses

This part discusses the methodology and equations used to calculate the experimental stress values for each specimen tested on the test benches previously identified in Section 4.3.1. These methods and equations can be referenced in Appendix H1 through H5.

For the ten (10) tensile (TEN) tests performed on the MTS Landmark test machine (with and without the extensometer), it was required to export and process the relevant tensile test data and curves recorded during each test on the dedicated computer system. From the processed data exports (see Table H-1 to Table H-4), the relevant yield (at 0.2 [%] strain line offset), ultimate tensile and offset loading values could be obtained. These values were then utilised in Equations (H-1) to (H-2) to calculate the ultimate tensile strength S_{ut} and yield strength S_y of each TEN test specimen. The average of these values was then calculated as the experimental EN19 (T-condition) material strength values. The relevant tensile specimen gauge extension measurements made with the extensometer were also exported, processed and utilised to calculate the material's Elasticity Modulus E using Equation (H-3). The average between this and the directly measured values (of extensometer) was assumed as the material stiffness of each specimen. The average of these values, in turn, was then calculated as the experimental material stiffness. Reference can be made to Appendix H1.1 and H1.2 for a more detailed illustration and discussion of the above TEN test specimens and experimental material strength calculations.

These TEN test results are reported in Table J-1 and discussed in Section 5.2.1 of the next chapter.

The eight (8) uniaxial axial (AX) fatigue tests, also performed on the MTS Landmark, similarly required the exporting and processing of test data. The axial fatigue amplitude values could be obtained from these processed data sets (provided in Table H-8 to Table H-10). The negligibly small and unavoidable midrange loading values (much like TEN test offset loading) were also obtained and subtracted from the experimental amplitude values. These experimental loading amplitudes were then utilised in Equation (H-7) to calculate the resultant fully reversed axial fatigue stress amplitude $\sigma_{axial;a}$ for each test (using post-test failure point diameter, as discussed in Section 4.3.2.1). Reference can be made to Appendix H2 for a more detailed illustration and discussion of the above AX fatigue test specimens and experimental fatigue stress calculations. These AX fatigue test loads and stresses are reported in Table H-10 (experimental loading amplitudes) and Table J-2 and are also discussed later in Section 5.2.2.

For the seven (7) uniaxial bending (B) fatigue tests performed on the bending fatigue test bench, it was required to calculate the experimental cantilever bending forces from the load cell calibration curve (see Figure A-6) for each test specimen. These forces were then utilised in Equations (H-8) and (H-9), along with the specimen diameter and the critical stress position (see Figure H-14) to calculate the resultant fully reversed bending fatigue stress amplitude $\sigma_{bending;a}$ for each test. The diameters and critical stress positions used were post-test failure point measurements, as mentioned in Section 4.3.2.1. Reference can be made to Appendix H3 for a more detailed illustration and discussion of the above B fatigue test specimens and experimental fatigue stress calculations. These B fatigue test results are reported in Table J-3 and discussed later in Section 5.2.2. Spec8 of the B fatigue tests had manufacturing defects (omitted).

For the nine (9) uniaxial torsion (T) fatigue tests performed on the newly developed torsion fatigue test bench, the nominal loading (centrifugal force and resultant torsion moment) was calculated with Equation (H-10). This calculation was done at the relevant test speed of each test for the chosen centrifugal mass piece, radial position on the wheels and the corresponding moment lever length (see Appendix E2). From the nominal (ungained) moment and the experimental torsional loading gain value, the fully reversed torsion fatigue stress amplitude τ_a could then be calculated for each test specimen using Equation (H-11). These experimental gain G_T values were measured with the DANTEC system for four (4) T fatigue test specimens (see Appendix H4.2 parts 1 and 2c). For the unmeasured specimens, the values were assumed equal to the calculated theoretical gain values (based on the verification measurement results in Section 4.4.2.4). Reference can be made to Appendix H4.1 and H4.2 part 2c for a more detailed illustration and discussion of the

above T fatigue test specimens, experimental fatigue stress and gain calculations. The relevant T fatigue test results are reported in Table J-4 and discussed later in Section 5.2.2.

The seventeen (17) biaxial bending-torsion (BT) fatigue tests performed on the biaxial fatigue test bench similarly required the calculation of the nominal loading ($F_{centrifugal}$ and $M_{B/T}$) using Equation (4-3) below. This calculation was done at the chosen test speed N of 38 [Hz] of each BT fatigue test for the chosen centrifugal mass piece m_{centr}, radius r_{wheel} and moment lever length L_{lever} (see Appendix E2). With the nominal moments (ungained and equal) and the experimental bending and torsion loading gain values $G_{B/T}$, the fully reversed out-of-phase bending and torsion fatigue stress amplitudes $\sigma_{bending;a}$ and τ_a could be calculated using Equations (4-4) and (4-5) below. These equations are repeated here from Equations (H-16) to (H-19) in Appendix H5.1.

$$M_{B/T}\,[N.m] = 2\left(F_{centrifugal}L_{lever}\right)\,[N.m] = \; 2(m_{centr}r_{wheel}(2\pi N)^2 L_{lever})\,[N.m] \qquad (4\text{-}3)$$

$$\sigma_{bending;a}\,[MPa] = \left\{\left[\frac{32\,M_B\,[N.m]}{\pi d_{spec}^3\,[m^3]}\right] / 10^6\right\} G_B \qquad (4\text{-}4)$$

$$\tau_a\,[MPa] = \left\{\left[\frac{16\,M_T\,[N.m]}{\pi d_{spec}^3\,[m^3]}\right] / 10^6\right\} G_T \qquad (4\text{-}5)$$

$$\lambda\,[-] = \tau_a \; / \sigma_{bending;a} \qquad (4\text{-}6)$$

where d_{spec} : is the BT fatigue specimen test zone diameter (Appendix D5)

m_{centr} : is the sum of relevant bolt, nut and washer masses (Appendix E2)

The above experimental gain values G_B and G_T were obtained from the measured displacements with the DANTEC system for the three (3) measured BT fatigue test specimens. For the unmeasured specimens, the gains were calculated from the gains of the measured specimens based on the centrifugal nut used (see previous Table 4-8 and discussion). Reference can be made to Appendix H5.1 and H5.2 part 2b for a more detailed illustration and discussion of the above BT fatigue test specimens, the experimental fatigue stress and the bending-torsion gain calculations. The relevant BT fatigue test results are reported in Table J-5 and discussed later in Section 5.2.3.

4.6.2 Fatigue Limit Strength Estimation

This part references the experimental fatigue limit and fatigue failure definitions previously provided in Section 4.4.3.

It was assumed that a manual estimation method for each experimental fatigue limit value would be appropriate for the fatigue tests performed. This assumption was made because the various uniaxial fatigue tests were performed supplementary to the biaxial tests. Their respective fatigue limit values (specifically f_{-1} and t_{-1}) were required to evaluate the chosen fatigue criteria (see Table 4-1). A more appropriate or analytical fatigue limit estimation method was not considered due to the limited uniaxial fatigue test data (limited material quantity and, thus, specimen allocation for each test type). The chosen manual estimation method was regarded as sufficient since it was deemed less appropriate to estimate these fatigue limits from the literature due to the inherent material variability with the EN19 (T-condition) steel in this study.

These fatigue limit strengths were estimated using the infinite life specimen (no failure after defined 1.5 x10^6 cycles) with the highest fatigue stress value. Suppose this specimen was tested at a stress level similar to a non-infinite life specimen (e.g., that failed at cycle count < 10^6); the next lower stressed infinite life specimen was then considered. This was done until the fatigue limit obtained was appropriate. This value was then assumed as the fully reversed uniaxial axial, bending or torsion fatigue limit, respectively, and used for each criterion evaluation.

It should be noted that no claim was made that the resultant uniaxial fatigue limit values obtained were the absolute limit values of the material. The experimentally obtained values (reported in Appendix J2 to J4) were assumed as more appropriate experimental estimates. These values might have been different if more specimens were tested in each uniaxial fatigue test type. As later discussed in Section 5.2.2, these values were compared with the relevant theoretical ranges or equivalent values to ensure appropriateness and validity.

4.6.3 Uncertainty Analysis

This part discusses the experimental uncertainties for the tensile and fatigue test stresses (see previous Section 4.6.1). A 95 [%] confidence interval (e.g., two standard deviations or $1.96Z_{\alpha/2}$) was assumed for all the resultant stress uncertainties calculated with the following equations.

TENSILE Tests – Experimental Uncertainties

The monotonic tensile strength uncertainties $u(S_{ut;spec})$ and $u(S_{y;spec})$ of each tensile (TEN) test was calculated with Equations (4-7) and (4-8) below. The specimen *diameter* and *tensile force* uncertainty were respectively considered for this. The MTS Landmark tensile load uncertainty was assumed as the average (0.247 [%] of the applied load) of the reported error percentages over the 10 - 40 [kN] loading range in the tension and compression calibration certificates of the machine (see Appendix A1). The four partial derivative values (sensitivity) for the equations below were obtained as the linear trendline slope values shown respectively in Figure K-1 (a) and (b). For this, the specimen diameter was varied by 0.3 [mm] (the largest variation in specimen diameter measurements), and the tensile forces were varied by the assumed 0.247 [%] MTS load uncertainty to obtain these sensitivity values. These partial derivatives (and those that follow for other tests) were also analytically checked and confirmed.

$$1.96u(S_{ut;spec}) = 1.96\sqrt{\left(\frac{\partial S_{ut}}{\partial d}u(d)\right)^2 + \left(\frac{\partial S_{ut}}{\partial F_{UTS}}u(F_{UTS})\right)^2} \tag{4-7}$$

$$1.96u(S_{y;spec}) = 1.96\sqrt{\left(\frac{\partial S_{y}}{\partial d}u(d)\right)^2 + \left(\frac{\partial S_{y}}{\partial F_{Y}}u(F_{Y})\right)^2} \tag{4-8}$$

where $u(d)$: is the TEN specimen diameter standard deviation (Appendix D1) [mm]

$\frac{\partial S_{ut}}{\partial d}$ and $\frac{\partial S_{y}}{\partial d}$: is the ultimate/yield tensile strength sensitivity [MPa/mm] to change in d

$u(F_{UTS})$: is the ultimate force uncertainty calculated as 0.247 [%] of F_{UTS} [kN]

$\frac{\partial S_{ut}}{\partial F_{UTS}}$: is the ultimate tensile strength sensitivity [MPa/kN] to change in F_{UTS}

$u(F_Y)$: is the yield force uncertainty calculated as 0.247 [%] of F_Y [kN]

$\frac{\partial S_{y}}{\partial F_{Y}}$: is the yield strength sensitivity [MPa/kN] to change in F_Y

The ultimate tensile strength and yield strength uncertainties $u(S_{ut})$ and $u(S_y)$ on the average tensile strength values from the test specimens were calculated as combined uncertainty values using Equations (4-9) and (4-10) below. For this, the standard deviation (denoted as $S_{ut;stdev}$ and $S_{y;stdev}$) of the respectively calculated tensile test $S_{ut;spec}$ and $S_{y;spec}$ values and the maximum specimen uncertainty values calculated from Equations (4-7) and (4-8) above were utilised. Therefore, the square root of the sum of the squared 'average' and 'scatter' uncertainties.

$$1.96u(S_{ut}) = 1.96\sqrt{\left(S_{ut;stdev}\right)^2 + \left(u\left(S_{ut;spec}\right)_{max}\right)^2} \tag{4-9}$$

$$1.96u(S_y) = 1.96\sqrt{\left(S_{y;stdev}\right)^2 + \left(u\left(S_{y;spec}\right)_{max}\right)^2} \tag{4-10}$$

The material stiffness uncertainty $u(E)$ on the average experimental E_{avg} value of the last five tensile tests was calculated as only the standard deviation of the per-specimen average $E_{avg;spec}$. This per specimen average was obtained between the 'measured' and 'calculated' values of the extensometer (see Table J-1). Considering only the standard deviation was due to the negligible engineering strain measurement uncertainty of 0.04 [%] (of measured strain, see Table 4-4 on pg.76). This value was reported for the 25 [mm] nominal gauge length extensometer in the calibration certificate in Figure B-6. It was also due to the small differences observed between the direct extensometer measurement E_{ext} values (see Table H-4) and those calculated from the extensometer data E_{calc} (see Table H-3). For these, a maximum deviation of 1.47 [GPa] was obtained. Therefore, a per specimen-based uncertainty on $E_{avg;spec}$ was not considered. All the above experimental TEN test uncertainties are provided in Table J-1 and Table K-1, and will later be discussed in Section 5.2.1.

AXIAL Fatigue Tests – Experimental Uncertainties

The axial fatigue stress amplitude uncertainty $u(\sigma_{axial;a})$ of each axial (AX) fatigue test was calculated with Equation (4-11) below. Consideration was made for the specimen *diameter* uncertainty and the *axial fatigue load amplitude* uncertainty, respectively. The load amplitude uncertainty was assumed as the same value (0.247 [%] of applied load) as the tensile test loading above. The two partial derivatives (sensitivity) for the equation below were obtained as the linear trendline slope values shown in Figure K-2 (a) and (b). These values were also analytically checked, and a maximum difference of 0.6 [%] was obtained between the analytical and manual method sensitivity values. For this, the specimen diameter was also varied by 0.3 [mm] and the axial fatigue load amplitude varied by the assumed 0.247 [%] MTS load uncertainty to obtain

these sensitivity values. All the above experimental AX fatigue test uncertainties are provided in Table K-2 and will later be discussed in Section 5.2.2.

$$1.96u\left(\sigma_{axial;a}\right) = 1.96\sqrt{\left(\frac{\partial\sigma_{axial;a}}{\partial d}u(d)\right)^2 + \left(\frac{\partial\sigma_{axial;a}}{\partial F_{axial;a}}u\left(F_{axial;a}\right)\right)^2} \quad (4\text{-}11)$$

where $u(d)$: is the AX specimen diameter standard deviation (Appendix D2) [mm]

$\frac{\partial\sigma_{axial;a}}{\partial d}$: is the axial fatigue stress sensitivity [MPa/mm] to change in d

$u\left(F_{axial;a}\right)$: is the axial fatigue load uncertainty calculated as 0.247 [%] of $F_{axial;a}$ [kN]

$\frac{\partial\sigma_{axial;a}}{\partial F_{axial;a}}$: is the axial fatigue stress sensitivity [MPa/kN] to change in $F_{axial;a}$

BENDING Fatigue Tests – Experimental Uncertainties

The bending fatigue stress amplitude uncertainty $u\left(\sigma_{bending;a}\right)$ of each bending (B) fatigue test was calculated with Equation (4-12) below. Consideration was made for the specimen *diameter* uncertainty, the *cantilever length* and *force* uncertainty, and the *break position* uncertainty. The four partial derivatives (sensitivity) for the equation below were obtained as the linear trendline slope values shown in Figure K-3 (a) through (d). For these sensitivity values, the specimen diameter was again varied by 0.3 [mm], and the cantilever length was varied by half the conservatively measured 8.6 [mm] value for where the load cell applied the cantilever force (see Figure K-3 (b)). The cantilever force was varied by the maximum 7.5 [N] load cell deviation value measured for the respective specimens (non-ideal machined straightness). The cantilever force was calculated from the load cell calibration curve, and thus no other uncertainty was assumed. Finally, the experimental break position was varied by 2 [mm] (the deviation value, from the ideal 61 [mm], of the post-test break position average). The above experimental B fatigue test uncertainties are provided in Table K-3 and later discussed in Section 5.2.2. Reference can be made to Equations (H-8) and (H-9) for the relevance of each uncertainty.

$$1.96u\left(\sigma_{bending;a}\right) = \cdots \quad (4\text{-}12)$$

$$1.96\sqrt{\left(\frac{\partial\sigma_{bending;a}}{\partial d}u(d)\right)^2 + \left(\frac{\sigma_{bending;a}}{\partial L_{cantilever}}u(L_{cantilever})\right)^2 + \left(\frac{\sigma_{bending;a}}{\partial F_{cantilever}}u(F_{cantilever})\right)^2 + \left(\frac{\sigma_{bending;a}}{\partial x_{break;exp}}u\left(x_{break;exp}\right)\right)^2}$$

where $u(d)$: is the B specimen diameter standard deviation (Appendix D3) [mm]

$\frac{\partial\sigma_{bending;a}}{\partial d}$: is the bending fatigue stress sensitivity [MPa/mm] to change in d

$u(L_{cantilever})$: is the specimen cantilever length uncertainty (see Figure K-3 (b)) [mm]

$\frac{\partial \sigma_{bending;a}}{\partial L_{cantilever}}$: is the bending fatigue stress sensitivity [MPa/mm] to change in $L_{cantilever}$

$u(F_{cantilever})$: is the specimen cantilever force uncertainty (Table J-3) [N]

$\frac{\partial \sigma_{bending;a}}{\partial F_{cantilever}}$: is the bending fatigue stress sensitivity [MPa/N] to change in $F_{cantilever}$

$u\left(x_{break;exp}\right)$: is the specimen experimental break position uncertainty (Table K-3) [mm]

$\frac{\partial \sigma_{bending;a}}{\partial x_{break;exp}}$: is the bending fatigue stress sensitivity [MPa/mm] to change in $x_{break;exp}$

TORSION Fatigue Tests – Experimental Uncertainties

The torsional fatigue stress amplitude uncertainty $u(\tau_a)$ of each torsion (T) fatigue test was calculated with Equation (4-13) below (based on nominal shear stress). Consideration was made for the specimen *diameter* uncertainty, the *material stiffness* uncertainty and the *diameter-gain-stress* uncertainty. The latter diameter uncertainty was different from the former in that it was used to determine the effect of the torsion loading gain, as influenced by a change from a measured (using DANTEC) to an unmeasured specimen's diameter, on the fatigue stress amplitude. This second $u(d)_2$ value was, therefore, 'calculated' as the change in diameter values of two specimens tested with a similar centrifugal nut (as in Table J-4), and not like the first $u(d)_1$ value being a specimen's diameter 'measurement' standard deviation (as in Table D-4).

These uncertainties were selected based on the utilisation of these input parameters in the static FEM simulation models (e.g., in Appendix I1) to obtain the experimental (and theoretically calculated) gain values of the T fatigue specimens (using Equation (H-14) from Appendix H4.1 and H4.2 part 1, 2b and 2c respectively). Therefore, the T fatigue stress uncertainties were considered differently than the previous test uncertainties (TEN, AX and B). For these T fatigue test stress uncertainties, it was assumed that the uncertainties associated with the torsion moment calculations in Equation (H-10) would be incorporated into the above-considered uncertainties. The centrifugal nut masses, radial positions, forces and lever lengths would be incorporated through their use in the relevant static FEM simulations performed to obtain the below-discussed partial derivative values. The centrifugal nut radial positions (on wheels) were assumed not to influence the torsion gain values since the appropriate moment lever lengths were used (Appendix E2) and therefore assumed independent for each nut. That is, only the moment inducing centrifugal force magnitudes changed due to a nut's arbitrarily different radial position.

The four partial derivatives (sensitivity) for the equation below were obtained as the linear trendline slope values shown in Figure K-4 (a) through (j). For this, the specimen diameter was varied by 0.3 [mm], and the material stiffness (experimentally measured value of 211.17 [GPa]) was varied by the calculated standard deviation value (of 1.479 [GPa], see Table J-1), whilst assuming constant gain values. Note that the diameter-gain-stress partial derivative values were obtained for the four (4) T fatigue specimens measured with the DANTEC system during testing (with either NUT5 or NUT10). These values were then inferred for the other specimens (not measured) for calculating the relevant torsion stress amplitude uncertainties of the specimens tested with similar centrifugal nuts. For these partial derivative values, the diameter was also varied by 0.3 [mm] to obtain the influence on the experimental torsional gain (from Equation (H-14)) and then subsequently the stress value (from Equation (H-11)). Reference can be made to each figure pair of the measured specimens in Figure K-4 (c):(d), (e):(f), (g):(h) and (i):(j), respectively. The above experimental T fatigue test uncertainties are provided in Table K-4 and will later be discussed in Section 5.2.2.

$$1.96u(\tau_a) = 1.96\sqrt{\left(\frac{\partial\tau_a}{\partial d}u(d)_1\right)^2 + \left(\frac{\partial\tau_a}{\partial E}u(E)\right)^2 + \left(\frac{\partial G_T}{\partial d}\frac{\partial\tau_a}{\partial G_T}u(d)_2\right)^2} \quad (4\text{-}13)$$

where $u(d)_1$: is the T specimen diameter standard deviation (Appendix D4) [mm]

$\frac{\partial\tau_a}{\partial d}$: is the torsion fatigue stress sensitivity [MPa/mm] to change in $d_{(1)}$

$u(E)$: is the material Elasticity Modulus uncertainty (Table J-1) [GPa]

$\frac{\partial\tau_a}{\partial E}$: is the torsion fatigue stress sensitivity [MPa/GPa] to change in E

$u(d)_2$: is the T specimen diameter difference $|d_{measured} - d_{unmeasured}|$ [mm]

$\frac{\partial G_T}{\partial d}$: is the torsion gain sensitivity [-/mm] to change in $d_{(2)}$

$\frac{\partial\tau_a}{\partial G_T}$: is the torsion fatigue stress sensitivity [MPa/-] to change in G_T

BENDING-TORSION Fatigue Tests – Experimental Uncertainties

The bending-torsion fatigue stress amplitude uncertainties $u(\sigma_{bending;a})$ and $u(\tau_a)$ of each bending-torsion (BT) fatigue test was calculated with Equations (4-14) and (4-15) below. Consideration was made for the specimen *diameter* uncertainty, the *material stiffness* uncertainty and the *diameter-gain-stress* uncertainty for each loading component of the biaxial loading condition. The latter diameter uncertainty was again different from the former in that it was used

to determine the effect of the bending and torsion loading gains, as influenced by a change from a measured (using DANTEC) to an unmeasured specimen's diameter, on the fatigue stress amplitudes. This second $u(d)_2$ value was, therefore, 'calculated' as the change in diameter values of two specimens tested with a similar centrifugal nut (as in Table J-5), and not like the first $u(d)_1$ value being a specimen's diameter 'measurement' standard deviation (as in Table D-5).

These uncertainties were selected based on the utilisation of these input parameters in the static FEM simulation models (e.g., in Appendix I2) to obtain the experimental gain values of the BT fatigue specimens (using Equation (H-22) from Appendix H5.1 and H5.2 part 1, 2a and 2b respectively). The BT fatigue stress uncertainties were considered differently than the previous test uncertainties (TEN, AX and B). For these BT fatigue test stress uncertainties, it was assumed that the uncertainties associated with the bending and torsion moment calculations in Equation (H-16) would be incorporated into the above-considered uncertainties. The centrifugal nut masses, radial positions, forces and lever lengths would be incorporated through their use in the relevant static FEM simulations performed to obtain the below-discussed partial derivative values. The centrifugal nut radial positions (on wheels) were again assumed not to influence the bending and torsion gain values since the appropriate moment lever lengths were used (Appendix E2) and therefore assumed independent for each nut. That is, only the moment inducing centrifugal force magnitudes changed due to a nut's different radial position.

The eight partial derivative values (sensitivity) for the equations below were obtained as the linear trendline slope values shown in Figure K-5 (a) through (h). For this, the specimen diameter was varied by 0.3 [mm], and the material stiffness (of 211.17 [GPa]) was also varied by the value of 1.479 [GPa] (see Table J-1) whilst assuming constant gain values. Note that the diameter-gain-stress partial derivative values were obtained for the three (3) BT fatigue specimens measured with the DANTEC DIC system during testing (with either NUT4, 5 or 9). These values were then inferred for the other specimens (not measured) for calculating the relevant bending and torsion stress amplitude uncertainties of the specimens tested with similar centrifugal nuts. For these partial derivative values, the diameter was also varied by 0.3 [mm] to obtain the influence on the experimental bending and torsion gain (from Equation (H-22)), and then subsequently, the stress values (from Equations (H-17) and (H-18)). Reference can be made to each figure pair of the measured specimens in Figure K-5 (c):(d), (e):(f) and (g):(h), respectively. The above experimental BT fatigue test uncertainties are provided in Table K-5 and will later be discussed in Section 5.2.3.

$$1.96u\left(\sigma_{bending;a}\right) = 1.96\sqrt{\left(\frac{\partial\sigma_{bending;a}}{\partial d}u(d)_1\right)^2 + \left(\frac{\partial\sigma_{bending;a}}{\partial E}u(E)\right)^2 + \left(\frac{\partial G_B}{\partial d}\frac{\partial\sigma_{bending;a}}{\partial G_B}u(d)_2\right)^2} \quad (4\text{-}14)$$

$$1.96u(\tau_a) = 1.96\sqrt{\left(\frac{\partial\tau_a}{\partial d}u(d)_1\right)^2 + \left(\frac{\partial\tau_a}{\partial E}u(E)\right)^2 + \left(\frac{\partial G_T}{\partial d}\frac{\partial\tau_a}{\partial G_T}u(d)_2\right)^2} \quad (4\text{-}15)$$

where $u(d)_1$: is the BT specimen diameter standard deviation (Appendix D5) [mm]

$\frac{\partial\sigma_{bending;a}}{\partial d}$ and $\frac{\partial\tau_a}{\partial d}$: is the bending/torsion fatigue stress sensitivity [MPa/mm] to change in $d_{(1)}$

$u(E)$: is the material Elasticity Modulus uncertainty (Table J-1) [GPa]

$\frac{\partial\sigma_{bending;a}}{\partial E}$ and $\frac{\partial\tau_a}{\partial E}$: is the bending/torsion fatigue stress sensitivity [MPa/GPa] to change in E

$u(d)_2$: is the BT specimen diameter difference $|d_{measured} - d_{unmeasured}|$ [mm]

$\frac{\partial G_T}{\partial d}$ and $\frac{\partial G_T}{\partial d}$: is the bending/torsion gain sensitivity [-/mm] to change in $d_{(2)}$

$\frac{\partial\sigma_{bending;a}}{\partial G_B}$ and $\frac{\partial\tau_a}{\partial G_T}$: is the bending/torsion fatigue stress sensitivity [MPa/-] to change in G_B/G_T

Experimental Testing – General Uncertainty Considerations

For the estimated uniaxial fatigue limits of AX, B and T (reported in Section 5.2.2 later), too few fatigue limit data points were obtained to calculate an uncertainty on the limit. This was because only one experimental test data set was obtained for each test type performed on EN19 (T-condition). Therefore, the previously discussed experimental stress uncertainties of each uniaxial fatigue test type were the only ones considered.

Concerning the fatigue-failure cycle counts N_f obtained in each experimental fatigue test, only the T and BT fatigue tests for which an experimental cycle count uncertainty could be reported. For these tests, the maximum uncertainty in the measured fatigue failure cycle count was assumed as 2326 cycles for BT (38 [Hz] test speed) and a maximum of 2448 cycles for T (40 [Hz] maximum test speed) for 1 min of testing due to the dedicated timer settings as discussed in Section 4.5.1. The AX fatigue failure cycle counts were recorded accurately to the nearest half cycle (e.g., 0.5 cycles on the MTS DAQ system). The B fatigue failure cycle counts were recorded accurately to the nearest complete cycle (e.g., one cycle on the mechanical cycle counter).

The experimental T and BT fatigue test measurements had minor test speed uncertainties for each test bench, as from the DANTEC displacement measurement sinusoidal curves (later

provided in Sections 5.2.2 and 5.2.3). This uncertainty was attributed to the inherent test bench motor slip. The maximum test speed deviations from the values set on the VSD of each test bench were 0.74 [Hz] (or 1.85 [%]) for the T fatigue test bench and 0.57 [Hz] (or 1.51 [%]) for the BT fatigue test bench. The test speeds had to be adapted by these values to overlay displacement measurement data points appropriately. The speed (not measured) was set and electronically controlled for the AX fatigue tests on the MTS computer system. The test speeds for the B fatigue tests were measured with the tachometer.

For the multiaxial fatigue criterion evaluations (discussed in Section 4.7 next), it was assumed that the uniaxial and biaxial fatigue stress uncertainties considered in the previous parts sufficiently accounted for the relevant experimental fatigue stress uncertainties. It was therefore assumed appropriate if no further consideration was made for any subsequent uncertainties in the respective criterion stress or failure parameter predictions.

4.7 Multiaxial Fatigue Data and Criteria Evaluation

As stated previously in Section 4.1, the primary purpose of the experimental testing performed in this study was to generate the relevant material tensile, uniaxial and biaxial fatigue strength data sets required to evaluate the three fatigue criteria (in Table 4-1 on pg.63). These experimental tests were performed according to the relevant test and measurement procedures (Appendix G and H) using the test benches and measurement equipment (Section 4.3). For each experimental test, the appropriate test considerations were made (Section 4.4) for the test specimens, the induced loading and the fatigue testing definitions. The resultant material strength and fatigue limit test results were obtained from the stress calculation and estimation methods previously discussed for each test type in Section 4.6.

From these results, the out-of-phase biaxial bending-torsion fatigue stress and cycle count data (in Table J-5) and the uniaxial bending f_{-1} and torsion t_{-1} fatigue limit estimates (in Table J-3 and Table J-4) were utilised to evaluate each fatigue criterion model (provided in Section 3.3). These evaluations with the experimental test data were done according to the method reported for each criterion in the literature to obtain the uniaxial equivalent stress value σ_{eq} [MPa] of each biaxial fatigue test data point ($\sigma_{bending;a}$; τ_a) [8, 9]. After these stresses were calculated with the criteria, the relevant error-index I [%] values were calculated (using Equation (3-1)) for each assumed 'infinite life' test (no failure after 1.5 x 10^6 cycles). The error-index only applies to fatigue life cycle counts larger or equal to the conventional definition of 10^6 cycles [9]. The error-index values essentially compared the calculated σ_{eq} value of the infinite life tests (LHS of each criterion)

with the uniaxial fatigue limit or parameter (RHS of each criterion) proposed by each criterion. These criteria evaluation results are provided in Appendix L1 through L3. As discussed at the end of Section 4.6.3, no criteria equivalent stress uncertainties were considered.

An S-N curve was generated for each criterion evaluation using the σ_{eq} values, and corresponding experimental fatigue cycle counts N_f. On each of these fatigue curves, the related criterion fatigue limit (RHS of models, based on the uniaxial fatigue limits) was added for illustration with the experimental σ_{eq} values. Also included in these curves was the estimated experimental biaxial fatigue limit value (based on the relevant equivalent stress), similarly obtained as with the uniaxial fatigue limit estimations (method in Section 4.6.2). The two fatigue limits were compared (using Equation (3-2)) to determine the percentage difference between what each criterion claims to be the fatigue limit and what was estimated for the experimental biaxial fatigue test data (from the criterion's σ_{eq} values). The in-phase and out-of-phase multiaxial bending-torsion fatigue limit data (Table 4-2) of (Z) Zenner *et al.* [45] were included in the criteria evaluations and added to these S-N curves to compare the σ_{eq} values with the associated criterion fatigue limits.

These S-N curves and the comparison results of each fatigue criterion are later provided and discussed in Section 5.2.4. Three separate fatigue curves were generated for this because each criterion calculates σ_{eq} differently. That is, using nominal stress amplitudes σ_a and τ_a like PPD, or critical plane stress amplitudes N_a and C_a like C&S and L&M. It was also done due to each criterion respectively considering the bending fatigue limit f_{-1} (like C&S), the torsion fatigue limit t_{-1} (like PPD) or a material parameter λ (like L&M, not the same λ value as in Equation (4-6)).

The second set of curves (in the normal-shear stress plane) was also generated using each fatigue criterion model (elliptic curves – inequalities) and the bending and torsion fatigue stresses (see Section 3.3 for each criterion σ_{eq} using e.g., σ_a; τ_a or N_a; C_a). These curves were plotted with the failed and un-failed test data to illustrate the theoretical 'safe' (inside) and 'unsafe' (outside) zones divided by each criterion curve and how well these criteria estimate or account for the experimentally biaxial fatigue stress results. Stress values lying directly on or near these model curves were, therefore, indicative of a biaxial fatigue stress condition equivalent to the presumed fatigue limit of a criterion (RHS fatigue limit value). These curves are also later provided and discussed in Section 5.2.4.

For the multiaxial (biaxial) and uniaxial fatigue 'data' comparisons, it was deemed most appropriate if the relevant literature data (in Table 4-2) were normalised (as in Figure 4-1 and Figure 4-2) and then supplemented with the experimental fatigue test data. Two S-N curves were used for this, one for the biaxial fatigue test data (based on the bending stress) and the other for

all three uniaxial fatigue tests. From these curves (end of Section 5.2.2 and 5.2.3), comparisons could be made for each test type and data set.

4.8 Conclusion

This experimental methodology chapter consisted of four main parts. The first part discussed the specific multiaxial loading condition, criteria, test material and literature data used for this study. All the appropriate experimental testing and measurement equipment for generating the relevant material and fatigue strength data were then identified and discussed. The principal measurement system verification was also discussed, which showed that the system is used correctly and measures correctly and that the speckle pattern generation procedure is appropriate.

The second part discussed all the essential experimental test considerations to ensure suitable test data generation on each test bench. This included considerations for the test specimens (e.g., geometry, machining and polishing), the experimental loading (e.g., verification measurements, pre-test measurements and test bench or instrument calibration) and the required fatigue testing definitions. These verification measurements for the T and BT fatigue test benches showed that the experimental test measurements are appropriate. It was shown that theoretical loading gains could only be used on the T fatigue test bench and not for the BT test bench.

The third part discussed the primary experimental testing and measurement methodology for out-of-phase biaxial bending-torsion fatigue. After this, the methodology for experimental stress calculation and uncertainty analysis was discussed for each test type performed. The chapter was ultimately concluded with a discussion on the chosen multiaxial fatigue criteria evaluation and comparison methods, which included using the applicable data reported from the literature. The results of all the experimental material and fatigue strength tests performed in this study are provided in the next chapter.

CHAPTER 5 – EXPERIMENTAL RESULTS

5.1 Introduction

The previous chapters discussed this study's literature, theory and experimental methodology considerations. This chapter aims to provide the results of all the experimental material and fatigue strength tests performed. After that, the resultant multiaxial fatigue criteria evaluations, comparisons and discussions are provided.

5.2 Results and Discussion

Note that experimental uncertainties reported in all the results are done with 95 [%] confidence intervals, and their relevant equations can be referenced in Section 4.6.3.

5.2.1 Monotonic Tensile Tests

The experimental monotonic tensile properties of EN19 (T-condition) are summarised in Table 5-1 below. These average material strengths were obtained from the tensile (TEN) tests performed at room temperature. These results, the material chemical composition (Table 4-5) and the material certificate values (Appendix M) provided adequate characterisation of the material. Post-test tensile fracture zone photos of an arbitrary tensile specimen can be viewed in Figure J-1, and reference can be made to Table J-1 and Figure J-2 for the complete tensile test data set.

Table 5-1: EN19 (T-condition) alloy steel – monotonic tensile test results

Monotonic Tensile Properties		
S_{ut} [MPa]	S_y [MPa]	E [GPa]
961.28 ± 102.77	858.99 ± 103.28	211.17 ± 2.89

The greatest ultimate tensile and yield strength uncertainty was obtained as 4.7 [%] of the calculated tensile stress (for Spec3). These uncertainty values can be referenced in Table K-1 and Figure J-2. The combined uncertainties are provided next to each of the average experimental monotonic tensile properties in Table 5-1 above. These uncertainty values can be referenced in Table J-1.

A comparison between the experimental and material certificate (Figure M-2) tensile strengths of EN19 (T-condition) showed a negligible difference of 0.6 [%] for S_{ut} and 1.1 [%] for S_y. No E value was reported on the material certificate. These tensile strengths also compared very well with most of the available tensile data reported in the literature for EN19 alloy steels (Table 4-2). For the experimental tensile stiffness E value, reference was made to the relevant Li *et al.* [16] data in Table 4-2 (from three different sources), and a maximum difference of 5.3 [%] was observed. The EN19 (T-condition) material compared best with the last AISI 4140 / EN19 material in Table 4-2, based on all three tensile properties reported in Table 5-1 above.

The above experimental uncertainties and comparisons with the relevant data confirmed that the experimental monotonic tensile properties were appropriate for subsequent calculations. It also confirmed the appropriateness of the experimental tensile (TEN) test methodology for obtaining the relevant test data (reference Sections 4.4 and 4.6).

5.2.2 Uniaxial Fatigue Tests

This uniaxial fatigue test results section is divided into two parts. The first part provides the official experimental torsion (T) fatigue test measurement results. These measurement results are discussed here since they provided the loading gain values used to calculate the T fatigue stresses. The experimental loading on the T fatigue test bench is also shown to be as expected. The second part provides the experimental uniaxial axial (AX), bending (B) and torsion (T) fatigue limit test results and a comparison with the literature data.

5.2.2.1 Torsion Fatigue Test Bench – Experimental Measurement Results

As stated at the end of the torsion (T) fatigue test-bench verification measurements in Section 4.4.2.4, it was required to measure the torsional displacement of four T fatigue specimens during official testing using the DANTEC (Appendix H4.2 parts 1 and 2c). These specimens were tested at the three speeds that had the lowest theoretical vs experimental gain difference (Table 4-7 pg.98). The results of these four measurements, the corresponding experimental gain calculations (G_T from Equation (H-14)) and the comparisons with theoretical gain values ($G_{T;theoretical}$ from Equation (F-4)) are summarised in Table 5-2 below.

The table and Figure 5-1 results below (circles) showed that the experimental and theoretical torsional gain values were equivalent for each measured specimen. The calculated gain difference values (Equation (H-15)) were very similar to those obtained during the test bench verification measurements (Table 4-7). The gain difference values were suitably low, with 3.22

[%] being the most significant calculated difference between experimentally measured and theoretically calculated torsional gains. The small differences confirmed that the methodologies considered for the experimental and theoretical torsion gain calculation were correct, and the DANTEC measured appropriately.

Table 5-2: T fatigue experimental measurement results – experimental vs theoretical torsion gain

			V ref point	Gauge P1-P2 Displacement - @ E = E_{exp} = 211.174GPa			
Specimen #	**Diameter**	**N**	**Theoretical G_T**	**NX FEM**	**DANTEC**	**Experimental G_T**	**Difference G_T**
	[mm]	**[Hz]**	**[-]**	**[mm]**	**[mm]**	**[-]**	**[%]**
EN19T-T-Spec-1	6.548	27.5	1.176	0.06255	0.07275	1.163	1.09
EN19T-T-Spec-5	6.523	35.0	1.345	0.12740	0.16584	1.302	3.22
EN19T-T-Spec-8	6.571	40.0	1.456	0.13087	0.19433	1.485	1.98
EN19T-T-Spec-9	6.558	40.0	1.490	0.14315	0.21549	1.505	1.03

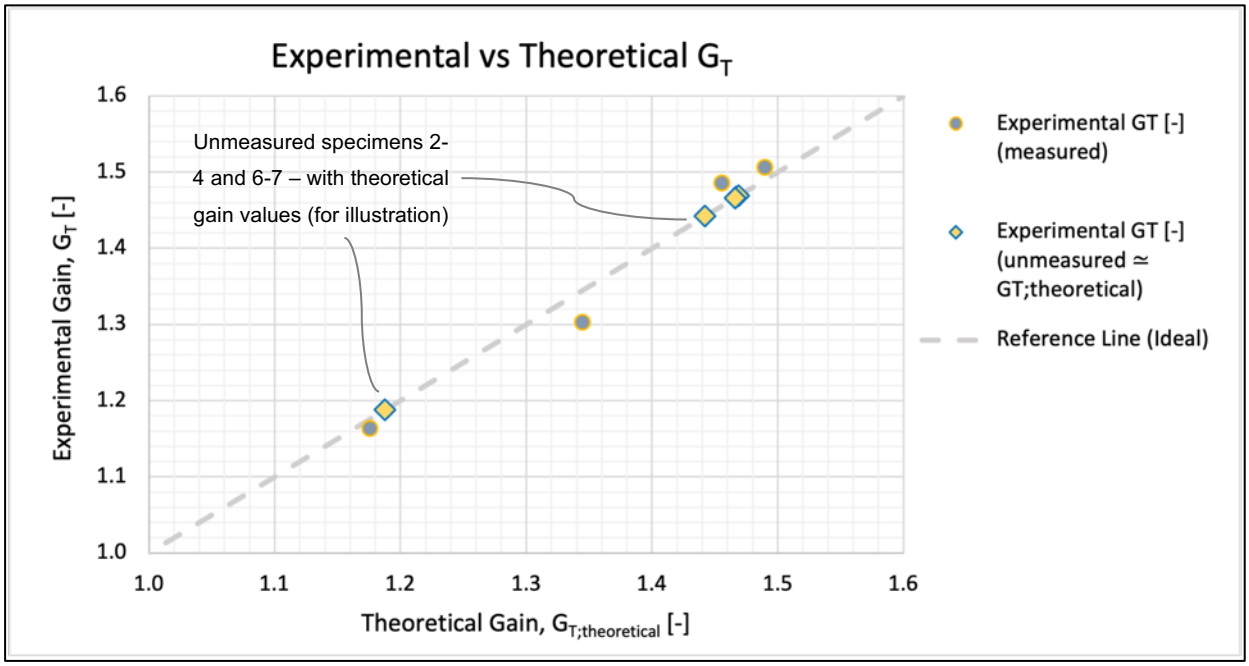


Figure 5-1: T fatigue experimental measurement results – experimental vs theoretical torsion gain and assumed experimental gains

The experimental (measured) and theoretical gains compared well. The negligibly small influence of specimen diameter uncertainty on the torsion gain was also considered (see Figure K-4). It was shown to be valid and sufficient to set the remaining experimental T fatigue specimen (unmeasured) experimental gain values equal to the theoretically calculated values (diamonds in Figure 5-1 for illustration with the measured specimen gain values). The five torsion fatigue

specimens for which this was done are Spec2-4 and Spec6-7, respectively. These experimental torsion gain values $G_T \simeq G_{T;th}$ were then utilised (Equation (H-11)) to calculate the fully reversed torsion fatigue stresses of the unmeasured specimens. The torsion fatigue stresses of Spec1, 5, 8 and 9 were calculated using the G_T values from Table 5-2. The experimental T fatigue loading gains and stresses can be referenced in Table J-4.

From the above experimental torsion displacement measurements with the DANTEC, generation of the fully reversed sinusoidal displacement (loading) curves for each of the four specimens measured was also possible. These curves were generated from the scattered displacement data (e.g., Spec8 in Figure H-27) using the procedure discussed at the end of Appendix H4.2 part 2c and are illustrated in Figure H-28. The experimental torsion displacement curve of Spec9 is provided in Figure 5-2 below, showing that the expected form of the experimental torsion fatigue loading induced by the test bench on the specimen was correct. These curves provided confidence that all torsion fatigue test loading was correct.

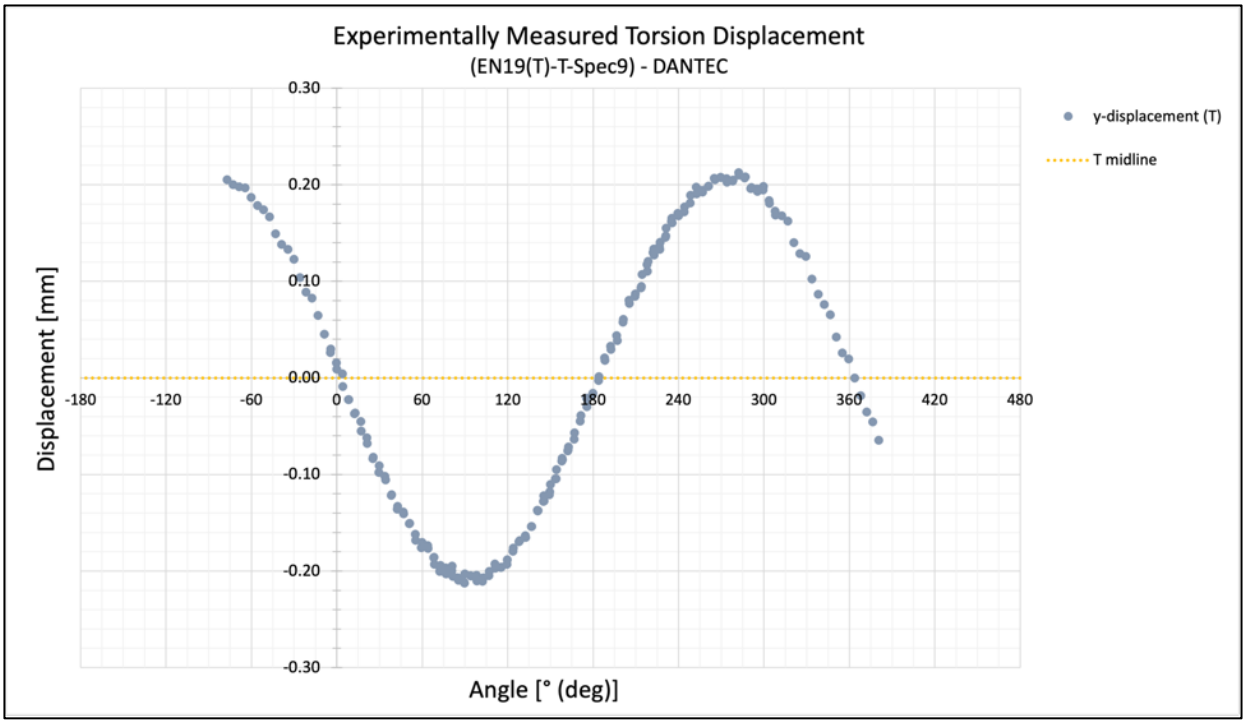


Figure 5-2: T fatigue experimental measurement – sinusoidal torsion displacement curve of Spec9

5.2.2.2 Uniaxial Fatigue Test Results

The experimental fully reversed uniaxial fatigue limit estimates of EN19 (T-condition) are summarised in Table 5-3 below. These fatigue limits were estimated according to the method

discussed previously in Section 4.6.2, and they are illustrated on the experimental axial (AX), bending (B), and torsion (T) fatigue strength S-N curves in Figure 5-3 to follow. In these curves, the uniaxial fatigue stresses are also shown along with the 'runout' arrows on tests with assumed infinite life. Post-test fatigue fracture plane photos of an arbitrary AX, B and T specimen can be viewed in Figure J-3, Figure J-4 and Figure J-5, respectively. Reference can be made to Table J-2, Table J-3 and Table J-4 for the complete uniaxial fatigue test data sets.

Table 5-3: EN19 (T-condition) alloy steel – uniaxial fatigue limit test results

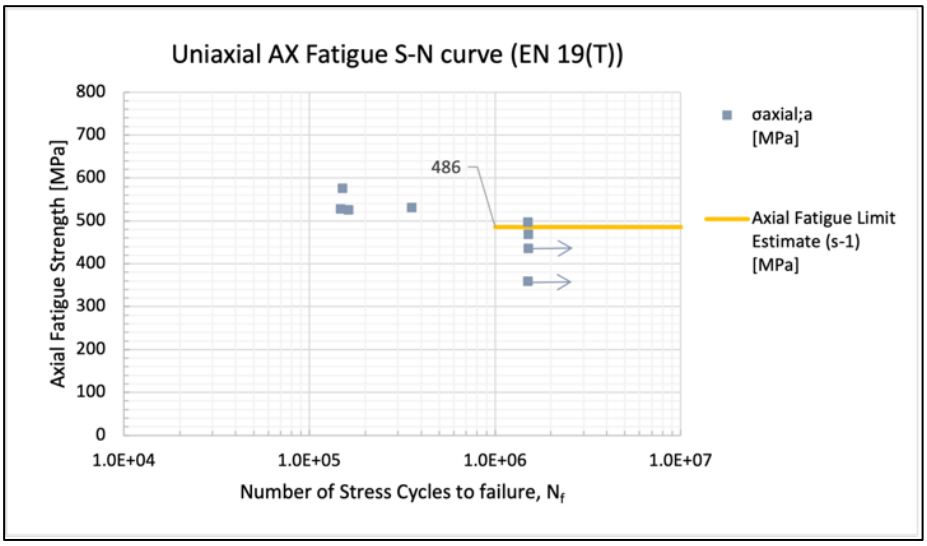
Uniaxial Fatigue Limit Strength Estimates				
s_{-1} [MPa]	f_{-1} [MPa]	t_{-1} [MPa]	t_{-1} / f_{-1} [-]	f_{-1} / t_{-1} [-]
486	510	354	0.694	1.441

According to the calculated t_{-1} / f_{-1} ratio above and the material type classification definition $0.577 < t_{-1} / f_{-1} < 0.833$ provided for the criteria (Table 4-1), the EN19 (T-condition) test material is regarded as a 'hard metal' [8, 10]. Therefore, all three criteria identified are applicable (evaluation results in Section 5.2.4).

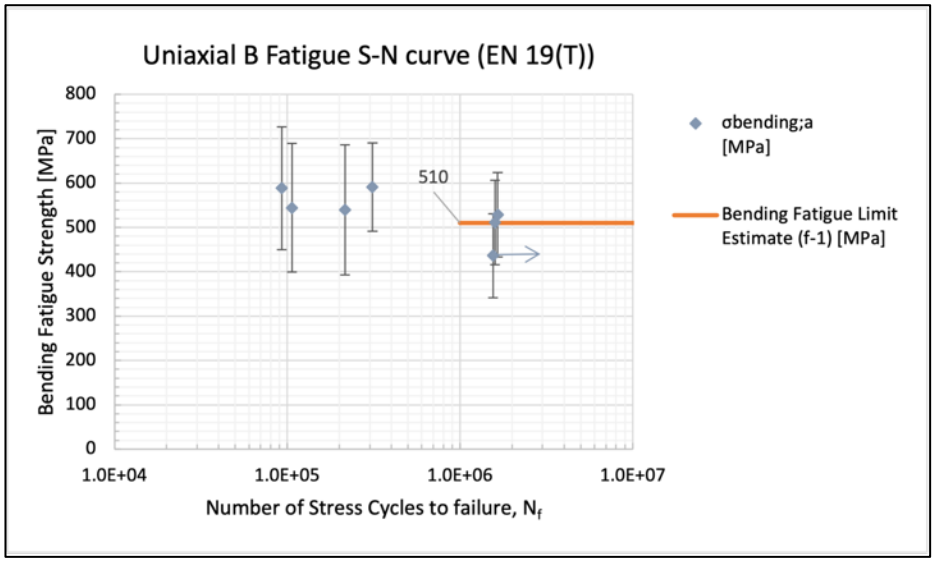
The greatest axial fatigue stress uncertainty was obtained as 2.6 [%] (for Spec4). The axial fatigue stress uncertainties were low and not incorporated into Figure 5-3 (a) below using error bars. These uncertainty values can be referenced in Table K-2.

The bending fatigue stress uncertainties were all quite significant (shown with error bars in Figure 5-3 (b)). The most significant bending fatigue stress uncertainty was 27.2 [%] (for Spec4). These uncertainty values can be referenced in Table K-3. This table shows that the cantilever length and specimen break position uncertainties largely contributed to each specimen bending stress uncertainty. This influence was due to the significant uncertainties in both these test parameters, which caused a maximum stress uncertainty of 47.5 [MPa] and 52.3 [MPa], respectively. The associated bending stress sensitivity to changes in these parameters was also significant (Figure K-3 (b) and (c)). The contribution of the specimen diameter and load cell force uncertainties on the bending stress uncertainty was smaller. However, also significant enough to cause a maximum stress uncertainty of 18.5 [MPa] and 25.6 [MPa], respectively.

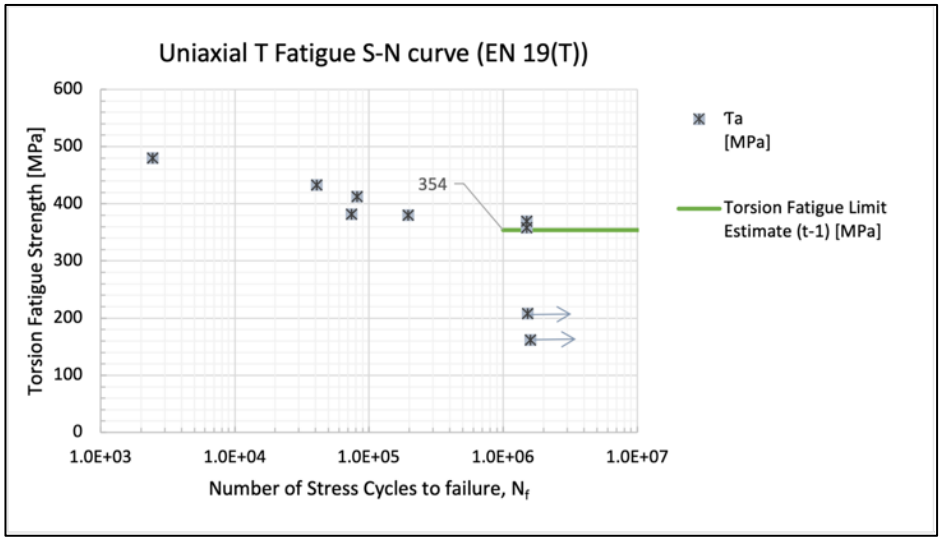
The greatest torsion fatigue stress uncertainty was obtained as 6.7 [%] (for Spec1). The torsion fatigue stress uncertainties were low and were not incorporated into Figure 5-3 (c) using error bars. The torsion uncertainty values can be referenced in Table K-4.



(a)



(b)



(c)

Figure 5-3: Experimental uniaxial fatigue S-N curves and fatigue limits – (a) AX fatigue, (b) B fatigue and (c) T fatigue

The three uniaxial fatigue limit estimates were compared with a graph of various carbon steel, alloy steel and wrought iron fatigue limits in Figure 5-4 below [3, Fig. 6-17]. This comparison was made as an informal means of showing the correctness of the fatigue limit estimates based on the typical values reported in the literature. This included the Zenner (Z), Susmel (SUS) and Li (JL) literature data (Table 4-2 on pg.67). The comparison shows that the experimental fatigue limits (callouts) were within the expected range or spread of fatigue limit data typically reported for alloy steels (black dots). The data callout values on the three experimental fatigue limits provide the ratio of the modified fatigue limit estimate to the EN19 (T-condition) ultimate tensile strength (Table 5-1). The fatigue limits were all modified for the loading type by dividing s_{-1}/0.85, f_{-1}/1 and t_{-1}/0.59 [3].

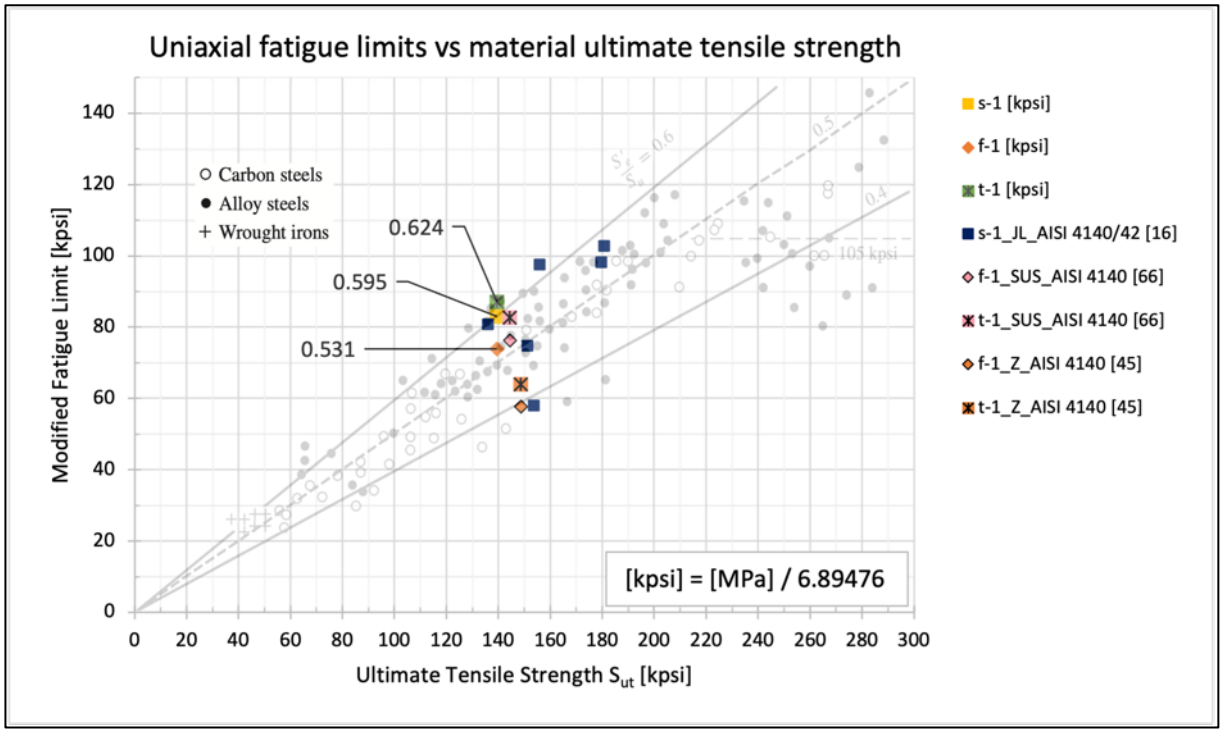


Figure 5-4: Experimental uniaxial fatigue limits (callouts) compared with literature fatigue limit data

The second comparison was between the experimental axial (AX), bending (B), and torsion (T) fatigue strength data and limit estimates (from Figure 5-3) and the uniaxial fatigue limit data from the literature. The comparison was made on an S-N curve (Figure 5-5 below), which supplemented the previously provided literature data graph (Figure 4-1 on pg.65) with the normalised uniaxial fatigue data from Table J-2 (AX), Table J-3 (B) and Table J-4 (T), respectively. The normalisation of stresses was discussed above in Figure 2-8 on pg.33. It is shown in the comparative S-N curve that the uniaxial B data and limit compared best with the SUS material's bending fatigue limit (0.531 vs pink diamond). The uniaxial AX data and limit compared best with

the second JL material axial fatigue limit data point (0.506 vs blue square, the last value of JL in Table 4-2). Lastly, the uniaxial T data and limit were closest to the SUS material's torsion fatigue limit (0.368 vs pink asterisk/square). The Z material's uniaxial bending and torsion fatigue limits (orange diamond and asterisk/square) did not compare well with either the experimental f_{-1} or t_{-1} fatigue limits in this study.

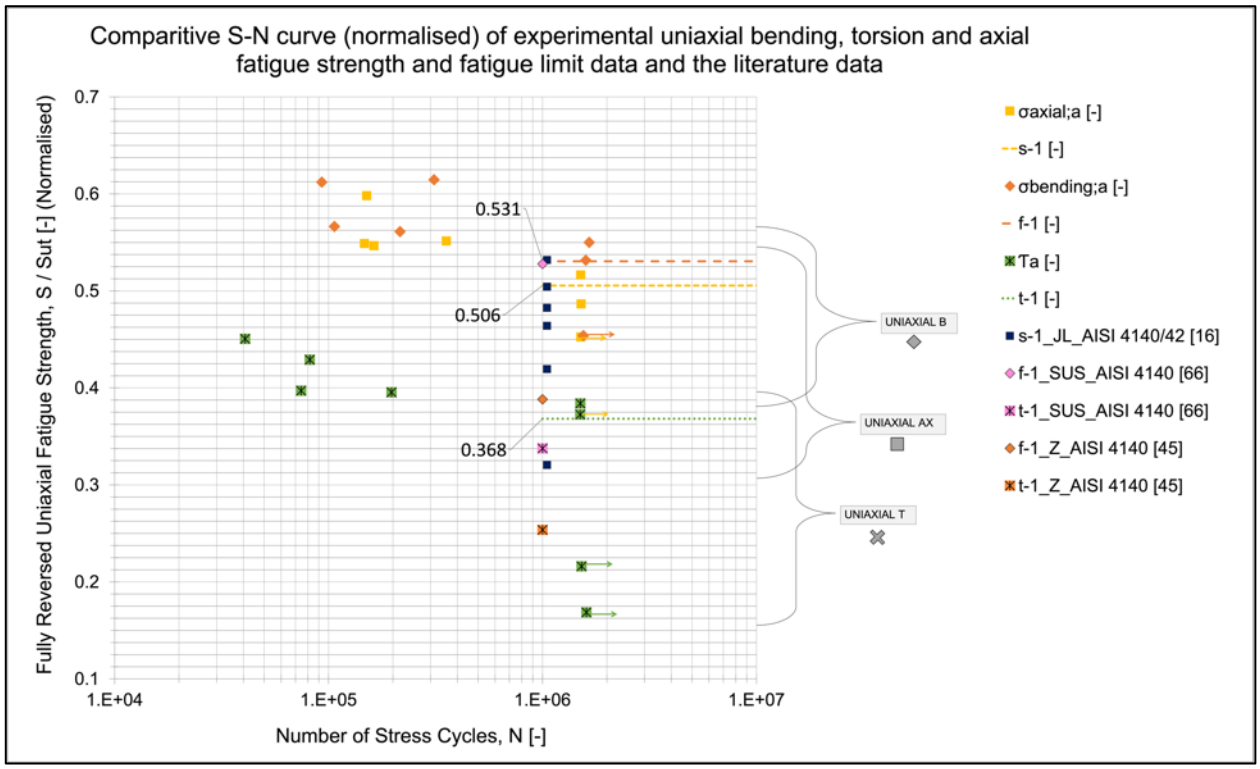


Figure 5-5: Comparative S-N curve (normalised) – experimental AX, B and T fatigue strength and limit data comparison with literature uniaxial fatigue limit data

The comparisons between experimental and literature uniaxial fatigue limit data (in Figure 5-4 and Figure 5-5 above) showed that the experimental fatigue limits were appropriate for use in the relevant criteria evaluations (Section 5.2.4). For these evaluations, the reported experimental uniaxial fatigue limits s_{-1}, f_{-1} and t_{-1} were deemed more appropriate values for the EN19 (T-condition) steel (Section 4.6.2). The limit estimates that could have been obtained from similar EN19 materials in the literature were considered less appropriate.

5.2.3 Biaxial Fatigue Tests

This biaxial fatigue test results section is also divided into two parts. The first part provides the official experimental bending-torsion (BT) fatigue test measurement results. These measurement

results are discussed here since they provided the loading gain values used to calculate all the BT fatigue stresses. The experimental out-of-phase loading on the BT fatigue test bench is also shown to be as expected, and the principal stress rotation phenomenon was observed during testing. The second part provides the experimental biaxial fatigue test results and a comparison with the literature data.

5.2.3.1 Bending-Torsion Fatigue Test Bench – Experimental Measurement Results

The BT fatigue tests required measuring three specimens' experimental bending and torsion displacement using the DANTEC (Appendix H5.2 parts 1 and 2b). This was done to obtain and compare the experimental bending and torsion loading gain values at the equivalent gain test speed of 38 [Hz]. These measurements were performed as from the methodology discussed in Section 4.5.2. The results of these measurements and the corresponding gain calculations (G_B and G_T from Equation (H-22)) are summarised in Table 5-4 below.

Table 5-4: BT fatigue experimental measurement results – experimental bending and torsion gain comparison

			Gauge P1-P2 Displacement - @ E = E_{exp} = 211.174GPa						
Specimen #	Diameter	N	NX FEM B	NX FEM T	DANTEC B	DANTEC T	Experimental G_B	Experimental G_T	Difference G_B vs G_T
	[mm]	[Hz]	[mm]	[mm]	[mm]	[mm]	[-]	[-]	[%]
EN19T-BT-Spec-3	6.560	38	0.17201	0.08588	0.24560	0.12758	1.428	1.486	4.04
EN19T-BT-Spec-9	6.563	38	0.18073	0.09024	0.24793	0.12317	1.372	1.365	0.51
EN19T-BT-Spec-15	6.571	38	0.17333	0.08655	0.24069	0.11247	1.389	1.299	6.42

The results showed that the experimental bending and torsion gain values G_B and G_T were similar, and the calculated gain differences were low. This confirmed that at the test speed of 38 [Hz], an experimental equivalent loading gain point was reached, and the biaxial nominal stress amplitude ratio λ was closest to the required 0.5 [-] value for each test. The most significant calculated difference (Equation (H-23)) was 6.42 [%]. This difference was attributed to the 0.9 [%] specimen diameter difference between Spec15 (measured) and Spec18 = 6.629 [mm] (on which the test speed is based). Due to the slightly smaller Spec15 diameter, the 38 [Hz] test speed may have been too low for Spec15, thus causing G_T to be smaller than G_B (see Figure 4-17 on pg.102). The slightly larger gain differences for Spec15 may also be attributed to the difference between the VSD test speed setting (38 [Hz]) and the actual test speed (37.48 [Hz]) for the sinusoidal displacement curve forming (see Figure H-38). These minor test speed differences (maximum 1.51 [%], attributed to motor slip) are discussed in Appendix H5.2 part 2b.

As discussed at the end of Section 4.5.2, it was deemed appropriate to utilise the measured test specimen gain values in Table 5-4 to calculate the un-measured specimen gain values. The specimen diameter changes and their effect on each biaxial loading gain value were considered (Figure K-5). This inference was made for the remaining BT fatigue test specimens (Spec1-2, 4-8, 10-14 and 16-17), tested with similar centrifugal mass pieces as Spec3, 9 or 15 above (see Table 4-8 on pg.109). The experimentally measured or calculated bending and torsion gain values were then utilised (Equation (H-17) and (H-18)) to calculate the fully reversed bending and torsion fatigue stress amplitudes shown in Figure 5-8 (a) and (b) hereafter. All the experimental BT gains and stresses can be referenced in Table J-5, along with the average experimental λ = 0.49 [-].

From the above experimental bending and torsion displacement measurements with the DANTEC, it was possible (like with the T fatigue) to generate the fully reversed out-of-phase biaxial sinusoidal displacement (loading) curves for each specimen. These curves were generated from the scattered bending-torsion displacement data (e.g., Spec9 in Figure H-37) using the procedure discussed at the end of Appendix H5.2, part 2b. They are illustrated in Figure H-38. The experimental out-of-phase bending-torsion displacement curve of Spec3 is provided in Figure 5-6 below. It is shown that the expected form of the biaxial out-of-phase induced loading of the test bench at 38 [Hz] was experimentally correct.

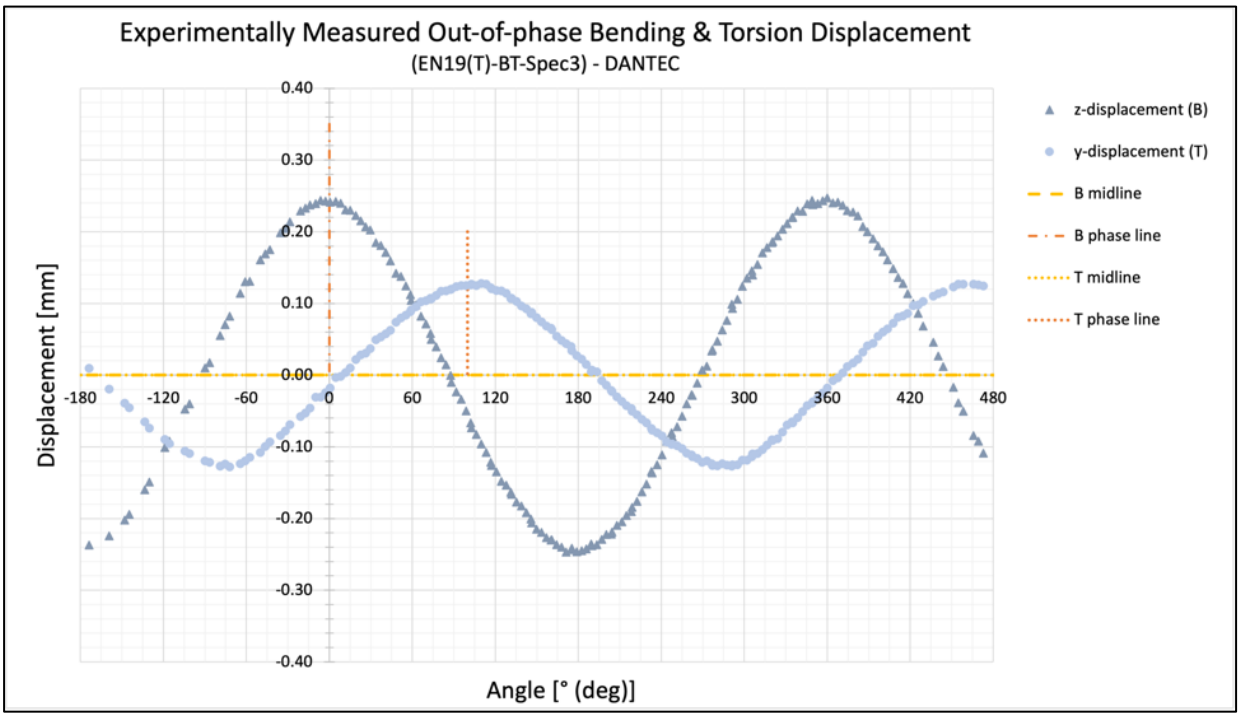


Figure 5-6: BT fatigue experimental measurements – sinusoidal bending and torsion displacement curves

Also illustrated in Figure 5-7 below is the *true principal strain* vector rotation observed during the experimental BT test measurements with the DANTEC. The images showed how the principal strain direction changes (blue lines in the test zone centre) with respect to the specimen's vertical axis (defined as x-direction in the DANTEC image coordinate system). This phenomenon was discussed in Section 3.2, where Mohr stress circles were used to theoretically illustrate the rotating principal stresses of the chosen out-of-phase bending-torsion loading condition. Therefore, the expected rotation in the principal stresses was shown from the experimental DANTEC measurements. For illustration, the Mohr circles (yellow) are indicated on each image for the relevant point of the loading cycle (reference Figure 3-1 on pg.44). The vertical yellow lines represent the Mohr circle σ-axis and the horizontal line the τ-axis. The red arrows indicate the principal stress axis direction as previously in the Mohr circles.

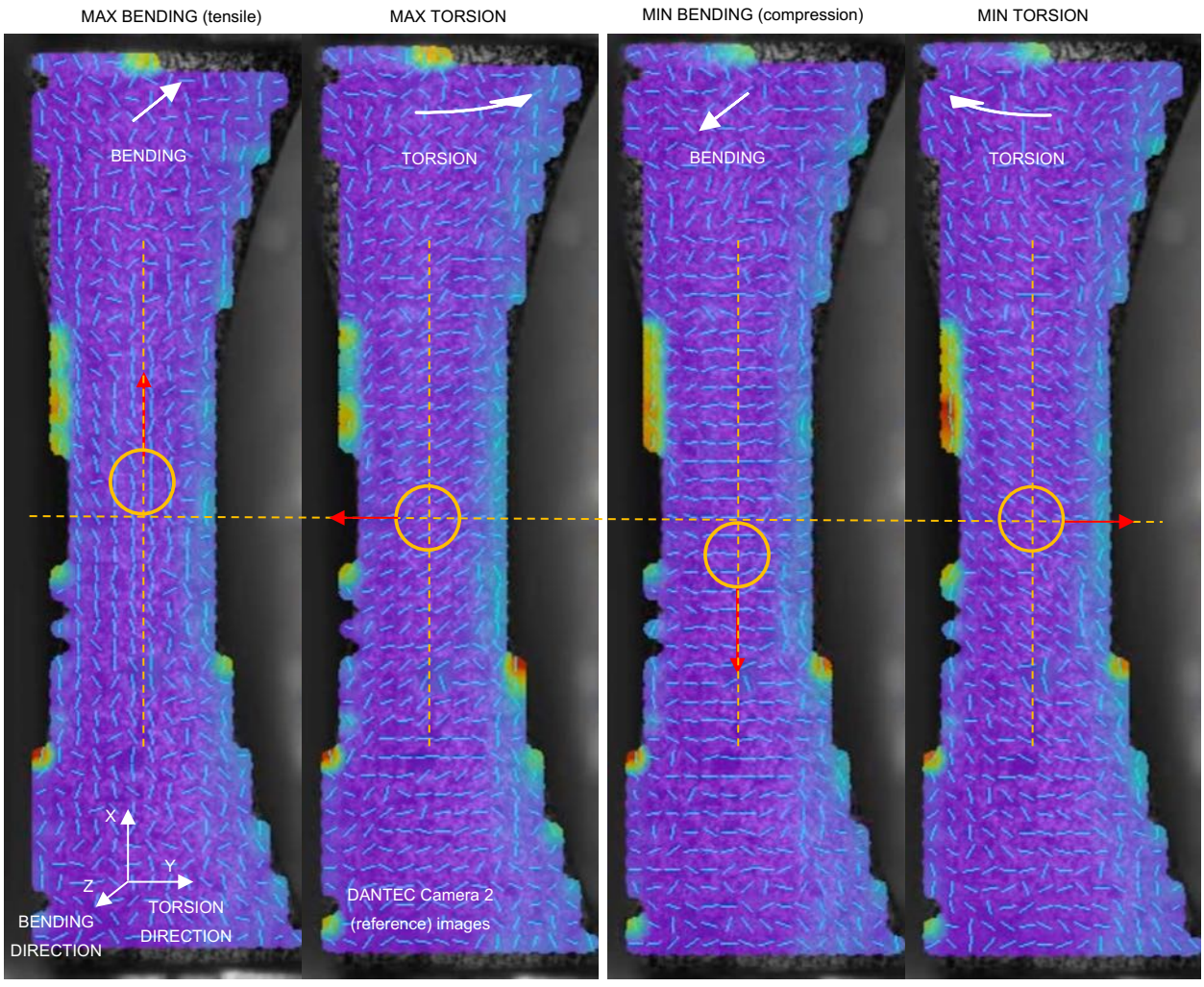


Figure 5-7: BT fatigue experimental measurements – DANTEC rotating true principal strain vectors

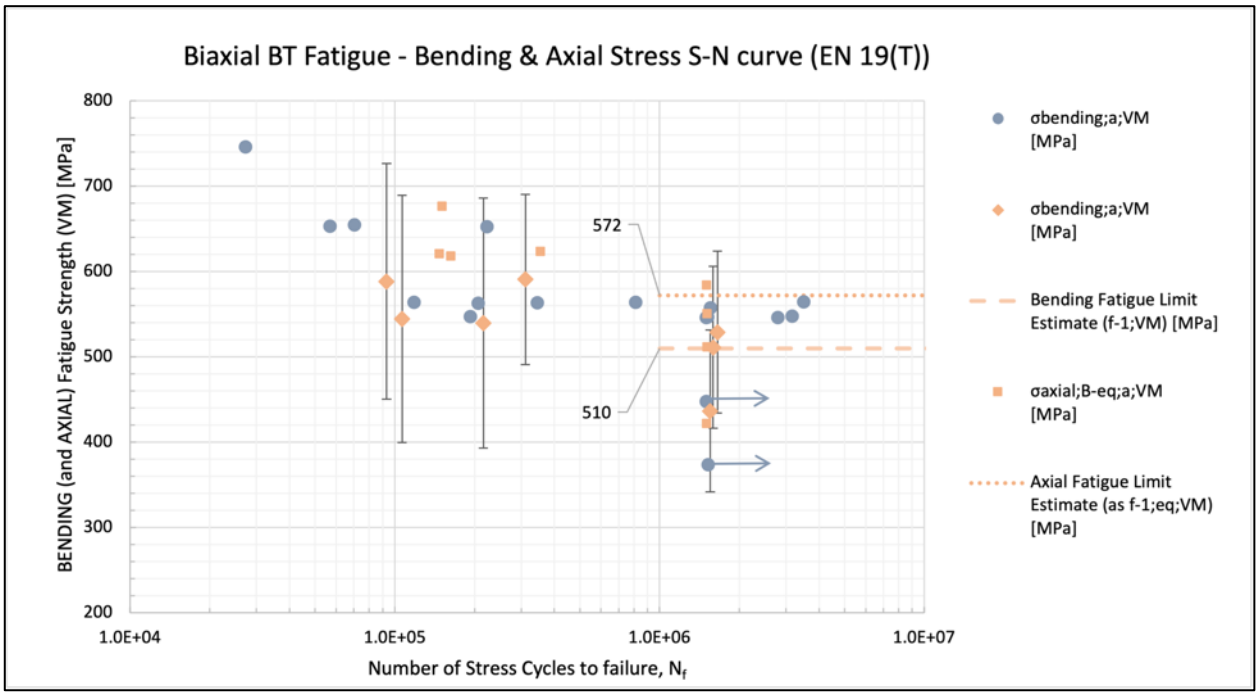
These curves and images provided further confidence that all biaxial out-of-phase bending-torsion fatigue test loading was correct. The only minor difference observed was the phase angle difference from the expected 90 [°] for all three measured test specimens. However, this was attributed to the observed difference in the test speeds (mentioned above). The experimental nominal displacement amplitude ratio (~0.5 [-]) could be seen from these curves. The BT fatigue test data generated on this test bench was considered correct and appropriate for evaluating the fatigue criteria.

5.2.3.2 Biaxial Fatigue Test Results

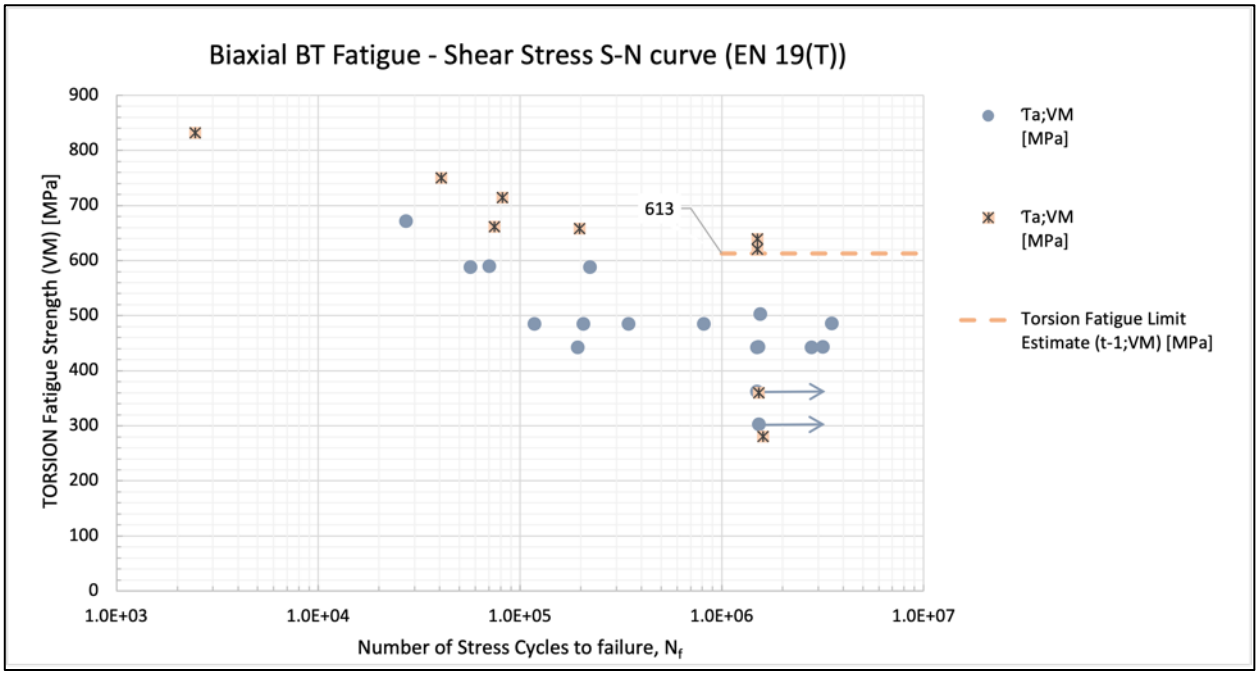
The experimental out-of-phase biaxial fatigue test data is summarised in the respective normal and shear fatigue strength S-N curves in Figure 5-8 below. These graphs included the uniaxial axial (AX), bending (B) and torsion (T) fatigue stresses and limit estimates (orange icons and lines) for comparison with the biaxial fatigue stress components (blue circles). As from the experimental measurement results discussed in the previous part, the biaxial BT fatigue strength data was shown to be experimentally sound. Reasons for considering the bending and torsion stress components of the biaxial loading condition on separate S-N curves were discussed in Section 3.2. These two S-N curves are based on the Von Mises (VM) stresses to allow direct comparisons between the stresses on each graph. The uniaxial axial fatigue data in Figure 5-8 (a) was converted to an equivalent bending fatigue data set by dividing the axial fatigue stresses by 0.85. Post-test fatigue fracture plane photos of an arbitrary BT specimen can be viewed in Figure J-6. Reference can be made to Table J-5 for the complete biaxial fatigue test data set.

The largest fully reversed bending, and torsion fatigue (nominal) stress uncertainties were obtained as 2.6 [%] and 3.0 [%], respectively (for Spec1). Reference can be made to Table K-5 for the biaxial fatigue stress component uncertainties. Both the bending and torsion fatigue stress uncertainties were low and not incorporated into the S-N curves of Figure 5-8. The uniaxial fatigue stresses (orange) and associated uncertainties on these graphs were previously discussed in Section 5.2.2.

From the S-N curves in Figure 5-8 below (based on shear and normal VM stress, respectively), the significant spread in experimental fatigue life to failure can be seen from all the repeated (and extended life) tests at respective biaxial stress levels. The fatigue life spread (10^5 to $3x10^6$ cycles) is primarily observed around the inflexion point stress levels of 400 to 550 [MPa] VM. This expected widespread fatigue life to failure agreed with what was previously illustrated in Figure 4-18 on pg.104 (S-N curve of typical carbon steel fatigue strengths).



(a)



(b)

Figure 5-8: Experimental biaxial fatigue S-N curves – (a) bending (and axial) fatigue strength and (b) torsion fatigue strength

Figure 5-8 (a) shows that the 'biaxial' bending fatigue strength (blue circles) of the material was comparable to both the uniaxial AX and B fatigue strength and limit estimate data. The biaxial bending fatigue strength 'limit' seemed equivalent to the uniaxial B fatigue limit estimate (orange dashed line). This suggested that a torsional stress component in the biaxial loading condition did

not influence the bending fatigue stress component. Conversely, Figure 5-8 (b) shows that the material's 'biaxial' torsion fatigue strength (blue circles) was not as comparable to the uniaxial T fatigue strengths and limit estimate.

Between the VM stress-based curves, it is also observed that biaxial fatigue failure can be assumed to be due to the bending stress component. That is because it was the dominant VM stress component of the biaxial stress condition in each specimen. The bending stress was between 100 – 150 [MPa] VM higher than the torsion if one positioned a fatigue limit line below each stress component's data points at the inflexion point. If the λ value were to be 2 (e.g., T > B), then failure may be presumed to be caused by the torsion stress component, as it would then be the dominant VM stress component of the biaxial stress condition.

Due to the 90 [°] out-of-phase angle between the two biaxial loading components, it is observed that an independent change in the torsion stress component (Figure 5-8 (b)) would not affect the bending stress component (Figure 5-8 (a)). That is, if the nominal stress amplitude ratio λ were changed to a value other than the chosen 0.5 [-] (B > T, inherent to the test bench working principle and method of testing), it would result in an independent change of either the bending or the torsion stress component. Therefore, it is suggested that the two stress components of this biaxial loading condition on a specimen can change independently primarily due to the specific phase angle tests conducted.

For the discussion that follows, the comparison between the experimental BT fatigue data (above) and the usable literature BT fatigue data from Zenner *et al.* [45] (Z) (see Table 4-2 on pg.67) bears reference. This comparison was made similarly to that previously done with the experimental uniaxial fatigue limits and the literature's uniaxial fatigue data. The purpose was to show and determine the suitability of the experimental fatigue data for the fatigue criteria evaluations (next section), as stated at the end of Section 4.7.

Regarding Figure 5-8 (b) above, the observed difference between the experimental t_{-1} value (354 [MPa], or 613 [MPa] VM) and the presumed biaxial torsion stress component's fatigue 'limit' value (estimated as 231 [MPa], or 400 [MPa] VM) was calculated as 35 [%]. A similar calculation with the Z material t_{-1} value (260 [MPa]) and biaxial torsion stress component value, reported as a biaxial 'fatigue limit stress condition', of τ_a (137 [MPa]) provided a larger 47 [%] difference. The difference observed between the experimental biaxial torsion fatigue stress and uniaxial torsion fatigue limit data also existed for the Z material. It was previously shown in Figure 5-4 that the Z material's uniaxial torsion t_{-1} and bending f_{-1} fatigue limits do not compare well with the SUS or experimental uniaxial fatigue limits.

Regarding the normalised S-N curve in Figure 5-9 below (based on the biaxial bending stress), it is shown that a significant difference exists between the Z material's (orange) in- and out-of-phase bending fatigue stress values (reported as a biaxial 'fatigue limit stress condition') and the Z uniaxial bending fatigue limit (orange dotted line). For the experimental (blue) out-of-phase bending fatigue stresses (at the inflexion point) and uniaxial fatigue limit, this difference is not observed (similar to previous Figure 5-8 (a)). Therefore, the Z material's biaxial fatigue limit data is again questioned since, unlike the experimental data, it is shown that the biaxial bending fatigue limit stresses (IP and OP) are lower than the material's bending fatigue limit.

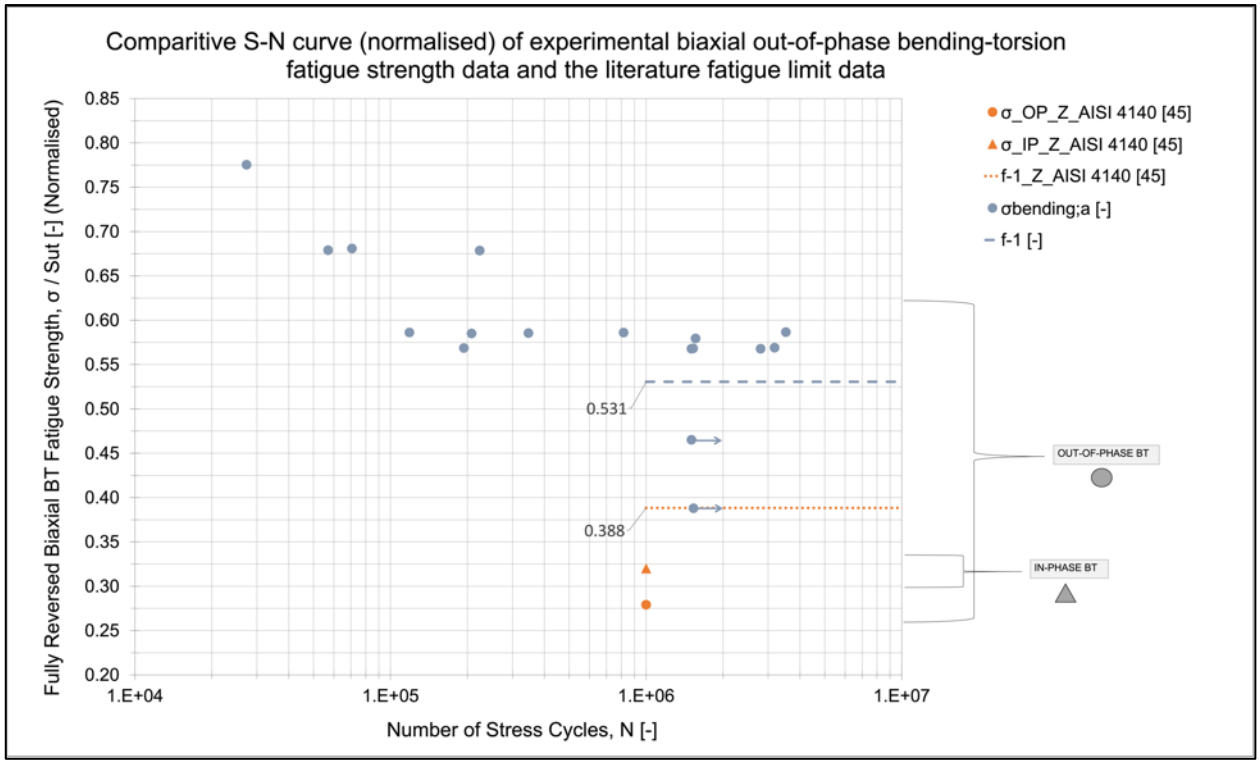


Figure 5-9: Comparative S-N curve (normalised) – experimental BT fatigue strength data comparison with literature biaxial fatigue limit data

The experimental biaxial BT fatigue limit data (based on bending) did not compare with the Z material's biaxial fatigue limit data in the normalised S-N graph above. The Z data appropriateness for criteria evaluations is ultimately questioned because of these and the previously observed differences with the uniaxial fatigue limit data. However, the experimental BT fatigue data was considered experimentally correct based on the experimental verification measurement results previously discussed. Therefore, the whole fatigue data set for EN19 (T-condition) was deemed appropriate for the multiaxial fatigue criteria evaluations, and these evaluation results will be provided next.

5.2.4 Multiaxial Fatigue Criteria Evaluations

The experimental uniaxial fatigue limit estimates from Section 5.2.2 and the biaxial (multiaxial) out-of-phase bending-torsion (BT) fatigue strength data from Section 5.2.3 above were utilised (discussion in Section 4.7) to evaluate each of the chosen multiaxial fatigue criteria (Table 4-1). These evaluation results can be referenced in Appendix L1 through L3.

Although the previous comparisons of the experimental and Z material fatigue data suggested that the Z data (for AISI 4140 / EN19) may be questionable, it was still included as part of these criteria evaluations for comparison (on the S-N curves only). This was done due to the material and data set's reference and use in the literature. It was also the only BT fatigue limit data appropriate for this study (see Table 4-2). In general, for the criteria evaluations to follow, a criterion prediction is regarded correct (or appropriate) if the presumed fatigue limit (solid yellow lines) of the criterion is equivalent to the estimated fatigue limit (dashed blue lines) of the evaluated experimental BT fatigue limit data. Note that for each criterion evaluation in this section, the experimental and Z material BT fatigue limit data are not compared (not normalised).

Papadopoulos 1994/1997 – Critical Plane Criterion

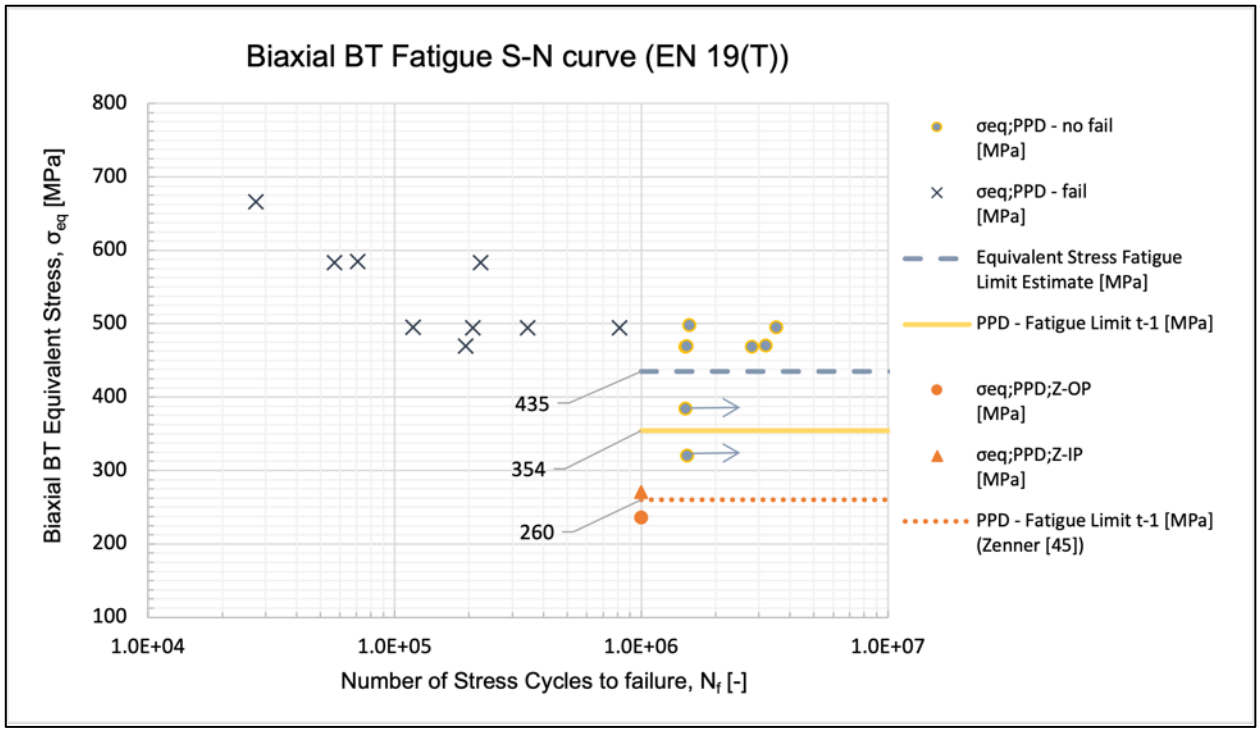
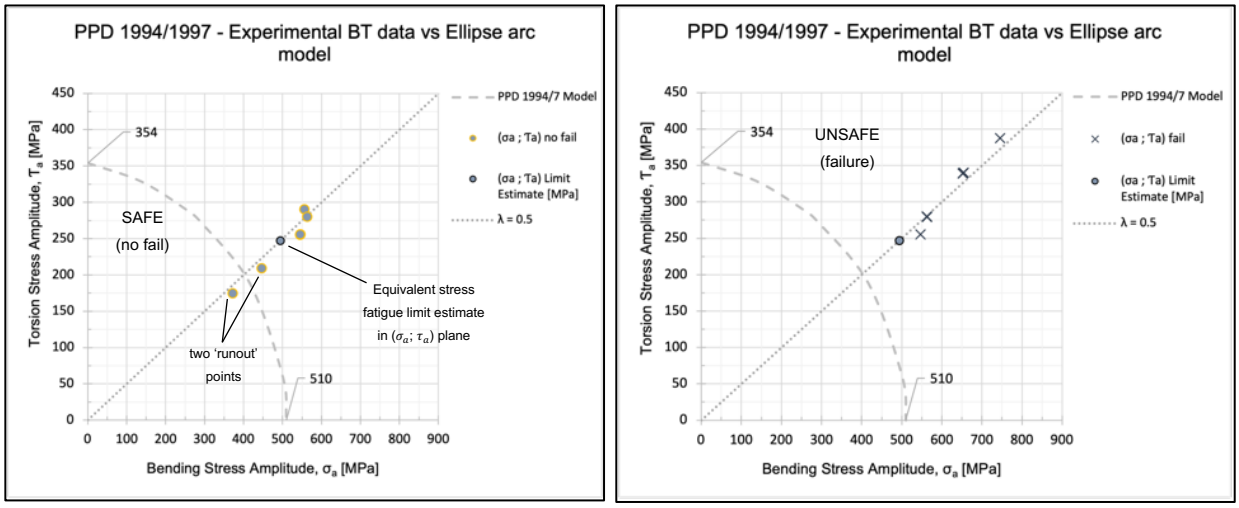


Figure 5-10: Biaxial BT fatigue S-N curve – experimental BT equivalent fatigue strength comparison with uniaxial T fatigue limit (PPD)

In Figure 5-10 above, it can be seen that the equivalent biaxial BT fatigue strength values from the PPD critical plane criterion evaluation (Equation (3-3)) were roughly 100 [MPa] higher than the proposed biaxial fatigue limit (t_{-1} for PPD, solid yellow line). The respective error-index values (from Equation (3-1), in Table L-1) of test points at fatigue life cycles > 10^6 reflected these notable differences (26.2 [%] on average). The differences were between the 'uniaxial equivalent stresses' (LHS, blue/yellow circles) and the uniaxial torsion fatigue limit for the criterion (RHS, solid yellow line). Therefore, the PPD multiaxial fatigue criterion suggests the biaxial BT fatigue limit is at a lower equivalent stress condition based on t_{-1} than what was obtained for the experimental test data (with fixed average λ = 0.49 [-]). This experimental BT fatigue limit (dashed blue line, based on PPD equivalent stress) was estimated as 435 [MPa] (method in Section 4.6.2). The Z material's BT fatigue limit data (orange) showed a good comparison with the PPD criterion proposed fatigue limit value (t_{-1}, dotted orange line).



(a) (b)

Figure 5-11: Biaxial BT fatigue stress data – experimental nominal bending-torsion fatigue strengths vs PPD ellipse arc model: (a) no fail tests and (b) failed tests

The conservativeness mentioned above of the PPD criterion model is also shown above in the 'un-failed' (Figure 5-11 (a)) and 'failed' (Figure 5-11 (b)) experimental BT fatigue stress graphs (on σ_a; τ_a plane). These graphs show that each test's out-of-phase biaxial BT fatigue stress conditions compared well with the ideal theoretical λ = 0.5 [-] (diagonal dotted line). The callout values at the ends of the criterion model on the σ_a and τ_a axes represent the fully reversed uniaxial B and T fatigue limits, respectively. These graphs reflected a similar result to the S-N curve above. The PPD criterion (dashed arc) underestimates the biaxial out-of-phase BT fatigue strength for tests that did not fail due to fatigue (blue/yellow circles). That is for the 1.5 x 10^6 cycle limit definition (Section 4.4.3) or even past 2 x 10^6 cycles (extended life tests). It is also shown concerning the PPD model curve that tests that failed due to fatigue (blue crosses) experienced

too large biaxial BT fatigue stresses to be considered safe against fatigue failure. The stresses in these tests were also larger than the estimated experimental BT fatigue limit (dark blue/black circle) stress condition based on the PPD equivalent stress.

Carpinteri and Spagnoli 2001 – Critical Plane Criterion

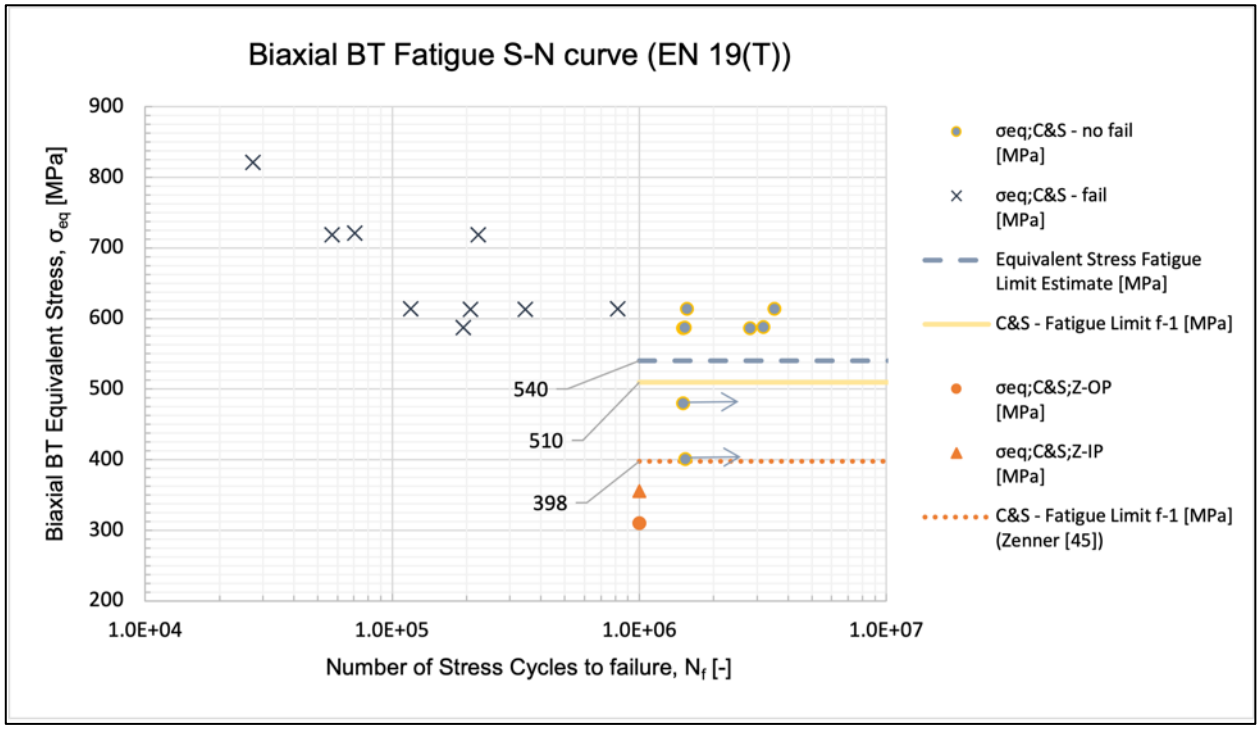
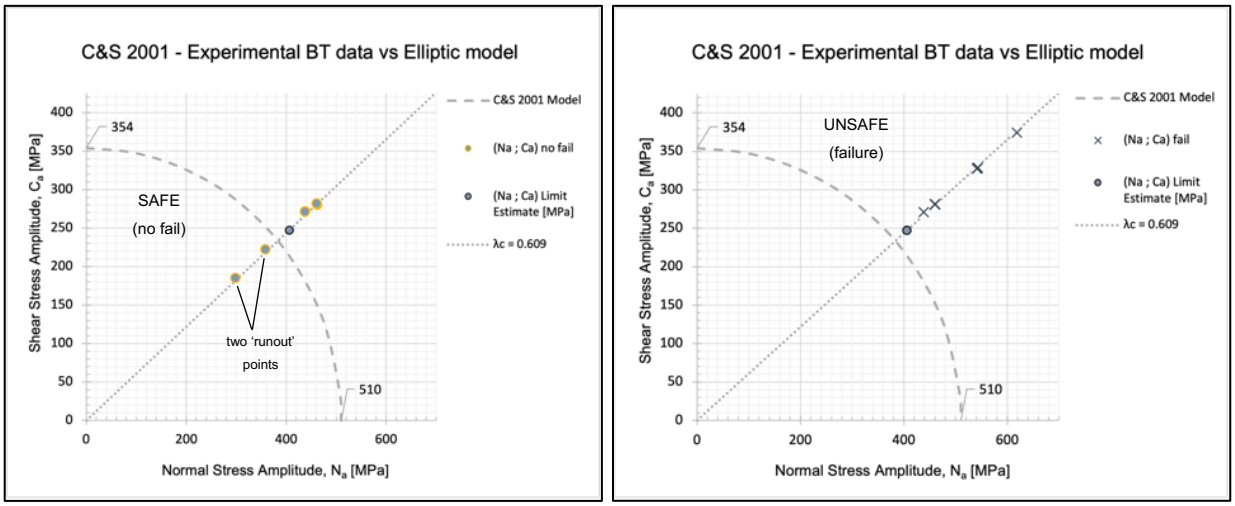


Figure 5-12: Biaxial BT fatigue S-N curve – experimental BT equivalent fatigue strength comparison with uniaxial B fatigue limit (C&S)

It can be seen in Figure 5-12 above that the equivalent biaxial BT fatigue strength values from the C&S critical plane criterion evaluation (Equation (3-4)) were roughly 60 [MPa] higher than the proposed biaxial fatigue limit (f_{-1} for C&S, solid yellow line). The respective error-index values (in Table L-2) of the test points at fatigue life cycles > 10^6 reflected much smaller differences (9.2 [%] on average). These differences were between the 'uniaxial equivalent stresses' (LHS, blue/yellow circles) and the uniaxial bending fatigue limit for the criterion (RHS, solid yellow line). Therefore, the C&S multiaxial fatigue criterion suggests the biaxial BT fatigue limit to be very close to the material's uniaxial bending fatigue limit value. This was similarly observed for the previously compared experimental biaxial bending fatigue strength and f_{-1} values in Figure 5-8 (a) (VM stresses) and in Figure 5-9 (normalised bending stresses). The experimental BT fatigue limit (dashed blue line, based on C&S equivalent stress) was estimated as 540 [MPa]. The Z material's

BT fatigue limit data (orange) did not show as good a comparison with the C&S criterion proposed fatigue limit value (f_{-1}, dotted orange line). A similar result was observed for the Z data in the normalised S-N curve in Figure 5-9 on pg.138. The C&S criterion effectively overestimates the fatigue limit strength of the Z material, as the in-phase (IP) and out-of-phase (OP) equivalent stress data points shown were reported as the biaxial BT fatigue limit of that EN19 material (see Table 4-2).



(a) (b)

Figure 5-13: Biaxial BT fatigue stress data – experimental critical plane fatigue stresses vs C&S elliptic model: (a) no fail tests and (b) failed tests

For the C&S criterion, it is shown above with the 'un-failed' (Figure 5-13 (a)) and 'failed' (Figure 5-13 (b)) experimental BT fatigue test stresses on the critical plane (N_a; C_a), that the criterion model is less conservative in its predictions. The normal and shear stress conditions on the identified critical plane of each test (from the procedure with Equation (3-4)) compared well with the C&S criterion model. These graphs also showed that the normal and shear stresses on the critical plane were in very good agreement with the critical plane stress amplitude ratio estimated as λ_C = 0.609 [-] (diagonal dotted line). This ratio differs from the λ value, which had an experimental average of 0.49 [-] for all BT fatigue tests. The callout values at the ends of the criterion model on the N_a and C_a axes similarly represent the fully reversed uniaxial B and T fatigue limits obtained from the criterion under uniaxial loading conditions. These graphs reflected a similar result to the S-N curve above. The C&S criterion (dashed arc) appropriately estimates the out-of-phase biaxial BT fatigue strength for tests that did not fail due to fatigue (blue/yellow circles). More specifically, the C&S criterion correctly estimates the non-failure of the two test data points that were assumed to have infinite life (runout arrows in Figure 5-12). These two data points are located inside the criterion model arc (considered the 'safe' zone) in Figure 5-13 (a) above. It is also shown concerning the C&S model curve that tests which failed due to fatigue (blue crosses)

experienced biaxial BT fatigue stresses that were larger than what the criterion considers safe against fatigue failure. Again, the stresses in these tests were larger than the estimated BT fatigue limit (dark blue/black circle) stress condition on the critical plane of C&S.

Liu and Mahadevan 2005 – Critical Plane Criterion

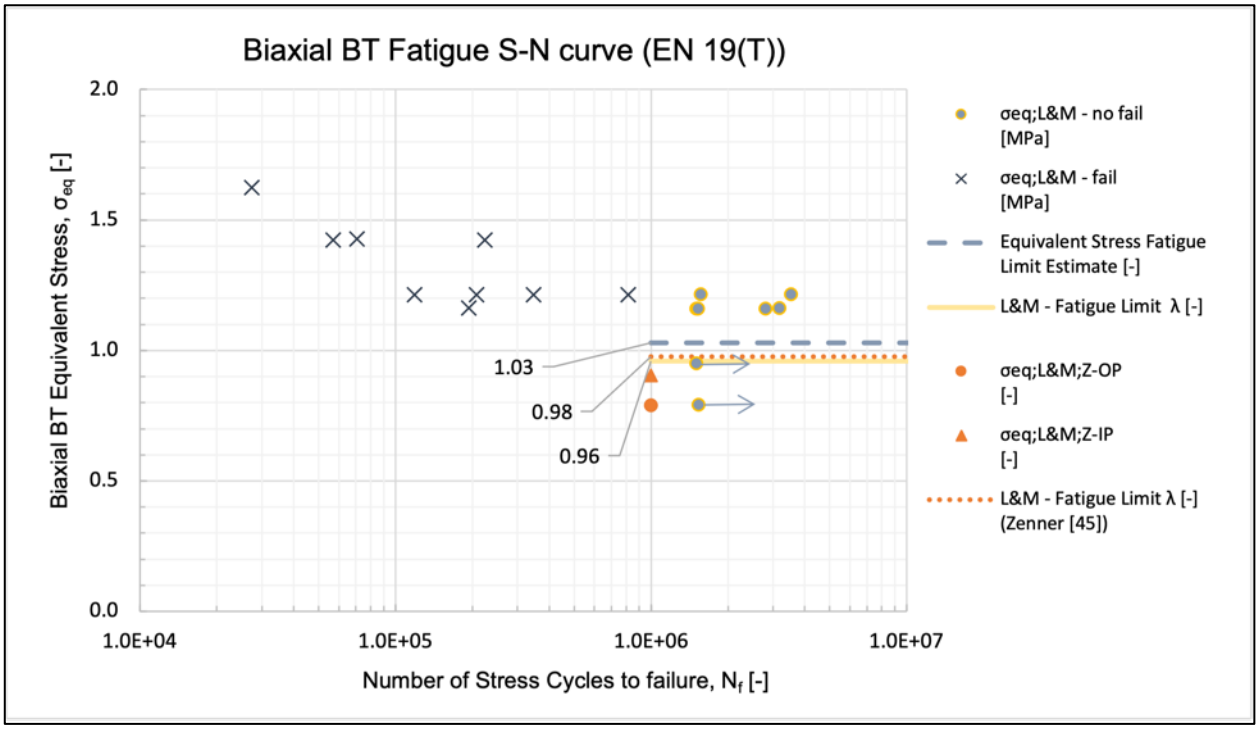
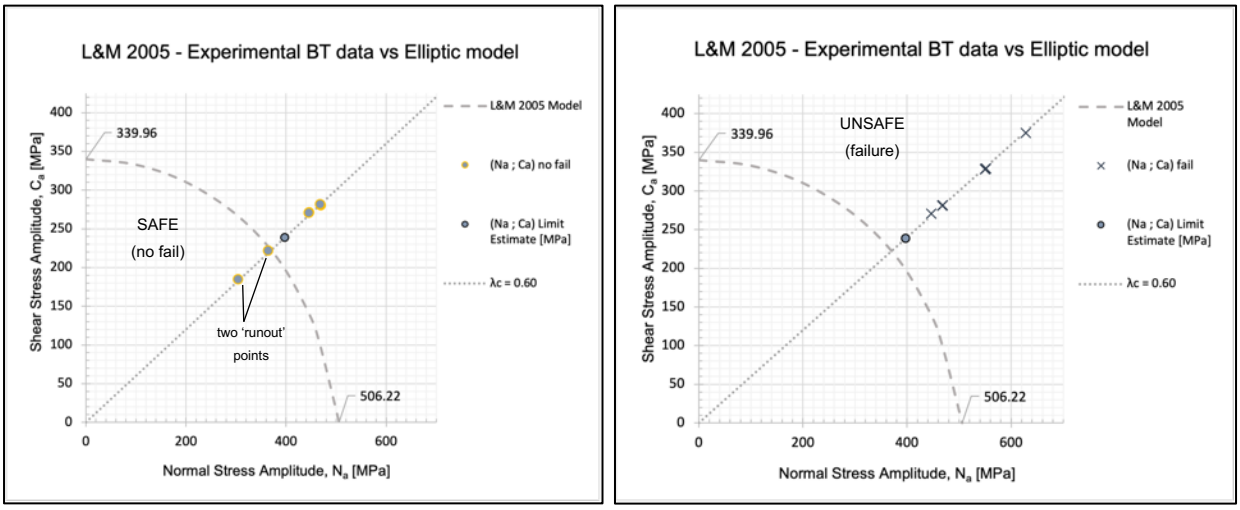


Figure 5-14: Biaxial BT fatigue S-N curve – experimental BT equivalent fatigue strength comparison with uniaxial fatigue limit parameter (L&M)

In Figure 5-14 above, it can be seen that the equivalent biaxial BT fatigue strength values from the L&M critical plane criterion evaluation (Equation (3-8)) were roughly 0.2 [-] higher than the proposed biaxial fatigue limit (λ 'material parameter' for L&M, solid yellow line). Note that this λ value (Equation (3-9)) should not be confused with the nominal stress amplitude 'ratio' λ value (Equation (4-6), for the BT loading condition tested). The L&M λ value was used in the same form reported in the literature to stay true to the original notation (RHS) used for this criterion. The respective error-index values (in Table L-3) of the test points at fatigue life cycles > 10^6 reflected slightly larger differences (14.8 [%] on average) than for C&S. These differences were between the 'uniaxial equivalent stresses' (LHS, blue/yellow circles) and the fatigue limit parameter for the criterion (RHS, solid yellow line). Therefore, the L&M multiaxial fatigue criterion suggests that the biaxial BT fatigue limit is also close to the fatigue limit parameter value for the material (similar to

C&S). The experimental BT fatigue limit (dashed blue line, based on L&M equivalent stress) was estimated as 1.03 [-]. The Z material's BT fatigue limit data (orange) also did not compare well with the L&M criterion proposed fatigue limit value (λ 'material parameter', dotted orange line). For this, the L&M criterion also overestimates (like C&S) the fatigue limit strength of the Z material.



(a) (b)

Figure 5-15: Biaxial BT fatigue stress data – experimental critical plane fatigue stresses vs L&M elliptic model: (a) no fail tests and (b) failed tests

For the L&M criterion, it is shown above with the 'un-failed' (Figure 5-15 (a)) and 'failed' (Figure 5-15 (b)) experimental BT fatigue test stresses on the critical plane (N_a; C_a), the criterion is slightly more conservative in its predictions than C&S. The normal and shear stress conditions on the identified critical plane of each test (from the procedure with Equation (3-7)) also compared well with the L&M criterion model. These graphs also showed that the normal and shear stresses on the critical plane were in very good agreement with the critical plane stress amplitude ratio estimated as λ_C = 0.60 [-] (diagonal dotted line). This ratio differs from both the above-mentioned λ values, which had values 0.49 [-] (biaxial) and 0.96 [-] (L&M) for all BT tests and the uniaxial fatigue limits. The callout values at the ends of the criterion model on the N_a and C_a axes represent critical plane stresses different from what was previously the case for both PPD and C&S. These graphs reflected a similar result to the S-N curve above. The L&M criterion (dashed arc) also appropriately estimates the out-of-phase biaxial BT fatigue strength for tests that did not fail due to fatigue (blue/yellow circles). The L&M criterion also correctly estimates the non-failure of the two test data points that were assumed to have infinite life (runout arrows in Figure 5-14). The two data points were located inside and on the criterion model arc (the 'safe' zone) in Figure 5-15 (a) above. As with the previous two criteria, it was also shown concerning the L&M model curve that the tests which failed due to fatigue failure (blue crosses) experienced BT fatigue stresses that were larger than what the criterion considers safe against fatigue failure. The stresses in

these tests also were larger than the estimated BT fatigue limit (dark blue/black circle) stress on the critical plane of L&M.

Critical Plane Criteria Comparison

Like the separate discussion of the criteria in previous paragraphs, it was not deemed appropriate to directly compare the equivalent stress values of each criterion with each other. This was because each criterion (Equations (3-3) through (3-7)) considers or calculates the 'uniaxial equivalent stress' value (LHS) differently. The criteria also considered three different 'uniaxial fatigue limit' values (t_{-1} – PPD, f_{-1} – C&S and λ – L&M) as the limiting (RHS) value for the evaluated test data (LHS). It was deemed more appropriate to compare the three criteria based on a percentage difference value (Equation (3-2)). This value is calculated between the proposed criterion fatigue limit (RHS, previous yellow solid lines) and the limit estimated for the evaluated experimental BT fatigue data (the previous blue dashed lines). These percentage differences are illustrated in Figure 5-16 below.

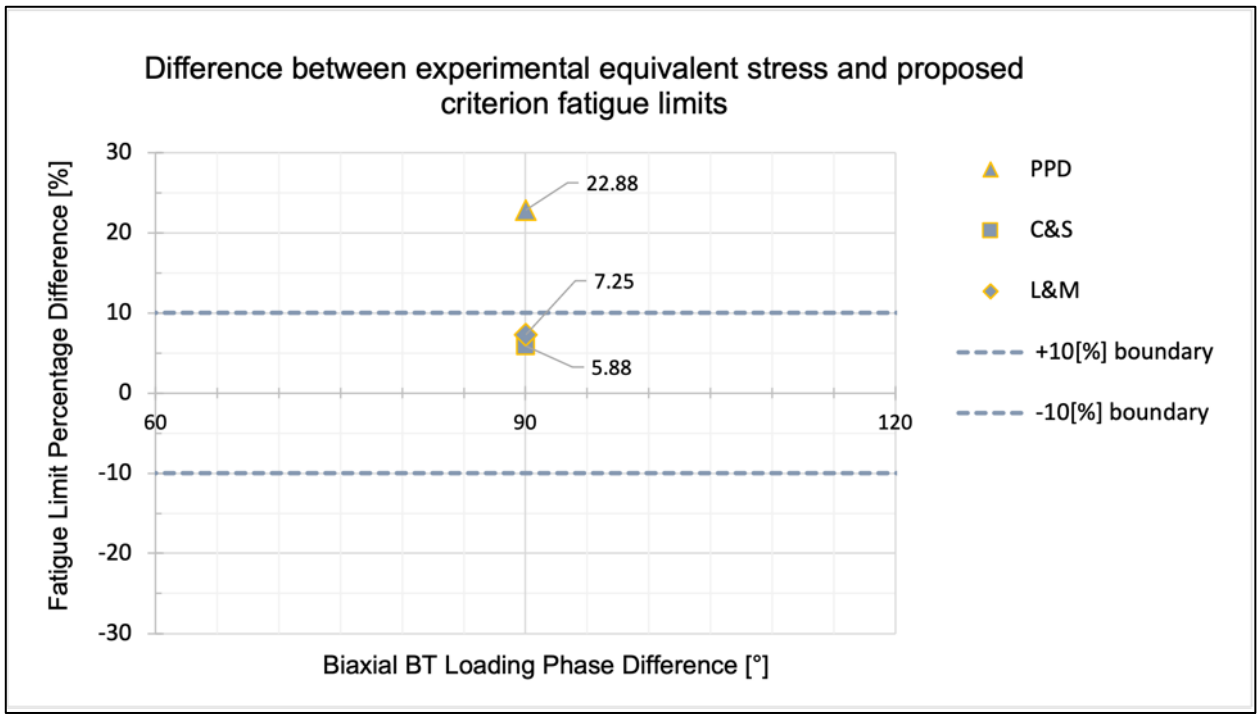


Figure 5-16: Multiaxial BT fatigue failure criteria – experimental BT fatigue limit estimate comparison with criteria proposed uniaxial fatigue limit

This approach was an informal way to compare the respective fatigue limit values for each criterion ([%] of points shown) and correspondingly the criteria with each other based on the

loading condition and material. That is, 90 [°] out-of-phase bending-torsion, with λ = 0.5 [-], on EN19 (T-condition) alloy steel. For the comparisons, 10 [%] boundary lines were assumed to show the range for which a criterion was considered to be accurate in its evaluation of the experimental BT fatigue test data (typically used error band, also in [9]).

The comparisons showed that all three multiaxial fatigue criteria made conservative (underestimated) fatigue limit estimates. It is also seen in this graph (and the S-N curves) that the PPD criterion was far more conservative than the C&S and L&M criteria. The C&S criterion was the least conservative, and its equivalent fatigue strengths (for the experimental data) compared better with the uniaxial fatigue limit it proposes for assessing the fatigue data.

5.3 Conclusion

This chapter provided the experimental results of the four main parts considered in this study. The first part was the characterisation of the EN19 (T-condition) test material through monotonic tensile (TEN) testing. These results showed to be in good comparison with the values reported in the multiaxial fatigue literature (Table 4-2) and on the material certificate (Figure M-2).

The second part was the experimental testing of EN19 (T-condition) under fully reversed uniaxial axial (AX), bending (B) and torsion (T) fatigue loading. The experimental T fatigue test measurements showed a very good comparison of the theoretical and experimental torsion loading gain values. The fully reversed torsion fatigue loading ‘form’ was also shown to be appropriate using the experimental sinusoidal displacements measured with the DANTEC during testing. Comparing the estimated experimental uniaxial fatigue limits with the available literature data showed that the values were appropriate for use in the fatigue criteria evaluations.

The third and most significant part was the experimental fully reversed out-of-phase biaxial bending-torsion (BT) fatigue testing of EN19 (T-condition). The experimental BT fatigue test measurements showed that equivalent bending and torsion loading gains were obtained at the chosen experimental test speed of 38 [Hz]. The experimental bending and torsion stresses were calculated with these gains, and an average λ = 0.49 [-] was obtained for the tests. The fully reversed biaxial bending and torsion fatigue loading ‘form’, ‘phase difference’ and ‘loading ratio’ were shown to be appropriate using the experimental sinusoidal displacements measured with the DANTEC during testing. With the DANTEC measurements, the principal stress rotation phenomenon reported in the literature and theory chapter was also experimentally observed, which confirmed that the appropriate out-of-phase loading was induced.

The respective comparisons between the experimental BT and uniaxial fatigue test data on VM-based S-N curves showed under 90 [°] out-of-phase bending-torsion loading with λ = 0.49 [-] that the material's uniaxial bending fatigue limit strength is reached. However, not for the uniaxial torsion fatigue limit strength. It was also shown that the biaxial bending stress component is the dominant VM stress under this loading condition. Due to this, it is considered that this bending loading component causes biaxial fatigue failure. The material's biaxial fatigue limit strength is seemingly determined by the maximum VM stress component rather than a combination of the stress components. For the 90 [°] phase difference between the bending and torsion loading components, it was also observed that an independent change in the torsion stress component (through λ) would not influence the bending stress component. Therefore, the loading components are considered to be independent.

All the above experimental uniaxial and biaxial fatigue test uncertainties, except for the uniaxial bending (B) fatigue tests, were sufficiently small. The uniaxial axial (AX) fatigue limit data set had very low test uncertainties, and it was considered a bending equivalent reference for the B fatigue tests. This bending equivalent fatigue data was within the uncertainty ranges of the B fatigue tests, and both the AX and B fatigue limits were deemed appropriate.

The comparisons between the experimental uniaxial fatigue data with the relevant literature data showed that the experimental data was appropriate for use in the fatigue criteria evaluations. These data comparisons showed that the Zenner (Z) material's uniaxial fatigue limits did not compare well with the experimental and Susmel (SUS) uniaxial fatigue limits. From the experimental biaxial BT fatigue strength data comparison with the Z material's biaxial BT fatigue limit data (based on the normalised bending stress), much less agreement exists. The Z data did not compare well with the experimental data or its own uniaxial bending fatigue limit. Therefore, the appropriateness of the Z multiaxial fatigue data set for evaluating fatigue criteria was questioned. Based on the verification measurements, the experimental biaxial BT fatigue data was still considered appropriate for criteria evaluations. The Z data was also considered for the evaluations performed in this study (since being the only literature multiaxial fatigue data set).

The chapter concluded by providing these multiaxial fatigue criteria evaluation results. These evaluations were performed for each criterion with (1) the experimental uniaxial and biaxial BT fatigue data sets and (2) the above-mentioned Zenner (Z) data.

(1) With these criteria evaluation results and the average error-index values, respectively, it was shown that the PPD criterion is much more conservative (underestimated) in its biaxial fatigue limit evaluation than what the C&S and L&M criteria are. The C&S and L&M criteria made appropriate and comparable evaluations of the biaxial fatigue limit data. The L&M criterion

was shown to be slightly more conservative than the C&S criterion, yet still much less than the PPD criterion. None of the criteria overestimates the experimental biaxial fatigue limit of EN19 (T-condition).

Comparing the criteria based on the percentage difference value between the presumed criterion and the estimated experimental BT fatigue limit showed that the C&S and L&M criteria may be considered better for biaxial fatigue limit evaluations (differences < 10 [%]). That is, specifically for the chosen biaxial fatigue loading condition, the material and the experimental uniaxial and biaxial fatigue test data. The PPD criterion may be too conservative for the considered BT loading condition and not necessarily for EN19 (T-condition) since it is an appropriate hard metal for the criterion.

(2) From these results, it was shown that only the PPD criterion evaluation is in agreement with the Z fatigue limit data. The C&S and L&M criteria overestimate (non-conservative) the Z material's (EN19) biaxial fatigue limit. Therefore, the validation of these criteria in the literature with this Z data (and others) is questioned. Therefore, more data is required to investigate these observations further and assess the criteria (not done in this study).

It was ultimately considered that the Zenner (Z) multiaxial fatigue data on AISI 4140 may be untrustworthy, which also implies that the criteria (especially PPD) may be untrustworthy based on the following:

- All the experimental fatigue test data sets are verified and shown through experimental measurements and data comparisons with literature to be appropriate.
- All three criteria have conservative yet inconsistent evaluations of this study's verified experimental fatigue test data. Only the C&S and L&M presumed fatigue limits show good agreement with the experimental biaxial BT fatigue limit of EN19 (T-condition).
- The PPD criterion has the only evaluation in excellent agreement with the Z material's fatigue limit data, whilst C&S and L&M overestimate the fatigue limit of the Z material.
- The Z material data may be inappropriate for evaluating the three fatigue criteria.

The last chapter discusses the research conclusions and recommendations for this study.

CHAPTER 6 – CONCLUSIONS AND RECOMMENDATIONS

6.1 Introduction

This chapter summarises the efforts and results discussed in the preceding chapters. This summary is done by first providing an overview of the research study and the main findings. Next, a discussion is provided on the critique and recommendations based on the results obtained. Further research recommendations are also made, and the contribution of this study is also briefly discussed. A conclusion on this experimental research study is ultimately provided at the end.

6.2 Study Overview and Main Findings

Chapter 1 identified that appropriate fatigue failure criteria are required to assess and predict a component's fatigue resistance under complex multiaxial fatigue loading conditions. The literature reports on the various fatigue criteria and the differences and inconsistencies between their fatigue limit predictions for metals. These discrepancies remain unresolved due to the testing and validation of the criteria with repeatedly used multiaxial fatigue data sets that the literature argues to be old, insufficient and often incorrect. These data sets are also not reported with any experimental uncertainty in the literature. The correctness, applicability and trustworthiness of these data sets are therefore questioned, and consequently, so are the criteria validated with them.

The testing and evaluating of multiaxial fatigue criteria (under question in the literature and this study) requires specific material strength properties. The literature review efforts in this study showed that discrepancies exist for the data sets as many of the required material strength properties were unreported, questioned, and repeatedly referenced in fatigue criteria review studies in the literature. The literature data applicable to this study also showed little data for proper and meaningful fatigue criteria evaluations.

Therefore, this research study's main objective was to generate new fatigue data and perform a complete evaluation for a single ferrous metal under uniaxial and out-of-phase biaxial loading. It was also part of this objective to have enough data points to enable meaningful trends. The results of these experimental tests, and the relevant fatigue data previously identified from the literature, would then be used to evaluate each of the chosen multiaxial fatigue criteria. These evaluations were primarily performed to answer the main research question: can the multiaxial fatigue criteria

in the literature be trusted based on the fatigue data used to validate them that may be untrustworthy?

In Chapter 2, a comprehensive literature review on multiaxial fatigue provided an abundance of existing fatigue failure criteria often considered in review and comparison studies. The reported multiaxial fatigue data sets (uniaxial and biaxial loading) were also identified from these and other studies. The study's limitations to ferrous metals and out-of-phase bending-torsion loading determined the relevant data and criteria. The biaxial loading condition was limited to 90 [°] out-of-phase bending-torsion loading with λ = 0.5 [-]. A summary and categorisation of the criteria and data sets were made, and the relevant ferrous metals commonly used for testing were also identified. The ferrous metal type was limited to only those classified in the literature as ductile or hard metals. This limitation resulted from the fatigue criteria applying to such metal types. A generalised discussion was provided for how fatigue criteria are evaluated and what material properties are required. The literature data to consider was made evident.

Chapter 2 also showed from the tabulated and graphically illustrated fatigue data that a lack of data exists. It was also shown that key material strength parameters required for criteria evaluation are not reported. The repeated use of some multiaxial fatigue data sets was also observed. The literature data, which could be used for comparison with this study's experimental fatigue data, and evaluation of the relevant criteria were ultimately shown to be very few. From the 67 fatigue criteria obtained in the literature, only 12 were considered appropriate based on this study's loading condition and experimental testing (in HCF) limitations. The criteria consisted of 9 critical-plane and 3 empirical-based criteria. They were each discussed further regarding their reported material applicability, completeness and description, ease of use and requirement for additional material parameters. From this discussion, it was evident that most of these criteria were not appropriate for evaluation. Consequently, only the relevant ones were chosen to evaluate the experimental data in this study. This selection was made later in the experimental methodology chapter.

Chapter 3 provided the theoretical discussion of the chosen fatigue loading condition and fatigue criteria and also the critical plane theory on which these criteria models are based. For the chosen experimental fatigue loading condition, it was shown with the Mohr circle theory that the induced stresses behave according to what is reported in the literature. This behaviour included the rotating principal stress phenomenon and the constant maximum shear stress experienced on a material plane. It was also discussed why a conventional Von Mises (VM) stress calculation is not suitable for obtaining the combined bending-torsion loading effect in a component when the loading components are out-of-phase. The theory chapter provided and discussed the relevant equations and models for the chosen critical plane fatigue criteria. A discussion on the critical

plane theory endeavoured to explain the critical plane and, with an example derivation of the one criterion, illustrate how it is typically considered. From the criteria models, identification of the required material strength properties for their evaluation followed. These material properties included the fully reversed uniaxial bending and torsion fatigue limits and the out-of-phase biaxial bending-torsion stresses. Identification of these properties assisted in determining the required experimental material tests performed and, consequently, the testing and measurement equipment.

Chapter 4 discussed the experimental methodology followed to generate this new material and fatigue strength data set. In the first part of the chapter, the specific experimental selections and motivations were discussed. For this, the previously mentioned out-of-phase biaxial bending-torsion loading condition choice was further motivated. After that, based on this loading condition, the three most relevant and appropriate multiaxial fatigue criteria were chosen from those discussed in the literature chapter. These included the Papadopoulos (PPD), Carpinteri and Spagnoli (C&S), and the Liu and Mahadevan (L&M) critical plane criteria. These criteria had the simplest and least cumbersome solution methods and did not require additional material parameters to allow solving them. However, they only applied to hard metals (ferrous in this study). The experimental test material was chosen as AISI 4140 / EN19 (T-condition) alloy steel from the criteria identification and consideration of the materials most reported on in the literature. According to the relevant criteria definitions and the generally reported properties of this steel in the literature, it is regarded as a hard metal. The only usable literature data sets for comparison and criteria evaluation purposes were identified with the test material identification. These data sets were ultimately reduced to the Zenner (Z) multiaxial fatigue data set and the Susmel (SUS) and Li (JL) uniaxial fatigue data sets.

The second part of the experimental methodology chapter identified and discussed the testing and measurement equipment based on the required material strength properties for the chosen criteria evaluations. The test benches included the MTS Landmark (tensile and axial fatigue tests), the TERCO MT205G (bending fatigue tests), the Torsion fatigue test bench (torsion fatigue tests), and the Biaxial Fatigue Test Bench M1 (bending-torsion fatigue tests). The additional tensile tests provided the necessary EN19 (T-condition) material characterisation, and the uniaxial axial fatigue tests served as a reference for the bending fatigue tests. The principal measurement instrument of the study was the DANTEC Digital Image Correlation (DIC) System, which was used to measure specimen displacements on the torsion (T) and bending-torsion (BT) fatigue test benches. Secondary verification of the DANTEC was performed prior to the experimental test measurements. The results of this verification provided sufficient measurement certainty and confirmed that the DANTEC system and general usage procedure are understood.

In the third part, additional experimental considerations for the specimens and the test bench loading were made to ensure that the experimental test data in this study can be trusted. The individual test specimens were machined according to standard, and the literature reported geometries relevant to each test type. All specimen surfaces were polished to ensure surface condition effects were mitigated and negligibly small. Specimen diameters were also properly measured multiple times to allow appropriate stress calculations. Test bench calibrations were performed, and calibration certificates were consulted for the relevant loading considerations of the tensile (TEN), axial (AX) fatigue and bending (B) fatigue test benches. Based on the theoretical loading gain observations made for the torsion and bending-torsion fatigue test benches, it was required to perform verification measurements.

For the torsion fatigue test bench, this entailed verification of the test bench loading and the test bench measurement set-up with the DANTEC. These displacement measurements and associated static FEM simulations showed that the DANTEC measures the loading on the test bench correctly, and the theoretical and experimental loading gains are comparable. The verification measurements characterised the test bench loading gain for the bending-torsion fatigue test bench. They were done to determine the relevant loading gain responses and the equivalent experimental loading gain point. These displacement measurements (also using static FEM simulations) showed that separate theoretical consideration of the bending and torsion loading component for gain is incorrect. The equivalent experimental loading gain test speed was obtained as 38 [Hz], and subsequent bending-torsion tests were performed at this speed. The appropriate experimental fatigue stresses were calculated with the relevant torsion and bending-torsion gain values. These official experimental gains were obtained from selected torsion and bending-torsion fatigue test measurements with the DANTEC. The DANTEC displacement measurements from these official tests showed that both the torsion and out-of-phase bending-torsion fatigue loading had the proper form. The rotating principal stress phenomenon was also observed in these experimental measurements for the bending-torsion fatigue tests.

The appropriate experimental stress calculation methodologies were considered for the EN19 (T-condition) material strength tests performed. The required uniaxial fatigue limits for criteria evaluations were also suitably estimated. For each test type, a complete experimental uncertainty analysis was performed.

The results in Chapter 5 showed that the experimental test uncertainties were sufficiently small, and only the uniaxial bending fatigue tests had pronounced uncertainties. However, the bending fatigue limit was comparable to the axial fatigue limit (in equivalent bending form). The comparisons between the experimental bending-torsion and uniaxial fatigue data showed that the biaxial bending stress component is the dominant VM stress. This biaxial bending stress

component's fatigue limit strength was equivalent to the uniaxial axial and bending fatigue limits. The biaxial bending-torsion fatigue failure of the material was presumed to be caused by this maximum VM stress component and not the combination of the two biaxial components.

Comparisons were also performed between the experimental and literature fatigue data. The experimental uniaxial fatigue limit data was appropriate and comparable with the uniaxial fatigue limits from the literature. Of the uniaxial fatigue limits in the literature, the Zenner data was shown to be least comparable with the experimental fatigue limits and the Susmel data. The out-of-phase biaxial bending-torsion data was shown not to be comparable with the literature data of Zenner, and the Zenner data also did not compare well with its uniaxial bending fatigue limit. Based on these comparisons, the Zenner material fatigue data as a whole was questioned.

The evaluation results of the fatigue criteria with the experimental fatigue data showed that the Papadopoulos criterion is much more conservative than the Carpinteri and Spagnoli and the Liu and Mahadevan criteria. The Papadopoulos criterion severely underestimates the out-of-phase bending-torsion fatigue limit strength of EN19 (T-condition). The Carpinteri and Spagnoli and the Liu and Mahadevan criteria appropriately estimated the material's fatigue limit strength under these loading conditions. A comparison of the criteria based on the percentage difference values between criteria fatigue limits and experimental fatigue limit estimates showed that the Papadopoulos criterion might be considered too conservative. That is, for the experimental loading condition and material.

The supplementary evaluation results of the criteria with the Zenner material data showed that only the Papadopoulos criterion's evaluation of the fatigue limit data was in agreement. The Carpinteri and Spagnoli and the Liu and Mahadevan criteria overestimate the Zenner material's fatigue limit.

It is evident from this study that the multiaxial fatigue data sets from the literature used for criteria validations are questionable. The discrepancies reported for the criteria and the data sets in the literature were also observed in this study. It is concluded that the Zenner multiaxial fatigue data on AISI 4140 might be considered untrustworthy. However, this implied that the evaluated fatigue criteria might be untrustworthy due to inconsistent evaluation results. It is apparent that more (and new) complex multiaxial fatigue data is required, and the literature criteria require further assessment.

6.3 Critique and Recommendations

This section provides the critique and recommendations on the research study and the experimental testing performed. This discussion is centred primarily on the generation of more multiaxial fatigue test data to investigate the differences observed for the criteria in this study.

- It is suggested that more extended-life testing be performed on the bending-torsion fatigue test bench using the same loading condition and a similar EN19 (T-condition) material. The experimental fatigue limit definition should be increased from $1.5x10^6$ to above $3x10^6$, and it will require a wider variety of centrifugal mass pieces to induce loading on the test bench. These long-life tests will provide data points well past the conventional fatigue limit definition of $1x10^6$. Further experimental fatigue limit strength certainty of the material compared with the criteria fatigue limits will be obtained.
- It is suggested that alternative out-of-phase biaxial bending-torsion fatigue test loading conditions be attempted on the existing bending-torsion fatigue test bench using a similar EN19 (T-condition) material. This testing can, as a first, be done with the centrifugal mass pieces spaced at 90 [°] apart on the bilateral wheels. Note that a different loading condition on this test bench has not yet been tested or confirmed. However, doing this may provide a different phase angle and biaxial stress amplitude ratio for the bending-torsion loading. Consequently, different data set entries (e.g., with other phase angles) of the literature data sets can be used for the same material type. Criteria evaluations with these data sets may determine if the chosen criteria show the influence of different loading conditions. It may also determine if they apply more to a specific loading condition.
- A more in-depth characterisation of the biaxial bending-torsion fatigue test bench is suggested. This is because it was observed from the experimental displacement measurements with the DANTEC that the two loading component vibration modes influence each other. It is suggested that complete FEM modal analyses of the test bench be done to investigate the significant differences observed between the separate theoretical consideration and experimental gain responses of the loading. From this, the quantification of the test bench damping may also be obtained.
- It is recommended that the uniaxial bending fatigue test bench be adapted to using a better and possibly digital load cell to induce the cantilever bending forces. The cantilever force cell should also have less lateral rigidity, allowing for unopposed sideways deflection of machined specimens that are not ideally straight. This improvement will provide better loading measurements and reduce the sizable experimental uncertainty on the uniaxial bending fatigue data.

- It is cautioned that the criteria and data in the literature cannot simply be assumed correct or trustworthy based on the reported (in the literature) and shown (in this study) variations in the fatigue limit strength properties and criteria predictions for a hard ferrous metal. For the loading condition and material tested, the Carpinteri and Spagnoli criterion is recommended based on its comparable prediction of the experimental out-of-phase biaxial fatigue limit. The Liu and Mahadevan criterion (slightly more conservative) is additionally recommended.
- It is recommended that further research be done to simplify the critical plane fatigue criteria with tedious solution methods, unknown model parameters and inadequate evaluation method descriptions. This might allow more criteria to be used in better and more complete comparative studies to determine criteria applicability and limitations for metals. Specific loading condition focussed investigations should also be done with the criteria to determine which provide varying prediction results for different loading conditions.

6.3.1 Areas of Further Research

- It is proposed that the experimental testing in this study be repeated, but with more test specimens in each test type and a similar EN19 (T-condition) material. This testing should be done with more than the recommended 10-15 specimens, especially in the HCF region and around the experimental fatigue limit strength. Doing this will provide additional data and reaffirm the results and fatigue strength trends obtained in this study's experimental test program. Additionally, it will also reaffirm the experimental methodology that was implemented.
- It is proposed to perform more tests on the bending fatigue test bench using the same loading condition but with other hard ferrous metals. These tests include the required uniaxial fatigue limit tests for criteria, and examples include EN30B or EN24 alloy steel and their relevant derivatives. Doing this will provide the necessary data to re-evaluate the same three criteria of this study and determine if their fatigue limit estimates are less or more conservative if the hard metal composition and strength are different. That is, regarding the presumed criteria fatigue limit and the experimentally estimated biaxial out-of-phase fatigue limit (based on each criterion's equivalent stress). It will also allow using other literature data sets, which can then be compared and evaluated with the criteria.
- It is additionally proposed that tests be done using ductile metals, which may include EN8 carbon steel, for example. Therefore, further performing the relevant additional fatigue tests to assess the Papadopoulos, Carpinteri and Spagnoli, and Liu and Mahadevan criteria. That is even if they are reported to apply to hard metals primarily. Further material applicability may

be confirmed from these evaluations of the criteria on ductile metals. It will also show if the criteria have similar or different fatigue limit estimates as with the hard metal in this study.

- It is suggested that Scanning Electron Microscope (SEM) analyses of the test material be performed to investigate if there is a statistical correlation between the rotating principal stresses, metallographic grains and boundaries and fatigue damage on the critical plane.

6.4 Contribution of the research

The research study showed that the multiaxial fatigue data set from the literature might be untrustworthy. It was shown that the fatigue limit strengths (uniaxial and biaxial) of this data set did not compare well with the other uniaxial literature data or the experimental fatigue data. Different fatigue limit evaluations with the criteria were also obtained for this data set than those for the experimental fatigue data. Therefore, it implied that the fatigue criteria are questioned, and they may not all be considered applicable for 90 [°] out-of-phase bending-torsion loading with λ = 0.5 [-] on EN19 (T-condition). The critical plane criteria evaluations showed that different and conservative experimental fatigue limit strength estimates are obtained for this material and loading condition. However, it was shown that the Carpinteri and Spagnoli and the Liu and Mahadevan (criteria might have better prediction capability. Implicated implicitly implied

The experimental fatigue data generated in this study was verified and shown to be experimentally sound, and uncertainties were small (except for bending). The data is therefore considered trustworthy and can contribute to existing data to test and validate criteria under the specific loading and material. The biaxial fatigue data from this study provided insight into what the literature considers the most damaging loading condition. The rotating principal stress phenomenon was also observed in the experimental measurements. For this loading condition, it was shown that the dominant VM stress component (bending) seemingly determines the material's fatigue limit strength. Due to the specific out-of-phase angle, independence was observed between the bending and torsion loading components when 90 [°] out of phase. For EN19 (T-condition) steel, it was shown that the uniaxial bending fatigue limit strength is equivalent to the biaxial bending component's fatigue limit strength. The experimental data of this study can also be compared with the new data sets generated from the suggestions above. The additional data may provide for further assessments of the relevant fatigue criteria.

6.5 Conclusion

The discrepancies reported in the literature for multiaxial fatigue data and criteria were shown to be of valid concern from this study. Apart from the data sets being argued in the literature as old, insufficient and often incomplete, it was also shown that a general lack of data exists and key material strength properties are often not reported. Based on a comparison with the verified experimental data, the literature data set was ultimately questioned for its applicability in fatigue criteria evaluations. It was shown that the fatigue criteria in this study have varying fatigue limit estimation capabilities on both verified experimental data and the literature data. Of the three fatigue criteria evaluated, the Carpinteri and Spagnoli and the Liu and Mahadevan criteria seemed to have better and less conservative experimental fatigue limit estimation capability for the specific loading condition and material considered. However, they overestimated the fatigue limit from the literature data set, and the Papadopoulos criterion was the only one that did not. Based on the literature data sets, the fatigue criteria were ultimately questioned. More and new fatigue data sets are required to investigate further and test the literature criteria.

BIBLIOGRAPHY

[1] M. De Freitas, "Multiaxial fatigue: From materials testing to life prediction," *Theoretical and Applied Fracture Mechanics,* vol. 92, pp. 360-372, 2017.

[2] D. L. McDiarmid, "A new analysis of fatigue under combined bending and twisting," *Aeronautical Journal,* vol. 78, pp. 325 - 329, 1974.

[3] R. G. Budynas and J. K. Nisbett, *Fatigue Failure Resulting from Variable Loading*, 10th ed. (Shigley's Mechanical Engineering Design). New York: McGraw-Hill Education, 2015, p. 1082.

[4] C. Lu, J. Melendez, and J. M. Martínez-Esnaola, "Multiaxial fatigue criterion considering the influence of out-of-phase failure and loading condition," (in English), *Int J Fatigue,* Article vol. 114, pp. 323-330, 2018, doi: 10.1016/j.ijfatigue.2018.06.006.

[5] E. Santecchia *et al.*, "A Review on Fatigue Life Prediction Methods for Metals," *Adv. Mater. Sci. Eng.,* Review Article vol. Vol 2016, pp. 1-26, 2016, doi: 9573524.

[6] T. Lassen and A. Spagnoli, "Fatigue Crack Paths In Shafts Subjected to Bending and Torsion," *Materials Science,* 2013.

[7] D. L. McDiarmid, "FATIGUE UNDER OUT-OF-PHASE BENDING AND TORSION," (in English), *Fatigue Fract Eng Mater Struct,* Article vol. 9, no. 6, pp. 457-475, 1987, doi: 10.1111/j.1460-2695.1987.tb00471.x.

[8] I. V. Papadopoulos, "A new criterion of fatigue strength for out-of-phase bending and torsion of hard metals," (in English), *Int J Fatigue,* Article vol. 16, no. 6, pp. 377-384, 1994, doi: 10.1016/0142-1123(94)90449-9.

[9] M. V. Pereira, F. A. Darwish, M. C. Teixeira, and R. A. Gonçalves, "Multiaxial High Cycle Fatigue Criteria Based on Fracture Plane Identification: Applicability to Metallic Materials," (in English), *J Mater Eng Perform,* Article vol. 28, no. 8, pp. 4740-4750, August 2019, doi: 10.1007/s11665-019-04242-5.

[10] I. V. Papadopoulos, P. Davoli, C. Gorla, M. Filippini, and A. Bernasconi, "A comparative study of multiaxial high-cycle fatigue criteria for metals," (in English), *Int J Fatigue,* Article vol. 19, no. 3, pp. 219-235, 1997, doi: 10.1016/S0142-1123(96)00064-3.

[11] F. Ellyin, "A General Fatigue Theory and Its Application to Out-of-Phase Cyclic Loading," *Journal of Engineering Materials and Technology,* Research Article vol. 115, pp. 411 - 416, 1993.

[12] A. Fatemi and D. F. Socie, "A CRITICAL PLANE APPROACH TO MULTIAXIAL FATIGUE DAMAGE INCLUDING OUT-OF-PHASE LOADING," (in English), *Fatigue Fract Eng Mater Struct,* Article vol. 11, no. 3, pp. 149-165, 1988, doi: 10.1111/j.1460-2695.1988.tb01169.x.

[13] A. Fatemi and P. Kurath, "Multiaxial fatigue life predictions under the influence of mean-stresses," *Journal of Engineering Materials and Technology,* vol. 110, pp. 380-388, 1988.

[14] C. Froustey and S. Lasserre, "Multiaxial fatigue endurance of 30NCD16 steel," *Int J Fatigue,* vol. 11, no. 2, pp. 169-175, 1989.

[15] I. V. Papadopoulos, "EXPLORING THE HIGH-CYCLE FATIGUE BEHAVIOUR OF METALS FROM THE MESOSCOPIC SCALE," *J. Mech. Behavior Mater.,* vol. 6, p. 93, 1996.

[16] J. Li, Y. Qiu, H. Wang, and Z. Wang, "Evalutation of the Methods for Estimating the Fully Reversed Unnotched Fatigue Limits of Steels," *Adv. Mater. Sci. Eng.,* Research Article pp. 1-11, 2019.

[17] *TERCO Material Testing Laboratory Brochure*. (2014). Sweden. Accessed: 5 February 2022. [Online]. Available: https://www.tercosweden.com/products/material-testing/

[18] C. M. Sonsino, "Multiaxial fatigue of welded joints under in-phase and out-of-phase local strains and stresses," *Int J Fatigue,* vol. 17, 1, pp. 55-70, 1995.

[19] P. Luo, W. Yao, L. Susmel, Y. Wang, and X. Ma, "A survey on multiaxial fatigue damage parameters under non-proportional loadings," *Fatigue Fract Eng Mater Struct,* Review vol. 40, pp. 1323-1342, 2017, doi: 10.1111/ffe.12659.

[20] I. V. Papadopoulos, "Long life fatigue under multiaxial loading," (in English), *Int J Fatigue,* Article vol. 23, no. 10, pp. 839-849, 2001, doi: 10.1016/S0142-1123(01)00059-7.

[21] J. Papuga, M. Nesládek, J. Kuželka, and J. Jurenka, "Differences in the response to in-phase and out-of-phase multiaxial high-cycle fatigue loading," (in English), *Frat. Integrita Strutr.,* Article vol. 13, no. 50, pp. 163-183, 2019, doi: 10.3221/IGF-ESIS.50.15.

[22] D. F. Socie, "Multiaxial Fatigue Damage Models," *Journal of Engineering Materials and Technology,* vol. 109, pp. 293-298, 1987.

[23] D. F. Socie, "Critical plane approaches for multiaxial fatigue damage assessment," *Advances in multiaxial fatigue,* pp. 7-36, 1993.

[24] I. V. Papadopoulos and V. P. Panoskaltsis, "Invariant formulation of a gradient dependent multiaxial high-cycle fatigue criterion," (in English), *Eng Fract Mech,* Article vol. 55, no. 4, pp. 513-528, 1996, doi: 10.1016/S0013-7944(96)00047-1.

[25] S. K. Gupta, T. M. Fesich, X. Schuler, V. Bhasin, K. K. Vaze, and E. Roos, "A CRITICAL PLANE BASED MODEL FOR FATIGUE ASSESSMENT UNDER FIXED AND ROTATING PRINCIPAL DIRECTION LOADING," New Delhi, India, 6-11 November 2011, 2011, 624.

[26] Y. Lee, M. E. Barkey, and H. Kang, "Chapter 5: Stress-Based Multiaxial Fatigue Analysis," in *Metal Fatigue Analysis Handbook*, (Practical Problem-Solving Techniques for Computer-Aided Engineering. USA: Elsevier Inc., 2012, ch. 5, pp. 161-211.

[27] S. Chattopadhyay, "INVESTIGATION OF PROPORTIONAL AND NON-PROPORTIONAL LOADINGS USING MOHR'S CIRCLE," presented at the ASEE Annual Conference, 2012, AC 2012 - 3221.

[28] A. F. Brown, "Shaft Fatigue Testing for Out-of-phase Loading Scenarios: Project 11 (AvW-1)," North-West University of Potchefstroom, 2020.

[29] D. Skibicki and J. Sempruch, "Use of a load non-proportionality measure in fatigue under out-of-phase combined bending and torsion," (in English), *Fatigue Fract Eng Mater Struct,* Article vol. 27, no. 5, pp. 369-377, 2004, doi: 10.1111/j.1460-2695.2004.00757.x.

[30] M. Firat, "A numerical analysis of combined bending-torsion fatigue of SAE notched shaft," *Finite Elements in Analysis and Design,* vol. 54, pp. 16-27, 2012.

[31] F. Morel, "A critical plane fatigue model applied to out-of-phase bending and torsion load conditions," (in English), *Fatigue Fract Eng Mater Struct,* Article vol. 24, no. 3, pp. 153-164, 2001, doi: 10.1046/j.1460-2695.2001.00390.x.

[32] X. Pan *et al.*, "Thermal-mechanical fatigue behavior and lifetime prediction of P92 steel with different phase angles," *Int J Fatigue,* vol. 109, pp. 126-136, 2018.

[33] S. Lasserre and C. Froustey, "Multiaxial fatigue of steel--testing out of phase and in blocks: validity and applicability of some criteria," *Int J Fatigue,* Research Article vol. 14, no. 2, pp. 113 - 120, 1992.

[34] I. V. Papadopoulos, "A HIGH-CYCLE FATIGUE CRITERION APPLIED IN BIAXIAL AND TRIAXIAL OUT-OF-PHASE STRESS CONDITIONS," (in English), *Fatigue Fract Eng Mater Struct,* Article vol. 18, no. 1, pp. 79-91, 1995, doi: 10.1111/j.1460-2695.1995.tb00143.x.

[35] D. L. McDiarmid, "Fatigue behaviour under out-of-phase bending and torsion," *Aeronautical Journal,* vol. 85, pp. 118-122, 1981.

[36] K. Dang Van and I. V. Papadopoulos, "Multiaxial fatigue failure criterion: a new approach," in *Third International Conference on Fatigue and Fatigue Thresholds - Fatigue '87*, 1987, pp. 997-1008.

[37] P. W. Beaver, "Multiaxial Fatigue and Fracture - A Literature Review," Defence Science and Technology Organisation Aeronautical Research Laboratories, Melbourne, 410, July 1984.

[38] A. Carpinteri and A. Spagnoli, "Multiaxial high-cycle fatigue criterion for hard metals," *Int J Fatigue,* vol. 23, pp. 135-145, 2001.

[39] P. Davoli, A. Bernasconi, M. Filippini, S. Foletti, and I. V. Papadopoulos, "Independence of the torsional fatigue limit upon a mean shear stress," (in English), *Int J Fatigue,* Article vol. 25, no. 6, pp. 471-480, 2003, doi: 10.1016/S0142-1123(02)00174-3.

[40] Y. Y. Wang and W. X. Yao, "Evaluation and comparison of several multiaxial fatigue criteria," (in English), *Int J Fatigue,* Article vol. 26, no. 1, pp. 17-25, 2004, doi: 10.1016/S0142-1123(03)00110-5.

[41] G. Stanfield, "Discussion on the strength of metals under combined alternating stresses," *Institution of Mechanical Engineers (Great Britain),* vol. 131, p. 93, 1935.

[42] T. Nishihara and M. Kawamoto, "The strength of metals under combined bending and twisting with phase difference," *Memoirs College of Engineering,* vol. XI, pp. 85 - 112, 1945.

[43] H. J. Gough, "Some experiments on the resistance of metals to fatigue under combined stresses," *Aeronautical Research Council Reports and Memoranda,* vol. 2522, 1951.

[44] W. N. Findley, "COMBINED-STRESS FATIGUE STRENGTH OF 76S-T61 ALUMINUM ALLOY WITH SUPERIMPOSED MEAN STRESSES AND CORRECTIONS FOR YIELDING," *NACA TN2924,* 1953.

[45] H. Zenner, R. Heidenreich, and I. Richter, "Fatigue Strength under Nonsynchronous Multiaxial Loading," *Zeitschrift fuer Werkstofftechnik / Materials Technology and Testing,* vol. 16, no. 3, pp. 101-112, 1985.

[46] F. B. Stulen and H. N. Cummings, "A failure criterion for multi-axial fatigue stresses," *Proceedings - American Society for Testing Materials,* vol. 54, pp. 822-835, 1954.

[47] J. Marin, "Interpretation of Fatigue Strengths for Combined Stresses," *Proceedings of the International Conference on Fatigue of Metals,* 10-14 September 1956, pp. 184-194, 1956.

[48] W. N. Findley, "A theory for the effect of mean stress on fatigue of Metals Under Combined Torsion and Axial Load or Bending," *Journal of Engineering for Industry,* vol. 81, 4, pp. 301-305, 1959.

[49] R. Smith, P. Watson, and T. Topper, "A stress strain function for the fatigue of metals," *J Mater Eng Perform,* vol. 5, 4, pp. 767-778, 1970.

[50] D. L. McDiarmid, "A criterion of fatigue failure under out-of-phase multi-axial stresses.," in *CANCAM 77 : proceedings, sixth Canadian Congress of Applied Mechanics, May 30 to June 3, 1977, University of British Columbia*, 1977, pp. 245-246.

[51] I. V. Papadopoulos, "Critical plane approaches in high-cycle fatigue: On the definition of the amplitude and mean value of the shear stress acting on the critical plane," (in English), *Fatigue Fract Eng Mater Struct,* Article vol. 21, no. 3, pp. 269-285, 1998, doi: 10.1046/j.1460-2695.1998.00459.x.

[52] I. V. Papadopoulos and K. Dang Van, "CHAPTER 3: Multiaxial fatigue limit criterion of metals: A mesoscopic scale approach, High cycle metal fatigue in the context of mechanical design," in *HIGH-CYCLE METAL FATIGUE: FROM THEORY TO APPLICATIONS*, vol. 392 of CISM International Centre for Mechanical Sciences, I. V. D. V. Papadopoulos, K. Ed., illustrated ed.: Springer, 1999, ch. 3.

[53] I. V. Papadopoulos, "High-cycle fatigue criterion applied in biaxial and triaxial out-of-phase stress conditions," *Fatigue Fract Eng Mater Struct,* vol. 18, 1, pp. 79-91, 2007, doi: 10.1111/j.1460-2695.1995.tb00143.x.

[54] Z. Yu, S. Zhu, Q. Liu, and Y. Liu, "Multiaxial Fatigue Damage Parameter and Life Prediction without Any Additional Material Constants," *Materials - MDPI,* vol. 10, 923, pp. 1-15, 2017, doi: 10.3390/ma10080923.

[55] D. Rozumek and Z. Marciniak, "The investigation of crack growth in specimens with rectangular cross-sections under out-of-phase bending and torsional loading," (in English), *Int J Fatigue,* Article vol. 39, pp. 81-87, 2012, doi: 10.1016/j.ijfatigue.2011.02.013.

[56] G. Morettini, C. Braccesi, F. Cianetti, S. M. J. Razavi, K. Solberg, and L. Capponi, "Collection of experimental data for multiaxial fatigue criteria verification," *Fatigue Fract Eng Mater Struct,* vol. 43, pp. 162-176, 2019.

[57] A. Bernasconi, S. Foletti, and I. V. Papadopoulos, "A study on combined torsion and axial load fatigue limit tests with stresses of different frequencies," (in English), *Int J Fatigue,* Article vol. 30, no. 8, pp. 1430-1440, 2008, doi: 10.1016/j.ijfatigue.2007.10.003.

[58] C. Sun and Q. Song, "A Method for Predicting the Effects of Specimen Geometry and Loading Condition on Fatigue Strength," *Metals,* vol. 2018, no. 811, 8, pp. 1-13, 2018.

[59] D. Ion, K. Lorand, D. Mircea, and M. Karoly, "The equivalent stress concept in multiaxial fatigue," *Journal of Engineering Studies and Research,* vol. 17, 2, pp. 53-62, 2011.

[60] G. Sines, "FAILURE OF MATERIALS UNDER COMBINED REPEATED STRESSES WITH SUPERIMPOSED STATIC STRESSES," *NACA TN3495,* 1955.

[61] W. Macek and N. Mucha, "Evaluation of fatigue life calculation algorithm of the multiaxial stress-based concept applied to S355 steel under bending and torsion," *Mechanics and Mechanical Engineering,* vol. 21, no. 2017, 4, pp. 935-951, 2017.

[62] H. E. Boyer, Ed. *Atlas of Fatigue Curves*. Materials Park, Ohio: ASM International, 1986, p. 534.

[63] F. Morel, "A critical plane approach for life prediction of high cycle fatigue under multiaxial variable amplitude loading," *Int J Fatigue,* vol. 22, 2000, pp. 101-119, 2000.

[64] F. Ogawa, Y. Shimizu, S. Bressan, T. Morishita, and T. Itoh, "Bending and torsion fatigue-testing machine developed for multiaxial non-proportional loading," (in English), *Metals,* Article vol. 9, no. 10, 2019, Art no. 1115, doi: 10.3390/met9101115.

[65] S. B. Lee, "Out-of-phase bending and torsion fatigue of steel," *In Brown MW, Miller KJ, editors. Biaxial and Multiaxial fatigue, EGF3. London: Mechanical Engineering Publications,* vol. 6, pp. 12-34, 1989.

[66] L. Susmel, "On the overall accuracy of the Modified Wöhler Curve Method in estimating high-cycle multiaxial fatigue strength," *Frat. Integrita Strutr.,* vol. 16, pp. 5-17, April 2011, doi: 10.3221/IGF-ESIS.16.01.

[67] A. Karolczuk, M. Kurek, and T. Łagoda, "Fatigue Life of Aluminum Alloy 6082 T6 Under Constant and Variable Amplitude Bending with Torsion," *Journal of Theoretical and Applied Mechanics,* vol. 53, 2, pp. 421-430, 2015, doi: DOI: 10.15632/jtam-pl.53.2.421.

[68] M. Filippini, S. Foletti, I. V. Papadopoulos, and C. M. Sonsino. *A multiaxial fratigue life criterion for non-symmetrical and non-proportional elasto-plastic deformation, European Structural Integrity Society*, vol. 31, pp. 383-400, 2003.

[69] E. El Magd and S. Mielke, "Dauerfestigkeit bei überlagerter zweiachsiger statischer Beanspruchung," *Konstruktion,* vol. 29, pp. 253-257, 1977.

[70] S. Mielke, "Festigkeitsverhalten metallischer Werkstoffe unter zweiachsiger schwingender Beanspruchung mit verschiedenen Spannungszeitverläufen," PhD, RWTH Aachen, 1980.

[71] H. Zenner and J. Liu, "On the fatigue limit of ductile materials under complex multiaxial loading," *Int J Fatigue,* vol. 22, no. 2, pp. 137-145, 2000.

[72] J. Papuga, "A survey on evaluating the fatigue limit under multiaxial loading," *Int J Fatigue,* vol. 33, 2, pp. 153-165, 2011.

[73] R. Heidenreich, I. Richter, and H. Zenner, "Schubspannung sintensitätshpothese—Weitere experimentalle und theorestische," *Konstruktion,* vol. 36, pp. 99-104, 1984.

[74] A. Troost, O. Akin, and F. Klubberg, "Dauerfestigkeitsverhalten metallischer Werkstoffe bei zweiachsiger Beanspruchung durch drei phasenverschoben schwingende Lastspannungen," *Konstruktion,* vol. 39, no. 479-488, 1987.

[75] T. Palin-Luc and S. Lasserre, "An energy-based criterion for high cycle multiaxial fatigue," *Eur J Mech A/Solids,* vol. 17, no. 2, pp. 237-251, 1998.

[76] J. Papuga, S. Parma, and M. Ružicka, "Systematic validation of experi- mental data usable for verifying the multiaxial fatigue prediction methods," *Frat. Integrita Strutr.,* vol. 10, no. 38, pp. 106-113, 2016.

[77] I. V. Papadopoulos and K. Dang Van, "NUCLEATION OF FISSURES IN POLYCYCLIC FATIGUE UNDER MULTIAXIAL LOADING," *Arch. Mech.,* vol. 40, p. 759, 1988.

[78] H. Achtelik, M. Kurek, M. Kurek, K. Kluger, R. Pawliczek, and T. Lagoda, "Non-Standard Fatigue Stands for Material Testing Under Bending and Torsion Loadings," in *AIP Conference Proceedings*, 2018, vol. 2029: AIP, 29 October 2018.

[79] C. Vieira, R. Barbieri, and G. O. Verran, "Prototype of a Torsion Fatigue Machine Based on Unbalance Rotation," *9th Congresso Brasileiro de Engenharia de Frabricação,* 2017, doi: DOI: 10.26678/ABCM.COBEF2017.COF2017-0526.

[80] P. A. Hilton. "Rotating Fatigue Machine (Analogue Version) HSM19." P.A. Hilton Limited. https://www.p-a-hilton.co.uk/products/strength-materials-hsm/rotating-fatigue-machine-analogue-version (accessed 17 August, 2022).

[81] M. Shariyat, "Three energy-based multiaxial HCF criteria for fatigue life determination in components under random non-proportional stress fields," *Fatigue Fract Eng Mater Struct,* vol. 32, no. 10, pp. 785-808, 2009.

[82] A. Lottering, "Torsional Fatigue Test Bench Design," North-West University: Potchefstroom Campus, 2021.

[83] "DANTEC DYNAMICS." https://www.dantecdynamics.com (accessed 18 September, 2022).

[84] P. Strzelecki, T. Tomaszewski, and J. Sempruch, "A method for determining a complete S-N curve using maximum likelihood," presented at the 22nd International Conference, Svratka, Czech Republic, 9-12 May 2016, 2016. [Online]. Available: https://www.engmech.cz/improc/2016/128bo_o_fra.pdf.

[85] *Standard Practice for Strain-Controlled Fatigue Testing*, ASTM standard E 606 - 92, 1998.

[86] *Standard Test Methods for Tension Testing of Metallic Materials*, ASTM standard E8/E8M - 13a, 2013.

[87] P. E. Carrion and N. Shamsaei, "Strain-based fatigue data for Ti-6Al-4V ELI under fully-reversed and mean strain loads," *Data in Brief,* Data Article vol. 7, pp. 12-15, 2016.

[88] A. A. Azeez, "Fatigue Failure and Testing Method," Bachelor's Bachelor's Thesis, Mechanical Engineering and Production Technology, Mechatronics, University of Applied Sciences, 2013.

[89] E. Jansons, J. Lugevics, and K. A. Gross, "Surface Roughness Measure that Best Correlates to Ease of Sliding," *Engineering for Rural Development,* vol. 25, pp. 687-695, 2016.

[90] N. Alang, N. Razak, and A. Miskam, "Effect of surface Roughness on Fatigue Life of Notched Carbon Steel," *International Journal of Engineering & Technology,* vol. 11, 1, pp. 160-163, 2011.

[91] S. S. Rao, "Free Vibration of SDOF Systems & Harmonically Excited Vibration," in *Mechanical Vibrations*, N. Dias, M. Bayman, and S. Patra Eds., 6th ed. Harlow, United Kingdom: Pearson Education Limited, 2018, ch. 2 & 3, pp. 153-294 & 297-402.

[92] J. J. Rozentals, "The design of structures supporting vibrating screens," *Civil Engineering = Siviele Ingenieurswese,* vol. 1975, no. 7, pp. 163-168, 1975, doi: doi:10.10520/AJA10212019_19842.

[93] Q. Wang, T. D. Feese, and B. C. Pettinato, "Torsional Natural Frequencies: Measurement vs Prediction," in *Forty-Second Turbomachinery Symposium*, Houstonn, Texas, September 30 - October 3 2013: Texas A&M University, pp. 1-29.

APPENDICES

A. EXPERIMENTAL TEST EQUIPMENT

A1. MTS Landmark Tensile Test Machine

The MTS Landmark servo-hydraulic tensile test system (Figure A-1 below) is a test machine commonly used for testing specimens made of various materials (steel, composites, polymers) under axial loading (tension, compression, axial fatigue) to obtain various monotonic material strength properties (yield strength, ultimate tensile strength, Elasticity Modulus, Poisson ratio, fatigue limit, strain behaviour). Therefore, the machine inherently only induces a uniaxial loading condition (which may also be cyclic). Adaptations or replacement of the specimen wedge grip heads can provide alternative biaxial loading conditions; however, these are less common.

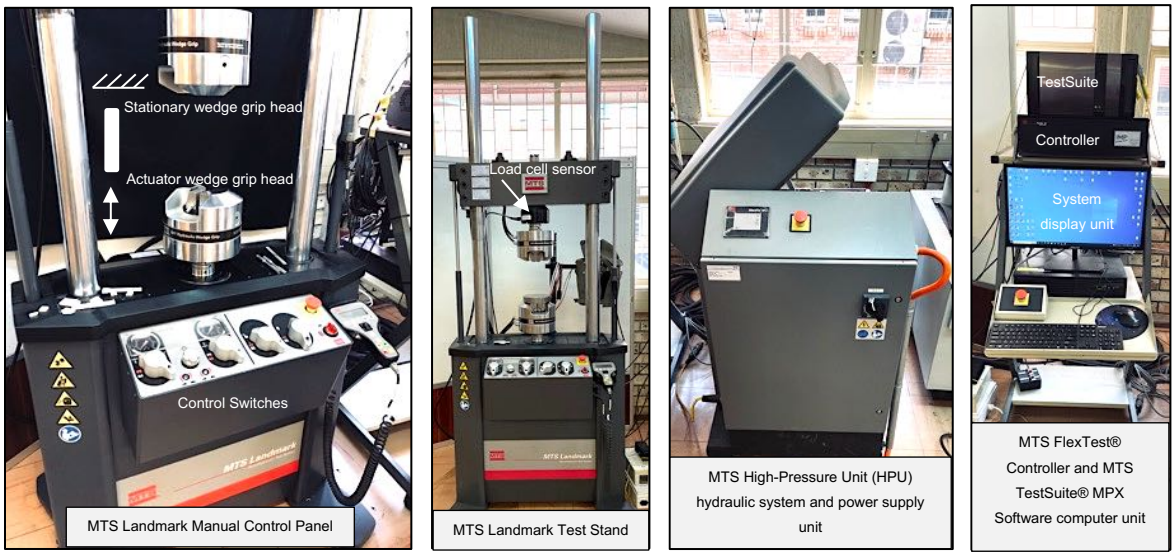


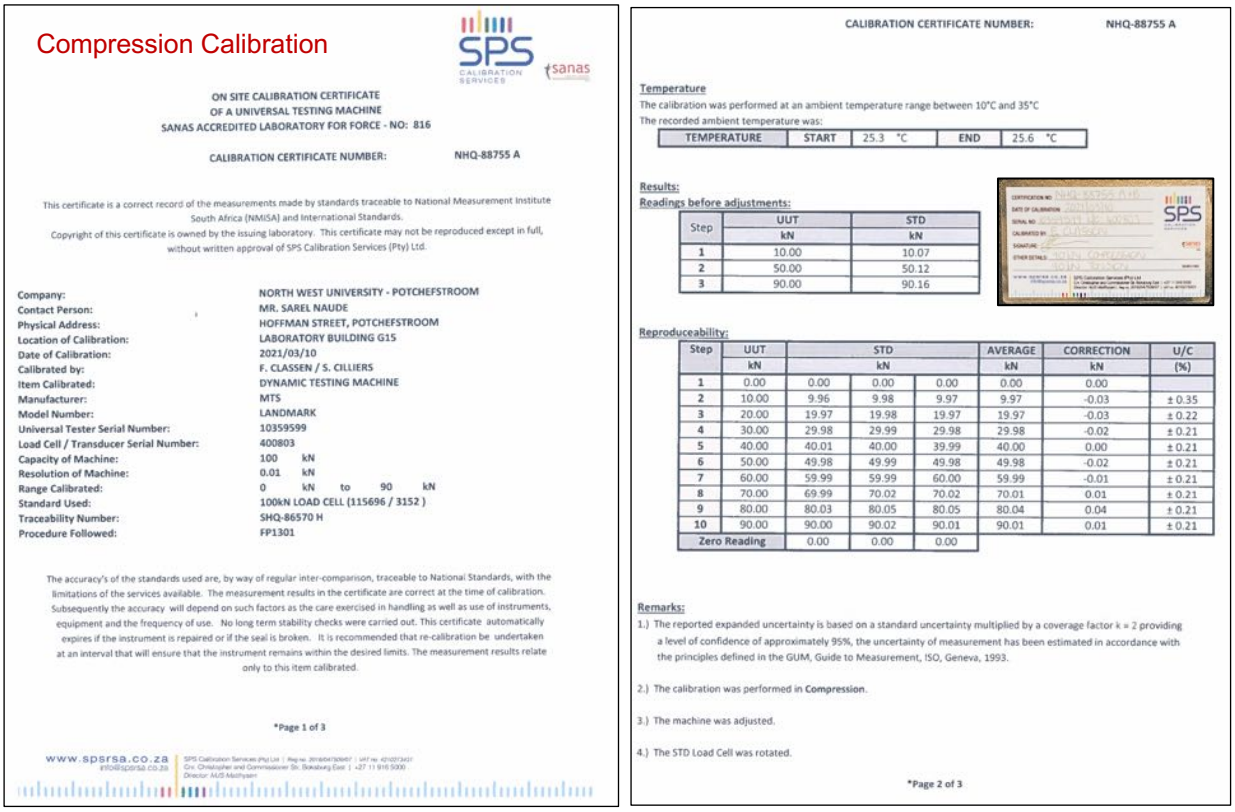
Figure A-1: MTS Landmark – test system and components

The tensile test machine is powered by an MTS High-Pressure Unit (HPU) hydraulic system, which drives the hydraulically actuated wedge grip heads. An external hydraulic fluid cooling system also forms part of this HPU system. The wedge grip heads are positioned with the control switches (or software) and controlled by the MTS FlexTest® 4.0 digital controller along with the MTS TestSuite® software (TW Elite program for tension and compression tests and Multipurpose Elite program for fatigue tests) in synchronicity with the HPU during a test. A 100 [kN] load cell sensor (black cylinder) connected to the top (stationary during a test) hydraulic wedge grip head measures the axial loading exerted on a tensile or fatigue test specimen. Displacement sensors measure and monitor the 'load train displacement' (which includes the bottom hydraulic actuator,

machine deflection and grip slippage) displacement and position relative to a zero position during a test. All measurements or readings are routed to the computer system (controller and software), where it is recorded and processed for each test.

The typical test procedure (tensile, compression or fatigue) for this machine consists of the following:

- Switching on the HPU, the hydraulic cooling system and the computer system.
- Activation of the hydraulic system through pressurisation and positioning the actuator head on the control program in preparation for loading a specimen.
- Selecting the appropriate test program (TW Elite or Multipurpose Elite) for the test to be performed and setting all required test parameters (loading type, loading cycle, cycle count).
- Loading and properly clamping the test specimen in the wedge grip heads.
- Zeroing the clamping offset load by zeroing the actuator position in the control program.
- Running the test according to a pre-defined procedure in each test program and appropriate tensile test rate of 3 [mm/min] (0.05 [mm/s]) until specimen failure occurs and is detected by the machine through the loadcell reading and the system interlocks (shuts down for safety).
- Processing (where required) and exporting test data for external evaluation.



Compression Calibration

SPS CALIBRATION SERVICES

sanas

ON SITE CALIBRATION CERTIFICATE
OF A UNIVERSAL TESTING MACHINE
SANAS ACCREDITED LABORATORY FOR FORCE - NO: 816

CALIBRATION CERTIFICATE NUMBER: NHQ-88755 A

This certificate is a correct record of the measurements made by standards traceable to National Measurement Institute South Africa (NMISA) and International Standards.
Copyright of this certificate is owned by the issuing laboratory. This certificate may not be reproduced except in full, without written approval of SPS Calibration Services (Pty) Ltd.

Company:	NORTH WEST UNIVERSITY - POTCHEFSTROOM
Contact Person:	MR. SAREL NAUDE
Physical Address:	HOFFMAN STREET, POTCHEFSTROOM
Location of Calibration:	LABORATORY BUILDING G15
Date of Calibration:	2021/03/10
Calibrated by:	F. CLASSEN / S. CILLIERS
Item Calibrated:	DYNAMIC TESTING MACHINE
Manufacturer:	MTS
Model Number:	LANDMARK
Universal Tester Serial Number:	10359599
Load Cell / Transducer Serial Number:	400803
Capacity of Machine:	100 kN
Resolution of Machine:	0.01 kN
Range Calibrated:	0 kN to 90 kN
Standard Used:	100kN LOAD CELL (115696 / 3152)
Traceability Number:	SHQ-86570 H
Procedure Followed:	FP1301

The accuracy's of the standards used are, by way of regular inter-comparison, traceable to National Standards, with the limitations of the services available. The measurement results in the certificate are correct at the time of calibration. Subsequently the accuracy will depend on such factors as the care exercised in handling as well as use of instruments, equipment and the frequency of use. No long term stability checks were carried out. This certificate automatically expires if the instrument is repaired or if the seal is broken. It is recommended that re-calibration be undertaken at an interval that will ensure that the instrument remains within the desired limits. The measurement results relate only to this item calibrated.

*Page 1 of 3

www.spsrsa.co.za

CALIBRATION CERTIFICATE NUMBER: NHQ-88755 A

Temperature
The calibration was performed at an ambient temperature range between 10°C and 35°C
The recorded ambient temperature was:

TEMPERATURE	START	25.3 °C	END	25.6 °C

Results:
Readings before adjustments:

Step	UUT kN	STD kN
1	10.00	10.07
2	50.00	50.12
3	90.00	90.16

Reproduceability:

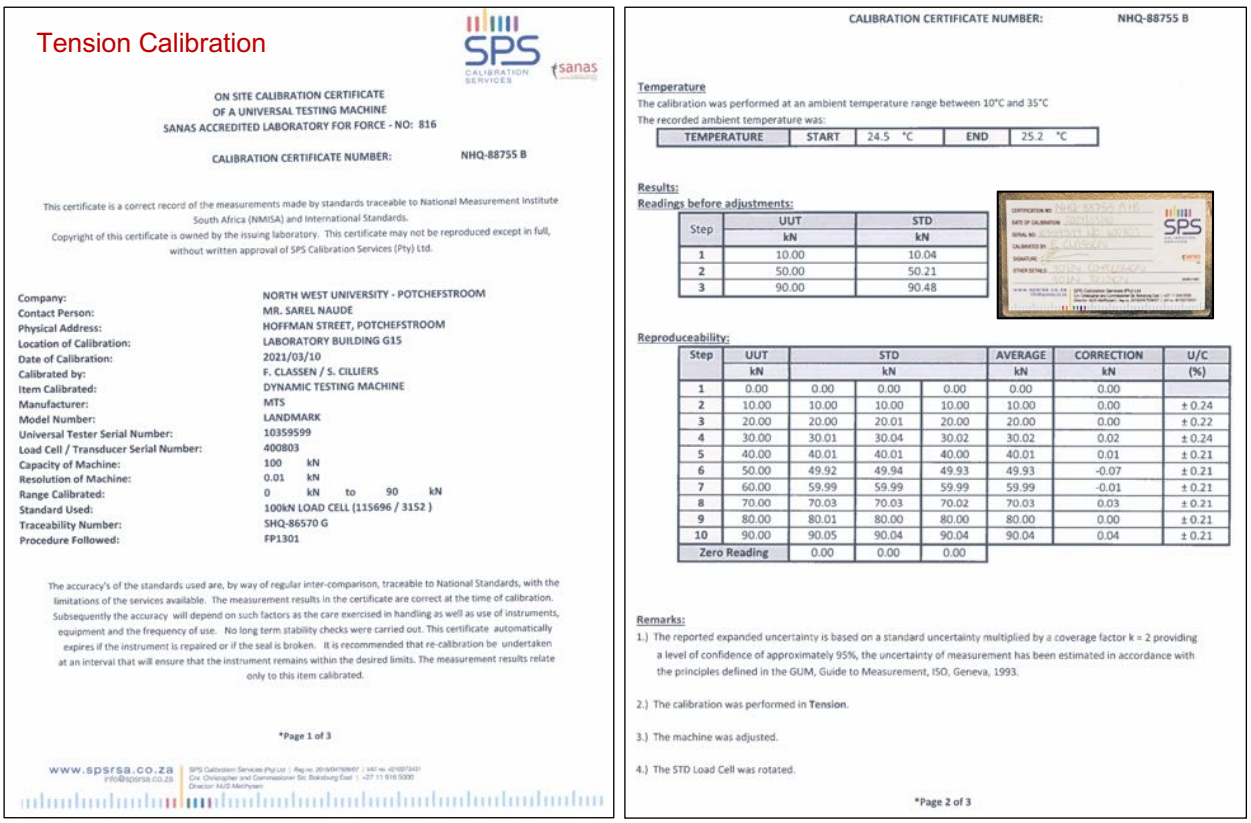
Step	UUT kN	STD kN			AVERAGE kN	CORRECTION kN	U/C (%)
1	0.00	0.00	0.00	0.00	0.00	0.00	
2	10.00	9.96	9.98	9.97	9.97	-0.03	± 0.35
3	20.00	19.97	19.98	19.97	19.97	-0.03	± 0.22
4	30.00	29.98	29.99	29.98	29.98	-0.02	± 0.21
5	40.00	40.01	40.00	39.99	40.00	0.00	± 0.21
6	50.00	49.98	49.99	49.98	49.98	-0.02	± 0.21
7	60.00	59.99	59.99	60.00	59.99	-0.01	± 0.21
8	70.00	69.99	70.02	70.02	70.01	0.01	± 0.21
9	80.00	80.03	80.05	80.05	80.04	0.04	± 0.21
10	90.00	90.00	90.02	90.01	90.01	0.01	± 0.21
Zero Reading		0.00	0.00	0.00			

Remarks:
1.) The reported expanded uncertainty is based on a standard uncertainty multiplied by a coverage factor k = 2 providing a level of confidence of approximately 95%, the uncertainty of measurement has been estimated in accordance with the principles defined in the GUM, Guide to Measurement, ISO, Geneva, 1993.
2.) The calibration was performed in Compression.
3.) The machine was adjusted.
4.) The STD Load Cell was rotated.

*Page 2 of 3

Figure A-2: MTS Landmark – compression calibration certificate

The MTS Landmark machine is typically calibrated annually by an external third-party company, as illustrated with the certificates in Figure A-2 above and Figure A-3 below. These typically include individual calibrations of all the modes of operation or channels of measurement of the machine (e.g., compression and tension – load cell, displacement – actuator head movement, extensometer). For the tests performed on this machine in this study (tensile tests and axial fatigue tests), only the loadcell calibrations were considered. This is due to the applied load being the only relevant test parameter primarily considered for processing test results. Because of the mechanical movement or play in the whole load train of the machine during testing, the displacement readings (and calibration thereof) were not considered viable test parameters for results processing. The last calibrations on this machine were performed on 10 March 2021.



Tension Calibration

ON SITE CALIBRATION CERTIFICATE
OF A UNIVERSAL TESTING MACHINE
SANAS ACCREDITED LABORATORY FOR FORCE - NO: 816

CALIBRATION CERTIFICATE NUMBER: NHQ-88755 B

This certificate is a correct record of the measurements made by standards traceable to National Measurement Institute South Africa (NMISA) and International Standards.
Copyright of this certificate is owned by the issuing laboratory. This certificate may not be reproduced except in full, without written approval of SPS Calibration Services (Pty) Ltd.

Company:	NORTH WEST UNIVERSITY - POTCHEFSTROOM
Contact Person:	MR. SAREL NAUDE
Physical Address:	HOFFMAN STREET, POTCHEFSTROOM
Location of Calibration:	LABORATORY BUILDING G15
Date of Calibration:	2021/03/10
Calibrated by:	F. CLASSEN / S. CILLIERS
Item Calibrated:	DYNAMIC TESTING MACHINE
Manufacturer:	MTS
Model Number:	LANDMARK
Universal Tester Serial Number:	10359599
Load Cell / Transducer Serial Number:	400803
Capacity of Machine:	100 kN
Resolution of Machine:	0.01 kN
Range Calibrated:	0 kN to 90 kN
Standard Used:	100kN LOAD CELL (115696 / 3152)
Traceability Number:	SHQ-86570 G
Procedure Followed:	FP1301

The accuracy's of the standards used are, by way of regular inter-comparison, traceable to National Standards, with the limitations of the services available. The measurement results in the certificate are correct at the time of calibration. Subsequently the accuracy will depend on such factors as the care exercised in handling as well as use of instruments, equipment and the frequency of use. No long term stability checks were carried out. This certificate automatically expires if the instrument is repaired or if the seal is broken. It is recommended that re-calibration be undertaken at an interval that will ensure that the instrument remains within the desired limits. The measurement results relate only to this item calibrated.

*Page 1 of 3

www.spsrsa.co.za

CALIBRATION CERTIFICATE NUMBER: NHQ-88755 B

Temperature
The calibration was performed at an ambient temperature range between 10°C and 35°C
The recorded ambient temperature was:

TEMPERATURE	START	24.5 °C	END	25.2 °C

Results:
Readings before adjustments:

Step	UUT kN	STD kN
1	10.00	10.04
2	50.00	50.21
3	90.00	90.48

Reproduceability:

Step	UUT kN	STD kN			AVERAGE kN	CORRECTION kN	U/C (%)
1	0.00	0.00	0.00	0.00	0.00	0.00	
2	10.00	10.00	10.00	10.00	10.00	0.00	± 0.24
3	20.00	20.00	20.01	20.00	20.00	0.00	± 0.22
4	30.00	30.01	30.04	30.02	30.02	0.02	± 0.24
5	40.00	40.01	40.01	40.00	40.01	0.01	± 0.21
6	50.00	49.92	49.94	49.93	49.93	-0.07	± 0.21
7	60.00	59.99	59.99	59.99	59.99	-0.01	± 0.21
8	70.00	70.03	70.03	70.02	70.03	0.03	± 0.21
9	80.00	80.01	80.00	80.00	80.00	0.00	± 0.21
10	90.00	90.05	90.04	90.04	90.04	0.04	± 0.21
Zero Reading	0.00	0.00	0.00				

Remarks:
1.) The reported expanded uncertainty is based on a standard uncertainty multiplied by a coverage factor k = 2 providing a level of confidence of approximately 95%, the uncertainty of measurement has been estimated in accordance with the principles defined in the GUM, Guide to Measurement, ISO, Geneva, 1993.
2.) The calibration was performed in Tension.
3.) The machine was adjusted.
4.) The STD Load Cell was rotated.

*Page 2 of 3

Figure A-3: MTS Landmark – tension calibration certificate

The experimental test procedure for this machine's tensile and axial fatigue tests are provided in Appendix G1 and G2.

A2. TERCO MT 205G Rotating Cantilever Bending Fatigue Test Bench

The TERCO MT 205G rotating cantilever bending fatigue test bench (Figure A-4 below) is the most common bending fatigue test bench used. That is, testing metal specimens under bending fatigue loading to obtain the fully reversed uniaxial bending fatigue limits. The machine, therefore, inherently only induces a fully reversed uniaxial cyclic loading condition.

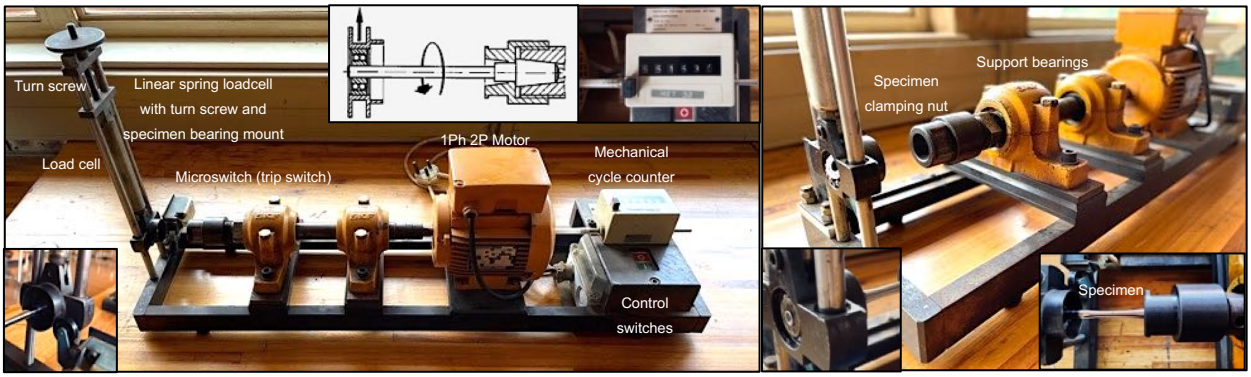


Figure A-4: TERCO MT 205G – bending fatigue test bench and components

The bending fatigue test bench is powered by a single-phase 2-pole electrical motor with a maximum speed of 50 [Hz]. This motor is connected with a plastic tube to a mechanical cycle counter on the back, which records the loading cycles of each test (1:1 ratio). On the other side, the motor drives a rigidly supported shaft through two large pillow block bearings. At the tip of the shaft is a specimen clamping nut which fastens a taper-ended cantilever specimen into the tapered female shaft end. The tip of the cantilever specimen is inserted (before fastening with the nut) through an 8 [mm] ID self-aligning ball bearing housed in the bottom mount (24 [mm] inner race bushing, see Figure G-1) of the linear spring load cell. The load cell is in the 'zero' position vertically, with the microswitch lever pressing against the load cell mount. This load cell (300 [N] maximum) is adjusted with a turn screw at the top to exert a linear upward force on the tip of the specimen, which induces the cantilever moment along the specimen length with the maximum at the clamping nut side. The microswitch is enabled when loading is applied. The counter is zeroed, and the motor is turned on to run the test. The test runs until specimen failure, where the load cell pulls up and away from the microswitch, which cuts power to the motor and stops the test and the cycle count accumulation. Test results are then recorded, and a new test is started. The formal experimental test procedure for the bending fatigue tests done on this test bench is provided in Appendix G3. The working principle of specimen loading induced on this test bench is also schematically illustrated in Figure H-14 of Appendix H3.

Because of the age of this fatigue test bench in the laboratory, it was required to perform a load cell calibration to ensure that the correct cantilever forces were applied and considered for calculation in the experimental tests performed on this bench. This calibration procedure is provided below.

Load Cell Calibration Procedure

The linear spring load cell was calibrated by using 5 [kg] and 10 [kg] mass pieces whose measured masses are reported in Appendix E1 and shown in Figure E-1. For the calibration (at room temperature) of the load cell, the following steps were followed (see Figure A-5 below):

- The bending fatigue test bench was rotated on the lab bench so that the load cell mount was positioned over the edge of the lab bench.
- Plastic cable ties were looped through the ball-bearing inner race and hung over the bottom frame strut of the test bench with a steel hook tying the cable tie loops together at the bottom.
- The load cell was positioned into a vertical position with the turn screw that would allow full downward extension of the internal spring once mass pieces were hung on the cable tie loops.
- Cable tie loops were fastened to each mass piece to assist in hanging them on the steel hook.
- The mass pieces were then hung on the steel hook in an additive manner, increasing the applied weight on the load cell.
- The load cell force reading was then recorded.



Figure A-5: Bending fatigue test bench – calibration process

These steps were done for measurements with 10 [kg] and then 5 [kg] hanging mass increments (reference weight values in the second column of the table) to assess the sensitivity of the load cell. For each of the increments, measurements were taken five times from the load cell scale (engraved on the inner cylinder that extends downwards). These measurements could only be

measured to the nearest 5 [N] value as this is the resolution of the engraved scale on the load cell. The measurements are reported in Table A-1, and the resultant calibration curve is illustrated in Figure A-6 below. A gravitational acceleration constant of 9.81 [m/s^2] was used to calculate the hanging mass piece weight values in Newton.

Table A-1: Bending fatigue test bench – load cell force measurements

10kg Weight Increments (5N resolution load cell)	Measurement #	Ref Weight [N]	Force Measurement [N] - 10kg increments								Error [N]	Error [%]
			1	2	3	4	5	AVG	STDEV			
	0	**0**	0	0	0	0	0	**0**	0.000	[N]	**0**	-
	1	**98.04**	85	85	85	85	85	**85**	0.000	[N]	**13**	13.3
	2	**196.10**	175	170	175	175	175	**174**	2.236	[N]	**22**	11.3
	3	**294.07**	245	265	265	265	265	**261**	8.944	[N]	**33**	11.2

5kg Weight Increments (5N resolution load cell)	Measurement #	Ref Weight [N]	Force Measurement [N] - 5kg increments								Error [N]	Error [%]
			1	2	3	4	5	AVG	STDEV			
	0	**0**	0	0	0	0	0	**0**	0.000	[N]	**0**	-
	1	**49.02**	40	40	40	40	40	**40**	0.000	[N]	**9**	18.4
	2	**97.97**	85	85	85	85	85	**85**	0.000	[N]	**13**	13.2
	3	**147.06**	130	130	130	130	130	**130**	0.000	[N]	**17**	11.6
	4	**196.01**	175	175	175	175	175	**175**	0.000	[N]	**21**	10.7
	5	**245.12**	220	225	220	225	225	**223**	2.739	[N]	**22**	9.0
	6	**294.07**	265	265	265	265	265	**265**	0.000	[N]	**29**	9.9

From the calibration curve in Figure A-6 below, it is seen that the load cell spring is, in fact, linear. However, what is considered to be due to the age of the test bench and the load cell, it can also be seen that the load cell measurement (force reading on the scale) is lower, proportional to the applied reference mass piece weights. Both weight increment methods gave similar measurement results. The linear trendline slope, through the 5 [kg] increment measurements (more data points), indicates a slightly stiff load cell spring since the applied force is larger than that read from the load cell. The trendline is also a good representation of both mass increment measurement methods.

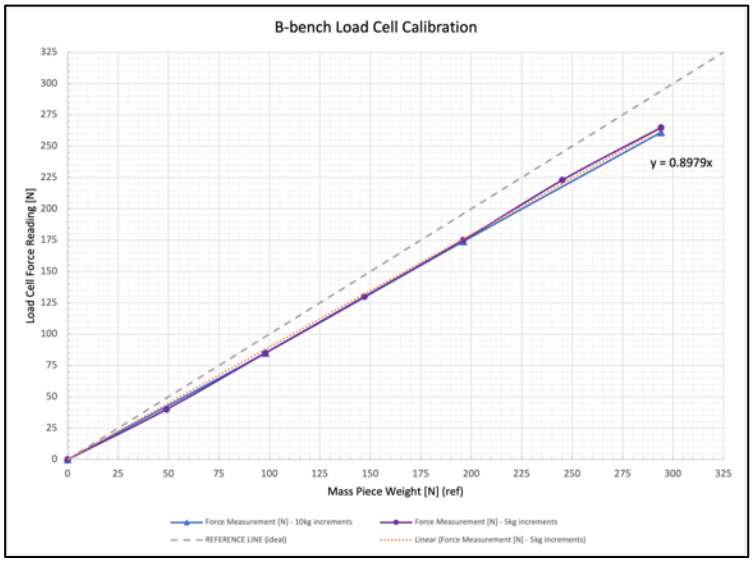


Figure A-6: Bending fatigue test bench – calibration curves

A3. Torsion Fatigue Test Bench

The uniaxial torsion fatigue bench (Figure A-7 and Figure A-8 below) was designed and built in an undergraduate design project [82] to test specimens primarily made of steel under torsion fatigue loading to obtain the fully reversed uniaxial torsion fatigue limit. The test bench inherently only induces a fully reversed uniaxial cyclic loading condition on a specimen. This test bench is based on the concept of the biaxial bending-torsion fatigue test bench (see Appendix A4 next) with the added lever-head stem constraints to suppress induced bending due to centrifugal forces.

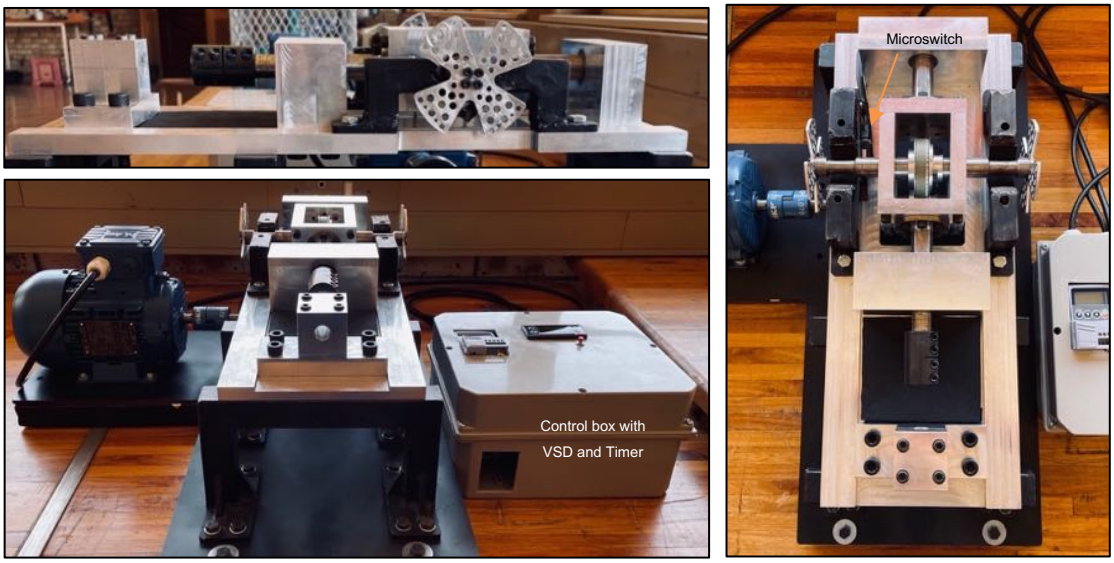


Figure A-7: Torsion Fatigue Test Bench

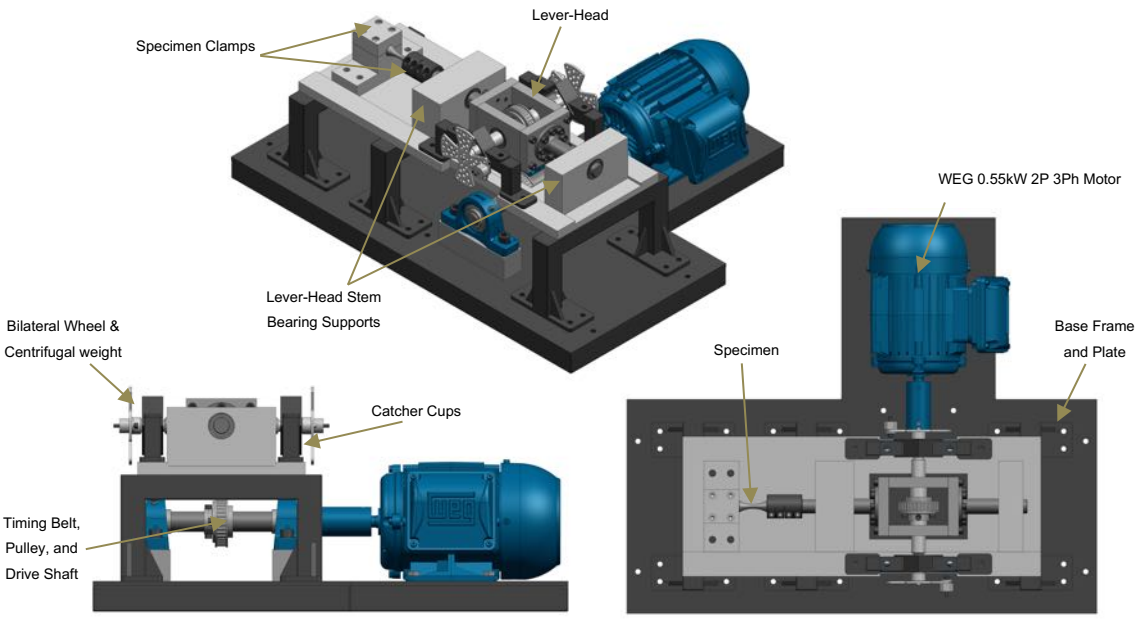


Figure A-8: Torsion Fatigue Test Bench – components

The torsion fatigue test bench is powered by a three-phase 2-pole electrical motor controlled by a VSD. A timer controller connected to the VSD records the elapsed time of each fatigue test, along with the test speed set on the VSD, which provides the cycle count of fatigue loading cycles. The motor (maximum speed 50 [Hz]) is connected to the bottom shaft and pulley, which drives the lever-head shaft through a timing belt and a second pulley (1:1 ratio). Rotation of the lever-head shaft then rotates the attached bilateral wheels, which have mass pieces attached to them at a specific radial position from the axis of rotation (180° apart). These rotating mass pieces induce centrifugal forces in opposite directions on each end of the wheel shaft. The magnitude of these forces can be altered by changing the mass pieces, their radial positions or the test speed on the VSD. However, test speeds on this test bench are dictated by the specimen diameter and material strength. The forces induce a torsional moment around the central axis of the head and, consequently, the specimen's longitudinal axis due to the perpendicular distance (moment lever) at which these forces act from this axis. Therefore, a sinusoidal fully reversed torsional moment is induced on the rigidly clamped specimen (Aluminum mount at the bottom) that is fastened with a coupling to the bottom end of the twisting lever-head stem. The loading principle of this test bench is illustrated schematically in Figure A-9 below. This torsional loading continues until the specimen fails due to fatigue, allowing excessive twisting of the top specimen half (attached to the lever-head). This causes the lever-head shaft's left end to trigger the microswitch, which stops the VSD power to the motor and pauses the timer. Test results can therefore be recorded, and a new test is started. The formal experimental test procedure for the torsion fatigue tests done on this test bench is provided in Appendix G4.

Because this test bench is new, it was required to perform verification measurements of the induced torsional loading on a specimen. These measurements and the procedures followed are provided in Appendix H4.

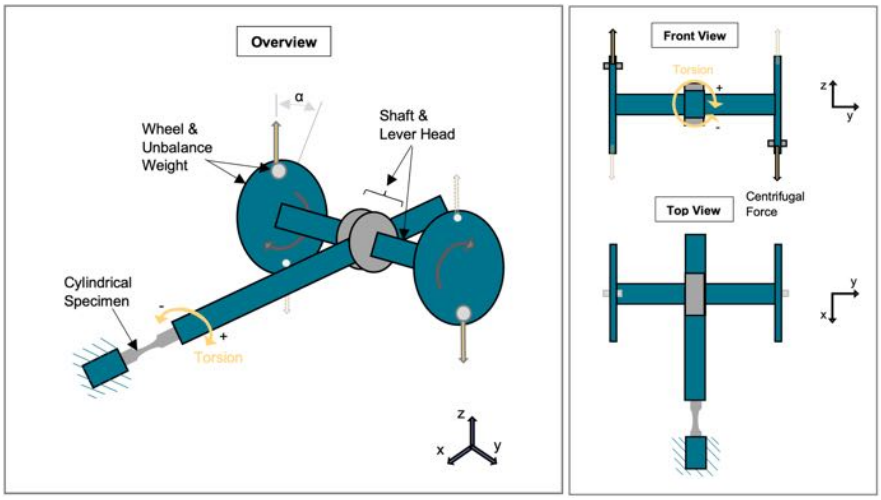


Figure A-9: Torsion Fatigue Test Bench – working principle

A4. Biaxial Fatigue Test Bench M1 Bending-Torsion

The biaxial out-of-phase bending-torsion fatigue bench (Figure A-10 and Figure A-11 below) was designed and built in an undergraduate project [28] to test specimens primarily made of steel to obtain the fully reversed biaxial bending-torsion fatigue limit. This test bench can induce both fully reversed uniaxial bending, and biaxial out-of-phase fully reversed bending-torsion loading on a specimen. This test bench is based on the concept of a biaxial out-of-phase bending-torsion fatigue test bench proposed by Ogawa *et al.* [64].



Figure A-10: Biaxial Fatigue Test Bench M1 Bending-Torsion

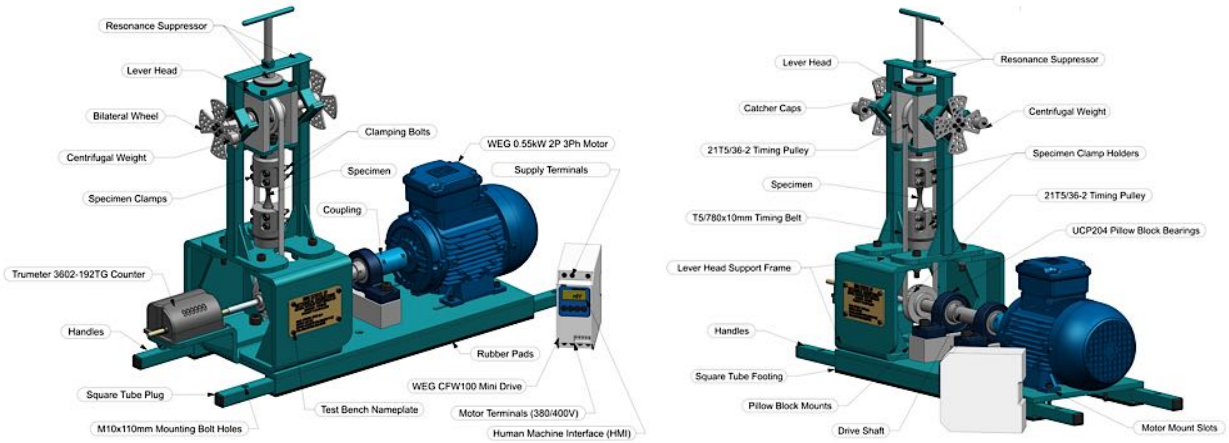


Figure A-11: Biaxial Fatigue Test Bench M1 Bending-Torsion – components

The biaxial bending-torsion fatigue test bench is powered by a three-phase 2-pole electrical motor controlled by a VSD. A timer controller connected to the VSD records the elapsed time of each fatigue test, along with the test speed set on the VSD, which provides the cycle count of fatigue loading. The motor (maximum speed 50 [Hz]) is connected to the bottom shaft and pulley, which drives the lever-head shaft from below with a timing belt and a second pulley (1:1 ratio). Rotation of the lever-head shaft then rotates the attached bilateral wheels, which have mass pieces attached to them at a specific radial position from the axis of rotation (180° apart). These rotating mass pieces induce centrifugal forces in opposite directions on each end of the wheel shaft. The magnitude of these forces can be altered by changing the mass pieces, their radial positions or the test speed on the VSD. However, test speeds on this test bench are dictated by the specimen diameter. The forces act at respective points of wheel rotation and induce fully reversed 90° out-of-phase bending and torsion moments on the rigidly clamped specimen (at steel mount at the bottom) that is fastened with a second steel clamp to the bottom end of the lever-head. The loading principle of this test bench is illustrated schematically in Figure A-12 below. This biaxial loading continues until the specimen fails due to fatigue, allowing excessive displacement of the top specimen half (attached to the lever-head). This causes the lever-head shaft's left or right end to trigger one of the microswitches, which stops the VSD power to the motor and pauses the timer. Test results can therefore be recorded, and a new test is started. The formal experimental test procedure for the biaxial fatigue tests on this bench is provided in Appendix G5. Because this test bench is new, it was required to perform verification measurements of the induced biaxial bending and torsion loading on a specimen. These measurements and the procedures followed are provided in Appendix H5.

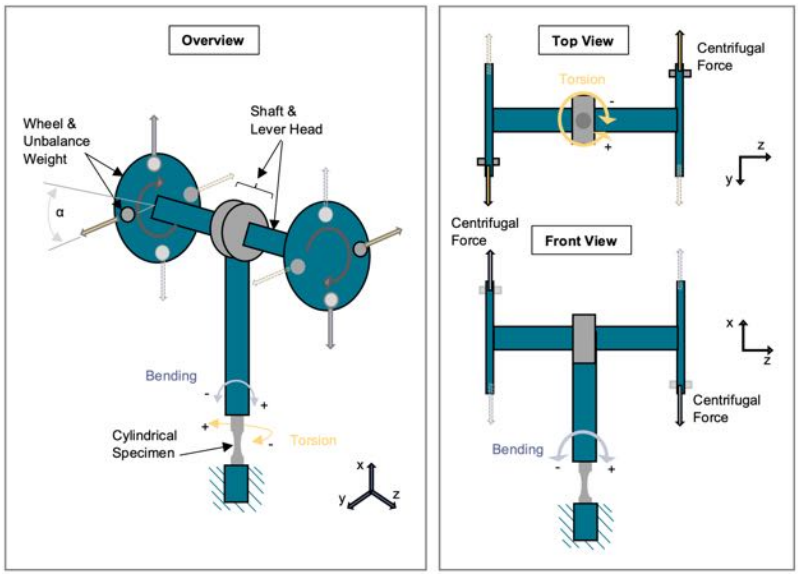


Figure A-12: Biaxial Fatigue Test Bench M1 Bending-Torsion – working principle

B. EXPERIMENTAL MEASUREMENT EQUIPMENT

B1. Mitutoyo Absolute Digital Vernier and SMIEC Micrometre



Figure B-1: Mitutoyo Absolute Digital Vernier and SMIEC Micrometre

The digital vernier in Figure B-1 above was used to measure all the experimental test specimen diameters (test zone after polishing). These measurements were made by closing the calliper jaw tips (thinnest part of jaws) on the cylindrical specimen test diameter areas and recording the diameter measurement (with 0.01 [mm] resolution). This was done ten (10) times for each test specimen, and the diameters are reported in Appendix D1 through D5.

Because the various experimental test specimen diameters (and other measurements or markings) were measured with this vernier, it was required to confirm the measurement accuracy of the digital vernier to ensure that it measures correctly. This verification was done using a 25 [mm] micrometre and corresponding 25 [mm] length calibration cylinder. The procedure followed for this is provided below, and the measurements are reported in Table B-1 below:

- The micrometre calibration cylinder was measured three times with the micrometre.
- The same calibration cylinder was measured with the digital vernier three times.

- Continuous room temperature measurements were made during the above measurements (the calibration cylinder was allowed to acclimatise to room temperature, see Appendix B3).
- The difference in cylinder measurements (using the micrometre as a reference) was then calculated and plotted in the graph shown in Figure B-2 below.

Table B-1: Mitutoyo Absolute Digital Vernier – vernier size measurements

25mm Micrometer Cylinder Measurement	Measrmnt #	Micrometre [mm]	Cylinder Measurement [mm]		
			Vernier [mm]	Error [mm]	Error [%]
	0	**0**	0	**0.000**	-
	1	**25.00**	25.00	**0.000**	0.00
	2	**25.02**	24.99	**0.030**	0.12
	3	**25.00**	25.00	**0.000**	0.00

Room Temp Measurement	Measrmnt #	Temperature Measurement [°C]					
		1	2	3	4	AVG [°C]	STDEV [°C]
	1	26.9	26.8	27.1	27.0	**26.85**	0.071

From Table B-1 above and Figure B-2 below, it can be seen at an average room temperature of 26.85 [°C] that the digital vernier measures accurately. A negligible difference of 0.12 [%] was obtained between these cylinder size measurements.

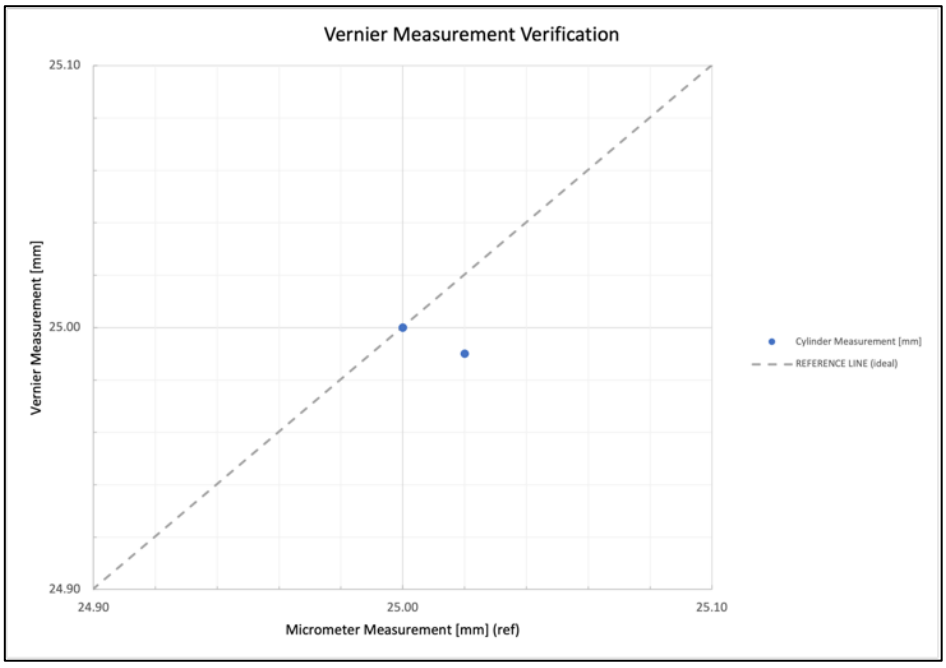


Figure B-2: Mitutoyo Absolute Digital Vernier – vernier size measurement results

B2. SARTORIUS BP110S and PRW30++ Microscale



(a)



(b)

Figure B-3: Microscales – (a) SARTORIUS BP110S and (b) PRW30++

The microscales (respectively with 0.1 [mg] and 0.1 [g] resolution) in Figure B-3 above were used to measure various experimental masses (like those reported in Appendix E). These measurements were made on each scale according to the general measurement steps below:

- Switch on the microscale and allow it to stabilise with the reading displayed on the digital display.
- Then, 'zero' or 'tare' this mass reading before placing a mass object on the scale platform.
- Place the mass object on the scale platform, wait for stabilised reading and record the measurement.

As an informal control measurement for each microscale, a set of calibration mass pieces (stored in the laboratory) were also measured. The mass pieces, with ideal and known masses, were measured on each microscale to check the scale measurement accuracy. These measurements, which were correct for each calibration mass piece, were not recorded since the microscales were both 'zeroed' or 'tared' with the dedicated buttons before recording a mass. Performing an official scale calibration was considered unnecessary as long as this 'zeroing' step was done before placing a mass piece on any one of the scales.

B3. FLUKE 52 K/J Thermocouple Thermometer



Figure B-4: FLUKE 52 K/J Thermocouple Thermometer

The thermocouple thermometer in Figure B-4 above (0.1 [°C] resolution) was used for temperature measurements during the monotonic tensile tests (average 22.68 [°C] obtained) and some other secondary test measurements. This thermometer was, at the time, the available and most accurate temperature-measuring device available in the laboratory. It was recently calibrated for other high- and low-temperature applications in the laboratory and gave satisfactory measurement results. It was therefore considered accurate enough for the room temperature ranges considered. However, to ensure accurate temperature measurements, this thermometer was used according to the general procedure below:

- Switch on the thermometer and lay it down on a surface near where temperature measurement is required for a test specimen.
- Allow sufficient time (1-3 minutes) for the thermometer to stabilise in the reading on the screen and prevent touching or holding of the thermocouple metal casing/stem. Also, do not place it near a secondary heat or airflow source.
- Record room temperature readings, at the start, during or at the end of a test as required.

For these measurements, it was assumed that if a test specimen is allowed enough time before a test in the room where the test and temperature measurement was performed, the specimen material will attain a temperature equivalent to that of the room atmosphere. Thus, it was assumed that the room temperature measurement could be conservatively used as that of the specimen since no direct on-specimen temperatures were measured.

B4. MTS Extensometer 634.31F-24

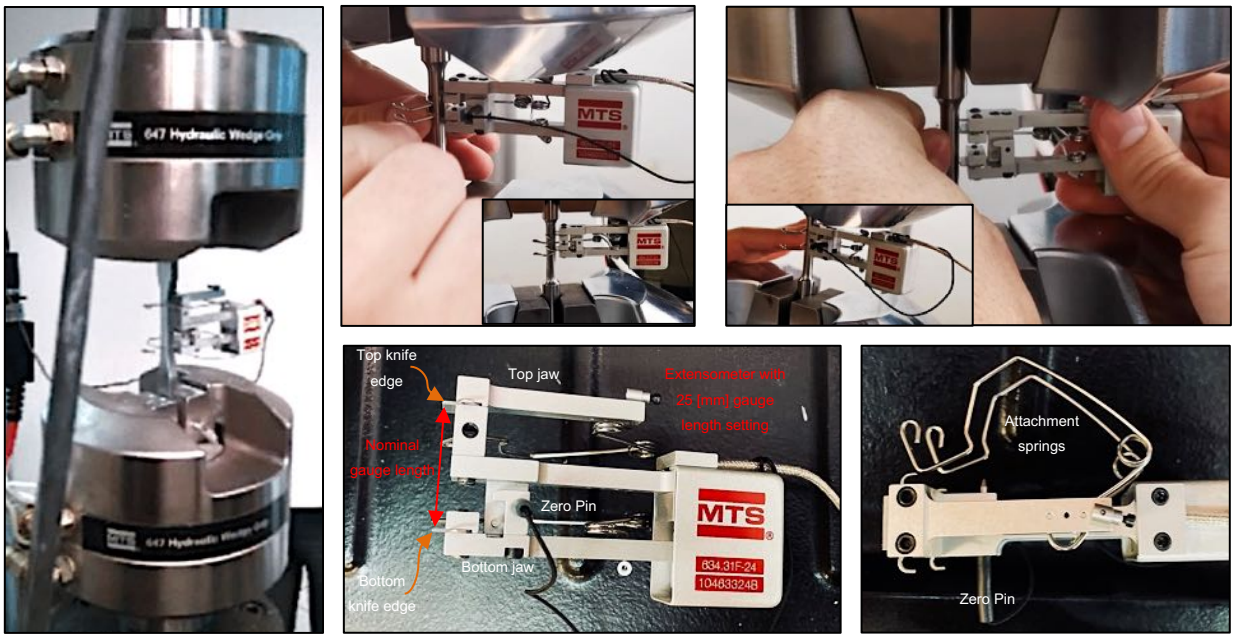


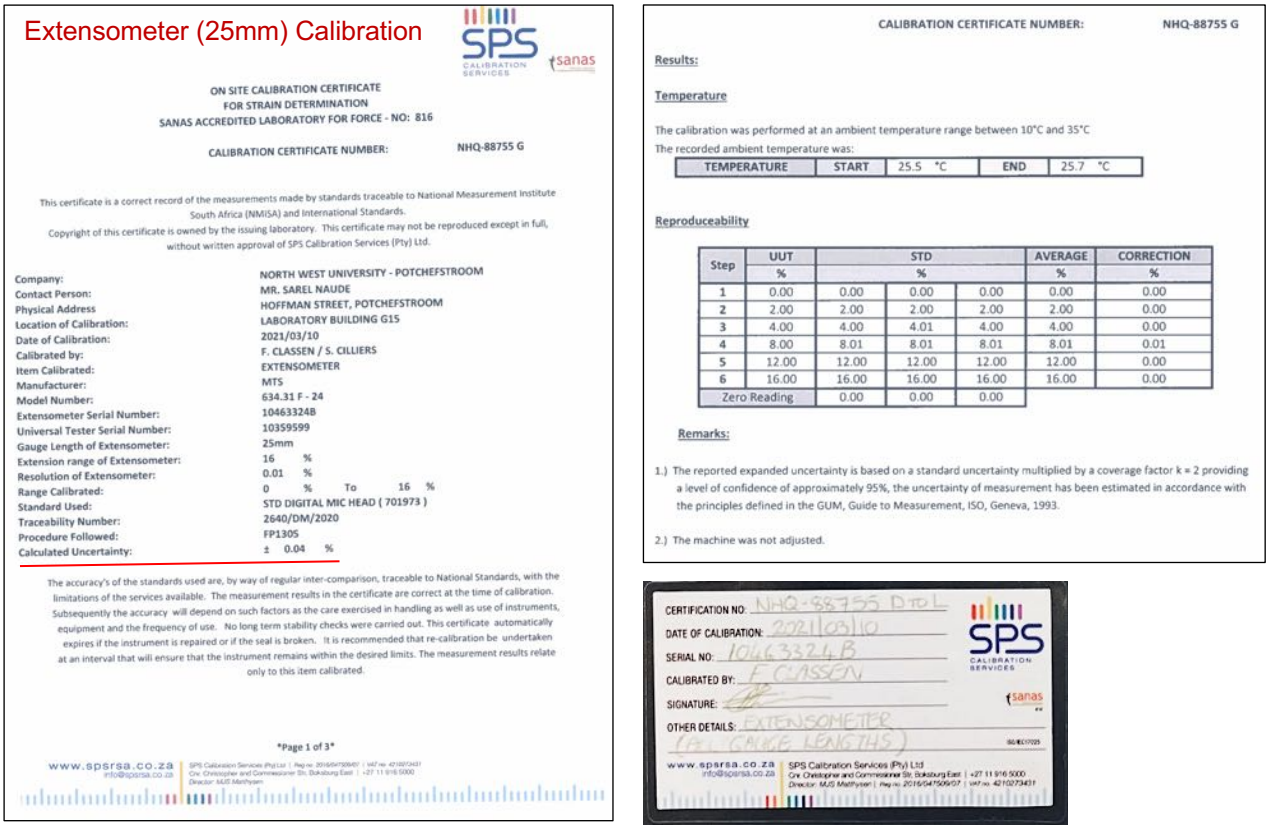
Figure B-5: MTS Extensometer 634.31F-24 – components

The MTS 634.31F-24 Extensometer (Figure B-5 above) is a static-rated axial strain measurement sensor used to take on-surface contact measurements of the specimen gauge section strain during tensile, compression or fatigue testing. For this study, the extensometer was only used during some of the experimental tensile tests performed on the MTS Landmark machine (see Appendix A1) to measure the direct specimen gauge area strain and the material's experimental Elasticity Modulus. Using the extensometer is considered standard practice for these strain measurements. This is due to the MTS Landmark machine's load train displacement measurements typically being less reliable due to machine deflection, grip deflection and grip slippage being incorporated into the displacement readings measured during each test.

The extensometer used in this study had the recommended straight knife edges (for round specimens). Its nominal gauge length was extended to 25 [mm] (distance between the knife edges) with the accompanying jaw extension kit components (to cover the recommended 70-80 [%] of 32.8 [mm] ASTM E8 tensile specimen gauge length). The extensometer has a -85 [°C] to +120 [°C] temperature range and a measuring range of +16 [%] to -8 [%] strain (for 25 [mm] gauge length) according to the specification sheet of the measurement device.

The typical procedure for measuring with this device involves connecting the extensometer to a multipin port on the MTS Landmark tensile test machine and activating it within the appropriate

software program on the MTS computer system. The standard tensile test procedure (clamping of a specimen) is followed (see Appendix G1) before proceeding with the extensometer measurement. Once the tensile test specimen is loaded into the MTS machine and all the test parameters are set in the relevant test procedure program on the computer, the extensometer is mounted onto the specimen gauge area. This is done with the zero pin still inserted (holding the parallel jaws together) when pressure is applied on the knife edges through the attachment springs that pull around the cylindrical specimen (preferably polished surface to ensure proper knife edge location on the specimen surface). The extensometer is positioned on the specimen, whilst the attachment springs apply light pressure in as vertical (axial extension) a direction as possible. The attachment springs are also located such that each applies pressure directly across from the knife edge on the other side of the cylindrical test specimen. The zero pin is removed, and the extensometer strain signal channel on the computer is zeroed. The tensile test (in the strain procedure environment) is then run, and the extensometer measures the specimen strain during the elastic extension part of the tensile test. Once the strain measurement procedure reaches these predefined region limits, a message notifies the user to remove the extensometer from the specimen. The tensile test is then continued until the ultimate tensile fracture of the specimen. This experimental test procedure for using the extensometer on the MTS Landmark tensile test machine is provided in Appendix H1.



Extensometer (25mm) Calibration

SPS CALIBRATION SERVICES

sanas

ON SITE CALIBRATION CERTIFICATE
FOR STRAIN DETERMINATION
SANAS ACCREDITED LABORATORY FOR FORCE - NO: 816

CALIBRATION CERTIFICATE NUMBER: NHQ-88755 G

This certificate is a correct record of the measurements made by standards traceable to National Measurement Institute South Africa (NMiSA) and International Standards.
Copyright of this certificate is owned by the issuing laboratory. This certificate may not be reproduced except in full, without written approval of SPS Calibration Services (Pty) Ltd.

Company:	NORTH WEST UNIVERSITY - POTCHEFSTROOM
Contact Person:	MR. SAREL NAUDE
Physical Address	HOFFMAN STREET, POTCHEFSTROOM
Location of Calibration:	LABORATORY BUILDING G15
Date of Calibration:	2021/03/10
Calibrated by:	F. CLASSEN / S. CILLIERS
Item Calibrated:	EXTENSOMETER
Manufacturer:	MTS
Model Number:	634.31 F - 24
Extensometer Serial Number:	10463324B
Universal Tester Serial Number:	10359599
Gauge Length of Extensometer:	25mm
Extension range of Extensometer:	16 %
Resolution of Extensometer:	0.01 %
Range Calibrated:	0 % To 16 %
Standard Used:	STD DIGITAL MIC HEAD (701973)
Traceability Number:	2640/DM/2020
Procedure Followed:	FP1305
Calculated Uncertainty:	± 0.04 %

The accuracy's of the standards used are, by way of regular inter-comparison, traceable to National Standards, with the limitations of the services available. The measurement results in the certificate are correct at the time of calibration. Subsequently the accuracy will depend on such factors as the care exercised in handling as well as use of instruments, equipment and the frequency of use. No long term stability checks were carried out. This certificate automatically expires if the instrument is repaired or if the seal is broken. It is recommended that re-calibration be undertaken at an interval that will ensure that the instrument remains within the desired limits. The measurement results relate only to this item calibrated.

Page 1 of 3

www.spsrsa.co.za

CALIBRATION CERTIFICATE NUMBER: NHQ-88755 G

Results:

Temperature

The calibration was performed at an ambient temperature range between 10°C and 35°C
The recorded ambient temperature was:

TEMPERATURE	START	25.5 °C	END	25.7 °C

Reproduceability

Step	UUT	STD			AVERAGE	CORRECTION
	%	%			%	%
1	0.00	0.00	0.00	0.00	0.00	0.00
2	2.00	2.00	2.00	2.00	2.00	0.00
3	4.00	4.00	4.01	4.00	4.00	0.00
4	8.00	8.01	8.01	8.01	8.01	0.01
5	12.00	12.00	12.00	12.00	12.00	0.00
6	16.00	16.00	16.00	16.00	16.00	0.00
Zero Reading		0.00	0.00	0.00		

Remarks:

1.) The reported expanded uncertainty is based on a standard uncertainty multiplied by a coverage factor k = 2 providing a level of confidence of approximately 95%, the uncertainty of measurement has been estimated in accordance with the principles defined in the GUM, Guide to Measurement, ISO, Geneva, 1993.

2.) The machine was not adjusted.

CERTIFICATION NO: NHQ-88755 D to L
DATE OF CALIBRATION: 2021/03/10
SERIAL NO: 10463324B
CALIBRATED BY: F. CLASSEN
SIGNATURE:
OTHER DETAILS: EXTENSOMETER (25 mm GAUGE LENGTHS)

SPS CALIBRATION SERVICES
sanas

www.spsrsa.co.za
SPS Calibration Services (Pty) Ltd

Figure B-6: MTS Extensometer 634.31F-24 – 25 [mm] calibration certificate

The MTS Extensometer is typically calibrated annually by an external third-party company, as illustrated with the certificate in Figure B-6 above. This typically includes individual calibrations of all the extensometer gauge length settings used for measurement on the MTS Landmark machine. For the tensile tests performed on this machine in this study, only the reported extensometer uncertainty (+- 0.04 [%] strain) from the calibration certificate is considered for the measured strains used compared with the DANTEC DIC System secondary verification measurements. The last calibrations of this extensometer were performed on 10 March 2021.

B5. Lutron DT-2234BL Digital Tachometer



Figure B-7: Lutron DT-2234BL Digital Tachometer

The Lutron DT-2234BL Digital Tachometer (Figure B-7 above) is an optical (laser type) rotational speed measurement device commonly used to measure the speed of shafts rotating. This Class 2 red diode laser (645 [nm] wavelength) tachometer has a distance measurement range of 0.05 to 2 [m] (minimum reflector tape size 10 [mm]) and a speed measurement range of 10 to 99 999 [rpm] (at 0.1 [rpm] resolution and 0.05 [%] accuracy).

For this study, the tachometer was used to measure the bending (B) fatigue test speed during each test according to the general measurement procedure below:

- With the B fatigue test running, point the laser lens to the area between the support bearings (see Figure A-4), where the reflector tape is fixed to the rotating shaft.
- Hold the tachometer in a horizontal position (with the display oriented upwards) and in line with the shaft level with the shaft perpendicular to the tachometer.
- Press and hold the button on the right side of the device and allow the measurement to stabilise.
- Record the speed reading (in [rpm]) on display and repeat the measurement three times.

B6. DANTEC Dynamics Q400 DIC System

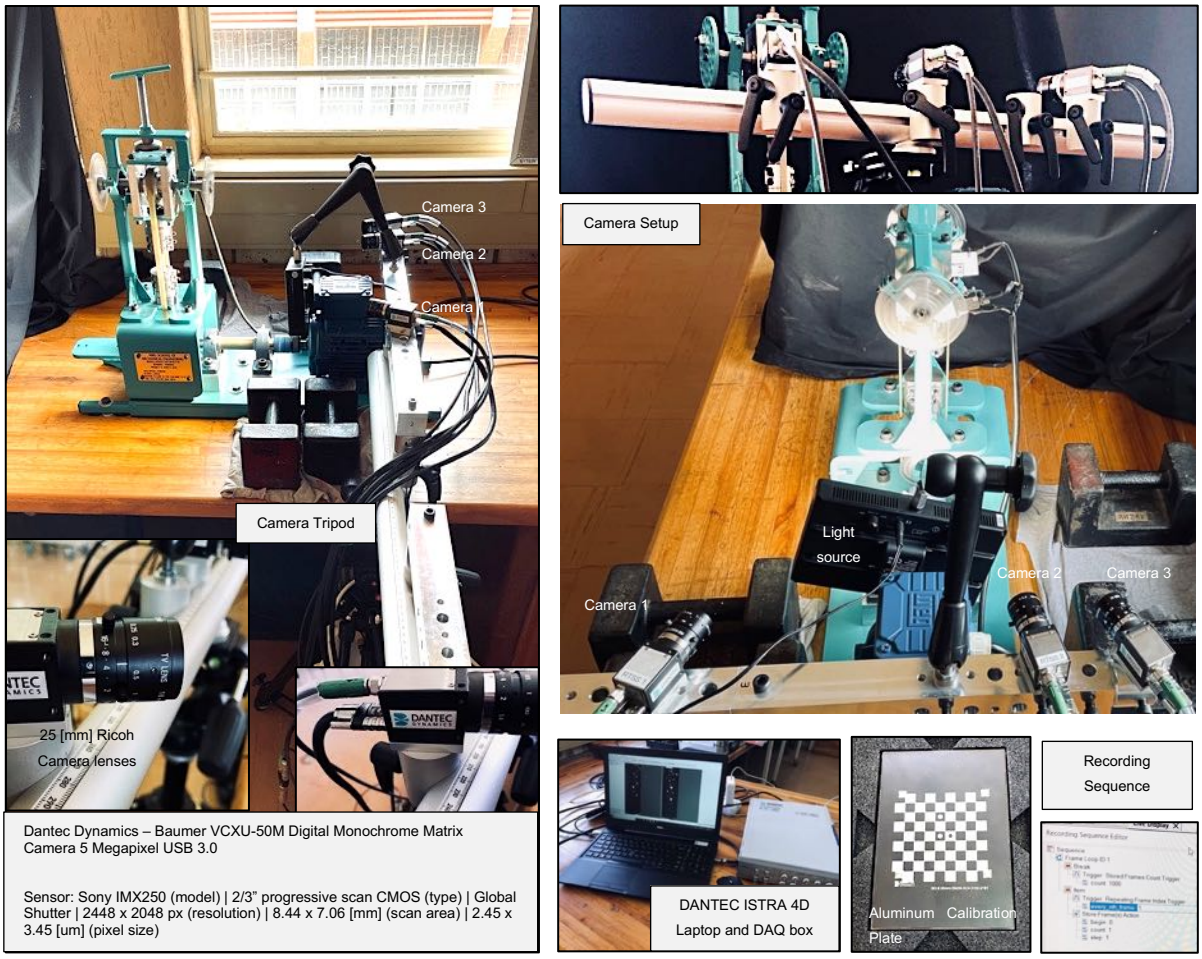


Figure B-8: DANTEC Dynamics Q400 DIC System – components and setup

The DANTEC Dynamics high-speed camera system (Figure B-8 above) uses full-field image analysis and correlation to determine an object's three-dimensional (3D) displacement under loading. Two to three cameras are used to take a set of consecutive photos of a speckle pattern on the pre-prepped test object that experiences the loading. Accompanying DIC software (ISTRA 4D) then applies a digital mesh on the test object's surface to track the movement of the speckles between the overlapping mesh elements with respect to a calibrated and defined 3D coordinate system of the cameras. Evaluation of the speckle correlation results then provides the displacement measurements from the software. This measurement system is commonly used in material testing (for stress, strain and displacement measurement), fracture mechanics (crack growth studies) and high-speed applications (dynamic measurements of up to 500 [Hz], depending on the camera views and object size). Figure B-8 above shows the system, its components and cameras and their setup for test measurement on the BT fatigue test bench.

A general procedure associated with a DIC measurement using this system involves the following:

- Creating a speckle pattern on the test object surface (Figure B-10 below) with white (background) and black (foreground/speckle) spray paint.
- Setting up the tripod, cabling, cameras, lighting, and computer and activating the system in the ISTRA 4D software program (Figure B-8).
- Specifying the region of interest (on the object) for measurement within the full camera view, as shown in Figure B-9, where only the speckled specimen surface is in focus and meshed.
- Adjusting camera focus, aperture, exposure time, lighting and frame rate.
- Performing a camera calibration using a dedicated calibration plate to establish the 3D coordinate system and camera positions within it (different from measurement coordinates).
- Specifying the recording/acquisition sequence (quantity of photos and rate).
- Perform image acquisition/recording and an evaluation (correlation with green mesh).
- Defining a user/measurements coordinate system for measured displacement directions and digital gauge points/lines from which measurements are obtained on the specimen surface.
- Visualise results with graphs and displacement colour fields within the software or from exported results data (x, y, z displacements or coordinates).

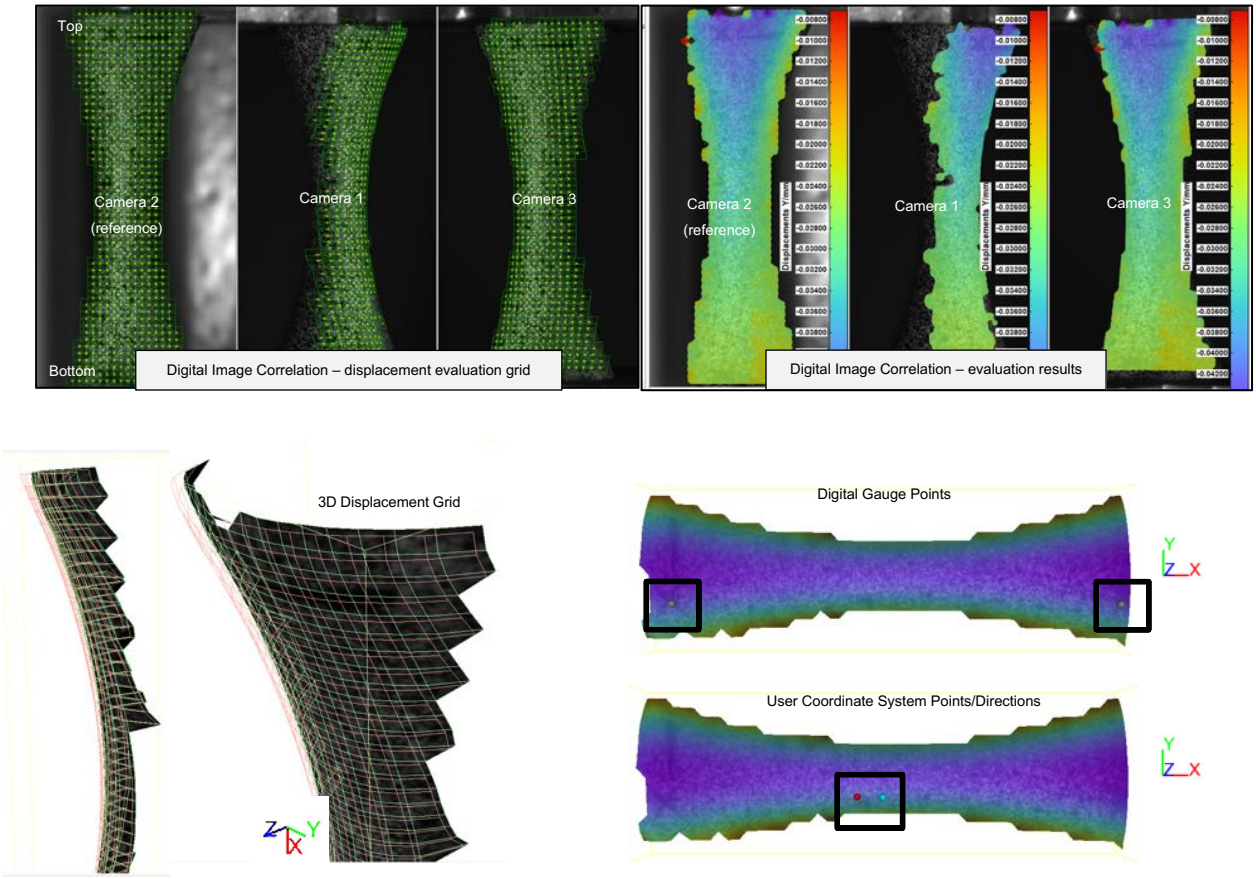


Figure B-9: DANTEC Dynamics Q400 DIC System – measurement illustration

Specimen surface preparation (polishing) and DIC speckle pattern generation on the specimen surface is fundamental to the correctness, accuracy and completeness of the DIC measurements made with this camera system. Figure B-10 below illustrates the typical process of preparing a surface speckle pattern on a polished arbitrary test specimen. The general steps followed for this include:

- Polishing a machined test specimen to ensure a smooth surface (mirror-like in the case of metals) with no visible grooves, pits or scratches (see Appendix C6). Note that specimen diameter should be measured prior to spraying on the speckle pattern.
- Taping the specimen ends (non-measured parts of the specimen) closed with masking tape to prevent spray paint from building up in the specimen clamping components of a test bench.
- Spraying a white (matte) background for the speckle pattern on the specimen area that should be measured (thin as possible layer that conceals metallic reflection/sheen)- allowing it to dry.
- Spraying the black (matte) foreground speckles over the entire white specimen surface with a spray-can method known as the ‘fallout’ method. Gentle spraying from far enough distance. The speckle size should range from very fine (mist-like) speckles to slightly larger speckles (still fine relative to specimen size), and they should be evenly distributed (even density of all speckle sizes) over the entire white background on the specimen. Allow sufficient drying time.
- Removing masking tape and making the required markings on the specimens for where digital gauge points/lines will be placed in the software to obtain measurements.

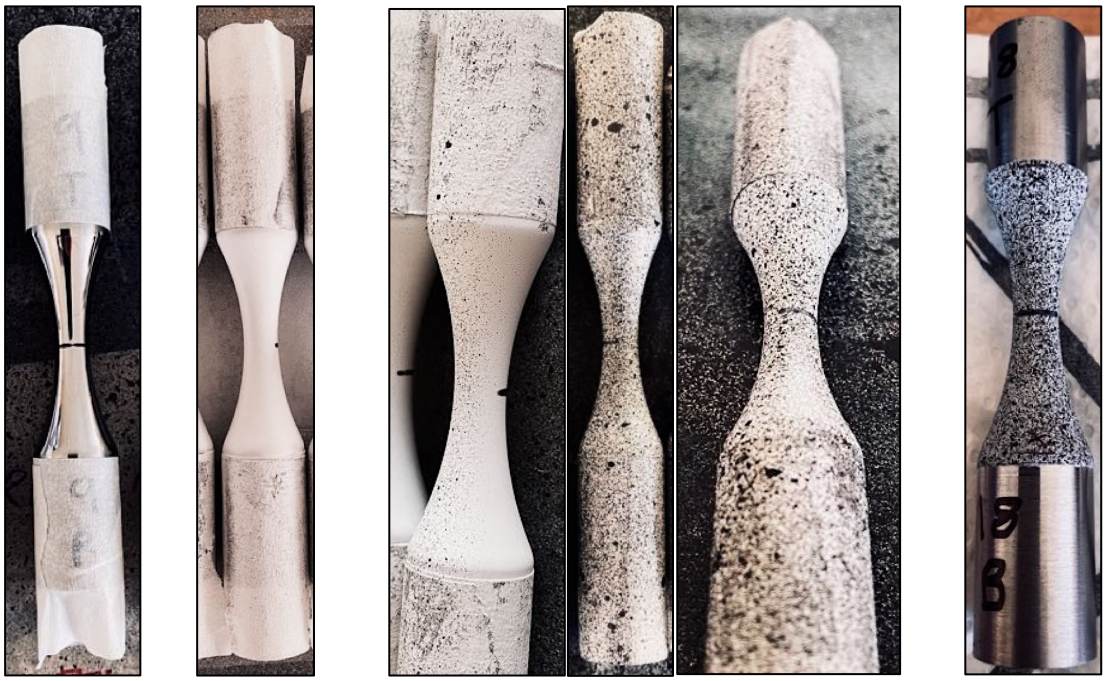


Figure B-10: DANTEC Dynamics Q400 DIC System – speckle pattern preparation

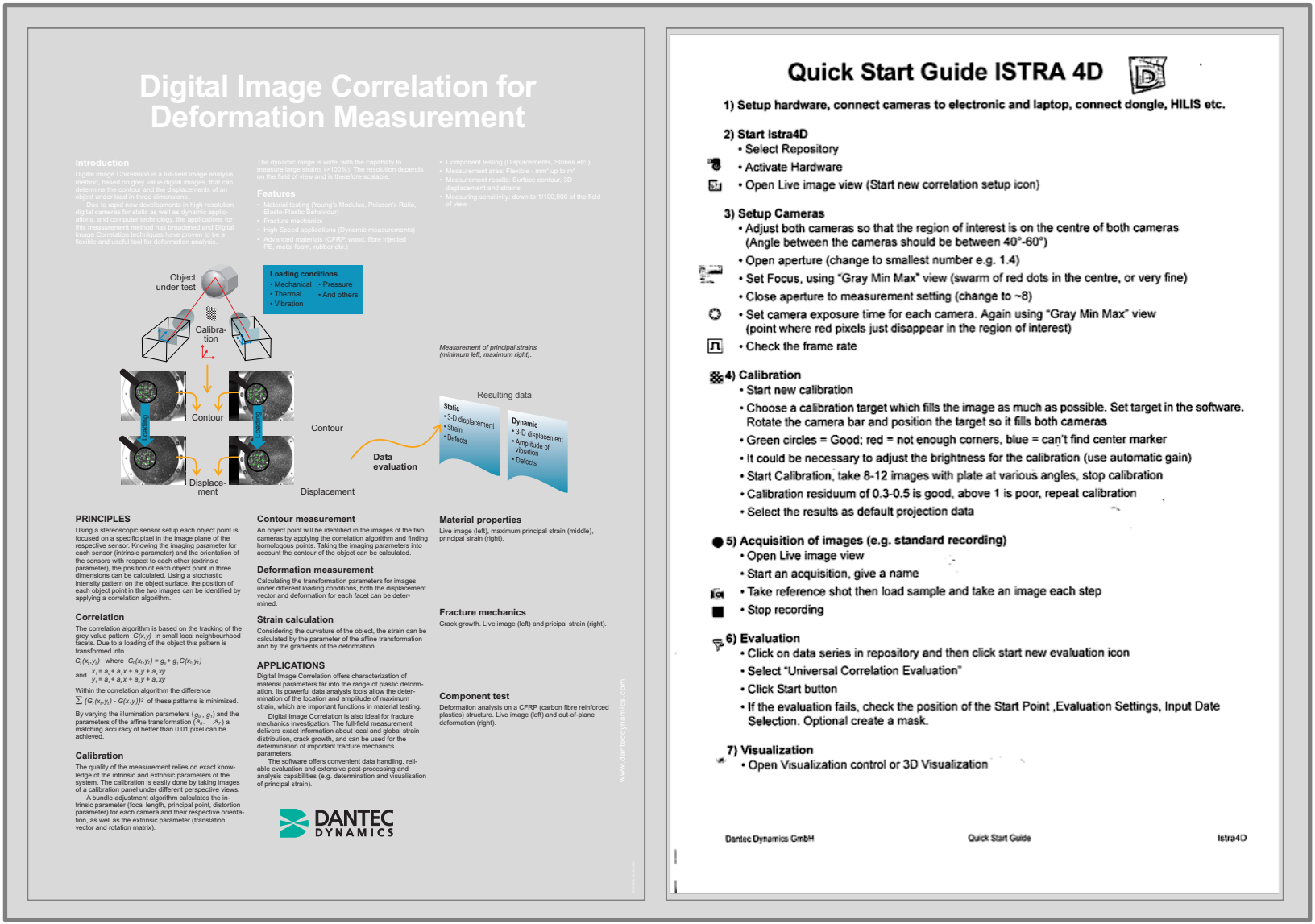


Figure B-11: DANTEC Dynamics Q400 DIC System – measurement and guide [83]

B7. RS Pro EZM-3735 Digital Timer Controller and WEG CFW100 VSD



(a) (b)

Figure B-12: (a) WEG CFW100 Mini Drive VSD and (b) RS Pro EZM-3735 Digital Timer Controller

The digital timer relay was incorporated into the torsion (T) and bending-torsion (BT) test bench control boxes to assist in recording the elapsed time of each fatigue test. This timer is connected to the VSD via a small 12 [V] control/logic board that allows the VSD relay switches to start, pause and stop the digital timer count during testing. A small red reset button is also incorporated to allow timer resetting prior to starting consecutive tests. The VSD is connected to the 3-phase 2-pole motor of each test bench and continuously provides power to the motor at a pre-defined test speed (specific to each bench and specimen diameter). With the test speed and the elapsed time (hour: minute) recorded from the VSD and timer controller, the fatigue cycle counts were calculated (3600 x speed [Hz] x time [hr]) for each test specimen.

B8. Aptina CMOS Digital Camera Microscope



Figure B-13: Aptina CMOS Digital Camera Microscope

C. SPECIMEN DETAIL AND PREPARATION

C1. Monotonic Tensile Test Specimens

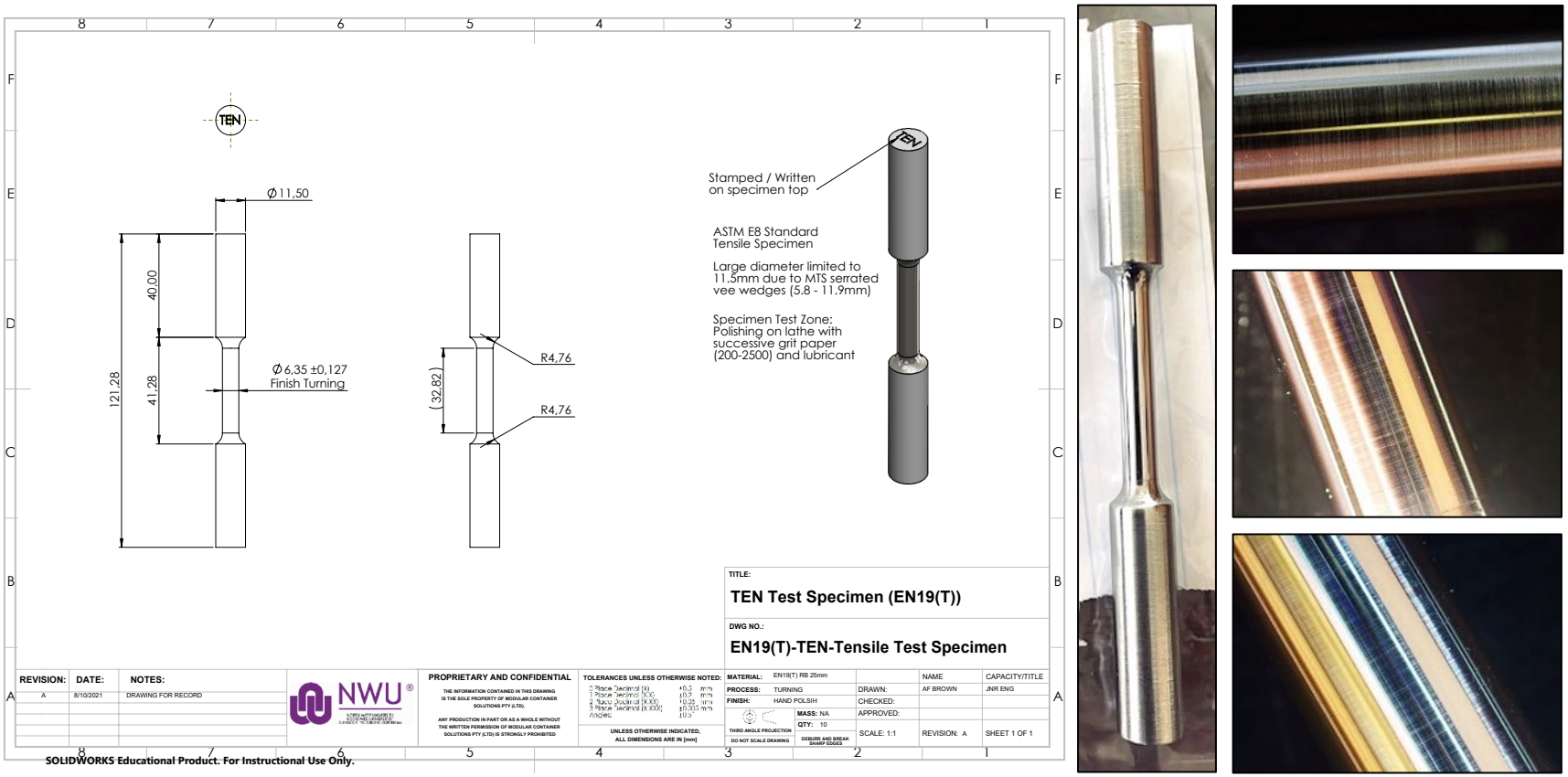


Figure C-1: Tensile (TEN) specimen – geometry and surface finish

C2. Axial Fatigue Test Specimens

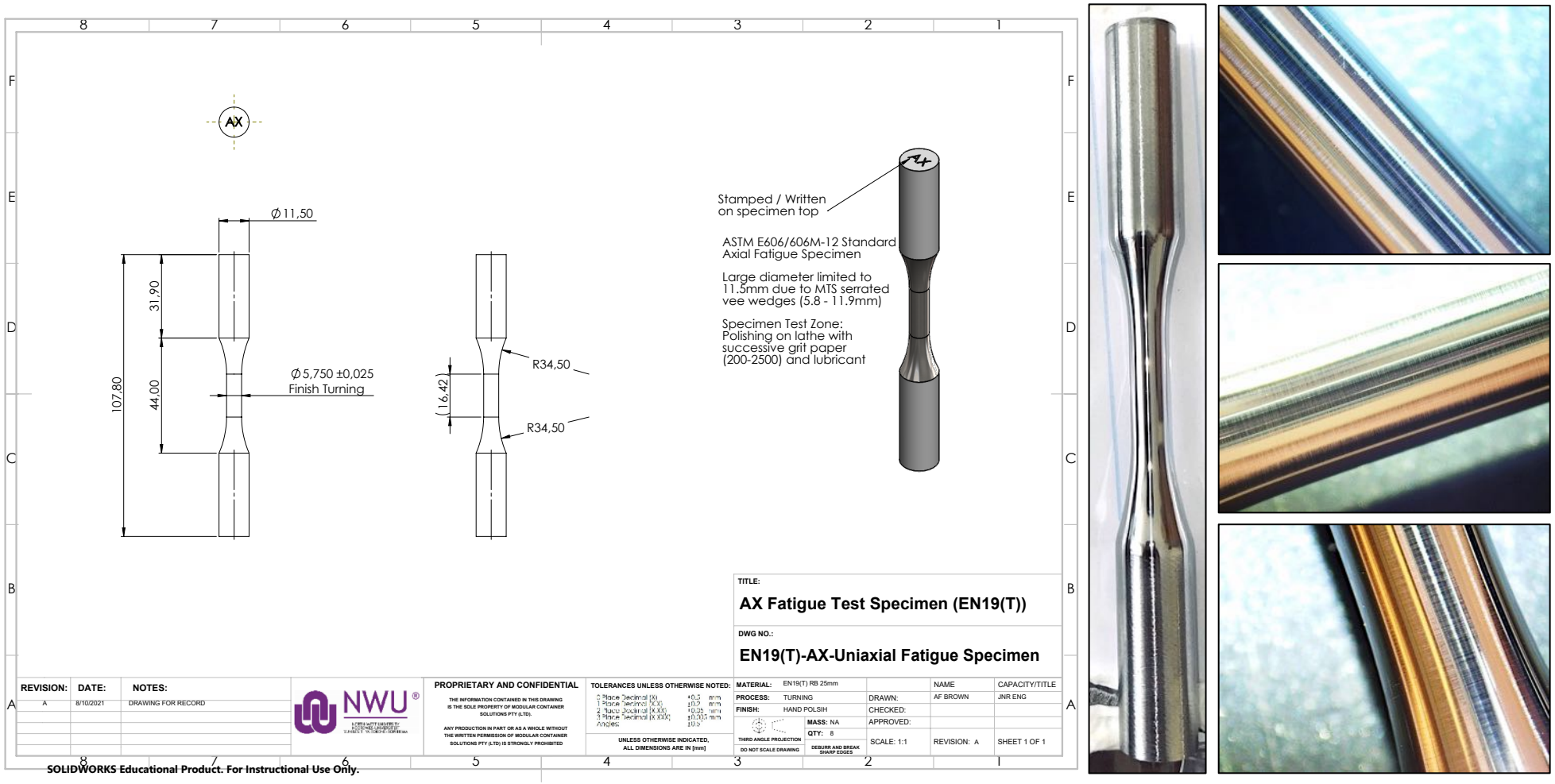


Figure C-2: Axial (AX) fatigue specimen – geometry and surface finish

C3. Bending Fatigue Test Specimens

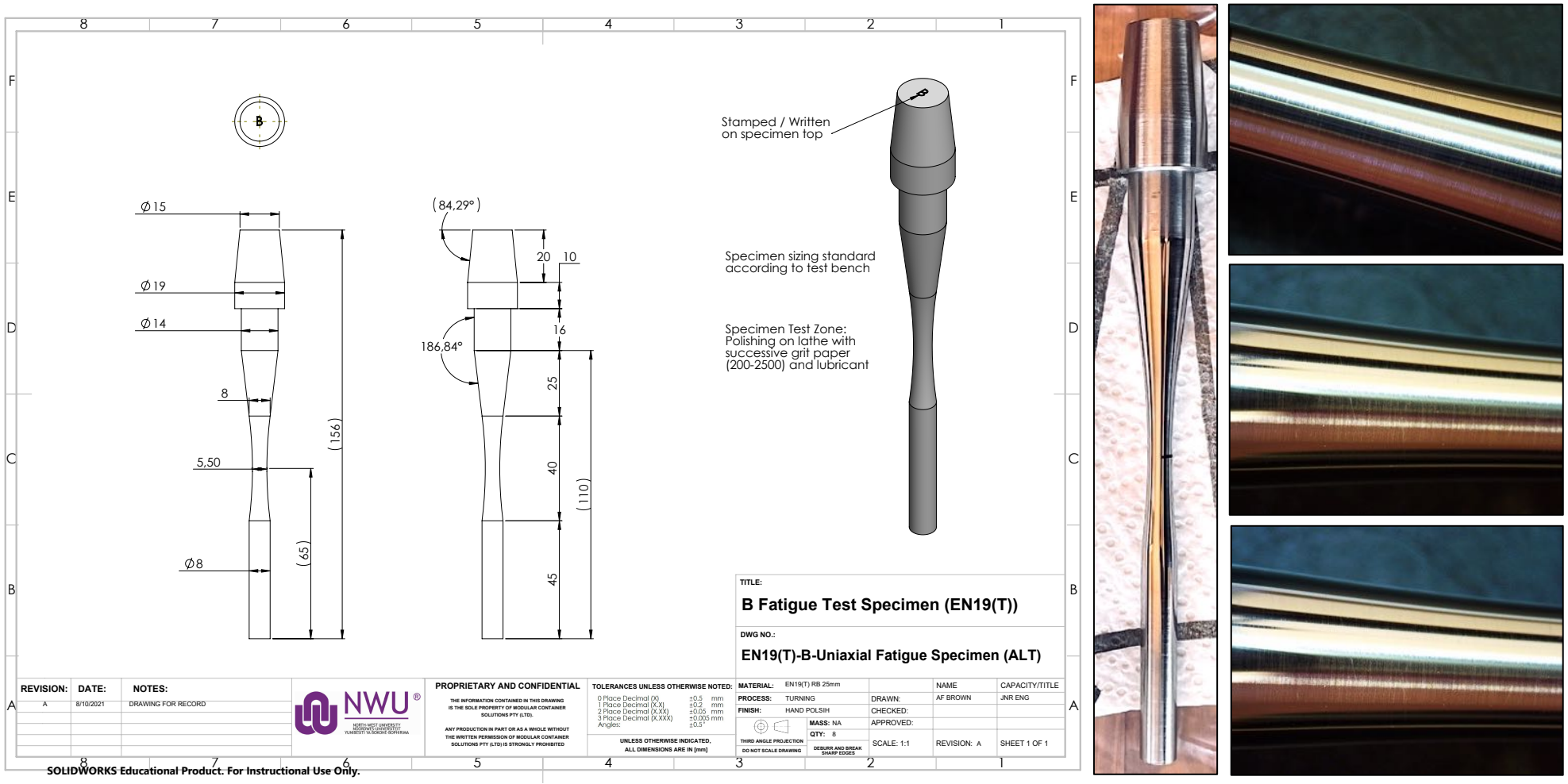


Figure C-3: Bending (B) fatigue specimen – geometry and surface finish

C4. Torsion Fatigue Test Specimens

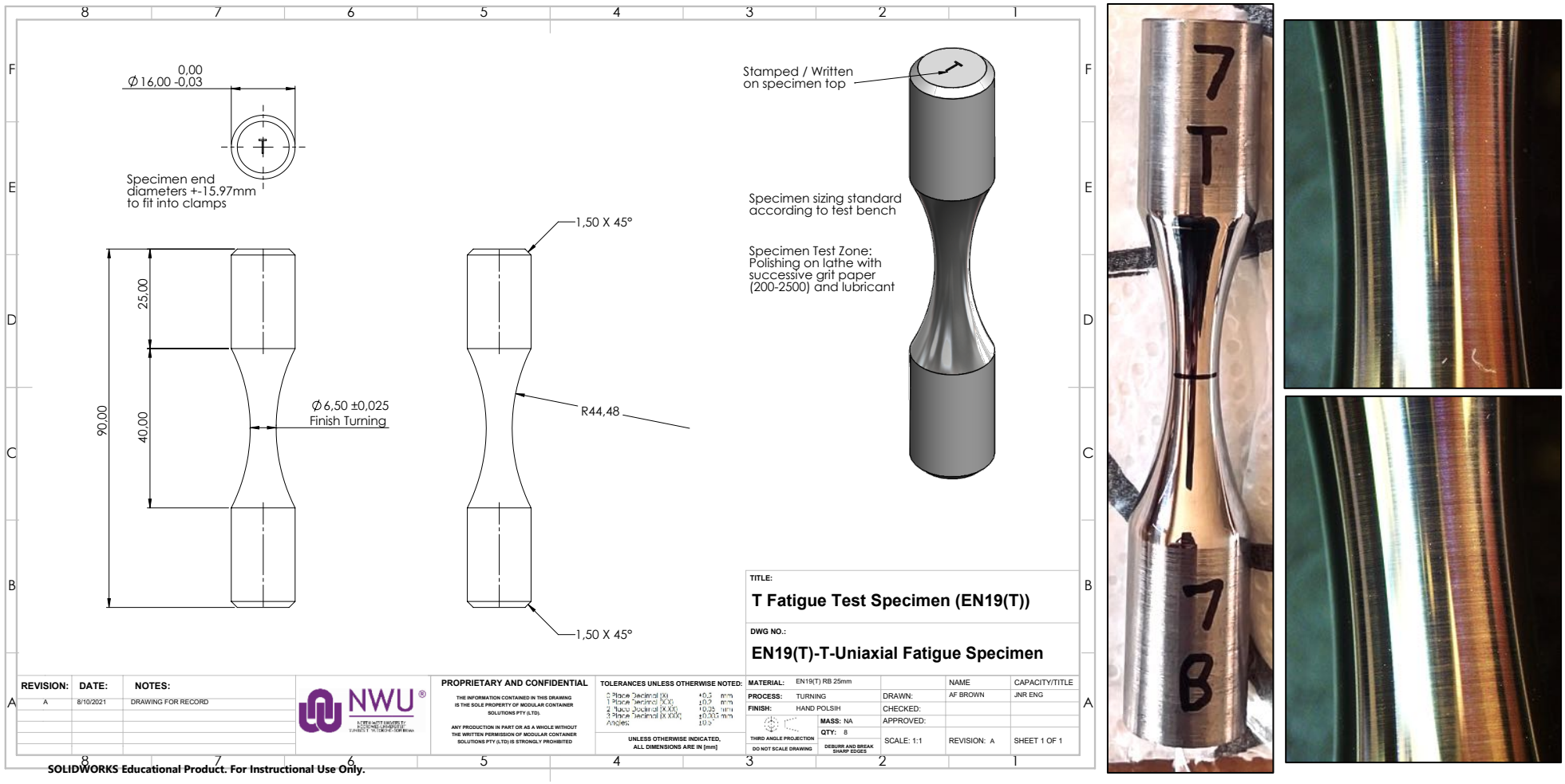


Figure C-4: Torsion (T) fatigue specimen – geometry and surface finish

C5. Bending-Torsion Fatigue Test Specimens

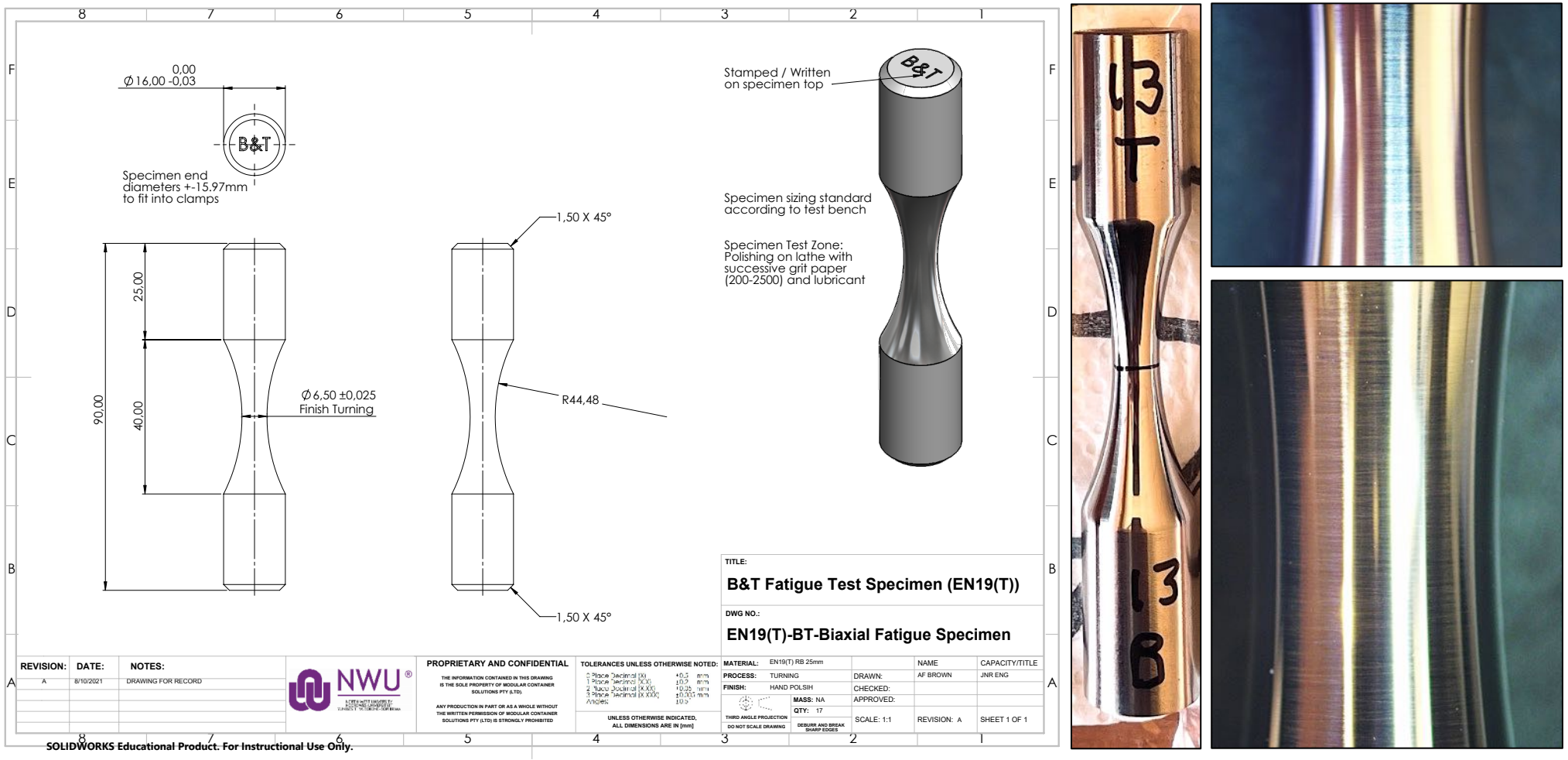


Figure C-5: Bending-Torsion (BT) fatigue specimen – geometry and surface finish

C6. Specimen Manufacturing, Management and Polishing

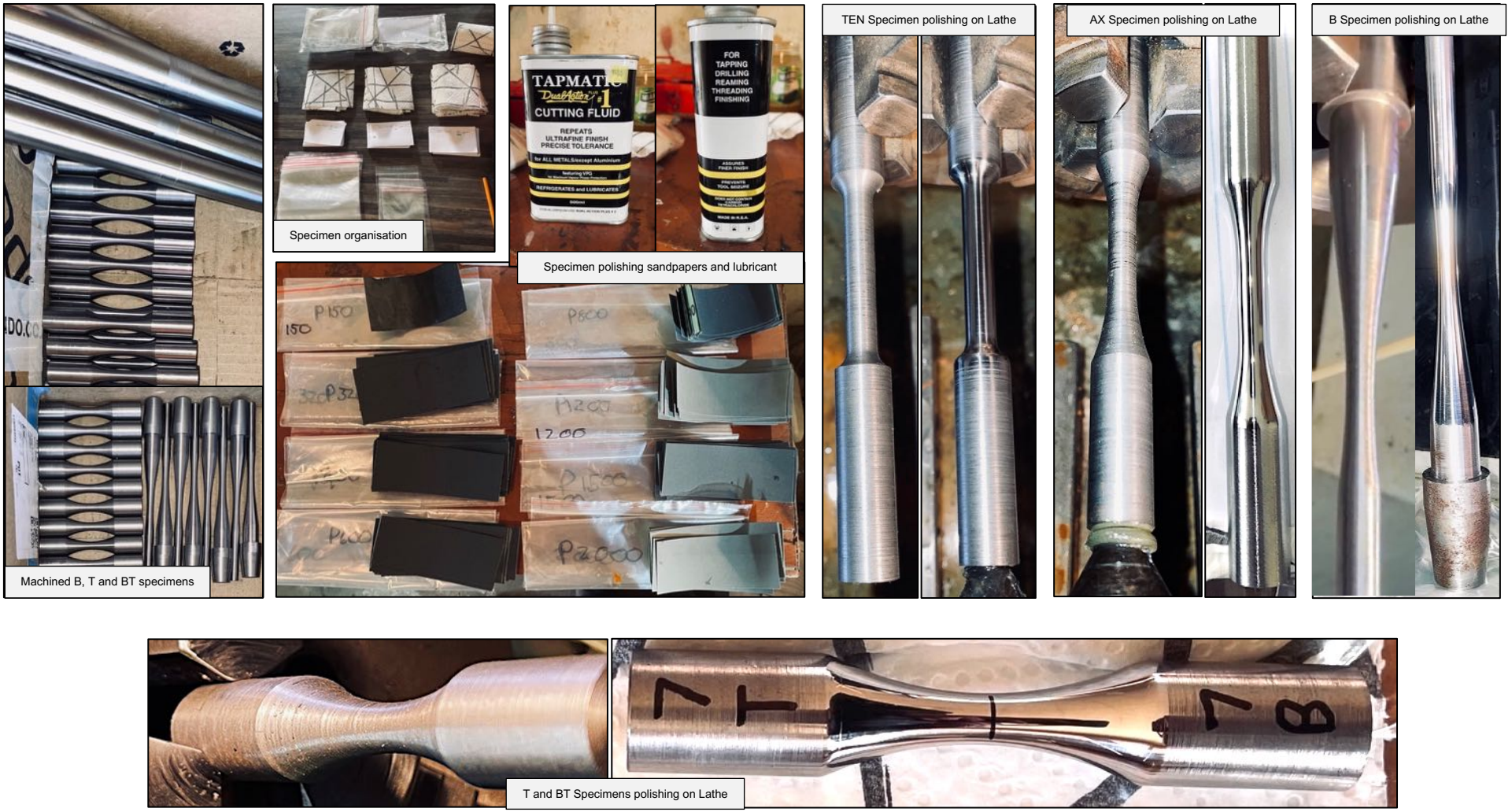


Figure C-6: Test Specimens – manufacturing, management and polishing

The general procedure used for experimental TEN, AX, B, T and BT test specimen surface polishing (see Figure C-6 above) involved:

- Mounting the specimen in the lathe and using a tailstock centre to prevent unmounted tip deflection during hand polishing.
- Running a steady stream of lubricating fluid over the specimen whilst running the lathe at 2750 [rpm] (speeding up the polishing process).
- Polishing the specimen with successively finer roughness grit sandpaper pieces with the lubrication stream continuously running over hand and specimen (rotating).
- Moving hand gripping the sandpaper along the full gauge length of the rotating specimen at various rates to create a ‘cross-hatch’ type polishing pattern and slowing down this movement with each successive grit.
- Visually inspect the specimen surface for visibly larger or rougher grooves (mainly concentric to specimen diameter) or unpolished areas after each grit before proceeding to the next.
- Finishing with the last grit sandpaper (P2000) at a slow rate of longitudinal hand movement and lightest applied pressure until no more visible scratches, rings, lines or grooves are observed with the naked eye (both while specimen is rotating and stationary).
- Removing specimen from the lathe and properly drying off all residual lubrication liquid (using a microfibre cloth in an axial direction) whilst not scratching the polished specimen surface.
- Allowing the specimen to air dry from any remaining moisture and packaging into a sealable bag (allocated for each specimen) with a piece of tissue paper to prevent scratching and rust.

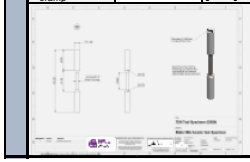
D. SPECIMEN DIAMETER MEASUREMENTS

Each test specimen's test zone diameter was measured ten (10) times using the digital vernier and tabulated to obtain the average diameter.

D1. Monotonic Tensile Test Specimen Diameters

Table D-1: Tensile (TEN) specimens – diameter measurements

TENSILE (MTS) Specimen Dims		ASTM E8	
L_{spec}	121.28	[mm]	Nom Diam
$L_{testzone}$	41.28	[mm]	6.35mm
L_{clamp}	40.00	[mm]	



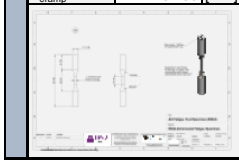


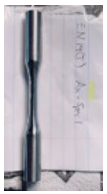
TENSILE (MTS)	Specimen #	Diameter Measurement - PRE-TEST												
		1	2	3	4	5	6	7	8	9	10	AVG	STDEV	
	EN19T-TEN-Spec-1	6.22	6.28	6.26	6.19	6.23	6.23	6.28	6.19	6.20	6.21	**6.229**	0.034	[mm]
	EN19T-TEN-Spec-2	6.48	6.46	6.43	6.38	6.37	6.35	6.32	6.33	6.31	6.33	**6.376**	0.061	[mm]
	EN19T-TEN-Spec-3	6.37	6.36	6.35	6.33	6.27	6.30	6.26	6.21	6.20	6.20	**6.285**	0.067	[mm]
	EN19T-TEN-Spec-4	6.08	6.09	6.09	6.11	6.09	6.10	6.07	6.05	6.04	6.03	**6.075**	0.027	[mm]
	EN19T-TEN-Spec-5	6.23	6.17	6.19	6.16	6.23	6.17	6.14	6.12	6.19	6.20	**6.180**	0.036	[mm]
*	EN19T-TEN-Spec-6	6.18	6.17	6.16	6.16	6.15	6.14	6.12	6.13	6.12	6.11	**6.144**	0.024	[mm]
*	EN19T-TEN-Spec-7	6.18	6.16	6.18	6.18	6.15	6.14	6.19	6.13	6.16	6.15	**6.162**	0.020	[mm]
*	EN19T-TEN-Spec-8	6.32	6.35	6.32	6.35	6.25	6.28	6.24	6.25	6.24	6.19	**6.279**	0.054	[mm]
*	EN19T-TEN-Spec-9	6.33	6.36	6.33	6.36	6.31	6.29	6.28	6.31	6.26	6.27	**6.310**	0.035	[mm]
*	EN19T-TEN-Spec-10	6.40	6.39	6.40	6.42	6.35	6.34	6.32	6.35	6.30	6.25	**6.352**	0.053	[mm]

D2. Axial Fatigue Test Specimen Diameters

Table D-2: Axial (AX) fatigue specimens – diameter measurements

AXIAL Specimen Dims		ASTME606	
L_{spec}	107.80	[mm]	Nom Diam
$L_{testzone}$	44.00	[mm]	5.75mm
L_{clamp}	31.90	[mm]	



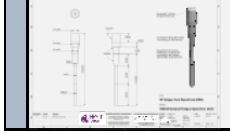


AXIAL	Specimen #	Diameter Measurement - AFTER TESTING @ FAILURE POINT												
		1	2	3	4	5	6	7	8	9	10	AVG	STDEV	
	EN19T-AX-Spec-1	5.82	5.83	5.83	5.82	5.80	5.81	5.80	5.81	5.79	5.80	**5.811**	0.014	[mm]
	EN19T-AX-Spec-2	5.68	5.67	5.71	5.72	5.70	5.68	5.66	5.65	5.72	5.71	**5.690**	0.025	[mm]
	EN19T-AX-Spec-3	5.70	5.70	5.68	5.74	5.70	5.73	5.73	5.71	5.71	5.73	**5.713**	0.019	[mm]
	EN19T-AX-Spec-4	5.73	5.67	5.68	5.73	5.72	5.77	5.75	5.72	5.69	5.74	**5.720**	0.032	[mm]
	EN19T-AX-Spec-5	5.66	5.68	5.74	5.68	5.70	5.69	5.63	5.66	5.65	5.63	**5.672**	0.034	[mm]
	EN19T-AX-Spec-6	5.65	5.60	5.65	5.65	5.64	5.62	5.64	5.65	5.67	5.66	**5.643**	0.020	[mm]
	EN19T-AX-Spec-7	5.74	5.69	5.69	5.74	5.73	5.76	5.68	5.69	5.73	5.76	**5.721**	0.031	[mm]
	EN19T-AX-Spec-8	5.70	5.69	5.69	5.71	5.71	5.72	5.72	5.70	5.74	5.73	**5.711**	0.017	[mm]
	EN19T-AX-Spec-9	-	-	-	-	-	-	-	-	-	-	-	-	[mm]
	EN19T-AX-Spec-10	-	-	-	-	-	-	-	-	-	-	-	-	[mm]

D3. Bending Fatigue Test Specimen Diameters

Table D-3: Bending (B) fatigue specimens – diameter measurements

BENDING Specimen Dims		bench/custom	
L_{spec}	156.00	[mm]	Nom Diam
$L_{testzone}$	40.00	[mm]	5.5mm
L_{clamp}	30.00	[mm]	
$L_{cantilever}$	114.00	[mm]	





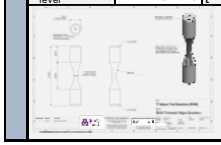
BENDING	Specimen #	Diameter Measurement - AFTER TESTING @ FAILURE POINT												
		1	2	3	4	5	6	7	8	9	10	AVG	STDEV	
	EN19T-B-Spec-1	5.49	5.49	5.49	5.48	5.48	5.50	5.52	5.49	5.50	5.49	**5.493**	0.012	[mm]
	EN19T-B-Spec-2	5.44	5.42	5.43	5.43	5.42	5.41	5.42	5.42	5.43	5.42	**5.424**	0.008	[mm]
	EN19T-B-Spec-3	5.55	5.53	5.55	5.56	5.55	5.57	5.54	5.55	5.56	5.56	**5.552**	0.011	[mm]
	EN19T-B-Spec-4	5.59	5.80	5.76	5.74	5.75	5.71	5.74	5.73	5.75	5.77	**5.734**	0.056	[mm]
	EN19T-B-Spec-5	5.55	5.53	5.54	5.54	5.55	5.55	5.57	5.54	5.53	5.55	**5.545**	0.012	[mm]
	EN19T-B-Spec-6	5.65	5.73	5.60	5.70	5.66	5.65	5.64	5.61	5.62	5.64	**5.650**	0.040	[mm]
	EN19T-B-Spec-7	5.61	5.62	5.60	5.60	5.61	5.60	5.59	5.60	5.61	5.59	**5.603**	0.009	[mm]
	EN19T-B-Spec-8	na	na	na	na	na	na	na	na	na	na	-	-	[mm]
	EN19T-B-Spec-9	-	-	-	-	-	-	-	-	-	-	-	-	[mm]
	EN19T-B-Spec-10	-	-	-	-	-	-	-	-	-	-	-	-	[mm]

Note that B-Spec8 was omitted due to a manufacturing error/inconsistency (near the critical stressed area) that would have caused improper test results.

D4. Torsion Fatigue Test Specimen Diameters

Table D-4: Torsion (T) fatigue specimens – diameter measurements

TORSION Specimen Dims		bench specif	
L_{spec}	90.00	[mm]	Nom Diam
$L_{testzone}$	40.00	[mm]	6.5mm
L_{clamp}	25.00	[mm]	
L_{lever}	115-118	[mm]	



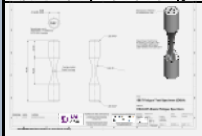


TORSION	Specimen #	Diameter Measurement - PRE-TEST												
		1	2	3	4	5	6	7	8	9	10	AVG	STDEV	
	EN19T-T-Spec-1	6.54	6.54	6.54	6.57	6.54	6.58	6.57	6.55	6.53	6.52	**6.548**	0.019	[mm]
	EN19T-T-Spec-2	6.52	6.52	6.53	6.51	6.51	6.54	6.52	6.51	6.56	6.54	**6.526**	0.016	[mm]
	EN19T-T-Spec-3	6.52	6.52	6.54	6.54	6.54	6.55	6.54	6.53	6.57	6.53	**6.538**	0.015	[mm]
	EN19T-T-Spec-4	6.53	6.53	6.55	6.56	6.57	6.56	6.55	6.55	6.56	6.55	**6.551**	0.013	[mm]
	EN19T-T-Spec-5	6.53	6.51	6.53	6.52	6.53	6.52	6.54	6.52	6.51	6.52	**6.523**	0.009	[mm]
	EN19T-T-Spec-6	6.53	6.51	6.53	6.53	6.53	6.55	6.54	6.53	6.53	6.54	**6.532**	0.010	[mm]
	EN19T-T-Spec-7	6.57	6.57	6.57	6.58	6.57	6.60	6.59	6.60	6.59	6.58	**6.582**	0.012	[mm]
	EN19T-T-Spec-8	6.58	6.54	6.58	6.60	6.57	6.58	6.57	6.56	6.56	6.57	**6.571**	0.016	[mm]
	EN19T-T-Spec-9	6.56	6.56	6.54	6.57	6.57	6.57	6.55	6.54	6.56	6.56	**6.558**	0.011	[mm]
	EN19T-T-Spec-10	-	-	-	-	-	-	-	-	-	-	-	-	[mm]

D5. Bending-Torsion Fatigue Test Specimen Diameters

Table D-5: Bending-Torsion (BT) fatigue specimens – diameter (and length) measurements

B&T Specimen Dims		bench specif	
L_{spec}	90.16	[mm]	Nom Diam
$L_{testzone}$	40.00	[mm]	6.5mm
L_{clamp}	25.00	[mm]	
L_{lever}	101-104	[mm]	



Nom Length
90mm

B&T



Specimen #	Diameter Measurement - PRE-TEST												
	1	2	3	4	5	6	7	8	9	10	AVG	STDEV	
EN19T-BT-Spec-1	6.53	6.51	6.51	6.52	6.53	6.55	6.53	6.52	6.53	6.54	**6.527**	0.013	[mm]
EN19T-BT-Spec-2	6.52	6.52	6.53	6.52	6.54	6.54	6.55	6.57	6.53	6.52	**6.534**	0.016	[mm]
EN19T-BT-Spec-3	6.57	6.57	6.56	6.55	6.55	6.58	6.55	6.55	6.57	6.55	**6.560**	0.012	[mm]
EN19T-BT-Spec-4	6.55	6.55	6.54	6.57	6.56	6.54	6.53	6.55	6.56	6.53	**6.548**	0.013	[mm]
EN19T-BT-Spec-5	6.56	6.55	6.56	6.56	6.55	6.54	6.56	6.55	6.56	6.53	**6.552**	0.010	[mm]
EN19T-BT-Spec-6	6.55	6.53	6.57	6.54	6.55	6.55	6.58	6.57	6.56	6.54	**6.554**	0.016	[mm]
EN19T-BT-Spec-7	6.56	6.55	6.59	6.55	6.55	6.57	6.56	6.58	6.57	6.55	**6.563**	0.014	[mm]
EN19T-BT-Spec-8	6.54	6.52	6.54	6.53	6.53	6.54	6.56	6.53	6.54	6.56	**6.539**	0.013	[mm]
EN19T-BT-Spec-9	6.56	6.58	6.56	6.57	6.56	6.57	6.55	6.55	6.56	6.57	**6.563**	0.009	[mm]
EN19T-BT-Spec-10	6.64	6.65	6.65	6.65	6.64	6.66	6.67	6.64	6.66	6.67	**6.653**	0.012	[mm]
EN19T-BT-Spec-11	6.56	6.56	6.59	6.56	6.57	6.56	6.57	6.56	6.59	6.56	**6.568**	0.012	[mm]
EN19T-BT-Spec-12	6.58	6.59	6.57	6.56	6.56	6.58	6.57	6.57	6.58	6.55	**6.571**	0.012	[mm]
EN19T-BT-Spec-13	6.53	6.52	6.53	6.54	6.56	6.53	6.54	6.56	6.53	6.55	**6.539**	0.014	[mm]
EN19T-BT-Spec-14	6.58	6.56	6.59	6.58	6.58	6.57	6.58	6.57	6.57	6.59	**6.577**	0.009	[mm]
EN19T-BT-Spec-15	6.59	6.56	6.57	6.56	6.58	6.56	6.58	6.57	6.56	6.58	**6.571**	0.011	[mm]
EN19T-BT-Spec-16	6.57	6.56	6.56	6.57	6.57	6.57	6.59	6.58	6.58	6.59	**6.574**	0.011	[mm]
EN19T-BT-Spec-17	6.60	6.59	6.59	6.60	6.57	6.57	6.58	6.59	6.59	6.61	**6.589**	0.013	[mm]
EN19T-BT-Spec-18	6.63	6.64	6.64	6.65	6.62	6.63	6.62	6.61	6.64	6.61	**6.629**	0.014	[mm]
Specimen #	**LENGTH Measurement**												
	1	2	3	4	5	6	7	8	9	10	AVG	STDEV	
EN19T-BT-Spec-1	90.02	89.98	89.99	90.01	89.99	90.01	90.00	89.98	90.00	90.02	**90.000**	0.015	[mm]
EN19T-BT-Spec-2	89.87	89.85	89.85	89.85	89.89	89.90	89.87	89.88	89.89	89.88	**89.873**	0.018	[mm]
EN19T-BT-Spec-3	89.96	89.99	90.00	90.03	90.02	90.03	90.00	89.98	89.99	90.01	**90.001**	0.022	[mm]
EN19T-BT-Spec-4	90.08	90.06	90.05	90.06	90.08	90.05	90.04	90.05	90.07	90.09	**90.063**	0.016	[mm]
EN19T-BT-Spec-5	89.98	89.97	89.97	89.97	89.97	90.03	89.99	89.98	89.99	89.98	**89.983**	0.018	[mm]
EN19T-BT-Spec-6	90.18	90.18	90.18	90.19	90.19	90.19	90.18	90.18	90.19	90.17	**90.183**	0.007	[mm]
EN19T-BT-Spec-7	90.06	90.06	90.07	90.07	90.07	90.05	90.06	90.05	90.05	90.03	**90.057**	0.013	[mm]
EN19T-BT-Spec-8	90.02	90.02	90.04	89.98	89.99	90.00	89.97	89.96	90.00	90.02	**90.000**	0.025	[mm]
EN19T-BT-Spec-9	89.89	89.90	89.92	89.94	89.89	89.91	89.93	89.93	89.92	89.91	**89.914**	0.017	[mm]
EN19T-BT-Spec-10	89.95	89.96	89.97	89.98	90.00	90.01	89.97	89.96	89.94	89.97	**89.971**	0.021	[mm]
EN19T-BT-Spec-11	90.02	90.00	90.03	90.04	90.02	90.02	89.99	90.02	90.04	90.01	**90.019**	0.016	[mm]
EN19T-BT-Spec-12	90.06	90.06	90.06	90.06	90.07	90.08	90.07	90.08	90.09	90.07	**90.070**	0.011	[mm]
EN19T-BT-Spec-13	90.04	90.04	90.06	90.06	90.03	90.02	90.00	90.00	90.03	90.02	**90.030**	0.021	[mm]
EN19T-BT-Spec-14	90.06	90.02	90.00	90.00	90.00	90.00	90.00	90.03	90.02	90.01	**90.014**	0.020	[mm]
EN19T-BT-Spec-15	90.16	90.16	90.18	90.17	90.15	90.16	90.13	90.14	90.14	90.16	**90.155**	0.015	[mm]
EN19T-BT-Spec-16	90.45	90.45	90.45	90.45	90.46	90.48	90.47	90.48	90.46	90.48	**90.463**	0.013	[mm]
EN19T-BT-Spec-17	90.04	90.03	90.04	90.04	90.06	90.07	90.03	90.04	90.05	90.06	**90.046**	0.013	[mm]
EN19T-BT-Spec-18	89.99	90.00	90.00	90.00	89.99	90.01	89.99	89.99	90.01	89.99	**89.997**	0.008	[mm]

E. MASS MEASUREMENTS

E1. Calibration Mass Pieces

The load cell calibration masses for the bending (B) fatigue test bench (Figure E-1 below) were measured ten (10) times each and tabulated as in Table E-1 below. The appropriate average masses for calculating the weight (in [N]) were obtained as the reference masses for the calibration (see Figure A-5 and Figure A-6). For these mass measurements, the larger PRW30++ microscale was used (see Appendix B2).

Table E-1: Calibration mass pieces – mass measurements

Mass piece #/ID		Mass Measurment [kg]													
		1	2	3	4	5	6	7	8	9	10	AVG	STDEV		Weight [N]
1	**5.0kg**	4.9968	4.9968	4.9966	4.9966	4.9967	4.9965	4.9966	4.9968	4.9964	4.9963	**4.9966**	0.0002	[kg]	**49.02**
2	**5.0kg**	4.9907	4.9904	4.9902	4.9900	4.9904	4.9902	4.9902	4.9904	4.9903	4.9904	**4.9903**	0.0002	[kg]	**48.96**
1	**10.0kg**	9.9940	9.9940	9.9941	9.9939	9.9940	9.9938	9.9930	9.9939	9.9938	9.9940	**9.9939**	0.0003	[kg]	**98.04**
2	**10.0kg**	9.9958	9.9959	9.9967	9.9957	9.9956	9.9957	9.9957	9.9956	9.9956	9.9957	**9.9958**	0.0003	[kg]	**98.06**



Figure E-1: Calibration weights

E2. Centrifugal Mass Pieces

The centrifugal mass piece pairs (Figure E-2 below) were measured ten (10) times each and tabulated as in Table E-2 below. The appropriate average masses that induce the centrifugal forces on the torsion (T) and bending-torsion (BT) test benches were obtained (see Figure A-7 and Figure A-10). For these mass measurements, the smaller SARTORIUS BP110S microscale was used and was zeroed before each measurement (see Appendix B2). Each mass piece pair (e.g., NUT1-1, BOLT2-2 or washer) was first measured and etched/ground with a Dremel to ensure that both NUT 1's for example (one for the left wheel and one for the right) had the same masses (or very close to it). The mass measurements for each NUT 1 (and others) were tabulated (as measurements 1, 2, …) as the average value between the two NUT 1 masses. The average of the ten (10) NUT 1 measurements was ultimately considered as the single mass value of each NUT 1. The exact process was followed for all the other centrifugal mass pieces (bolts and washers).

Table E-2: Centrifugal mass pieces – mass measurements

Bolts	Centrifugal Bolt Mass Measurement [g]											
	1	2	3	4	5	6	7	8	9	10	AVG [g]	STDEV [g]
BOLT 1 (M5x25)	4.5793	4.5798	4.5797	4.5796	4.5795	4.5797	4.5797	4.5796	4.5795	4.5798	**4.5796**	0.0002
BOLT 2 (M4x25)	2.7859	2.7859	2.7859	2.7855	2.7856	2.7858	2.7858	2.7860	2.7856	2.7859	**2.7858**	0.0002
Washer pair	3.6966	3.6966	3.6966	3.6967	3.6968	3.6967	3.6967	3.6966	3.6965	3.6966	**3.6966**	0.0001

	Nuts	L_{lever} B&T [mm]	L_{lever} T [mm]	Centrifugal Nut Mass Measurement [g]											
				1	2	3	4	5	6	7	8	9	10	AVG [g]	STDEV [g]
BOLT 1	**NUT 1**	**97.85**	**110.72**	10.9095	10.9095	10.9093	10.9089	10.9097	10.9099	10.9093	10.9092	10.9093	10.9093	**10.9094**	0.0003
BOLT 1	**NUT 2**	**98.39**	**111.26**	12.7738	12.7740	12.7743	12.7739	12.7742	12.7741	12.7738	12.7741	12.7740	12.7743	**12.7740**	0.0002
BOLT 1	**NUT 3**	**98.92**	**111.79**	14.4665	14.4662	14.4669	14.4664	14.4666	14.4665	14.4666	14.4667	14.4667	14.4652	**14.4664**	0.0005
BOLT 2	**NUT 4**	**99.47**	**112.35**	17.6665	17.6664	17.6664	17.6667	17.6665	17.6664	17.6667	17.6665	17.6663	17.6664	**17.6665**	0.0001
BOLT 2	**NUT 5**	**100.53**	**113.40**	21.8780	21.8777	21.8776	21.8781	21.8778	21.8778	21.8779	21.8777	21.8779	21.8776	**21.8778**	0.0002
BOLT 1	**NUT 6**	**96.89**	**109.77**	6.2321	6.2320	6.2321	6.2323	6.2321	6.2320	6.2321	6.2320	6.2322	6.2321	**6.2321**	0.0001
BOLT 1	**NUT 7**	**96.59**	**109.47**	5.0781	5.0781	5.0781	5.0781	5.0781	5.0779	5.0780	5.0782	5.0782	5.0781	**5.0781**	0.0001
BOLT 1	**NUT 8**	**96.18**	**109.05**	3.7520	3.7521	3.7521	3.7520	3.7519	3.7519	3.7519	3.7519	3.7520	3.7519	**3.7519**	0.0001
BOLT 2	**NUT 9**	**101.17**	**114.04**	24.7627	24.7629	24.7628	24.7627	24.7627	24.7627	24.7626	24.7625	24.7625	24.7624	**24.7626**	0.0002
BOLT 2	**NUT 10**	**101.96**	**114.83**	28.3069	28.3073	28.3070	28.3070	28.3067	28.3069	28.3070	28.3069	28.3068	28.3070	**28.3069**	0.0002

All nuts were machined from EN8 steel, whereas steel bolts and washers were purchased. The corresponding bolt of each nut is indicated to the left in the table above. Each nut-bolt pair was used with the washers to fasten to each wheel (summing the relevant masses for centrifugal force calculation). The use of the washers (for all bolts) was especially required for the smaller M4x25 [mm] Allen Cap bolts since their heads were slightly too small for the 6 [mm] diameter holes on the bilateral wheels. The general geometric dimensions of the centrifugal nuts are illustrated in Figure E-3 below, along with a schematic of the bilateral wheels (T and BT test bench, lasered Aluminium plates) showing the radial positions where nut-bolt pieces could be fastened. For respective nuts, these dimensions were adapted (depth or outside diameter) to provide a good enough variety of centrifugal masses (as measured) for experimental testing on each fatigue test bench (T and BT).



Figure E-2: Centrifugal mass pieces

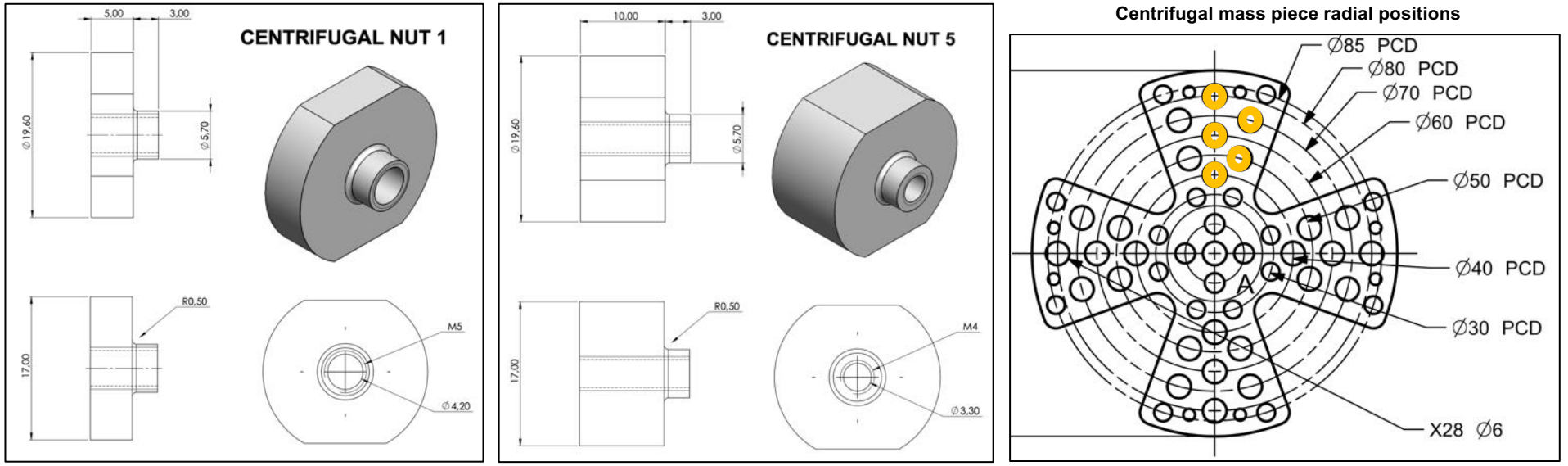
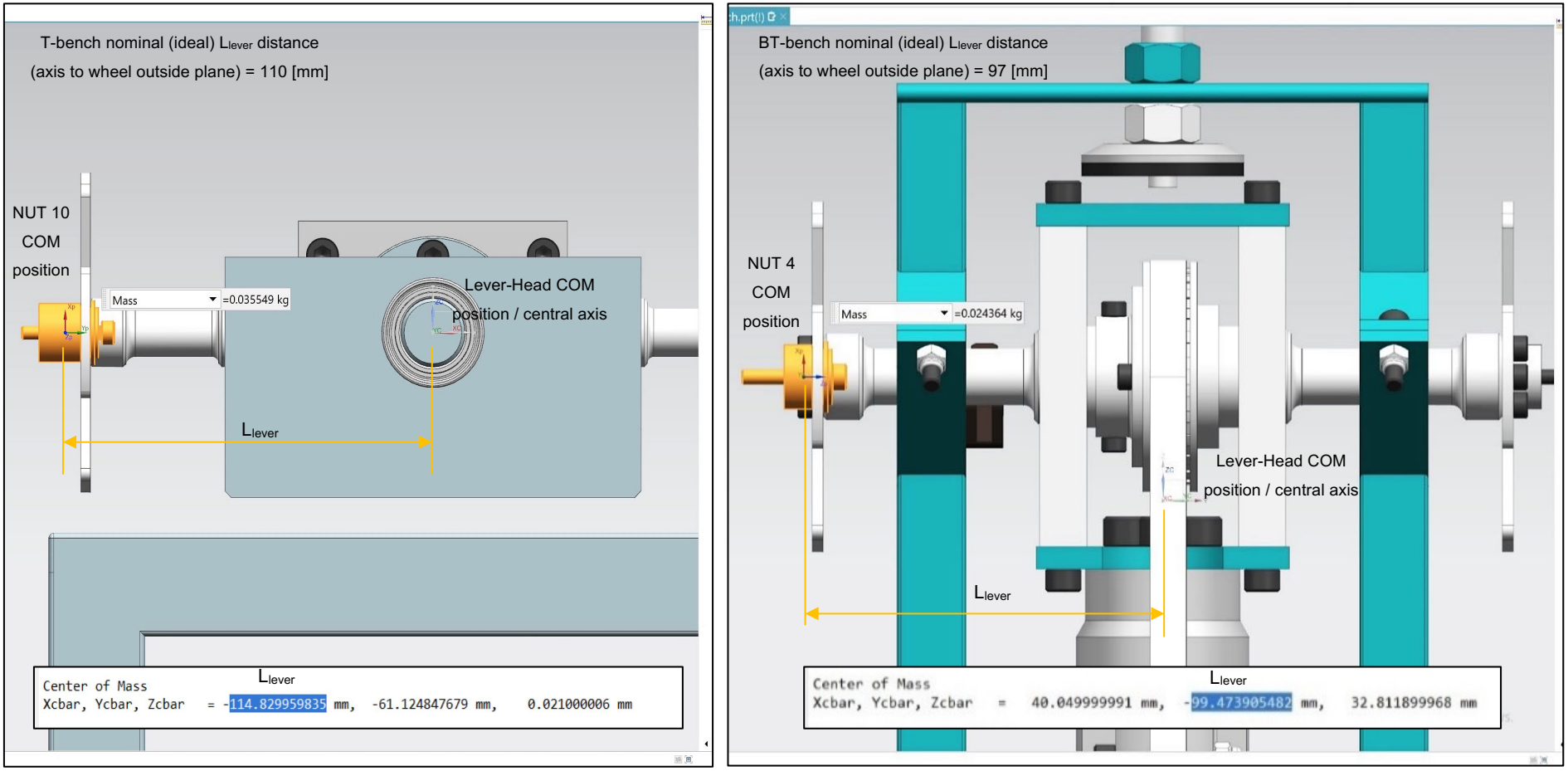


Figure E-3: Centrifugal mass pieces – general nut geometry and radial position options on bilateral wheels

The centrifugal mass piece units (nut-bolt-washers) were fastened with the nut on the outside face (furthest from the central lever-head axis) of each bilateral wheel of the T and BT test benches (at radial positions 20, 25, 30, 35 or 40 [mm]). Each centrifugal mass piece unit has its own centre of mass (COM). Therefore, it was required to obtain/measure the COM distances (moment lever length, L_{lever} in Table E-2 above) from the central axis of the lever-head in each test bench's Siemens NX12 CAD assembly model. This was primarily done to ensure that the correct bending and torsion moments are calculated from the induced centrifugal forces (for each nut) that act at these measured distances (moment levers) from the lever-head central axis. Examples of how this was done for each centrifugal mass unit are illustrated in Figure E-4 below. It will be shown in Appendix F2 that doing this was appropriate since the inherent COM position of a centrifugal mass piece (because of size differences) correspondingly influences the torsional gain. That is, due to different polar mass moment of inertia for each nut considered (see Table F-1).



(a) (b)

Figure E-4: Centrifugal mass pieces – COM distance measurements in (a) T fatigue and (b) BT fatigue test bench CAD model

E3. Bending-Torsion Fatigue Test Bench Head Mass

The biaxial fatigue test bench (Figure A-10) lever-head mass (illustrated in Figure E-5 below) was measured ten (10) times and tabulated as in Table E-3 below. The appropriate average head mass for the bending-torsion (BT) specimen bending modal analyses was obtained (discussed next in Appendix F3) and used in the Siemens NX12 FEA-Nastran environment. The larger PRW30++ microscale was used for these mass measurements, and it was zeroed before each measurement (see Appendix B2). Figure G-2 can be referenced for illustration of how the lever-head would be removed from the test bench and measured.

Table E-3: BT fatigue test bench – lever-head mass measurements

B&T LeverHead	Head Mass Measurment [kg]											
	1	2	3	4	5	6	7	8	9	10	AVG [kg]	STDEV [kg]
Aluminum X-wheels	2.1495	2.1524	2.1459	2.1513	2.1497	2.1524	2.1457	2.1413	2.1489	2.1541	**2.1491**	0.0039
										$m_{leverHead}$	**2.1491**	0.0039

The COM position of this leaver head mass value was obtained from the Siemens NX12 CAD assembly model of the BT fatigue test bench. This is illustrated in Figure E-5 below (selected orange parts of lever-head). For this, every component in the 3D model was assigned the appropriate material properties (steel or Aluminium) to ensure the accuracy of this theoretical COM position.

A user-defined coordinate system was added to the 3D model at the indicated COM position. Digital dimensions were then measured from the specimen inserted at the bottom to this coordinate system. The primary dimension required was the distance from the lever-head COM to the top edge of the specimen hourglass test zone (gauge area). This dimension, 83.16 [mm], was used to extend the top cylinder part of a BT specimen model (originally 25 [mm] long) to provide a point/surface (COM position) to which the lever-head's measured mass is attached (as a mass element) for modal analyses. The assumption for this is that the extended top specimen cylinder effectively represents all the components of the lever-head and their COM (top specimen clamp, bottom head plate, bearing mounts) that fastens to the top of the specimen. The procedure and results of the modal analyses for bending resonance frequencies and gain are further discussed and provided in Appendix F1 and F3.

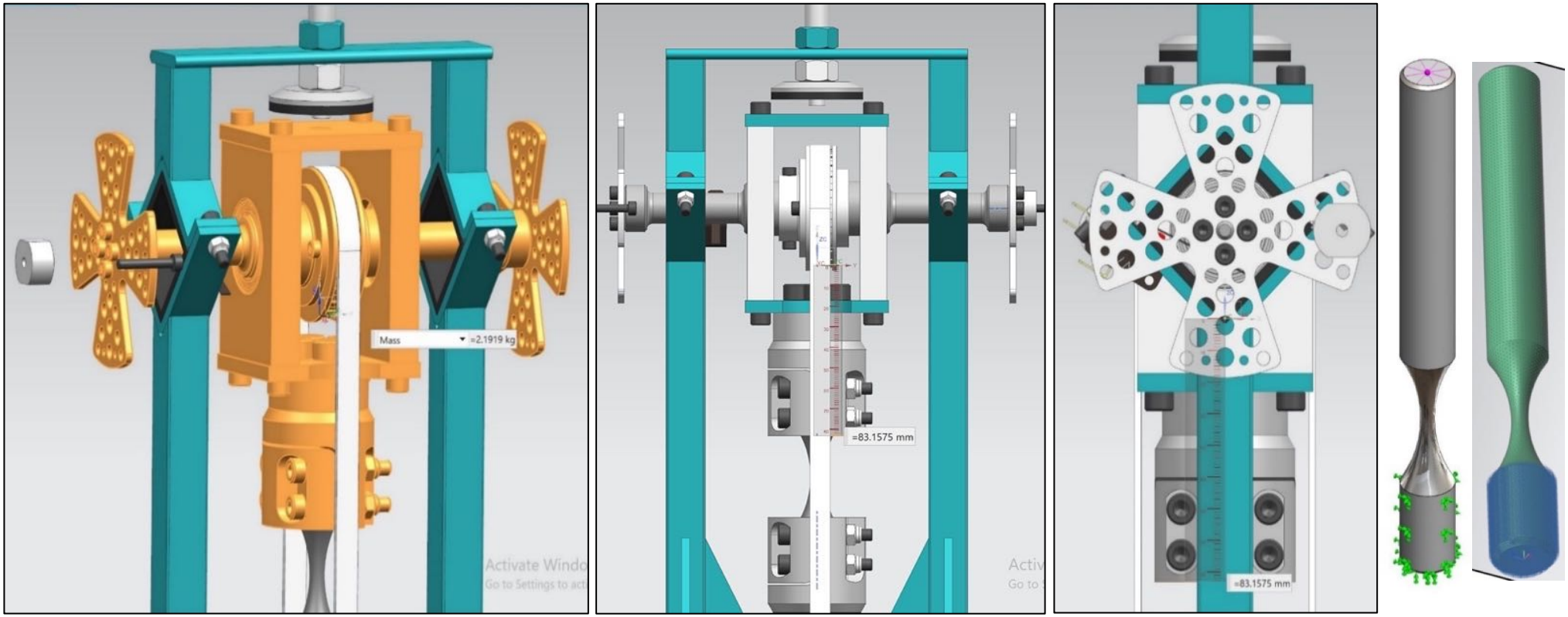


Figure E-5: BT fatigue test bench – lever-head theoretical COM position

F. RESONANCE FREQUENCY AND GAIN CONSIDERATIONS

F1. Methodology for Theoretical Resonance Frequencies and Gain

The theoretical gain discussions to follow include, for completeness and comparative purposes, all three the possible lever-head configurations of each test bench (T or BT) listed below. The **second configuration** was the **primary** one considered and implemented. These configurations include:

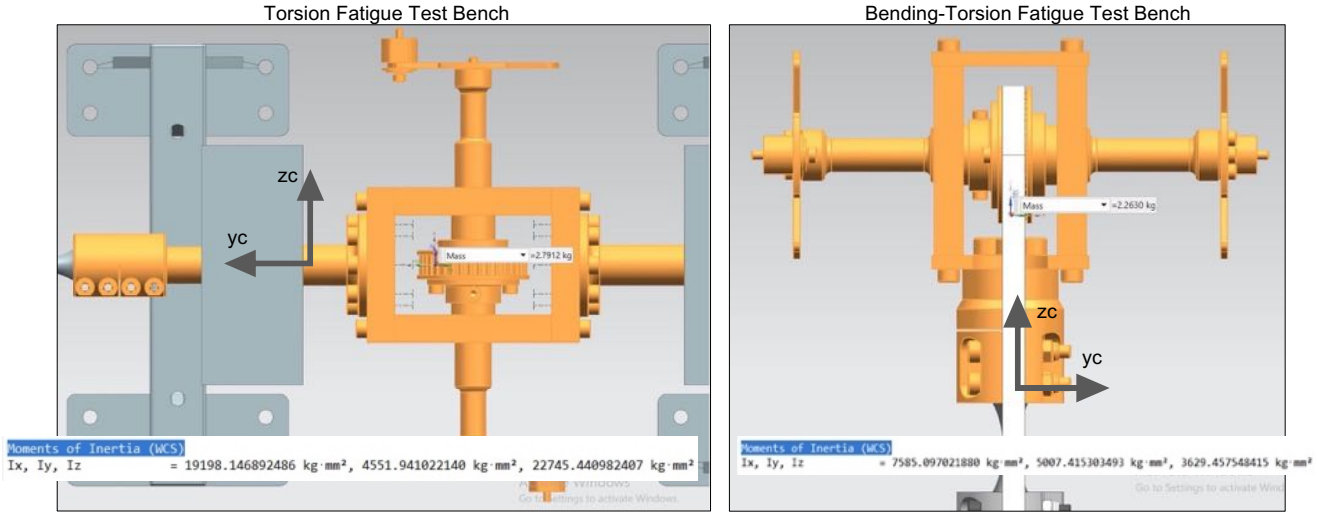
- The ***original lever-head*** configuration (designed) consists of a *steel shaft* and *two steel bilateral wheels* (6 [mm] thick for T and 5 [mm] thick BT bench). This configuration is shown with the ***dashed line curves*** in the theoretical gain curve graphs (in Figure F-6 and Figure F-7 to come), and the relevant natural frequency values of this configuration are identified with the subscript *"**T-T_orig**"*, *"**B-BT_orig**"* or *"**T-BT_orig**"*.
- The ***Aluminium cross-wheel lever-head*** configuration consists of a *steel shaft* and *two 3 [mm] thick Aluminium cross-shaped bilateral wheels*. This configuration is shown with the ***solid line curves*** in the theoretical gain curve graphs (in Figure F-6 and Figure F-7 to come), and the relevant natural frequency values of this configuration are identified with the subscript *"**T-T_XW**"*, *"**B-BT_XW**"* or *"**T-BT_XW**"*.
- The ***Aluminium cross-wheel and Aluminium shaft lever-head*** configuration consist of an *Aluminium shaft* and *two 3 [mm] thick Aluminium cross-shaped bilateral wheels*. This configuration is shown with the ***dotted line curves*** in the theoretical gain curve graphs (in Figure F-6 and Figure F-7 to come), and the relevant natural frequency values of this configuration are identified with the subscript *"**T-T_XWS**"*, *"**B-BT_XWS**"* or *"**T-BT_XWS**"*.

Configurations 2 and 3 above involve the shaft and/or bilateral wheel changes (from steel to Aluminium) that were considered to address the adverse torsional loading gain influence on a test specimen in each test bench. However, the **second lever-head configuration (XW)** was the chosen configuration with which all **experimental testing** was performed on each test bench. The reason for choosing this lever-head configuration (XW) was because more lever-head mass reduction (with configuration 3) would have only been beneficial in further decreasing the torsional loading gain response, which was not required. A lighter lever-head in the bending-torsion bench would have also unavoidably shifted the bending gain response curve too far (higher values) for an arbitrary specimen diameter. An appropriate test speed (below motor maximum) at which the biaxial loading components both have equal gain values (preferred test point) would not be attainable.

TORSION Gain

The theoretical torsional resonance frequency $N_{c;T}$ (of the specimen) and the resultant loading gain G_T (at arbitrary test speed) was considered for the torsion (T) fatigue and the bending-torsion (BT) fatigue test bench using the following method:

- First, the *polar mass moment of inertia* J_0 [kg.m^2] of the entire lever-head assembly in the NX12 CAD test bench model was measured for each of the ten (10) centrifugal nut/bolt options that could be used to induce loading on a specimen. This moment of inertia was measured for the coordinate system axis around which torsional loading would be induced. That is the yc-axis for the T bench model and the zc-axis for the BT-bench model, as shown in Figure F-1 below. Reference Table F-1 and Table F-2 of Appendix F2 and F3 for the values.



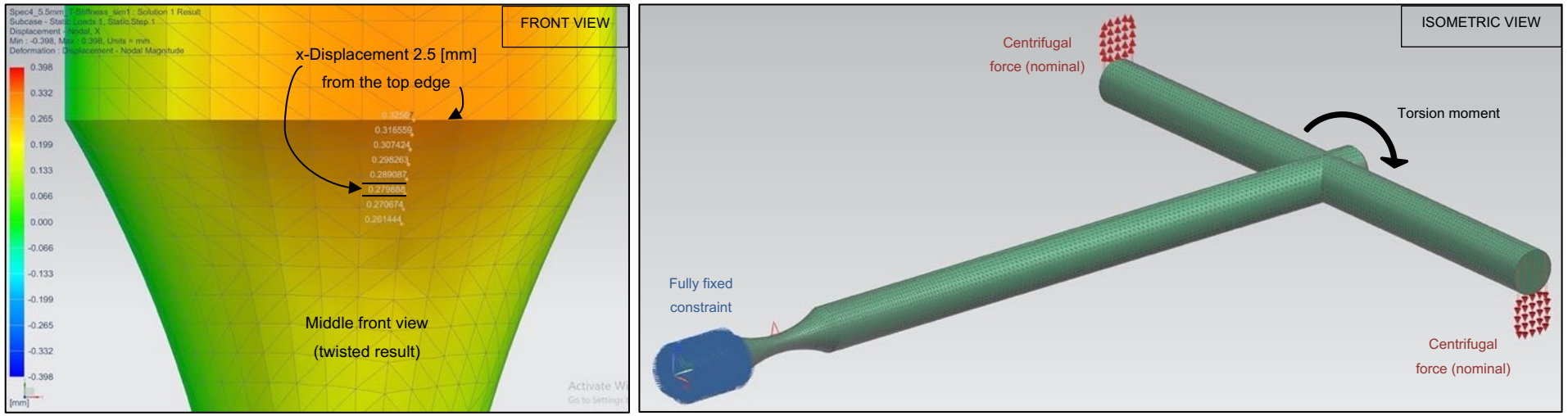
(a) (b)

Figure F-1: (a) T fatigue and (b) BT fatigue test bench – polar mass moments of inertia measurement

- The second step was to calculate the theoretical *torsional stiffness* k_t [N.m/rad] from the measured *torsional angular displacement* θ [rad] of five specimens (5.5 – 7.5 [mm] diameters) under the same *torsional moment* M_t [N.m] in a static FEM simulation using NX12. The stiffness of each specimen was calculated using Equation (F-1) below (from [91]). The angular displacement was, in fact, an inferred calculation (using Equation (F-2) below from [91]). That, with the measured linear x displacement of a point on the specimen surface at a specific radial position r (cylindrical) 2.5 [mm] from the top edge (where the DANTEC would measure torsion displacement), as shown in Figure F-2 below. The static FEM simulation model had a 1 [mm] 3D tetrahedral (CTETRA10) mesh throughout, and 'steel' material was assigned (E_{NX} = 206.9 [GPa]). The specimen model was fully constrained at the bottom, and forces were applied on the tip of each lever arm (representing the lever-head of each test bench), which in turn induced the necessary torsional moment (20 [N.m]) on the specimen. The theoretical stiffness calculation result for each specimen is reported (same for both test benches) in Table F-1 and Table F-2 of Appendix F2 and F3 to follow.

$$k_t = M_t / \theta \tag{F-1}$$

$$\theta = \text{asin}\,(x / r) \tag{F-2}$$



(a) (b)

Figure F-2: Torsional angular displacement – (a) inferring linear x-displacement measurement from (b) static FEM model

- The third step was to calculate the theoretical *torsional resonance frequency* $N_{c;T}$ [Hz] for each of the five considered specimen diameters by substituting the previously identified *polar mass moment of inertia* J_0 [kg.m^2] value of each test bench (T or BT) lever-head (for arbitrarily chosen centrifugal nut piece) and the corresponding specimen *torsional stiffness* k_t [N.m/rad] value into Equation (F-3) below (from [91]). These resonance frequency values are reported for each specimen diameter (rows) and each lever-head configuration (columns) of the test benches in Table F-1 and Table F-2.

$$N_{c;T-T} \; or \; N_{c;T-BT} = \left(\left(\frac{k_t}{J_0}\right)^{1/2}\right) / 2\pi \tag{F-3}$$

- The fourth step was to calculate the theoretical *torsional resonance frequency* $N_{c;T-T;XW}$ or $N_{c;T-BT;XW}$ [Hz] of an arbitrarily sized experimental torsion or bending-torsion fatigue test specimen being considered, and under loading of an arbitrarily chosen centrifugal nut piece by performing linear interpolation (with respect to test specimen diameter) between the ones calculated and reported in the relevant table of each test bench (previous steps). The linear interpolation for intermediate resonance frequency values of a test specimen was assumed appropriate since the calculated $N_{c;T}$ values demonstrated a linear dependency on the diameter of a specimen over the small range of considered diameters (see Figure F-3 on the next page). The arbitrary test specimen resonance frequencies are reported for each test bench (and configuration) at the bottom of Table F-1 and Table F-2.
- The fifth and final step was calculating the theoretical *torsional loading gain* G_T [-] of the arbitrarily sized torsion or bending-torsion fatigue test specimen being considered. That is, for an arbitrarily chosen centrifugal nut piece (for $N_{c;T}$) and test/forced speed/frequency N [Hz], using Equation (F-4) below (from [91-93]). Alternatively, a range of test speeds N [Hz] can be substituted into Equation (F-4) to generate a specimen's torsional loading gain response curve. This curve is illustrated in Figure F-6 (green) and Figure F-7 (pink) of Appendix F2 and F3 to follow for each test bench. Note that N here is the test speed in [Hz] or [rpm] and is not to be confused with the fatigue cycle count N_f [-].

$$G_T = \frac{1}{1-\left(\frac{N}{N_{c;T}}\right)^2} \quad \text{or with damping,} \quad G_T = \frac{1}{\left\{\left[1-\left(\frac{N}{N_{c;T}}\right)^2\right]^2 + \left[2\zeta\frac{N}{N_{c;T}}\right]^2\right\}^{1/2}} \tag{F-4}$$

For the gain equation, it was assumed that there was no experimental damping ζ [-] for either of the test benches' lever-head movements (undamped harmonic vibration). That is, even if there is inherent test bench damping due to, e.g., bearings. However, it could not be appropriately measured experimentally. Instead, as discussed in Section 4.4.2.4 and provided in Appendix H4 and H5, it was decided to perform direct experimental displacement measurements on selected T or BT test specimens during testing. Comparing these displacements with static FEM simulation displacements (under nominal loading, as if G_T = 1) provided the test specimens' experimentally induced loading gain.

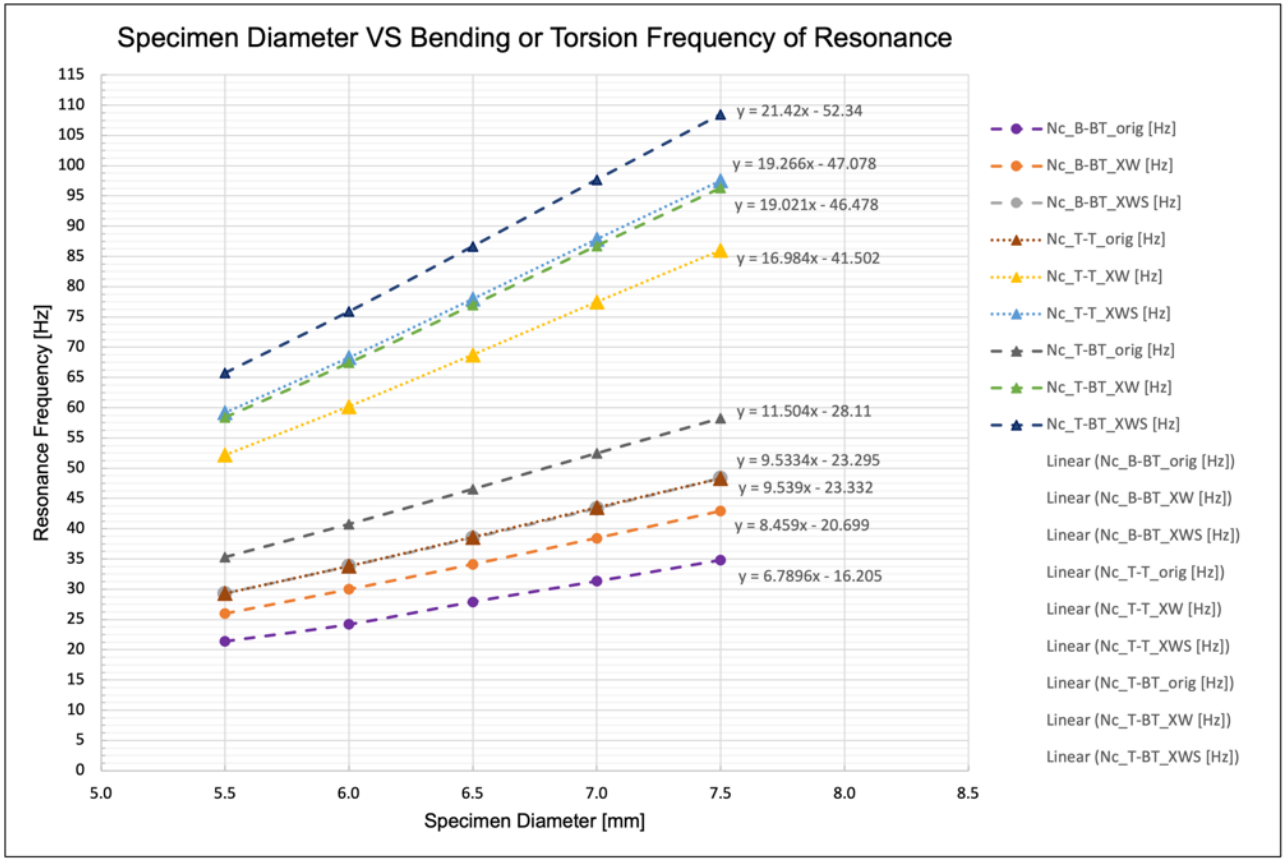
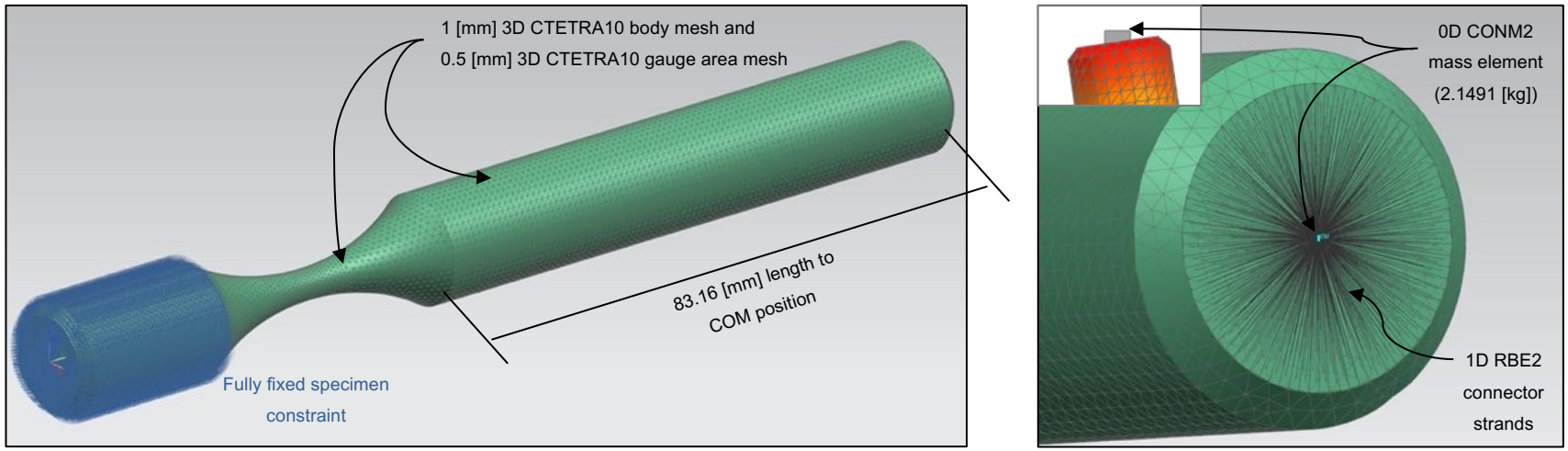


Figure F-3: Linear dependency of torsion and bending resonance frequencies on specimen diameter

BENDING Gain

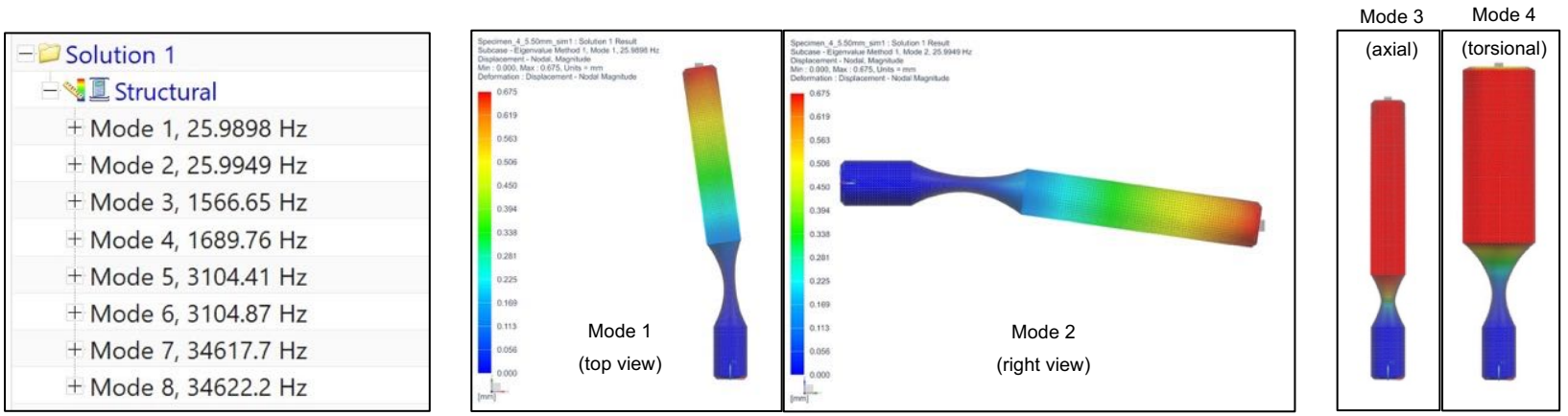
The theoretical bending resonance frequency $N_{c;B}$ (of the specimen) and the resultant loading gain G_B (at arbitrary test speed) was only considered for the bending-torsion (BT) test bench using the method below. That is because negligible bending is induced in the T test bench (theoretically).

- First, the true *lever-head mass* $m_{leverHead}$ [kg] of the entire lever-head assembly that fastens to a test specimen in the BT test bench had to be measured. This was done using the large microscale (Figure B-3 (b)) and is reported in Table E-3 with an average mass of 2.1491 [kg].
- The second step was identifying the *theoretical centre of mass* (COM) *position* of the BT test bench lever-head in the NX12 CAD assembly model. A user-defined coordinate system was assigned to this position. The distance (83.16 [mm]) from this COM position to the top edge of the specimen hourglass gauge area was measured (see Appendix E3 and Figure E-5). Negligible specimen length uncertainty (influencing this measurement) was measured for all the BT specimens (see Appendix D5).
- The third step was to generate the modal analysis FEM model of a BT test specimen (geometry in Figure C-5). The specimen's top cylinder part (originally 25 [mm]) was extended by 58.16 [mm] to provide a point/surface for the theoretical COM position of the lever-head (see Figure E-5).
- The fourth step was (see Figure F-4 on the next page):
  (1) to *assign a material* (steel) to the model,
  (2) to apply a *1.0 [mm] 3D tetrahedral mesh* on the specimen model using *CTETRA10 3D elements,*
  (3) to apply a *0.5 [mm] 3D tetrahedral mesh refinement* on the hourglass *gauge area* of the specimen,
  (4) to apply a *fully fixed constraint* to the bottom of the specimen model,
  (5) to add a *1D rigid body element connector* (RBE2) to the top face of the specimen and
  (6) to finally attach a *0D concentrated mass element* (CONM2) to the RBE2 element centre node and assign the measured lever-head mass value (2.1491 [kg]) to the CONM2 element. Note centrifugal nut masses are not included in this mass, with a negligible contribution.
- The fifth step was to run/solve the modal analysis FEM model to obtain the Mode 1 and Mode 2 theoretical *bending resonance frequencies* N_c [Hz] for each of the five specimen diameters (see example in Figure F-5 below). The average of these bending resonance frequencies $N_{c;B-BT}$ [Hz] is reported for each specimen diameter (5.5 to 7.5 [mm]) in the yellow columns of Table F-3 in Appendix F3. Similarly, this was done using the SolidWorks Student software package, and results were very similar to those obtained using Siemens NX12.



(a) (b)

Figure F-4: BT specimen modal analysis FEM model – (a) CTETRA10 meshed body and fixed constraint with (b) CONM2 element and RBE2 connector



(a) (b) (c)

Figure F-5: BT specimen modal analysis results – (a) theoretical mode 1 to 8 resonance frequencies, (b) bending resonance mode 1 and 2 specimen shapes, and (c) additional mode 3 and 4 shapes

- The sixth step was to calculate the theoretical *bending resonance frequency* $N_{c;B-BT;XW}$ [Hz] of an arbitrarily sized experimental bending-torsion fatigue test specimen being considered by performing linear interpolation (with respect to test specimen diameter) between the ones simulated for the test bench (see the previous step). Linear interpolation for test specimen resonance values was assumed appropriate since the frequency values $N_{c;B-BT}$ (average between bending modes 1-2) demonstrated a linear dependency on the specimen diameter over the small range of considered diameters (see Figure F-3). The arbitrary test specimen bending resonance frequency values are reported at the bottom of Table F-3 in Appendix F3 to follow (for each BT test bench configuration).
- The seventh and final step was to calculate the theoretical *bending loading gain* G_B [-] of the arbitrarily sized bending-torsion fatigue test specimen being considered at an arbitrary test/forced speed/frequency N [Hz], using the previous Equation (F-4) (from [91-93]). Alternatively, a range of test speeds N [Hz] can be substituted into this equation to generate the bending loading gain response curve of the specimen, as was done for illustration in Figure F-7 (purple) of Appendix F3 to follow.

For the gain equation used, it was again assumed that no experimental damping ζ [-] was present for the BT test bench lever-head movement (undamped harmonic vibration). That is because it could also not be appropriately measured for this test bench. Instead, as discussed in Section 4.4.2.4 and provided in Appendix H5, it was decided to perform direct experimental displacement measurements on a selected BT test specimen during testing. Comparing these displacements with static FEM simulation displacements (under nominal loading, as if G_B = 1) provided the test specimens' experimentally induced bending loading gain. In these measurements, it was also shown (later in Appendix H5) that the experimental gain response was very different (lower and shifted curve) from the theoretically calculated gain, which further reinforced the decision to perform direct experimental displacement measurements instead.

The preferred test point (or test speed) for the BT fatigue tests is where both the G_T and G_B reach the same value (for XW configuration). It was shown (see Figure F-7) that each BT fatigue test specimen had to pass through its bending resonance frequency (where G_B >>>) to get to this condition of equal biaxial loading gain for testing. This, however, had no direct concern or influence (for damaging the specimens) during this study since a bending resonance suppressor was previously designed and implemented to address this problem (shown in Figure A-10 and Figure A-11) during the initial tests done on this BT fatigue test bench [28].

F2. Torsion Fatigue Test Bench – Resonance Frequencies and Gain

Table F-1: T fatigue test bench – theoretical polar mass moments of inertia and torsional resonance frequencies

T-bench Lever Head - Polar MASS Moments of Inertia		no nuts $J_{0;NX_WCS}$ [kg.m^2]	NUT 1 $J_{0;NX_WCS}$ [kg.m^2]	NUT 2 $J_{0;NX_WCS}$ [kg.m^2]	NUT 3 $J_{0;NX_WCS}$ [kg.m^2]	NUT 4 $J_{0;NX_WCS}$ [kg.m^2]	NUT 5 $J_{0;NX_WCS}$ [kg.m^2]	NUT 6 $J_{0;NX_WCS}$ [kg.m^2]	NUT 7 $J_{0;NX_WCS}$ [kg.m^2]	NUT 8 $J_{0;NX_WCS}$ [kg.m^2]	NUT 9 $J_{0;NX_WCS}$ [kg.m^2]	NUT 10 $J_{0;NX_WCS}$ [kg.m^2]
Original steel 6mm thick wheels (0.4073kg ea)	Ix	0.020668	0.020726	0.020733	0.020741	0.020761	0.020779	0.020709	0.020704	0.020699	0.020978	0.020993
Original steel shaft (0.5258kg)	**Iy**	**0.012718**	**0.013889**	**0.013938**	**0.013986**	**0.014116**	**0.014255**	**0.013779**	**0.013744**	**0.013708**	**0.014364**	**0.014448**
Total head mass = 3.4804kg	Iz	0.031032	0.032260	0.032317	0.032372	0.032521	0.032678	0.032134	0.032094	0.032053	0.032986	0.033084
Aluminum 3mm thick Xwheels (0.02709kg ea)	Ix	0.019050	0.019113	0.019122	0.019130	0.019151	0.019171	0.019096	0.019090	0.019084	0.019184	0.019198
Original steel shaft (0.5258kg)	**Iy**	**0.003593**	**0.003984**	**0.004037**	**0.004090**	**0.004226**	**0.004359**	**0.003874**	**0.003842**	**0.003807**	**0.004450**	**0.004552**
Total head mass = 2.7201kg	Iz	0.021641	0.022094	0.022155	0.022216	0.022374	0.022525	0.021967	0.021929	0.021890	0.022629	0.022745
Aluminum 3mm thick Xwheels (0.02709kg ea)	Ix	0.018854	0.018921	0.018930	0.018939	0.018962	0.018982	0.018902	0.018897	0.018891	0.018996	0.019011
Aluminum shaft (0.1821kg)	**Iy**	**0.002579**	**0.002969**	**0.003022**	**0.003076**	**0.003212**	**0.003344**	**0.002860**	**0.002827**	**0.002793**	**0.003435**	**0.003537**
Total head mass = 2.3764kg	Iz	0.020450	0.020907	0.020968	0.021030	0.021189	0.021342	0.020779	0.020741	0.020701	0.021446	0.021563

							T- specimen: Torsional resonance frequency ($N_{C;T;T}$)						
Specimen / SIM Nr	Diameter [mm]	Mt [Nm]	Radius of Measure [mm]	x-Displ NX [mm]	Θ [rad]	kt [Nm/rad]	$\omega_{n_T\text{-}T_orig}$ [rad/s]	$Nc_T\text{-}T_orig$ [Hz]	ω_{n_XW} [rad/s]	$Nc_T\text{-}T_XW$ [Hz]	ω_{n_XWS} [rad/s]	$Nc_T\text{-}T_XWS$ [Hz]	
Specimen 1	5.50	20.00	6.84	0.279888	0.04093	488.64	183.91	**29.27**	327.64	**52.15**	371.66	**59.15**	
Specimen 2	6.00	20.00	6.89	0.211640	0.03073	650.92	212.26	**33.78**	378.15	**60.18**	428.96	**68.27**	
Specimen 3	6.50	20.00	6.94	0.163492	0.02356	848.78	242.38	**38.58**	431.82	**68.73**	489.84	**77.96**	
Specimen 4	7.00	20.00	6.99	0.129696	0.01856	1077.85	273.14	**43.47**	486.61	**77.45**	551.99	**87.85**	
Specimen 5	7.50	20.00	7.04	0.106027	0.01506	1328.30	303.22	**48.26**	540.19	**85.97**	612.78	**97.53**	
								V		V		V	
								V		V		V	
							$N_{C;T\text{-}T;orig}$	39.05	$N_{C;T\text{-}T;XW}$	69.56	$N_{C;T\text{-}T;XWS}$	78.91	[Hz]
								2342.77		4173.77		4734.57	[rpm]
					for current specimen torsion G=1		$N_{run;T\text{-}T;orig}$	55.22	$N_{run;T\text{-}T;XW}$	98.38	$N_{run;T\text{-}T;XWS}$	111.59	[Hz]
								3313.18		5902.61		6695.69	[rpm]
					% of motor maximum speed (3000 rpm)			110.44		196.75		223.19	[%]
					Time to 1 million cycles			5.03		2.82		2.49	[hrs]

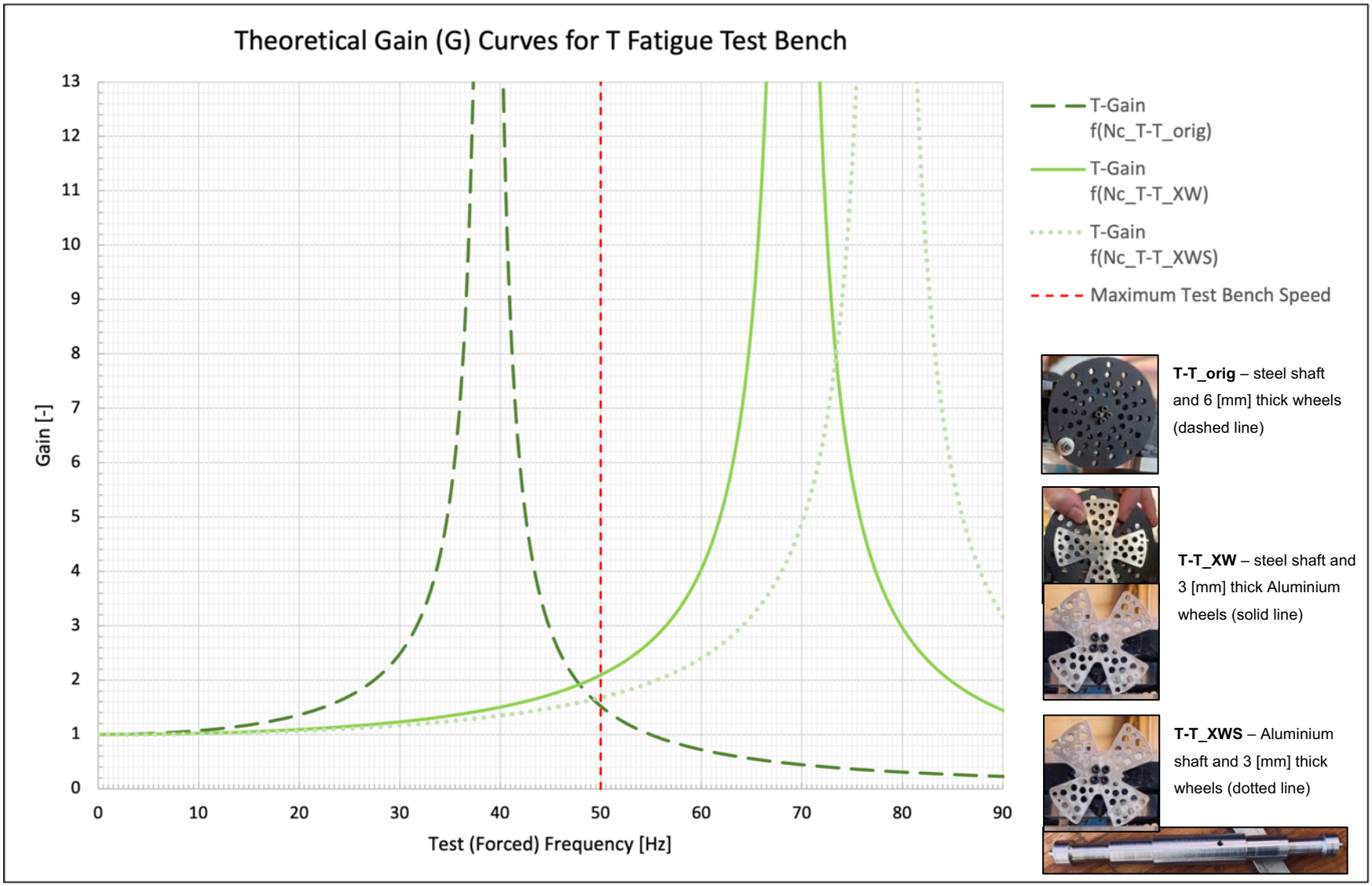


Figure F-6: T fatigue test bench - theoretical torsion loading gain curves

F3. Bending-Torsion Fatigue Test Bench – Resonance Frequencies and Gain

Table F-2: BT fatigue test bench – theoretical polar mass moments of inertia and torsional resonance frequencies

BT-bench Lever Head - Polar MASS Moments of Inertia		no nuts $J_{0;NX_WCS}$ [kg.m^2]	NUT 1 $J_{0;NX_WCS}$ [kg.m^2]	NUT 2 $J_{0;NX_WCS}$ [kg.m^2]	NUT 3 $J_{0;NX_WCS}$ [kg.m^2]	NUT 4 $J_{0;NX_WCS}$ [kg.m^2]	NUT 5 $J_{0;NX_WCS}$ [kg.m^2]	NUT 6 $J_{0;NX_WCS}$ [kg.m^2]	NUT 7 $J_{0;NX_WCS}$ [kg.m^2]	NUT 8 $J_{0;NX_WCS}$ [kg.m^2]	NUT 9 $J_{0;NX_WCS}$ [kg.m^2]	NUT 10 $J_{0;NX_WCS}$ [kg.m^2]
Original steel 5mm thick wheels (0.3353kg ea)	Ix	0.013478	0.013835	0.013887	0.013941	0.014065	0.014198	0.013724	0.013691	0.013656	0.014624	0.014733
Original steel shaft (0.5078kg)	Iy	0.006312	0.006402	0.006415	0.006428	0.006456	0.006487	0.006373	0.006365	0.006356	0.006844	0.006874
Total head mass = 2.8089kg	**Iz**	**0.009089**	**0.009420**	**0.009467**	**0.009514**	**0.009636**	**0.009752**	**0.009324**	**0.009295**	**0.009265**	**0.009833**	**0.009923**
Aluminum 3mm thick Xwheels (0.02679kg ea)	Ix	0.006791	0.007105	0.007150	0.007195	0.007309	0.007422	0.007013	0.006985	0.006957	0.007499	0.007585
Original steel shaft (0.5078kg)	Iy	0.004837	0.004911	0.004920	0.004929	0.004954	0.004976	0.004890	0.004884	0.004877	0.004991	0.005007
Total head mass = 2.1919kg	**Iz**	**0.002774**	**0.003114**	**0.003162**	**0.003210**	**0.003334**	**0.003455**	**0.003015**	**0.002985**	**0.002954**	**0.003537**	**0.003629**
Aluminum 3mm thick Xwheels (0.02679kg ea)	Ix	0.005720	0.006044	0.006089	0.006136	0.006254	0.006369	0.005949	0.005920	0.005891	0.006446	0.006535
Aluminum shaft (0.1758kg)	Iy	0.004511	0.004594	0.004604	0.004615	0.004643	0.004669	0.004570	0.004563	0.004556	0.004683	0.004701
Total head mass = 1.8600kg	**Iz**	**0.002007**	**0.002347**	**0.002394**	**0.002443**	**0.002567**	**0.002687**	**0.002247**	**0.002217**	**0.002186**	**0.002769**	**0.002862**

							BT- specimen: Torsional resonance frequency ($N_{C;T;BT}$)					
Specimen / SIM Nr	Diameter [mm]	Mt [Nm]	Radius of Measure [mm]	x-Displ NX [mm]	ϴ [rad]	kt [Nm/rad]	ωn_T-BT_orig [rad/s]	Nc_T-BT_orig [Hz]	ωn_XW [rad/s]	Nc_T-BT_XW [Hz]	ωn_XWS [rad/s]	Nc_T-BT_XWS [Hz]
Specimen 1	5.50	20.00	6.84	0.279888	0.04093	488.64	221.91	**35.32**	366.92	**58.40**	413.20	**65.76**
Specimen 2	6.00	20.00	6.89	0.211640	0.03073	650.92	256.12	**40.76**	423.49	**67.40**	476.90	**75.90**
Specimen 3	6.50	20.00	6.94	0.163492	0.02356	848.78	292.47	**46.55**	483.59	**76.97**	544.59	**86.67**
Specimen 4	7.00	20.00	6.99	0.129696	0.01856	1077.85	329.58	**52.45**	544.95	**86.73**	613.69	**97.67**
Specimen 5	7.50	20.00	7.04	0.106027	0.01506	1328.30	365.88	**58.23**	604.96	**96.28**	681.27	**108.43**
								\/		\/		\/
								\/		\/		\/
							$N_{c;T-BT;orig}$	47.12	$N_{c;T-BT;XW}$	77.90	$N_{c;T-BT;XWS}$	87.73 [Hz]
								2826.92		4674.19		5263.76 [rpm]
						for current specimen torsion G=1	$N_{run;T-BT;orig}$	66.63	$N_{run;T-BT;XW}$	110.17	$N_{run;T-BT;XWS}$	124.07 [Hz]
								3997.87		6610.30		7444.08 [rpm]
						% of motor maximum speed (3000 rpm)		133.26		220.34		248.14 [%]
						Time to 1 million cycles		4.17		2.52		2.24 [hrs]

Table F-3: BT fatigue test bench – theoretical bending resonance frequencies

Specimen / SIM	Diameter [mm]	NX12 - Original 2020 (2.7787kg true head mass) Mode 1 Nc [Hz]	Mode 2 Nc [Hz]	Mode 3/4/6 Nc [Hz]	Nc_B-BT_orig [Hz]	NX12 - XW (2.1491kg true head mass) Mode 1 Nc [Hz]	Mode 2 Nc [Hz]	Nc_B-BT_XW [Hz]	NX12 - XWS (1.86kg theoretical head mass) Mode 1 Nc [Hz]	Mode 2 Nc [Hz]	Nc_B-BT_XWS [Hz]
Specimen 1	5.50	21.397	21.401	1613.090	**21.40**	25.990	25.995	**25.99**	29.317	29.323	**29.32**
Specimen 2	6.00	24.189	24.191	1809.600	**24.19**	29.964	29.973	**29.97**	33.799	33.809	**33.80**
Specimen 3	6.50	27.915	27.918	2095.120	**27.92**	34.118	34.122	**34.12**	38.484	38.488	**38.49**
Specimen 4	7.00	31.323	31.328	2345.100	**31.33**	38.436	38.443	**38.44**	43.352	43.361	**43.36**
Specimen 5	7.50	34.803	34.808	2598.400	**34.81**	42.903	42.906	**42.90**	48.389	48.393	**48.39**

BT- specimen: Bending resonance frequency ($N_{C;B}$)

					V			V			V	
			$N_{c;B\text{-}BT;orig}$	28.24	[Hz]		$N_{c;B\text{-}BT;XW}$	34.53	[Hz]		$N_{c;B\text{-}BT;XWS}$	38.95	[Hz]
				1694.63	[rpm]			2072.09	[rpm]			2337.19	[rpm]
for current specimen bending G=1			$N_{run;B\text{-}BT;orig}$	39.94	[Hz]		$N_{run;B\text{-}BT;XW}$	48.84	[Hz]		$N_{run;B\text{-}BT;XWS}$	55.09	[Hz]
				2396.57	[rpm]			2930.37	[rpm]			3305.29	[rpm]
% of motor maximum speed (3000 rpm)				79.89	[%]			97.68	[%]			110.18	[%]
Time to 1 million cycles				6.95	[hrs]			5.69	[hrs]			5.04	[hrs]



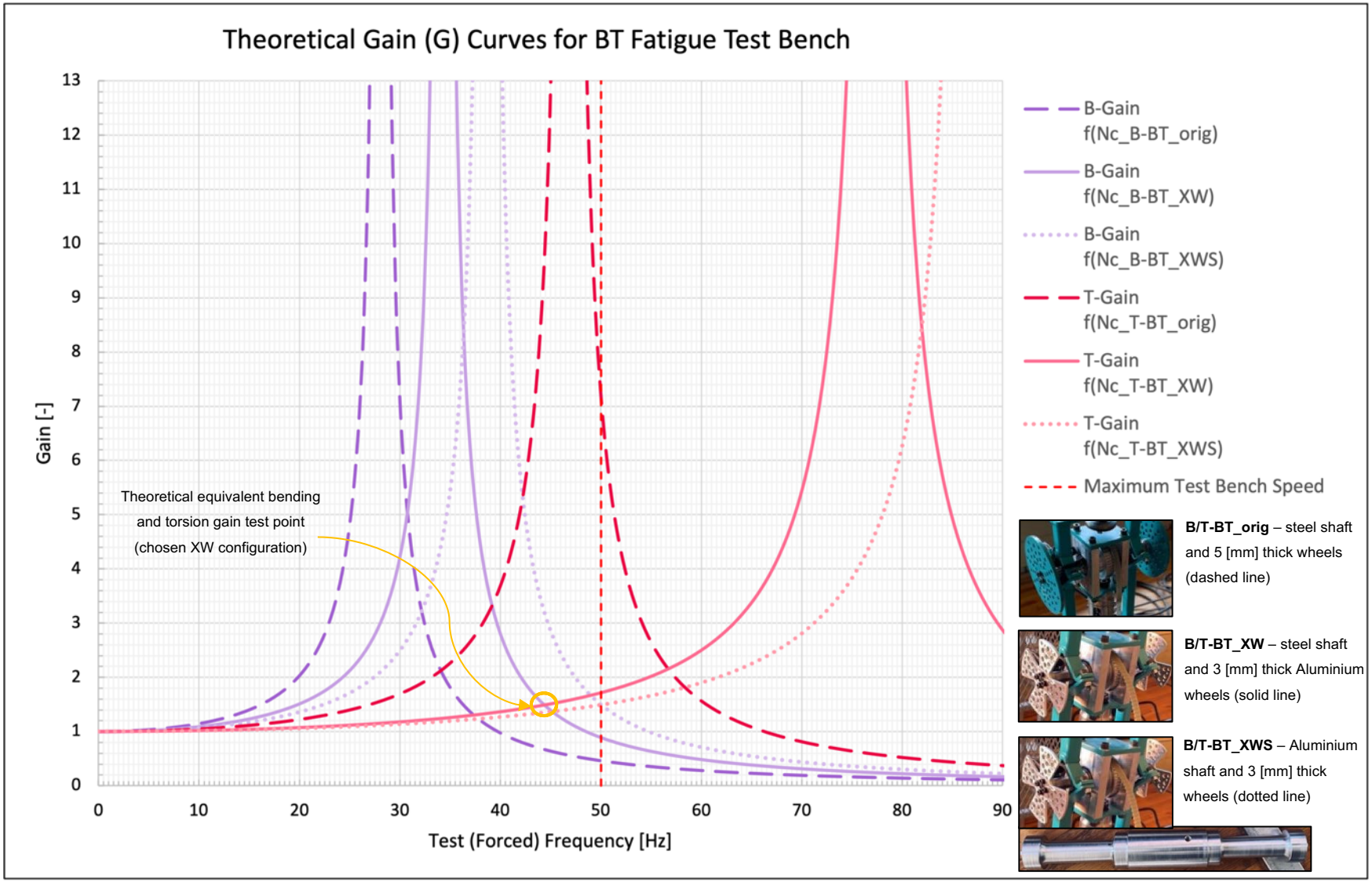


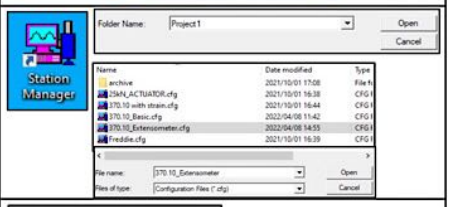
Figure F-7: BT fatigue test bench - theoretical bending and torsion loading gain curves

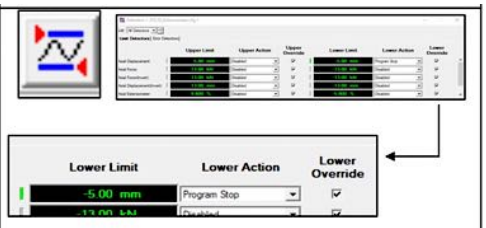
G. EXPERIMENTAL TEST PROCEDURES

G1. Monotonic Tensile Test Procedure

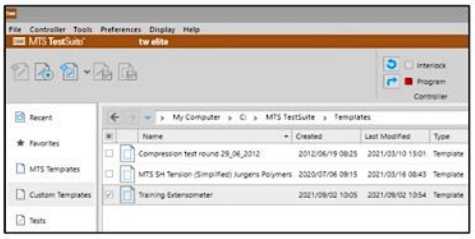
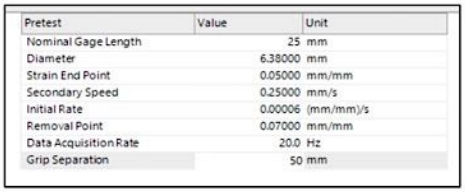
The experimental test procedure for the tensile (TEN) tests performed in this study is provided in Table G-1 below (without MTS Extensometer, see later Table H-5). The relevant room temperature measurements were made, using the procedure in Appendix B3, at the start and end of each test and reported as in Table J-1. Reference can be made to Figure A-1 for the MTS test system component designations.

Table G-1: Monotonic tensile test procedure

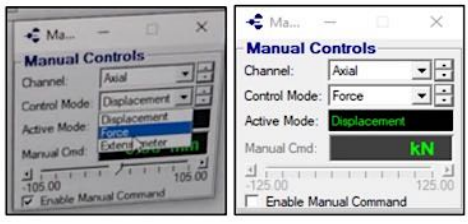
	PART A | MACHINE ACTIVATION	
1	Switch on the whole MTS machine (hydraulics box, computer and chiller) as with usual procedure (do not yet open any applications on the computer desktop). **a)** Before continuing with test steps below, you can/should perform a simple tensile test to warm up the MTS hydraulic system (removes inaccuracy of first tests). Or, perform a cyclic loading/movement of the actuator for 10-15min at ± 10-15Hz with no specimens or actual testing being recorded (ask Mr. Sarel for help on this). After warm-up of machine is done, re-close all open windows (e.g. station manager etc.) before proceeding to next steps.	
2	Open "Station Manager" on the desktop, open the "Project1" folder, select the "370.10_Basic.cfg" configuration file and select "Open". **a)** The Station Manager has to be opened with the above ".cfg" file. E.g., if the "370.10_Extensometer.cfg" file was previously opened/used for a extensometer tensile test, shut down and close all Station Manager and TW Elite (orange/brown icon) programs/windows, and restart with the above step.	
3.1	After Station Manager opened, locate and select/check the "Exclusive Control" tick-box on the right hand side (RHS) under "Station Controls".	
3.2	Select the "Reset" button next to the "Interlock 1" that has red light/bar next to it.	
3.3	Then, activate the hydraulic system of the MTS by incrementally selecting, with +-5 second rest/wait between each button selection, the "HPU-J25" and "HSM-J28A" buttons (1 red, 2 yellow, 3 green horizontal bars). Only select the next button at each once the button stops flickering, until all three buttons are selected and green, for the two hydraulic systems.	
4	Under the "Station Controls", locate and select the "Manual Command" button (one of 6 below the blue text heading, above the exclusive control check box) (it has two large blue arrows pointing up and down). Set the "Control Mode" to "Displacement" and at the bottom select/tick the "Enable Manual Command" option. **a)** This is done for safety purposes to override the program while your hands will be working between the actuators. **b)** You should 'zero' the position of the MTS actuator (bottom one) by entering value "0mm" into the lower black box, and pressing enter. The actuator will now set at its vertical zero point (for displacement up or down that will occur during test), ready for tensile specimen to be loaded and test to be performed.	

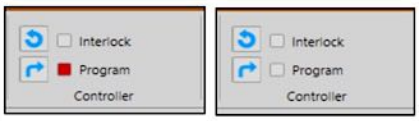
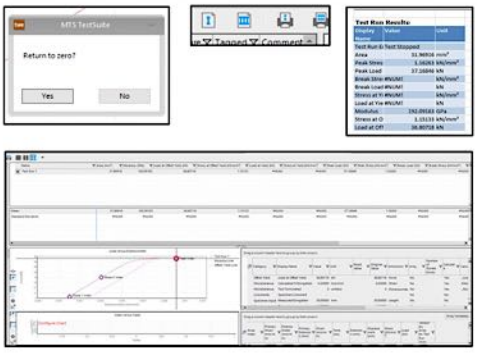
5	Under the "Station Controls", locate and select the "Detectors" button (one of 6 below the blue text heading, above the exclusive control check box) (it has two small red arrows and two blue lines with triangles in between). A wide window will open with black boxes (12) and green numbers (ensure the "Limit Detectors" tab in this window is selected). **a)** In the "Detectors" window, under the "Lower Limit" column, set the "Axial Displacement" row value (green) to -5mm, and in the dropdown next to it, select "Program Stop" as the "Lower Action" (green bar will appear next to -5mm value). **b)** This is done to prevent the MTS from compressing the actuators together by more than 5mm for any reason whatsoever (a safety setting).	

PART B | TEST- PROGRAM SETUP

6.1	Now locate the "TW Elite" program icon (orange/brown) on the desktop of the computer, and open the program.	
6.2	When the program is open, select the "Custom Templates" directory in the left hand side (LHS) pane of the window. Then double click the "MTS SH Tension (Simplified) Jurgens Polymers" template to open it.	
7	Specify the "Nominal Gage Length" in the "Monitor" tab of the TW Elite test suite window that opened. This is the nominal **gage length of** your **specimen.** Specify the specimen diameter. NOTE: figure here is just illustrative	
8	Right click on the black "Load" block at the bottom left of the screen and select "Zero Signal" to zero the kN reading BEFORE loading test specimen into actuator clamps (see next steps).	

PART C | TEST - SPECIMEN MOUNTING

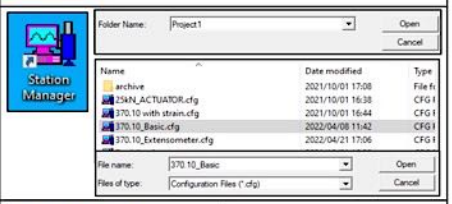
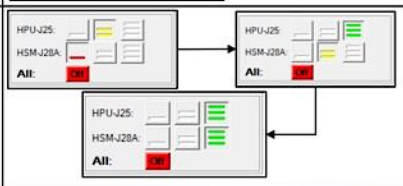
9.1	Load the tensile test specimen (dog-bone ASTM E8, preferrably polished) into the MTS wedge grips (as would be done with normal tensile test). **First** clamp the specimen into the **bottom actuator wedge grip** (actuator set at zero vertical position, ref step 7). **Second,** lower the top head and **clamp the top wedge grip** onto specimen. Then lock the top wedge grip head with the turn switch (third from the left). NOTE: do not yet switch the red bunny/turtle button to the rabbit side (red light on).	
9.2	AFTER loading the specimen, go to the "Manual Controls" window previously opened, and set the "Control Mode" from "Displacement" (as it was left like in step 7) to "Force" (with the "Enable Manual Command" option still selected/ticked). **a)** Now enter 'zero' as the kN value in the bottom black box and press enter. The resultant compressive/tensile force of the actuator wedge clamps is now zero'ed away (caused by clamping of specimen). **b)** Leave the "Control Mode" with the "Force" selected, and uncheck the "Enable Manual Command" tick box and then minimize the "Manual Controls" window.	
10	Finally **turn** the bunny/turtle button (**interlock** speed) **to** the **rabbit** (right) side (**red light** comes **on**). Ensure the top wedge grip is locked in position before continuing with the test (see step 14.1).	

11	Reset the "Interlock" (anticlockwise circular arrow) at the top of the window in the "Controller" group. The red light next to "Program" will turn off, and testing may proceed. NOTE: if step 10 is not done (rabbit switched on) then this interlock in this step will not reset, and the red light next to "Program" will stay on. Starting test will not be allowed and MTS will give a pop-up message about interlock problems.	
	PART D | TEST- RUN	
12	Go to the open TW Elite test suite window, and press big GREN PLAY arrow under "Test Controls" group to START the test. Press OK and let the test run (± 20-30 seconds).	
13	After test completed (specimen break detected by MTS): **a**) Select "NO" in the "Return to Zero" window that opens. You will be directed to the processed results window. For data, select File -> Export -> Raw Data, and save in your folder. For graphs, select the button with the blue "I" (single test result Excel) to obtain and save graphic results as Excel file in your folder. For multiple tests combined in one Excel, select the blue "III" button.	
"14"	IF **MORE TESTS** ARE TO BE PERFORMED: Remove the broken specimen halves from MTS grips. - Re-do step 4 and check step 5. Restart procedure at step 7 through to here. Got to the "Monitor" tab at the top of the "TW Elite" programme window (window showing the current results) to start entering the new specimen's details.	

G2. Axial Fatigue Test Procedure

The experimental test procedure for the axial fatigue (AX) tests performed in this study is provided in Table G-2 below. Reference can be made to Figure A-1 for the MTS test system component designations.

Table G-2: Axial fatigue test procedure

	PART A | MACHINE ACTIVATION	
1	Switch on the whole MTS machine (hydraulics box, computer and chiller) as with usual procedure (do not yet open any applications on the computer desktop). **a)** Before continuing with test steps below, you can/should perform a simple tensile test to warm up the MTS hydraulic system (removes inaccuracy of first tests). Or, perform a cyclic loading/movement of the actuator for 10-15min at ± 10-15Hz with no specimens or actual testing being recorded (ask Mr. Sarel for help on this). After warm-up of machine is done, re-close all open windows (e.g. station manager etc.) before proceeding to next steps. **NOTE:** At least 2-3 tensile tests have to be performed for the material to test here before continuing. Test results from that will be required here (e.g. actuator max displacement after specimen fails/snaps in tension).	
2	Open "Station Manager" on the desktop, open the "Project1" folder, select the "370.10_Basic.cfg" configuration file and select "Open". **a)** The Station Manager has to be opened with the above ".cfg" file. E.g., if the "370.10_Extensometer.cfg" file was previously opened/used for a extensometer tensile test, shut down and close all Station Manager and TW Elite (orange/brown icon) programs/windows, and restart with the above step.	
3.1	After Station Manager opened, locate and select/check the "Exclusive Control" tick-box on the right hand side (RHS) under "Station Controls".	
3.2	Select the "Reset" button next to the "Interlock 1" that has red light/bar next to it.	
3.3	Then, activate the hydraulic system of the MTS by incrementally selecting, with +-5 second rest/wait between each button selection, the "HPU-J25" and "HSM-J28A" buttons (1 red, 2 yellow, 3 green horizontal bars). Only select the next button at each once the button stops flickering, until all three buttons are selected and green, for the two hydraulic systems.	
"4"	Under the "Station Controls", locate and select the "Manual Command" button (one of 6 below the blue text heading, above the exclusive control check box) (it has two large blue arrows pointing up and down). Set the "Control Mode" to "Displacement" and at the bottom select/tick the "Enable Manual Command" option. **a)** This is done for safety purposes to override the program while your hands will be working between the actuators. **b)** You should 'zero' the position of the MTS actuator (bottom one) by entering value "0mm" into the lower black box, and pressing enter. The actuator will now set at its vertical zero point (for displacement up or down that will occur during test), ready for axial fatigue specimen to be loaded and test to be performed. **NOTE:** this will be formally done later in the program setup in the "Multipurpose Elite" application by "Parking" the channels.	

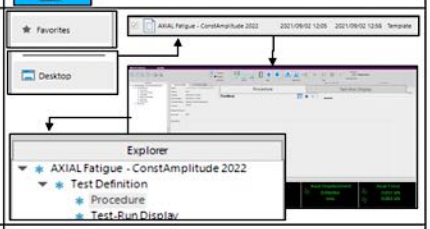
PART B | TEST- PROGRAM SETUP

5.1 Now locate the "Multipurpose Elite" program icon (purple) on the desktop of the computer, and open the program.

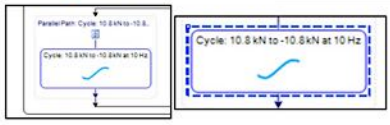


5.2 When the program is open, select the "Desktop" (or "Favorites") directory in the left hand side (LHS) pane of the window.
Then select the "AXIAL Fatigue - ConstAmplitude 2022" template by double clicking on it.

When the application window opens with the "Explorer" pane on the left hand side, select "Procedure" under the "Test Definition" dropdown. The procedure block diagram will open to the right of the window.

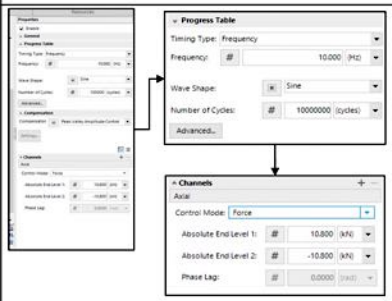


6.1 In the procedure block diagram window, you should scroll down to the bottom and select the block marked "Cycle".
Select this block. Upon selecting it, the "Properties" window will appear on the right hand side of the screen.



6.2 In the "Properties" window, you can now set the cyclic axial fatigue parameters.

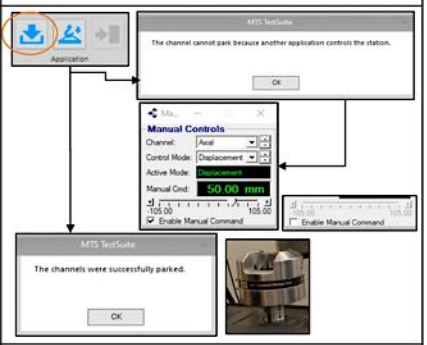
a) Set the "Frequency" to any preferred value below or equal to 10Hz. Setting it to a value higher than 10Hz causes the 'induced' peak load (what the MTS measures during test with its load cell) to sometimes not actually reaching the 'commanded' peak load (what you tell the MTS to induce). Thus you will think you are inducing 10kN but infact the specimen is actually only experiencing 8 or 9kN. Testing too fast = incorrect load.
b) If you want the specimen to undergo full fatigue fracture (break in two, theoretically at 1x10^6), set the "Number of Cycles" value to a value much larger than the theoretical fatigue limit (e.g. 1x10^8). If you do not want the specimen to fracture, set it to the preferred cycle count.
c) Set the "Absolute End Level 1" (maxima) and the "Absolute End Level 2" (minima) to your preferred sinusoidal loading peak load values.
(Level 1 = Level 2 is fully reversed loading, Level 1 ≠ Level 2 is loading with a midrange value)



7 The hydraulic actuator should now be zero'ed into its vertical position (if step 4 hasn't been done yet) before continuing.
This is done by selecting the "Park Channel" button in the Application's group at the top of the current Multipurpose window.

NOTE: ensure that the top hydraulic wedge grip head is moved sufficiently up away from the bottom actuator before clicking this button to zero the position.
NOTE: if the message pops up with "...another application controls the station", you should first go to the "Manual Controls" window (see step 4) and uncheck the "Enable Manual Command" tickbox. Then try again by clicking on the "Park Channel" button.

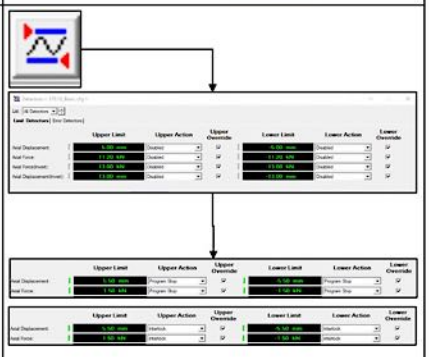
The hydraulic actuator is now parked at its vertical zero position (like was done in step 4) and the loading of the specimen can now commence.



8 Under the "Station Controls", locate and select the "Detectors" button (one of 6 below the blue text heading, above the exclusive control check box) (it has two small red arrows and two blue lines with wave in between). A wide window will open with black boxes (12) and green numbers (ensure the "Limit Detectors" tab in this window is selected).

a) In the "Detectors" window, under the "Lower Limit" and the "Upper Limit" columns, set the "Axial Displacement" row values (green) to the same but opposite sign values.
These values should be slightly larger than the maximum displacement that is measured in a tensile test of the same material (e.g. tensile test = 5mm, then set it here to 5.5mm).
In the dropdown next to each, select "Program Stop" OR "Interlock" as the "Lower Action" (green bar will appear next to value).
NOTE:
"Program Stop" will just stop the whole test if specified cycle count is reached or specimen fails/fractures (only use if you are present during the axial fatigue test cycle).
"Interlock" will shutdown the whole MTS once the specified cycle count is reached or specimen fails/fractures (use this if you are NOT present during the axial fatigue test cycle to prevent damaging the machine or crushing the specimen).

b) In the "Detectors" window, under the "Lower Limit" and the "Upper Limit" columns, set the "Axial Force" row values (green) to the same but opposite sign values.
These values should be slightly larger than the maximum specified cyclic force that was entered for this axial fatigue test, see step 6.2 (e.g. specified force = 10kN, then set it here to 10.5kN).
In the dropdown next to each, select "Program Stop" OR "Interlock" as the "Lower Action" (green bar will appear next to value).
This is done so that the MTS does not crush the fatigue specimen when it fails/fractures. That is, you are setting a threshold for the maximum compressive force that is allowed



9 Right click on the black "Axial Force" channel/block at the bottom left of the screen and select "Zero Signal" to zero the kN reading BEFORE loading test specimen into actuator clamps (see next steps).

NOTE: this zeroing step of the channel (not the actual force, mainly noise) should not be done whatsoever after this when proceeding with the next steps as it will again add an offset reading on the measure force (which is zero'ed in step 10.2 below)



PART C | TEST - SPECIMEN MOUNTING

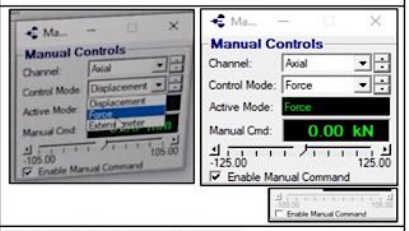
10.1 Load the axial fatigue test specimen (dog-bone ASTM E606/606M-12, highly polished up to 2000 grit sand paper and lubricant or better) into the MTS wedge grips.
First clamp the specimen into the **bottom actuator wedge grip** (actuator set at zero vertical position, ref step 7).
Second, lower the top head and **clamp the top wedge grip** onto specimen. Then lock the top wedge grip head with the turn switch (third from the left).

NOTE: do not yet switch the red bunny/turtle button to the rabbit side (red light on).



10.2 AFTER loading the specimen, go to the "Manual Controls" window previously opened, and set the "Control Mode" from "Displacement" (as it was left like in step 4/7) to "Force" (with the "Enable Manual Command" option selected/ticked).

a) Now enter 'zero' as the kN value in the bottom black box and press enter.
The resultant compressive/tensile force of the actuator wedge clamps is now zero'ed away (caused by clamping of specimen).
b) Leave the "Control Mode" with the "Force" selected, and uncheck the "Enable Manual Command" tick box and then minimize the "Manual Controls" window.
(if this box is not unchecked after zeroing the load, the test will not be able to start when pressing the green play button later on)



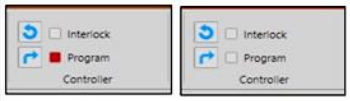
10.3 Only now **turn** the bunny/turtle button (**interlock** speed) **to** the **rabbit** (right) side (**red light** comes **on**).

Ensure the top wedge grip is locked in position before continuing with the test (see step 10.1).



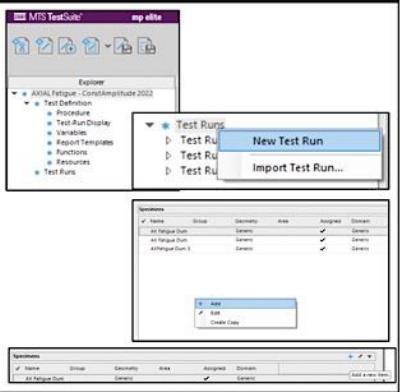
11 Reset the "Interlock" (anticlockwise circular arrow) at the top of the window in the "Controller" group. The red light next to "Program" will turn off, and testing may proceed.

NOTE: if step 10.3 is not done (rabbit switched on) then this interlock in this step will not reset, and the red light next to "Program" will stay on. Starting test will not be allowed and MTS will give a pop-up message about interlock problems.

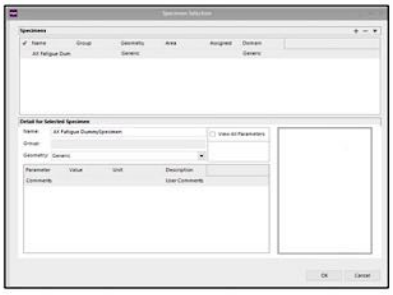


PART D | TEST- RUN

12.1 Go to the open Mulitpurpose Elite test suite window.
In the left window pane ("Explorer"), right click on the "Test Runs" dropdown and select "New Test Run" (the "New Test Run" button in the top left corner of this application window can also be selected in the ribbon).
A window will open where you can right click on the blank white space or on the "plus" signe next to the window title to "Add" a new test.

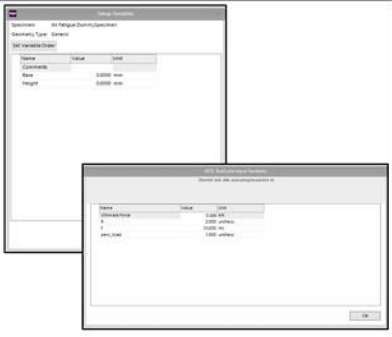


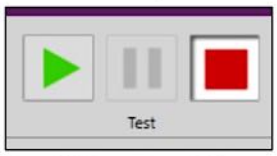
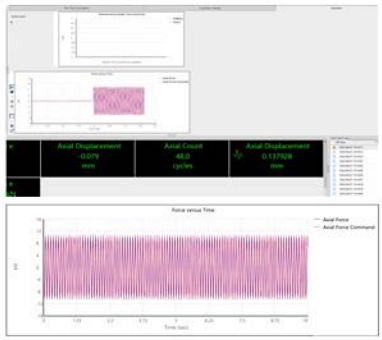
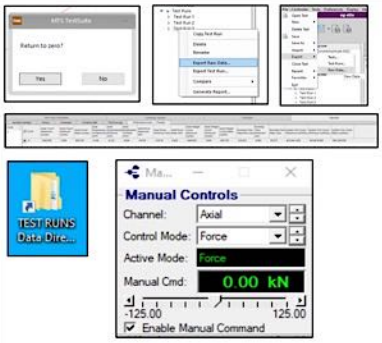
12.2 A "Specimen Selection" window will open next.
In this window you can specify the name of the test specimen etc.
Press "OK" when done.



12.3 The next two windows that open can be "ignored" and just press "OK".
(The "Setup Variables" and "MTS TestSuite Input Variables" windows).

This is because all the inputs here have already been specified in steps 6.1 to 8 and any values entered here will not have any influence on the test.



12.4	Zero all the channel signals at the bottom of the Multipurpose Elite application window now. **NOTE**: Do not zero the "Axial Force" furthest to the left (see reason in step 9). The rest of the channels can be zero'ed because they are only indications of the set test parameters.	
13	In the open Mulitpurpose Elite test suite window, press big GREN PLAY arrow under "Test Controls" group to START the test. The running test window will open and a load vs time graph will display the "Axial force" and the "Axial Force Command" cyclic loads. Leave the test to run (until specified cycle count or until fracture of specimen).	 
14	After test completed (specimen break detected by MTS or max cycle count reached): **a)** Select "NO" in the "Return to Zero" window that opens (if it appears). You will be directed to the processed results window. For data, select File -> Export -> Raw Data, and save in your folder, OR right click on the test run in the "Explorer" pane of the window and export it there. The tests that you performed can be located in the "TEST RUNS Data Directory" shortcut on the computer desktop (if you forgot to export something during test day). **NOTE**: If the specimen was not tested to fracture (with specified cycle count), then you should first go and zero the test force in the "Manual Controls" window once the test stopped before removing specimen from the wedge grips. This is done to prevent injury or damaging the machine.	
"15"	IF **MORE TESTS** ARE TO BE PERFORMED: Remove the fractured/whole specimen pieces from MTS wedge grips. - Re-do step 4. Restart procedure at step 5.2 through to here.	

G3. Bending Fatigue Test Procedure

The experimental test procedure for the bending fatigue (B) tests is provided below. Reference can be made to Figure A-4 for the test bench component designations.

Preparing/Running Test

- Ensure that the motor power supply is switched off and do an overall check on the test bench (e.g., are the bearing bolts properly fastened, is the microswitch working, and is the counter tube connected to the motor shaft).
- Insert a bending fatigue specimen, tip first, into the specimen clamping nut (loosened off the shaft) from the threaded side (without damaging the polished test zone surface) until the specimen presses against the small diameter flange inside the nut.
- With care, insert the cantilever tip of the specimen into the load cell bearing and push it through (again without scratching the specimen surface) until the clamping nut with the specimen can be positioned back over the shaft end for the tapered end of the specimen to then guide into the shaft.
- Fasten the clamping nut onto the threaded shaft end by hand first, ensuring the microswitch wheel is in position against the load cell bearing mount (in 'test' position – cannot be set after specimen fastening). The load cell bearing should be positioned (using the turn screw) directly across the shaft centre (to ensure the specimen is not bent pre-test). See Figure G-1 below for an illustration of the three steps for an arbitrary cantilever bending fatigue specimen.

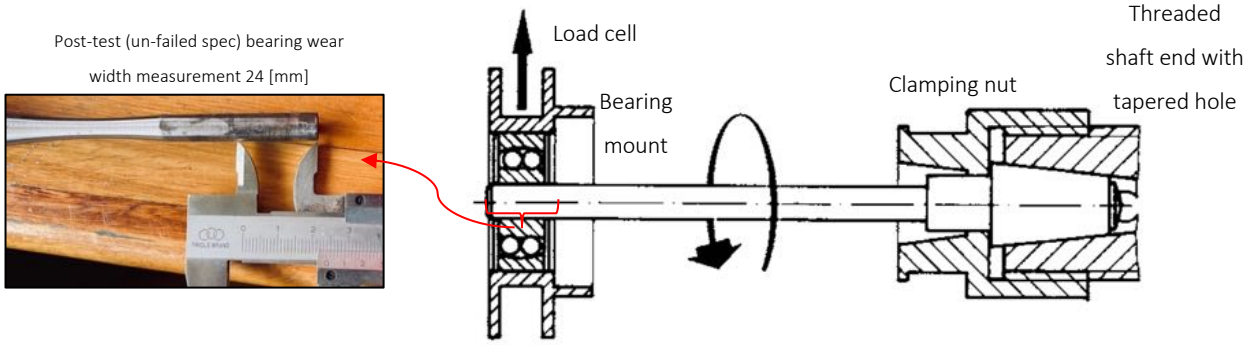


Figure G-1: B fatigue test specimen mounting and loading schematic [17]

- Using the appropriate tools, properly fasten the clamping nut onto the shaft end (threaded shaft end turning into the nut) and thus 'mounting' the test specimen for the test to be conducted.
- Check after this that the load cell reading is 0 (no cantilever force applied after the specimen mounting into the shaft end).

- With the mounted bending fatigue specimen in the unloaded condition, switch on the test bench and take the first test speed measurement using the tachometer. Ensure that the mechanical cycle counter is counting up the cycles during this. Stop the test.
- Set the required load cell force (according to the calibration curve and the preferred cantilever test load) using the turn screw at the top and again ensuring the microswitch is in position for the test to run. Notate the test load cell if not already pre-calculated.
- Ensure the mechanical cycle counter is set to zero by holding the red side button and pressing down on the black button.
- Start the test by pressing the green I/O button on the control switches.
- Let the test proceed whilst continuously monitoring the test bench to ensure no anomalies.

Test Termination or Specimen Failure

- Upon specimen failure, the test is automatically stopped with the micro switch released (from the ‘closed’ position against the bearing mount), and the counter is paused. Manual termination may be required via the red I/O button if the micro switch was not released or no specimen failure occurred after the defined cycle count. The load cell pulls up and away when the specimen does fail.
- Notate the fatigue cycle count from the counter. Switch off the control box power supply.
- Loosen the specimen clamping nut (containing broken specimen half) and carefully remove it from the nut.
- Place the (un)failed specimen in a sealable bag marked with the test specimen number (Spec#), diameter, specimen material, cycles to failure, cantilever force and the test date.

G4. Torsion Fatigue Test Procedure

The experimental test procedure for this study's torsion fatigue (T) tests is provided below (without measuring with DANTEC DIC System). Reference can be made to Figure A-8 for the test bench component designations.

Preparing/Running Test

- Ensure that the VSD power supply is switched off and do an overall check on the test bench (e.g., are wheel and lever-head bolts properly fastened?).
- Fasten the chosen centrifugal weights (identical) to the bilateral wheels (180° apart) at the radius position of choice (20, 25, 30, 35 or 40 [mm]).
- Insert a torsion fatigue specimen through the bottom aluminium specimen clamp (without damaging the polished test zone surface) and orient the specimen with markings on it into the correct position (as viewed from the top of the test bench).
- Securely fasten the x4 bolts of the bottom clamp to firmly grip the specimen whilst ensuring the top end is pressing against the lever-head stem inside the coupling.
- Now, ensure that the unfastened side of the specimen (coupling side) is loose enough to level out the lever-head position so that the wheel shaft is in a horizontal position before fastening the coupling onto the head stem and specimen.
- Only now may the x4 bolts at the top (coupling) be fastened to grip the specimen firmly. Ensure that the lever-head shaft is horizontal throughout this fastening before securely fastening the bolts. Take precaution not to twist the specimen when fastening the top coupling bolts.
- Switch the control box power supply on and observe the '*rdY*' (ready) message on the VSD HMI and confirm the timer is on and zeroed by pressing the small red button below it.
- Perform a micro switch function check by manually triggering both the switches and observing the *F091* error code on the HMI of the VSD. The pause sign (yellow) will show on the timer.
- Ensure the correct test speed and start-up time (2.5 [s]) setting by verifying the values of VSD parameters *P121* and *P100,* using the HMI buttons *P*, Δ and ∇.
- Start the test by pressing the I/O button on VSD (the timer will start to count elapsed time).
- Let the test proceed whilst continuously monitoring the test bench to ensure no anomalies.

Test Termination or Specimen Failure

- Upon specimen failure, the micro switch is triggered, the test is automatically stopped, and the timer is paused (manual termination may be required via VSD HMI if the micro switch is not triggered or there is no specimen failure).

- Notate the elapsed test time from the timer and test speed from the VSD. Switch off the control box power supply.
- Loosen the specimen clamping bolts and carefully remove the specimen halves from the clamps.
- Place the failed specimen sections in a sealable bag marked with the test specimen number (Spec#), diameter, specimen material, cycles to failure, centrifugal weight designation, mass and radius and the test date.
- Remove the centrifugal weights from the wheels.

G5. Bending-Torsion Fatigue Test Procedure

The experimental test procedure for this study's biaxial out-of-phase bending-torsion fatigue (BT) tests is provided below (without measuring with DANTEC DIC System). Reference can be made to Figure A-11 for the test bench component designations.

Preparing/Running Test

- Ensure that the VSD power supply is switched off and do an overall check on the test bench (e.g., the wheel and the lever-head bolts are properly fastened).
- Fasten the chosen centrifugal weights (identical) to the bilateral wheels (180° apart) at the radius position of choice (20, 25, 30, 35 or 40 [mm]).
- Loosen the suppression system bolts and remove the system from the catchers.
- Lifting the lever-head out of the way (derailed the timing belt), insert the specimen into the bottom specimen clamp (without damaging the polished test zone surface) and turn it with the left "L" and the right "R" labels in the correct position (viewed from the front of the test bench).
- Securely fasten the x4 bolts of the bottom clamp to grip the specimen firmly.
- Raise the lever-head and lower it over the specimen whilst inserting the specimen side marked "top" into the attached top clamp.
- Re-apply and fasten the suppression system to the catchers, and with moderate tightening, apply suppression on the lever-head top plate, cantering it over the specimen.
- Only now may the x4 bolts of the top clamp be tightened to grip the specimen firmly. Ensure that the lever-head and the motor shafts are parallel before securely fastening the top clamp bolts. Take precaution not to twist or bend the specimen when fastening the top clamp bolts of the lever-head (moderate suppression applied for this).
- Re-rail the timing belt over the pulleys and securely fasten the front pillow block bearing mount bolts (loosened after a previous test).
- Switch the control box power supply on and observe the '*rdY*' (ready) message on the VSD HMI and confirm the timer is on and zeroed by pressing the small red button below it.
- Perform a micro switch function check by manually triggering both the switches and observing the *F091* error code on the HMI of the VSD. The pause sign (yellow) will show on the timer.
- Ensure the correct test speed and start-up time (2.5 [s]) setting by verifying the values of VSD parameters *P121* and *P100,* using the HMI buttons *P*, Δ and ∇.
- Place the cover frame over the test bench and ensure all the cables are cleared away from the rotating components of the test bench. Apply additional suppression with the screw.
- Start the test by pressing the I/O button on VSD (the timer will start to count elapsed time).
- After 2 to 3 seconds, unscrew the suppression on the lever head all the way to the top.
- Let the test proceed whilst continuously monitoring the test bench to ensure no anomalies.

Test Termination or Specimen Failure

- Upon specimen failure, the micro switch is triggered, the test is automatically stopped, and the timer is paused (manual termination may be required via VSD HMI if the micro switch is not triggered or there is no specimen failure).
- Notate the elapsed test time from the timer and test speed from the VSD. Switch off the control box power supply.
- Remove the cover frame over the test bench.
- De-rail the timing belt, loosen the specimen clamping bolts and carefully remove the specimen halves from the clamps.
- Place the failed specimen sections in a sealable bag marked with the test specimen number (Spec#), diameter, specimen material, cycles to failure, centrifugal weight designation, mass and radius and the test date.
- Remove the centrifugal weights from the wheels.

Figure G-2 on the next page depicts these experimental procedure steps in the form of a general process flow diagram for further clarity. Reference can be made to Figure A-11 for the test bench component designations.

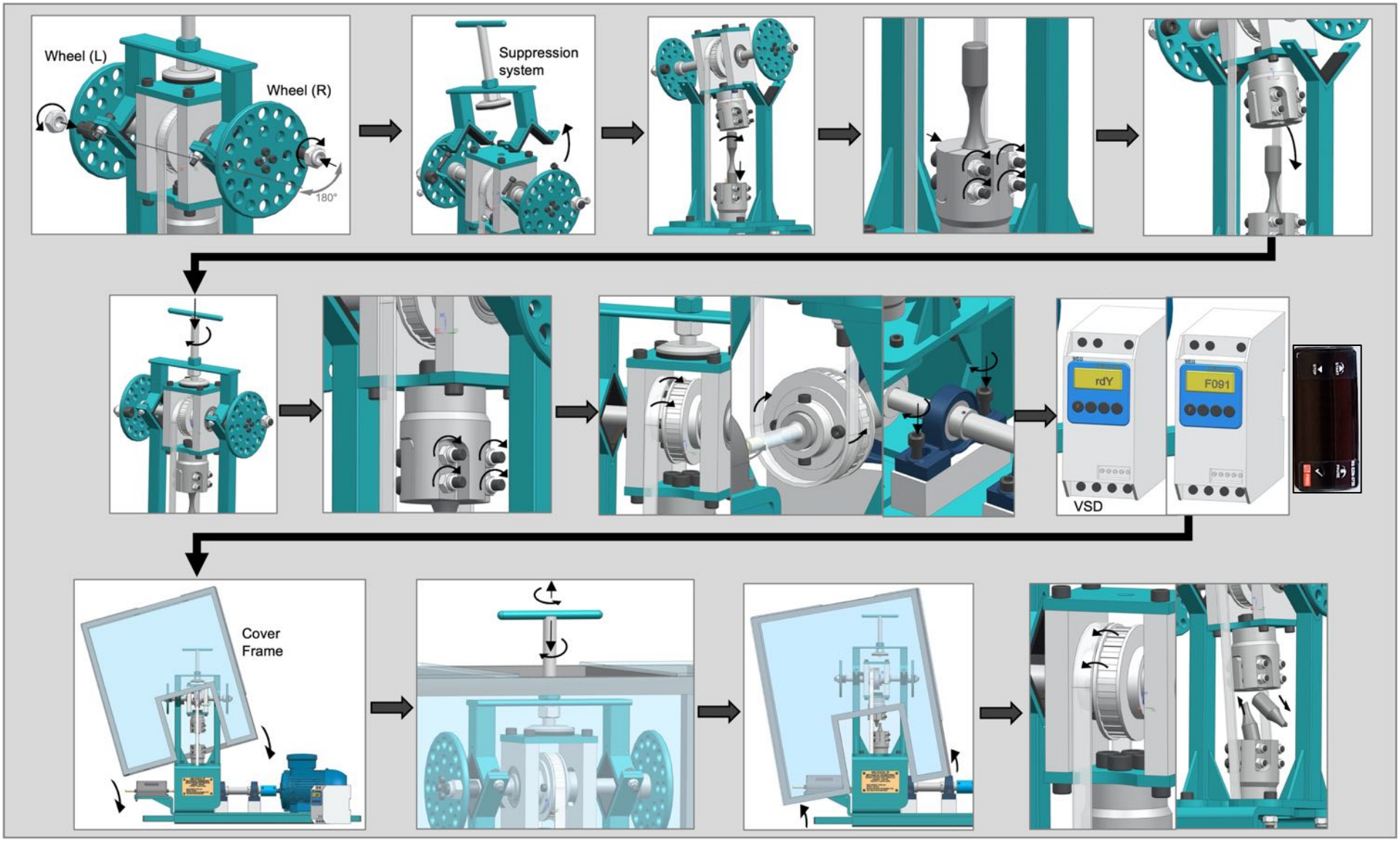


Figure G-2: BT fatigue test procedure – flow diagram

H. EXPERIMENTAL TEST MEASUREMENTS AND CALCULATIONS

H1. Monotonic Tensile Test Measurements and Calculations

H1.1. Tensile Test Measurements and Calculations

The first five (5) monotonic tensile (TEN) tests (Spec1-Spec5, shown in Figure H-1 on the next page) were performed according to the TEN test procedure previously provided in Table G-1. The tests were performed with a tensile test rate of 3 [mm/min] (0.05 [mm/s]) as recommended for steels on this machine in the laboratory. The recorded test measurement data for each specimen is provided in Table H-1 (condensed) and Table H-2 to follow. The MTS TW Elite program-generated tensile test curves are illustrated in Figure H-2 (a) after these tables. The tensile force offset values F_{offset} (due to clamping forces, specimen slippage) are reflected in Table H-1 at the start of each tensile test (first non-zero value). The resultant monotonic tensile material strengths S_{ut} and S_y of Spec1 to Spec5, respectively, were calculated using Equation (H-1) and (H-2) below and are provided in Table J-1 and Figure J-2.

$$S_{ut}\,[MPa] = \left[\frac{F_{UTS}\,[kN]}{A\,[mm^2]}\right]1000 = \left[\frac{F_{peak}\,[kN] - F_{offset}\,[kN]}{\frac{\pi}{4}d_{spec}^2\,[mm^2]}\right]1000 \qquad \text{(H-1)}$$

$$S_{y}\,[MPa] = \left[\frac{F_{Y}\,[kN]}{A\,[mm^2]}\right]1000 = \left[\frac{F_{0.2\%;yield-offset}\,[kN] - F_{offset}\,[kN]}{\frac{\pi}{4}d_{spec}^2\,[mm^2]}\right]1000 \qquad \text{(H-2)}$$

where d_{spec} : is the measured Spec1 to Spec5 diameters (Appendix D1)

The 0.2 [%] strain yield-offset load $F_{0.2\%;yield-offset}$ value was obtained from the load-extension test curves by overlaying the MTS TW Elite program-generated test curve on a blank Excel graph. Positioning of a data point marker to the appropriate offset line and curve intersection position on the graph followed, and finally subtracting the corresponding F_{offset} value from this point for each tensile test specimen (see example in Figure H-2 (b)). The reason for using this method is that the EN19 (T-condition) alloy steel not having or illustrating a well-defined yield strength point for the tensile tests (curves). This phenomenon is generally the case for high-strength alloy steels and is an acceptable method for obtaining yield strength. Also, the MTS TW Elite tensile test procedure does not provide the correct yield load value after each test (tables) as it does with the ultimate/peak load value (due to this unclear yield point). The room temperature measurements are reported in Table J-1 for all five tests (with the other tensile (extensometer) test results). These values are also illustrated in the post-test images in Figure H-1 below and were measured with the procedure discussed in Appendix B3.

PRE-TEST



POST-TEST

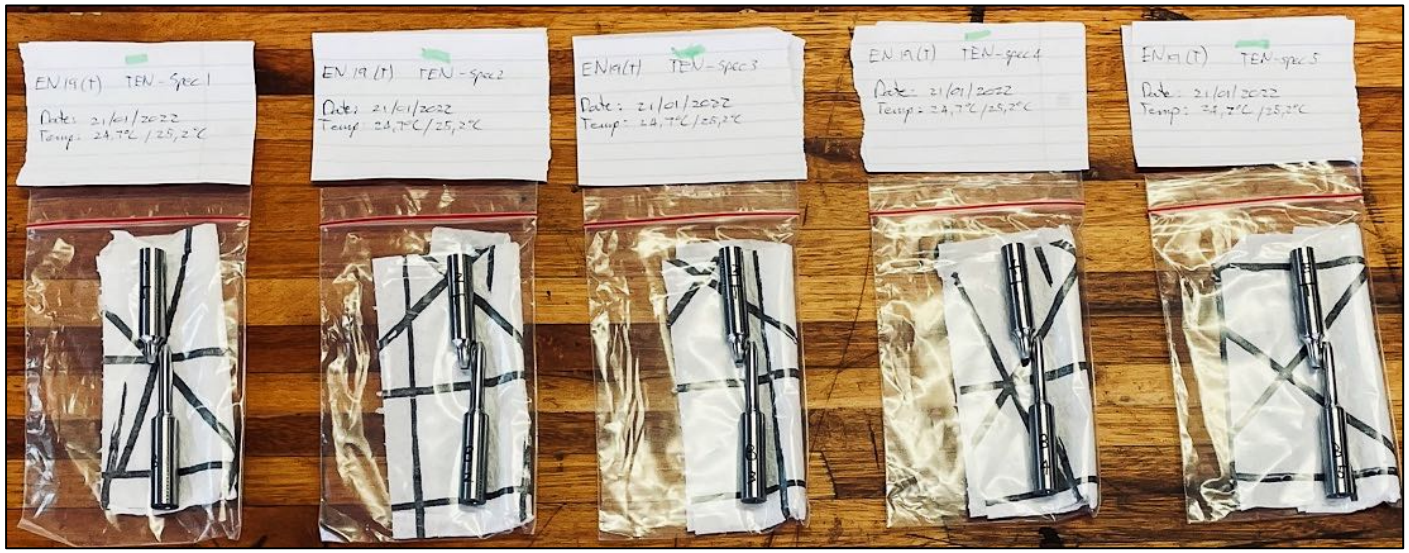


Figure H-1: TEN test Spec1 to Spec5 – pre and post-test images

Table H-1: TEN test Spec1 to Spec5 measurements – DAQ data exports

Peak Load	28,696	[kN]	Peak Load	29,972	[kN]	Peak Load	30,946	[kN]	Peak Load	28,840	[kN]	Peak Load	30,817	[kN]
SPECIMEN 1 - DAQ Data			SPECIMEN 2 - DAQ Data			SPECIMEN 3 - DAQ Data			SPECIMEN 4 - DAQ Data			SPECIMEN 5 - DAQ Data		
Displacement	Load	Time	Displacement	Load	Time	Displacement	Load	Time	Displacement	Load	Time	Displacement	Load	Time
[mm]	[kN]	[s]	[mm]	[kN]	[s]	[mm]	[kN]	[s]	[mm]	[kN]	[s]	[mm]	[kN]	[s]
0,01408	**1,67993**	0,25977	0,00539	**1,43819**	0,14063	0,00702	**1,79084**	0,13770	0,00703	**1,70518**	0,14063	0,00815	**1,61284**	0,15332
0,01895	2,01168	0,35938	0,01055	1,96634	0,24023	0,01250	2,23772	0,23730	0,01244	2,09986	0,24023	0,01392	2,01867	0,25293
0,02380	2,42751	0,45898	0,01581	2,37056	0,33984	0,01457	2,59494	0,33691	0,01716	2,48747	0,33984	0,01833	2,42257	0,35254
:	:	:	:	:	:	:	:	:	:	:	:	:	:	:
:	:	:	:	:	:	:	:	:	:	:	:	:	:	:
4,93651	17,89897	98,67383	5,21164	18,42638	104,23242	4,75497	20,05643	95,06543	5,19407	18,15879	103,83398	5,44347	19,52081	108,82715
4,96911	-0,57799	98,77344	5,21333	-0,22213	104,33203	4,76118	0,17677	95,16504	5,21124	0,03370	103,93359	5,50100	-0,59692	108,92676
4,94519	-0,12323	98,83008	5,21920	0,10167	104,34082	4,76292	-0,18556	95,17383	5,20961	-0,08538	103,97266	5,45426	0,13179	108,97168

Table H-2: TEN test Spec1 to Spec5 measurements – DAQ data tables (peak loads)

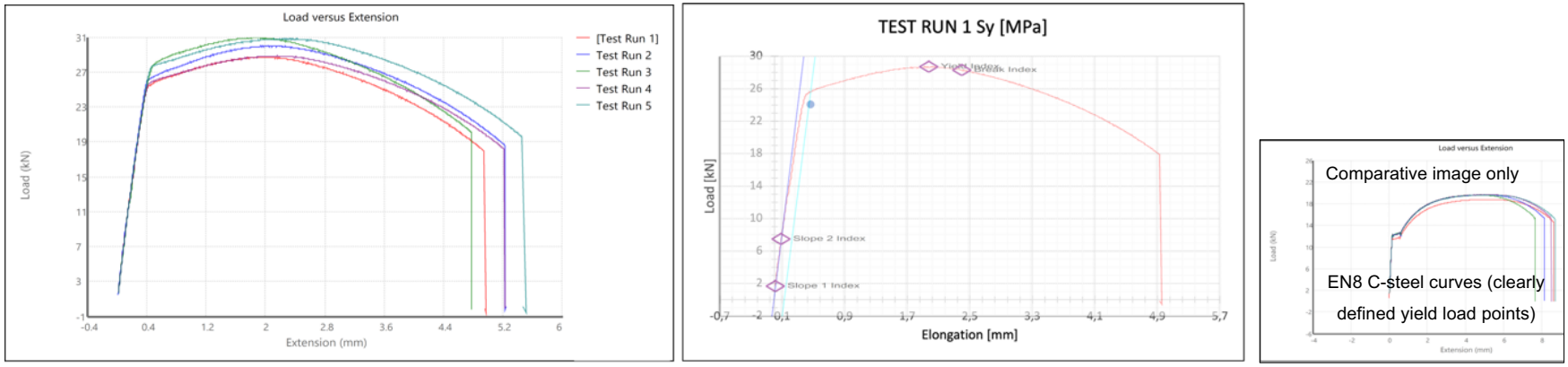
Test Run Results:	Spec1	
Display Name	**Value**	**Unit**
Test Run End Reason	Break Detected	
Peak Stress	1,1	kN/mm²
Peak Load	**28,696**	**kN**
Strain at Break	0,037	mm/mm
Modulus	190,799	kN/mm²
Width	6,500	mm
Thickness	4,000	mm

Test Run Results:	Spec2	
Display Name	**Value**	**Unit**
Test Run End Reason	Break Detected	
Peak Stress	1,2	kN/mm²
Peak Load	**29,972**	**kN**
Strain at Break	0,041	mm/mm
Modulus	197,665	kN/mm²
Width	6,500	mm
Thickness	4,000	mm

Test Run Results:	Spec3	
Display Name	**Value**	**Unit**
Test Run End Reason	Break Detected	
Peak Stress	1,2	kN/mm²
Peak Load	**30,946**	**kN**
Strain at Break	0,034	mm/mm
Modulus	187,368	kN/mm²
Width	6,500	mm
Thickness	4,000	mm

Test Run Results:	Spec4	
Display Name	**Value**	**Unit**
Test Run End Reason	Break Detected	
Peak Stress	1,1	kN/mm²
Peak Load	**28,840**	**kN**
Strain at Break	0,041	mm/mm
Modulus	188,897	kN/mm²
Width	6,500	mm
Thickness	4,000	mm

Test Run Results:	Spec5	
Display Name	**Value**	**Unit**
Test Run End Reason	Break Detected	
Peak Stress	1,2	kN/mm²
Peak Load	**30,817**	**kN**
Strain at Break	0,045	mm/mm
Modulus	189,421	kN/mm²
Width	6,500	mm
Thickness	4,000	mm



(a) (b)

Figure H-2: TEN test Spec1 to Spec5 – (a) load vs extension curves and (b) yield load estimation method

H1.2. Tensile Test (Extensometer) Measurements and Calculations

The last five (5) monotonic tensile (TEN) tests (Spec6-Spec10, shown in Figure H-3 on the next page) were performed according to the TEN test (extensometer) procedure provided in Table H-5 (to follow). For each of these tests, the tensile rate (usually 0.05 [mm/s] for steels) was initially lower according to pre-set extensometer test program parameters. The TEN test measurement data (including extensometer strain) for each specimen is provided in Table H-3 (condensed) and Table H-4 to follow. After this, the MTS TW Elite program tensile test curves are illustrated in Figure H-5. The tensile force offset values (due to clamping forces and specimen slippage) were again reflected in Table H-3 at the start of each tensile test (first non-zero value). The experimental monotonic tensile material strengths S_{ut} and S_y of Spec6 to Spec10 were calculated using the previously provided Equations (H-1) and (H-2). The yield and peak loads are obtained from Table H-4 (use of the extensometer). The results were tabulated in Table J-1 alongside the preceding TEN tests (Appendix H1.1) of Spec1-Spec5.

The relevant specimen gauge engineering strain ε measurements (shown in Figure H-4) were also obtained (fourth columns, Table H-3) in these last five TEN tests due to the use of the extensometer (Appendix B4). These strain measurements and corresponding load values were then utilised in Equation (H-3) below to obtain the calculated Modulus of Elasticity E_{calc} values for each tensile test specimen. They are reported in Table J-1 next to the MTS direct measured E_{ext} values from the extensometer measurement (see Table H-4). The average $E_{avg;spec}$ value of the measured and calculated values was considered the E of each test specimen. The E_{calc} values were calculated (from Table H-3 load and strain data) over the most linear range of each test (see Figure H-4 and Figure H-5). That is, between the first data point and the data point where the modulus line (turquoise) stopped touching the tensile test curve. That is, between the 'slope 1 index' and 'slope 2 index' markers of each curve, which is also how the software obtains the 'measured' E_{ext} values. All extensometer strains were measured (according to pre-sets) past the 'slope 2 index' to allow for the slope (E) calculation between the index points in the most linear region of the curves.

$$E\ [GPa] = \frac{\Delta\sigma\ [MPa]}{\Delta\varepsilon\ [strain]} = \frac{\left(\frac{F\,[kN]}{\frac{\pi}{4}d_{spec}^2\,[mm^2]}\right)_{index2} - \left(\frac{F\,[kN]}{\frac{\pi}{4}d_{spec}^2\,[mm^2]}\right)_{index1}}{\varepsilon_{index2}\,[-] - \varepsilon_{index1}\,[-]} \tag{H-3}$$

where d_{spec} : is the measured Spec6 to Spec10 diameters (Appendix D1)

σ : is the tensile stress

The room temperature measurements are reported in Table J-1 for all five tensile (extensometer) tests. These values are also illustrated in the post-test images in Figure H-3 below and were measured according to the procedure discussed in Appendix B3.

PRE-TEST



POST-TEST

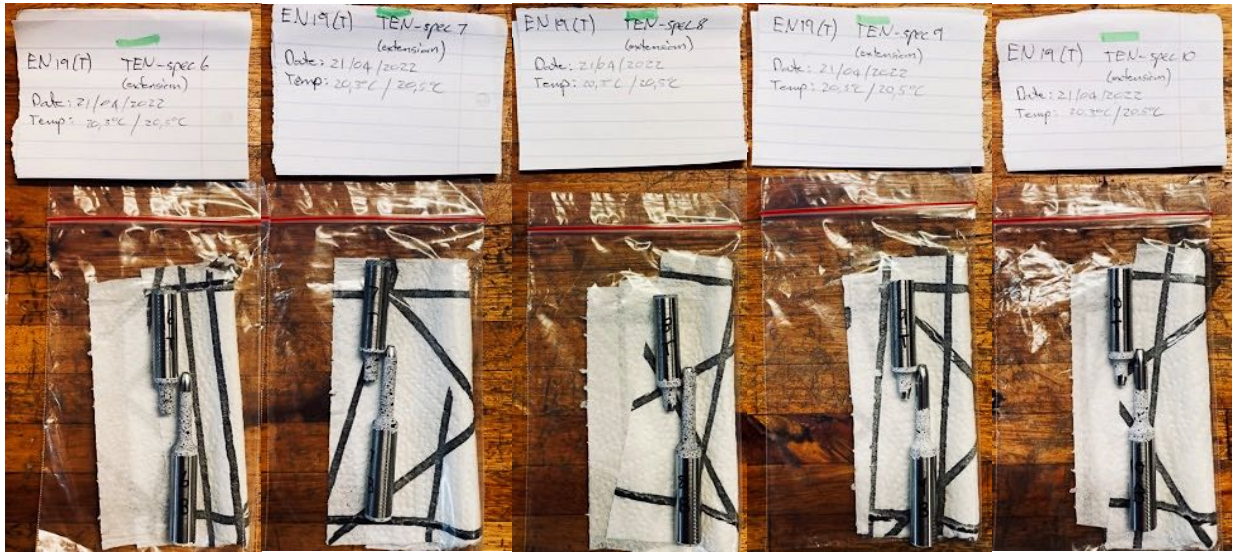


Figure H-3: TEN test Spec6 to Spec10 (Extensometer and DANTEC) – pre and post-test images

Table H-3: TEN test Spec6 to Spec10 measurements (Extensometer) – DAQ data exports

Calculated from 0 - point on TEN graph where modulus line stops touching the test curve (+- before yield kN)	0,5318	[MPa]
	0,0025	[-]
Calculated E-Modulus [GPa]	**210,6201**	

SPECIMEN 6 - Extensometer DAQ Data

(DANTEC)

DAQ Data Table	E-Modulus [GPa]	210,197
Calculated	E-Modulus [GPa]	210,620
	EXTENSION [mm]	0,25809
	STRAIN [-]	0,01032
	Diameter [mm]	6,144

File Path: C:\Users\MTS Landmark\Desktop\ANDREW 2022\03 EN19(T) TEN Tests
Test: Training Extensometer 10
Test Run: Test Run 3
Date: 2022/04/21 15:44:34

$E = \sigma / \varepsilon = (F/A) / (\Delta L/L)$
$\varepsilon = \Delta L / L$

Nominal Gauge Length [mm]: L = 25,0

Displacement [mm]	Load [kN]	Time [s]	Extensometer Strain ε [mm/mm] or [-]	EXTENSION (ΔL) [mm]
0,00514	**0,22236**	0,20801	0,00002	**0,00055**
0,00482	0,35097	0,25781	0,00004	**0,00105**
0,00875	0,54825	0,30762	0,00007	**0,00179**
:	:	:	:	:
0,22160	15,56211	3,04688	0,00247	**0,06181**
0,22555	15,77508	3,09668	0,00252	**0,06295**
0,23254	15,80682	3,14648	0,00252	**0,06296**
0,23495	15,98867	3,19629	0,00255	**0,06367**
0,23937	16,27940	3,24609	0,00258	**0,06462**
0,24468	16,52216	3,29590	0,00263	**0,06570**
0,24658	16,66821	3,34570	0,00265	**0,06614**
:	:	:	:	:
0,62616	27,90412	7,87793	0,00994	**0,24848**
0,63055	27,93002	7,92773	0,01007	**0,25177**
0,63516	27,74901	8,10254	0,01032	**0,25794**
0,63574	27,71789	8,15234	0,01035	**0,25865**
0,65	27,25	32,01	/\--- removal point	

Calculated from 0 - point on TEN graph where modulus line stops touching the test curve (+- before yield kN)	0,5497	[MPa]
	0,0026	[-]
Calculated E-Modulus [GPa]	**212,6973**	

SPECIMEN 7 - Extensometer DAQ Data

(DANTEC)

DAQ Data Table	E-Modulus [GPa]	211,431
Calculated	E-Modulus [GPa]	212,697
	EXTENSION [mm]	0,24846
	STRAIN [-]	0,00994
	Diameter [mm]	6,162

File Path: C:\Users\MTS Landmark\Desktop\ANDREW 2022\03 EN19(T) TEN Tests
Test: Training Extensometer 10
Test Run: Test Run 4
Date: 2022/04/21 16:04:05

$E = \sigma / \varepsilon = (F/A) / (\Delta L/L)$
$\varepsilon = \Delta L / L$

Nominal Gauge Length [mm]: L = 25,0

Displacement [mm]	Load [kN]	Time [s]	Extensometer Strain ε [mm/mm] or [-]	EXTENSION (ΔL) [mm]
-0,00570	**-0,41374**	0,20801	-0,00004	**-0,00093**
-0,00410	-0,27157	0,25781	-0,00002	**-0,00050**
-0,00165	-0,04585	0,30762	0,00001	**0,00025**
:	:	:	:	:
0,21754	15,03402	3,04688	0,00240	**0,05992**
0,21961	15,09302	3,09668	0,00240	**0,06009**
0,22466	15,31098	3,14648	0,00244	**0,06094**
0,22683	15,52882	3,19629	0,00247	**0,06174**
0,23424	15,81697	3,24609	0,00251	**0,06284**
0,23525	15,97935	3,29590	0,00255	**0,06368**
0,23857	16,22663	3,34570	0,00258	**0,06459**
:	:	:	:	:
0,59071	26,88861	7,57910	0,00945	**0,23627**
0,59594	26,89801	7,62891	0,00961	**0,24015**
0,60081	26,94102	7,67871	0,00975	**0,24371**
0,60704	26,93254	7,72852	0,00990	**0,24753**
0,63	26,34	34,96	/\--- removal point	

Calculated from 0 - point on TEN graph where modulus line stops touching the test curve (+- before yield kN)	0,5097	[MPa]
	0,0024	[-]
Calculated E-Modulus [GPa]	**209,5430**	

SPECIMEN 8 - Extensometer DAQ Data

(DANTEC)

DAQ Data Table	E-Modulus [GPa]	208,473
Calculated	E-Modulus [GPa]	209,543
	EXTENSION [mm]	0,25717
	STRAIN [-]	0,01029
	Diameter [mm]	6,279

File Path: C:\Users\MTS Landmark\Desktop\ANDREW 2022\03 EN19(T) TEN Tests
Test: Training Extensometer 10
Test Run: Test Run 5
Date: 2022/04/21 16:19:01

$E = \sigma / \varepsilon = (F/A) / (\Delta L/L)$
$\varepsilon = \Delta L / L$

Nominal Gauge Length [mm]: L = 25,0

Displacement [mm]	Load [kN]	Time [s]	Extensometer Strain ε [mm/mm] or [-]	EXTENSION (ΔL) [mm]
0,00194	**0,16633**	0,22363	0,00003	**0,00073**
0,00268	0,25441	0,27344	0,00005	**0,00131**
0,00685	0,49626	0,32324	0,00008	**0,00190**
:	:	:	:	:
0,22396	15,33188	3,06250	0,00238	**0,05940**
0,22594	15,52024	3,11230	0,00239	**0,05972**
0,23021	15,72374	3,16211	0,00243	**0,06067**
0,23434	15,94788	3,21191	0,00246	**0,06154**
0,23764	16,15952	3,26172	0,00250	**0,06242**
0,24083	16,33498	3,31152	0,00252	**0,06291**
0,24428	16,57141	3,36133	0,00255	**0,06385**
:	:	:	:	:
0,60378	27,03688	7,64453	0,00989	**0,24734**
0,60917	27,08720	7,69434	0,01003	**0,25071**
0,61320	26,90528	7,88672	0,01028	**0,25703**
0,61625	26,89541	7,93652	0,01032	**0,25791**
0,63	26,51	30,40	/\--- removal point	

Calculated from 0 - point on TEN graph where modulus line stops touching the test curve (+- before yield kN)	0,5042	[MPa]
	0,0024	[-]
Calculated E-Modulus [GPa]	**213,4144**	

SPECIMEN 9 - Extensometer DAQ Data

(DANTEC) Split

DAQ Data Table	E-Modulus [GPa]	212,067
Calculated	E-Modulus [GPa]	213,414
	EXTENSION [mm]	0,25715
	STRAIN [-]	0,01029
	Diameter [mm]	6,310

File Path: C:\Users\MTS Landmark\Desktop\ANDREW 2022\03 EN19(T) TEN Tests
Test: Training Extensometer 10
Test Run: Test Run 6
Date: 2022/04/21 16:34:34

$E = \sigma / \varepsilon = (F/A) / (\Delta L/L)$
$\varepsilon = \Delta L / L$

Nominal Gauge Length [mm]: L = 25,0

Displacement [mm]	Load [kN]	Time [s]	Extensometer Strain ε [mm/mm] or [-]	EXTENSION (ΔL) [mm]
0,00403	**0,10341**	0,20703	0,00001	**0,00021**
0,00312	0,27302	0,25684	0,00003	**0,00068**
0,00421	0,41293	0,30664	0,00006	**0,00147**
:	:	:	:	:
0,22120	15,09669	3,04590	0,00226	**0,05645**
0,22329	15,27395	3,09570	0,00228	**0,05704**
0,22667	15,58763	3,14551	0,00234	**0,05852**
0,23283	15,87150	3,19531	0,00237	**0,05928**
0,23664	16,08206	3,24512	0,00240	**0,05993**
0,24050	16,35714	3,29492	0,00245	**0,06117**
0,24464	16,66001	3,34473	0,00249	**0,06217**
:	:	:	:	:
0,64055	28,28401	8,07617	0,00985	**0,24636**
0,64525	28,32248	8,12598	0,01000	**0,25009**
0,65198	28,12573	8,32227	0,01028	**0,25690**
0,65205	28,06259	8,37207	0,01029	**0,25736**
0,67	27,75	34,07	/\--- removal point	

Calculated from 0 - point on TEN graph where modulus line stops touching the test curve (+- before yield kN)	0,5094	[MPa]
	0,0024	[-]
Calculated E-Modulus [GPa]	**212,1460**	

SPECIMEN 10 - Extensometer DAQ Data

(DANTEC) Split

DAQ Data Table	E-Modulus [GPa]	211,148
Calculated	E-Modulus [GPa]	212,146
	EXTENSION [mm]	0,25707
	STRAIN [-]	0,01028
	Diameter [mm]	6,352

File Path: C:\Users\MTS Landmark\Desktop\ANDREW 2022\03 EN19(T) TEN Tests
Test: Training Extensometer 10
Test Run: Test Run 7
Date: 2022/04/21 16:55:19

$E = \sigma / \varepsilon = (F/A) / (\Delta L/L)$
$\varepsilon = \Delta L / L$

Nominal Gauge Length [mm]: L = 25,0

Displacement [mm]	Load [kN]	Time [s]	Extensometer Strain ε [mm/mm] or [-]	EXTENSION (ΔL) [mm]
0,00336	**0,11898**	0,22461	0,00004	**0,00104**
0,00471	0,33676	0,27441	0,00006	**0,00160**
0,00622	0,54698	0,32422	0,00010	**0,00248**
:	:	:	:	:
0,22289	15,45204	3,06348	0,00231	**0,05779**
0,22650	15,72802	3,11328	0,00234	**0,05859**
0,23144	16,00304	3,16309	0,00239	**0,05964**
0,23618	16,26234	3,21289	0,00244	**0,06108**
0,24034	16,57590	3,26270	0,00248	**0,06192**
0,24240	16,77428	3,31250	0,00251	**0,06276**
0,24696	17,08381	3,36230	0,00256	**0,06400**
:	:	:	:	:
0,66057	29,00868	8,34277	0,00997	**0,24924**
0,66456	28,98860	8,39258	0,01007	**0,25179**
0,66902	28,86594	8,57031	0,01031	**0,25785**
0,67101	28,80034	8,62012	0,01032	**0,25811**
0,68	28,35	31,33	/\--- removal point	

Table H-4: TEN test Spec6 to Spec10 measurements (Extensometer) – DAQ data tables (peak and yield loads, E Modulus)

Test Run Results:	Spec6	
Display Name	**Value**	**Unit**
Test Run End Reason	Break Detected	
Area	29,64779	mm²
Peak Stress	1,03088	kN/mm²
Peak Load	**30,56318**	**kN**
Break Stress	1,03088	kN/mm²
Break Load	30,56318	kN
Stress at Yield	0,07622	kN/mm²
Load at Yield	2,25965	kN
Modulus	**210,19724**	**GPa**
Stress at Offset Yield	0,93246	kN/mm²
Load at Offset Yield	**27,64532**	**kN**
Calculated % Elongation	0,20000	mm/mm
Diameter	6,14400	mm

Test Run Results:	Spec7	
Display Name	**Value**	**Unit**
Test Run End Reason	Break Detected	
Area	29,82176	mm²
Peak Stress	1,00066	kN/mm²
Peak Load	**29,84137**	**kN**
Break Stress	1,00066	kN/mm²
Break Load	29,84137	kN
Stress at Yield	0,07803	kN/mm²
Load at Yield	2,32690	kN
Modulus	**211,43119**	**GPa**
Stress at Offset Yield	0,89222	kN/mm²
Load at Offset Yield	**26,60752**	**kN**
Calculated % Elongation	0,20000	mm/mm
Diameter	6,16200	mm

Test Run Results:	Spec8	
Display Name	**Value**	**Unit**
Test Run End Reason	Break Detected	
Area	30,96498	mm²
Peak Stress	0,96360	kN/mm²
Peak Load	**29,83783**	**kN**
Break Stress	0,96360	kN/mm²
Break Load	29,83783	kN
Stress at Yield	0,07303	kN/mm²
Load at Yield	2,26152	kN
Modulus	**208,47288**	**GPa**
Stress at Offset Yield	0,85719	kN/mm²
Load at Offset Yield	**26,54277**	**kN**
Calculated % Elongation	0,20000	mm/mm
Diameter	6,27900	mm

Test Run Results:	Spec9	
Display Name	**Value**	**Unit**
Test Run End Reason	Break Detected	
Area	31,27149	mm²
Peak Stress	0,99666	kN/mm²
Peak Load	**31,16692**	**kN**
Break Stress	0,99666	kN/mm²
Break Load	31,16692	kN
Stress at Yield	0,07054	kN/mm²
Load at Yield	2,20598	kN
Modulus	**212,06706**	**GPa**
Stress at Offset Yield	0,88873	kN/mm²
Load at Offset Yield	**27,79206**	**kN**
Calculated % Elongation	0,20000	mm/mm
Diameter	6,31000	mm

Test Run Results:	Spec10	
Display Name	**Value**	**Unit**
Test Run End Reason	Break Detected	
Area	31,68917	mm²
Peak Stress	0,99736	kN/mm²
Peak Load	**31,60560**	**kN**
Break Stress	0,99736	kN/mm²
Break Load	31,60560	kN
Stress at Yield	0,07575	kN/mm²
Load at Yield	2,40052	kN
Modulus	**211,14758**	**GPa**
Stress at Offset Yield	0,90075	kN/mm²
Load at Offset Yield	**28,54408**	**kN**
Calculated % Elongation	0,20000	mm/mm
Diameter	6,35200	mm

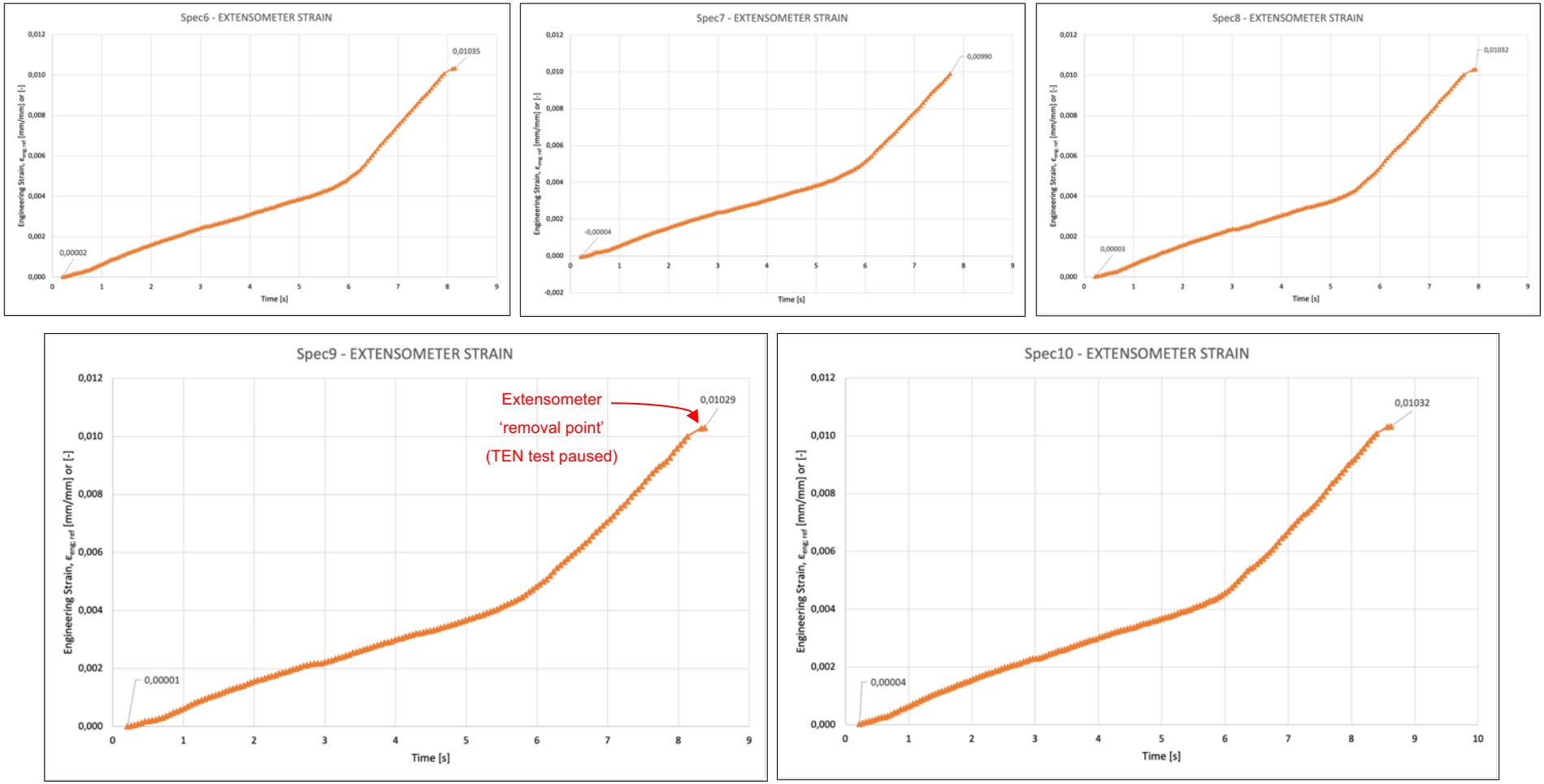


Figure H-4: TEN test Spec6 to Spec10 measurements – extensometer strain vs time curves

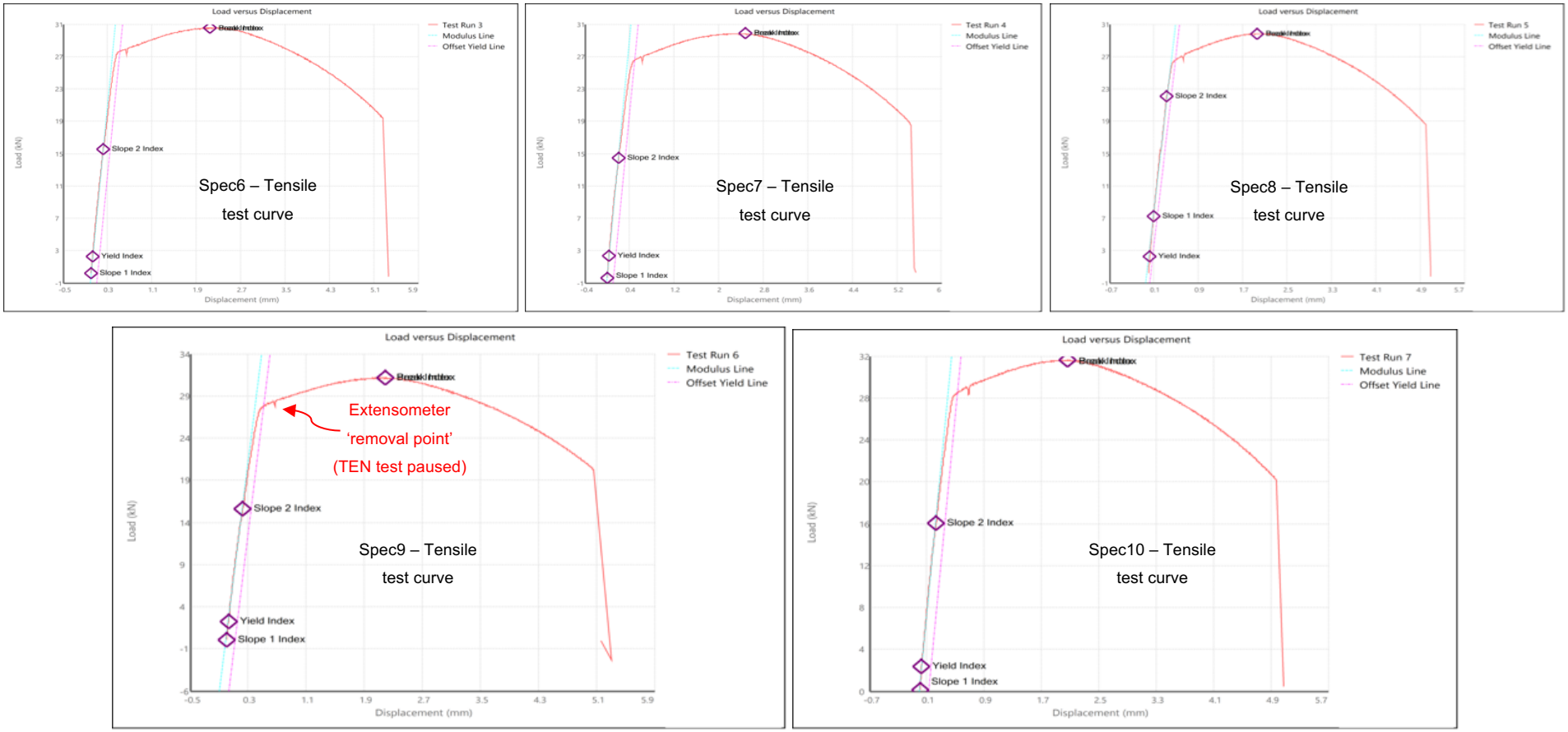
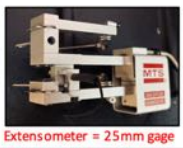
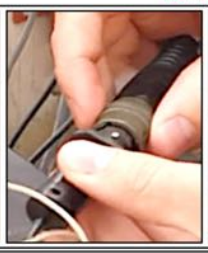
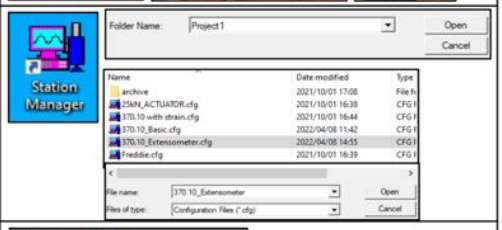
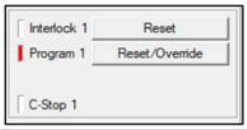
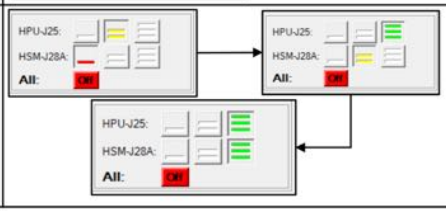
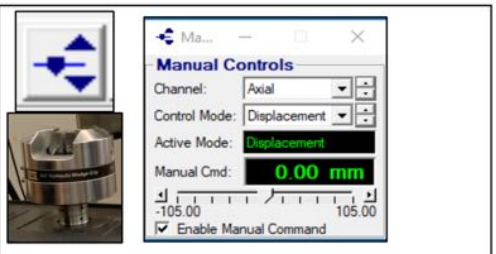
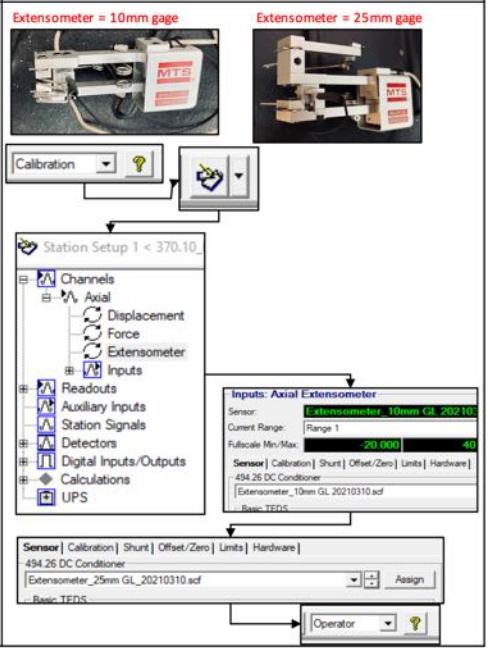


Figure H-5: TEN test Spec6 to Spec10 – load vs displacement curves

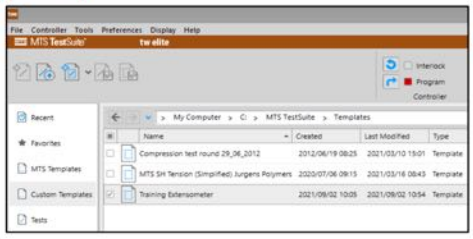
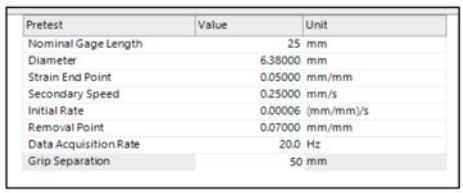
The experimental test procedure for the last five tensile (TEN) tests performed in this study, with extensometer measurement, is provided in Table H-5 below.

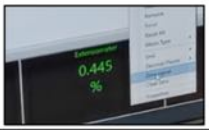
Table H-5: Monotonic tensile test (Extensometer) procedure

	PART A | MACHINE ACTIVATION	
1	Switch on the whole MTS machine (hydraulics box, computer and chiller) as with usual procedure (do not yet open any applications on the computer desktop). **a)** Before continuing with extensometer test steps below, you can/should perform a simple tensile test (with that procedure) to warm up the MTS hydraulic system (removes inaccuracy of first tests). Or, perform a cyclic loading/movement of the actuator for 10-15min at ± 10-15Hz with no specimens or actual testing being recorded (ask Mr. Sarel for help on this). After warm-up of machine is done, re-close all open windows (e.g. station manager etc.) before proceeding to next steps.	   Extensometer = 10mm gage  Extensometer = 25mm gage
2	Plug the Extensometer device (from its black plastic case in MTS cupboard) into the dedicated 5 pin plug located on the right cylinder pillar of the MTS bench (hangs in a bracket that is fixed to the pillar). The plugs lock together by twisting the ring over the interface of the two once plugged in. Hang the connected plugs back into the bracket on the MTS pillar and ensure the thin white cable of the extensometer is untwisted/uncoiled properly.	  
3	Open "Station Manager" on the desktop, open the "Project1" folder, select the "370.10_Extensometer.cfg" configuration file and select "Open". **a)** The Station Manager has to be opened with the above ".cfg" file, otherwise the Extensometer will not be picked up by the MTS, and no readings will be available. E.g., if the "370.10_Basic.cfg" file was previously opened/used for a normal tensile test, shut down and close all Station Manager and TW Elite (orange/brown icon) programs/windows, and restart with the above step.	
4.1	After Station Manager opened, locate and select/check the "Exclusive Control" tick-box on the right hand side (RHS) under "Station Controls".	
4.2	Select the "Reset" button next to the "Interlock 1" that has red light/bar next to it.	
4.3	Then, activate the hydraulic system of the MTS by incrementally selecting, with +-5 second rest/wait between each button selection, the "HPU-J25" and "HSM-J28A" buttons (1 red, 2 yellow, 3 green horizontal bars). Only select the next button at each once the button stops flickering, until all three buttons are selected and green, for the two hydraulic systems.	
5	Under the "Station Controls", locate and select the "Manual Command" button (one of 6 below the blue text heading, above the exclusive control check box) (it has two large blue arrows pointing up and down). Set the "Control Mode" to "Displacement" and at the bottom select/tick the "Enable Manual Command" option. **a)** This is done for safety purposes to override the program while your hands will be working between the actuators. **b)** You should 'zero' the position of the MTS actuator (bottom one) by entering value "0mm" into the lower black box, and pressing enter. The actuator will now set at its vertical zero point (for displacement up or down that will occur during test), ready for tensile specimen to be loaded and test to be performed.	

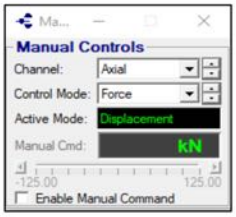
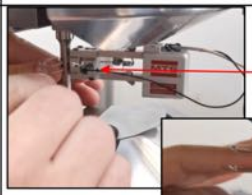
6	Under the “Station Controls”, locate and select the “Detectors” button (one of 6 below the blue text heading, above the exclusive control check box) (it has two small red arrows and two blue lines with triangles in between). A wide window will open with black boxes (12) and green numbers (ensure the “Limit Detectors” tab in this window is selected). **a**) In the “Detectors” window, under the “Lower Limit” column, set the “Axial Displacement” row value (green) to -5mm, and in the dropdown next to it, select “Program Stop” as the "Lower Action" (green bar will appear next to -5mm value). **b**) This is done to prevent the MTS from compressing the actuators together by more than 5mm for any reason whatsoever (a safety setting).	
"7"	**NOTE**: IF the extensometer’s gauge length (spacing between the two blade sharp edges) is change to 10mm or 25mm (using aluminum pieces from its case, making it bigger/smaller), then the “calibration” .scf file has to be re-selected/checked in the station manager before running a the test: **(only IF the "default25" or "default" version of the “370.10_Extensometer.cfg” configuration file was not explicitly selected when starting up the station manager app from step 2-3)** **(i)** Go to station manager window (already open). **(ii)** At the top LHS next to the red MTS symbol, look for the dropdown that says “Operator”. Change this to “Calibration” (enter password: Calibration). Then to the left of the dropdown, look for the button that says “Station Setup” and select it. **(iii)** A window will open. In the LHS pane of this window select the "+" sign next to 'Channels' and then next to 'Axial' and then click on 'Extensometer'. To the RHS, below the black box of with green lettering (fullsclae min/max), on the "Sensor" tab, change the calibration template (in first dropdown) to the one with the name that has the same [mm] value as that to which you extended or decreased the extensometer gauge length (spacing of the blade sharp edges). The dropdown shows all the saved calibration files with gauge lengths in the name. Select the ".scf" file with the most recent date (e.g., in the file name "Extensometer_25mm_GL_20210310.scf"), and select "Assign" next to dropdown arrow. Close the window. Set the Station Manager dropdown back to "Operator". (NOTE) If this is not done beforehand, the scaling of the extensometer will be out and the GPa reading for E Modulus will not be the correct value once the test is done and the results are obtained. (NOTE) If later a "Sensor change notification" window pops-up, just check that the	

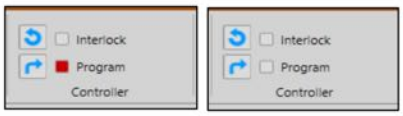
PART B | TEST- PROGRAM SETUP

8.1	Now locate the “TW Elite” program icon (orange/brown) on the desktop of the computer, and open the program.	
8.2	When the program is open, select the “Custom Templates” directory in the left hand side (LHS) pane of the window. Then double click the “Training Extensometer” template to open it. Note, the extensometer has to be plugged in before this template is opened (ref step 2).	
9.1	Specify the “Nominal Gage Length” in the “Monitor” tab of the TW Elite test suite window that opened. This is **not** the nominal **gage length of** your **specimen**, but the rather that of the extensometer. (That is, the distance between the extensometer’s blade edges (10mm or 25mm). Measure with vernier if uncertain to get the estimate distance. Extensometer aluminum pieces will provide precisely 10 or 25mm. Measuring it is just to confirm.)	
9.2	Specify the “diameter” for the tensile test specimen next.	
9.3	The “Strain End Point” must be set to a value previously defined for your specimen. This is the mm/mm value until which the extensometer will “measure” the strain used to calculate the E Modulus for results (Standard value: 0.01 mm/mm).	
9.4	Leave the “Secondary speed” at the standard 0.25mm/s and the “Initial Rate” at the standard 0.00006(mm/mm)/s.	

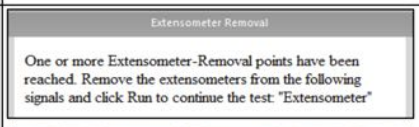
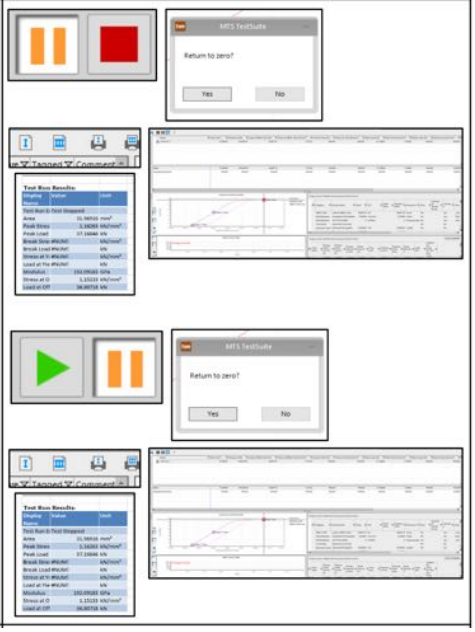
9.5	Set the “Removal Point” to a value slightly larger than that of the “Strain End Point" (Standard value: 0.03 mm/mm). This is the value reached during tensile test, at which the computer will give a message to remove the extensometer from the specimen (during test run). You can continue the test after this, to a complete normal tensile test to also obtain Sy and Sut for the specimen. Or you can select STOP (red block at top of window) after removing extensometer, if you just want to obtain the extensometer results from the tensile test.	
9.6	Leave “Data Acquisition Rate” at the standard 20Hz (may be set higher if needed).	
9.7	Specify the “Grip Separation” value from a manual measurement of the MTS machine's actuator grip seperation (wedge blocks inside actuators, flat face to flat face vertical distance measurement).	
10.1	Right click on the black “Extensometer” block at the bottom of the screen and select “Zero Signal” to zero the extensometer reading BEFORE loading test specimen into actuator clamps (see next steps).	 
10.2	Right click on the black “Load” block at the bottom left of the screen and select “Zero Signal” to zero the kN reading BEFORE loading test specimen into actuator clamps (see next steps).	 

PART C | TEST - SPECIMEN / EXTENSOMETER MOUNTING

11.1	Load the tensile test specimen (dog-bone ASTM E8, preferrably polished) into the MTS wedge grips (as would be done with normal tensile test). **First** clamp the specimen into the **bottom actuator wedge grip** (actuator set at zero vertical position, ref step 7). **Second,** lower the top head and **clamp the top wedge grip** onto specimen. Then lock the top wedge grip head with the turn switch (third from the left). NOTE: do not yet switch the red bunny/turtle button to the rabbit side (red light on) as it will be done after attaching the extensometer to specimen (steps to follow).	  
11.2	AFTER loading the specimen, go to the "Manual Controls" window previously opened, and set the “Control Mode” from "Displacement" (as it was left like in step 7) to “Force” (with the “Enable Manual Command” option still selected/ticked). **a**) Now enter ‘zero’ as the kN value in the bottom black box and press enter. The resultant compressive/tensile force of the actuator wedge clamps is now zero'ed away (caused by clamping of specimen). **b**) Leave the "Control Mode" with the "Force" selected, and uncheck the "Enable Manual Command" tick box and then minimize the "Manual Controls" window.	 
12.1	Mount the extensometer to the tensile test specimen’s gauge area. This is done by wrapping the large spring arms of the extensometer around the specimen, which presses the two parallel blades against the specimen cylinder. The blades must be alligned with each of the spring arms respectively. Ensure the extensometer is positioned as upright as possible on the specimen, with blades horisontal and centred on specimen gage area. NOTE, mounting the extensometer must be done with the black zero pin still in position between the extensometer arms. NOTE: photo's here are with the extensometer with 10mm gauge length (distance between blade edges). The same mounting procedure is done for the 25mm gaged extensometer.	 
12.2	Once the extensometer is securely mounted and centred on the specimen gauge area, remove the zero pin. See figures to the right. Do not move/touch the extensometer again when the zero pin is removed.	  

13	Finally **turn** the bunny/turtle button (**interlock** speed) **to** the **rabbit** (right) side (**red light** comes **on**). Ensure the top wedge grip is locked in position before continuing with the test (see step 14.1).	
14	Reset the "Interlock" (anticlockwise circular arrow) at the top of the window in the "Controller" group. The red light next to "Program" will turn off, and testing may proceed. NOTE: if step 12 is not done (rabbit switched on) then this interlock in this step will not reset, and the red light next to "Program" will stay on. Starting test will not be allowed and MTS will give a pop-up message about interlock problems.	

PART D | TEST- RUN

15	Go to the open TW Elite test suite window, and press big GREN PLAY arrow under "Test Controls" group to START the test. **a**) An "MTS TestSuite Input Variables" pop-up window will open. Confirm the "Grip Separation" and extensometer's "Nominal Gage Length" values here. Press OK. **b**) A second pop-up will appear. Confirm the specimen's test zone diameter here. Press OK. **c**) NOTE: when you press OK in this second window, a final window will pop-up stating that the official tensile test with extensometer measurement will start. Press OK and let the test run (± 5-9 seconds).	
16	A pop-up window will appear on the computer screen: Reading → 'One or more Extensometer-Removal points have been reached. Remove the extensometer(s) from the following signals and click Run to continue the test: "Extensometer" '. Do not click anything yet, FIRST NOW GENTLY REMOVE the EXTENSOMETER from the specimen (put zero pin back to not damage sensor), and put it down next to but away from the actuator. Take care to not move/damage the free moving arm of the extensometer until the zero pin is put back in. NOTE: This step should be done rather QUICKLY, but CAREFULLY since the tensile specimen is under immense tensile force now. A slight drop in the kN (load) value will be inevetable due to this pause in the tensile test run whilst removing the sensor. Therefore, if the test is to be continued (see next step at (b)), this pause in the test run should be kept as short as possible (before selecting PLAY button again).	 
17	You now have two options whilst ornage PAUSE is in action (must be determined before starting test): **a**) **ONE** is to press the big **RED STOP square** under the "Test Controls" This **TERMINATES** the **tensile extensometer test** with only extensometer measurements (extension and E Modulus data), and takes you to the processed results window. Press "okay" (thus ignore) on the "Measured Elongation" window that opens (usual value of 30mm). Select "NO" in the "Return to Zero" window that opens. You will be directed to the processed results window. For data, select File -> Export -> Raw Data, and save in your folder. For graphs, select the button with the blue "I" (single test result Excel) to obtain and save graphic results as Excel file in your folder. For multiple tests combined in one Excel, select the blue "III" button. **b**) **TWO** is to press the big **GREEN PLAY arrow** again under the "Test Controls" This will **CONTINUE** with a normal **tensile test** for further Sy and Sut measurements that can be obtained. Test will continue until "Break Detected" (specimen fractures in tension). Press "okay" (thus ignore) on the "Measured Elongation" window that opens (usual value of 30mm). Select "NO" in the "Return to Zero" window that opens. You will be directed to the processed results window. For data, select File -> Export -> Raw Data, and save in your folder. For graphs, select the button with the blue "I" (single test result Excel) to obtain and save graphic results as Excel file in your folder. For multiple tests combined in one Excel, select the blue "III" button.	

"18"	IF **MORE TESTS** ARE TO BE PERFORMED: **If option "b) CONTINUE" in previous step was done:** Remove the broken specimen halves from MTS grips. - Re-do step 5 and check step 6. Restart procedure at step 9.1 through to here. Got to the "Monitor" tab at the top of the "TW Elite" programme window (window showing the current results) to start entering the new specimen's details. **HOWEVER:** **If option "a) TERMINATE " in the previous step was done** Go to the "Manual Controls" window. Tick the "Enable Manual Command" box, then set the "Control Mode" to "Force" (the current tensile force on the specimen will be displayed). Incrementally (manually) lower that kN value by entering loads smaller than the one displayed, until reaching 0kN again. ONLY THEN, can you turn the interlock button to the turtle (the reverse of step 13), and start to unlock and open the grip clamps to remove the specimen (unbroken). *If the tensile force (statically present in tension) is not lowered to zero, the MTS grips will knock/split open under the tension when the grip clamps are opened. This might be hazardous and/or damage the MTS machine. - Re-do step 5 and check step 6. Restart procedure at step 9.1 through to here. Got to the "Monitor" tab at the top of the "TW Elite" programme window (window showing the current results) to start entering the new specimen's details.	

H1.3. DANTEC DIC System Verification Measurements and Calculations

The DANTEC DIC System secondary verification measurements were taken during the last five (5) tensile (TEN) tests on Spec6-Spec10 (see previous Appendix H1.2). The reason for this was so that the related extensometer strain measurement data on each specimen (see Table H-3 and Figure H-4) could be used, as a reference, to verify the accuracy of the DANTEC system strain measurements on the specimens.

The relevant DANTEC strain measurements were obtained using the general DIC measurement procedure, as provided in Appendix B6. For these measurements, the speckle patterns were prepared on the five test specimens according to the procedure and illustrations also provided in Figure B-10 of Appendix B6 and can be viewed in Figure H-3 (previous Appendix H1.2) or Figure H-7 (a) to follow. The DANTEC system setup with respect to the MTS Landmark tensile test machine (Appendix A1), the test specimen and the extensometer (Appendix B6) is illustrated in the schematic of Figure H-6 below (not to scale).

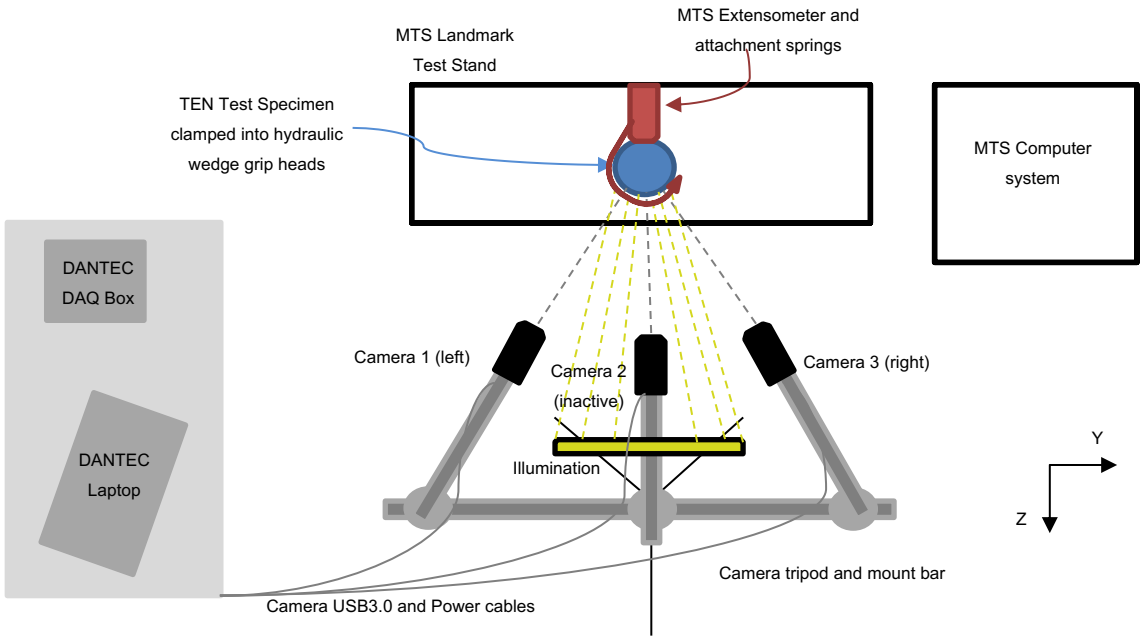


Figure H-6: TEN test Spec6 to Spec10 measurements – DANTEC DIC System setup schematic (top view)

The DANTEC system was positioned in front of the MTS Landmark test bench so to allow the cameras to view the specimen from the front (less obstruction from the extensometer and MTS test bench components) with the appropriate stereo angle between cameras 1 and 3 (recommended 30 – 60 [°] for proper 3D measurement of a cylindrical object). Camera 1 was used as the reference for measurements and correlation/evaluation of the recorded images for

each test. The positioning of the system (tripod and mount bar) did not change between different test measurements (especially after initial camera calibration).

Once a speckle pattern prepped TEN test specimen was appropriately loaded into the MTS test bench wedge grips, and the extensometer was appropriately attached to the specimen gauge, the DANTEC measurement commenced. For this, the camera recording sequence was set to take between 40 – 50 consecutive photos at a frame rate of about 2 [Hz], which allowed sufficient time (+-20-25 seconds) for the DANTEC strain measurement (at first measuring stationary test specimen) to 'overlap' the interval of extensometer strain measurement (+-7-9 seconds). The DANTEC recording sequence was started first, after which the tensile test started immediately after this (extensometer measuring during the first few seconds of it). The tensile test ran just past the material yield point (a pre-set in the test procedure), at which the tensile test procedure automatically paused the test on the computer (notifying removal of the extensometer). Reference can be made to Figure H-5, where extensometer removal points are indicated. Throughout this, the DANTEC recorded the extensometer part of the tensile test and the last part where the test was paused (holding the specimen in static tension). After the DANTEC completed the set recording sequence, the extensometer was removed, and the tensile test procedure immediately resumed. The test then ran, according to the standard tensile test rate/procedure, until the tensile test concluded due to the specimen failing in tension (see Figure H-5).

The above was done for all five tests. The last two test specimen speckle patterns (Spec9 and Spec10, shown in Table H-6) were prepared with a 'split' between the top and bottom halves of the specimens. These acted as control measurements to ensure that the spray paint layer on the gauge length surfaces (of Spec6-Spec8) did not experience subordinate or mutually influential deformations or strains between the top and bottom of a specimen.

After all the measurements were concluded, the extensometer strain data sets were exported and processed as described in Appendix H1.2 to obtain the direct experimental specimen gauge strain measurements (reported in Table H-3 and Figure H-4). For the DANTEC measurements, however, it was first required to perform the necessary image processing using the ISTRA 4D software on the dedicated DANTEC computer.

This involved defining digital masks (with a start point in each) on the speckle pattern surfaces visible to the cameras (Figure H-7 (a)). This mask specified the evaluation area and excluded any reflective (e.g., attachment springs) or unfocussed image areas from the correlation to be performed (search/focus area for software to track speckle movements). After this, the appropriate image correlations were performed to obtain the evaluated areas on the specimens (Figure H-7 (b) and (c)) from which digital measurement data could be extracted. The next step was to define a static measurement coordinate system (different from the camera 'calibration'

coordinate system) for the evaluated images by using the engineering principal strain 1 vector orientations and the indicated best-fit plane area (light blue geometric field) on the evaluated specimen surface as a reference to appropriately orient the coordinate system x-axis (turquois asterisk) and z-axis position (red asterisk) as in Figure H-7 (d). Customarily for long or cylindrical-shaped specimens, the x-axis direction is oriented along the longitudinal length of the specimen (above or below the z-axis origin position) and inside the best-fit plane area. Suppose the x-axis was positioned to the right or left of the z-axis origin. In that case, it may lead to inappropriate coordinate system definition and, thus, incorrect displacement and strain measurement data (which bears reference to this coordinate system). The principal strain 1 vector orientations and the best-fit plane are independent of the defined coordinate system, thus serving as appropriate references for the axes positioning.

Since the required measurement quantity was the specimen gauge area strain (on the front), it was required to next define a digital line gauge element in the software on the surface of the specimen. This was done within the available colour field (area for attainable measurement data) between the extensometer attachment springs. Again, using the principal strain 1 vectors and best-fit plane fields as references for the best longitudinal positioning and orientation of the line gauge (Figure H-8 (a) and (b)). Ultimately the required line gauge strain, extension and length data was exported (over all the recorded steps/images – complete data set) and processed as illustrated in Table H-6 and Figure H-9. The DANTEC line strain measurement values $\varepsilon_{eng\ (DANTEC)}$ were calculated with Equation (H-5) below using the appropriate maximum line strain value extracted from the processed data (in Table H-6). These strain values were identified on each specimen's line strain curve (last point of measured strain, at flattening of the curve). This strain was then compared with the extensometer-measured strain value $\varepsilon_{eng;\,ref\ (Extensometer)}$ (in Table H-3 and Figure H-4) as calculated with Equation (H-4) below. The difference between the two measured strains was calculated as a percentage value using Equation (H-6) after that (extensometer as reference) and reported in Table H-7 (to follow below).

$$\varepsilon_{eng;\,ref\ (Extensometer)}\ [-] = (\varepsilon_{max}\ [-] - \ \varepsilon_{min}\ [-])_{extensometer} \tag{H-4}$$

$$\varepsilon_{eng\ (DANTEC)}\ [-] = \frac{\varepsilon_{eng;Line1;max}\ [\mu strain]}{10^6} \tag{H-5}$$

$$Difference\ [\%] = \left(\frac{\varepsilon_{eng;\,DANTEC}\ [-] - \varepsilon_{eng;\,ref;\,Extensometer}[-]}{\varepsilon_{eng;\,ref;\,Extensometer}\ [-]}\right) 100 \tag{H-6}$$

It should be noted that the unit for extensometer data was 'strain' [mm/mm] or [-] (as shown in Figure H-4 previously), and for the DANTEC line gauge element, it was 'micro strain' [μstrain] (as shown in Figure H-9 to follow). The appropriate conversions were therefore done to obtain the 'strain' values for comparison (as shown in Figure H-10 to follow).

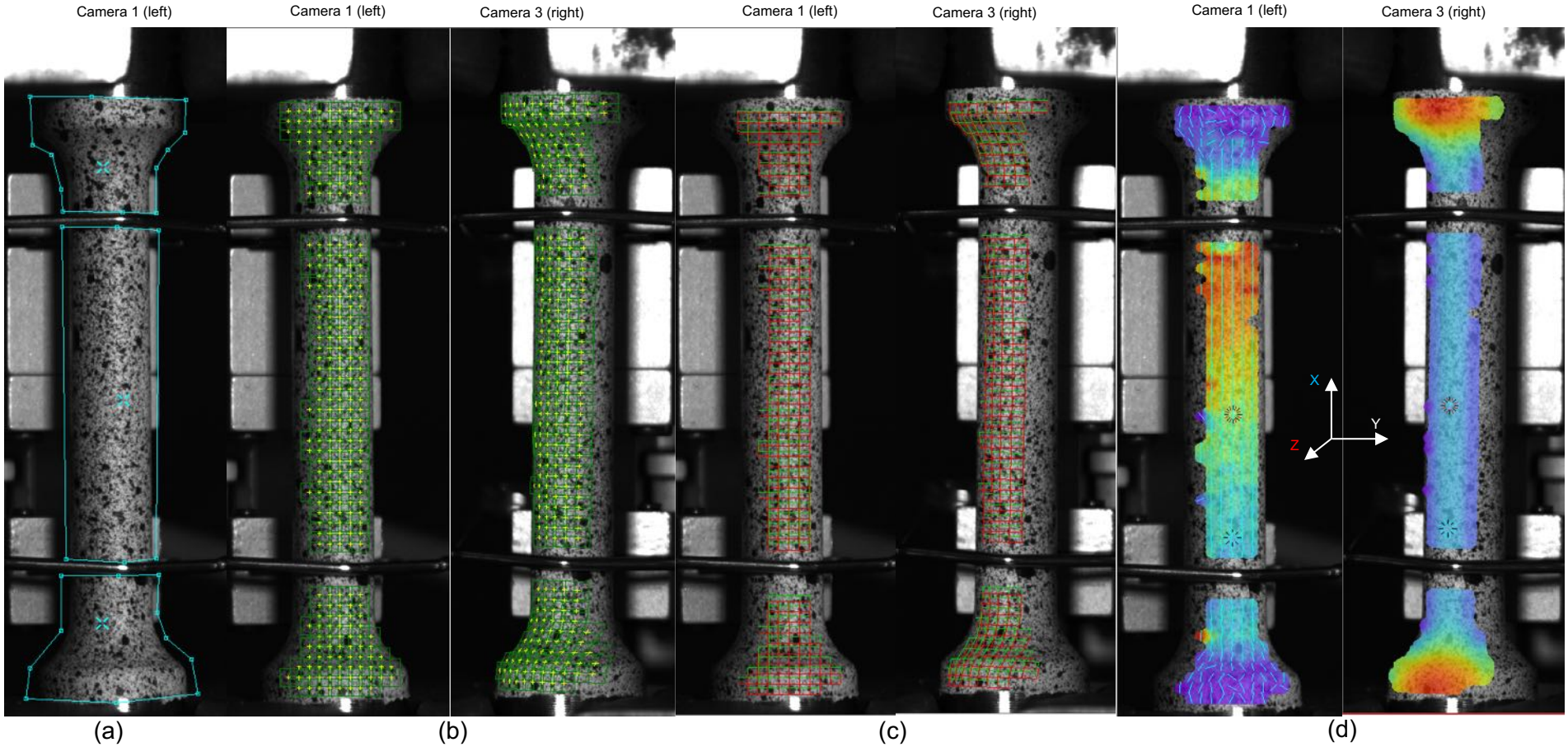


Figure H-7: TEN test Spec6 (Extensometer and DANTEC) – DANTEC (a) mask and start point definition, (b) evaluation grid, (c) displacement grid and (d) measurement (user) coordinate system definition

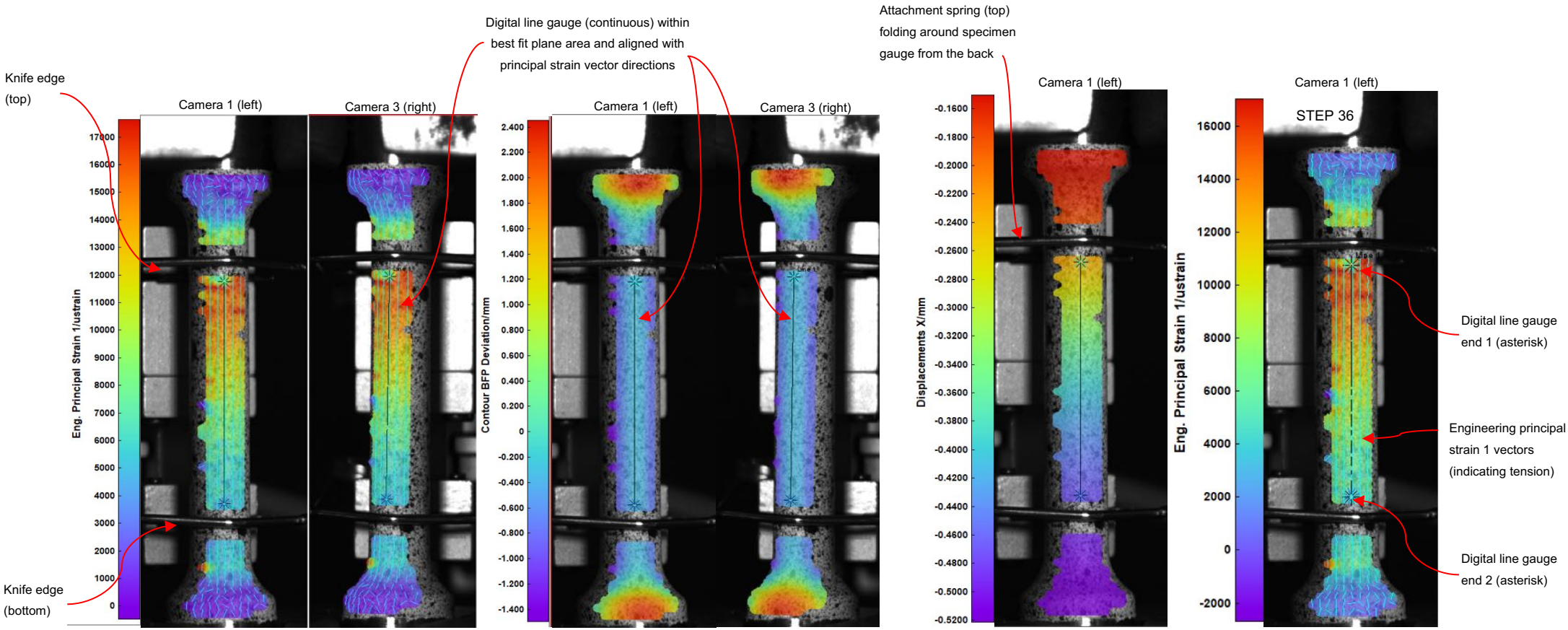


Figure H-8: TEN test Spec6 (Extensometer and DANTEC) – DANTEC (a) line gauge element definition and positioning, (b) specimen extension measurement

Table H-6: TEN test Spec6 to Spec10 measurements – DANTEC DAQ data exports from ISTRA 4D measurements

SPECIMEN 6 - Dantec Data

Line strain is already in deltaL form

STATIC Coord Syst (defined)	LINE GAUGE

Step No.	Line 1 (Reference Step: 0) Gauge Length / Gauge Length	Line 1 (Reference Step: 0) Length Change / Length Change	Line 1 (Reference Step: 0) Gauge Strain / Eng. Line Strain
	Centiux/mm	Displacement/mm	Strain/ustrain
0	22,5223	0,0000	0,0000
1	22,5229	0,0005	23,8419
2	22,5227	0,0003	14,6627
3	22,5227	0,0004	16,5701
4	22,5222	-0,0001	-5,6424
5	22,5230	0,0007	29,8023
6	22,5221	-0,0002	-8,2951
7	22,5227	0,0003	14,1859
8	22,5231	0,0008	33,3786
9	22,5229	0,0006	27,0605
10	22,5235	0,0011	49,5911
11	22,5226	0,0003	12,9938
12	22,5229	0,0005	23,2458
13	22,5229	0,0006	27,2989
14	22,5225	0,0002	7,0334
15	22,5222	-0,0001	-5,7817
16	22,5226	0,0003	12,8746
17	22,5276	0,0053	233,5310
18	22,5352	0,0129	571,4890
19	22,5447	0,0224	994,2050
20	22,5530	0,0307	1361,9700
21	22,5611	0,0388	1722,2200
22	22,5688	0,0465	2063,9900
23	22,5753	0,0529	2350,0900
24	22,5810	0,0587	2606,2500
25	22,5897	0,0674	2980,8400
26	22,5949	0,0726	3221,5100
27	22,6020	0,0796	3535,6300
28	22,6083	0,0860	3817,3200
29	22,6156	0,0933	4140,7300
30	22,6234	0,1011	4487,6300
31	22,6351	0,1127	5005,3600
32	22,6560	0,1336	5932,8100
33	22,6803	0,1580	7013,9200
34	22,7058	0,1835	8147,0000
35	22,7322	0,2099	9317,9900
36	22,7528	0,2305	10232,1600
37	22,7547	0,2323	10315,2000
38	22,7543	0,2320	10300,8000
39	22,7552	0,2329	10339,1000
40	22,7558	0,2335	10366,1000
41	22,7555	0,2332	10352,6000
42	22,7557	0,2334	10361,3000
43	22,7560	0,2337	10375,3000
44	22,7568	0,2345	10412,5000
45	22,7564	0,2340	10391,8000
46	22,7569	0,2345	10412,8000
47	22,7576	0,2352	10444,2000
48	22,7577	0,2353	10448,6000
49	22,7578	0,2354	10453,5000
50	22,7582	0,2359	10471,9000

STEP 16 – 36

SPECIMEN 7 - DANTEC DAQ Data

Line strain is already in deltaL form

STATIC Coord Syst (defined)	LINE GAUGE

Step No.	Line 1 (Reference Step: 0) Gauge Length / Gauge Length	Line 1 (Reference Step: 0) Length Change / Length Change	Line 1 (Reference Step: 0) Gauge Strain / Eng. Line Strain
	Centiux/mm	Displacement/mm	Strain/ustrain
0	23,1156	0,0000	0,0000
1	23,1162	0,0006	25,6300
2	23,1159	0,0003	13,5899
3	23,1164	0,0007	31,4713
4	23,1154	-0,0002	-8,0599
5	23,1163	0,0007	28,3718
6	23,1152	-0,0004	-16,7489
7	23,1163	0,0007	30,6368
8	23,1166	0,0009	41,0080
9	23,1154	-0,0002	-10,0732
10	23,1153	-0,0003	-12,4574
11	23,1167	0,0010	44,9419
12	23,1165	0,0009	36,8357
13	23,1158	0,0002	7,8678
14	23,1159	0,0003	12,1593
15	23,1154	-0,0002	-8,9407
16	23,1165	0,0009	38,1470
17	23,1161	0,0004	18,2390
18	23,1159	0,0003	12,0401
19	23,1153	-0,0004	-16,1529
20	23,1209	0,0053	229,8360
21	23,1302	0,0145	626,4250
22	23,1409	0,0253	1094,9400
23	23,1475	0,0318	1377,7900
24	23,1569	0,0413	1784,8000
25	23,1647	0,0490	2120,7300
26	23,1717	0,0561	2427,3400
27	23,1781	0,0625	2704,0200
28	23,1838	0,0682	2950,4300
29	23,1922	0,0766	3314,3800
30	23,1991	0,0834	3610,0100
31	23,2052	0,0896	3876,0900
32	23,2171	0,1014	4387,7400
33	23,2316	0,1159	5015,8500
34	23,2547	0,1390	6014,7000
35	23,2788	0,1632	7058,1400
36	23,3057	0,1901	8222,5800
37	23,3344	0,2187	9462,7100
38	23,3590	0,2434	10529,2000
39	23,3647	0,2491	10774,3000
40	23,3651	0,2494	10790,3000
41	23,3659	0,2503	10826,9000
42	23,3662	0,2506	10841,3000
43	23,3668	0,2512	10865,1000
44	23,3676	0,2519	10898,6000
45	23,3688	0,2532	10951,9000
46	23,3689	0,2532	10955,6000
47	23,3685	0,2529	10940,0000
48	23,3688	0,2531	10950,8000
49	23,3687	0,2531	10949,8000
50	23,3702	0,2546	11014,7000
51	23,3698	0,2541	10993,7000
52	23,3701	0,2545	11008,7000

STEP 19 – 38

SPECIMEN 8 - DANTEC DAQ Data

Line strain is already in deltaL form

STATIC Coord Syst (defined)	LINE GAUGE

Step No.	Line 1 (Reference Step: 0) Gauge Length / Gauge Length	Line 1 (Reference Step: 0) Length Change / Length Change	Line 1 (Reference Step: 0) Gauge Strain / Eng. Line Strain
	Centiux/mm	Displacement/mm	Strain/ustrain
0	24,3037	0,0000	0,0000
1	24,3038	0,0001	5,6028
2	24,3043	0,0006	24,9147
3	24,3044	0,0007	30,5176
4	24,3045	0,0008	33,2934
5	24,3028	-0,0009	-37,1337
6	24,3049	0,0013	52,2137
7	24,3035	-0,0002	-7,9870
8	24,3042	0,0006	22,6486
9	24,3030	-0,0007	-28,7294
10	24,3030	-0,0007	-28,4910
11	24,3047	0,0010	41,1272
12	24,3034	-0,0002	-9,5964
13	24,3054	0,0017	71,0487
14	24,3041	0,0005	19,7887
15	24,3044	0,0007	28,3718
16	24,3045	0,0009	36,0012
17	24,3049	0,0012	50,9024
18	24,3088	0,0052	213,0270
19	24,3204	0,0168	689,2680
20	24,3303	0,0266	1094,4600
21	24,3386	0,0350	1439,3300
22	24,3473	0,0436	1791,6200
23	24,3538	0,0501	2060,6500
24	24,3617	0,0581	2389,4300
25	24,3670	0,0634	2607,5800
26	24,3743	0,0707	2907,4000
27	24,3836	0,0799	3288,3900
28	24,3891	0,0854	3514,7700
29	24,3955	0,0918	3777,6200
30	24,4042	0,1005	4136,5600
31	24,4181	0,1145	4709,2400
32	24,4408	0,1372	5643,4900
33	24,4632	0,1595	6562,7100
34	24,4895	0,1858	7644,4200
35	24,5164	0,2127	8751,7500
36	24,5376	0,2339	9624,9600
37	24,5407	0,2370	9753,3500
38	24,5407	0,2371	9754,1800
39	24,5408	0,2371	9755,8500
40	24,5410	0,2374	9767,0600
41	24,5419	0,2382	9801,7500
42	24,5424	0,2388	9823,6800
43	24,5442	0,2406	9898,9000
44	24,5431	0,2394	9852,4100
45	24,5435	0,2398	9868,3800
46	24,5427	0,2391	9836,2000
47	24,5437	0,2400	9876,4900
48	24,5436	0,2399	9872,5600
49	24,5442	0,2405	9894,9700

STEP 17 – 37

SPECIMEN 9 - Dantec Data

Line strain is already in deltaL form

STATIC Coord Syst (defined)	LINE GAUGE

Step No.	Line 1 (Reference Step: 0) Gauge Length / Gauge Length	Line 1 (Reference Step: 0) Length Change / Length Change	Line 1 (Reference Step: 0) Gauge Strain / Eng. Line Strain
	Centiux/mm	Displacement/mm	Strain/ustrain
0	24,5587	0,0000	0,0000
1	24,5592	0,0005	20,5040
2	24,5590	0,0004	15,0204
3	24,5600	0,0013	54,5979
4	24,5604	0,0017	69,8566
5	24,5593	0,0007	27,5373
6	24,5591	0,0004	17,5238
7	24,5589	0,0003	10,2520
8	24,5591	0,0004	17,0469
9	24,5590	0,0003	11,9209
10	24,5600	0,0014	55,9092
11	24,5600	0,0013	54,1210
12	24,5601	0,0015	59,2470
13	24,5660	0,0073	299,2150
14	24,5769	0,0182	742,4350
15	24,5864	0,0277	1129,2700
16	24,5952	0,0366	1488,8000
17	24,6024	0,0437	1780,5100
18	24,6097	0,0511	2079,3700
19	24,6171	0,0585	2380,2500
20	24,6231	0,0644	2622,2500
21	24,6311	0,0724	2947,8100
22	24,6386	0,0799	3255,1300
23	24,6447	0,0860	3502,1300
24	24,6525	0,0938	3819,4700
25	24,6590	0,1004	4086,7300
26	24,6689	0,1102	4487,7500
27	24,6825	0,1238	5042,2000
28	24,7020	0,1434	5838,3900
29	24,7241	0,1654	6736,7600
30	24,7517	0,1931	7862,4500
31	24,7752	0,2166	8818,5100
32	24,8020	0,2433	9906,5300
33	24,8262	0,2675	10078,8000
34	24,8075	0,2488	10132,7000
35	24,8069	0,2482	10107,0000
36	24,8076	0,2489	10135,4000
37	24,8084	0,2498	10169,7000
38	24,8080	0,2493	10150,9000
39	24,8095	0,2509	10216,0000
40	24,8094	0,2508	10211,1000
41	24,8111	0,2524	10277,4000
42	24,8113	0,2526	10287,2000
43	24,8100	0,2514	10235,0000
44	24,8110	0,2524	10276,4000
45	24,8105	0,2519	10256,1000
46	24,8114	0,2528	10291,8000

STEP 12 – 33

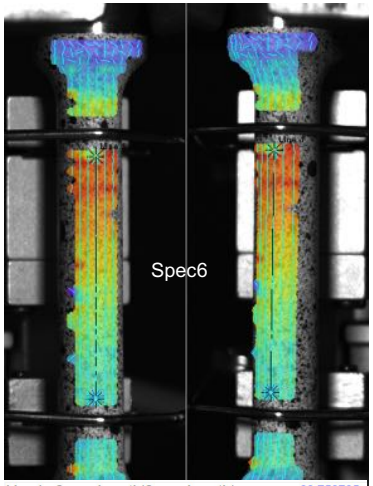
SPECIMEN 10 - Dantec Data

Line strain is already in deltaL form

STATIC Coord Syst (defined)	LINE GAUGE

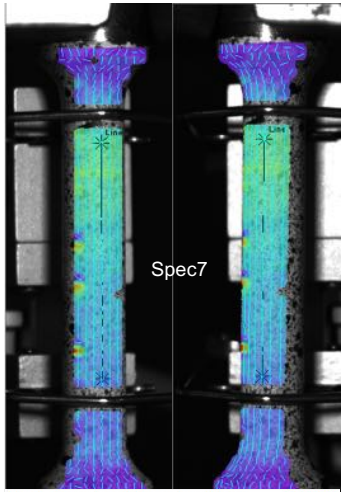
Step No.	Line 1 (Reference Step: 0) Gauge Length / Gauge Length	Line 1 (Reference Step: 0) Length Change / Length Change	Line 1 (Reference Step: 0) Gauge Strain / Eng. Line Strain
	Centiux/mm	Displacement/mm	Strain/ustrain
0	23,5366	0,0000	0,0000
1	23,5365	0,0000	-0,2980
2	23,5373	0,0007	29,6831
3	23,5365	0,0000	-1,3113
4	23,5369	0,0003	14,3051
5	23,5374	0,0009	38,1470
6	23,5370	0,0004	16,3162
7	23,5366	0,0001	2,2650
8	23,5373	0,0007	31,3520
9	23,5366	0,0001	3,9339
10	23,5371	0,0005	22,8882
11	23,5371	0,0005	21,8153
12	23,5361	-0,0005	-20,0272
13	23,5375	0,0010	41,3656
14	23,5359	-0,0007	-29,1467
15	23,5377	0,0011	47,0877
16	23,5375	0,0009	38,2662
17	23,5369	0,0003	14,3051
18	23,5374	0,0008	34,3123
19	23,5408	0,0043	182,5090
20	23,5485	0,0119	505,5670
21	23,5580	0,0214	910,1630
22	23,5654	0,0288	1224,8800
23	23,5744	0,0378	1607,6400
24	23,5824	0,0458	1946,0900
25	23,5888	0,0523	2221,7000
26	23,5946	0,0581	2467,7500
27	23,6014	0,0648	2755,2800
28	23,6092	0,0727	3087,1400
29	23,6155	0,0790	3356,2200
30	23,6202	0,0836	3552,4400
31	23,6274	0,0908	3859,2800
32	23,6344	0,0979	4158,5000
33	23,6419	0,1054	4476,3100
34	23,6540	0,1174	4989,6200
35	23,6751	0,1386	5888,2200
36	23,6984	0,1618	6875,7500
37	23,7132	0,1766	7504,3400
38	23,7327	0,1961	8333,4400
39	23,7544	0,2179	9256,4800
40	23,7586	0,2221	9434,9400
41	23,7574	0,2209	9383,4400
42	23,7569	0,2203	9360,3100
43	23,7578	0,2213	9400,6100
44	23,7581	0,2215	9412,1700
45	23,7577	0,2211	9395,3600
46	23,7573	0,2207	9377,4800
47	23,7576	0,2210	9390,5900
48	23,7577	0,2211	9394,6500
49	23,7581	0,2215	9412,4300
50	23,7581	0,2215	9410,8800
51	23,7573	0,2208	9379,5100
52	23,7570	0,2204	9366,0400
53	23,7571	0,2206	9370,6800

STEP 18 – 40



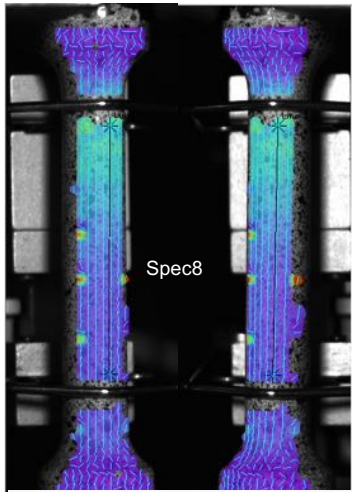
Line 1 - Gauge Length/Gauge Length/mm: 22.752785
Line 1 - Length Change/Length Change/mm: 0.230452
Line 1 - Gauge Strain/Eng. Line Strain/ustrain: 10232.1

STEP 36



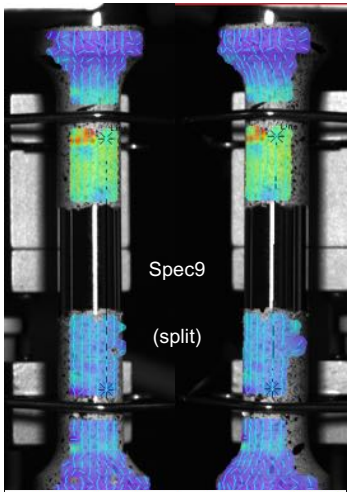
Line 1 - Gauge Length/Gauge Length/mm: 23.359016
Line 1 - Length Change/Length Change/mm: 0.243387
Line 1 - Gauge Strain/Eng. Line Strain/ustrain: 10529.2

STEP 38



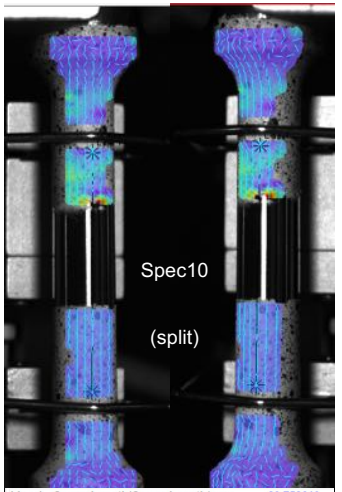
Line 1 - Gauge Length/Gauge Length/mm: 24.540710
Line 1 - Length Change/Length Change/mm: 0.237041
Line 1 - Gauge Strain/Eng. Line Strain/ustrain: 9753.346680

STEP 37



Line 1 - Gauge Length/Gauge Length/mm: 24.806179
Line 1 - Length Change/Length Change/mm: 0.247520
Line 1 - Gauge Strain/Eng. Line Strain/ustrain: 10078.8

STEP 33



Line 1 - Gauge Length/Gauge Length/mm: 23.758619
Line 1 - Length Change/Length Change/mm: 0.222067
Line 1 - Gauge Strain/Eng. Line Strain/ustrain: 9434.938477

STEP 40

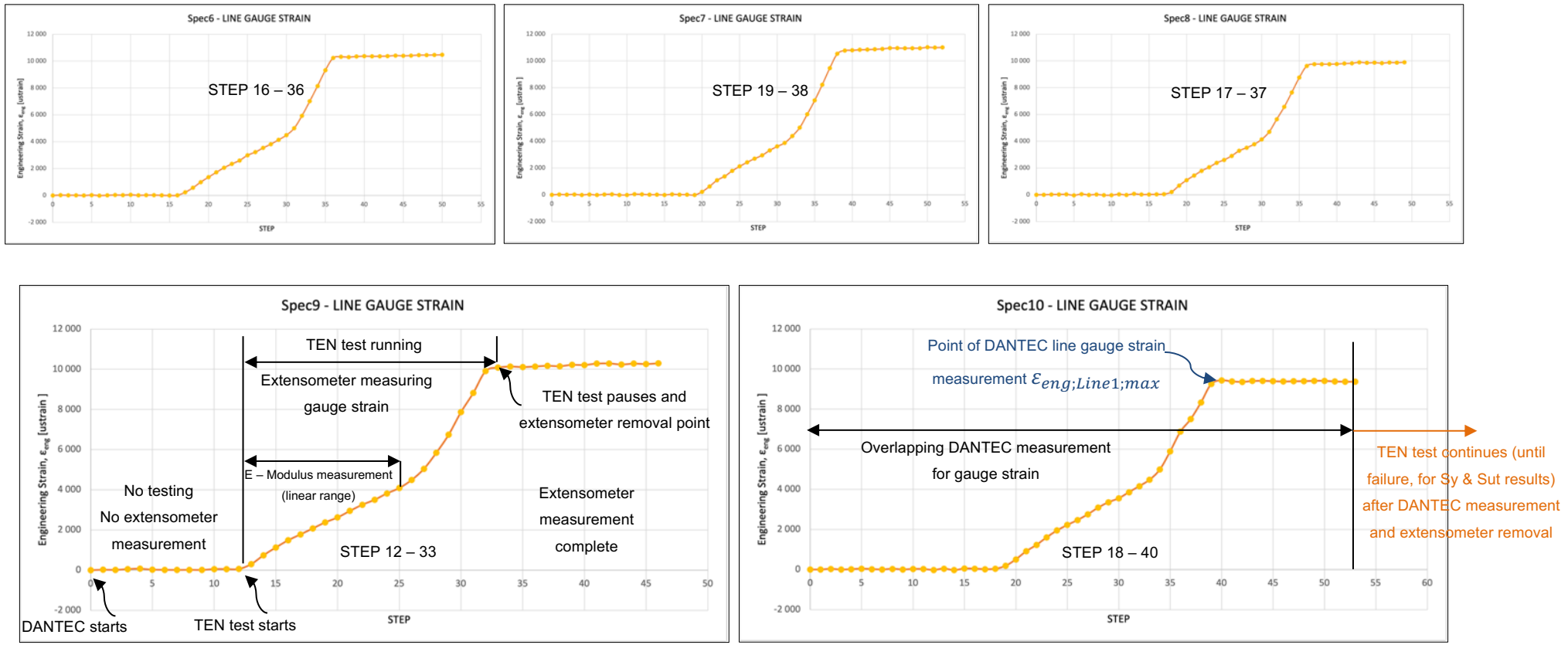


Figure H-9: TEN test Spec6 to Spec10 measurements – DANTEC digital line gauge strain curves

Table H-7: TEN test Spec6 to Spec10 verification measurement results – Extensometer vs DANTEC

EN 19 (T)		Specimen #	Diameter	Engineering Strain - ε_{eng}			
				Extensometer $\varepsilon_{eng;ref}$	Uncertainty +- 0.04 [%] $\varepsilon_{eng;ref}$	DANTEC ε_{eng}	Difference
LINE GAUGE 1 strain			[mm]	[-]	[-]	[-]	[%]
redid mask/line	(DANTEC)	**EN19T-TEN-Spec-6**	6.144	0.01032	0.00000413	0.01023	-0.89
redid mask/line	(DANTEC)	**EN19T-TEN-Spec-7**	6.162	0.00994	0.00000398	0.01053	5.95
redid mask/line	(DANTEC)	**EN19T-TEN-Spec-8**	6.279	0.01029	0.00000411	0.00975	-5.19
redid mask/line	(DANTEC)split	**EN19T-TEN-Spec-9**	6.310	0.01029	0.00000411	0.01008	-2.02
redid mask/line	(DANTEC)split	**EN19T-TEN-Spec-10**	6.352	0.01028	0.00000411	0.00943	-8.25

From the verification measurements and the compared results in Table H-7 above, it is clear that the DANTEC strain measurements were sufficiently accurate given the experimental measurement procedure and the identified test constraints and faults, as discussed in Section 4.4.2.4. It can also be seen (Figure H-4 in Appendix H1.2 and Figure H-9 above) that both measurement instruments measured similar strain responses for each TEN test specimen. This comparable response is illustrated with the 'overlay' curves in Figure H-10 below. For each test specimen, the strain curves have very similar forms, which implied that the DANTEC strain measurements also accurately captured the specimen tensile extension during each test in reference to the extensometer. The primary differences were observed between the maximum strain measurement values of the two instruments. The DANTEC verification, therefore, provided sufficient confidence in the system's measurement accuracy and capability to permit further use in the relevant torsion fatigue (T) and bending-torsion fatigue (BT) test bench measurements which are discussed further in Appendix H4 and H5 to follow.

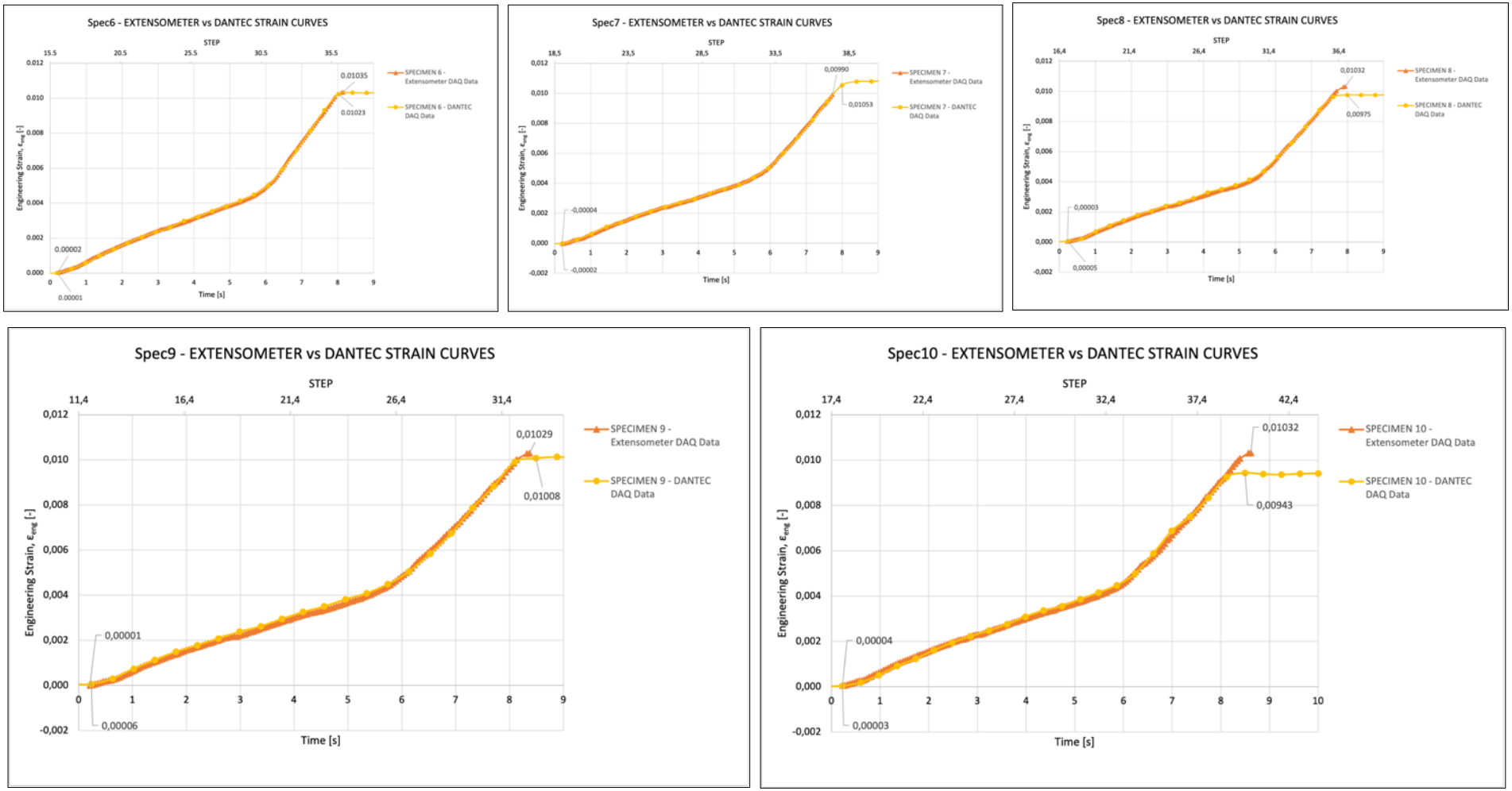


Figure H-10: TEN test Spec6 to Spec10 measurements – DANTEC (strain-step) and Extensometer (strain-time) overlay curves

H2. Axial Fatigue Test Measurements and Calculations

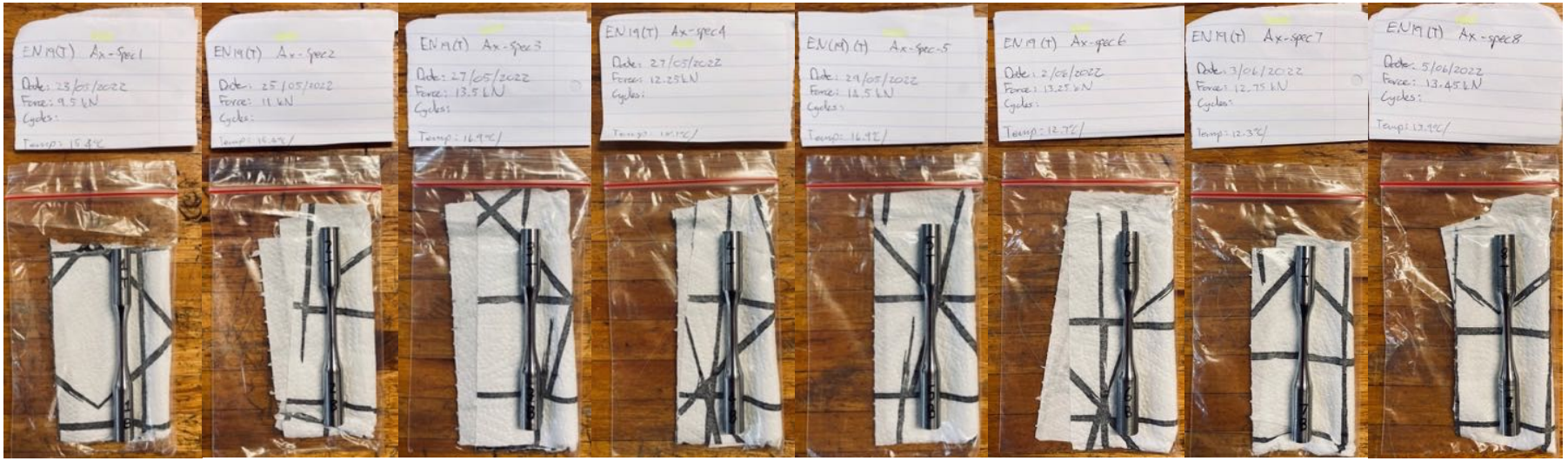
All eight (8) uniaxial axial fatigue (AX) tests (Spec1-Spec8, shown in Figure H-11 on the next page) were conducted according to the AX fatigue test procedure (force-controlled testing) previously provided in Table G-2, with the only exception the axial fatigue test speed of 12 [Hz]. The reason was to shorten the test duration (without exceeding the recommended test speed of 10 [Hz] too much) since continuous runs were preferred, and power interruptions influenced testing. Three of the eight tests (on Spec2, Spec4 and Spec5), therefore, had to be interrupted and restarted (with the appropriate method) due to this to prevent the MTS Landmark machine from damaging (crushing or pulling) the specimens once the hydraulic HPU lost and regained power. An example of this is illustrated for Spec2 in Table H-9.

For the AX fatigue tests conducted, no specific experimental test loading measurements were made using the DANTEC DIC system, the extensometer or any other measurement device (e.g., strain gauges). However, in-test *cyclic loading* and *fatigue cycle count* measurements were obtained from each test's recorded MTS DAQ data exports. These measurements are provided in Table H-8 (shortened due to thousands of points) and in Table H-9 (end-of-test results on MTS, Spec1-Spec3) to follow. The measured axial fatigue loading curves are also illustrated after this in Figure H-12. The negligible axial fatigue loading midrange values $F_{axial;m}$ (much like previously discussed tensile test force offset values F_{offset}) were calculated from the exported MTS DAQ data of each test and reported in Table H-8 (top). The corresponding axial fatigue loading amplitude values of each test $F_{axial;a}$ were also calculated from this data. Subtracting the negligibly small midrange loading values obtained (due to clamping and specimen slippage during testing) from the amplitude values ultimately provided the experimental fully reversed axial fatigue loading value $F_{axial;a;Experimental}$ for each test. These fatigue amplitude values were also compared with the theoretical axial fatigue amplitude values (pre-test input on the MTS test program), which are reported in Table H-10 and illustrated in Figure H-13. The calculated difference [%] between these test values was negligibly small and indicated that the expected theoretical axial fatigue loading was experimentally appropriate for each specimen. The fully reversed axial fatigue stress amplitude $\sigma_{axial;a}$ value for each test was calculated with Equation (H-7) below. These stresses are tabulated in Table J-2 and used in the uniaxial axial fatigue S-N curve with the experimental fatigue cycle counts N_f [-] (provided after each test as in Table H-9).

$$\sigma_{axial;a}\,[MPa] = \left[\frac{F_{axial;a;Experimental}\,[kN]}{A\,[mm^2]}\right]1000 = \left[\frac{F_{axial;a}\,[kN] - F_{axial;m}[kN]}{\frac{\pi}{4}d_{spec}^2\,[mm^2]}\right]1000 \qquad \text{(H-7)}$$

where d_{spec} : is the AX fatigue specimen test zone diameter (Appendix D2)

PRE-TEST



POST-TEST

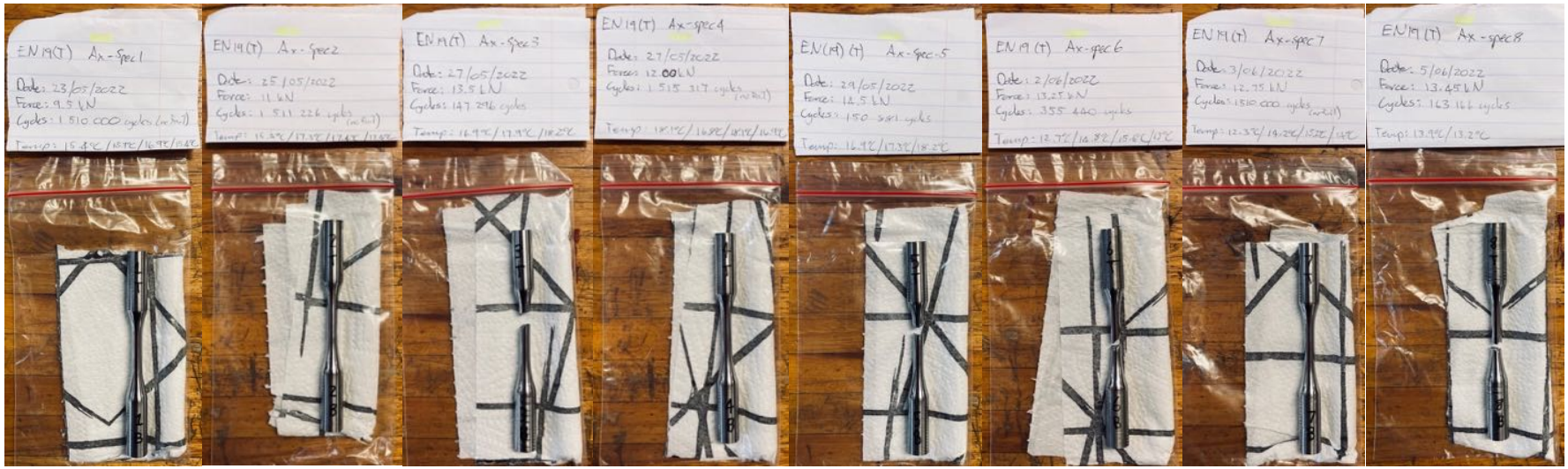


Figure H-11: AX fatigue test Spec1 to Spec8 – pre and post-test images

Table H-8: AX fatigue test Spec1 to Spec8 measurements – DAQ data exports

Specimen 1 - MTS DAQ Data

Axial MTS Data Export (partial inport)

MAX value F_{AX} (400->1000)	9,511	[kN]
MIN value F_{AX} (400->1000)	-9,507	[kN]
Recorded Cycles count	1510000	[-]
F_{AX_a}	9,509	[kN]
F_{AX_m}	0,002	[kN]

Cycle count	Axial Displacement [mm]	Axial Force [kN]	Axial Integer Count [-]	Run Time [s]
2	-0,00605	-0,636	2	5,2
2,5	0,08107	6,826	2,5	5,2
3,5	-0,12099	-9,872	3,5	5,3
4	0,11526	9,677	4	5,3
4,5	-0,08096	-6,250	4,5	5,4
5	0,00113	0,154	5	5,4
5,5	0,07459	6,141	5,5	5,5
6,5	-0,11339	-9,469	6,5	5,5
7	0,11850	9,698	7	5,6
7,5	-0,08385	-6,688	7,5	5,6
8	0,00946	0,854	8	5,7
8,5	0,06317	5,482	8,5	5,7
9,5	-0,11117	-9,089	9,5	5,8
10	0,11478	9,630	10	5,8
10,5	-0,08987	-7,241	10,5	5,9
11	0,01991	1,699	11	5,9
11,5	0,05318	4,664	11,5	6,0
12	-0,10659	-8,799	12	6,0
13	0,11611	9,589	13	6,1
13,5	-0,09565	-7,672	13,5	6,1
14	0,02872	2,438	14	6,2
14,5	0,04367	4,003	14,5	6,2
15	-0,10098	-8,377	15	6,3
16	0,11578	9,543	16	6,3
16,5	-0,08849	-8,044	16,5	6,4
17	0,03833	3,173	17	6,4
17,5	0,03759	3,358	17,5	6,5
18	-0,09585	-7,975	18	6,5
19	0,11678	9,595	19	6,6
19,5	-0,10224	-8,396	19,5	6,6
20	0,04664	3,946	20	6,7

Specimen 2 - MTS DAQ Data

Axial MTS Data Export (partial inport)

MAX value F_{AX} (400->1000)	11,086	[kN]
MIN value F_{AX} (400->1000)	-11,060	[kN]
Recorded Cycles count	1511226	[-]
F_{AX_a}	11,073	[kN]
F_{AX_m}	0,013	[kN]

Cycle count	Axial Displacement [mm]	Axial Force [kN]	Axial Integer Count [-]	Run Time [s]
2	0,05625	4,426	2	5,2
2,5	0,03375	3,070	2,5	5,2
3	-0,10323	-8,630	3	5,3
4	0,13973	11,135	4	5,3
4,5	-0,11906	-9,827	4,5	5,4
5	0,06539	5,136	5	5,4
5,5	0,02419	2,181	5,5	5,5
6	-0,09775	-8,093	6	5,5
7	0,13759	10,997	7	5,6
7,5	-0,12208	-10,146	7,5	5,6
8	0,07311	5,797	8	5,7
8,5	0,01555	1,429	8,5	5,7
9	-0,08638	-7,377	9	5,8
10	0,13568	10,777	10	5,8
10,5	-0,12294	-10,364	10,5	5,9
11	0,08143	6,386	11	5,9
11,5	0,00650	0,581	11,5	6,0
12	-0,08041	-6,844	12	6,0
13	0,13277	10,615	13	6,1
13,5	-0,12675	-10,626	13,5	6,1
14	0,09050	7,207	14	6,2
14,5	-0,00472	-0,339	14,5	6,2
15	-0,07266	-6,221	15	6,3
16	0,12790	10,235	16	6,3
16,5	-0,12923	-10,805	16,5	6,4
17	0,09861	7,755	17	6,4
17,5	-0,01465	-1,211	17,5	6,5
18	-0,06164	-5,447	18	6,5
18,5	0,12248	9,986	18,5	6,6
19,5	-0,12783	-10,925	19,5	6,6
20	0,10694	8,321	20	6,7

Specimen 3 - MTS DAQ Data

Axial MTS Data Export (partial inport)

MAX value F_{AX} (400->1000)	13,548	[kN]
MIN value F_{AX} (400->1000)	-13,523	[kN]
Recorded Cycles count	147296	[-]
F_{AX_a}	13,536	[kN]
F_{AX_m}	0,012	[kN]

Cycle count	Axial Displacement [mm]	Axial Force [kN]	Axial Integer Count [-]	Run Time [s]
3	-0,14174	-11,566	3	5,3
4	0,17504	13,931	4	5,3
4,5	-0,14727	-11,785	4,5	5,4
5	0,06690	5,229	5	5,4
5,5	0,03856	3,637	5,5	5,5
6	-0,13400	-10,778	6	5,5
7	0,16950	13,773	7	5,6
7,5	-0,14910	-12,090	7,5	5,6
8	0,07419	5,994	8	5,7
8,5	0,02790	2,727	8,5	5,7
9	-0,12136	-10,008	9	5,8
10	0,16900	13,573	10	5,8
10,5	-0,15282	-12,459	10,5	5,9
11	0,08618	6,822	11	5,9
11,5	0,01287	1,475	11,5	6,0
12	-0,11372	-9,239	12	6,0
13	0,16361	13,143	13	6,1
13,5	-0,15502	-12,753	13,5	6,1
14	0,09479	7,647	14	6,2
14,5	0,00096	0,437	14,5	6,2
15	-0,10257	-8,402	15	6,3
16	0,15901	12,809	16	6,3
16,5	-0,15967	-12,987	16,5	6,4
17	0,10548	8,432	17	6,4
17,5	-0,01215	-0,553	17,5	6,5
18	-0,09286	-7,551	18	6,5
19	0,15462	12,525	19	6,6
19,5	-0,16072	-13,206	19,5	6,6
20	0,11472	9,176	20	6,7
20,5	-0,02264	-1,429	20,5	6,7
21	-0,08163	-6,682	21	6,8

Specimen 4 - MTS DAQ Data

Axial MTS Data Export (partial inport)

MAX value F_{AX} (400->1000)	12,047	[kN]
MIN value F_{AX} (400->1000)	-12,020	[kN]
Recorded Cycles count	1515317	[-]
F_{AX_a}	12,033	[kN]
F_{AX_m}	0,013	[kN]

Cycle count	Axial Displacement [mm]	Axial Force [kN]	Axial Integer Count [-]	Run Time [s]
2	0,05784	4,673	2	5,2
2,5	0,03479	3,382	2,5	5,2
3	-0,11729	-9,569	3	5,3
4	0,14886	12,156	4	5,3
4,5	-0,13350	-10,716	4,5	5,4
5	0,06498	5,437	5	5,4
5,5	0,02474	2,574	5,5	5,5
6	-0,10981	-8,871	6	5,5
7	0,14508	12,012	7	5,6
7,5	-0,13662	-11,028	7,5	5,6
8	0,07473	6,197	8	5,7
8,5	0,01386	1,688	8,5	5,7
9	-0,10221	-8,231	9	5,8
10	0,14272	11,858	10	5,8
10,5	-0,14185	-11,342	10,5	5,9
11	0,08197	6,884	11	5,9
11,5	0,00071	0,690	11,5	6,0
12	-0,09444	-7,528	12	6,0
13	0,14092	11,586	13	6,1
13,5	-0,14153	-11,535	13,5	6,1
14	0,09080	7,610	14	6,2
14,5	-0,01174	-0,299	14,5	6,2
15	-0,08505	-6,787	15	6,3
16	0,13544	11,247	16	6,3
16,5	-0,14352	-11,694	16,5	6,4
17	0,09947	8,314	17	6,4
17,5	-0,02158	-1,225	17,5	6,5
18	-0,07517	-6,061	18	6,5
18,5	0,13066	10,933	18,5	6,6
19,5	-0,14536	-11,872	19,5	6,6
20	0,10765	9,021	20	6,7

Specimen 5 - MTS DAQ Data

Axial MTS Data Export (partial inport)

MAX value F_{AX} (400->1000)	14,538	[kN]
MIN value F_{AX} (400->1000)	-14,528	[kN]
Recorded Cycles count	150881	[-]
F_{AX_a}	14,533	[kN]
F_{AX_m}	0,005	[kN]

Cycle count	Axial Displacement [mm]	Axial Force [kN]	Axial Integer Count [-]	Run Time [s]
2	0,08439	6,611	2	5,2
2,5	0,02709	2,820	2,5	5,2
3	-0,12692	-10,710	3	5,3
4	0,18137	14,590	4	5,3
4,5	-0,16321	-13,372	4,5	5,4
5	0,09196	7,310	5	5,4
5,5	0,01488	1,774	5,5	5,5
6	-0,11814	-9,864	6	5,5
7	0,17580	14,304	7	5,6
7,5	-0,16524	-13,668	7,5	5,6
8	0,10231	8,235	8	5,7
8,5	0,00220	0,630	8,5	5,7
9	-0,10927	-9,051	9	5,8
10	0,17201	13,954	10	5,8
10,5	-0,17127	-13,998	10,5	5,9
11	0,11402	9,094	11	5,9
11,5	-0,00824	-0,375	11,5	6,0
12	-0,09817	-8,137	12	6,0
13	0,16293	13,524	13	6,1
13,5	-0,16894	-14,167	13,5	6,1
14	0,12284	9,906	14	6,2
14,5	-0,02151	-1,466	14,5	6,2
15	-0,09024	-7,219	15	6,3
15,5	0,15480	13,082	15,5	6,3
16,5	-0,17344	-14,376	16,5	6,4
17	0,13142	10,677	17	6,4
17,5	-0,03044	-2,457	17,5	6,5
18	-0,07632	-6,254	18	6,5
18,5	0,14985	12,591	18,5	6,6
19,5	-0,17523	-14,465	19,5	6,6
20	0,13784	11,380	20	6,7

Specimen 6 - MTS DAQ Data

Axial MTS Data Export (partial inport)

MAX value F_{AX} (400->1000)	13,257	[kN]
MIN value F_{AX} (400->1000)	-13,274	[kN]
Recorded Cycles count	355440	[-]
F_{AX_a}	13,266	[kN]
F_{AX_m}	0,009	[kN]

Cycle count	Axial Displacement [mm]	Axial Force [kN]	Axial Integer Count [-]	Run Time [s]
2	0,05992	4,431	2	5,2
2,5	0,05155	4,425	2,5	5,2
3	-0,14181	-11,754	3	5,3
4	0,17874	13,779	4	5,3
4,5	-0,14690	-11,897	4,5	5,4
5	0,07083	5,377	5	5,4
5,5	0,03965	3,443	5,5	5,5
6	-0,13088	-10,762	6	5,5
7	0,17084	13,309	7	5,6
7,5	-0,14798	-12,131	7,5	5,6
8	0,08139	6,267	8	5,7
8,5	0,02859	2,478	8,5	5,7
9	-0,11916	-9,820	9	5,8
10	0,16876	13,178	10	5,8
10,5	-0,15154	-12,409	10,5	5,9
11	0,09453	7,257	11	5,9
11,5	0,01689	1,441	11,5	6,0
12	-0,10708	-8,959	12	6,0
13	0,16575	12,936	13	6,1
13,5	-0,15461	-12,783	13,5	6,1
14	0,10337	7,991	14	6,2
14,5	0,00472	0,424	14,5	6,2
15	-0,09579	-8,134	15	6,3
16	0,16292	12,717	16	6,3
16,5	-0,15635	-12,897	16,5	6,4
17	0,11460	8,877	17	6,4
17,5	-0,00539	-0,410	17,5	6,5
18	-0,08625	-7,236	18	6,5
19	0,15964	12,410	19	6,6
19,5	-0,15565	-12,961	19,5	6,6
20	0,12493	9,642	20	6,7

Specimen 7 - MTS DAQ Data

Axial MTS Data Export (partial inport)

MAX value F_{AX} (400->1000)	12,760	[kN]
MIN value F_{AX} (400->1000)	-12,761	[kN]
Recorded Cycles count	1510000	[-]
F_{AX_a}	12,761	[kN]
F_{AX_m}	0,001	[kN]

Cycle count	Axial Displacement [mm]	Axial Force [kN]	Axial Integer Count [-]	Run Time [s]
2	0,04500	3,052	2	5,1
2,5	0,06872	5,742	2,5	5,2
3	-0,14055	-11,867	3	5,2
4	0,17262	13,303	4	5,3
4,5	-0,12682	-10,544	4,5	5,3
5	0,05404	3,844	5	5,4
5,5	0,05942	4,803	5,5	5,4
6	-0,13071	-11,101	6	5,5
7	0,16787	13,097	7	5,5
7,5	-0,13128	-10,938	7,5	5,6
8	0,06394	4,691	8	5,6
8,5	0,04638	3,796	8,5	5,7
9	-0,12116	-10,318	9	5,7
10	0,16510	12,894	10	5,8
10,5	-0,13413	-11,332	10,5	5,8
11	0,07470	5,611	11	5,9
11,5	0,03470	2,871	11,5	5,9
12	-0,11221	-9,637	12	6,0
13	0,16238	12,709	13	6,0
13,5	-0,13807	-11,696	13,5	6,1
14	0,08463	6,426	14	6,1
14,5	0,02487	1,996	14,5	6,2
15	-0,10311	-8,890	15	6,2
16	0,15973	12,559	16	6,3
16,5	-0,14168	-12,003	16,5	6,3
17	0,09333	7,186	17	6,4
17,5	0,01262	0,933	17,5	6,4
18	-0,09434	-8,187	18	6,5
19	0,15637	12,266	19	6,5
19,5	-0,14444	-12,248	19,5	6,6
20	0,10298	7,935	20	6,6

Specimen 8 - MTS DAQ Data

Axial MTS Data Export (partial inport)

MAX value F_{AX} (400->1000)	13,457	[kN]
MIN value F_{AX} (400->1000)	-13,485	[kN]
Recorded Cycles count	163166	[-]
F_{AX_a}	13,471	[kN]
F_{AX_m}	0,014	[kN]

Cycle count	Axial Displacement [mm]	Axial Force [kN]	Axial Integer Count [-]	Run Time [s]
2	0,02059	1,012	2	5,2
2,5	0,08754	7,345	2,5	5,2
3,5	-0,15090	-12,679	3,5	5,3
4	0,16930	13,382	4	5,3
4,5	-0,11951	-9,795	4,5	5,4
5	0,02906	1,993	5	5,4
5,5	0,07604	6,428	5,5	5,5
6	-0,14553	-12,174	6	5,5
7	0,16919	13,501	7	5,6
7,5	-0,12516	-10,378	7,5	5,6
8	0,04106	3,005	8	5,7
8,5	0,06533	5,572	8,5	5,7
9	-0,13866	-11,619	9	5,8
10	0,16898	13,546	10	5,8
10,5	-0,13262	-10,977	10,5	5,9
11	0,05301	4,000	11	5,9
11,5	0,05439	4,676	11,5	6,0
12	-0,13111	-11,036	12	6,0
13	0,16886	13,484	13	6,1
13,5	-0,13773	-11,491	13,5	6,1
14	0,06407	4,951	14	6,2
14,5	0,04173	3,720	14,5	6,2
15	-0,12366	-10,414	15	6,3
16	0,16785	13,461	16	6,3
16,5	-0,14306	-11,926	16,5	6,4
17	0,07538	5,909	17	6,4
17,5	0,03115	2,730	17,5	6,5
18	-0,11630	-9,776	18	6,5
19	0,16532	13,340	19	6,6
19,5	-0,14682	-12,304	19,5	6,6
20	0,08596	6,798	20	6,7

Table H-9: AX fatigue test Spec1 to Spec3 measurements – DAQ data tables (post-test results for fatigue cycle count)

Pre-Test Variables | Runtime Values | Monitor | Results

Variable Summary | History | Hysteresis | Variable Chart | Test Run Log | DAQ: Axial Count, ... - (Timed)

Spec1 AX Fatigue test cycle count

Cycle	Axial Count Maximum (cycles)	Axial Count Minimum (cycles)	Axial Count Mean (cycles)	Axial Displacement Maximum (mm)	Axial Displacement Minimum (mm)	Axial Displacement Mean (mm)	Axial Force Maximum (kN)	Axial Force Minimum (kN)	Axial Force Mean (kN)	Axial Integer Count Maximum (cycles)	Axial Integer Count Minimum (cycles)	Axial Integer Count Mean (cycles)	Running Time Maximum (sec)	Running Time Minimum (sec)	Running Time Mean (sec)	System Tick Count Maximum (unitless)	System Tick Count Minimum (unitless)	System Tick Count Mean (unitless)
0	1510000.500	2.000	755001.250	0.214	-0.121	0.046	9.698	-9.872	-0.087	1510000.500	2.000	755001.250	125838.414	5.161	62921.788	129761672.000	908420.000	65335046.000

Spec1 (full test run – stopped due to predefined 1.5×10^6 fatigue cycle count reached without specimen failure)

Spec2 (first) AX Fatigue test time

Program | Controller | Power | Axial | Application | Test

Running Time: 10:54:34

Pre-Test Variables | Runtime Values | Monitor | Results

Variable Summary | History | Hysteresis | Variable Chart | Test Run Log | DAQ: Axial Count, ... - (Timed)

Spec2 (first) AX Fatigue test cycle count

Cycle	Axial Count Maximum (cycles)	Axial Count Minimum (cycles)	Axial Count Mean (cycles)	Axial Displacement Maximum (mm)	Axial Displacement Minimum (mm)	Axial Displacement Mean (mm)	Axial Force Maximum (kN)	Axial Force Minimum (kN)	Axial Force Mean (kN)	Axial Integer Count Maximum (cycles)	Axial Integer Count Minimum (cycles)	Axial Integer Count Mean (cycles)	Running Time Maximum (sec)	Running Time Minimum (sec)	Running Time Mean (sec)	System Tick Count Maximum (unitless)	System Tick Count Minimum (unitless)
0	471226.000	2.000	235614.000	0.147	-0.139	0.004	11.128	-11.108	0.010	471226.000	2.000	235614.000	39274.051	5.146	19639.599	198134572.000	157

Spec2 (second) AX Fatigue test time

Controller | Power | Axial | Application | Test

Running Time: 24:04:32

Pre-Test Variables | Runtime Values | Monitor | Results

Variable Summary | History | Hysteresis | Variable Chart | Test Run Log | DAQ: Axial Count, ... - (Timed)

Spec2 (second) AX Fatigue test cycle count (test restarted)

Cycle	Axial Count Maximum (cycles)	Axial Count Minimum (cycles)	Axial Count Mean (cycles)	Axial Displacement Maximum (mm)	Axial Displacement Minimum (mm)	Axial Displacement Mean (mm)	Axial Force Maximum (kN)	Axial Force Minimum (kN)	Axial Force Mean (kN)	Axial Integer Count Maximum (cycles)	Axial Integer Count Minimum (cycles)	Axial Integer Count Mean (cycles)	Running Time Maximum (sec)	Running Time Minimum (sec)	Running Time Mean (sec)	System Tick Count Maximum (unitless)	System Tick Count Minimum (unitless)
0	1040000.500	2.000	520001.250	0.140	-0.159	-0.010	11.135	-11.120	0.007	1040000.500	2.000	520001.250	86671.734	5.166	43338.450	89110188.000	3636

Spec2 AX Fatigue test cycle counts summed to obtain N_f (similarly done for Spec4 and Spec5)

Spec2 (two test runs – loadshedding and no failure)

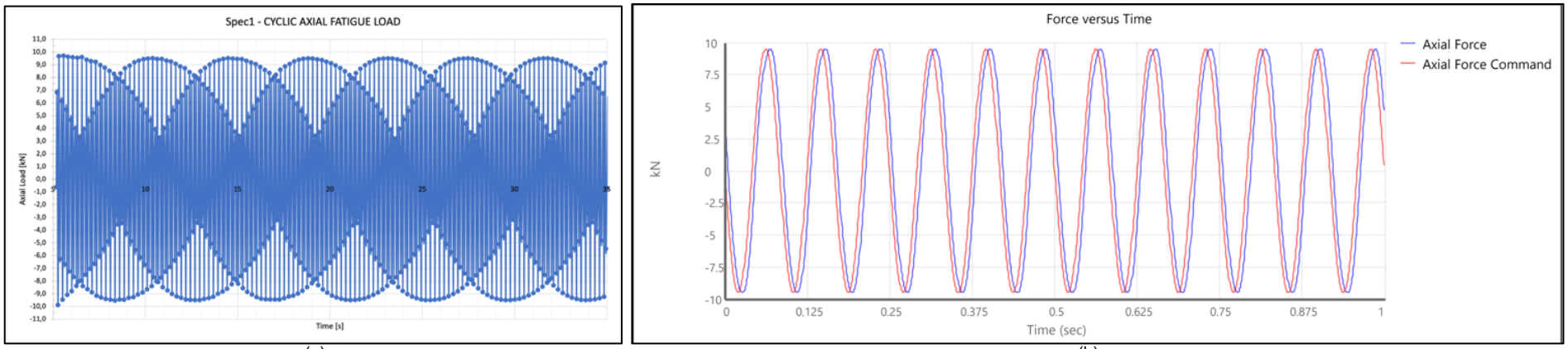
Pre-Test Variables | Runtime Values | Monitor | Results

Variable Summary | History | Hysteresis | Variable Chart | Test Run Log | DAQ: Axial Count, ... - (Timed)

Spec3 AX Fatigue test cycle count

Cycle	Axial Count Maximum (cycles)	Axial Count Minimum (cycles)	Axial Count Mean (cycles)	Axial Displacement Maximum (mm)	Axial Displacement Minimum (mm)	Axial Displacement Mean (mm)	Axial Force Maximum (kN)	Axial Force Minimum (kN)	Axial Force Mean (kN)	Axial Integer Count Maximum (cycles)	Axial Integer Count Minimum (cycles)	Axial Integer Count Mean (cycles)	Running Time Maximum (sec)	Running Time Minimum (sec)	Running Time Mean (sec)	System Tick Count Maximum (unitless)	System Tick Count Minimum (unitless)	System Tick Count Mean (unitless)
0	147296.000	3.000	73649.500	4.927	-0.170	2.378	13.931	-13.604	0.163	147296.000	3.000	73649.500	12279.681	5.266	6142.473	13274976.000	705975.000	6990475.500

Spec3 (full test run – stopped due to specimen fatigue failure)



(a) (b)

Figure H-12: AX fatigue test Spec1 – cyclic axial fatigue load vs time curve from (a) exported DAQ data and (b) MTS display (in-test)

The primary reason for the difference between sinusoidal curve forms in Figure H-12 (a) and (b) above is attributed to the difference in test speed (set at 12 [Hz]) and the MTS load sampling rate, which was 20 [Hz] and not adaptable. However, similar maximum and minimum axial load values were still obtained, as illustrated in Table H-10 and Figure H-13 below. The largest difference between load values was calculated as 0.55 [%] (theoretical axial load the reference). It can also be seen from Figure H-12 (b) that the 'axial force command' (HPU system and MTS software) continuously reached similar maxima load values as the measured 'axial force' (with 90 [kN] load cell). This observation was a good indication that the increased axial fatigue test speed (10 [Hz] recommended to the slightly accelerated 12 [Hz]) did not influence this load command and experimentally induced load measurement, as is the reason for the lower recommended test speed.

Uncertainties on the calculated experimental axial fatigue stress with the MTS (DAQ Data Exports) loading uncertainty are discussed in Section 4.6.3 and provided later in Appendix K2.

Table H-10: AX fatigue test Spec1 to Spec8 results – experimental loading

Specimen #	Diameter	Test Speed	\/ ref point Theoretical Axial Load	Experimental Result Experimental Cycle Count	Experimental Axial Load	Difference
	[mm]	[Hz]	[kN]	[-]	[kN]	[%]
EN19T-AX-Spec-1	5.811	12	9.500	1510000	9.507	0.07
EN19T-AX-Spec-2	5.690	12	11.000	1511226	11.060	0.55
EN19T-AX-Spec-3	5.713	12	13.500	147296	13.523	0.17
EN19T-AX-Spec-4	5.720	12	12.000	1515317	12.020	0.16
EN19T-AX-Spec-5	5.672	12	14.500	150881	14.528	0.20
EN19T-AX-Spec-6	5.643	12	13.250	355440	13.257	0.05
EN19T-AX-Spec-7	5.721	12	12.750	1510000	12.760	0.08
EN19T-AX-Spec-8	5.711	12	13.450	163166	13.457	0.05

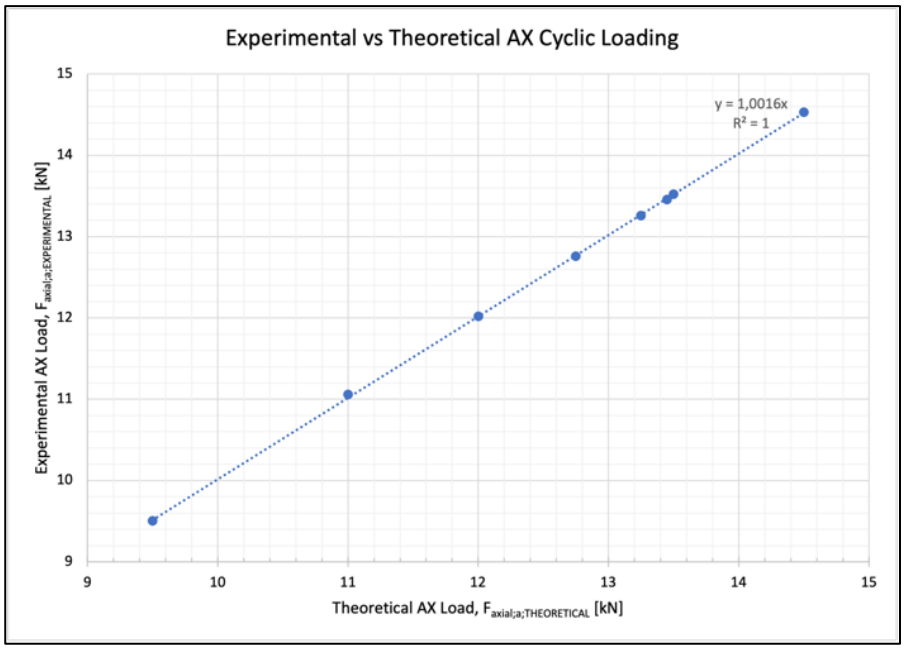


Figure H-13: AX fatigue test Spec1 to Spec8 results – experimental vs theoretical loading

H3. Bending Fatigue Test Measurements and Calculations

All seven (7) uniaxial bending fatigue (B) tests (Spec1-Spec7, shown in Figure H-16 to follow) were conducted according to the B fatigue test procedure previously provided in Appendix G3. An average test speed of 49.71 [Hz] was measured for all tests using the digital tachometer (see Appendix B5 for description and procedure).

For the B fatigue tests conducted, it was unreasonable to perform experimental loading measurements of the test specimens using, e.g., the DANTEC DIC system or strain gauges since the specimen was constantly rotating. However, measurements for the cantilever bending force and fatigue cycle count were made before and after each test. The experimental cantilever bending force $F_{cantilever}$ was calculated by dividing the load cell force reading $F_{load\ cell}$ (set with turn screw) with the calibration curve slope value of 0.8979 (reference calibration in Figure A-6 of Appendix A2). This cantilever force was conservatively assumed to be applied through the centre of the load cell bearing inner race bushing (24 [mm] width), thus 12 [mm] from the bending fatigue specimen tip (see Figure H-14 below). This cantilever force, the theoretical cantilever length $L_{cantilever}$ and the expected specimen failure position x_{break} (pre-test marking at 61 [mm]) were then used to calculate the rotating cantilever bending moment $M_{B;cantilever}$ (illustrated in Figure H-15 to follow). The bending moment was calculated with Equation (H-8) below at the hourglass test zone centre (x_{break}). Using this bending moment, the calculation of the induced fully reversed bending stress amplitude $\sigma_{bending;a}$ using Equation (H-9) followed (with specimen diameter at x_{break}). After each bending fatigue test (that failed), the fatigue failure position $x_{break;exp}$ and the diameter (at that point) were re-measured, and the experimental bending moment and stress re-calculated (orange marked specimens in Appendix D3). The experimental cantilever bending force, moment and fatigue stress are reported for each test specimen in Table J-3. The test results are used in the uniaxial bending fatigue S-N curve with the experimental fatigue cycle counts N_f (recorded after each test from the cycle counter).

$$M_{B;cantilever}\ [N.m] = F_{cantilever} L_{cantilever}\ [N.m] - F_{cantilever} x_{break;exp}\ [N.m] \qquad \text{(H-8)}$$

$$\sigma_{bending;a}\ [MPa] = \left[\frac{32\ M_{B;cantilever}\ [N.m]}{\pi d_{spec}^3\ [m^3]}\right] / 10^6 \qquad \text{(H-9)}$$

where d_{spec} : is the B fatigue specimen test zone diameter (Appendix D3)

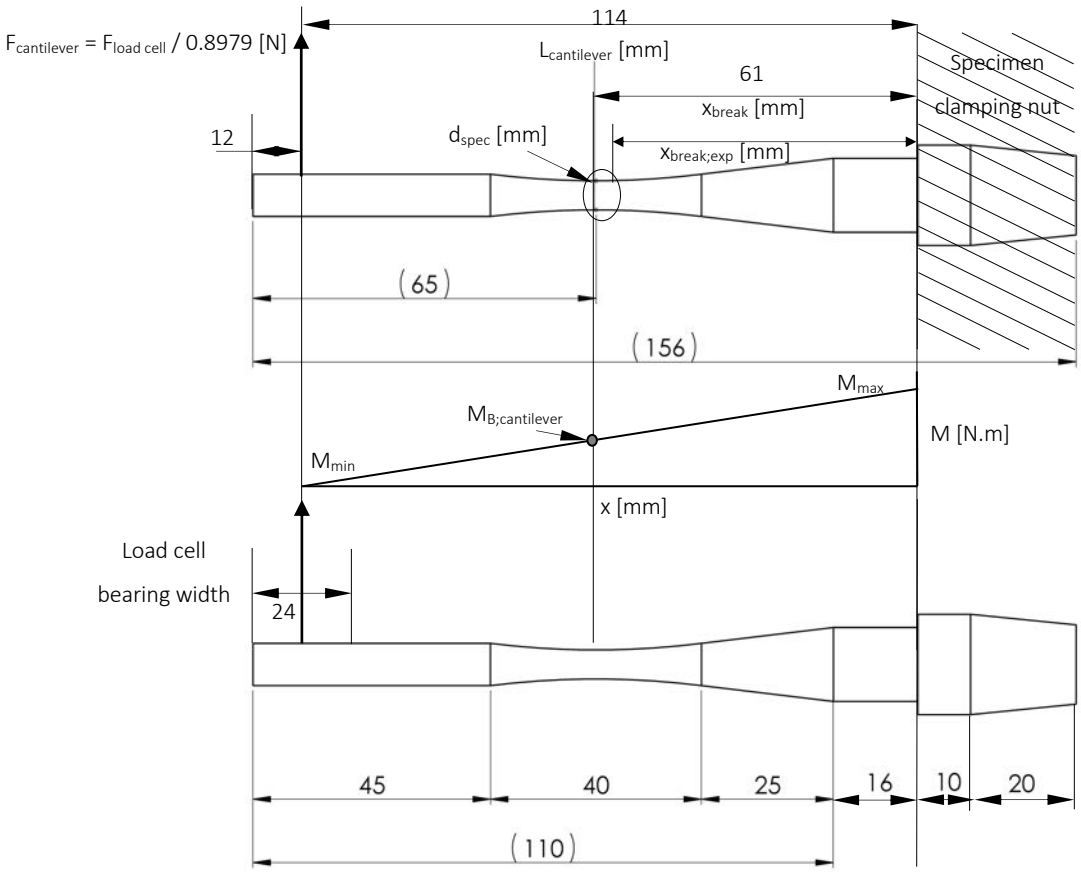


Figure H-14: B fatigue test specimen – cantilever loading schematic

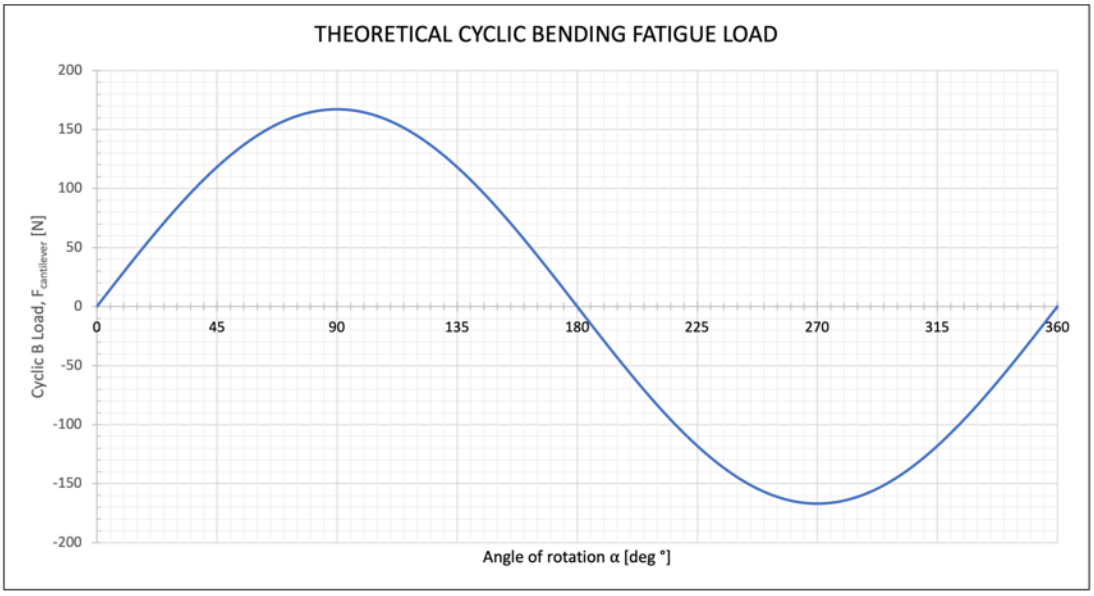


Figure H-15: B fatigue test specimen – sinusoidal loading vs rotation angle curve

PRE-TEST



POST-TEST



Figure H-16: B fatigue test Spec1 to Spec7 – pre and post-test images

H4. Torsion Fatigue Test Measurements and Calculations

H4.1. Experimental Torsion Fatigue Test Measurements and Calculations

All nine (9) uniaxial torsion fatigue (T) tests (Spec1-Spec9, shown in Figure H-18 to follow) were conducted according to the T fatigue test procedure previously provided in Appendix G4 at respectively chosen test speeds (each speed measured with the DANTEC).

For the experimental T fatigue tests conducted, it was not deemed feasible to make experimental loading measurements of the test specimens with measurement devices (e.g., strain gauges) other than the non-contact DANTEC DIC system (discussed in Appendix B6 and secondary verification measurement in Appendix H1.3). The displacement measurements from the DANTEC were required for processing the tests. The use of the DANTEC system was primarily due to the high testing frequencies and physical test bench constraints regarding sensor mounting and secondary vibrations during testing. The measurements made with this system were 3D displacement measurements of predefined specimen markings on the fatigue test specimen surfaces. These displacement measurements (in parts 1 and 2c of Appendix H4.2) were utilised with the appropriate Siemens NX12 static FEM theoretical displacement measurements of the same specimen (discussed in Appendix I1). With them, the experimental torsional loading gain G_T [-] was calculated (theoretical discussion in previous Appendix F1 to F2) using Equation (H-14) from the last parts 2b and 2c of Appendix H4.2 hereafter.

The nominal centrifugal force $F_{centrifugal}$ [N] induced on each test specimen was calculated with the chosen centrifugal mass piece m_{centr} [kg] (see Appendix E2) at the chosen radial position r_{wheel} [m] (see Figure E-3) and test speed N [Hz] (set on VSD). This centrifugal force was assumed to act through the mass piece COM position (on each wheel) at a distance L_{lever} [m] (moment lever) from the lever-head central axis (theoretical value for each mass piece, see Table E-2 and Figure E-4). With the centrifugal force and this moment lever length, it was then possible to calculate the nominal torsional moment using Equation (H-10) below. Reference may be made to Figure H-17 below for the T test bench working principle. Using this torsional moment on each test specimen then allowed for the calculation of the experimentally induced fully reversed torsional stress amplitude τ_a [MPa] using Equation (H-11) below (as induced in the hourglass centre). The centrifugal mass pieces, their masses and radii, the test speeds, centrifugal forces and resulting torsional moments and stresses are reported for each test specimen in Table J-4. The uniaxial torsion fatigue S-N curve is generated with the experimental fatigue cycle counts N_f [-] (calculated for each test from elapsed test time and test speed) these stresses.

$$M_T\ [N.m] = 2\left(F_{centrifugal}L_{lever}\right)\ [N.m] = \ 2(m_{centr}r_{wheel}(2\pi N)^2 L_{lever})\ [N.m] \qquad \text{(H-10)}$$

$$\tau_a\,[MPa] = \left\{\left[\frac{16\,M_T\,[N.m]}{\pi d_{spec}^3\,[m^3]}\right] / 10^6\right\} G_T \qquad \text{(H-11)}$$

where d_{spec} : is the T fatigue specimen test zone diameter (Appendix D4)

m_{centr} : is the sum of relevant bolt, nut and washer masses (Appendix E2)

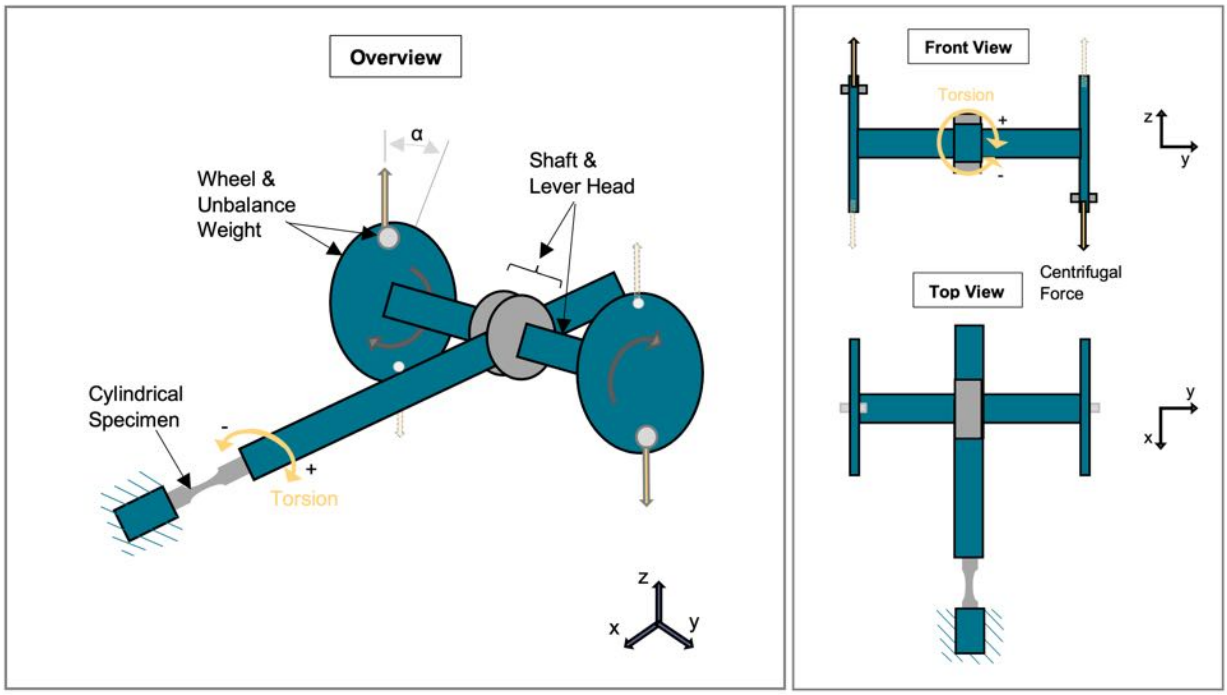
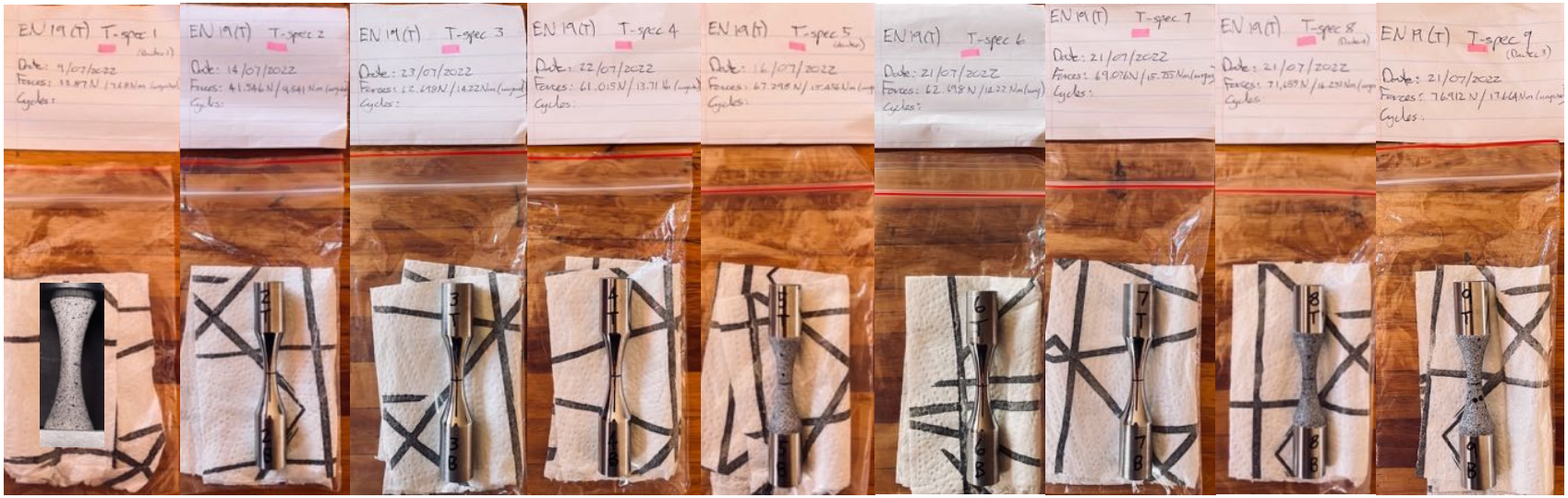


Figure H-17: Torsion fatigue test bench – working principle (repeat)

PRE-TEST



POST-TEST



Figure H-18: T fatigue test Spec1 to Spec9 – pre and post-test images

H4.2. Torsion Fatigue Loading Verification - DANTEC Measurements and Calculations

1) DANTEC System Set-Up and Measurement Procedure

The relevant DANTEC displacement measurements for the experimental torsion loading gain calculation were obtained using the general DIC measurement procedure (see Appendix B6). For these measurements, the speckle patterns were prepared on the respective torsion fatigue (T) test specimens according to the procedure and illustrations provided in Figure B-10 of Appendix B6 and can be viewed in Figure H-21 (a) to follow. The DANTEC system setup with respect to the torsion fatigue test bench (Appendix A3) and the fatigue test specimen is illustrated in the schematic of Figure H-19 below (not to scale).

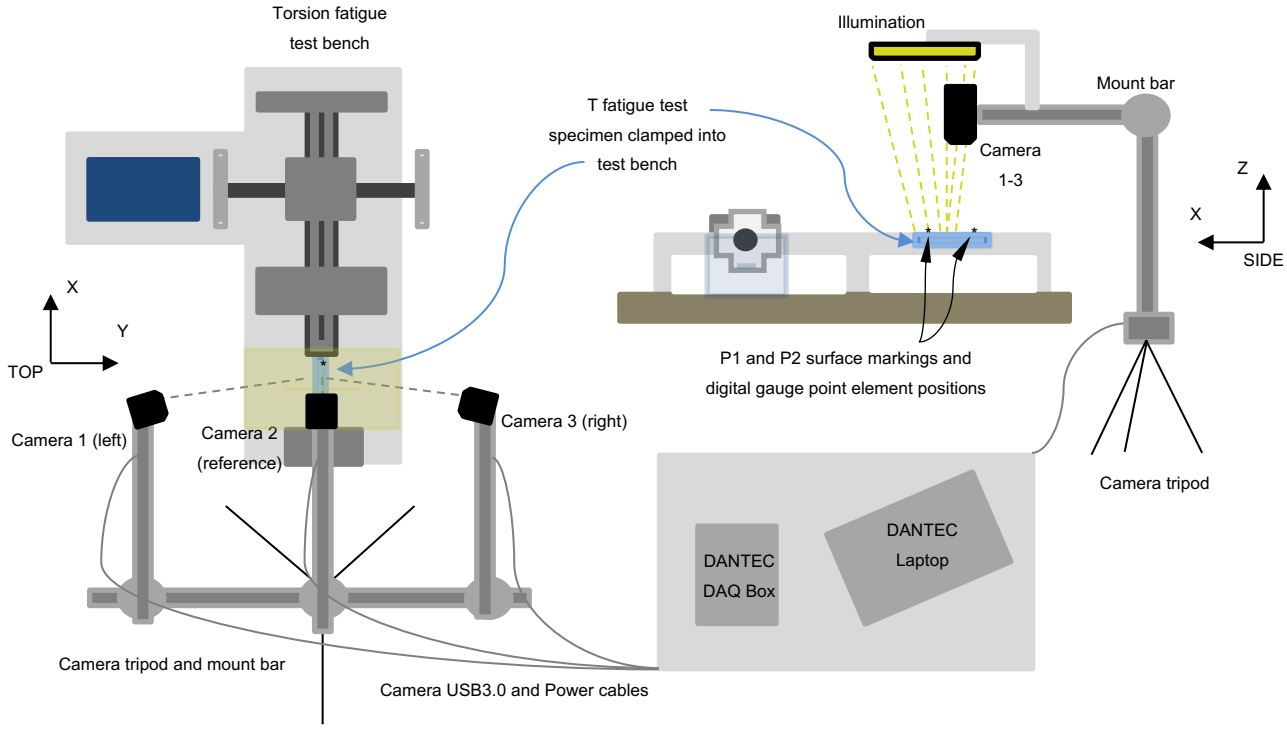


Figure H-19: T fatigue test specimen measurement – DANTEC DIC System setup schematic (side and top view)

The DANTEC system was positioned on the floor in front of and over above the torsion fatigue test bench. That is, to allow the downward-facing cameras to view the specimen from the top with the appropriate stereo angle between cameras 1 and 3 (recommended 30 – 60 [°] for proper 3D measurement of a cylindrical object) and camera 2 in the middle. Camera 2 was used as the reference for measuring and evaluating the recorded images for each test. The system's positioning (tripod and mount bar) was set up similarly for each test measurement.

It should be noted that the T fatigue test bench was mounted (as a whole) with four M10x110mm steel bolts to the laboratory workbench. However, the workbench was not as securely fastened to its support frame at this location. This necessitated the use of four mass pieces (50 [kg] total, see Figure H-20 (a) below) to suppress the excessive workbench corner and, thus, test bench displacements (in the x and z-directions, see Figure H-21 (c) coordinate system). These were detected during the first experimental displacement measurement (27.5 [Hz] test speed) on the fatigue specimen with the DANTEC (discussed in the section to follow). The added workbench masses lowered the excessive displacements as shown for the x, y and z-displacement curves of both pre and post-weight DANTEC measurements on the same specimen (EN19T-T-Spec1) in Figure H-20 (b) below. The test bench also inherently experienced rigid body displacements due to its working principle (imbalance forces) and the induced loading. These mass pieces were subsequently used for each experimental displacement measurement after that.

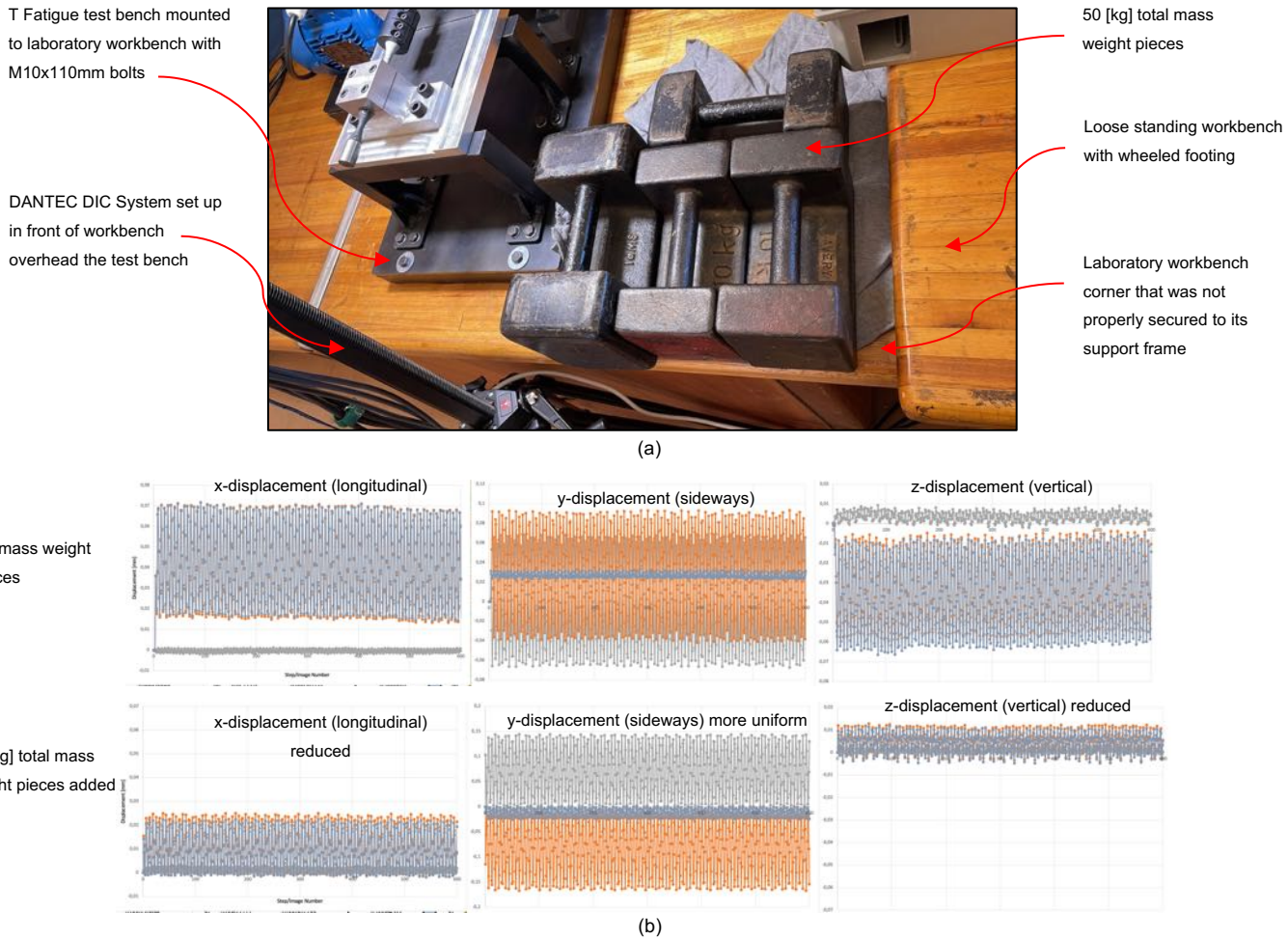


Figure H-20: T fatigue test bench – (a) experimental displacement stabilisation weights and (b) pre and post-displacement measurements

Once a speckle pattern prepped T fatigue test specimen (see Figure H-21 (a) to follow) was appropriately loaded and fastened into the T test bench clamps (surface markings oriented

towards the cameras above), the DANTEC displacement measurement could commence. For this, the camera recording sequence was set to take 500-600 consecutive photos at the highest possible frame rate. This rate depended on the lighting, focal length, resolution, camera calibration and the defined region of interest (specimen view) in the respective camera image views. The highest frame rates varied between 171 [Hz] and 194 [Hz] for the T specimen displacement measurements. The DANTEC recording sequence was initiated (recording for 3-3.5 [s]) about 10 [s] after the start of each torsion fatigue test, allowing specimen loading and the test bench to stabilise. After the DANTEC completed the pre-set recording sequence, the fatigue test (then measured) continued to run until specimen failure or until the defined fatigue limit cycle count was reached and the test manually stopped. After a displacement measurement was concluded, it was required to perform the necessary image processing using the ISTRA 4D software on the dedicated DANTEC computer.

This process entailed performing the appropriate image correlations to obtain the evaluated areas on the specimen surface (Figure H-21 (b)) from which digital measurement data could be extracted. The next step was to define a static measurement coordinate system (different from the camera ‘calibration’ coordinate system) for the image evaluations. This was done using the indicated best-fit sphere area illustrated on the evaluated specimen surface (purple geometric field, shown in Figure H-22) as a reference. That is, to appropriately orient the coordinate system x-axis (turquois asterisk) and z-axis position (red asterisk) in-line with the surface markings (for gauge points) as in Figure H-21 (c). Customarily for cylindrical specimens, and in this case, the hourglass-shaped gauge area, the x-axis direction is oriented along the longitudinal length of the specimen (above or below the z-axis origin position) and inside the mentioned best-fit sphere area. If the x-axis were positioned to the right or left of the z-axis origin (around the cylinder), it would lead to inappropriate coordinate system definition and, thus, incorrect displacement measurement data (references to this coordinate system). The best-fit sphere is independent of this defined coordinate system, thus serving as an appropriate reference for the coordinate axes positioning.

Since the required measurement quantity was the torsional displacement (y-direction), it was required to next define two digital point gauge elements within the available colour field on the specimen surface. This was done by placing each digital gauge point element (P1 and P2, with P3 irrelevant) on the small cross markings at the top and bottom of the specimen (marked at 2 [mm] from the edges of the specimen gauge area). Reference the evaluated camera images in the software in Figure H-22 and in Figure H-21 (a) and (c). These cross markings were measured (using the digital vernier) and marked in line with each other (longitudinally) on the surface of each specimen prior to each DANTEC measurement. The reason for measuring the torsional twist of a specimen from the linear (translational) y-displacement of each gauge point element was that

the DANTEC could not provide out-of-plane (depth) measurements other than the linear z-displacement of each point. Also, due to the DANTEC being a non-contact measurement, the specimen longitudinal axis could not be defined within the ISTRA 4D software. Therefore, an angular displacement measurement around this axis was not possible to describe the torsional displacement. The ISTRA 4D software and relevant image correlation and evaluation environment also did not have any digital gauge elements for this (besides a line gauge element used for the DANTEC verification in Appendix H1.3). It was also decided that calculating an angular displacement from the combined y and z-displacement measurements would not be feasible (in polar coordinate form). Since too many uncertainties could arise from the specimens (geometry) and DANTEC measurements (setup and procedure).

For each of these digital gauge point elements, the relevant displacement (and coordinate) data was ultimately exported over all the evaluated images (500-600 total) from the ISTRA 4D software and processed to obtain the relevant torsion displacement amplitude. This amplitude was further utilised with the theoretical displacement obtained with the static FEM simulation to compare and calculate the experimental torsional gain. This procedure is discussed in the next section (of this Appendix H4.2) and in Appendix I1 for each of the three different torsion displacement measurements performed on the T fatigue test bench.

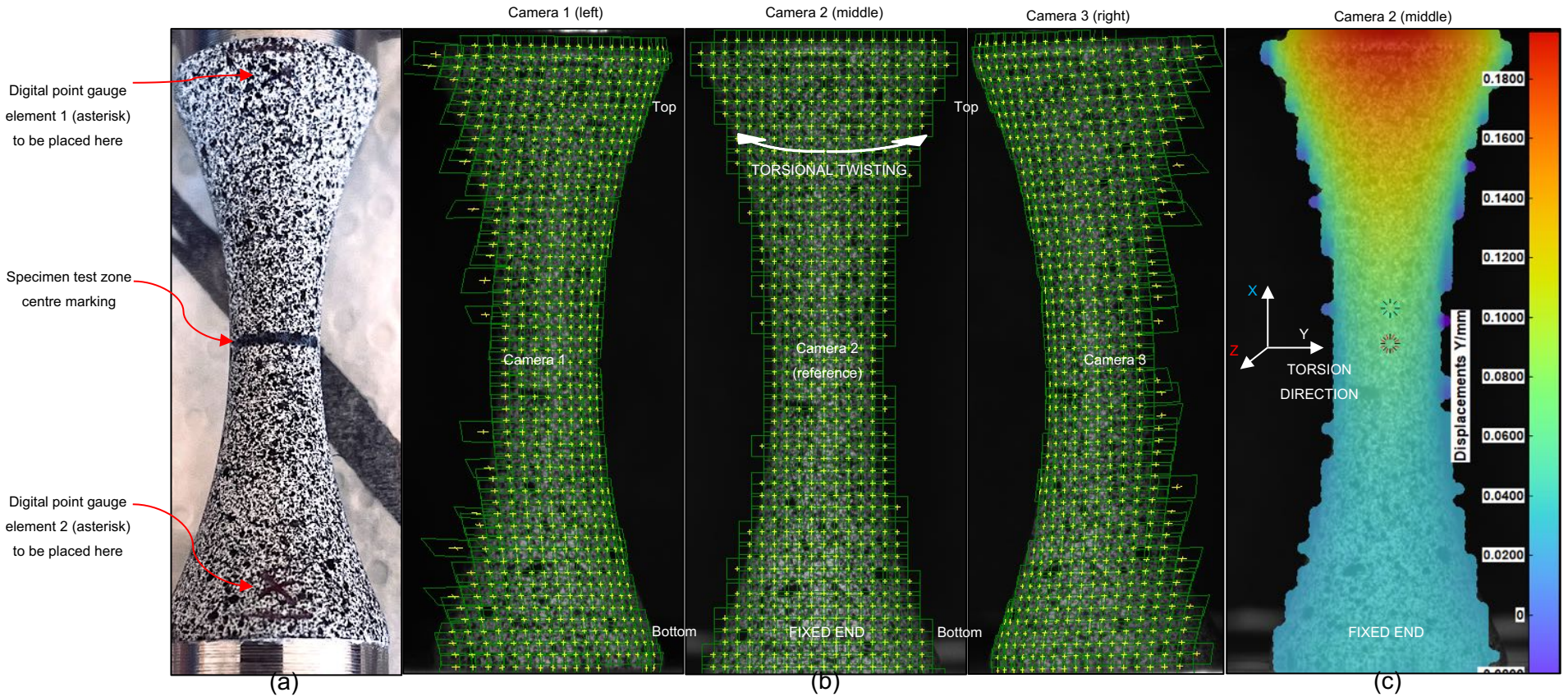


Figure H-21: T fatigue test specimen – DANTEC (a) prepared specimen speckle pattern and markings, (b) evaluation grid and (c) measurement (user) coordinate system definition

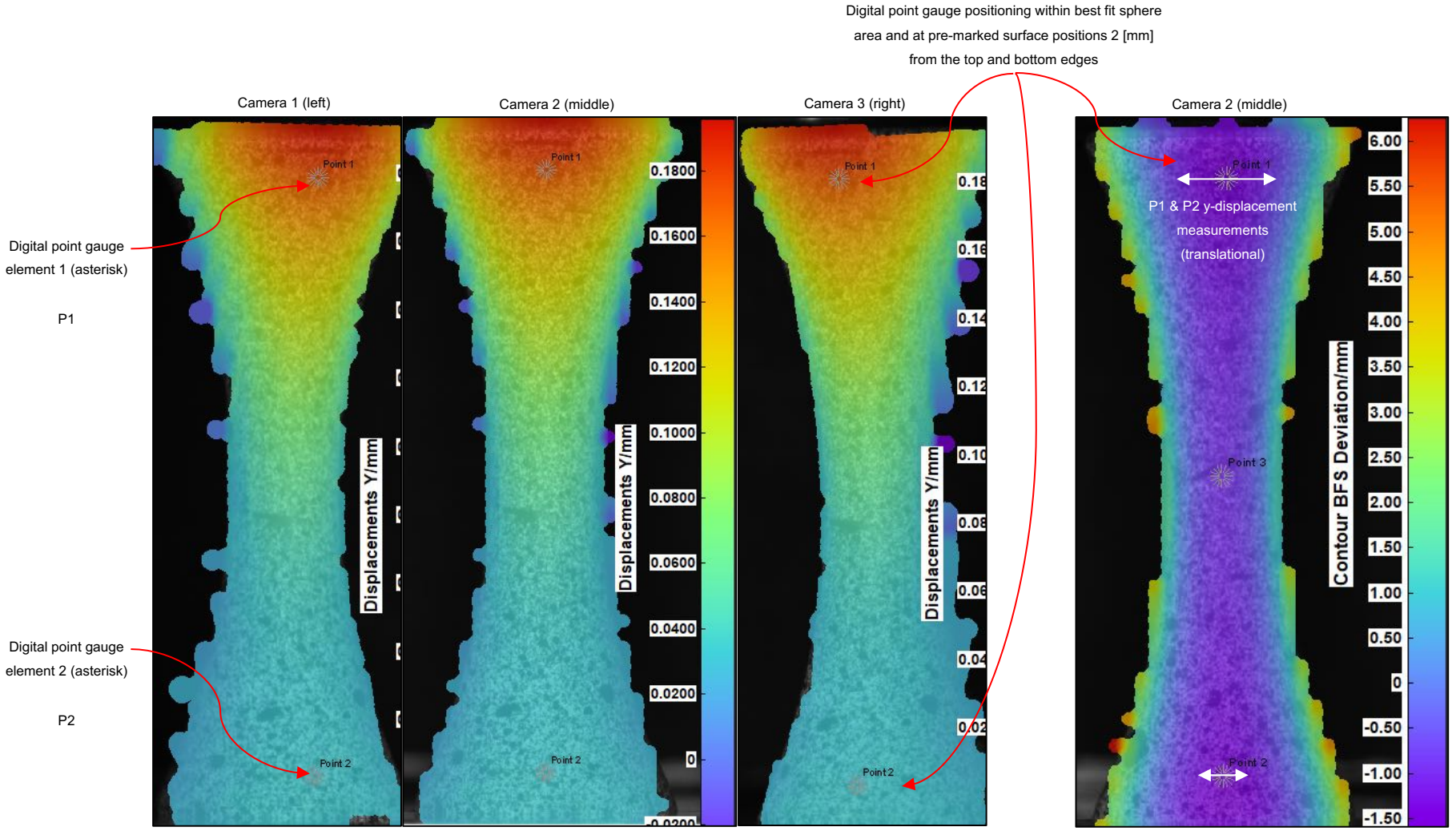


Figure H-22: T fatigue test specimen – DANTEC point gauge elements definition and positioning within best fit sphere area

2) DANTEC Torsion Displacement Measurements and Calculations

a) Torsional Loading Verification

Since the T fatigue test bench was so new to the laboratory, and no formal experimental testing or measurements had been performed before this study, it was proposed to perform an informal torsional loading verification measurement on an arbitrary test specimen using the DANTEC. This specimen was an EN19 (R-condition) steel specimen (left over from previous tests) with a measured average diameter of 6.364 [mm] (using the digital vernier). This specimen was used prior to this measurement to explore the general T fatigue test bench operation using various centrifugal mass pieces. For the verification measurement, the T fatigue test bench was not run with centrifugal mass pieces but instead loaded with a hanging scale (with confirmed mass measurement) pulling upwards on one of the lever-head wheels (see Figure H-23 below). This digital hang scale was filmed during the measurements to obtain the maximum achieved pulling weight (in [kg], converted to [N]). It was also zeroed prior to each measurement. The DANTEC continuously measured the resultant specimen twist (as in the previous section, over 500 image steps). The relevant displacement data was exported and processed to obtain the maximum nett displacement (in the y-direction) of the two digital gauge points ($\Delta y_{max} = y_{1,max} - y_{2,max}$) corresponding to the moment of maximum pulling force on the wheel (see Figure H-24 below). The measurements were then compared with the specimen's theoretical torsional displacement from the static FEM simulations (see Figure H-24 below, measured at the P1 position, 3 [mm] from the top edge). The results of the three displacement comparisons are provided in Table H-11 below.

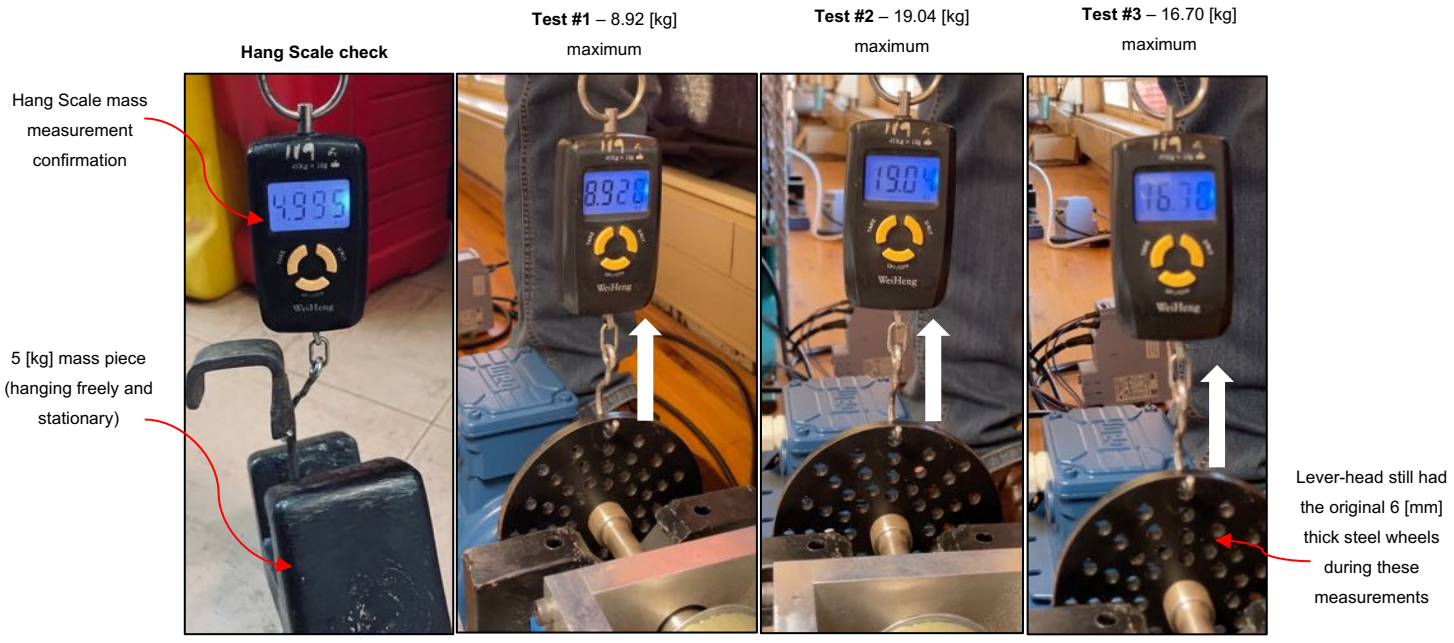


Figure H-23: Hang scale test #1 to #3 – hang scale loading on wheel

It should be noted that the user-defined measurement coordinate system of the DANTEC was differently defined from that previously shown (see Figure H-21 (c)). The x-axis direction was inverted due to the speckle pattern flaking off in the specimen centre (because of the previous tests on the specimen mentioned earlier). For this reason, the y-displacement measurements were also inverted in direction and thus illustrated below as 'decreasing' values instead of the expected increasing values (positive twisting). However, the absolute values of these displacements were the relevant ones to consider for comparison with the FEM model. The observed offset in the P1 and P2 y-displacements are attributed to the unavoidable rigid body y-displacement (accounted for by P2) of the test bench itself under the hang scale loads pulling upward and the cameras not being positioned precisely above the specimen.

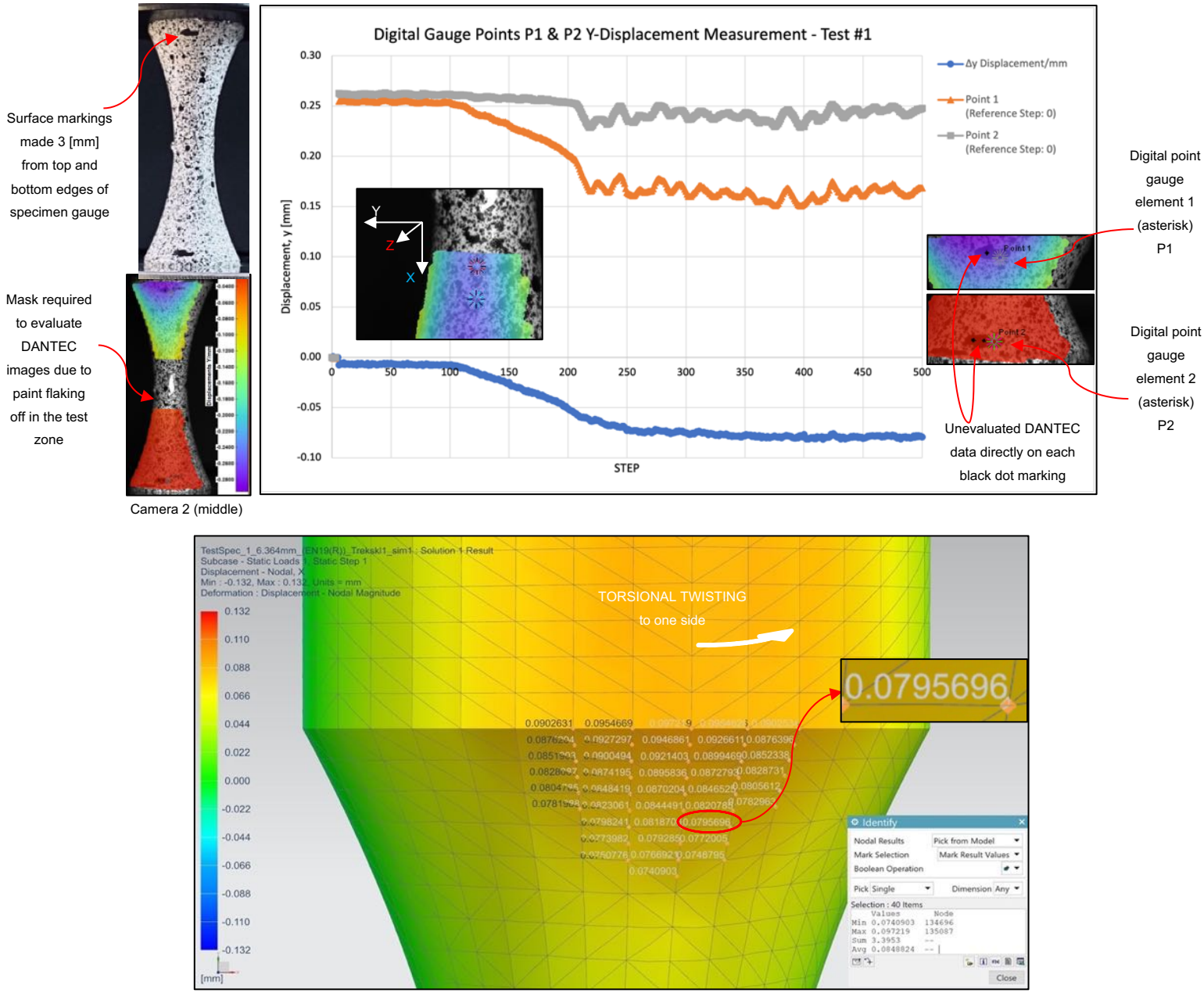


Figure H-24: Hang scale test #1 – DANTEC and static FEM displacement measurement

For the stat FEM model, the hang scale load was assumed to be applied in the middle of the wheel plate width (6 [mm] thick) for the moment calculation. The moment lever distance to this point was theoretically measured as 110 [mm] in the test bench's CAD assembly model. The specimen model had the corresponding diameter measured ten (10) times for the test specimen before testing. The specimen model was loaded and constrained, similar to that illustrated in Figure I-1 (Appendix I1). The theoretical P1 displacement measurement in the FEM simulation was made slightly off-centre (to the right) due to the digital gauge point positionings also being slight to the right of the black dot markings on the specimen surface. This was due to the black dot markings having some 'unrecorded' DANTEC measurement data directly on each dot (see Figure H-24 above), purely due to the dots being large and black (relative to other speckles). The surface markings were adapted for the official experimental specimen measurements (parts b and c after this) to the small cross markings previously shown in Figure H-21 (a).

Table H-11: Hang scale test #1 to #3 – measurement comparison

										Gauge P1-P2 Displacement - @ E = E_{NX} = 206.9GPa		
EN 19 (R)		Specimen #	Diameter	Hang Scale Test #	Hang Scale Maximum Load			S_y / T_{VM}		NX FEM	DANTEC	Difference
			[mm]		[kg]	[N]	[N.m]	[MPa]		[mm]	[mm]	[%]
hangscale	(DANTEC)	EN19R-T-Spec-1	6.364	1	8.92	87.51	9.63	1.99		0.07957	0.07603	4.45
hangscale	(DANTEC)			2	19.04	186.78	20.55	0.93		-	0.24271	-
hangscale	(DANTEC)			3	16.70	163.83	18.02	1.07		-	0.13098	-
xwheels	gains verify-->	EN19R-T-Spec-2	6.368	-	-	-	-	-		-	-	-

The percentage difference value was calculated with Equation (H-12) below, using the FEM result as a reference (ideally loaded and constrained) and in terms of displacements.

$$Difference\ [\%] = ABS\big((DANTEC - NX\ FEM)\ /\ NX\ FEM\big)100 \qquad \text{(H-12)}$$

The results clearly show that only the first hang scale test (#1) had a suitably low and valid displacement difference. For tests #2 and #3, the comparison between DANTEC and FEM displacement measurements could not be performed since τ_{VM} exceeded the yield strength S_y (657 [MPa] [28]) of the material during test #2 (FEM not valid for plastic deformation). The specimen was, therefore, presumed to have sheared off under the higher applied hang scale loads. These results are further discussed in Section 4.4.2.4 for the T test bench verification measurements. Due to test #1 having the only valid and acceptable measurement difference, it was decided to instead perform different T test bench load-verification measurements with the DANTEC using centrifugal mass pieces. These are discussed in the next part, and they were performed on a second, un-tested EN19 (R-condition) steel T specimen (shown in Table H-11 above).

b) Torsional Loading Gain Measurement – Speed Range

Before performing the official experimental T fatigue test measurements (next part), it was considered appropriate first to measure the loading gain of the second EN19 (R-condition) steel specimen. These measurements were made for various test speeds on the T fatigue test bench. That is, to compare the specimen's experimentally measured torsional gain response (under fully reversed torsional loading) with the theoretically calculated gain response (discussed in Appendix F1 and F2). It was also to check the assumptions made for test bench damping in the latter calculation and the method used to obtain the specimen torsional resonance frequency.

The general DIC measurement and speckle pattern preparation procedures were considered (see Appendix B6) for the experimental gain measurements of the specimen (with an average diameter of 6.368 [mm]). That, along with the specific system setup and torsional displacement measurement procedure described at the beginning of this Appendix H4.2 in part 1. For the specimen loading, it was decided to use the lightest centrifugal mass piece (NUT 8, see Appendix E2) at the 35 [mm] radial position on the wheels. This nut was used to avoid excessive torsional stresses at each test speed, which could damage the specimen and thus influence subsequent measurements at other speeds. The test speeds were chosen as 25, 30, 35, 40 and 45 [Hz], at which each DANTEC displacement measurement was made on the specimen. The test bench was stopped for each measurement, speed set, and restarted. The specimen (diameter 6.368 [mm]), the mass piece and its radial position were kept constant for all five measurements, with only the test speed incrementally increasing.

The displacement measurements (500 image steps) at the five speeds were exported from the ISTRA 4D software for each digital gauge point (P1 and P2). They were processed as illustrated in Table H-12 (all five speeds) and Figure H-25 (illustrative raw data graph for 40 [Hz] speed). After this, they were used to calculate the relevant experimental torsional displacement amplitudes Δy_a [mm] using Equation (H-13) below (middle columns in Table H-12). Note should be taken at this point that these displacements were already 'experimentally gained'. The induced torsion moments and, thus, stresses in the specimen were, therefore, not nominal values (as theoretically calculated for each speed, mass piece, and radius). That is, the torsional loading gain G_T [-] that would be required to calculate the shear stress with Equation (H-11) (in Appendix H4.1) was already included; however not been quantified yet (calculation using the two displacement measurements for each test speed to follow below).

$$\Delta y_a \ [mm] = \left[\Delta y_{max}\,[mm] - \ \Delta y_{min}\,[mm]\right] / 2 \qquad \text{(H-13)}$$

where Δy_{max} : is the image step-wise P1 to P2 maximum difference, $(y_1 - y_2)_{max}$

Δy_{min} : is the image step-wise P1 to P2 minimum difference, $(y_1 - y_2)_{min}$

The next step was to obtain the corresponding theoretical torsional displacements (single-sided y-displacement) of the P1 gauge point, 2 [mm] from the top edge (pre-measured and marked on the specimen) to compare with the above calculated experimental displacement amplitudes. Using only the P1 measurement for the theoretical displacement measurement is due to the ideal theoretical specimen model bottom constraint in FEM (thus, no theoretical rigid body displacement, as accounted for by P2 in the DANTEC measurement). This displacement was obtained from the static FEM specimen model (same diameter), loaded with the theoretically induced centrifugal force (nominal values, see Table H-13 to follow) at each speed. That is, the FEM displacement provided the 'ungained' torsional displacement. This theoretical measurement method and the static FEM model are illustrated and discussed in Appendix I1 hereafter.

With the experimental torsional displacement amplitude ('gained') from the equation above and the theoretical ('ungained') torsional displacement from the static FEM measurement for each test speed, it was then possible to calculate the experimental torsional loading gain G_T [-] using Equation (H-14) below. That is, assuming the theoretical FEM measurement as a reference. The relevant displacement measurements and induced gain calculation results are reported in Table H-13 to follow.

$$G_T\,[-] = DANTEC\,[mm] \,/\, NX\ FEM\,[mm] \tag{H-14}$$

where $DANTEC$: is the experimentally measured y-displacement of test specimen

$NX\ FEM$: is the theoretically measured (nominal) y-displacement of test specimen

These experimental gains were then compared with the theoretical torsional loading gains $G_{T;th}$ [-] from Equation (F-4) (for the considered specimen, speed and mass piece). For this, a percentage difference value was calculated for each test speed measurement using Equation (H-15) below and reported in Table H-13.

$$Difference\,[\%] = ABS\left(\left(G_T - G_{T;th}\right) / \,G_{T;th}\right)100 \tag{H-15}$$

The above torsional loading verification method (with the gain calculation) was considered better than the previous hang scale measurement method since it appropriately considered the actual torsional loading and induced displacements and corresponding stresses experienced by a specimen. This method was similarly used to obtain the official experimental torsional loading gain measurements, as discussed in the last part (to follow).

Table H-12: T specimen measurements – DANTEC DAQ data exports from ISTRA 4D measurements

x-displacement (P1&P2)

	Point 1 (Reference Step: 0)	TOP of specimen	Point 2 (Reference Step: 0)	BOTTOM of specimen	Top - Bottom
Step No.	x Displacement/mm	Uncertainty of x Displacement/mm	x Displacement/mm	Uncertainty of x Displacement/mm	Δx Displacement/mm
0	0	0,0001175	0	0,000344017	0
1	0,000145247	0,000167446	-0,000101649	0,000408216	0,000246896
2	1,24759E-05	0,000168921	0,000218999	0,000404723	-0,000206523
3	2,96863E-05	0,000166323	1,95232E-05	0,000398905	1,01631E-05
4	0,0288659	0,000194384	0,0291863	0,000402103	-0,0003204

y-displacement (P1&P2)

	Point 1 (Reference Step: 0)	TOP of specimen	Point 2 (Reference Step: 0)	BOTTOM of specimen	Top - Bottom
Step No.	y Displacement/mm	Uncertainty of y Displacement/mm	y Displacement/mm	Uncertainty of y Displacement/mm	Δy Displacement/mm
0	0	0,000145634	0	0,000394133	0
1	7,36609E-05	0,000194662	6,7674E-07	0,000456822	-7,29842E-05
2	-6,40458E-05	0,000195694	-1,26133E-05	0,000453647	5,14325E-05
3	1,57723E-05	0,000192934	3,46268E-05	0,000447704	1,88545E-05
4	0,0244777	0,000222852	0,0118827	0,000451511	-0,012595

z-displacement (P1&P2)

	Point 1 (Reference Step: 0)	TOP of specimen	Point 2 (Reference Step: 0)	BOTTOM of specimen	Top - Bottom
Step No.	z Displacement/mm	Uncertainty of z Displacement/mm	z Displacement/mm	Uncertainty of z Displacement/mm	Δz Displacement/mm
0	0	0,000241295	0	0	0,000583349	0
1	0,000295293	0,000295237	1	0,000752439	0,00064723	-0,000457146
2	-0,000382009	0,000295134	2	0,000262095	0,000644796	-0,000644104
3	-0,000182288	0,000291583	3	-0,000018877	0,00063796	-0,000163411
4	-0,0330295	0,000330226	4	-0,0341392	0,000643996	0,0011097

25 [Hz] Test Speed – exported xyz-displacement data

x-displacement (P1&P2)

	Point 1 (Reference Step: 0)	TOP of specimen	Point 2 (Reference Step: 0)	BOTTOM of specimen	Top - Bottom
Step No.	x Displacement/mm	Uncertainty of x Displacement/mm	x Displacement/mm	Uncertainty of x Displacement/mm	Δx Displacement/mm
0	0	0,000128837	0	0	0,000314095	0
1	-0,000219519	0,000174115	1	-0,000032553	0,000378969	-0,000186966
2	-0,000250828	0,000174467	2	-0,000117653	0,000376465	-0,000133175
3	-0,000116161	0,000176583	3	-0,000223761	0,000374488	0,0001076
4	-0,00714679	0,000206579	4	-0,00703739	0,000369696	-0,0001094

y-displacement (P1&P2)

	Point 1 (Reference Step: 0)	TOP of specimen	Point 2 (Reference Step: 0)	BOTTOM of specimen	Top - Bottom
Step No.	y Displacement/mm	Uncertainty of y Displacement/mm	y Displacement/mm	Uncertainty of y Displacement/mm	Δy Displacement/mm
0	0	0,000162669	0	0	0,000363687	0
1	-5,23592E-05	0,00020621	1	0,000520077	0,000427986	-0,000572436
2	-7,03352E-05	0,000207296	2	0,000256649	0,000424815	-0,000326984
3	0,00015048	0,000209457	3	0,000313693	0,000422713	-0,000163213
4	0,0140083	0,000240812	4	0,00485968	0,000418748	0,00914862

z-displacement (P1&P2)

	Point 1 (Reference Step: 0)	TOP of specimen	Point 2 (Reference Step: 0)	BOTTOM of specimen	Top - Bottom
Step No.	z Displacement/mm	Uncertainty of z Displacement/mm	z Displacement/mm	Uncertainty of z Displacement/mm	Δz Displacement/mm
0	0	0,000269853	0	0	0,00053877	0
1	-0,000305076	0,00031607	1	0,000470339	0,000607539	-0,000775415
2	-0,000108851	0,000319193	2	0,00040997	0,000602145	-0,000518821
3	0,000225058	0,000321756	3	-1,44808E-05	0,000599502	0,000239539
4	0,0059589	0,00036053	4	0,00945973	0,000597618	-0,00350083

30 [Hz] Test Speed – exported xyz-displacement data

x-displacement (P1&P2)

	Point 1 (Reference Step: 0)	TOP of specimen	Point 2 (Reference Step: 0)	BOTTOM of specimen	Top - Bottom
Step No.	x Displacement/mm	Uncertainty of x Displacement/mm	x Displacement/mm	Uncertainty of x Displacement/mm	Δx Displacement/mm
0	0	0,000235051	0	0	0,000494199	0
1	-9,56672E-05	0,000255593	1	-8,00619E-05	0,000526237	-1,56053E-05
2	2,36363E-06	0,000259088	2	0,000444988	0,000525195	-0,000442624
3	-2,33339E-05	0,000259887	3	6,59409E-05	0,000526778	-8,92748E-05
4	0,034421	0,000270433	4	0,0336118	0,000528663	0,0008092

y-displacement (P1&P2)

	Point 1 (Reference Step: 0)	TOP of specimen	Point 2 (Reference Step: 0)	BOTTOM of specimen	Top - Bottom
Step No.	y Displacement/mm	Uncertainty of y Displacement/mm	y Displacement/mm	Uncertainty of y Displacement/mm	Δy Displacement/mm
0	0	0,000243773	0	0	0,000505294	0
1	4,80895E-05	0,000264068	1	5,98705E-05	0,000536749	-0,000011781
2	-7,64112E-05	0,000267484	2	5,99694E-05	0,000535761	-0,000136381
3	-7,66524E-05	0,000268282	3	0,000205984	0,000537292	-0,000282636
4	-0,0211364	0,000278682	4	0,0127137	0,000539148	-0,0338501

z-displacement (P1&P2)

	Point 1 (Reference Step: 0)	TOP of specimen	Point 2 (Reference Step: 0)	BOTTOM of specimen	Top - Bottom
Step No.	z Displacement/mm	Uncertainty of z Displacement/mm	z Displacement/mm	Uncertainty of z Displacement/mm	Δz Displacement/mm
0	0	0,000505078	0	0	0,000880293	0
1	1,95762E-05	0,000525471	1	8,49478E-05	0,000900945	-6,53716E-05
2	0,000120275	0,00052791	2	0,000445037	0,000901302	-0,000324762
3	0,000248059	0,000528912	3	0,000524354	0,000901614	-0,000276295
4	-0,0324782	0,000538439	4	-0,0344135	0,00090292	0,0019353

35 [Hz] Test Speed – exported xyz-displacement data

x-displacement (P1&P2)

	Point 1 (Reference Step: 0)	TOP of specimen	Point 2 (Reference Step: 0)	BOTTOM of specimen	Top - Bottom
Step No.	x Displacement/mm	Uncertainty of x Displacement/mm	x Displacement/mm	Uncertainty of x Displacement/mm	Δx Displacement/mm
0	0	0,000234463	0	0	0,000497206	0
1	0,000106135	0,000256204	1	-7,14996E-05	0,000532656	0,000177635
2	9,29085E-05	0,000258578	2	-2,46648E-05	0,000534153	0,000117573
3	8,90673E-05	0,000259004	3	-5,51382E-05	0,000531505	0,000144206
4	0,0138544	0,000276523	4	0,0119365	0,000529099	0,0019179

y-displacement (P1&P2)

	Point 1 (Reference Step: 0)	TOP of specimen	Point 2 (Reference Step: 0)	BOTTOM of specimen	Top - Bottom
Step No.	y Displacement/mm	Uncertainty of y Displacement/mm	y Displacement/mm	Uncertainty of y Displacement/mm	Δy Displacement/mm
0	0	0,000243162	0	0	0,000508368	0
1	-0,000117874	0,000264649	1	-0,000103228	0,000543243	-0,000014646
2	-0,000151199	0,000267056	2	-0,000253299	0,000544754	0,0001021
3	-0,00012582	0,000267443	3	-2,35795E-05	0,00054212	-0,000102241
4	-0,0700332	0,000284859	4	-0,0114816	0,000539797	-0,0585516

z-displacement (P1&P2)

	Point 1 (Reference Step: 0)	TOP of specimen	Point 2 (Reference Step: 0)	BOTTOM of specimen	Top - Bottom
Step No.	z Displacement/mm	Uncertainty of z Displacement/mm	z Displacement/mm	Uncertainty of z Displacement/mm	Δz Displacement/mm
0	0	0,000503813	0	0	0,000885646	0
1	-0,000114245	0,000525514	1	-0,000283398	0,000910413	0,000169153
2	0,000178584	0,000529272	2	0,000160899	0,000912507	0,000017685
3	-5,17232E-05	0,000528866	3	-0,000223127	0,000909907	0,000171404
4	-0,0116123	0,000548108	4	-0,010634	0,000909495	-0,0009783

40 [Hz] Test Speed – exported xyz-displacement data

x-displacement (P1&P2)

	Point 1 (Reference Step: 0)	TOP of specimen	Point 2 (Reference Step: 0)	BOTTOM of specimen	Top - Bottom
Step No.	x Displacement/mm	Uncertainty of x Displacement/mm	x Displacement/mm	Uncertainty of x Displacement/mm	Δx Displacement/mm
0	0	0,000224171	0	0	0,000477335	0
1	-7,56574E-05	0,00024572	1	0,000435686	0,000510455	-0,000511343
2	-0,000220242	0,000247318	2	-4,62111E-07	0,000512674	-0,00021978
3	3,20216E-05	0,000247268	3	0,000223095	0,000511389	-0,000191073
4	0,00907205	0,000266917	4	0,0120575	0,000512286	-0,00298545

y-displacement (P1&P2)

	Point 1 (Reference Step: 0)	TOP of specimen	Point 2 (Reference Step: 0)	BOTTOM of specimen	Top - Bottom
Step No.	y Displacement/mm	Uncertainty of y Displacement/mm	y Displacement/mm	Uncertainty of y Displacement/mm	Δy Displacement/mm
0	0	0,000232488	0	0,000488049	0
1	-0,000034827	0,000253644	1	-7,62037E-05	0,000520606	4,13767E-05
2	0,000256708	0,00025528	2	1,69784E-06	0,000522891	0,00025501
3	2,93227E-05	0,000255238	3	-0,000251997	0,000521602	0,00028132
4	0,125125	0,00027497	4	0,0374673	0,000522497	0,0876577

z-displacement (P1&P2)

	Point 1 (Reference Step: 0)	TOP of specimen	Point 2 (Reference Step: 0)	BOTTOM of specimen	Top - Bottom
Step No.	z Displacement/mm	Uncertainty of z Displacement/mm	z Displacement/mm	Uncertainty of z Displacement/mm	Δz Displacement/mm
0	0	0,000481696	0	0	0,000850212	0
1	0,000121797	0,000499756	1	-7,30799E-05	0,000872603	0,000194877
2	0,00021773	0,000502662	2	-0,000449918	0,000877029	0,000667648
3	4,39129E-05	0,000502799	3	-0,000428449	0,000875427	0,000472362
4	-0,00697178	0,000529229	4	-0,0118881	0,000876425	0,00491632

45 [Hz] Test Speed – exported xyz-displacement data

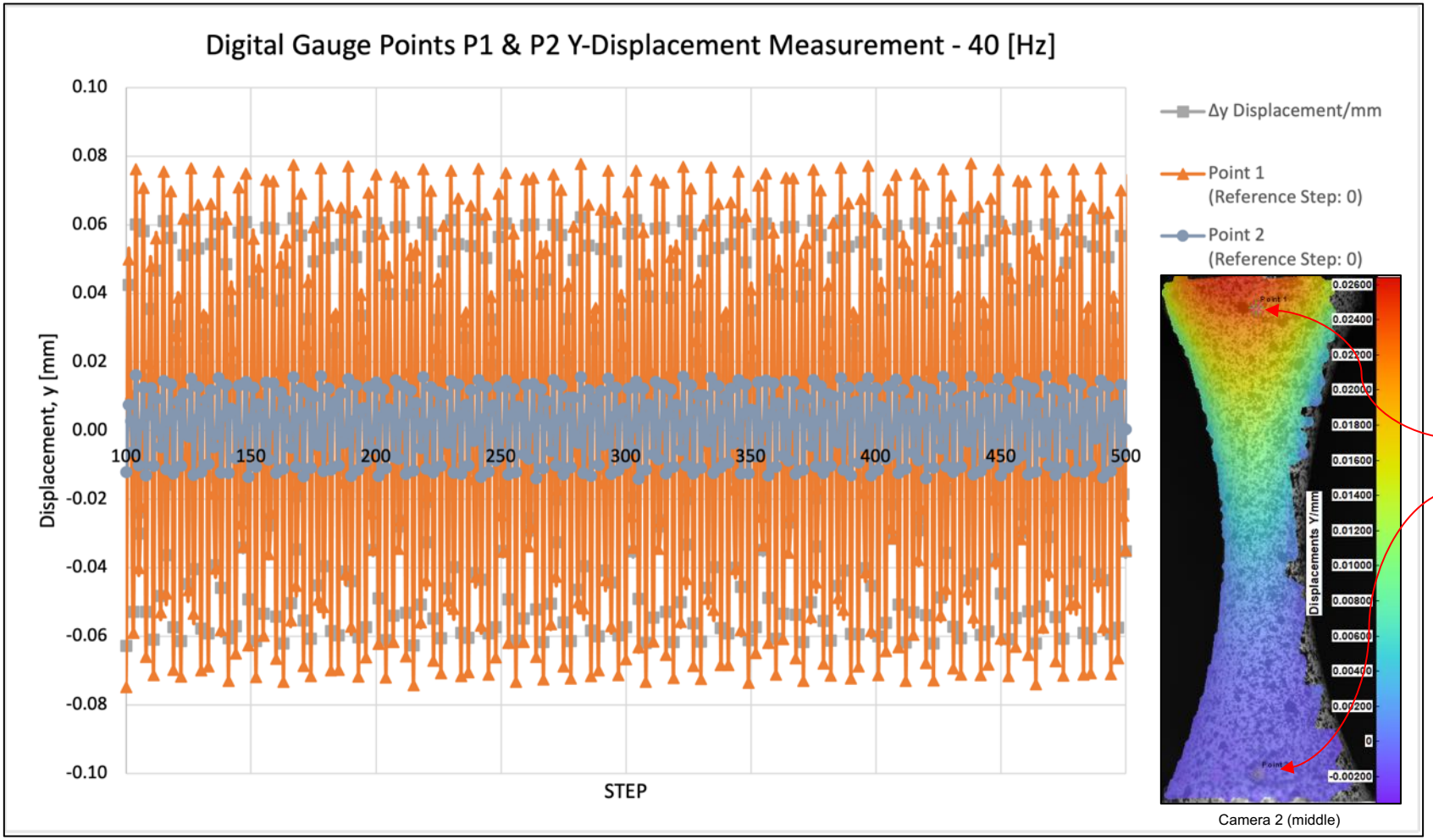
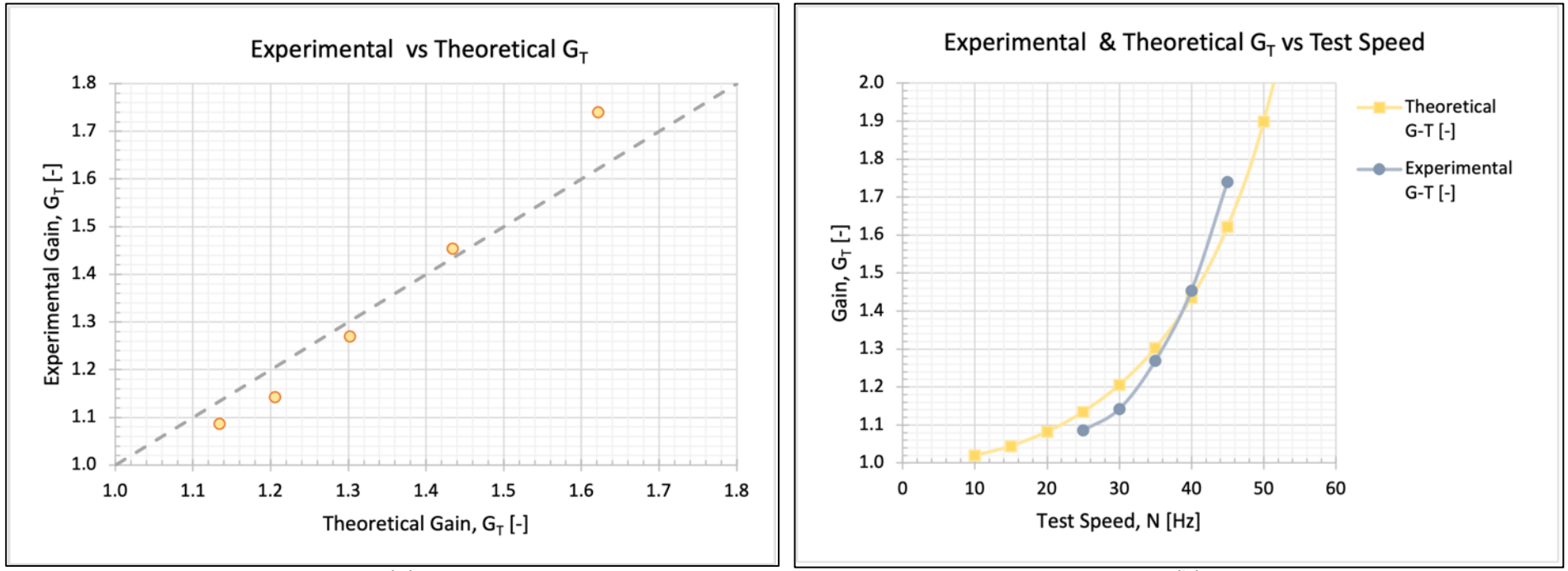


Figure H-25: T specimen measurements – DANTEC digital point gauge P1 and P2 y-displacement curves at 40 [Hz] test speed

Table H-13: T specimen measurements – experimental and theoretical gain

EN 19 (R)		Specimen #	Diameter	N	Nut 8 Bolt 1 (M5)	Radius	V Nominal V $F_{centrifugal}$	V Nominal V M_T	T-Stiffness k_t	V ref point Theoretical G_T	Gauge P1-P2 Displacement - @ E = E_{NX} = 206.9GPa NX FEM	DANTEC	Experimental G_T	Difference G_T
			[mm]	[Hz]	[g]	[mm]	[N]	[N.m]	[N.m/rad]	[-]	[mm]	[mm]	[-]	[%]
hang scale measurments -->		EN19R-T-Spec-1	6.364	-	-	-	-	-	-	-	-	-	-	-
xwheels	(DANTEC)	EN19R-T-Spec-2	6.368	25	12.028	35	10.387	2.266	786.96	1.134	0.02044	0.02221	1.086	-4.21
xwheels	(DANTEC)		6.368	30	12.028	35	14.958	3.262	786.92	1.205	0.02943	0.03363	1.142	-5.23
xwheels	(DANTEC)		6.368	35	12.028	35	20.359	4.440	786.94	1.302	0.04006	0.05086	1.269	-2.50
xwheels	(DANTEC)		6.368	40	12.028	35	26.592	5.800	786.92	1.435	0.05233	0.07608	1.454	1.35
xwheels	(DANTEC)		6.368	45	12.028	35	33.655	7.340	786.92	1.622	0.06623	0.11522	1.740	7.28

The torsional loading verification measurements (with the DANTEC and static FEM model) and the calculated torsional gains in Table H-13 above show that the experimental torsional gain response was very similar to the theoretical gain response. That is, for the considered specimen over the five test speeds and relevant centrifugal mass piece. The experimental vs theoretical torsional gain graph illustrates the similarity in Figure H-26 (a) and the two gain response curves in Figure H-26 (b) below. The gain comparison differences calculated (with Equation (H-15)) for each test speed were shown to be sufficiently low, with only the 30 [Hz] and 45 [Hz] having differences larger than 5 [%]. The low differences (over the considered speed range), therefore, implied that the experimental torsional loading gain was very similar to the calculated theoretical values with the assumption of little to no test bench damping (see Equation (F-4)). These results are further discussed in Section 4.4.2.4.



(a) (b)

Figure H-26: T specimen measurements – (a) experimental and theoretical gain comparison and (b) gain response curves

c) Experimental Torsional Loading Gain Measurement

For the official experimental T fatigue loading gain measurements, it was decided only to measure the specimens tested at different speeds or with different centrifugal mass pieces (both influential to torsion gain). These were Spec1, Spec5, Spec8 and Spec9. The similar diameters (6.548 [mm] on average) of the nine (9) uniaxial torsion fatigue (T) test specimens allowed for this (see Figure H-18 and Appendix D5). It was therefore assumed that the experimental gain of the specimens not measured with the DANTEC would be very similar to the theoretical values (based on previous part b results). That is, the experimental torsional loading gain (of the unmeasured specimens) could be set equal to the theoretically calculated gain (using Equation (F-4)) since the percentage difference between the two (at respective test speeds) was sufficiently low.

These four (4) experimental T fatigue test specimens were measured with the DANTEC system according to the general DIC measurement and speckle pattern preparation procedures (see Appendix B6) and the displacement measurement procedure described in part 1 of this Appendix H4.2. The initial approach for these experimental T fatigue tests was to start at low enough test speeds (and measure it with the DANTEC) using appropriate centrifugal mass pieces that would either cause ‘low’ HCF failure or not cause failure at all. The purpose was to obtain the ‘end points’ of the experimental torsion fatigue S-N curve between which remaining specimens could be tested. That is, at loading levels in-between the two endpoints (or curve limits). The above was done despite the previous results (see Table H-13 and Figure H-26 (b)), which showed that the 35 to 40 [Hz] range would be the test speeds where the theoretical and experimental torsional loading gains would have the closest values. Therefore, the likelihood of not having appropriately sized mass piece options or wheel radius positions for the chosen test speeds was mitigated.

Due to the above approach, Spec1 was measured at a test speed of 27.5 [Hz] and Spec5 at 35 [Hz]. Both these test specimens did not fail in torsional fatigue, even with the heaviest centrifugal mass pieces used in each test. For these two tests, the DANTEC displacement measurements (for P1 and P2, over 600 image steps) were exported from the ISTRA 4D software and processed as illustrated in Table H-14 (for all measured specimens) and Figure H-27 (raw data graph of Spec8 for illustration). The relevant experimental displacement amplitudes, theoretical displacement measurements, torsional gains and measurement differences were obtained using the same procedure and equations (Equation (H-13) to (H-15)) as discussed in the previous part.

Since the lower test speeds above did not cause for failure of the specimens, it was decided to increase the test speed to 40 [Hz] (see the previous part, the ideal test speed for equivalent theoretical and experimental gains). This speed was used for Spec9 first (using a large mass piece), which caused LCF failure, and then for Spec8 (using a mid-sized mass piece), which also caused LCF failure of the specimen. Therefore, the two end-points of the experimental torsion

fatigue S-N curve were obtained from this and the lower test speed measurements. All subsequent specimens were tested in between these test loading levels further to fill the S-N curve with data points in HCF. For Spec9 and Spec8, the DANTEC (Table H-14 and in Figure H-27) displacement data processing and static FEM measurements were also done with the procedure and equations of the previous part to obtain the experimental torsional gains and the difference values. These experimental measurement results are reported along with the previous Spec1 and Spec5 results in Table H-15 and Figure H-29 to follow. These results were also carried over to the experimental torsion fatigue testing results reported in Table J-4. There they were utilised, as described in Appendix H4.1 and Equation (H-11), to calculate the fully reversed torsion fatigue stresses, as reported in Table J-4.

For all four of the DANTEC displacement measurements performed on the T fatigue test bench, the resultant fully reversed (experimental torsion) sinusoidal displacement curves were also obtained, as shown in Figure H-28 to follow. These sinusoidal curves were obtained by 'collapsing' the semi-scattered Δy [mm] displacement values (as shown in Figure H-27) to a single sinusoid representative of the actual loading. The fullest curves obtained were those of the two 40 [Hz] test speed specimen measurements (Spec9 and Spec8). The 'collapsing' (or overlaying) of the DANTEC displacement data points onto each other was required primarily due to the scatter of the unprocessed data points caused by the difference in the test speed (of each specimen) and the camera frame rate speed (notes on each graph in Figure H-28). It was required to slightly lower the T fatigue specimen test speeds (from the 27.5, 35, and 40 [Hz] thought to be tested) by a maximum of 1.85 [%] to allow the proper overlaying of the scattered displacement data points (reported in the notes on each graph in Figure H-28). This lowering in the speed was necessary since the specified test bench speeds on the VSD were experimentally lower during each test and DANTEC measurement, which was attributed to the inherent motor slip present at each motor speed. These sinusoidal displacement curves illustrated that each specimen's experimentally induced torsional loading had the appropriate and expected fully reversed form. The curves also further verified the correctness of the experimental loading thought to be induced during each test.

Table H-14: T fatigue test Spec1, 5, 8 and 9 measurements – DANTEC DAQ data exports from ISTRA 4D measurements

x-displacement (P1&P2)

	Point 1 (Reference Step: 0)	TOP of specimen	Point 2 (Reference Step: 0)	BOTTOM of specimen	Top - Bottom
Step No.	x Displacement/mm	Uncertainty of x Displacement/mm	Step No.	x Displacement/mm	Uncertainty of x Displacement/mm	Δx Displacement/mm
0	0	0,000221139	0	0	0,000257279	0
1	0,0154849	0,00028068	1	0,0142933	0,000302458	0,0011916
2	0,00870845	0,000258156	2	0,00831457	0,000286775	0,00039388
3	0,00955897	0,00023335	3	0,00916625	0,000274361	0,000039272
4	-0,000575449	0,000248319	4	-0,000929511	0,000292952	0,000354062

y-displacement (P1&P2)

	Point 1 (Reference Step: 0)	TOP of specimen	Point 2 (Reference Step: 0)	BOTTOM of specimen	Top - Bottom
Step No.	y Displacement/mm	Uncertainty of y Displacement/mm	Step No.	y Displacement/mm	Uncertainty of y Displacement/mm	Δy Displacement/mm
0	0	0,000254987	0	0	0,000314281	0
1	-0,114826	0,000309366	1	-0,0113525	0,000353849	0,1034735
2	-0,0556307	0,000288327	2	-0,00483645	0,000339727	0,050794 25
3	-0,000852367	0,000266061	3	7,95603E-05	0,00032917	0,000931927
4	-0,0380012	0,000279934	4	-0,00961969	0,000345052	0,028381 51

z-displacement (P1&P2)

	Point 1 (Reference Step: 0)	TOP of specimen	Point 2 (Reference Step: 0)	BOTTOM of specimen	Top - Bottom
Step No.	z Displacement/mm	Uncertainty of z Displacement/mm	Step No.	z Displacement/mm	Uncertainty of z Displacement/mm	Δz Displacement/mm
0	0	0,00133834	0	0	0,00189431	0
1	0,0120348	0,00138153	1	0,00963106	0,00193332	0,00240374
2	0,00785165	0,00135984	2	0,00651609	0,00191538	0,00133556
3	0,000298543	0,00134928	3	0,000130502	0,00191086	0,000168041
4	-0,00112154	0,00136645	4	-0,0013123	0,00191817	0,00019076

27.5 [Hz] Test Speed of Spec1 – exported xyz-displacement data

x-displacement (P1&P2)

	Point 1 (Reference Step: 0)	TOP of specimen	Point 2 (Reference Step: 0)	BOTTOM of specimen	Top - Bottom
Step No.	x Displacement/mm	Uncertainty of x Displacement/mm	Step No.	x Displacement/mm	Uncertainty of x Displacement/mm	Δx Displacement/mm
0	0	0,000256193	0	0	0,000138382	0
1	0,000156085	0,000288192	1	-5,05384E-05	0,000182416	0,000206623
2	0,000118739	0,000288654	2	-2,59787E-05	0,000176195	0,000144718
3	3,07073E-05	0,000289278	3	0,000179595	0,000181618	-0,000148888
4	0,0143241	0,000338798	4	0,0141504	0,000268087	0,0001737

y-displacement (P1&P2)

	Point 1 (Reference Step: 0)	TOP of specimen	Point 2 (Reference Step: 0)	BOTTOM of specimen	Top - Bottom
Step No.	y Displacement/mm	Uncertainty of y Displacement/mm	Step No.	y Displacement/mm	Uncertainty of y Displacement/mm	Δy Displacement/mm
0	0	0,000441104	0	0	0,000370496	0
1	2,80922E-05	0,000467612	1	-9,75223E-05	0,000396215	-0,000125615
2	1,93715E-05	0,000468313	2	-8,00967E-05	0,000394142	-9,94682E-05
3	9,46713E-05	0,000468974	3	-0,000100722	0,00039616	-0,000195393
4	-0,180152	0,000507714	4	-0,0287896	0,00046171	0,1513624

z-displacement (P1&P2)

	Point 1 (Reference Step: 0)	TOP of specimen	Point 2 (Reference Step: 0)	BOTTOM of specimen	Top - Bottom
Step No.	z Displacement/mm	Uncertainty of z Displacement/mm	Step No.	z Displacement/mm	Uncertainty of z Displacement/mm	Δz Displacement/mm
0	0	0,00155106	0	0	0,00147068	0
1	-0,000164257	0,00159506	1	-0,000127862	0,00150948	-0,000036395
2	-0,000110673	0,00159736	2	0,000245334	0,00151231	-0,000356007
3	4,92045E-05	0,00159894	3	0,000250095	0,00151087	-0,000200891
4	-0,00407457	0,00164619	4	-0,00505955	0,00162372	0,00098498

35 [Hz] Test Speed of Spec5 – exported xyz-displacement data

x-displacement (P1&P2)

	Point 1 (Reference Step: 0)	TOP of specimen	Point 2 (Reference Step: 0)	BOTTOM of specimen	Top - Bottom
Step No.	x Displacement/mm	Uncertainty of x Displacement/mm	Step No.	x Displacement/mm	Uncertainty of x Displacement/mm	Δx Displacement/mm
0	0	0,000202407	0	0	0,000066622	0
1	-0,000130019	0,000241861	1	0,000169234	0,000111844	-0,000299253
2	-5,27594E-05	0,00024632	2	0,000363343	0,000110694	-0,000416102
3	-0,000316954	0,000249724	3	0,000106487	0,000112074	-0,000423441
4	-0,0339088	0,000306971	4	-0,0318741	0,000177011	-0,0020347

y-displacement (P1&P2)

	Point 1 (Reference Step: 0)	TOP of specimen	Point 2 (Reference Step: 0)	BOTTOM of specimen	Top - Bottom
Step No.	y Displacement/mm	Uncertainty of y Displacement/mm	Step No.	y Displacement/mm	Uncertainty of y Displacement/mm	Δy Displacement/mm
0	0	0,000243072	0	0	0,000103633	0
1	-7,36026E-05	0,000279157	1	-9,83129E-05	0,000138486	-2,47103E-05
2	-9,35777E-05	0,000282913	2	-0,000134213	0,000137712	-4,06353E-05
3	-6,36242E-06	0,000285435	3	0,000124093	0,000138635	0,000130455
4	0,108597	0,000345527	4	0,0209343	0,000202008	-0,0876627

z-displacement (P1&P2)

	Point 1 (Reference Step: 0)	TOP of specimen	Point 2 (Reference Step: 0)	BOTTOM of specimen	Top - Bottom
Step No.	z Displacement/mm	Uncertainty of z Displacement/mm	Step No.	z Displacement/mm	Uncertainty of z Displacement/mm	Δz Displacement/mm
0	0	0,00153466	0	0	0,000899677	0
1	0,000117365	0,00159401	1	-0,000113498	0,000929784	0,000230863
2	-0,000451276	0,00159207	2	0,000393881	0,000932532	-0,000845157
3	-0,000604099	0,00158233	3	-8,62821E-05	0,000929107	-0,000517817
4	0,00260304	0,00181882	4	0,00503719	0,0011143	-0,00243415

40 [Hz] Test Speed of Spec8 – exported xyz-displacement data

x-displacement (P1&P2)

	Point 1 (Reference Step: 0)	TOP of specimen	Point 2 (Reference Step: 0)	BOTTOM of specimen	Top - Bottom
Step No.	x Displacement/mm	Uncertainty of x Displacement/mm	Step No.	x Displacement/mm	Uncertainty of x Displacement/mm	Δx Displacement/mm
0	0	0,000178103	0	0	0,000079902	0
1	0,000233608	0,000223523	1	0,000204355	0,000148272	0,000029253
2	5,90813E-05	0,000226624	2	0,000322531	0,000141703	-0,00026345
3	0,000168781	0,00022574	3	-2,39587E-05	0,000140445	0,00019274
4	-0,00439878	0,00027814	4	-0,00533348	0,000170039	0,0009347

y-displacement (P1&P2)

	Point 1 (Reference Step: 0)	TOP of specimen	Point 2 (Reference Step: 0)	BOTTOM of specimen	Top - Bottom
Step No.	y Displacement/mm	Uncertainty of y Displacement/mm	Step No.	y Displacement/mm	Uncertainty of y Displacement/mm	Δy Displacement/mm
0	0	0,000214085	0	0	0,000124318	0
1	4,51383E-05	0,000254928	1	0,000122971	0,000177865	7,78327E-05
2	-0,000102484	0,000257479	2	-0,000147872	0,000172439	-0,000045388
3	-0,000168992	0,000256788	3	-0,000128274	0,00017125	0,000040718
4	-0,0973467	0,000308485	4	-0,00835144	0,000197914	0,08899526

z-displacement (P1&P2)

	Point 1 (Reference Step: 0)	TOP of specimen	Point 2 (Reference Step: 0)	BOTTOM of specimen	Top - Bottom
Step No.	z Displacement/mm	Uncertainty of z Displacement/mm	Step No.	z Displacement/mm	Uncertainty of z Displacement/mm	Δz Displacement/mm
0	0	0,00135442	0	0	0,00107942	0
1	0,000467224	0,00140339	1	0,000156152	0,00112025	0,000311072
2	0,00052677	0,00139983	2	-7,81625E-05	0,00111962	0,000604933
3	0,00115931	0,00140173	3	-0,00052096	0,00111641	0,00168027
4	-0,000254443	0,00153346	4	-0,00331477	0,00115723	0,003060327

40 [Hz] Test Speed of Spec9 – exported xyz-displacement data

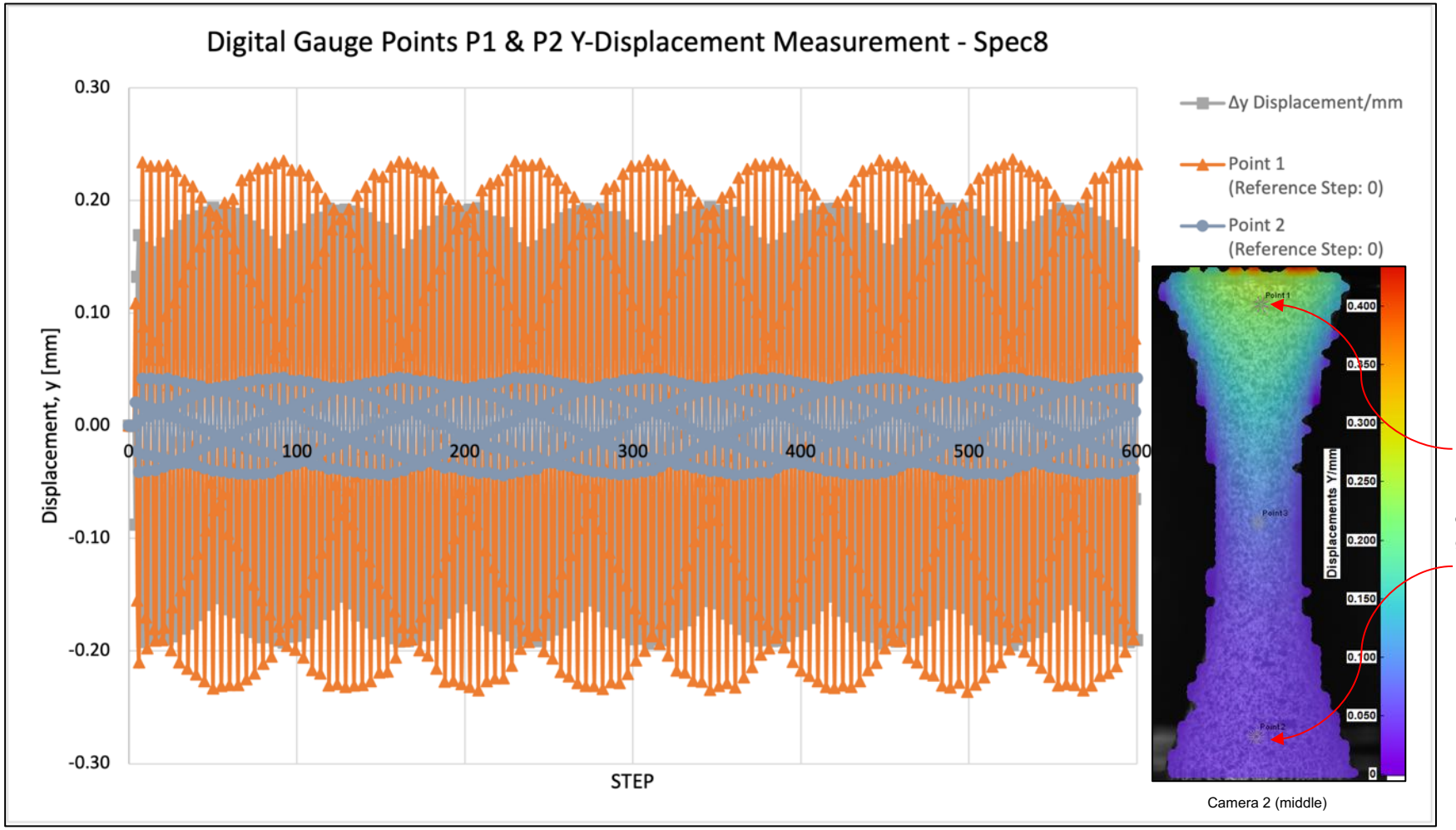


Figure H-27: T fatigue test Spec8 measurements – DANTEC digital point gauge P1 and P2 y-displacement curves at 40 [Hz] test speed

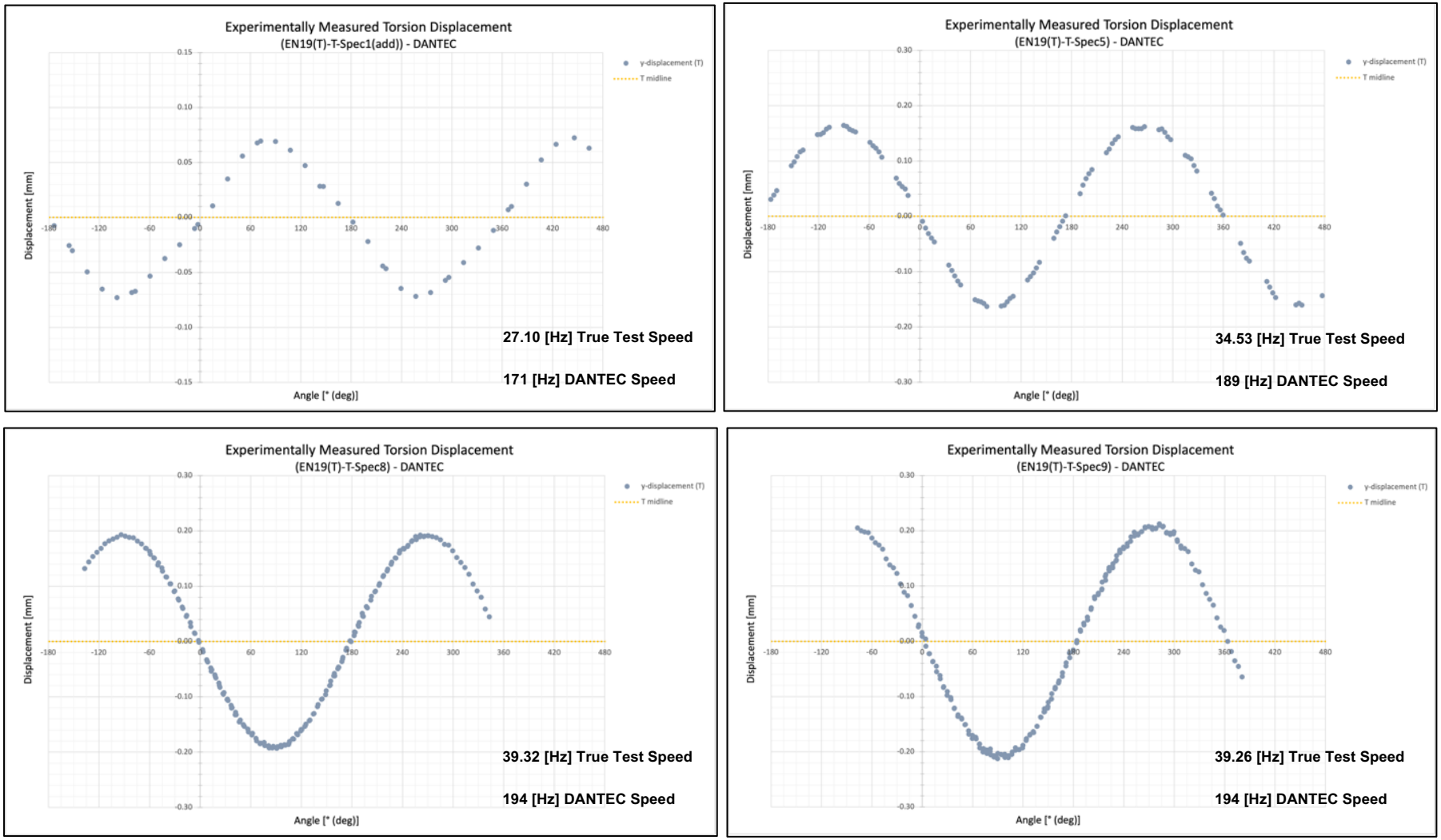


Figure H-28: T fatigue test Spec1, 5, 8 and 9 measurements – DANTEC sinusoidal displacement curves (collapsed)

Table H-15: T fatigue test Spec1, 5, 8 and 9 measurements – experimental and theoretical gain

EN 19 (T)	Specimen #	Diameter	N	Nut&Bolt Mass	Radius	V Nominal V $F_{centrifugal}$	V Nominal V M_T	T-Stiffness k_t	V ref point Theoretical G_T	Gauge P1-P2 Displacement - @ E = E_{exp} = 211.174GPa NX FEM	DANTEC	Experimental G_T	Difference G_T
		[mm]	[Hz]	[g]	[mm]	[N]	[N.m]	[N.m/rad]	[-]	[mm]	[mm]	[-]	[%]
(DANTEC)	EN19T-T-Spec-1	6.548	27.5	28.360	40	33.868	7.681	871.93	1.176	0.06255	0.07275	1.163	1.09
(DANTEC)	EN19T-T-Spec-5	6.523	35.0	34.789	40	67.298	15.456	861.29	1.345	0.12740	0.16584	1.302	3.22
(DANTEC)	EN19T-T-Spec-8	6.571	40.0	28.360	40	71.655	16.252	881.61	1.456	0.13087	0.19433	1.485	1.98
(DANTEC)	EN19T-T-Spec-9	6.558	40.0	34.789	35	76.912	17.664	876.05	1.490	0.14315	0.21549	1.505	1.03

The calculated torsional gain values reported in Table H-15 above and Figure H-29 below for the measured T fatigue specimens showed that the theoretical and experimental torsion loading gains were comparable for the considered test speeds. The calculated differences in the gains for each specimen were all very low. These low difference values supported the notion, previously revealed in Table H-13 that one may set the experimental torsion gain values equal to the theoretically calculated ones (unmeasured specimens) to calculate the stress under the assumption of no damping.

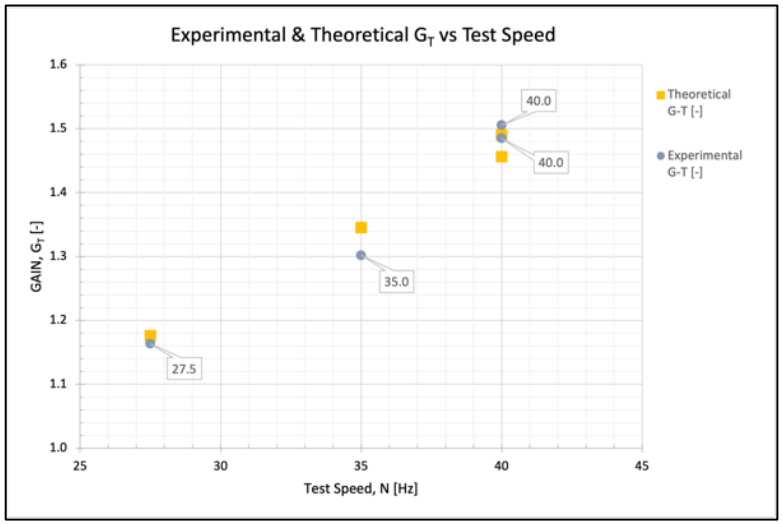


Figure H-29: T fatigue test Spec1, 5, 8 and 9 measurements – experimental and theoretical torsional gain at tested speeds

H5. Bending-Torsion Fatigue Test Measurements and Calculations

H5.1. Experimental Bending-Torsion Fatigue Test Measurements and Calculations

All seventeen (17) biaxial bending-torsion fatigue (BT) tests (Spec1-Spec17, shown in Figure H-31 to follow) were conducted according to the BT fatigue test procedure previously provided in Appendix G5. That is, with the experimentally determined test speed of 38 [Hz] for equivalent bending and torsion loading gain (as discussed in Appendix H5.2 part 2a).

For the BT fatigue tests conducted, it was not deemed feasible to make experimental loading measurements of the test specimens with measurement devices (e.g., strain gauges) other than the non-contact DANTEC system (discussed in Appendix B6 and secondary verification measurement in Appendix H1.3). These displacement measurements from the DANTEC were required for processing the tests. The use of the DANTEC system was primarily due to the high testing frequencies and physical test bench constraints regarding sensor mounting and secondary vibrations during testing. The measurements made with this system were 3D displacement measurements of predefined markings on the fatigue test specimen surfaces. These displacement measurements (in parts 1 and 2b of Appendix H5.2) were utilised along with the appropriate Siemens NX12 static FEM theoretical displacement measurements of the same specimen (discussed in Appendix I2). With the two displacements, the experimental bending loading and torsional loading gains G_B [-] and G_T [-] were calculated (theoretical discussion in previous Appendix F1 to F3) using Equation (H-22) in parts 2a and 2b of Appendix H5.2 hereafter.

The nominal centrifugal force $F_{centrifugal}$ [N] induced on each test specimen was calculated with the chosen centrifugal mass piece m_{centr} [kg] (see Appendix E2) at the chosen radial position r_{wheel} [m] (see Figure E-3) and test speed N [Hz] (set on VSD). This centrifugal force was assumed to act through the centrifugal mass piece COM position (on each wheel). This COM was at a distance L_{lever} [m] (moment lever) from the lever-head central axis (theoretical value for each mass piece, see Table E-2 and Figure E-4). With the centrifugal force and this moment lever length, it was then possible to calculate the nominal bending and torsional moment using Equation (H-16) below. Reference may be made to Figure H-30 below for the BT test bench working principle. Using this bending and torsional moments on each test specimen then allowed for the calculation of the experimentally induced fully reversed bending $\sigma_{bending;a}$ [MPa] and torsional τ_a [MPa] stress amplitudes using Equation (H-17) and (H-18) below (as induced in the hourglass centre). The experimental nominal stress amplitude ratio λ [-] (gained stresses) was also calculated for each test specimen using Equation (H-19) below. The centrifugal mass pieces, their masses and radii, the test speed (38 [Hz]), centrifugal force and resulting moment(s) and stresses are reported for each test specimen in Table J-5. The biaxial shear stress component and uniaxial

torsion fatigue S-N curves were generated. The biaxial bending stress component and uniaxial axial and bending fatigue S-N curves were generated separately. These curves are shown in the results with the experimental fatigue cycle counts N_f [-] (calculated for each test from elapsed test time and test speed).

$$M_{B/T}\,[N.m] = 2\left(F_{centrifugal} L_{lever}\right)\,[N.m] = \; 2\left(m_{centr} r_{wheel} (2\pi N)^2 L_{lever}\right)\,[N.m] \qquad \text{(H-16)}$$

$$\sigma_{bending;a}\,[MPa] = \left\{\left[\frac{32\,M_B\,[N.m]}{\pi d_{spec}^3\,[m^3]}\right] / 10^6\right\} G_B \qquad \text{(H-17)}$$

$$\tau_a\,[MPa] = \left\{\left[\frac{16\,M_T\,[N.m]}{\pi d_{spec}^3\,[m^3]}\right] / 10^6\right\} G_T \qquad \text{(H-18)}$$

$$\lambda\,[-] = \tau_a \; / \sigma_{bending;a} \qquad \text{(H-19)}$$

where d_{spec} : is the BT fatigue specimen test zone diameter (Appendix D5)

m_{centr} : is the sum of relevant bolt, nut and washer masses (Appendix E2)

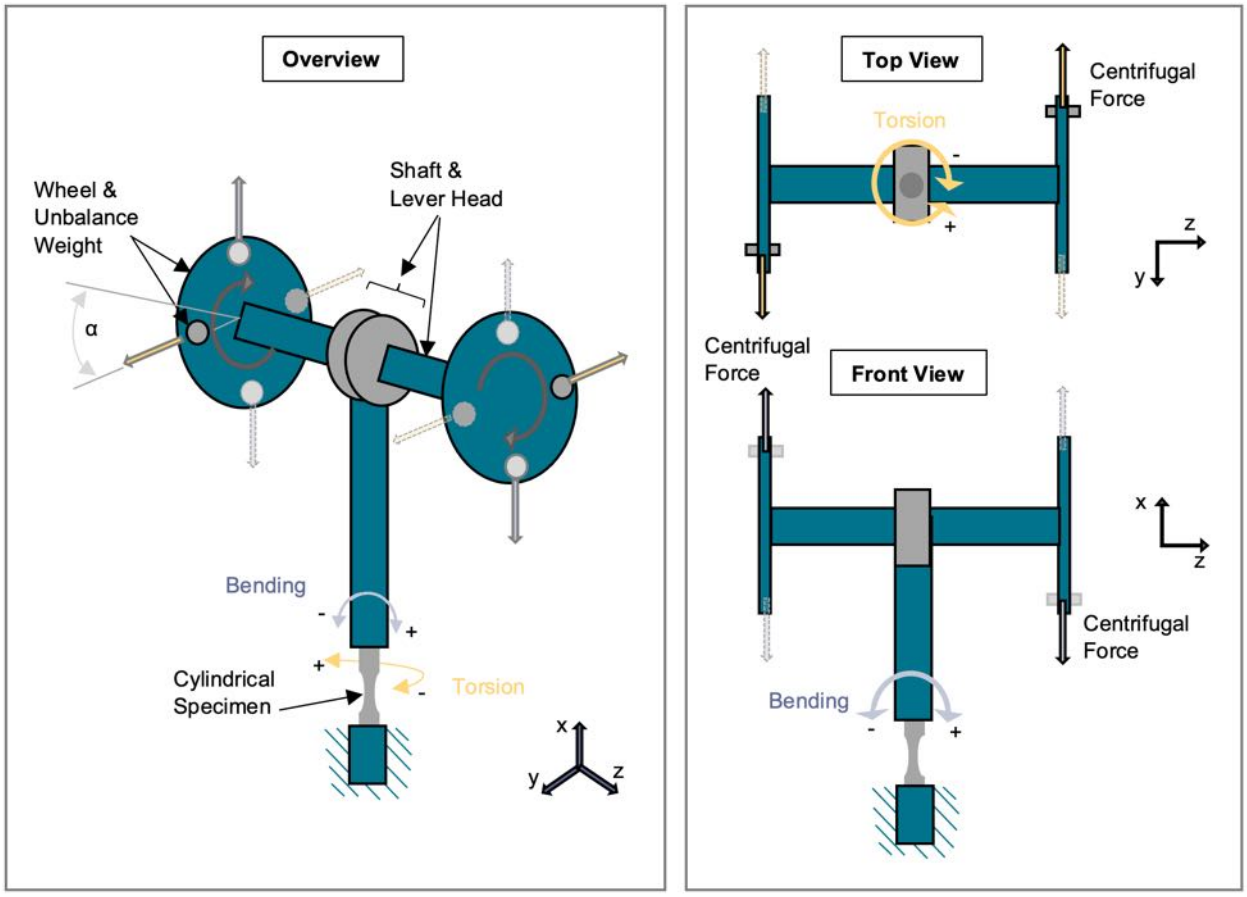
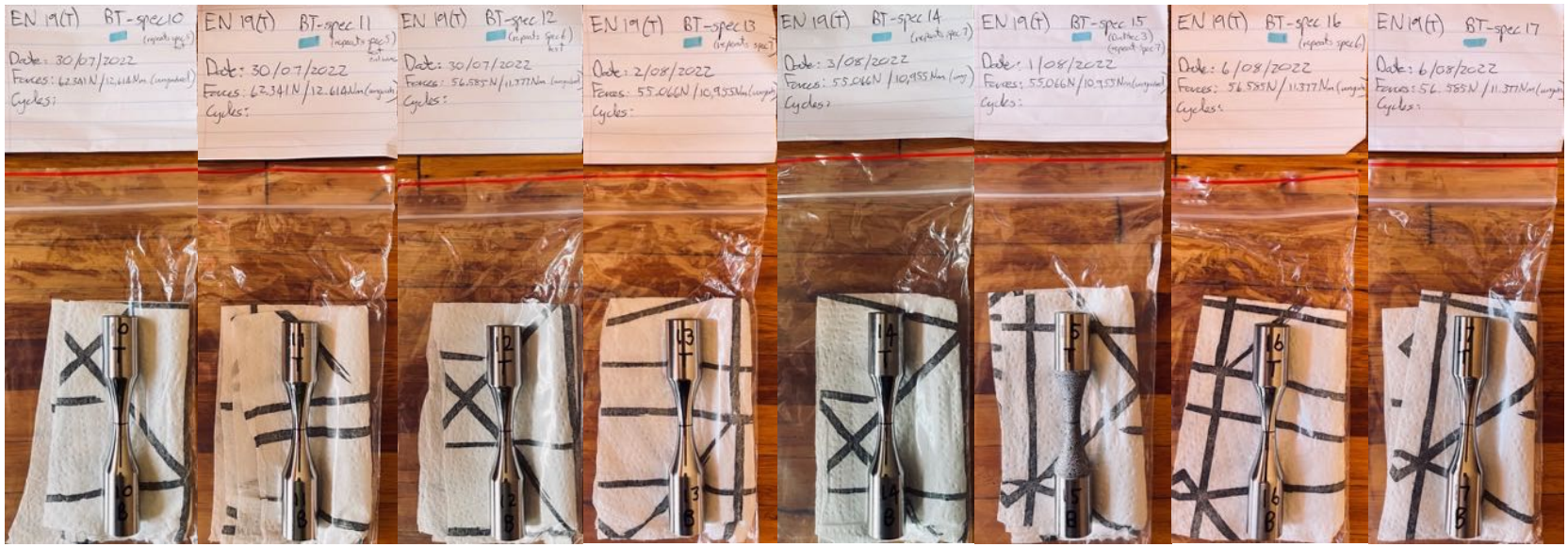


Figure H-30: Bending-Torsion fatigue test bench – working principle (repeat)


EN 19(T) BT-spec1
Date: 25/07/2022
Forces: 38,28 N / 7,491 Nm (unspiked)
Cycles:
EN 19(T) BT-spec2
Date: 26/07/2022
Forces: 45,377 N / 8,977 Nm (unspiked)
Cycles:
EN 19(T) BT-spec3 (Duplicate 1)
Date: 27/07/2022
Forces: 53,435 N / 10,512 Nm (unspiked)
Cycles:
EN 19(T) BT-spec4
Date: 28/07/2022
Forces: 71,347 N / 14,416 Nm (unspiked)
Cycles:
EN 19(T) BT-spec5
Date: 28/07/2022
Forces: 62,341 N / 12,614 Nm (unspiked)
Cycles:
EN 19(T) BT-spec6
Date: 28/07/2022
Forces: 56,585 N / 11,377 Nm (unspiked)
Cycles:
EN 19(T) BT-spec7
Date: 29/07/2022
Forces: 55,066 N / 10,955 Nm (unspiked)
Cycles:
EN 19(T) BT-spec8 (repeats spec7 but unspiked)
Date: 29/07/2022
Forces: 55,066 N / 10,955 Nm (unspiked)
Cycles:
EN 19(T) BT-spec9 (Duplicate 2) (repeats spec6 but unspiked)
Date: 1/08/2022
Forces: 56,585 N / 11,377 Nm (unspiked)
Cycles:


EN 19(T) BT-spec10 (repeats spec5 but unspiked)
Date: 30/07/2022
Forces: 62,341 N / 12,614 Nm (unspiked)
Cycles:
EN 19(T) BT-spec11 (repeats spec5) 2nd time
Date: 30/07/2022
Forces: 62,341 N / 12,614 Nm (unspiked)
Cycles:
EN 19(T) BT-spec12 (repeats spec4) hit
Date: 30/07/2022
Forces: 56,585 N / 11,377 Nm (unspiked)
Cycles:
EN 19(T) BT-spec13 (repeats spec3)
Date: 2/08/2022
Forces: 55,066 N / 10,955 Nm (unspiked)
Cycles:
EN 19(T) BT-spec14 (repeats spec7)
Date: 3/08/2022
Forces: 55,066 N / 10,955 Nm (unspiked)
Cycles:
EN 19(T) BT-spec15 (Duplicate 3) (repeats spec7)
Date: 1/08/2022
Forces: 55,066 N / 10,955 Nm (unspiked)
Cycles:
EN 19(T) BT-spec16 (repeats spec6)
Date: 6/08/2022
Forces: 56,585 N / 11,377 Nm (unspiked)
Cycles:
EN 19(T) BT-spec17
Date: 6/08/2022
Forces: 56,585 N / 11,377 Nm (unspiked)
Cycles:

POST-TEST



Figure H-31: BT fatigue test Spec1 to Spec17 – pre and post-test images

H5.2. Bending-Torsion Fatigue Loading Measurement - DANTEC Measurements and Calculations

1) DANTEC System Set-Up and Measurement Procedure

The relevant DANTEC displacement measurements for the experimental bending and torsion loading gain calculations were obtained using the general DIC measurement procedure (see Appendix B6). For these measurements, the speckle patterns were prepared on the bending-torsion fatigue (BT) test specimens according to the procedure and illustrations provided in Figure B-10 of Appendix B6 and can be viewed in Figure H-33 (a) to follow. The DANTEC system setup with respect to the biaxial bending-torsion fatigue test bench (Appendix A4) and the fatigue test specimen are illustrated in the schematic of Figure H-32 below (not to scale).

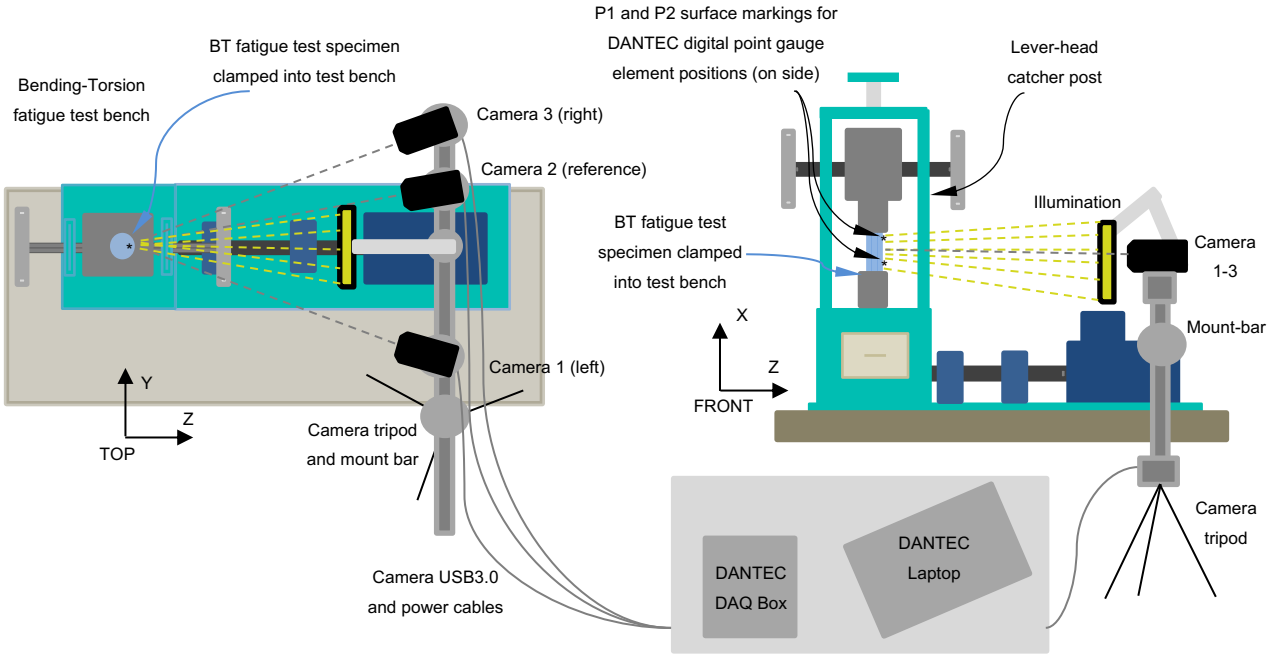


Figure H-32: BT fatigue test specimen measurement – DANTEC DIC System setup schematic (top and front view)

The DANTEC system was positioned on the floor in front of the laboratory workbench and slightly to the side. The DANTEC cameras were then positioned side-by-side on the mount-bar extension arms over the back of the bending-torsion fatigue test bench. This positioning was done to allow the cameras to view the specimen from the right-hand side (at a similar vertical level) with the appropriate stereo angle between cameras 1 and 3 (recommended 30 – 60 [°] for proper 3D measurement of a cylindrical object). Camera 2 was positioned off-centre on the extension arm (towards camera 3) due to the lever-head catcher post obstructing its view in the middle. It should be noted that the DANTEC extension arms, the camera cables and the illumination source were set up over the test bench motor such that nothing touched the test bench (vibrating) during test

measurement. The entire DANTEC system setup was free-standing (on the floor) from the test bench. Camera 2 was used as the reference for measuring and evaluating the recorded images for each test. The system positioning (tripod and mount bar) was set up similarly for all test measurements.

It should be noted that the BT fatigue test bench was mounted (as a whole) with six M10x110mm steel bolts to the laboratory workbench to the left of the T fatigue test bench. However, the workbench at this location was more securely fastened to its support frame than the T fatigue test bench (see Figure H-20). It was, therefore, not required to utilise the 50 [kg] mass pieces to stabilise the workbench (vibrations and displacements) under and around the BT test bench during testing. However, doing this would be an appropriate control to implement so that any unforeseen or excess test bench and workbench rigid body displacements would be minimised during the DANTEC measurements. Therefore, the mass pieces were packed all around the BT test bench at locations where the most vibration was felt during previous fatigue tests (see Figure B-8 of Appendix B6). These mass pieces were used during all subsequent experimental displacement measurements on the BT fatigue test bench.

Once a speckle pattern prepped BT fatigue test specimen (see Figure H-33 (a) to follow) was appropriately loaded and fastened into the BT fatigue test bench clamps (surface markings oriented towards the cameras on the right), the DANTEC displacement measurement could commence. For this, the camera recording sequence was set to take 600 consecutive photos at the highest possible frame rate. This rate depended on the lighting, focal length, resolution, camera calibration and the defined region of interest (specimen view) in the respective camera image views. The highest frame rate achieved was 195 [Hz] for the respective bending-torsion fatigue specimen displacement measurements. The DANTEC recording sequence was initiated (recording for 3-3.5 [s]) about 10 [s] after the start of each biaxial fatigue test, allowing specimen loading and the test bench to stabilise. After the DANTEC completed the pre-set recording sequence, the biaxial fatigue test (then measured) continued to run until specimen failure or until the defined fatigue limit cycle count was reached and the test manually stopped. After a displacement measurement was concluded, it was required to perform the necessary image processing using the ISTRA 4D software on the dedicated DANTEC computer.

This process entailed performing the appropriate image correlations to obtain the evaluated areas on the specimen surface (Figure H-33 (b)) from which digital measurement data could be extracted. The next step was to define a static measurement coordinate system (different from the camera ‘calibration’ coordinate system) for the image evaluations. This was done using the indicated best-fit sphere area illustrated on the evaluated specimen surface (purple geometric field, shown in Figure H-33 (c)) as a reference. That is, to appropriately orient the coordinate

system x-axis (turquois asterisk) and z-axis position (red asterisk) in-line with the surface markings (for gauge points). Customarily for cylindrical specimens, and in this case, the hourglass-shaped gauge area, the x-axis direction is oriented along the longitudinal length of the specimen (above or below the z-axis origin position) and inside the mentioned best-fit sphere area. Suppose the x-axis was positioned to the right or left of the z-axis origin (around the cylinder). In that case, it might lead to inappropriate coordinate system definition and, thus, incorrect displacement measurement data (references to this coordinate system). The best fit sphere is independent of this defined coordinate system, thus serving as an appropriate reference for the coordinate axes positioning.

Since the required measurement quantities were the bending (z-direction) and torsional (y-direction) displacements, it was required to next define two digital point gauge elements within the available colour field on the specimen surface. This was done by placing each digital gauge point element (P1 and P2) on the small cross markings at the top and bottom of the specimen (marked at 2 [mm] from the edges of the specimen gauge area). Reference the evaluated camera images in the software in Figure H-34 and Figure H-33 (a) and (c). These cross markings were measured (using the digital vernier) and marked in line with each other (longitudinally) on the surface of each specimen before each DANTEC measurement. The reason for measuring the torsional twist of a specimen from the linear (translational) y-displacement of each gauge point element was that the DANTEC could not provide out-of-plane (depth) measurements other than the linear z-displacement of each point (which provided the bending displacement). Also, due to the DANTEC being a non-contact measurement, the specimen longitudinal axis could not be defined within the ISTRA 4D software. Therefore, an angular displacement measurement around this axis was not possible to describe the torsional displacement. The ISTRA 4D software and relevant image correlation and evaluation environment also did not have any digital gauge elements for this (besides a line gauge element used for the DANTEC verification in Appendix H1.3). It was also decided that calculating an angular displacement from the combined y and z-displacement measurements would not be feasible (in polar coordinate form). Since too many uncertainties might arise from the specimens (geometry) and DANTEC measurements.

For each of these digital gauge point elements, the relevant displacement (and coordinate) data was ultimately exported over all the evaluated images (600 total) from the ISTRA 4D software and processed to obtain the relevant bending and torsion displacement amplitudes. These were then further utilised with the theoretical displacements obtained with the static FEM simulations to compare and calculate the experimental loading gains. This procedure is discussed in the next section (of this Appendix H5.2) and Appendix I2 for each of the two different BT displacement measurements performed on the BT fatigue test bench.

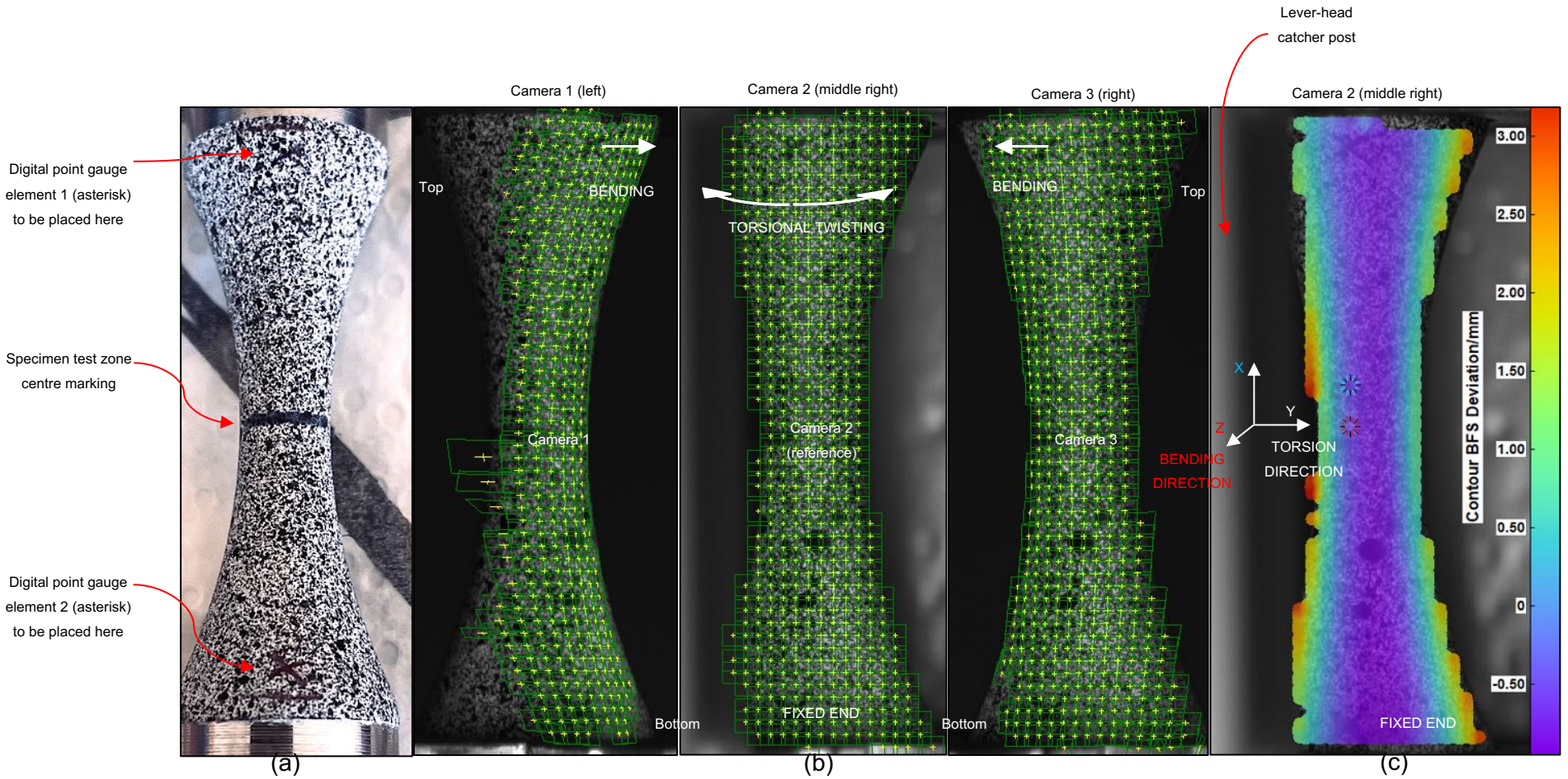


Figure H-33: BT fatigue test specimen – DANTEC (a) prepared specimen speckle pattern and markings, (b) evaluation grid and (c) measurement (user) coordinate system definition

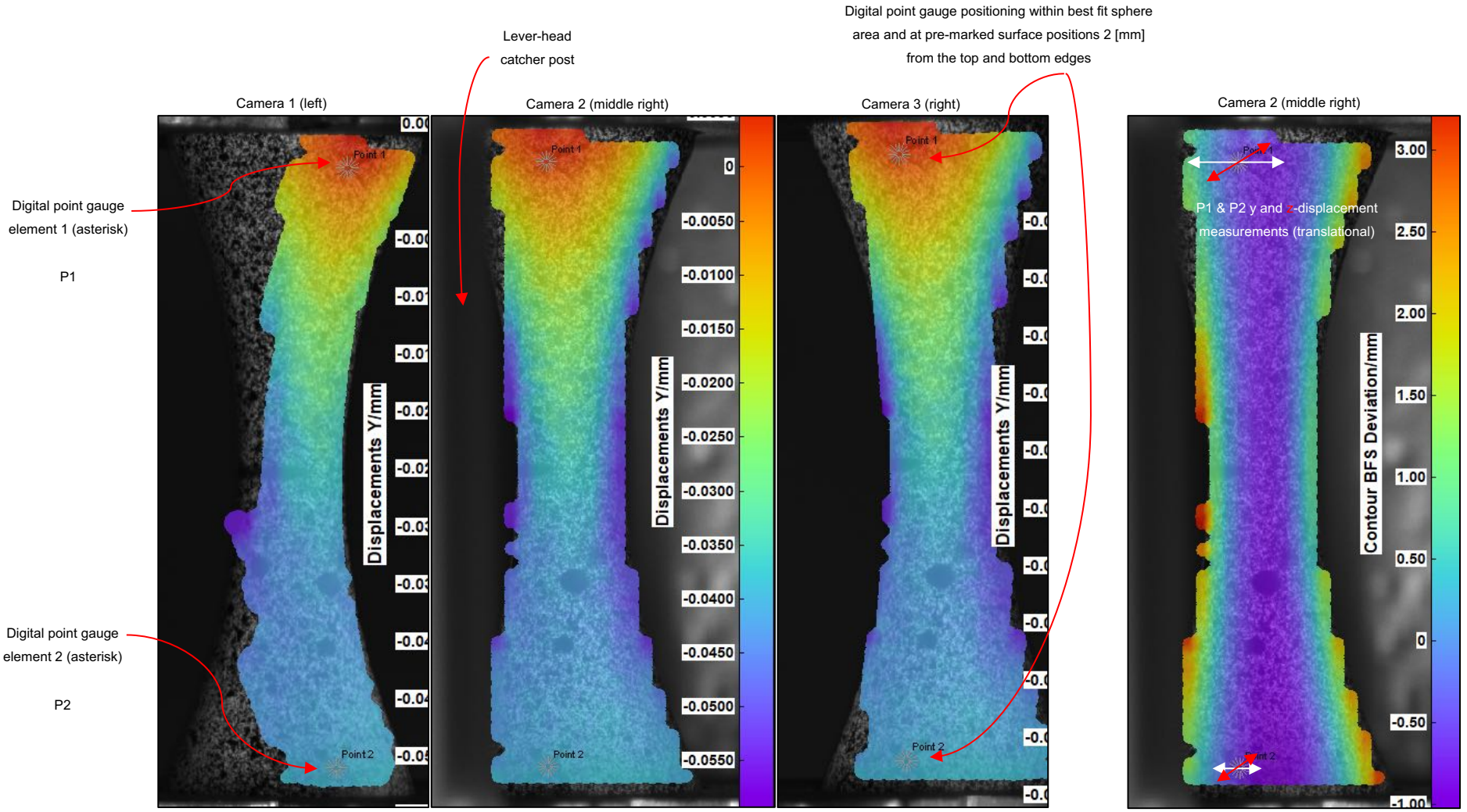


Figure H-34: BT fatigue test specimen – DANTEC point gauge elements definition and positioning within best fit sphere area

2) DANTEC Bending-Torsion Displacement Measurements and Calculations

a) Bending-Torsion Loading Gain Characterisation – Speed Range

Before performing the official experimental BT fatigue test measurements (next part), it was considered necessary first to measure the experimental loading gain of the last BT test specimen (Spec18, EN19(T) alloy steel). These measurements were made for a specifically chosen range of test speeds on the BT fatigue test bench, using the lightest and heaviest centrifugal mass pieces, respectively. The test speeds were chosen to include the preferred and theoretically equal biaxial loading gain point (from the specimen theoretical gain curves). This was done to determine if the specimen experimentally measured bending and torsion gain responses (under fully reversed out-of-phase biaxial loading) are comparable with the theoretically calculated gain responses (discussed in Appendix F1 and F3). That is if the theoretical considerations apply to this test bench. However, the primary purpose was to determine the experimental test speed where the biaxial loading components both have similar or equal gain values (past the bending resonance speed) to maintain the loading condition's nominal stress ratio.

The general DANTEC DIC measurement and speckle pattern preparation procedures were considered (see Appendix B6) for the experimental gain measurements of the specimen. That, along with the system setup and displacement measurement procedure described at the beginning of this Appendix H5.2 in part 1. For the specimen loading, it was decided to first use the lightest centrifugal mass piece (NUT 8, see Appendix E2) at the 25 [mm] radial position on the wheels for each test speed measurement. Thereafter, the heaviest mass piece (NUT 5 at the time, before NUT 9 and 10 manufacturing) was used at the same radius on the wheels. That is because the choice of centrifugal nut also influenced the torsional loading gain (both theoretical and experimental). Using NUT 8 first was to avoid excessive stresses at each test speed, which could damage the specimen and thus influence subsequent measurements with the heavier nut. The test speeds chosen were 28, 32, 37, 40, 44 and 48 [Hz], at which each DANTEC displacement measurement was made on the specimen for each nut. The test bench was stopped for each measurement, speed set, and restarted. The specimen (diameter 6.629 [mm]), the mass piece and its radial position were kept constant for all twelve measurements, with only the test speed incrementally increasing.

The displacement measurements (600 image steps) at the six speeds for each nut were exported from the ISTRA 4D software for each digital gauge point (P1 and P2). They were processed as illustrated in Table H-16 (shortened) and Figure H-35 (illustrative raw data graph for NUT 5 at 48 [Hz] speed only). After this, the displacements were used to calculate the relevant experimental bending displacement Δz_a [mm] and torsion displacement Δy_a [mm] amplitudes. These were calculated using Equation (H-20) and (H-21) below (middle and last columns in Table H-16). Note

should be taken at this point that these displacements were already 'experimentally gained'. The induced bending and torsion moments and, thus, stresses in the specimen were, therefore, not nominal values (as theoretically calculated for each speed, mass piece, and radius). That is, the bending loading gain G_B [-] and torsion loading gain G_T [-] that are required to calculate the bending and torsion stresses with Equation (H-17) and (H-18) (see Appendix H5.1) was already included. The calculation of these gains is done with the equations to follow next (using the displacements from the DANTEC and the FEM model).

$$\Delta y_a \ [mm] = \left[\Delta y_{max} \ [mm] - \ \Delta y_{min} \ [mm]\right] / 2 \tag{H-20}$$

$$\Delta z_a \ [mm] = \left[\Delta z_{max} \ [mm] - \ \Delta z_{min} \ [mm]\right] / 2 \tag{H-21}$$

where Δy_{max} : is the image-step wise P1 to P2 maximum difference, $(y_1 - y_2)_{max}$

Δy_{min} : is the image-step wise P1 to P2 minimum difference, $(y_1 - y_2)_{min}$

Δz_{max} : is the image-step wise P1 to P2 maximum difference, $(z_1 - z_2)_{max}$

Δz_{min} : is the image-step wise P1 to P2 minimum difference, $(z_1 - z_2)_{min}$

The next step was to obtain the corresponding theoretical bending and torsion displacements (single-sided y and z-displacement) of P1 gauge point, 2 [mm] from the top edge (pre-measured and marked on Spec18) to compare with the above calculated experimental displacement amplitudes. Using only the P1 measurement for the theoretical displacement measurement is due to the ideal theoretical specimen model bottom constraint in FEM (thus, no theoretical rigid body displacement, as accounted for by P2 in the DANTEC measurement). This displacement was obtained from the static FEM specimen model (same diameter), loaded with the theoretically induced centrifugal force (nominal values, see Table H-17 to follow) at each test speed (and nut). Therefore, the FEM displacements provided the 'ungained' bending and torsion displacements. This theoretical measurement method and the static FEM model are illustrated and discussed in Appendix I2 hereafter.

With the experimental displacement amplitudes ('gained') from above and the theoretical ('ungained') displacements from the static FEM measurement (for each test speed and nut), it was then possible to calculate the experimental loading gain responses for this test bench. That is, the bending loading gain G_B [-] and torsion loading gain G_T [-] using Equation (H-22) below. The theoretical FEM measurement is assumed as the reference. The relevant displacement measurements and induced gain calculation results are reported in Table H-17 to follow.

$$G_{B/T} \ [-] = DANTEC \ [mm] \ / \ NX \ FEM \ [mm] \tag{H-22}$$

where $DANTEC$: is the experimentally measured y or z-displacement of test specimen

$NX\ FEM$: is the theoretically measured (nominal) y or z-displacement of test specimen

These experimental gains were then compared (for illustrative purposes) with the theoretical loading gains $G_{B;th}$ [-] and $G_{T;th}$ [-] from Equation (F-4) (for the considered loading component, specimen, speed and mass piece). For this, a percentage difference value was calculated for each test speed (and nut) measurement using Equation (H-23) below and reported in Table H-17.

$$Difference\ [\%] = ABS\big((G - G_{th})\ /\ G_{th}\big)100 \tag{H-23}$$

The above bending-torsion loading characterisation method (with the gain calculations) was considered appropriate for measuring the actual bending and torsion loading displacements (and thus gains) for calculating the corresponding biaxial stresses experienced in a specimen.

This calculation method was similarly used to obtain the official experimental bending-torsion loading gain measurements as discussed in the last part 2b (to follow) of this appendix. The difference calculation with Equation (H-23) above was adapted for these measurements to be calculated between the respective experimental bending (reference) and torsion gain values instead of the theoretical and experimental gain values. That is because the characterisation measurements showed significant differences between theoretical and experimental gain responses on the bench. The official measurements (discussed in the next part) were therefore done to instead confirm an equivalent gain test point.

Table H-16: BT Spec18 measurement – DANTEC DAQ data exports from ISTRA 4D measurements

x-displacement (P1&P2) | y-displacement (P1&P2) - TORSION | z-displacement (P1&P2) - BENDING

28 [Hz] Test Speed of NUT 8 – exported xyz-displacement data

Step No.	Point 1 (Reference Step: 0) x Displacement/mm	TOP of specimen Uncertainty of x Displacement/mm	Point 2 (Reference Step: 0) x Displacement/mm	BOTTOM of specimen Uncertainty of x Displacement/mm	Top - Bottom Δx Displacement/mm
0	0	0,000386431	0	0,000496062	0
1	-0,000284894	0,000410366	0,000571699	0,00057841	-0,000856593
2	0,000330943	0,000412068	0,000547105	0,00057599	-0,000216162
3	-0,000310601	0,000412678	-0,000040895	0,00057615	-0,000269706
4	-0,0623336	0,000441589	-0,0119677	0,000618317	-0,0503659

Step No.	Point 1 (Reference Step: 0) y Displacement/mm	TOP of specimen Uncertainty of y Displacement/mm	Point 2 (Reference Step: 0) y Displacement/mm	BOTTOM of specimen Uncertainty of y Displacement/mm	Top - Bottom Δy Displacement/mm
0	0	0,000678368	0	0,00106957	0
1	-3,75536E-05	0,000695742	-0,000292529	0,00113108	0,000254975
2	0,000520567	0,000696803	-6,43561E-05	0,00113104	0,000584923
3	-0,000169607	0,00069762	-0,000587046	0,0011337	0,000417439
4	0,0403256	0,000718593	-0,0134491	0,00116996	0,0537747

Step No.	Point 1 (Reference Step: 0) z Displacement/mm	TOP of specimen Uncertainty of z Displacement/mm	Point 2 (Reference Step: 0) z Displacement/mm	BOTTOM of specimen Uncertainty of z Displacement/mm	Top - Bottom Δz Displacement/mm
0	0	0,00114589	0	0,00189934	0
1	-0,0022142	0,00116194	-0,0033261	0,00196761	0,0011119
2	-0,00214453	0,00116267	-0,0001593	0,00196948	-0,00198523
3	-0,00105237	0,00116391	0,000226179	0,00197505	-0,001278549
4	-0,176946	0,00118242	-0,0428455	0,00201877	-0,1341005

32 [Hz] Test Speed of NUT 8 – exported xyz-displacement data

Step No.	Point 1 (Reference Step: 0) x Displacement/mm	TOP of specimen Uncertainty of x Displacement/mm	Point 2 (Reference Step: 0) x Displacement/mm	BOTTOM of specimen Uncertainty of x Displacement/mm	Top - Bottom Δx Displacement/mm
0	0	0,000385116	0	0,000502084	0
1	0,000137334	0,000411766	0,000392137	0,000576984	-0,000254803
2	4,63267E-05	0,000411176	0,00025865	0,000583431	-0,000212323
3	0,00026872	0,0004102	9,21343E-05	0,000586575	0,000176586
4	-0,0377233	0,000437685	-0,00603034	0,000590771	-0,03169296

Step No.	Point 1 (Reference Step: 0) y Displacement/mm	TOP of specimen Uncertainty of y Displacement/mm	Point 2 (Reference Step: 0) y Displacement/mm	BOTTOM of specimen Uncertainty of y Displacement/mm	Top - Bottom Δy Displacement/mm
0	0	0,000676023	0	0,00108256	0
1	-0,000240865	0,000696071	-0,000116357	0,00113751	-0,000124508
2	0,000157019	0,000695439	-0,000574211	0,00114387	0,00073123
3	0,000135598	0,000694436	-7,43138E-05	0,00114865	0,000209912
4	0,105574	0,000718813	0,0049731 9	0,00115498	0,10060081

Step No.	Point 1 (Reference Step: 0) z Displacement/mm	TOP of specimen Uncertainty of z Displacement/mm	Point 2 (Reference Step: 0) z Displacement/mm	BOTTOM of specimen Uncertainty of z Displacement/mm	Top - Bottom Δz Displacement/mm
0	0	0,00114191	0	0,0019224	0
1	0,000524847	0,00116132	0,000785967	0,00198258	-0,00026112
2	0,000903829	0,00116047	0,000364859	0,00199109	0,00053897
3	0,0014069	0,00115917	0,00109156	0,00199883	0,00031534
4	-0,0837569	0,00118689	-0,0161313	0,00200908	-0,0676256

37, 40 and 44 [Hz]

48 [Hz] Test Speed of NUT 8 – exported xyz-displacement data

Step No.	Point 1 (Reference Step: 0) x Displacement/mm	TOP of specimen Uncertainty of x Displacement/mm	Point 2 (Reference Step: 0) x Displacement/mm	BOTTOM of specimen Uncertainty of x Displacement/mm	Top - Bottom Δx Displacement/mm
0	0	0,000395399	0	0,00050044	0
1	-0,000248543	0,000418711	0,000317638	0,00057344	-0,000566181
2	-0,000452324	0,000417365	-0,00016816	0,000568553	-0,000284164
3	-0,000399181	0,000419113	-5,08404E-05	0,000568754	-0,000348341
4	-0,0185368	0,000456692	0,00979309	0,000594	-0,02832989

Step No.	Point 1 (Reference Step: 0) y Displacement/mm	TOP of specimen Uncertainty of y Displacement/mm	Point 2 (Reference Step: 0) y Displacement/mm	BOTTOM of specimen Uncertainty of y Displacement/mm	Top - Bottom Δy Displacement/mm
0	0	0,000694093	0	0,00107901	0
1	-0,000305312	0,000711305	-0,000320809	0,0011341	0,000015497
2	-0,000283048	0,000710245	-0,000240042	0,00113169	-0,000043006
3	-0,000500942	0,000711777	-9,31275E-05	0,00112715	-0,000407815
4	0,153129	0,000745845	0,0035771	0,00114362	0,1495519

Step No.	Point 1 (Reference Step: 0) z Displacement/mm	TOP of specimen Uncertainty of z Displacement/mm	Point 2 (Reference Step: 0) z Displacement/mm	BOTTOM of specimen Uncertainty of z Displacement/mm	Top - Bottom Δz Displacement/mm
0	0	0,00117244	0	0,0019161	0
1	-0,000420259	0,00118874	-0,000674495	0,00197808	0,000254236
2	-0,000784085	0,00118766	0,000581093	0,00197678	-0,001365178
3	0,00010002	0,00118941	-0,00103963	0,00196689	0,00113965
4	-0,0566774	0,00122894	-0,00187716	0,00198195	-0,05480024

x-displacement (P1&P2) | y-displacement (P1&P2) - TORSION | z-displacement (P1&P2) - BENDING

28 [Hz] Test Speed of NUT 5 – exported xyz-displacement data

Step No.	Point 1 (Reference Step: 0) x Displacement/mm	TOP of specimen Uncertainty of x Displacement/mm	Point 2 (Reference Step: 0) x Displacement/mm	BOTTOM of specimen Uncertainty of x Displacement/mm	Top - Bottom Δx Displacement/mm
0	0	0,000388928	0	0,000498081	0
1	0,00015691	0,000415171	1,29853E-05	0,000568366	0,000133925
2	-0,000529603	0,00041124	-0,000288558	0,000560708	-0,000241045
3	0,000164425	0,000416417	-3,56407E-05	0,000576973	0,000200066
4	0,188496	0,000468785	-0,00515337	0,000603918	0,19364937

Step No.	Point 1 (Reference Step: 0) y Displacement/mm	TOP of specimen Uncertainty of y Displacement/mm	Point 2 (Reference Step: 0) y Displacement/mm	BOTTOM of specimen Uncertainty of y Displacement/mm	Top - Bottom Δy Displacement/mm
0	0	0,000682756	0	0,00107394	0
1	-0,000680955	0,000701619	-0,000521058	0,00113459	-0,000159897
2	-0,00062672	0,000700299	-0,00041565	0,00112488	-0,00021107
3	-0,00140807	0,000702702	-0,00093647	0,00113562	-0,0004716
4	-0,164641	0,000744336	-0,033717	0,00115606	-0,130924

Step No.	Point 1 (Reference Step: 0) z Displacement/mm	TOP of specimen Uncertainty of z Displacement/mm	Point 2 (Reference Step: 0) z Displacement/mm	BOTTOM of specimen Uncertainty of z Displacement/mm	Top - Bottom Δz Displacement/mm
0	0	0,0011533	0	0,00190711	0
1	-0,000666422	0,00117046	1	0,00288098	0,00198316	-0,00095452
2	0,00130931	0,00117018	2	0,00223704	0,00196837	-0,00092773
3	0,00180142	0,00117167	3	0,00096254	0,00197852	0,000838846
4	0,740417	0,00121292	4	0,186	0,00200065	0,554417

32 [Hz] Test Speed of NUT 5 – exported xyz-displacement data

Step No.	Point 1 (Reference Step: 0) x Displacement/mm	TOP of specimen Uncertainty of x Displacement/mm	Point 2 (Reference Step: 0) x Displacement/mm	BOTTOM of specimen Uncertainty of x Displacement/mm	Top - Bottom Δx Displacement/mm
0	0	0,000385082	0	0,00052517	0
1	-0,000205643	0,000407963	-0,000570959	0,000593599	0,000365316
2	0,000243993	0,000412413	2	0,000102146	0,000596202	0,000141847
3	-0,000247181	0,000412868	-3,47018E-06	0,000604495	-0,000243711
4	0,117777	0,000457977	4	0,0355262	0,000622988	0,0822508

Step No.	Point 1 (Reference Step: 0) y Displacement/mm	TOP of specimen Uncertainty of y Displacement/mm	Point 2 (Reference Step: 0) y Displacement/mm	BOTTOM of specimen Uncertainty of y Displacement/mm	Top - Bottom Δy Displacement/mm
0	0	0,000675978	0	0,00113224	0
1	0,000130272	0,000693776	1	0,000436228	0,00119129	-0,000305956
2	0,000291116	0,000696637	2	0,000526767	0,0011865	-0,000235651
3	0,000335497	0,000696463	3	0,000211131	0,00119151	0,000124366
4	0,0585033	0,00072947	4	-0,0214116	0,00121626	0,0799149

Step No.	Point 1 (Reference Step: 0) z Displacement/mm	TOP of specimen Uncertainty of z Displacement/mm	Point 2 (Reference Step: 0) z Displacement/mm	BOTTOM of specimen Uncertainty of z Displacement/mm	Top - Bottom Δz Displacement/mm
0	0	0,00114184	0	0,00201065	0
1	0,000482335	0,00115986	1	-0,000713013	0,00208474	0,001195348
2	-0,000137196	0,00116196	2	-0,00180711	0,00207245	0,001669914
3	0,000865937	0,00116113	3	0,000251011	0,00207766	0,000614926
4	0,403197	0,00119022	4	0,126461	0,00211498	0,276736

37, 40 and 44 [Hz]

48 [Hz] Test Speed of NUT 5 – exported xyz-displacement data

Step No.	Point 1 (Reference Step: 0) x Displacement/mm	TOP of specimen Uncertainty of x Displacement/mm	Point 2 (Reference Step: 0) x Displacement/mm	BOTTOM of specimen Uncertainty of x Displacement/mm	Top - Bottom Δx Displacement/mm
0	0	0,000393763	0	0,000526053	0
1	-0,000300097	0,000419312	1	0,000351397	0,00060358	-0,000651494
2	-0,000687167	0,000417938	2	-8,53455E-05	0,000594434	-0,000601822
3	-0,000249515	0,000418329	3	0,000193225	0,000613971	-0,00044274
4	0,0255548	0,000466684	4	0,024906	0,000648567	0,0006488

Step No.	Point 1 (Reference Step: 0) y Displacement/mm	TOP of specimen Uncertainty of y Displacement/mm	Point 2 (Reference Step: 0) y Displacement/mm	BOTTOM of specimen Uncertainty of y Displacement/mm	Top - Bottom Δy Displacement/mm
0	0	0,000691234	0	0,00113425	0
1	-0,000436476	0,000710835	1	-0,000252097	0,00119438	-0,000184379
2	-0,000822005	0,000710375	2	-0,00043627	0,00118696	-0,000385735
3	-0,00114473	0,000710724	3	-0,00043916	0,00119825	-0,00070557
4	0,180725	0,000750115	4	0,0200109	0,00124468	0,1607141

Step No.	Point 1 (Reference Step: 0) z Displacement/mm	TOP of specimen Uncertainty of z Displacement/mm	Point 2 (Reference Step: 0) z Displacement/mm	BOTTOM of specimen Uncertainty of z Displacement/mm	Top - Bottom Δz Displacement/mm
0	0	0,00116762	0	0,00201421	0
1	0,00144957	0,0011871	1	-0,000756546	0,00208352	0,002206116
2	-0,000242771	0,0011874	2	-0,00196101	0,00207482	0,001718239
3	-0,00149815	0,00118781	3	-0,00431155	0,00208349	0,0028134
4	0,0192498	0,00122837	4	-0,0109524	0,0021554	0,0302022

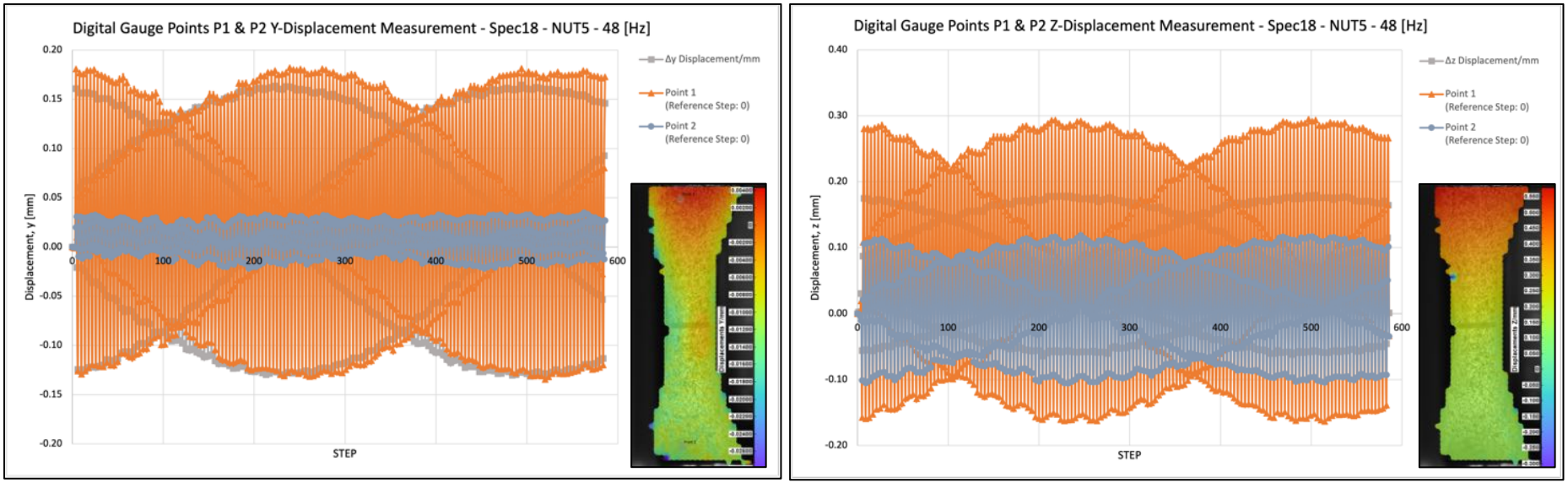


Figure H-35: BT Spec18 measurement – DANTEC digital point gauge P1 and P2 y (torsion) and z (bending) displacement curves at 48 [Hz] with NUT 5

The vertical axis y and z-displacement offsets observed in Figure H-35 above do not imply that the biaxial fatigue loading components were not fully reversed. The observed offsets are attributed to the resonance suppressor (see Figure A-10 and Figure A-11 in Appendix A4), which was applied prior to and during the start-up of each BT fatigue test and the above loading displacement measurements made with the DANTEC (at 189 [Hz] frame rate). When this suppressor is lightly screwed into the BT fatigue test bench lever head (only attached to the specimen at the bottom and thus free to move in y and z-directions), it unavoidably displaces the lever head slightly to the left (negative z-direction) and slightly forward (negative y-direction) with respect to the DANTEC user-defined coordinate system shown in Figure H-33 (c). The DANTEC has to capture 4 images (manually by the user) prior to each test measurement (test bench off, specimen not loaded with forces/moments, and only suppressed) for image correlation and evaluation purposes which serve as the reference position for those images then taken during the test specimen loading after that (speckle pattern then moving with respect to these reference images). Therefore, these reference images provide the ‘start’ or ‘zero load’ position of the

specimen (slightly skewed due to suppression). After each test was started, all subsequent displacement measurements refer to this 'zeroed' (suppressed) position of the measurement. However, the unscrewing of the suppressor (after starting the test) allowed the lever head to return to the actual 'zero' position. In this position, the lever-head twists and bends the specimen during a test. Therefore, this actual zero position (in test / in measurement position) had the displacement offset (in both y and z-direction) from the reference image's zero position equal to that caused by the suppression being applied prior to and at the start of the test and measurement. This offset is, therefore, not present (subtracted away), and the biaxial loading is considered fully reversed as theoretically calculated for the test bench based on its working principle and the centrifugal mass piece positions on the wheels.

Table H-17: BT Spec18 measurement – experimental and theoretical gain

EN 19 (T)		Specimen #	Diameter	N	Nut 8 Bolt 1 (M5)	Radius	V Nominal V $F_{centrifugal}$	V Nominal V M_B	V Nominal V M_T	T-Stiffness k_t	V ref point Theoretical G_B NUT8	V ref point Theoretical G_T NUT8	Gauge P1-P2 Displacement - @ E = E_{NX} = 206.9GPa NX FEM B	NX FEM T	DANTEC B	DANTEC T	Experimental G_B NUT8	Experimental G_T NUT8	Difference G_B	Difference G_T
			[mm]	[Hz]	[g]	[mm]	[N]	[N.m]	[N.m]	[N.m/rad]	[-]	[-]	[mm]	[mm]	[mm]	[mm]	[-]	[-]	[%]	[%]
(DANTEC)	NUT 8 (lightest)	EN19T-BT-Spec-18	6.629	28	12.028	25	9.307	1.790	1.790	927.60	2.714	1.112	0.02813	0.01390	0.32044	0.06184	11.391	4.450	319.73	300.21
(DANTEC)			6.629	32	12.028	25	12.156	2.338	2.338	927.60	5.709	1.152	0.03674	0.01815	0.21646	0.07387	5.892	4.070	3.20	253.30
(DANTEC)			6.629	37	12.028	25	16.252	3.126	3.126	927.58	9.735	1.214	0.04912	0.02427	0.09412	0.04020	1.916	1.657	80.32	36.47
(DANTEC)			6.629	40	12.028	25	18.994	3.654	3.654	927.59	3.463	1.260	0.05741	0.02836	0.07696	0.04136	1.341	1.458	61.29	15.74
(DANTEC)			6.629	44	12.028	25	22.983	4.421	4.421	927.58	1.788	1.332	0.06946	0.03432	0.06326	0.04922	0.911	1.434	49.06	7.67
(DANTEC)			6.629	48	12.028	25	27.352	5.261	5.261	927.56	1.168	1.422	0.08267	0.04084	0.05706	0.06098	0.690	1.493	40.91	5.01

		Specimen #	Diameter	N	Nut 5 Bolt 2 (M4)	Radius	V Nominal V $F_{centrifugal}$	V Nominal V M_B	V Nominal V M_T	T-Stiffness k_t	V ref point Theoretical G_B NUT5	V ref point Theoretical G_T NUT5	Gauge P1-P2 Displacement - @ E = E_{NX} = 206.9GPa NX FEM B	NX FEM T	DANTEC B	DANTEC T	Experimental G_B NUT5	Experimental G_T NUT5	Difference G_B	Difference G_T
			[mm]	[Hz]	[g]	[mm]	[N]	[N.m]	[N.m]	[N.m/rad]	[-]	[-]	[mm]	[mm]	[mm]	[mm]	[-]	[-]	[%]	[%]
(DANTEC)	NUT 5 (heaviest)	EN19T-BT-Spec-18	6.629	28	28.360	25	21.944	4.412	4.412	927.59	2.714	1.134	0.06932	0.03425	0.65722	0.20161	9.480	5.887	249.31	419.13
(DANTEC)			6.629	32	28.360	25	28.662	5.763	5.763	927.57	5.709	1.182	0.09055	0.04473	0.40149	0.12876	4.434	2.878	22.33	143.52
(DANTEC)			6.629	37	28.360	25	38.319	7.704	7.704	927.56	9.735	1.260	0.12105	0.05980	0.19705	0.09011	1.628	1.507	83.28	19.59
(DANTEC)			6.629	40	28.360	25	44.785	9.004	9.004	927.55	3.463	1.318	0.14148	0.06989	0.16172	0.09826	1.143	1.406	66.99	6.66
(DANTEC)			6.629	44	28.360	25	54.189	10.895	10.895	927.56	1.788	1.412	0.17119	0.08457	0.13786	0.11684	0.805	1.382	54.96	2.15
(DANTEC)			6.629	48	28.360	25	64.490	12.966	12.966	927.54	1.168	1.532	0.20373	0.10065	0.12196	0.14804	0.599	1.471	48.75	3.99

The biaxial loading characterisation measurements (with the DANTEC and static FEM model) and the bending and torsion loading gains in Table H-17 above show that the experimental gain responses were not similar to the theoretically calculated gain responses. That is, for the considered specimen over the six test speeds and each centrifugal nut. The bending and torsion loading gain response curves in Figure H-36 below also illustrate this. The individual gain comparison differences were considered more illustrative (with Equation (H-23)) for each nut and test speed. Figure H-36 below shows that the experimental bending loading gain influenced the torsion loading gain over the test speed ranges close to the bending resonance of the test specimen. This resonance was visually observed on the BT test bench during the DANTEC measurement tests. There was,

however, an experimental test speed range (around 37-40 [Hz]) where it appeared that this influence diminished, and the torsion loading component's gain started to near the theoretical values at each test speed as the bending gain further reduced. From the gain response curves, it appeared that a 38 [Hz] test speed would be the test speed, for both nuts (and others with intermediate masses), with the highest probability of having the most equivalent or similar experimental biaxial loading gains (to maintain λ ratio). These results and the reasons for the theoretical and experimental loading gain differences are discussed further in Section 4.4.2.4.

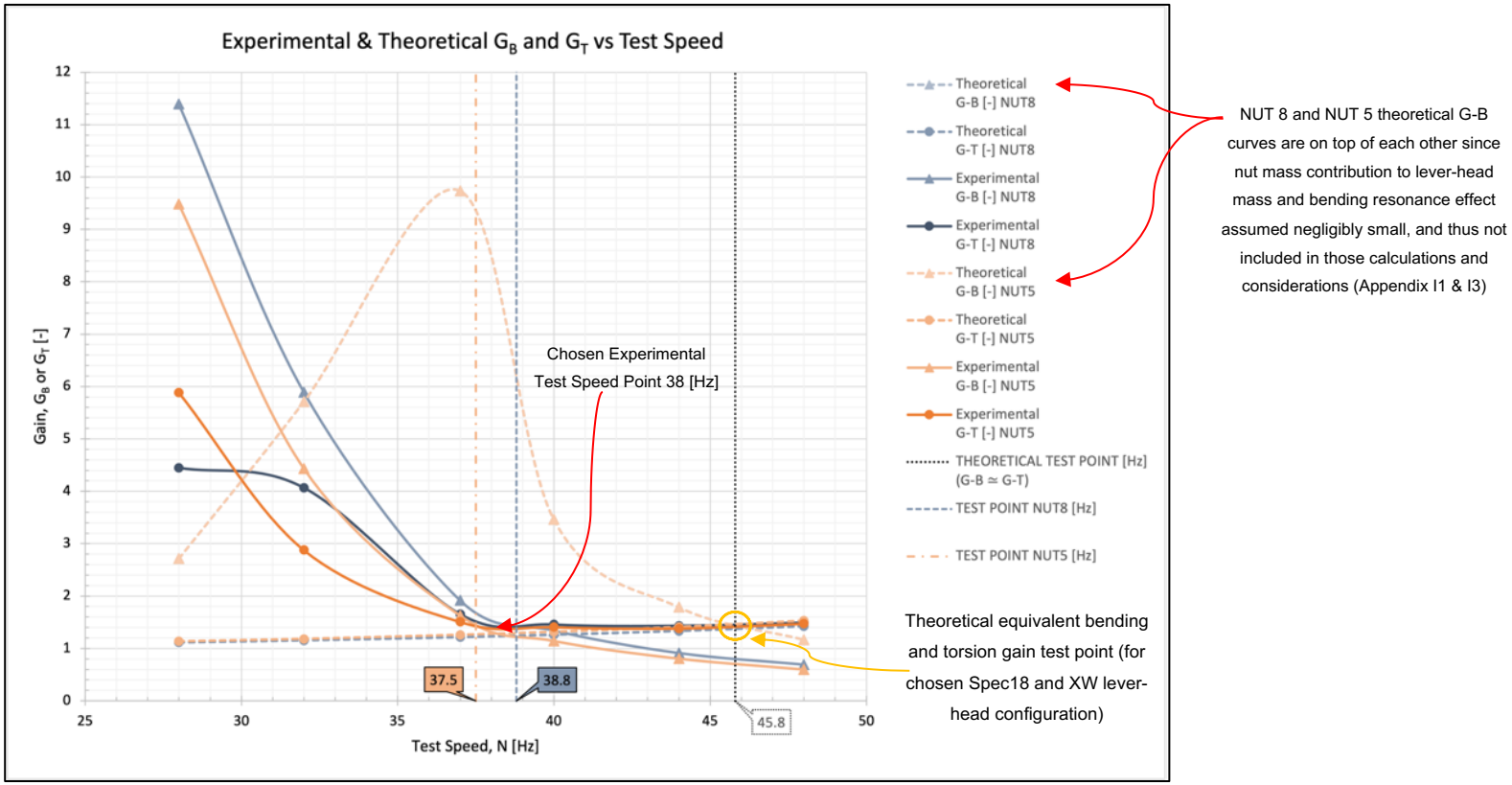


Figure H-36: BT Spec18 measurement – experimental and theoretical gain response curves

b) Experimental Bending-Torsion Measurement

For the official experimental BT fatigue loading gain measurements, it was decided only to measure the test specimens tested with different centrifugal mass pieces (which influence torsion gain). The appropriate test speed of 38 [Hz] was identified and kept constant for all BT tests (from Figure H-36 above). These were Spec3, Spec9 and Spec15. The similarly measured diameters (6.567 [mm] on average) of the seventeen (17) biaxial out-of-phase bending-torsion fatigue (BT) test specimens allowed for this (see Figure H-31 and Appendix D5). It was therefore assumed that the experimental gains of the specimens not measured with the DANTEC would be theoretically calculable from the measured ones (inferred). Therefore, if an unmeasured specimen was tested with the same centrifugal nut piece as a measured specimen (primarily NUT 4, 5 and 9, see Table J-5), this calculation was based on the sensitivity of each loading gain value to change in specimen diameter (further discussed in Section 4.6.3 and Appendix K5). It was therefore done for the 'repeated test conditions' (e.g., nut and speed) where the specimen diameter was the only test quantity being different. For these calculations, it was also assumed that a change in the radial position (thus centrifugal force, the moments and stresses) with the same test speed and nut did not influence the loading gain values. It was because no such effects of the loading magnitudes were observed in the theoretical bending and torsion resonance frequency and loading gain calculations discussed in Appendix F1 to F3.

These inferred gain calculations were done due to the results from the previous section showing disagreement between theoretical and experimental loading gains of both bending and torsion components on the BT fatigue test bench. It was also considered appropriate since the uncertainties showed (Appendix K4 to K5) that the small changes in specimen diameters have a negligible influence on the bending and torsion gain values. It was, therefore, not sufficient or correct to set the unmeasured specimen experimental gains equal to the corresponding theoretically calculated values from Equation (F-4). That is, for the bending or torsion loading components (as done with the unmeasured uniaxial T fatigue test specimens in part 2c of Appendix H4.2).

The relevant three (3) experimental BT fatigue test specimens were measured with the DANTEC system according to the general DIC measurement and speckle pattern preparation procedures (see Appendix B6) and the displacement measurement procedure described in part 1 of this Appendix H5.2. The initial approach for these experimental BT fatigue tests was to start with an appropriately sized centrifugal mass piece (and measure it with the DANTEC) that would either cause 'low' HCF failure or not cause failure. The purpose was to obtain the 'end points' of the experimental bending-torsion fatigue S-N curve (based on the bending stress), between which the remaining specimens could then be tested. That is, at intermediate loading levels in-between

the two endpoints (or curve limits). The above was done based on the previous results (see Table H-17 and Figure H-36), which showed that 38 [Hz] would be the test speed (irrespective of nut used) where the experimental bending and torsional loading gain values would be equivalent. Therefore, to maintain the nominal biaxial stress amplitude ratio of 0.5 for the chosen loading condition after applying experimental gains, see Equation (H-19)).

Due to the above approach, Spec3 was measured using NUT 9, Spec9 with NUT 5 and Spec15 with NUT 4 at the chosen wheel radius position for each nut. Ultimately, Spec3 and Spec15 did not fail in bending-torsion fatigue, whereas Spec9 did fail. For these three tests, the DANTEC displacement measurements (for P1 and P2, over 600 image steps) were exported from the ISTRA 4D software and processed as illustrated in Table H-18 (for all measured specimens) and Figure H-37 (raw data graphs of Spec9 for illustration). The relevant experimental displacement amplitudes, theoretical displacement measurements and gains were obtained using the same procedure and equations (Equation (H-20) to (H-22)) as discussed in the previous part (see Table H-19). The only exception from the last part is the official percentage difference calculation (Equation (H-23)). This calculation was done between the experimental gain values of bending (reference value) and torsion since, for the tests, the purpose was to test at a speed where ideally, they have equal values (and measure it). All subsequent specimens (not measured) were tested between the above loading levels using other radiuses for similar nuts on the wheels. That is since Spec3, 9 and 15 provided the end-points of the S-N curve, and they were measured. All the test results are provided for the experimental bending-torsion fatigue tests in Table J-5. The above gains (measured and inferred) were utilised in Equations (H-17) to (H-19) to calculate the fully reversed bending and torsion fatigue stresses.

For all three of the DANTEC displacement measurements performed on the BT fatigue test bench, the resultant fully reversed (experimental bending-torsion) out-of-phase sinusoidal displacement curves were also obtained (see Figure H-38 to follow). These sinusoidal curves were obtained by ‘collapsing’ the semi-scattered Δy [mm] and Δz [mm] displacement values (as shown in Figure H-37) to single sinusoids representative of the actual loading. The ‘collapsing’ (or overlaying) of the DANTEC displacement data points onto each other was required primarily due to the scatter of the unprocessed data points caused by the difference in test speed and camera frame rate speed (notes in Figure H-38). It was required to lower the BT fatigue specimen test speeds (from 38 [Hz]) by a maximum of 1.51 [%] to allow the proper overlaying of the data points. This was necessary since the specified test bench speed on the VSD was slightly lower during each test and DANTEC measurement, which was attributed to the inherent motor slip. These sinusoidal displacement curves illustrated that the experimentally induced bending-torsion loading had the appropriate fully reversed and out-of-phase form.

Table H-18: BT fatigue test Spec3, 9 and 15 measurements – DANTEC DAQ data exports from ISTRA 4D measurements

x-displacement (P1&P2)

Step No.	Point 1 (Reference Step: 0) x Displacement/mm	Point 1 Uncertainty of x Displacement/mm	Step No.	Point 2 (Reference Step: 0) x Displacement/mm	Point 2 Uncertainty of x Displacement/mm	Top - Bottom Δx Displacement/mm
0	0	0,000107413	0	0	0,000204274	0
1	-0,000257835	0,00022651	1	-0,00171224	0,000308183	0,001454405
2	0,000279143	0,000240231	2	-0,000742408	0,000303293	0,001021551
3	0,000578485	0,000253229	3	-0,00156341	0,000311036	0,002141895
4	0,0668698	0,000332121	4	-0,0193444	0,000353037	0,0862142

Step No.	Point 1 (Reference Step: 0) x Displacement/mm	Point 1 Uncertainty of x Displacement/mm	Step No.	Point 2 (Reference Step: 0) x Displacement/mm	Point 2 Uncertainty of x Displacement/mm	Top - Bottom Δx Displacement/mm
0	0	0,0017147	0	0	0,00106316	0
1	-0,000331934	0,0017308	1	-0,000311175	0,0010916	-0,000020759
2	-0,000487726	0,00173217	2	-0,000531517	0,00109556	0,000043791
3	-0,000346545	0,00173322	3	0,000160478	0,00109264	-0,000507023
4	0,0309407	0,00178872	4	-0,0220556	0,00114555	0,0529963

Step No.	Point 1 (Reference Step: 0) x Displacement/mm	Point 1 Uncertainty of x Displacement/mm	Step No.	Point 2 (Reference Step: 0) x Displacement/mm	Point 2 Uncertainty of x Displacement/mm	Top - Bottom Δx Displacement/mm
0	0	0,00110341	0	0	0,00145381	0
1	0,000130241	0,00111382	1	0,00025747	0,00148054	-0,000127229
2	0,000317217	0,001114	2	-0,000147571	0,00147788	0,000464788
3	-0,000348126	0,00111472	3	-0,000052393	0,00148087	-0,000295733
4	0,0679212	0,00113912	4	-0,0115709	0,00151547	0,0794921

y-displacement (P1&P2) - TORSION

Step No.	Point 1 (Reference Step: 0) y Displacement/mm	Point 1 Uncertainty of y Displacement/mm	Step No.	Point 2 (Reference Step: 0) y Displacement/mm	Point 2 Uncertainty of y Displacement/mm	Top - Bottom Δy Displacement/mm
0	0	0,000250432	0	0	0,00029223	0
1	-0,000462479	0,000322038	1	0,00111632	0,000372785	-0,001578799
2	0,00056124	0,000331625	2	0,00139277	0,00036903	-0,00083153
3	0,000151137	0,000340964	3	0,00186095	0,000375054	-0,001709813
4	-0,0222607	0,000406024	4	-0,0353876	0,00041149	0,0131269

Step No.	Point 1 (Reference Step: 0) y Displacement/mm	Point 1 Uncertainty of y Displacement/mm	Step No.	Point 2 (Reference Step: 0) y Displacement/mm	Point 2 Uncertainty of y Displacement/mm	Top - Bottom Δy Displacement/mm
0	0	0,00171597	0	0	0,00106356	0
1	0,000150756	0,00173206	1	-4,31856E-05	0,001092	0,000193942
2	-0,000385807	0,00173344	2	3,62754E-05	0,00109596	-0,000422082
3	0,000679165	0,00173449	3	0,00122848	0,00109304	-0,000549315
4	-0,153007	0,00178999	4	-0,00886513	0,00114595	-0,14414187

Step No.	Point 1 (Reference Step: 0) y Displacement/mm	Point 1 Uncertainty of y Displacement/mm	Step No.	Point 2 (Reference Step: 0) y Displacement/mm	Point 2 Uncertainty of y Displacement/mm	Top - Bottom Δy Displacement/mm
0	0	0,00110423	0	0	0,00145436	0
1	-0,000993325	0,00111464	1	0,000370298	0,00148109	-0,001363623
2	-0,00137584	0,00111483	2	-8,83521E-05	0,00147843	-0,00127488
3	-0,00127857	0,00111554	3	-1,24661E-05	0,00148143	-0,001266104
4	0,02563	0,00113995	4	-0,0142085	0,00151602	0,0398385

z-displacement (P1&P2) - BENDING

Step No.	Point 1 (Reference Step: 0) z Displacement/mm	Point 1 Uncertainty of z Displacement/mm	Step No.	Point 2 (Reference Step: 0) z Displacement/mm	Point 2 Uncertainty of z Displacement/mm	Top - Bottom Δz Displacement/mm
0	0	0,00147619	0	0	0,00137525	0
1	-0,000269486	0,00150688	1	-0,000984505	0,00139935	0,000715019
2	-0,000961077	0,00150708	2	-0,0012615	0,00140138	0,000300423
3	0,000388815	0,00150734	3	-0,00078798	0,00139892	0,001176795
4	0,436737	0,00155586	4	0,136746	0,00141615	0,299991

Step No.	Point 1 (Reference Step: 0) z Displacement/mm	Point 1 Uncertainty of z Displacement/mm	Step No.	Point 2 (Reference Step: 0) z Displacement/mm	Point 2 Uncertainty of z Displacement/mm	Top - Bottom Δz Displacement/mm
0	0	0,00191389	0	0	0,00112018	0
1	0,000785088	0,00192939	1	0,00121469	0,00114897	-0,000429602
2	0,00117353	0,0013909	2	0,00150053	0,00115311	0,001023477
3	3,93841E-05	0,00193183	3	0,00130064	0,00115025	-0,001261256
4	0,204768	0,00198715	4	0,0440449	0,00120352	0,1607231

Step No.	Point 1 (Reference Step: 0) z Displacement/mm	Point 1 Uncertainty of z Displacement/mm	Step No.	Point 2 (Reference Step: 0) z Displacement/mm	Point 2 Uncertainty of z Displacement/mm	Top - Bottom Δz Displacement/mm
0	0	0,0012327	0	0	0,00153405	0
1	0,000598169	0,00124301	1	0,00155479	0,00156116	-0,000956621
2	-0,00235499	0,00124313	2	-0,0010296	0,00155839	-0,00132539
3	-0,00172706	0,00124385	3	-0,000930573	0,00156151	-0,000796487
4	0,388728	0,00126878	4	0,134741	0,00159567	0,253987

38 [Hz] Test Speed of Spec3 – exported xyz-displacement data

38 [Hz] Test Speed of Spec9 – exported xyz-displacement data

38 [Hz] Test Speed of Spec15 – exported xyz-displacement data

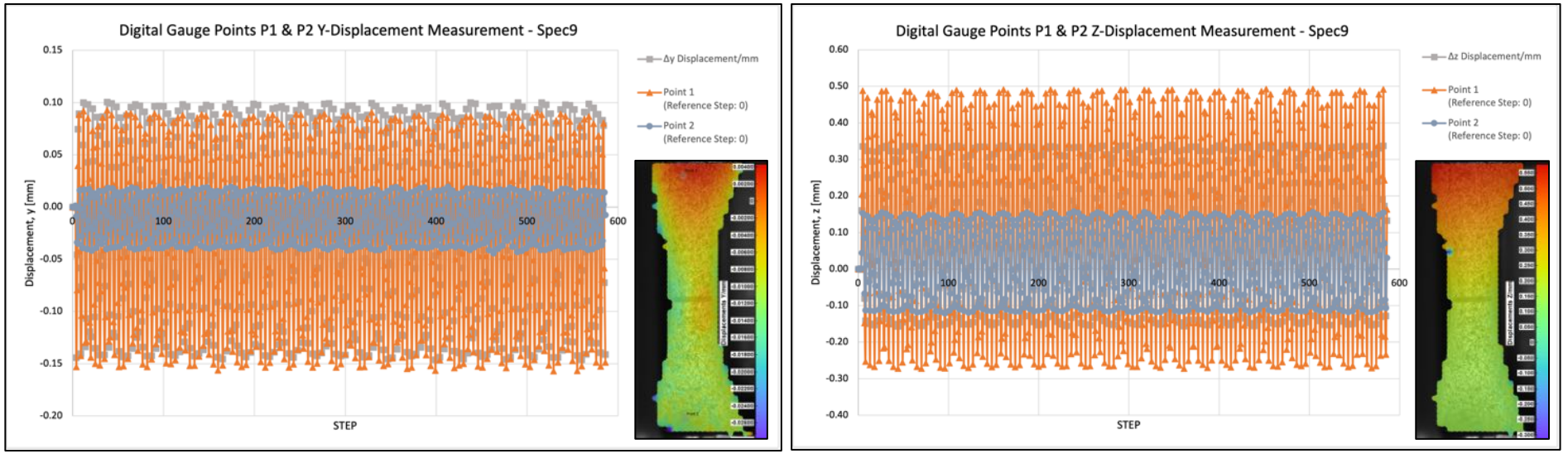


Figure H-37: BT fatigue test Spec9 measurements – DANTEC digital point gauge P1 and P2 y and z-displacement curves at 38 [Hz] test speed

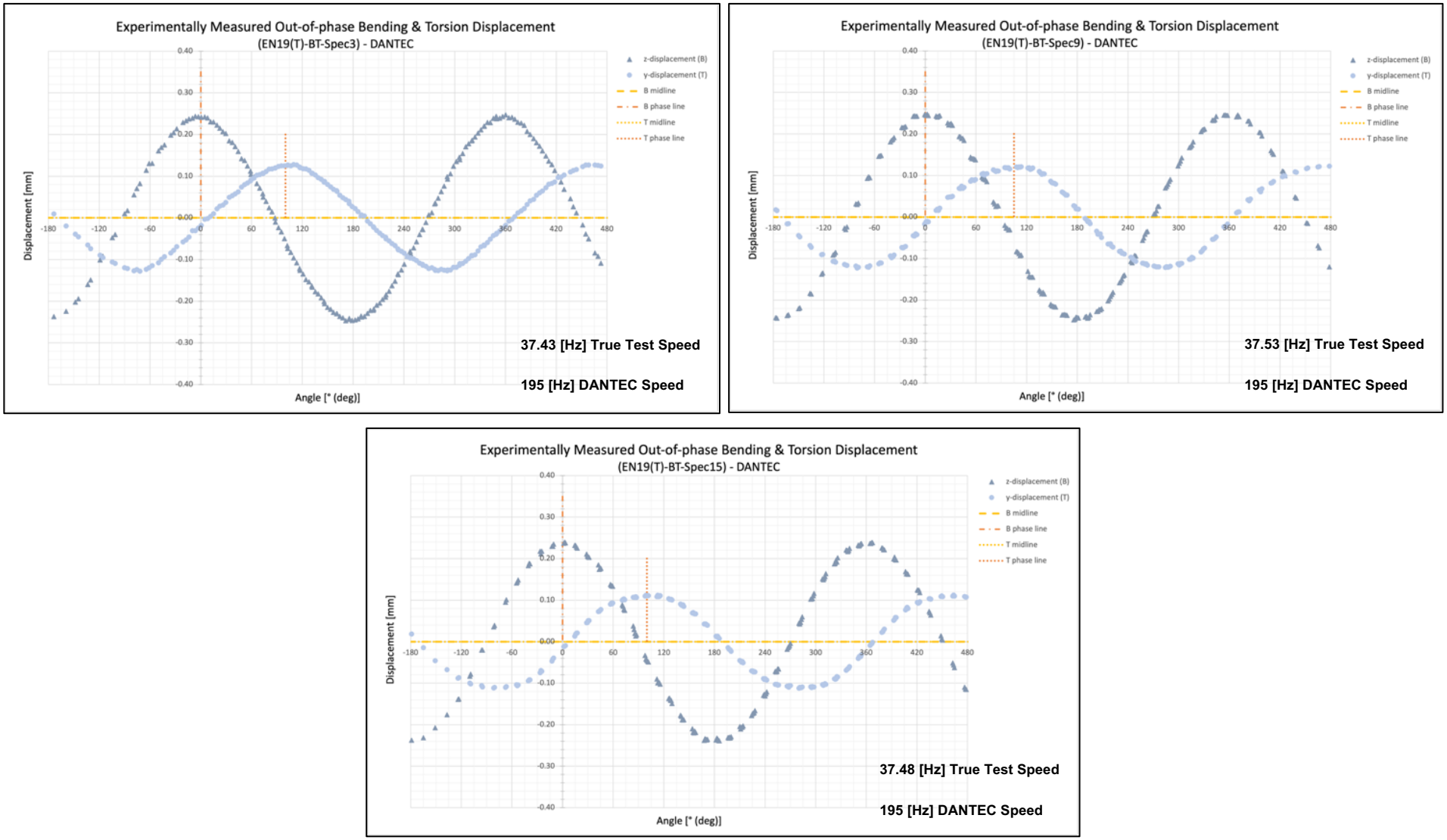


Figure H-38: BT fatigue test Spec3, 9 and 15 measurements – DANTEC sinusoidal displacement curves (collapsed)

Table H-19: BT fatigue test Spec3, 9 and 15 measurement – experimental gain comparison

EN 19 (T)		Specimen #	Diameter	N	Nut&Bolt Mass	Radius	V Nominal V			T-Stiffness k_t	Theoretical G_B	Theoretical G_T	Gauge P1-P2 Displacement - @ E = E_{exp} = 211.174GPa						
							$F_{centrifugal}$	M_B	M_T				NX FEM B	NX FEM T	DANTEC B	DANTEC T	Experimental G_B	Experimental G_T	Difference G_B vs G_T
			[mm]	[Hz]	[g]	[mm]	[N]	[N.m]	[N.m]	[N.m/rad]	[-]	[-]	[mm]	[mm]	[mm]	[mm]	[-]	[-]	[%]
NUT9	(DANTEC)	EN19T-BT-Spec-3	6.560	38	31.2450	30	53.435	10.812	10.812	893.80	4.914	1.300	0.17201	0.08588	0.24560	0.12758	1.428	1.486	4.04
NUT5	(DANTEC)	EN19T-BT-Spec-9	6.563	38	28.3602	35	56.585	11.377	11.377	895.13	4.958	1.290	0.18073	0.09024	0.24793	0.12317	1.372	1.365	0.51
NUT4	(DANTEC)	EN19T-BT-Spec-15	6.571	38	24.1489	40	55.066	10.955	10.955	898.66	5.078	1.276	0.17333	0.08655	0.24069	0.11247	1.389	1.299	6.42

The calculated experimental bending and torsion gain values in Table H-19 above showed that the theoretical and experimental bending and torsion gains were again not comparable. However, the calculated percentage differences between experimental G_B and G_T showed good agreement. The small differences showed that the chosen test speed, 38 [Hz], is the most appropriate point of testing for the biaxial loading components to have similar experimental gain values. The discussion for the vertical displacement axis offsets (not truly present) below Figure H-35, previously provided, is still valid for the displacement data curves of the official measurements in Figure H-37 in this section (as reflected by the sinusoidal curves in Figure H-38 above). The largest difference of 6.42 [%] was attributed to the difference in Spec15 and Spec18 (previously tested, see part 2a of this Appendix H5.2) diameters. In this, the gain response of Spec15 theoretically shifted (to the lower speed side of the graph illustrated in Figure H-36) with respect to that of Spec18. Therefore, the chosen 38 [Hz] might not have been the ideal test speed for Spec15 due to it being based on the larger Spec18 diameter and those measurements. These measurements are discussed further in Section 4.5.2, and the results are reported and discussed in Section 5.2.3.

I. EXPERIMENTAL TEST SIMULATIONS

I1. Theoretical Torsional Displacement Measurement

The static FEM simulations were performed in Siemens NX12 to obtain the theoretical torsional displacement measurements required for comparison or calculation with each relevant DANTEC displacement measurement, as discussed in Appendix H4.2 (parts 2a to 2c).

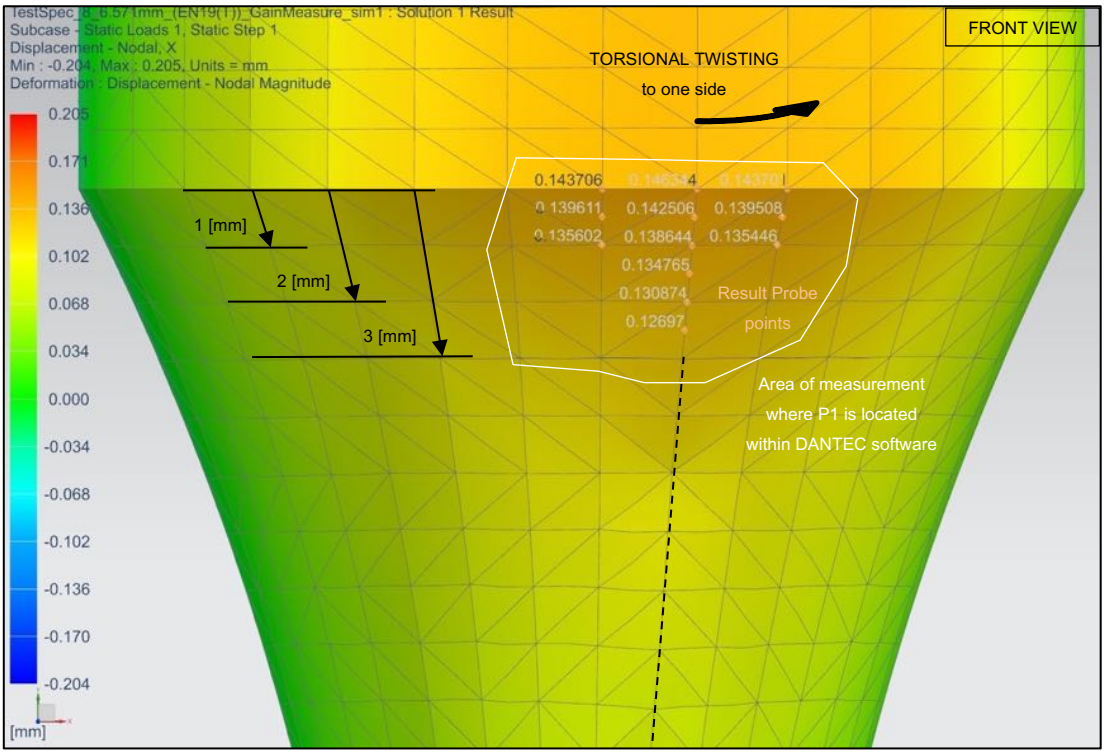
This simulation was done with a specimen FEM model generated to represent the specimen appropriately and the attached T fatigue test bench lever-head geometry, which was assumed to be rigid from the specimen coupling clamp upwards (see Figure I-1 (b) below). The specimen was modelled to have the exact measured hourglass test zone diameter and moment lever lengths relevant to each test specimen being measured with the DANTEC. The whole specimen model was meshed with a 2 [mm] 3D tetrahedral (CTETRA10 elements) mesh throughout, and a 1 [mm] mesh refinement was applied to the specimen gauge area.

The specimen models used for parts 2a and 2b in Appendix H4.2 were assigned the pre-defined 'steel' material in NX (E_{NX} = 206.9 [GPa]). It was necessary since the tested EN19 (R-condition) material properties were obtained from older tensile tests (unverified), and its experimental E value was unknown. These measurements were also only for loading investigation and verification purposes of EN19 (R-condition) specimens before the official experimental test measurements. For the official experimental measurements in Appendix H4.2 part 2c, the specimen FEM models were appropriately considered. The material assigned to this FEM model was a user-defined material in NX, which utilised the experimentally measured yield strength, ultimate tensile and Modulus of Elasticity property values for the EN19 (T-condition) alloy steel considered in this study (see Table J-1). See Figure I-2 in the following appendix for the negligibly small influence of E on the theoretical y-displacement (torsion) in NX.

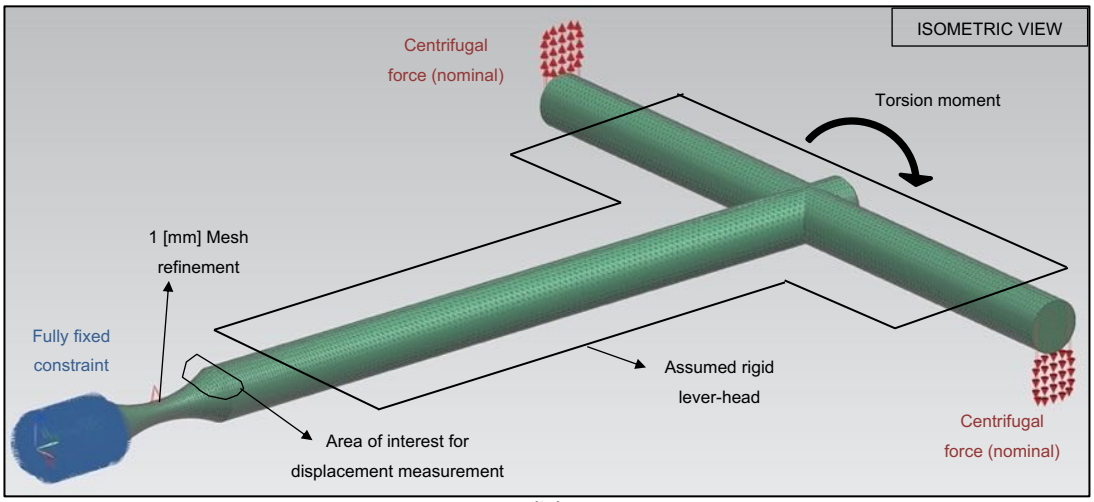
The calculated nominal (un-gained) centrifugal forces for each test were applied to the tips of the moment lever arms in the relevant directions that induce torsion on the specimen. The bottom of the specimen FEM model was fully constrained (fixed constraint) to represent the ideal experimental clamping condition.

Once the FEM model was solved, the relevant theoretical displacement was measured (result probe in NX, see Figure I-1 (a) below) at the corresponding P1 digital gauge element position. This gauge element is placed in the ISTRA 4D software on each test specimen's surface (on pre-marked cross markings). For this, the 1 [mm] refined mesh elements on the specimen gauge area were used to identify the correct point for the corresponding displacement value measurement. It

should be noted that in the NX FEM results, the x-direction displacement (shown below) corresponds to the relevant y-direction displacement with respect to the DANTEC coordinate system (shown in Figure H-19 or Figure H-21).



(a)



(b)

Figure I-1: Theoretical torsional displacement measurement – (a) NX FEM model y-displacement measurement and (b) static FEM model

I2. Theoretical Bending and Torsion Displacement Measurement

The static FEM simulations were performed in Siemens NX12 to obtain the theoretical bending and torsion displacement measurements required for comparison or calculation with the relevant DANTEC displacement measurement, as discussed in Appendix H5.2 (parts 2a to 2b).

This simulation was done with a specimen FEM model generated to represent the specimen appropriately and the attached BT fatigue test bench lever-head geometry, which was assumed to be rigid from the specimen clamp upwards (see Figure I-3 (b) below). The specimen was modelled to have the exact measured hourglass test zone diameter and moment lever lengths relevant to each test specimen being measured with the DANTEC. The whole specimen model was meshed with a 2 [mm] 3D tetrahedral (CTETRA10 elements) mesh throughout, and a 1 [mm] mesh refinement was applied to the specimen gauge area.

The specimen model used for part 2a in Appendix H5.2 was assigned the pre-defined 'steel' material in NX (E_{NX} = 206.9 [GPa]). It was necessary since the experimental Elasticity Modulus value of the EN19 (T-condition) test material was not yet determined at the time of these static FEM simulations for determining Spec18's theoretical bending and torsion displacements. Figure I-2 below illustrates the negligibly small influence of using the lower E_{NX} value instead of E_{exp} = 211.174 [GPa] (from Appendix H1.2 and Table J-1) on the measured displacements for bending (0.00470 [mm] or 1.9 [%] more) and torsion (0.00256 [mm] or 2 [%] more). The official test Spec18 was also used only to measure, investigate and affirm the experimental gain response of an EN19 (T-condition) BT fatigue specimen over a chosen test speed range using different centrifugal nuts.

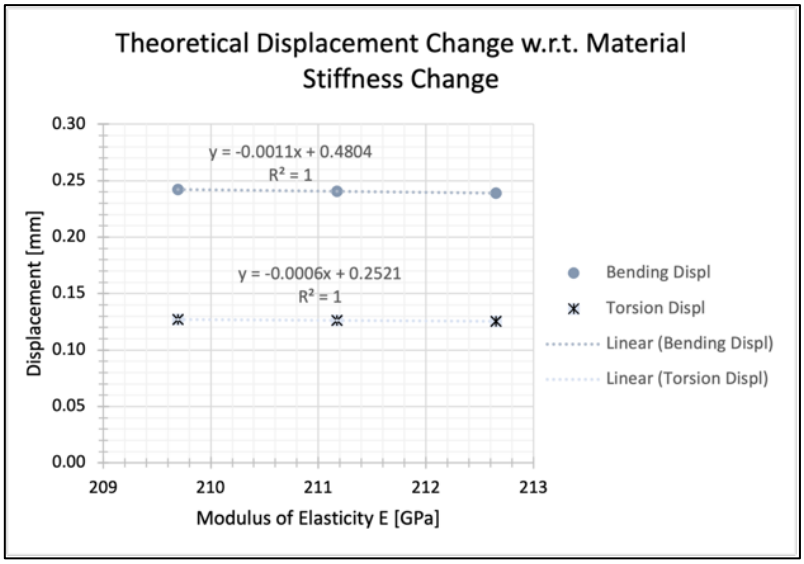
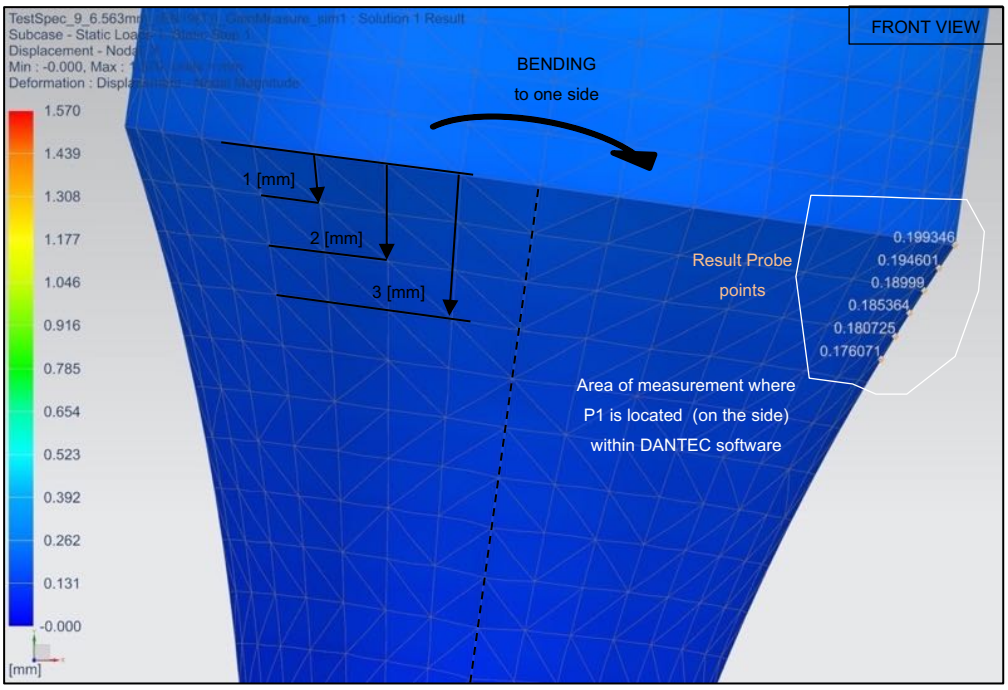


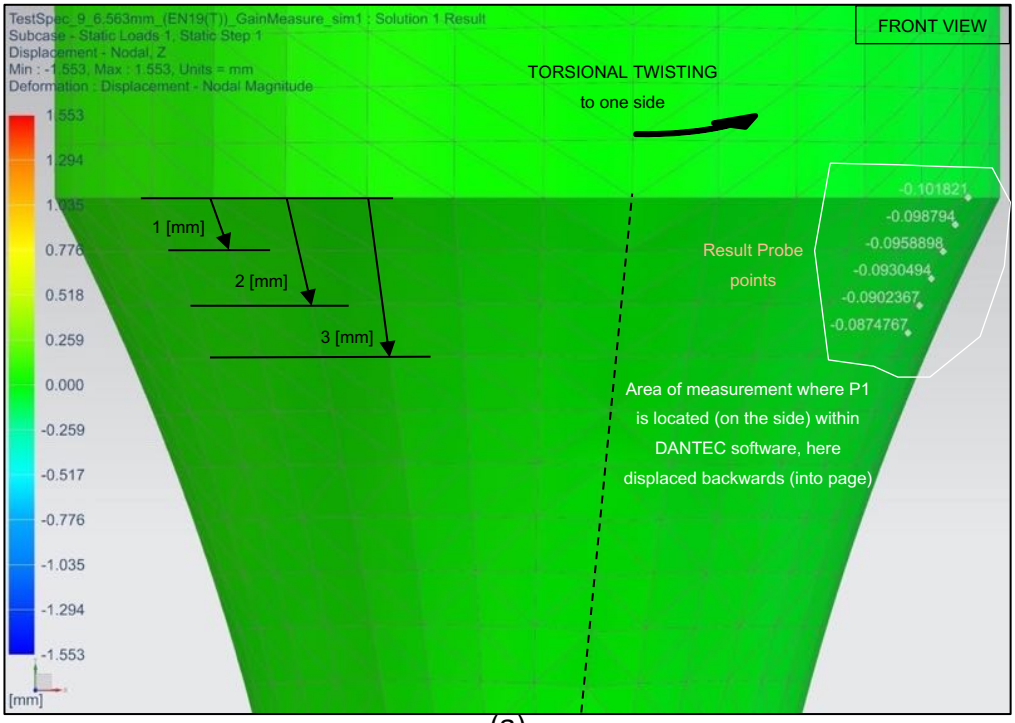
Figure I-2: Theoretical bending-torsion displacement vs FEM Elasticity Modulus

For the official experimental measurements in Appendix H5.2 part 2b, the specimen FEM models were appropriately considered with E_{exp}. The material assigned to these FEM models was a user-defined material in NX, which utilised the experimentally measured yield strength, ultimate tensile and Modulus of Elasticity property values for the EN19 (T-condition) alloy steel considered in this study (see Table J-1).

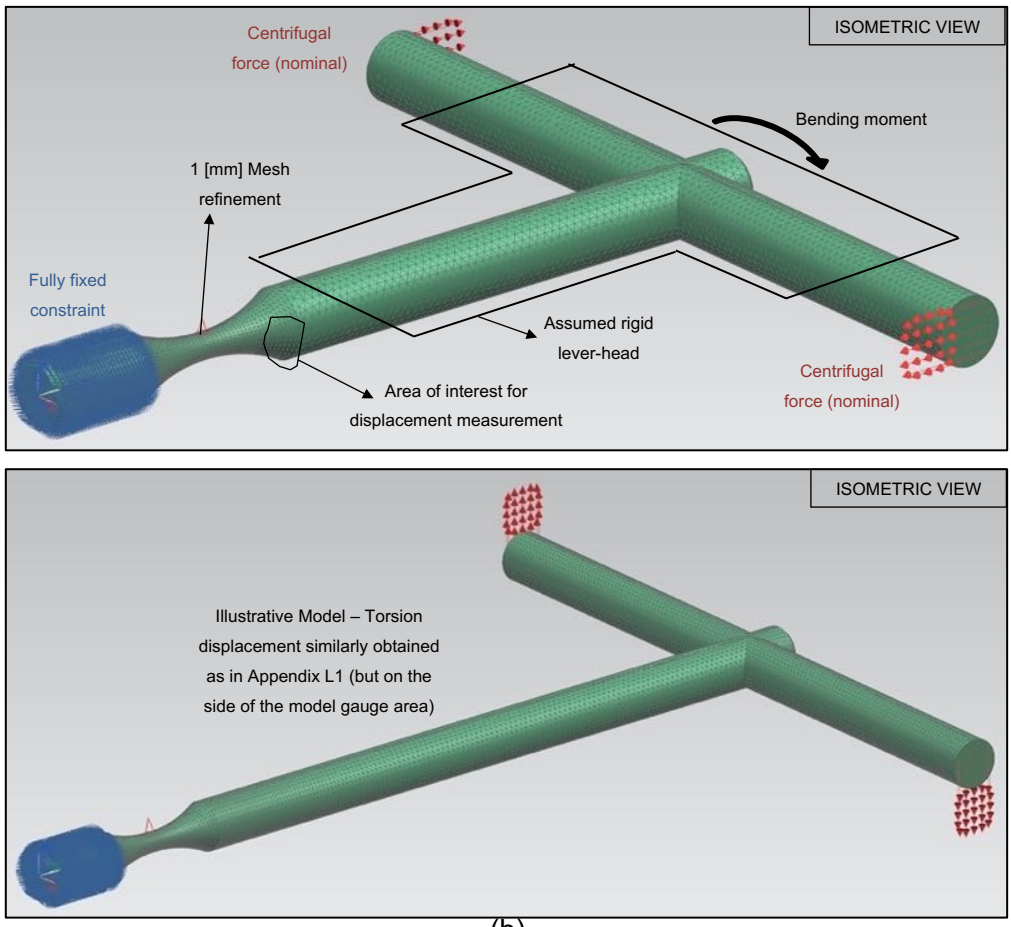
The calculated nominal (un-gained) centrifugal forces for each test were applied to the tips of the moment lever arms in the relevant directions that induce bending or torsion on the specimen. The bottom of the specimen FEM model was fully constrained (fixed constraint) to represent the ideal experimental clamping condition.

Once the FEM model was solved, the relevant theoretical displacement was measured (result probe in NX, see Figure I-3 (a) below) at the corresponding P1 digital gauge element position. This gauge element is placed in the ISTRA 4D software on each test specimen's surface (on pre-marked cross markings). For this, the 1 [mm] refined mesh elements on the specimen gauge area were used to identify the appropriate point for the corresponding displacement value measurement. It should be noted that in the NX FEM results, the x-direction displacement (shown below) corresponds to the relevant z-direction displacement (of bending), and the z-direction displacement corresponds to the relevant y-direction displacement (of torsion) with respect to the DANTEC coordinate system (shown in Figure H-32 and Figure H-33). The different 'directions' were due to the BT measurements all being made on the specimen's right-hand side face (marking positions) as if one were to stand in front of the test bench with the camera viewing from right to left (see Figure H-32).





(a)



(b)

Figure I-3: Theoretical bending-torsion displacement measurement – (a) NX FEM model y and z-displacement measurement and (b) static FEM model

J. EXPERIMENTAL TEST RESULTS

J1. Monotonic Tensile Test Results

Table J-1: Tensile (TEN) testing results

			S_{ut} [MPa]	961.28											
	EN 19 (T)		S_y [MPa]	858.99											
			E [GPa]	211.17	enter from MTS results/data/Excel		read from graph yield offset line MTS		enter from extensometer/calculations			enter from thermometer		
DATE	**Specimen #**	**Diameter [mm]**	**Cross Sectional Area [m^2]**		**UTS Load - F_{UTS} [kN]**	**$S_{ut;spec}$ [MPa]**	**YIELD Load - F_Y [kN]**	**$S_{y;spec}$ [MPa]**	**MODULUS of Elasticity [GPa]**		**$E_{avg;spec}$ [GPa]**	**Room TEMPERATURE start/end [°C]**		**T_{avg} [°C]**
21/01/2022	**EN19T-TEN-Spec-1**	6.229	0.00003047		27.016	886.53	24.070	789.86	Uncertainty inherent to extensometer is +- 0,04% of engineering strain ε [-] for 25mm nominal gauge length (calibration certificate)			24.7	25.2	24.95
21/01/2022	**EN19T-TEN-Spec-2**	6.376	0.00003193		28.534	893.66	24.762	775.53				24.7	25.2	24.95
21/01/2022	**EN19T-TEN-Spec-3**	6.285	0.00003102		29.155	939.76	26.309	848.02				24.7	25.2	24.95
21/01/2022	**EN19T-TEN-Spec-4**	6.075	0.00002899		27.135	936.15	24.295	838.17				24.7	25.2	24.95
21/01/2022	**EN19T-TEN-Spec-5**	6.180	0.00003000		29.204	973.59	26.187	873.01	E_{ext}	E_{calc}		24.7	25.2	24.95
21/04/2022	**EN19T-TEN-Spec-6**	6.144	0.00002965		30.341	1023.38	27.423	924.96	210.197	210.620	210.409	20.3	20.5	20.40
21/04/2022	**EN19T-TEN-Spec-7**	6.162	0.00002982		30.255	1014.53	27.021	906.09	211.431	212.697	212.064	20.3	20.5	20.40
21/04/2022	**EN19T-TEN-Spec-8**	6.279	0.00003096		29.671	958.23	26.376	851.81	208.473	209.543	209.008	20.3	20.5	20.40
21/04/2022	**EN19T-TEN-Spec-9**	6.310	0.00003127		31.064	993.35	27.689	885.43	212.067	213.414	212.741	20.3	20.5	20.40
21/04/2022	**EN19T-TEN-Spec-10**	6.352	0.00003169		31.487	993.61	28.425	897.00	211.148	212.146	211.647	20.3	20.5	20.40
	Material Certificate (post T-condition heat treatment):				**$S_{ut;avg}$**	**961.28**	**$S_{y;avg}$**	**858.99**		**E_{avg}**	**211.174**		**$T_{avg;TEN}$**	**22.68**
	S_{ut} = 955MPa ≃ 0.6 [%] from experimental results				**$S_{ut;stdev}$**	47.35	**$S_{y;stdev}$**	48.60		**E_{stdev}**	1.479		**$T_{stdev;TEN}$**	2.40
	S_y = 850MPa ≃ 1.1 [%] | (HBN10/3000 = 285)				**1.96u(S_{ut})**	**102.77**	**1.96u(S_y)**	**103.28**		**1.96u(E)**	**2.899**			

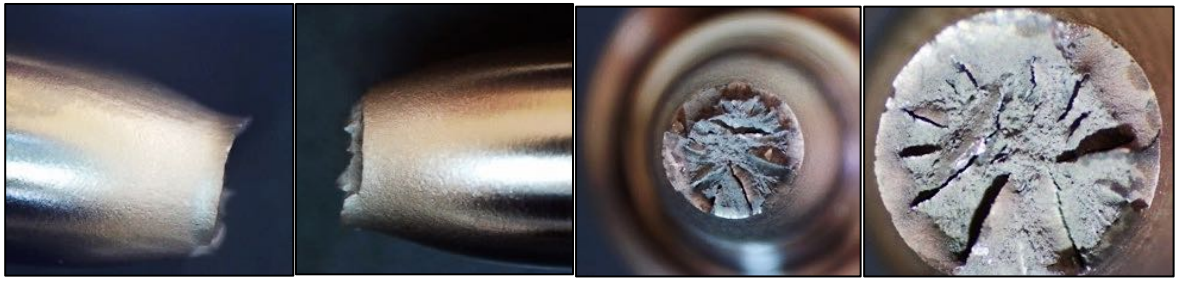


Figure J-1: Tensile (TEN) specimen fracture zone

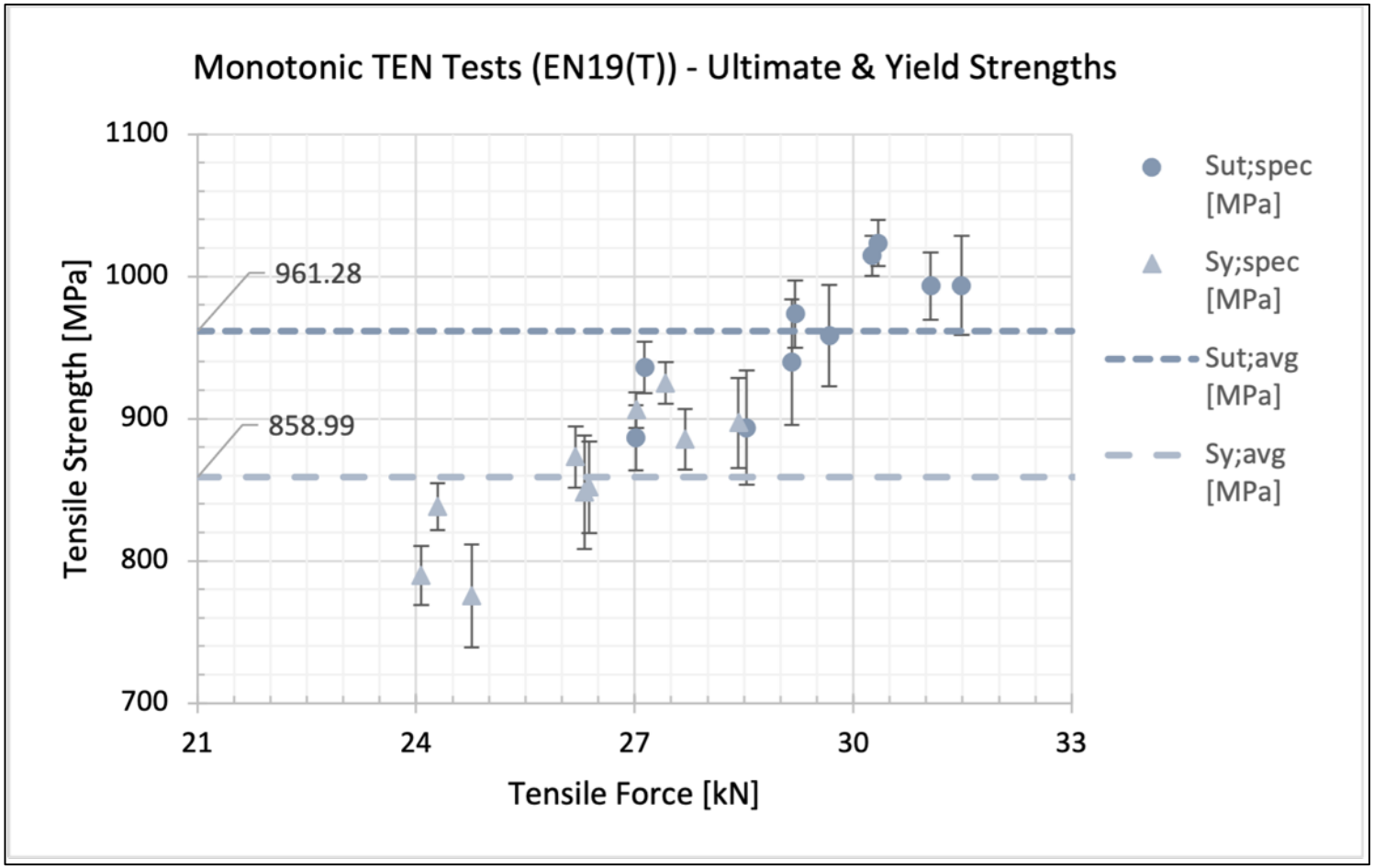


Figure J-2: Tensile (TEN) testing results – monotonic ultimate tensile and yield strengths

J2. Axial Fatigue Test Results

Table J-2: Axial (AX) fatigue testing results

	EN 19 (T)		S_{ut} [MPa] 961.28	$s_{-1;\,exp}$ 486 [MPa]	s_{-1} vs Sut	$f_{-1;equiv}$ [MPa]				enter		enter		
			S_y [MPa] 858.99	enter from data export	0.506	571.76	BT graphs							
DATE	Specimen #	Diameter [mm]	Cross Sectional Area [m^2]	$F_{axial;a;Theoretical}$ [kN]	$F_{axial;a;Experimental}$ [kN]	$\sigma_{axial;a}$ [MPa]	$\sigma_{axial;a;VM}$ [MPa]	$\sigma_{axial;B\text{-}eq;a;VM}$ [MPa]	% of Sut [%]	N [Hz]	$N_{f\,estimated}$ [-]	Test Time [hrs]	N_f [-]	Test Time Failure [hrs]	Notes
23/05/2022	EN19T-AX-Spec-1	5.811	0.00002652	9.500	9.507	358.47	358.47	421.73	37.29	12	274300	6.35	1510000	34.95	no fail
25/05/2022	EN19T-AX-Spec-2	5.690	0.00002543	11.000	11.060	434.97	434.97	511.73	45.25	12	255766	5.92	1511226	34.98	no fail
27/05/2022	EN19T-AX-Spec-3	5.713	0.00002563	13.500	13.523	527.56	527.56	620.65	54.88	12	53213	1.23	147296	3.41	fail
27/05/2022	EN19T-AX-Spec-4	5.720	0.00002570	12.000	12.020	467.75	467.75	550.29	48.66	12	301250	6.97	1515317	35.08	no fail
29/05/2022	EN19T-AX-Spec-5	5.672	0.00002527	14.500	14.528	574.98	574.98	676.45	59.81	12	45872	1.06	150881	3.49	fail
2/06/2022	EN19T-AX-Spec-6	5.643	0.00002501	13.250	13.257	530.08	530.08	623.63	55.14	12	118681	2.75	355440	8.23	fail
3/06/2022	EN19T-AX-Spec-7	5.721	0.00002571	12.750	12.760	496.38	496.38	583.97	51.64	12	367237	8.50	1510000	34.95	no fail
5/06/2022	EN19T-AX-Spec-8	5.711	0.00002562	13.450	13.457	525.31	525.31	618.02	54.65	12	337138	7.80	163166	3.78	fail

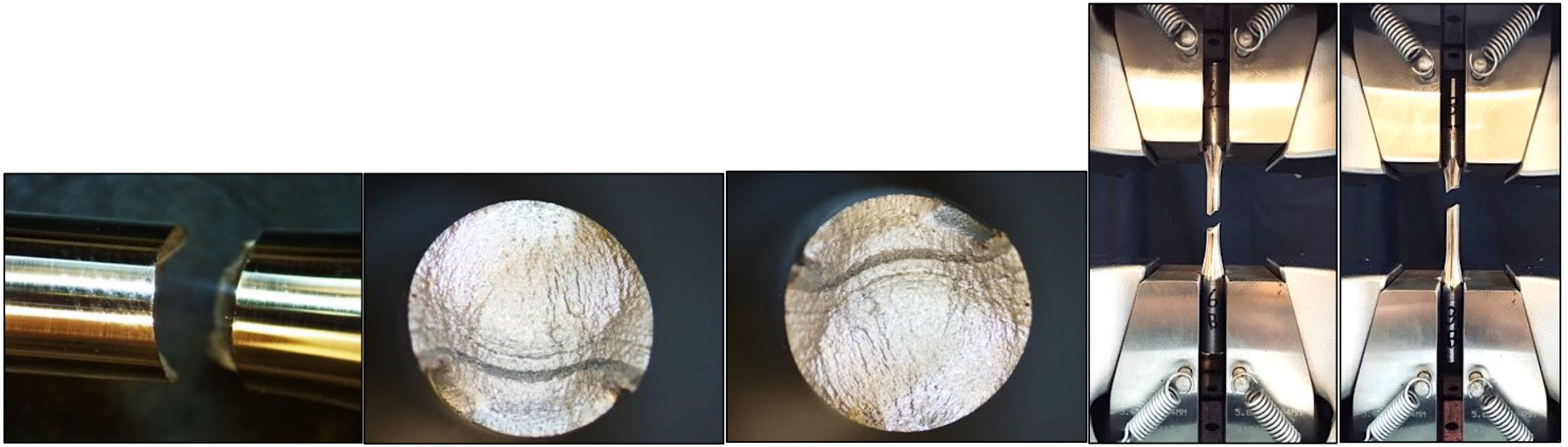


Figure J-3: Axial (AX) fatigue specimen fracture plane

J3. Bending Fatigue Test Results

Table J-3: Bending (B) fatigue testing results

	EN 19 (T)		S_{ut} [MPa]	961.28	$f_{-1;exp}$	510	[MPa]	f_{-1} vs Sut				measure		enter		enter		
			S_v [MPa]	858.99	enter		enter	0.531										
DATE	Specimen #	Diameter [mm]	Cross Sectional Area [m^2]		$F_{cantilever}$ [N]	$F_{load\ cell}$ [N]	$x_{break;exp}$ [mm]	$M_{B;cantilever}$ [N.m]	$\sigma_{bending;a}$ [MPa]	$\sigma_{bending;a;VM}$ [MPa]	% of Sut [%]	N [rpm]	N [Hz]	$N_{f;estimated}$ [-]	Test Time [hrs]	N_f [-]	Test Time Failure [hrs]	Notes
3/06/2022	EN19T-B-Spec-1	5.493	0.00002370		134	**120**	**61**	7.102	436.47	436.47	45.40	2983	49.72	647147	3.62	1551537	8.67	no fail - 2.5N uncert
6/06/2022	EN19T-B-Spec-2	5.424	0.00002311		173	**155**	**60.5**	9.256	590.80	590.80	61.46	2979	49.65	143932	0.81	311201	1.74	fail - 5N uncert
4/06/2022	EN19T-B-Spec-3	5.552	0.00002421		162	**145**	**61**	8.586	511.03	511.03	53.16	2981	49.68	707885	3.96	1594240	8.91	no fail - 2.5N uncert
6/06/2022	EN19T-B-Spec-4	5.734	0.00002582		173	**155**	**56.3**	9.984	539.42	539.42	56.11	2991	49.85	417325	2.33	215897	1.20	fail - 5N uncert
7/06/2022	EN19T-B-Spec-5	5.545	0.00002415		167	**150**	**61**	8.851	528.80	528.80	55.01	2982	49.70	879439	4.92	1653278	9.24	no fail - 2.5N uncert
8/06/2022	EN19T-B-Spec-6	5.650	0.00002507		167	**150**	**56.3**	9.643	544.56	544.56	56.65	2989	49.82	384824	2.15	106457	0.59	fail - 5N uncert
3/06/2022	EN19T-B-Spec-7	5.603	0.00002466		178	**160**	**56.9**	10.162	588.46	588.46	61.22	2972	49.53	19172	0.11	92923	0.52	fail - 7.5N uncert
NA	EN19T-B-Spec-8	-	-		-	-	-	-	-	-	-	-	-	-	-	-	-	**OMMITTED**

Note that Spec8 was omitted due to a manufacturing error/inconsistency that would have caused improper testing.

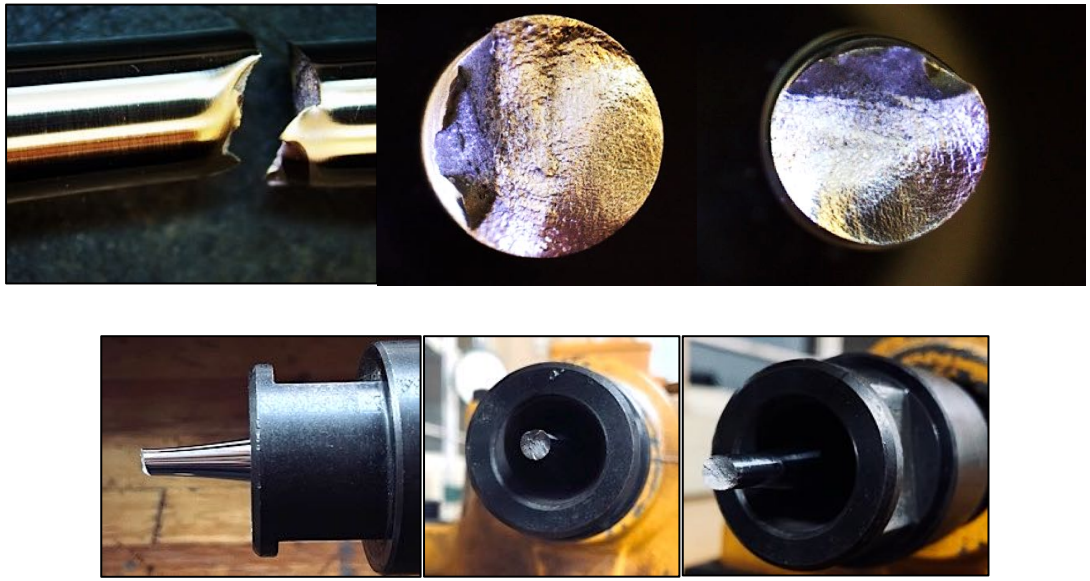


Figure J-4: Bending (B) fatigue specimen fracture plane

J4. Torsion Fatigue Test Results

Table J-4: Torsion (T) fatigue testing results

	EN 19 (T)		S_u [MPa]	961.28	$t_{-1;exp}$	354	[MPa]	t_{-1} vs Sut						Expemntly							
			S_y [MPa]	858.99	enter			0.368	enter	V Nominal V		enter	enter	V GAINED V			enter		enter		
DATE	Specimen #	Diameter [mm]	Cross Sectional Area [m^2]		Centrifugal Mass Piece			Radius [mm]	N [Hz]	$F_{centrifugal}$ [N]	M_T [N.m]	Theoretical G_T [-]	Experimental G_T [-]	T_a [MPa]	$T_{a;VM}$ [MPa]	% of Sut [%]	$N_{testimated}$ [-]	Test Time [hrs]	Test Time Failure [hrs]	N_f [-]	Notes
					Nut #	Bolt	Tot Mass [g]														
9/07/2022	EN19T-T-Spec-1	6.548	0.00003367		NUT 5	BOLT 2 (M4x25)	28.360	40	27.5	33.868	7.681	1.176	1.163	162.08	280.73	16.86	2088327	21.09	16.200	1603800	no fail - Dantec @171Hz
14/07/2022	EN19T-T-Spec-2	6.526	0.00003345		NUT 10	BOLT 2 (M4x25)	34.789	40	27.5	41.546	9.541	1.188	1.188	207.66	359.67	21.60	17331016	175.06	15.367	1521333	no fail
23/07/2022	EN19T-T-Spec-3	6.538	0.00003357		NUT 5	BOLT 2 (M4x25)	28.360	35	40.0	62.698	14.220	1.467	1.467	380.16	658.46	39.55	802741	5.57	1.367	196848	fail
22/07/2022	EN19T-T-Spec-4	6.551	0.00003371		NUT 4	BOLT 2 (M4x25)	24.149	40	40.0	61.015	13.710	1.442	1.442	358.13	620.30	37.26	1041187	7.23	10.417	1500048	no fail
16/07/2022	EN19T-T-Spec-5	6.523	0.00003342		NUT 10	BOLT 2 (M4x25)	34.789	40	35.0	67.298	15.456	1.345	1.302	369.18	639.45	38.41	576540	4.58	11.917	1501542	no fail - Dantec @189Hz
21/07/2022	EN19T-T-Spec-6	6.532	0.00003351		NUT 5	BOLT 2 (M4x25)	28.360	35	40.0	62.698	14.220	1.469	1.469	381.73	661.18	39.71	789329	5.48	0.517	74448	fail
21/07/2022	EN19T-T-Spec-7	6.582	0.00003403		NUT 9	BOLT 2 (M4x25)	31.245	35	40.0	69.076	15.755	1.466	1.466	412.52	714.51	42.91	485025	3.37	0.567	81648	fail
21/07/2022	EN19T-T-Spec-8	6.571	0.00003391		NUT 5	BOLT 2 (M4x25)	28.360	40	40.0	71.655	16.252	1.456	1.485	433.16	750.25	45.06	482117	3.35	0.283	40752	fail (LCF) - Dantec @194Hz
21/07/2022	EN19T-T-Spec-9	6.558	0.00003378		NUT 10	BOLT 2 (M4x25)	34.789	35	40.0	76.912	17.664	1.490	1.505	480.15	831.65	49.95	273849	1.90	0.017	2448	fail (LCF) - Dantec @194Hz

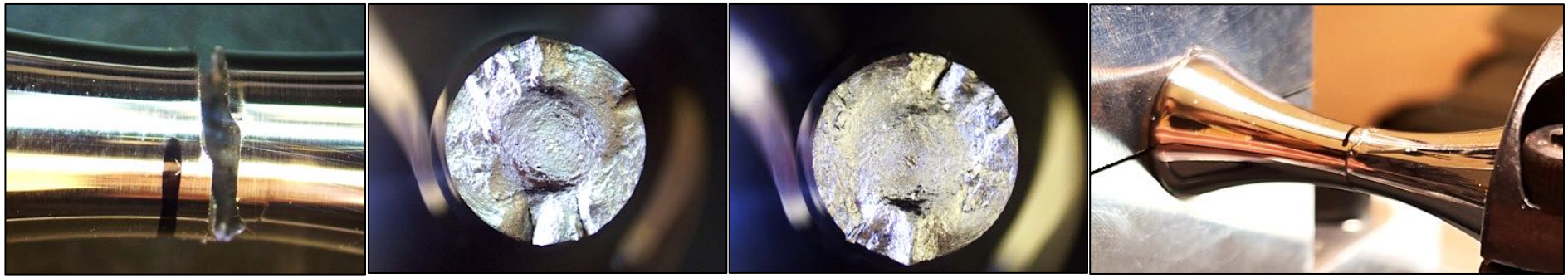


Figure J-5: Torsion (T) fatigue specimen fracture plane

J5. Bending-Torsion Fatigue Test Results

Table J-5: Bending-Torsion (BT) fatigue testing results

	EN 19 (T)		S_{ut} [MPa]	961.28																								
			S_y [MPa]	858.99						V Nominal V							Expemntly V GAINED V			Expemntly V GAINED V								
				enter				enter	enter	enter			enter	enter				V Nominal V						enter		enter		
DATE	Specimen #	Diameter [mm]	Cross Sectional Area [m²]	Centrifugal Mass Piece Nut #	Bolt	Tot Mass [g]	Radius [mm]	N [Hz]	$F_{centrifugal}$ [N]	M_T [N.m]	Theoretical G_B [-]	Theoretical G_T [-]	Experimental G_B [-]	Experimental G_T [-]	T_a [MPa]	$T_{a,VM}$ [MPa]	M_B [N.m]	$\sigma_{bending,a}$ [MPa]	$\sigma_{bending,a;VM}$ [MPa]	% of Sut [%]	λ [-]	$N_{f,estimated}$ [-]	Test Time Estim [hrs]	Test Time Real [hrs]	N_f [-]	Notes
25/07/2022	EN19T-BT-Spec-1	6.527	0.00003346	NUT 1	BOLT 1 (M5x25)	19.1856	35	38.0	38.280	7.491	4.473	1.260	1.359	1.269	174.12	301.58	7.491	372.86	372.86	38.79	0.47	565599	4.134	11.200	1532160	no fail
26/07/2022	EN19T-BT-Spec-2	6.534	0.00003353	NUT 3	BOLT 1 (M5x25)	22.7426	35	38.0	45.377	8.977	4.561	1.269	1.364	1.274	208.76	361.59	8.977	447.05	447.05	46.51	0.47	469652	3.433	11.000	1504800	no fail
27/07/2022	EN19T-BT-Spec-3	6.560	0.00003380	NUT 9	BOLT 2 (M4x25)	31.2450	30	38.0	53.435	10.812	4.914	1.300	1.428	1.486	289.75	501.87	10.812	557.01	557.01	57.94	0.52	774748	5.663	11.417	1561846	no fail - Dantec1 @195Hz
28/07/2022	EN19T-BT-Spec-4	6.548	0.00003367	NUT 9	BOLT 2 (M4x25)	31.2450	40	38.0	71.247	14.416	4.745	1.302	1.425	1.482	387.49	671.15	14.416	745.29	745.29	77.53	0.52	51764	0.378	0.200	27360	fail
28/07/2022	EN19T-BT-Spec-5	6.552	0.00003372	NUT 9	BOLT 2 (M4x25)	31.2450	35	38.0	62.341	12.614	4.800	1.301	1.428	1.485	339.10	587.33	12.614	652.24	652.24	67.85	0.52	202871	1.483	1.633	223394	fail
28/07/2022	EN19T-BT-Spec-6	6.554	0.00003374	NUT 5	BOLT 2 (M4x25)	28.3602	35	38.0	56.585	11.377	4.828	1.292	1.367	1.357	279.37	483.88	11.377	562.72	562.72	58.54	0.50	580091	4.240	2.533	346514	fail
29/07/2022	EN19T-BT-Spec-7	6.563	0.00003383	NUT 4	BOLT 2 (M4x25)	24.1489	40	38.0	55.066	10.955	4.958	1.277	1.384	1.293	255.20	442.03	10.955	546.52	546.52	56.85	0.47	885150	6.470	1.417	193846	fail
29/07/2022	EN19T-BT-Spec-8	6.539	0.00003358	NUT 4	BOLT 2 (M4x25)	24.1489	40	38.0	55.066	10.955	4.625	1.281	1.367	1.277	254.83	441.39	10.955	545.72	545.72	56.77	0.47	792233	5.791	11.000	1504800	no fail - repeats Spec7
1/08/2022	EN19T-BT-Spec-9	6.563	0.00003383	NUT 5	BOLT 2 (M4x25)	28.3602	35	38.0	56.585	11.377	4.958	1.290	1.372	1.365	279.77	484.58	11.377	562.38	562.38	58.50	0.50	604696	4.420	1.517	207526	fail - Dantec2 @195Hz - repeats Spec6
30/07/2022	EN19T-BT-Spec-10	6.653	0.00003476	NUT 9	BOLT 2 (M4x25)	31.2450	35	38.0	62.341	12.614	6.686	1.282	1.500	1.558	339.94	588.79	12.614	654.43	654.43	68.08	0.52	322353	2.356	0.517	70726	fail - repeats Spec5
30/07/2022	EN19T-BT-Spec-11	6.568	0.00003388	NUT 9	BOLT 2 (M4x25)	31.2450	35	38.0	62.341	12.614	5.032	1.298	1.439	1.496	339.27	587.63	12.614	652.66	652.66	67.90	0.52	218416	1.597	0.417	57046	fail - repeats Spec5
30/07/2022	EN19T-BT-Spec-12	6.571	0.00003391	NUT 5	BOLT 2 (M4x25)	28.3602	35	38.0	56.585	11.377	5.078	1.288	1.379	1.369	279.64	484.35	11.377	563.27	563.27	58.60	0.50	627411	4.586	5.967	816286	fail - repeats Spec6
2/08/2022	EN19T-BT-Spec-13	6.539	0.00003358	NUT 4	BOLT 2 (M4x25)	24.1489	40	38.0	55.066	10.955	4.625	1.281	1.367	1.277	254.83	441.39	10.955	545.72	545.72	56.77	0.47	792233	5.791	20.500	2804400	no fail - repeats Spec7
3/08/2022	EN19T-BT-Spec-14	6.577	0.00003397	NUT 4	BOLT 2 (M4x25)	24.1489	40	38.0	55.066	10.955	5.171	1.275	1.394	1.302	255.41	442.38	10.955	546.96	546.96	56.90	0.47	944128	6.902	23.267	3182926	no fail - repeats Spec7
1/08/2022	EN19T-BT-Spec-15	6.571	0.00003391	NUT 4	BOLT 2 (M4x25)	24.1489	40	38.0	55.066	10.955	5.078	1.276	1.389	1.299	255.54	442.60	10.955	546.14	546.14	56.81	0.47	918401	6.713	11.167	1527646	no fail - Dantec3 @195Hz - repeats Spec7
6/08/2022	EN19T-BT-Spec-16	6.574	0.00003394	NUT 5	BOLT 2 (M4x25)	28.3602	35	38.0	56.585	11.377	5.124	1.288	1.381	1.371	279.68	484.43	11.377	563.36	563.36	58.61	0.50	636141	4.650	0.867	118606	fail - repeats Spec6
6/08/2022	EN19T-BT-Spec-17	6.589	0.00003410	NUT 5	BOLT 2 (M4x25)	28.3602	35	38.0	56.585	11.377	5.368	1.285	1.392	1.382	279.91	484.81	11.377	563.82	563.82	58.65	0.50	681579	4.982	25.750	3522600	no fail - repeats Spec6
14/07/2022	EN19T-BT-Spec-18	6.629	0.00003451	-	-	-	-	-	-	-	-	-	-	-		-	-	-		-	-	-	-	-	-	Dantec - exp gain curves testing: Nut8&5

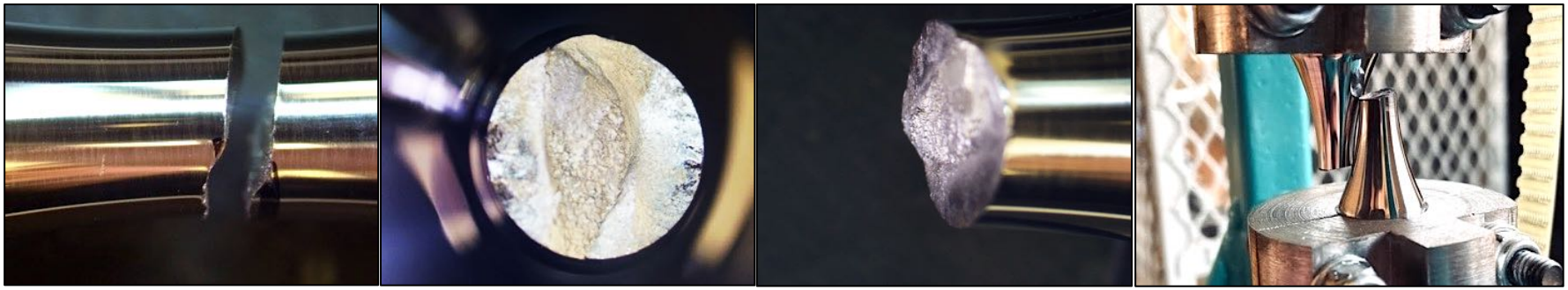


Figure J-6: Bending-Torsion (BT) fatigue specimen fracture plane

K. EXPERIMENTAL TEST UNCERTAINTIES

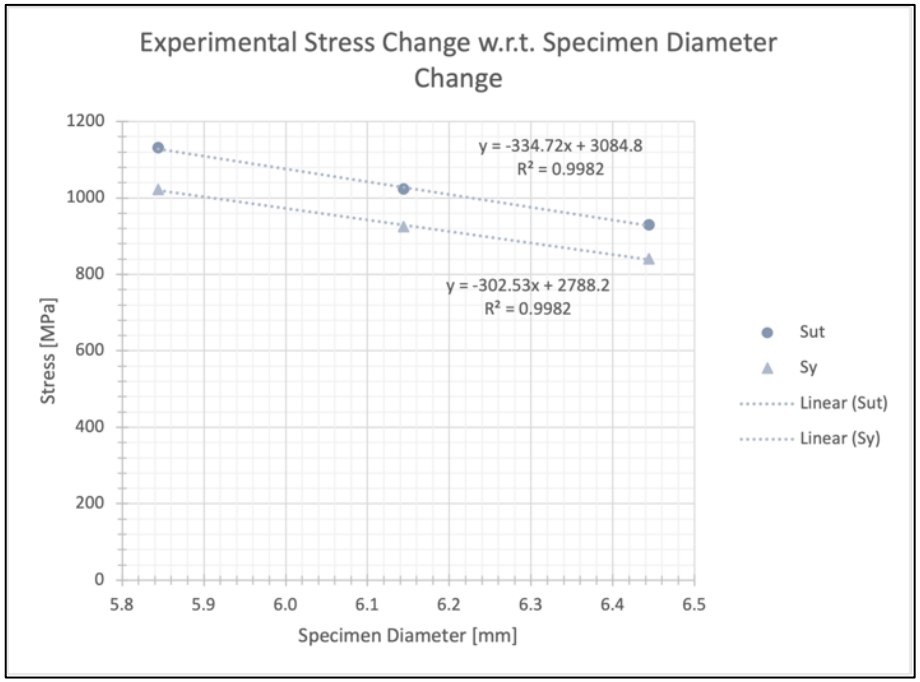
K1. Monotonic Tensile Test Uncertainties

Table K-1: Tensile (TEN) test result uncertainties

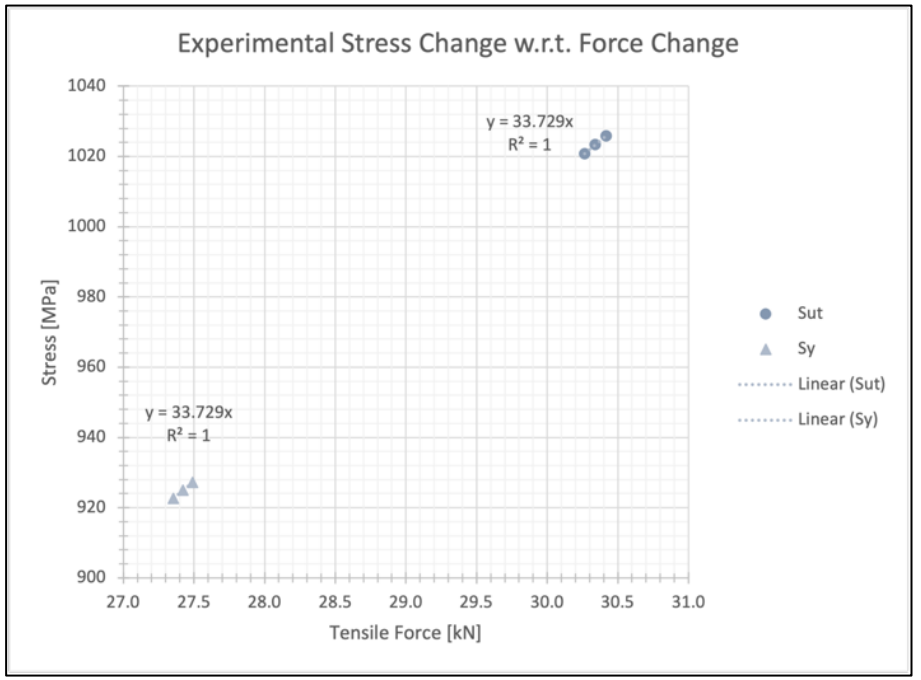
		Diameter -> Stress			Tensile Force -> Stress				95% confidence interval			
Specimen #	**Diameter [mm]**	**u(d) [mm]**	$\partial S_{ut} / \partial d$ **[MPa/mm]**	$\partial S_y / \partial d$ **[MPa/mm]**	**$u(F_{UTS})$ [kN]**	$\partial S_{ut} / \partial F_{UTS}$ **[MPa/kN]**	**$u(F_Y)$ [kN]**	$\partial S_y / \partial F_Y$ **[MPa/kN]**	**$1.96u(S_{ut;spec})$ [MPa]**	**$1.96u(S_{y;spec})$ [MPa]**	**$1.96u(S_{ut;spec})/S_{ut;spec}$ [%]**	**$1.96u(S_{y;spec})/S_{y;spec}$ [%]**
EN19T-TEN-Spec-1	6.229	**0.034**	334.72	302.53	**0.067**	33.73	**0.059**	33.73	**22.83**	**20.62**	**2.6%**	**2.6%**
EN19T-TEN-Spec-2	6.376	**0.061**	334.72	302.53	**0.070**	33.73	**0.061**	33.73	**40.14**	**36.26**	**4.5%**	**4.7%**
EN19T-TEN-Spec-3	6.285	**0.067**	334.72	302.53	**0.072**	33.73	**0.065**	33.73	**44.13**	**39.89**	**4.7%**	**4.7%**
EN19T-TEN-Spec-4	6.075	**0.027**	334.72	302.53	**0.067**	33.73	**0.060**	33.73	**18.11**	**16.36**	**1.9%**	**2.0%**
EN19T-TEN-Spec-5	6.180	**0.036**	334.72	302.53	**0.072**	33.73	**0.065**	33.73	**23.83**	**21.53**	**2.4%**	**2.5%**
EN19T-TEN-Spec-6	6.144	**0.024**	334.72	302.53	**0.075**	33.73	**0.068**	33.73	**16.30**	**14.73**	**1.6%**	**1.6%**
EN19T-TEN-Spec-7	6.162	**0.020**	334.72	302.53	**0.075**	33.73	**0.067**	33.73	**13.95**	**12.59**	**1.4%**	**1.4%**
EN19T-TEN-Spec-8	6.279	**0.054**	334.72	302.53	**0.073**	33.73	**0.065**	33.73	**35.65**	**32.21**	**3.7%**	**3.8%**
EN19T-TEN-Spec-9	6.310	**0.035**	334.72	302.53	**0.077**	33.73	**0.068**	33.73	**23.69**	**21.40**	**2.4%**	**2.4%**
EN19T-TEN-Spec-10	6.352	**0.053**	334.72	302.53	**0.078**	33.73	**0.070**	33.73	**34.93**	**31.57**	**3.5%**	**3.5%**

	Diameter [mm]	**UTS Force [kN]**	**Sut [MPa]**	**YIELD Force [kN]**	**Sy [MPa]**
/	**5.844**	30.341	1131.14	27.423	1022.36
EN19T-TEN-Spec-6	**6.144**	**30.341**	**1023.38**	**27.423**	**924.96**
\	**6.444**	30.341	930.31	27.423	840.84

	Diameter [mm]	**UTS Force [kN]**	**Sut [MPa]**	**YIELD Force [kN]**	**Sy [MPa]**
/	**6.144**	30.266	1020.85	27.355	922.67
EN19T-TEN-Spec-6	**6.144**	**30.341**	**1023.38**	**27.423**	**924.96**
\	**6.144**	30.416	1025.90	27.491	927.24



(a)



(b)

Figure K-1: Tensile (TEN) test result uncertainties – partial derivatives

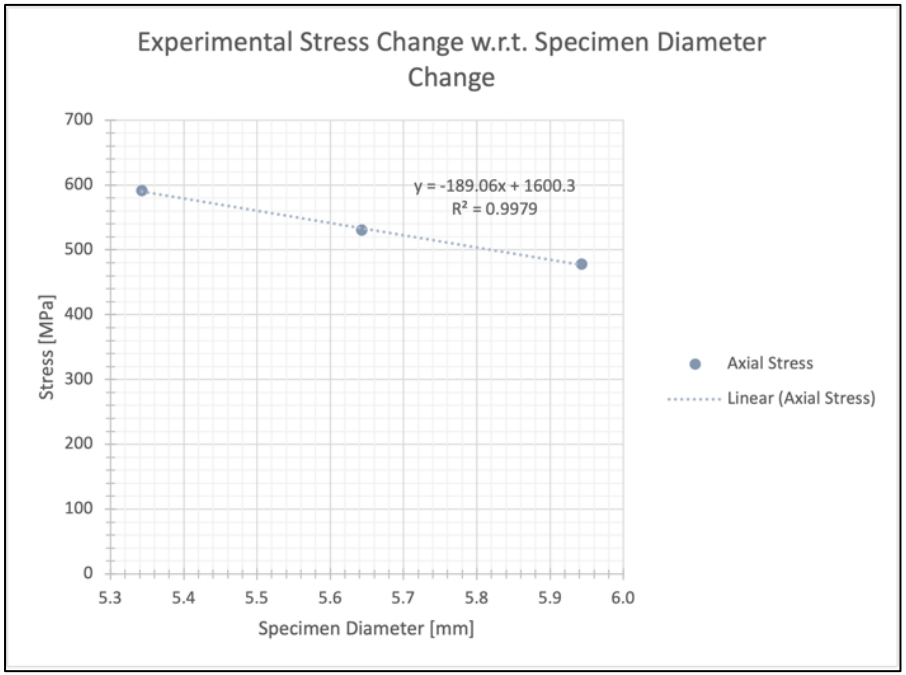
K2. Axial Fatigue Test Uncertainties

Table K-2: Axial (AX) fatigue test result uncertainties

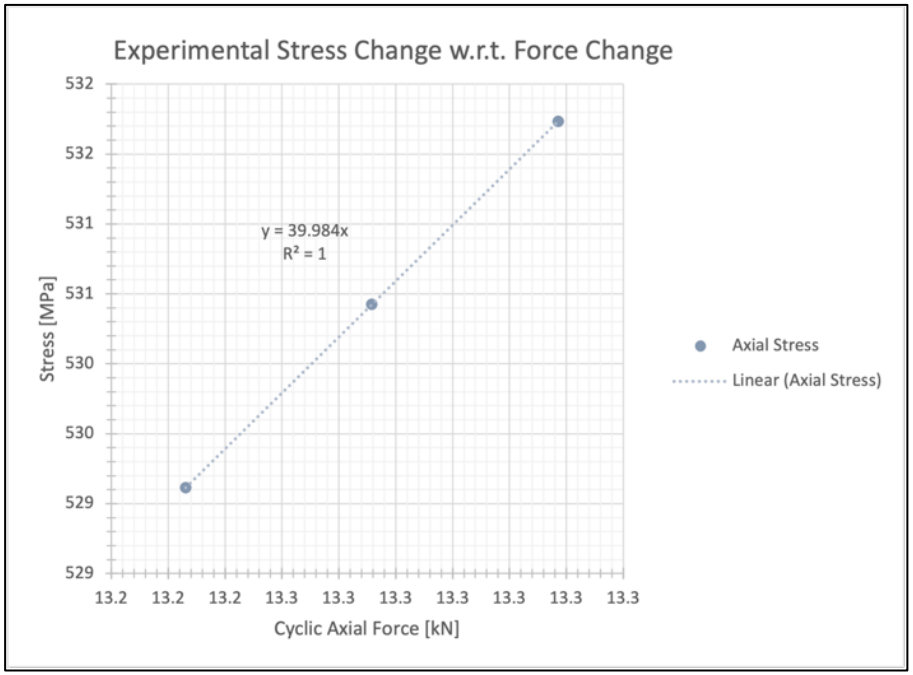
Specimen #	Diameter [mm]	Diameter -> Stress		Axial Force -> Stress		95% confidence interval	
		u(d) [mm]	$\partial\sigma_{axial;a} / \partial d$ [MPa/mm]	$u(F_{axial;a})$ [kN]	$\partial\sigma_{axial;a} / \partial F_{axial;a}$ [MPa/kN]	$1.96u(\sigma_{axial;a})$ [MPa]	$1.96u(\sigma_{axial;a})/\sigma_{axial;a}$ [%]
EN19T-AX-Spec-1	5.811	**0.014**	189.06	**0.023**	39.98	**5.40**	**1.5%**
EN19T-AX-Spec-2	5.690	**0.025**	189.06	**0.027**	39.98	**9.65**	**2.2%**
EN19T-AX-Spec-3	5.713	**0.019**	189.06	**0.033**	39.98	**7.47**	**1.4%**
EN19T-AX-Spec-4	5.720	**0.032**	189.06	**0.030**	39.98	**11.95**	**2.6%**
EN19T-AX-Spec-5	5.672	**0.034**	189.06	**0.036**	39.98	**12.76**	**2.2%**
EN19T-AX-Spec-6	5.643	**0.020**	189.06	**0.033**	39.98	**7.85**	**1.5%**
EN19T-AX-Spec-7	5.721	**0.031**	189.06	**0.032**	39.98	**11.65**	**2.3%**
EN19T-AX-Spec-8	5.711	**0.017**	189.06	**0.033**	39.98	**6.69**	**1.3%**

	Diameter [mm]	Cyclic Axial Force [kN]	Axial Stress [MPa]
/	**5.343**	13.266	591.66
EN19T-AX-Spec-6	**5.643**	**13.266**	**530.42**
\	**5.943**	13.266	478.23

	Diameter [mm]	Cyclic Axial Force [kN]	Axial Stress [MPa]
/	**5.643**	13.233	529.11
EN19T-AX-Spec-6	**5.643**	**13.266**	**530.42**
\	**5.643**	13.299	531.74



(a)



(b)

Figure K-2: Axial (AX) fatigue test result uncertainties – partial derivatives

K3. Bending Fatigue Test Uncertainties

Table K-3: Bending (B) fatigue test result uncertainties

		Diameter -> Stress		Cantilever length -> Stress		Break position -> Stress		Cantilever Force -> Stress		95% confidence interval	
Specimen #	**Diameter [mm]**	**u(d) [mm]**	$d\sigma_{bending;a} / dd$ **[MPa/mm]**	**u($L_{cantilever}$) [mm]**	$d\sigma_{bending;a} / dL_{cantilever}$ **[MPa/mm]**	**u($x_{break;exp}$) [mm]**	$d\sigma_{bending;a} / dx_{break;exp}$ **[MPa/mm]**	**u($F_{cantilever}$) [N]**	$d\sigma_{bending;a} / dF_{cantilever}$ **[MPa/N]**	**1.96u($\sigma_{bending;a}$) [MPa]**	**1.96u($\sigma_{bending;a}$)/$\sigma_{bending;a}$ [%]**
EN19T-B-Spec-1	5.493	**0.012**	330.12	**4.3**	11.043	**0.00**	11.043	**2.5**	3.415	**94.86**	**21.7%**
EN19T-B-Spec-2	5.424	**0.008**	330.12	**4.3**	11.043	**0.50**	11.043	**5.0**	3.415	**99.64**	**16.9%**
EN19T-B-Spec-3	5.552	**0.011**	330.12	**4.3**	11.043	**0.00**	11.043	**2.5**	3.415	**94.85**	**18.6%**
EN19T-B-Spec-4	5.734	**0.056**	330.12	**4.3**	11.043	**4.71**	11.043	**5.0**	3.415	**146.59**	**27.2%**
EN19T-B-Spec-5	5.545	**0.012**	330.12	**4.3**	11.043	**0.00**	11.043	**2.5**	3.415	**94.87**	**17.9%**
EN19T-B-Spec-6	5.650	**0.040**	330.12	**4.3**	11.043	**4.74**	11.043	**5.0**	3.415	**144.80**	**26.6%**
EN19T-B-Spec-7	5.603	**0.009**	330.12	**4.3**	11.043	**4.09**	11.043	**7.5**	3.415	**138.05**	**23.5%**

	Diameter [mm]	$L_{cantilever}$ [mm]	Bending Force [N]	x_{break} [mm]	Bending Stress [MPa]
/	**5.124**	114	173	60.5	700.77
EN19T-B-Spec-2	**5.424**	**114**	**173**	**60.5**	**590.80**
\	**5.724**	114	173	60.5	502.69

	Diameter [mm]	$L_{cantilever}$ [mm]	Bending Force [N]	x_{break} [mm]	Bending Stress [MPa]
/	**5.424**	109.7	173	60.5	543.32
EN19T-B-Spec-2	**5.424**	**114.0**	**173**	**60.5**	**590.80**
\	**5.424**	118.3	173	60.5	638.29

	Diameter [mm]	$L_{cantilever}$ [mm]	Bending Force [N]	x_{break} [mm]	Bending Stress [MPa]
/	**5.424**	114	173	58.5	612.89
EN19T-B-Spec-2	**5.424**	**114**	**173**	**60.5**	**590.80**
\	**5.424**	114	173	62.5	568.71

	Diameter [mm]	$L_{cantilever}$ [mm]	Bending Force [N]	x_{break} [mm]	Bending Stress [MPa]
/	**5.424**	114	166	60.5	565.19
EN19T-B-Spec-2	**5.424**	**114**	**173**	**60.5**	**590.80**
\	**5.424**	114	181	60.5	616.41

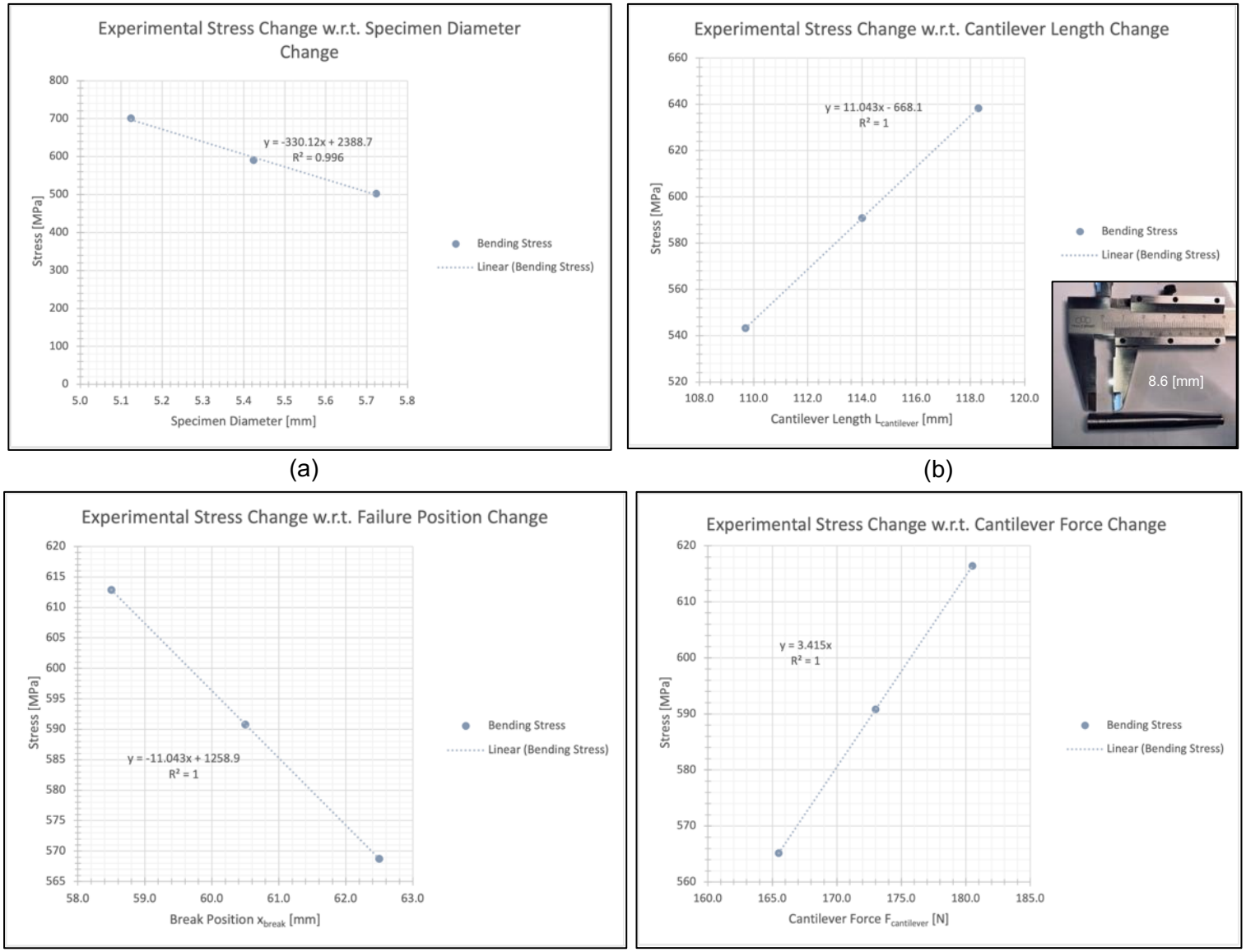


Figure K-3: Bending (B) fatigue test result uncertainties – partial derivatives

K4. Torsion Fatigue Test Uncertainties

Table K-4: Torsion (T) fatigue test result uncertainties

		Diameter -> Stress			Material Stiffness -> Stress			Diameter -> Gain -> Stress			95% confidence interval		
Specimen #	**Diameter [mm]**	**u(d) [mm]**	$\partial T_{a;VM} / \partial d$ **[MPa/mm]**	$\partial T_a / \partial d$ **[MPa/mm]**	**u(E) [GPa]**	$\partial T_{a;VM} / \partial E$ **[MPa/GPa]**	$\partial T_a / \partial E$ **[MPa/GPa]**	**u(d) [mm]**	$\partial T_{a;VM} / \partial d$ **[MPa/mm]**	$\partial T_a / \partial d$ **[MPa/mm]**	$1.96u(T_{a;VM})$ [MPa]	**$1.96u(T_a)$ [MPa]**	**$1.96u(T_a)/T_a$ [%]**
EN19T-T-Spec-1	6.548	**0.019**	390.81	225.63	**1.479**	4.05	2.34	**0.000**	8.29	4.79	18.89	**10.91**	**6.7%**
EN19T-T-Spec-2	6.526	**0.016**	390.81	225.63	**1.479**	4.05	2.34	**0.003**	19.13	11.04	17.23	**9.95**	**4.8%**
EN19T-T-Spec-3	6.538	**0.015**	390.81	225.63	**1.479**	4.05	2.34	**0.033**	21.93	12.66	16.36	**9.44**	**2.5%**
EN19T-T-Spec-4	6.551	**0.013**	390.81	225.63	**1.479**	4.05	2.34	**0.020**	21.93	12.66	15.35	**8.86**	**2.5%**
EN19T-T-Spec-5	6.523	**0.009**	390.81	225.63	**1.479**	4.05	2.34	**0.000**	19.13	11.04	13.81	**7.97**	**2.2%**
EN19T-T-Spec-6	6.532	**0.010**	390.81	225.63	**1.479**	4.05	2.34	**0.039**	21.93	12.66	14.26	**8.23**	**2.2%**
EN19T-T-Spec-7	6.582	**0.012**	390.81	225.63	**1.479**	4.05	2.34	**0.024**	24.46	14.12	15.09	**8.71**	**2.1%**
EN19T-T-Spec-8	6.571	**0.016**	390.81	225.63	**1.479**	4.05	2.34	**0.000**	21.93	12.66	16.94	**9.78**	**2.3%**
EN19T-T-Spec-9	6.558	**0.011**	390.81	225.63	**1.479**	4.05	2.34	**0.000**	24.46	14.12	14.61	**8.43**	**1.8%**

					T		Calcd	FEM NX
	Diameter [mm]	**unGained Force [N]**	**unGained Moment [N.m]**	**Expermntl GAIN T**	**ExpGained Force [N]**	**ExpGained Moment [N.m]**	**Torsion Stress VM [MPa]**	**Torsion Stress VM [MPa]**
/	**6.258**	76.912	17.664	1.505	115.781	26.590	957.08	962.62
EN19T-T-Spec-9	**6.558**	**76.912**	**17.664**	**1.505**	**115.781**	**26.590**	**831.65**	**837.97**
\	**6.858**	76.912	17.664	1.505	115.781	26.590	727.21	728.14

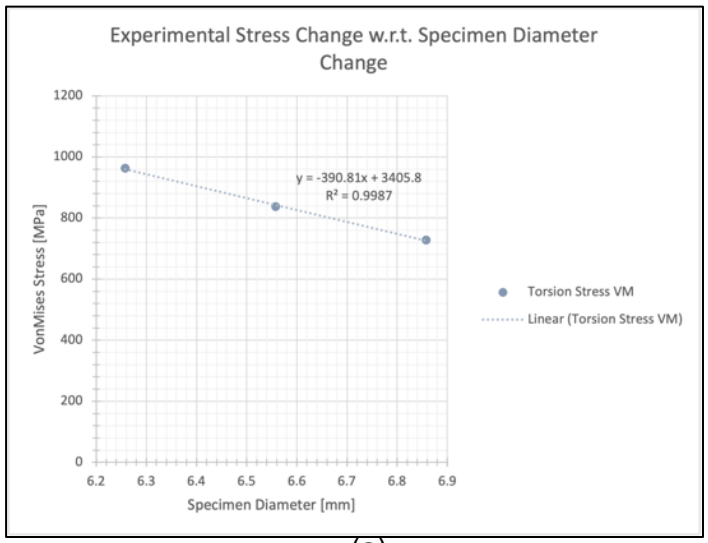
						T			FEM NX		V			FEM NX	
	Diameter [mm]	**E [GPa]**	**unGained Force [N]**	**unGained Moment [N.m]**	**Expermntl GAIN T**	**ExpGained Force [N]**	**ExpGained Moment [N.m]**	**Torsion Displ [mm]**	**Torsion Stress VM [MPa]**	-> Nom T Stress [MPa]	**ExpGained Force [N]**	**Torsion Displ [mm]**	**Torsion Stress VM [MPa]**	-> Nom T Stress [MPa]
/	**6.558**	209.695	76.912	17.664	1.489	114.519	26.300	0.218432	831.60	480.12	113.722	0.216912	824.96	476.29
EN19T-T-Spec-9	**6.558**	**211.174**	**76.912**	**17.664**	**1.489**	**114.519**	**26.300**	0.216911	**830.75**	479.63	**114.519**	0.216911	**830.75**	479.63
\	**6.558**	212.653	76.912	17.664	1.489	114.519	26.300	0.215402	831.19	479.89	115.321	0.216910	836.94	483.21

								Calcd	
	Diameter [mm]	**E [GPa]**	**unGained Force [N]**	**unGained Moment [N.m]**	**FEM NX [mm]**	**DANTEC [mm]**	**Expermntl GAIN T - spec1**	**Torsion Stress VM [MPa]**	-> Nom T Stress [MPa]
/	**6.248**	211.174	33.868	7.681	0.07284	0.072753	0.999	277.49	160.21
EN19T-T-Spec-1	**6.548**	**211.174**	**33.868**	**7.681**	**0.06255**	**0.072753**	**1.163**	**280.73**	162.08
NUT 5 \	**6.848**	211.174	33.868	7.681	0.05434	0.072753	1.339	282.49	163.09

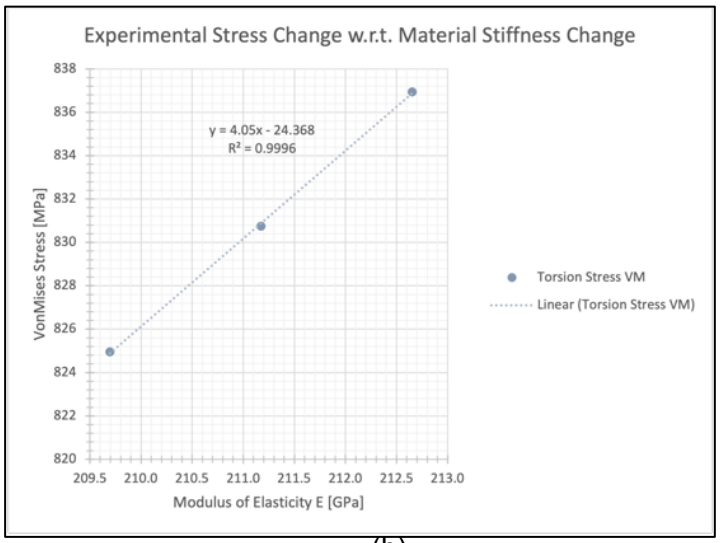
	Diameter [mm]	E [GPa]	unGained Force [N]	unGained Moment [N.m]	FEM NX [mm]	DANTEC [mm]	Expermntl GAIN T - spec5	Calcd Torsion Stress VM [MPa]	-> Nom T Stress [MPa]
/	**6.223**	211.174	67.298	15.456	0.14845	0.165845	1.117	632.05	364.91
EN19T-T-Spec-5	**6.523**	**211.174**	**67.298**	**15.456**	**0.12740**	**0.165845**	**1.302**	**639.45**	369.18
NUT 10 \	**6.823**	211.174	67.298	15.456	0.11061	0.165845	1.499	643.57	371.56

	Diameter [mm]	E [GPa]	unGained Force [N]	unGained Moment [N.m]	FEM NX [mm]	DANTEC [mm]	Expermntl GAIN T - spec8	Calcd Torsion Stress VM [MPa]	-> Nom T Stress [MPa]
/	**6.271**	211.174	71.655	16.252	0.15230	0.194325	1.276	741.73	428.24
EN19T-T-Spec-8	**6.571**	**211.174**	**71.655**	**16.252**	**0.13087**	**0.194325**	**1.485**	**750.25**	433.16
NUT 5 \	**6.871**	211.174	71.655	16.252	0.11376	0.194325	1.708	754.94	435.86

	Diameter [mm]	E [GPa]	unGained Force [N]	unGained Moment [N.m]	FEM NX [mm]	DANTEC [mm]	Expermntl GAIN T - spec9	Calcd Torsion Stress VM [MPa]	-> Nom T Stress [MPa]
/	**6.258**	211.174	76.912	17.664	0.16664	0.215487	1.293	822.14	474.66
EN19T-T-Spec-9	**6.558**	**211.174**	**76.912**	**17.664**	**0.14315**	**0.215487**	**1.505**	**831.65**	480.15
NUT 10 \	**6.858**	211.174	76.912	17.664	0.12439	0.215487	1.732	836.87	483.17

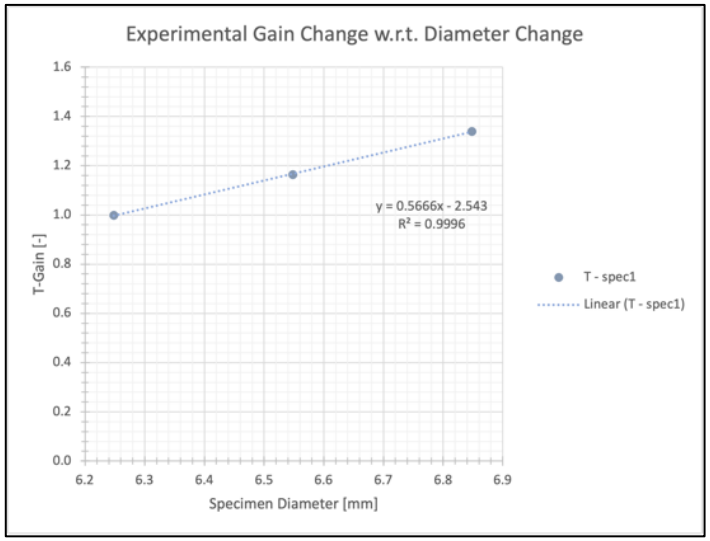


(a)

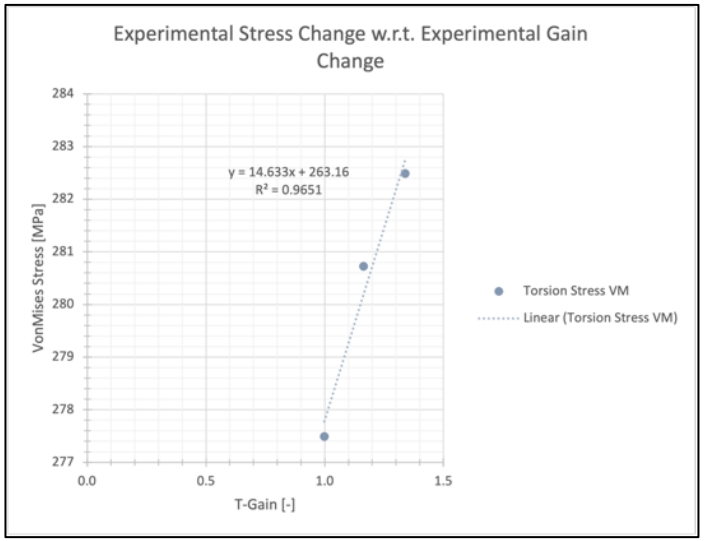


(b)

Spec1
(NUT 5)
27.5 [Hz]

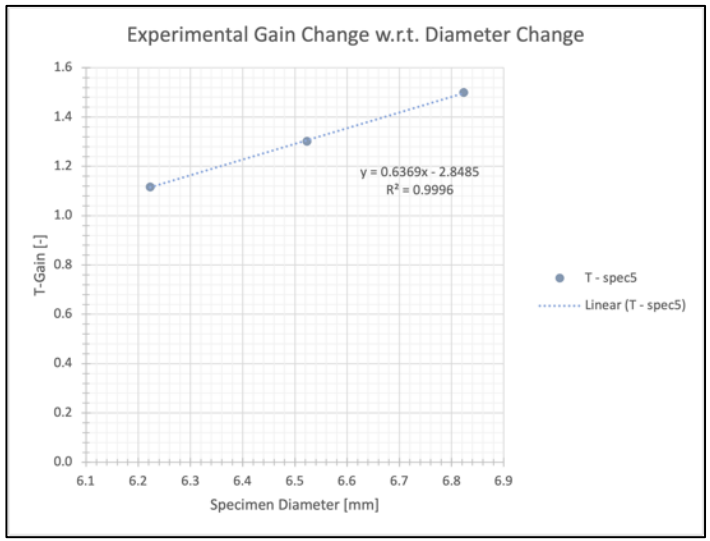


(c)

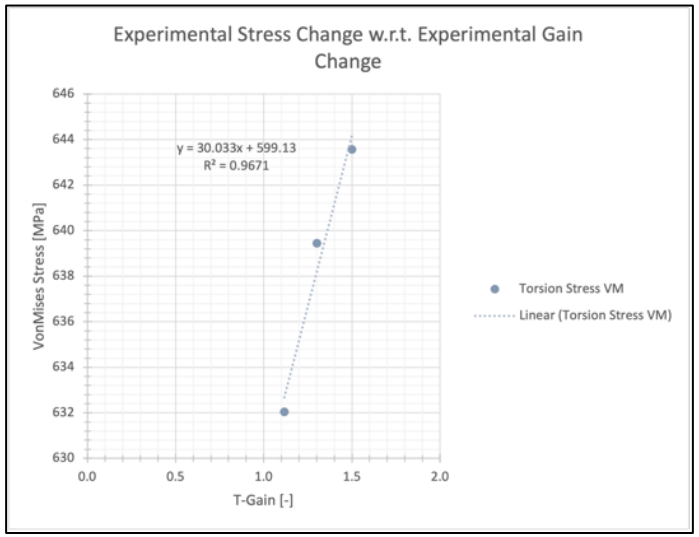


(d)

Spec5
(NUT 10)
35 [Hz]

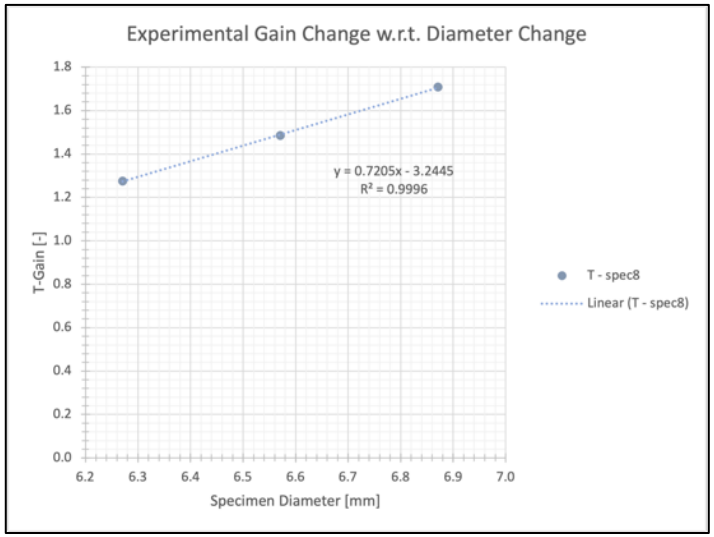


(e)

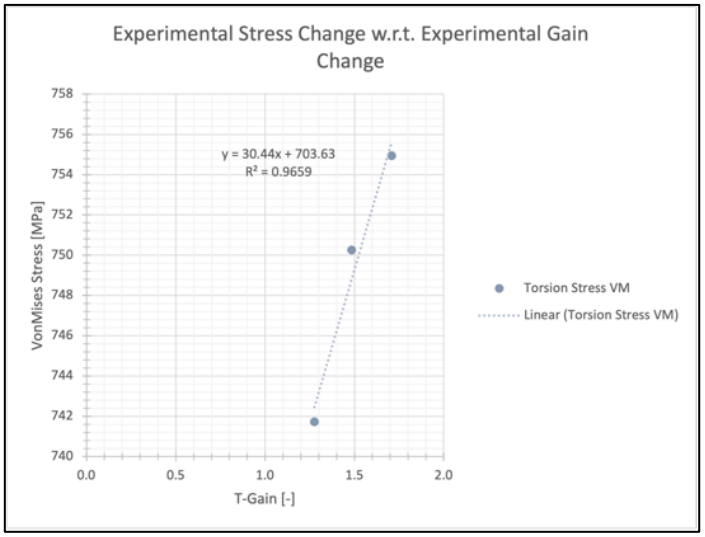


(f)

Spec8
(NUT 5)
40 [Hz]

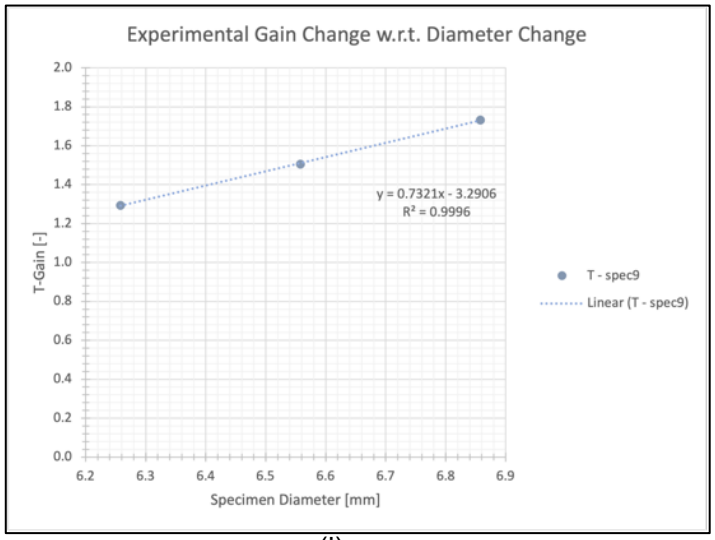


(g)

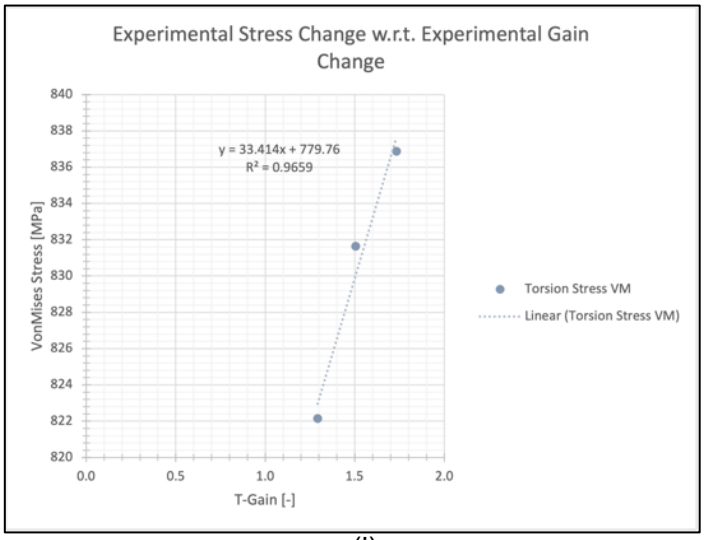


(h)

Spec9
(NUT 10)
40 [Hz]



(i)



(j)

Figure K-4: Torsion (T) fatigue test result uncertainties – partial derivatives

K5. Biaxial Bending-Torsion Test Uncertainties

Table K-5: Bending-Torsion (BT) fatigue test result uncertainties

		Diameter -> Stress				Material Stiffness -> Stress				Diameter -> Gain -> Stress				95% confidence interval				
Specimen #	Diameter [mm]	u(d) [mm]	$d\sigma_a$ / dd [MPa/mm]	$dT_{a;VM}$ / dd [MPa/mm]	dT_a / dd [MPa/mm]	u(E) [GPa]	$d\sigma_a$ / dE [MPa/GPa]	$dT_{a;VM}$ / dE [MPa/GPa]	dT_a / dE [MPa/GPa]	u(d) [mm]	$d\sigma_a$ / dd [MPa/mm]	$dT_{a;VM}$ / dd [MPa/mm]	dT_a / dd [MPa/mm]	**1.96u(σ_a) [MPa]**	1.96u($T_{a;VM}$) [MPa]	**1.96u(T_a) [MPa]**	**1.96u(σ_a)/σ_a [%]**	**1.96u(T_a)/T_a [%]**
EN19T-BT-Spec-1	6.527	**0.013**	239.10	231.81	133.83	**1.479**	2.52	2.33	1.34	**0.044**	32.86	26.56	15.33	**9.79**	9.11	**5.26**	**2.6%**	**3.0%**
EN19T-BT-Spec-2	6.534	**0.016**	239.10	231.81	133.83	**1.479**	2.52	2.33	1.34	**0.037**	32.86	26.56	15.33	**10.89**	10.25	**5.92**	**2.4%**	**2.8%**
EN19T-BT-Spec-3	6.560	**0.012**	239.10	231.81	133.83	**1.479**	2.52	2.33	1.34	**0.000**	23.80	16.80	9.70	**9.09**	8.54	**4.93**	**1.6%**	**1.7%**
EN19T-BT-Spec-4	6.548	**0.013**	239.10	231.81	133.83	**1.479**	2.52	2.33	1.34	**0.012**	23.80	16.80	9.70	**9.58**	9.02	**5.21**	**1.3%**	**1.3%**
EN19T-BT-Spec-5	6.552	**0.010**	239.10	231.81	133.83	**1.479**	2.52	2.33	1.34	**0.008**	23.80	16.80	9.70	**8.77**	8.22	**4.74**	**1.3%**	**1.4%**
EN19T-BT-Spec-6	6.554	**0.016**	239.10	231.81	133.83	**1.479**	2.52	2.33	1.34	**0.009**	33.95	29.19	16.85	**10.41**	9.85	**5.69**	**1.9%**	**2.0%**
EN19T-BT-Spec-7	6.563	**0.014**	239.10	231.81	133.83	**1.479**	2.52	2.33	1.34	**0.008**	32.86	26.56	15.33	**9.89**	9.33	**5.39**	**1.8%**	**2.1%**
EN19T-BT-Spec-8	6.539	**0.013**	239.10	231.81	133.83	**1.479**	2.52	2.33	1.34	**0.032**	32.86	26.56	15.33	**9.70**	9.08	**5.24**	**1.8%**	**2.1%**
EN19T-BT-Spec-9	6.563	**0.009**	239.10	231.81	133.83	**1.479**	2.52	2.33	1.34	**0.000**	33.95	29.19	16.85	**8.55**	8.00	**4.62**	**1.5%**	**1.7%**
EN19T-BT-Spec-10	6.653	**0.012**	239.10	231.81	133.83	**1.479**	2.52	2.33	1.34	**0.093**	23.80	16.80	9.70	**10.09**	9.09	**5.25**	**1.5%**	**1.5%**
EN19T-BT-Spec-11	6.568	**0.012**	239.10	231.81	133.83	**1.479**	2.52	2.33	1.34	**0.008**	23.80	16.80	9.70	**9.31**	8.76	**5.06**	**1.4%**	**1.5%**
EN19T-BT-Spec-12	6.571	**0.012**	239.10	231.81	133.83	**1.479**	2.52	2.33	1.34	**0.008**	33.95	29.19	16.85	**9.23**	8.67	**5.01**	**1.6%**	**1.8%**
EN19T-BT-Spec-13	6.539	**0.014**	239.10	231.81	133.83	**1.479**	2.52	2.33	1.34	**0.032**	32.86	26.56	15.33	**9.94**	9.33	**5.38**	**1.8%**	**2.1%**
EN19T-BT-Spec-14	6.577	**0.009**	239.10	231.81	133.83	**1.479**	2.52	2.33	1.34	**0.006**	32.86	26.56	15.33	**8.56**	8.01	**4.62**	**1.6%**	**1.8%**
EN19T-BT-Spec-15	6.571	**0.011**	239.10	231.81	133.83	**1.479**	2.52	2.33	1.34	**0.000**	32.86	26.56	15.33	**8.94**	8.39	**4.85**	**1.6%**	**1.9%**
EN19T-BT-Spec-16	6.574	**0.011**	239.10	231.81	133.83	**1.479**	2.52	2.33	1.34	**0.011**	33.95	29.19	16.85	**8.91**	8.35	**4.82**	**1.6%**	**1.7%**
EN19T-BT-Spec-17	6.589	**0.013**	239.10	231.81	133.83	**1.479**	2.52	2.33	1.34	**0.026**	33.95	29.19	16.85	**9.63**	9.05	**5.22**	**1.7%**	**1.9%**

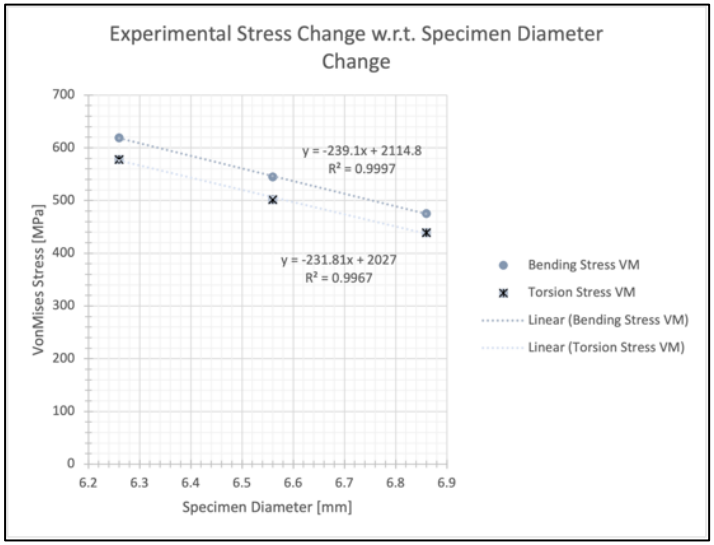
		unGained	unGained	Experimental GAIN		B		T		Calcd		FEM NX		-> Nom		
	Diameter [mm]	Force [N]	Moment [N.m]	B	T	ExpGained Force [N]	ExpGained Moment [N.m]	ExpGained Force [N]	ExpGained Moment [N.m]	Bending Stress VM [MPa]	Torsion Stress VM [MPa]	Bending Stress VM [MPa]	Torsion Stress VM [MPa]	T Stress [MPa]	NX vs Theortcl calc	
/	**6.260**	53.435	10.812	1.428	1.486	76.297	15.437	79.378	16.061	640.99	577.53	**618.84**	**578.19**	333.82	3.58	0.11
EN19T-BT-Spec-3	**6.560**	**53.435**	**10.812**	**1.428**	**1.486**	**76.297**	**15.437**	**79.378**	**16.061**	**557.01**	**501.87**	**544.84**	**501.68**	289.65	2.23	0.04
\	**6.860**	53.435	10.812	1.428	1.486	76.297	15.437	79.378	16.061	487.08	438.86	**475.38**	**439.11**	253.52	2.46	0.06

			unGained	unGained	Experimental GAIN		B		T		FEM NX - gained F		FEM NX		-> Nom	V	V	FEM NX - newgained F		FEM NX		-> Nom
	Diameter [mm]	E [GPa]	Force [N]	Moment [N.m]	B	T	ExpGained Force [N]	ExpGained Moment [N.m]	ExpGained Force [N]	ExpGained Moment [N.m]	Bending Displ [mm]	Torsion Displ [mm]	Bending Stress VM [MPa]	Torsion Stress VM [MPa]	T Stress [MPa]	ExpGained Force [N]	ExpGained Force [N]	Bending Displ [mm]	Torsion Displ [mm]	Bending Stress VM [MPa]	Torsion Stress VM [MPa]	T Stress [MPa]
/	**6.560**	209.695	53.435	10.812	1.398	1.469	74.717	15.118	78.513	15.886	0.24220	0.12708	**545.06**	**502.13**	289.90	74.196	77.963	0.24051	0.12619	**540.72**	**497.94**	287.49
EN19T-BT-Spec-3	**6.560**	**211.174**	**53.435**	**10.812**	**1.398**	**1.469**	**74.717**	**15.118**	**78.513**	**15.886**	0.24051	0.12619	**545.27**	**501.37**	289.47	**74.717**	**78.513**	0.24051	0.12619	**545.27**	**501.37**	289.47
\	**6.560**	212.653	53.435	10.812	1.398	1.469	74.717	15.118	78.513	15.886	0.23884	0.12532	**545.26**	**501.46**	289.52	75.239	79.058	0.24051	0.12619	**548.17**	**504.82**	291.46

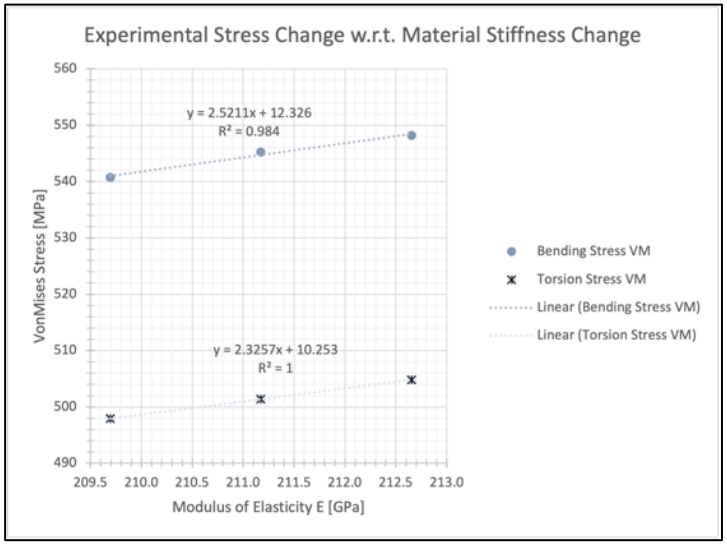
					FEM NX	FEM NX	DANTEC	DANTEC	Experimental GAIN		Calcd		-> Nom
	Diameter [mm]	E [GPa]	unGained Force [N]	unGained Moment [N.m]	B [mm]	T [mm]	B [mm]	T [mm]	B - spec3	T - spec3	Bending Stress VM [MPa]	Torsion Stress VM [MPa]	T Stress [MPa]
/	**6.260**	211.174	53.435	10.812	0.20091	0.10007	0.24560	0.12758	1.222	1.275	548.78	495.66	286.17
EN19T-BT-Spec-3	**6.560**	**211.174**	**53.435**	**10.812**	**0.17201**	**0.08588**	**0.24560**	**0.12758**	**1.428**	**1.486**	**557.01**	**501.87**	289.75
NUT 9 \	**6.860**	211.174	53.435	10.812	0.14879	0.07452	0.24560	0.12758	1.651	1.712	563.09	505.77	292.01

	Diameter [mm]	E [GPa]	unGained Force [N]	unGained Moment [N.m]	FEM NX B [mm]	FEM NX T [mm]	DANTEC B [mm]	DANTEC T [mm]	Experimental GAIN		Calcd Bending Stress VM [MPa]	Calcd Torsion Stress VM [MPa]	-> Nom T Stress [MPa]
									B - spec9	T - spec9			
/	**6.263**	211.174	56.585	11.377	0.21332	0.10683	0.24793	0.12317	1.162	1.153	548.25	470.98	271.92
EN19T-BT-Spec-9	**6.563**	**211.174**	**56.585**	**11.377**	**0.18073**	**0.09024**	**0.24793**	**0.12317**	**1.372**	**1.365**	**562.38**	**484.58**	279.77
NUT 5 \	**6.863**	211.174	56.585	11.377	0.15630	0.07829	0.24793	0.12317	1.586	1.573	568.65	488.46	282.01

	Diameter [mm]	E [GPa]	unGained Force [N]	unGained Moment [N.m]	FEM NX B [mm]	FEM NX T [mm]	DANTEC B [mm]	DANTEC T [mm]	Experimental GAIN		Calcd Bending Stress VM [MPa]	Calcd Torsion Stress VM [MPa]	-> Nom T Stress [MPa]
									B - spec15	T - spec15			
/	**6.271**	211.174	55.066	10.955	0.20454	0.10244	0.24069	0.11247	1.177	1.098	532.47	430.23	248.39
EN19T-BT-Spec-15	**6.571**	**211.174**	**55.066**	**10.955**	**0.17333**	**0.08655**	**0.24069**	**0.11247**	**1.389**	**1.299**	**546.14**	**442.60**	255.54
NUT 4 \	**6.871**	211.174	55.066	10.955	0.14994	0.07510	0.24069	0.11247	1.605	1.498	552.22	446.14	257.58

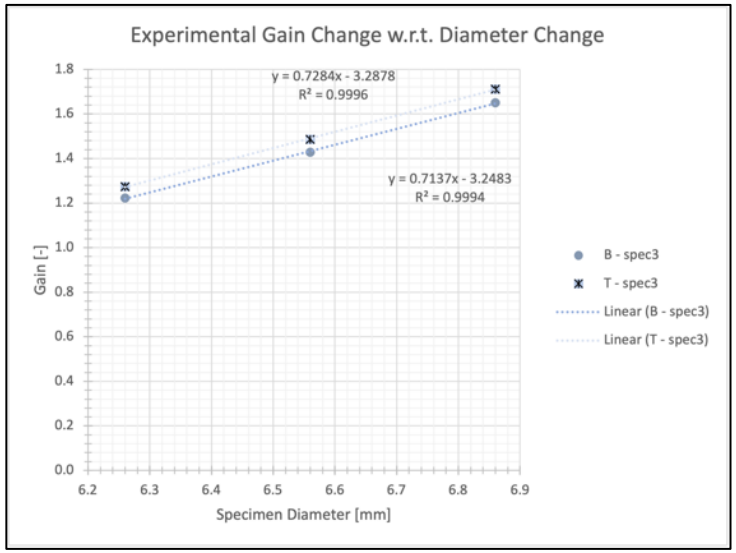


(a)

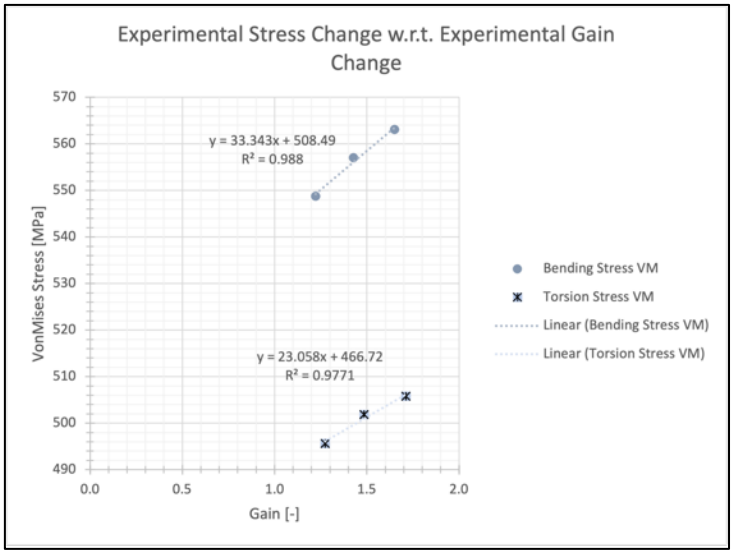


(b)

Spec3
(NUT 9)
38 [Hz]

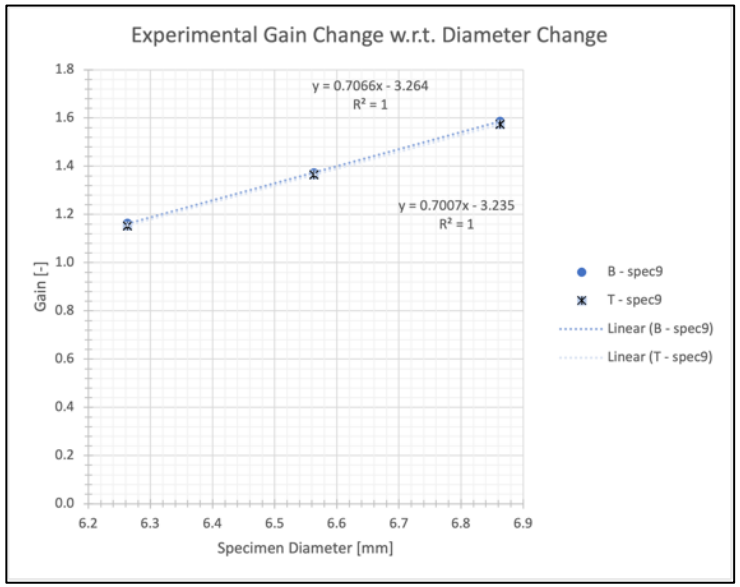


(c)

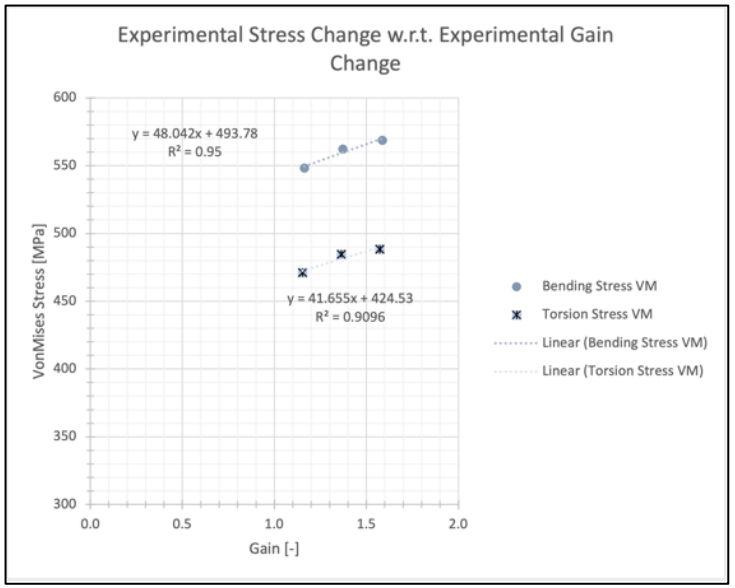


(d)

Spec9
(NUT 5)
38 [Hz]

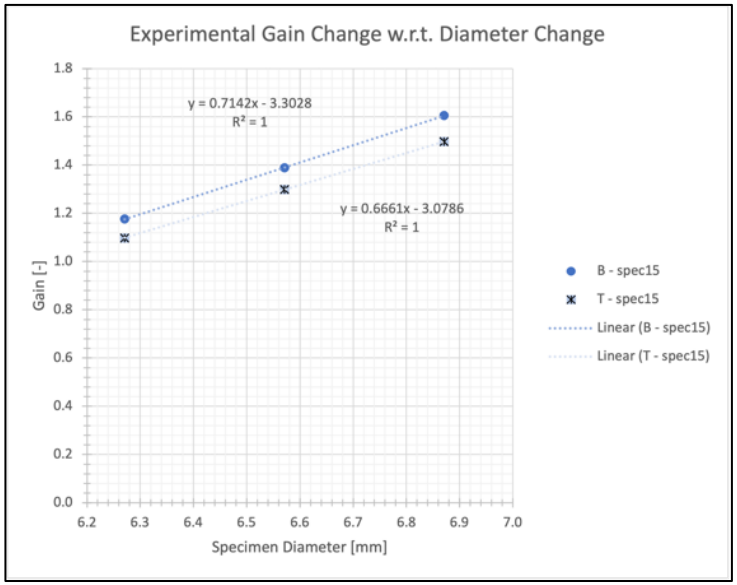


(e)

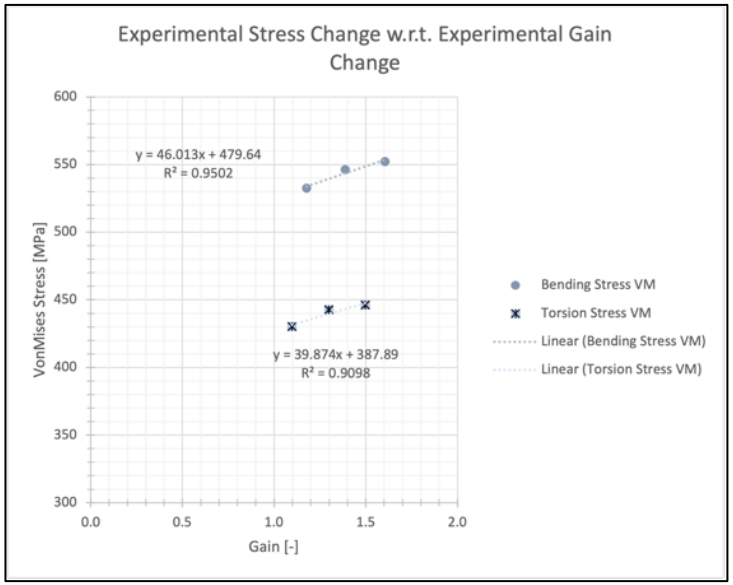


(f)

Spec15
(NUT 4)
38 [Hz]



(g)



(h)

Figure K-5: Bending-Torsion (BT) fatigue test result uncertainties – partial derivatives

L. MULTIAXIAL FATIGUE CRITERIA EVALUATION RESULTS

L1. Papadopoulos 1994/1997 – Critical Plane Criterion

Table L-1: Papadopoulos 1994/1997 criterion – equivalent multiaxial fatigue stress predictions

Specimen #	N_f [-]	λ [-]	Notes		T_a [MPa]	σ_a [MPa]	$\sigma_{eq;PPD}$ [MPa]	Err Indx I [%]
EN19T-BT-Spec-1	1532160	0.47	no fail	-	174.12	372.86	320.41	-9.5
EN19T-BT-Spec-2	1504800	0.47	no fail	-	208.76	447.05	384.17	8.5
EN19T-BT-Spec-3	1561846	0.52	no fail	Dantec1 @195Hz	289.75	557.01	497.91	40.7
EN19T-BT-Spec-4	27360	0.52	fail	-	387.49	745.29	666.08	
EN19T-BT-Spec-5	223394	0.52	fail	-	339.10	652.24	582.91	
EN19T-BT-Spec-6	346514	0.50	fail	-	279.37	562.72	494.19	
EN19T-BT-Spec-7	193846	0.47	fail	-	255.20	546.52	469.64	
EN19T-BT-Spec-8	1504800	0.47	no fail	repeats Spec7	254.83	545.72	468.95	32.5
EN19T-BT-Spec-9	207526	0.50	fail	Dantec2 @195Hz - repeats Spec6	279.77	562.38	494.27	
EN19T-BT-Spec-10	70726	0.52	fail	repeats Spec5	339.94	654.43	584.67	
EN19T-BT-Spec-11	57046	0.52	fail	repeats Spec5	339.27	652.66	583.25	
EN19T-BT-Spec-12	816286	0.50	fail	repeats Spec6	279.64	563.27	494.67	
EN19T-BT-Spec-13	2804400	0.47	no fail	repeats spec7	254.83	545.72	468.95	32.5
EN19T-BT-Spec-14	3182926	0.47	no fail	repeats spec7	255.41	546.96	470.01	32.8
EN19T-BT-Spec-15	1527646	0.47	no fail	Dantec3 @195Hz - repeats Spec7	255.54	546.14	469.63	32.7
EN19T-BT-Spec-16	118606	0.50	fail	repeats Spec6	279.68	563.36	494.75	
EN19T-BT-Spec-17	3522600	0.50	no fail	repeats Spec6	279.91	563.82	495.15	39.9

	Nf	Zenner et.al. 1985 [45]		$\sigma_{eq;PPD;Z-OP}$ [MPa]	
OP	1000000	137	286	236.27	-9.1
IP	1000000	157	328	270.89	4.2
				$\sigma_{eq;PPD;Z-IP}$ [MPa]	

L2. Carpinteri and Spagnoli 2001 – Critical Plane Criterion

Table L-2: Carpinteri and Spagnoli 2001 criterion – equivalent multiaxial fatigue stress predictions

β 90.0 [°]
ϕ 90.0 [°] ∨ enter after solver for specimen here onwards --> (N_a : C_a) 90° Out-Of-Phase B&T

Specimen #	N_f [-]	λ [-]	Notes		T_a [MPa]	σ_a [MPa]	a [MPa]	b [MPa]	$N_{max}=N_a$ [MPa]	ϕ_f [°]	ψ_f [°]	δ [°]	ψ_c [°]	ϕ_c [°]	a [MPa]	b [MPa]	N_a [MPa]	p [MPa]	q [MPa]	C_a [MPa]	$\sigma_{eq;C\&S}$ [MPa]	Err Indx I [%]
EN19T-BT-Spec-1	1532160	0.47	no fail	-	174.12	372.86	372.86	0.00	372.86	90.00	0.00	34.98	34.98	55.02	250.33	-163.57	299.03	175.14	59.67	185.03	400.59	-21.5
EN19T-BT-Spec-2	1504800	0.47	no fail	-	208.76	447.05	447.05	0.00	447.05	90.00	0.00	34.98	34.98	55.02	300.14	-196.12	358.53	209.99	71.55	221.84	480.30	-5.8
EN19T-BT-Spec-3	1561846	0.52	no fail	Dantec1 @195Hz	289.75	557.01	557.01	0.00	557.01	90.00	0.00	34.98	34.98	55.02	373.95	-272.20	462.53	261.64	99.31	279.85	613.58	20.3
EN19T-BT-Spec-4	27360	0.52	fail	-	387.49	745.29	745.29	0.00	745.29	90.00	0.00	34.98	34.98	55.02	500.36	-364.02	618.77	350.08	132.80	374.42	820.88	
EN19T-BT-Spec-5	223394	0.52	fail	-	339.10	652.24	652.24	0.00	652.24	90.00	0.00	34.98	34.98	55.02	437.89	-318.56	541.50	306.37	116.22	327.67	718.38	
EN19T-BT-Spec-6	346514	0.50	fail	-	279.37	562.72	562.72	0.00	562.72	90.00	0.00	34.98	34.98	55.02	377.79	-262.45	460.00	264.32	95.75	281.13	612.89	
EN19T-BT-Spec-7	193846	0.47	fail	-	255.20	546.52	546.52	0.00	546.52	90.00	0.00	34.98	34.98	55.02	366.91	-239.75	438.30	256.71	87.46	271.20	587.16	
EN19T-BT-Spec-8	1504800	0.47	no fail	repeats Spec7	254.83	545.72	545.72	0.00	545.72	90.00	0.00	34.98	34.98	55.02	366.38	-239.40	437.66	256.33	87.34	270.80	586.31	15.0
EN19T-BT-Spec-9	207526	0.50	fail	Dantec2 @195Hz - repeats Spec6	279.77	562.38	562.38	0.00	562.38	90.00	0.00	34.98	34.98	55.02	377.56	-262.83	460.03	264.16	95.88	281.02	612.82	
EN19T-BT-Spec-10	70726	0.52	fail	repeats Spec5	339.94	654.43	654.43	0.00	654.43	90.00	0.00	34.98	34.98	55.02	439.36	-319.35	543.16	307.40	116.50	328.74	720.64	
EN19T-BT-Spec-11	57046	0.52	fail	repeats Spec5	339.27	652.66	652.66	0.00	652.66	90.00	0.00	34.98	34.98	55.02	438.17	-318.72	541.83	306.57	116.27	327.88	718.82	
EN19T-BT-Spec-12	816286	0.50	fail	repeats Spec6	279.64	563.27	563.27	0.00	563.27	90.00	0.00	34.98	34.98	55.02	378.16	-262.70	460.45	264.58	95.84	281.40	613.49	
EN19T-BT-Spec-13	2804400	0.47	no fail	repeats spec7	254.83	545.72	545.72	0.00	545.72	90.00	0.00	34.98	34.98	55.02	366.38	-239.40	437.66	256.33	87.34	270.80	586.31	15.0
EN19T-BT-Spec-14	3182926	0.47	no fail	repeats spec7	255.41	546.96	546.96	0.00	546.96	90.00	0.00	34.98	34.98	55.02	367.21	-239.94	438.65	256.92	87.53	271.42	587.64	15.2
EN19T-BT-Spec-15	1527646	0.47	no fail	Dantec3 @195Hz - repeats Spec7	255.54	546.14	546.14	0.00	546.14	90.00	0.00	34.98	34.98	55.02	366.66	-240.06	438.26	256.53	87.58	271.07	587.01	15.1
EN19T-BT-Spec-16	118606	0.50	fail	repeats Spec6	279.68	563.36	563.36	0.00	563.36	90.00	0.00	34.98	34.98	55.02	378.22	-262.75	460.53	264.62	95.85	281.45	613.59	
EN19T-BT-Spec-17	3522600	0.50	no fail	repeats Spec6	279.91	563.82	563.82	0.00	563.82	90.00	0.00	34.98	34.98	55.02	378.52	-262.96	460.90	264.83	95.93	281.67	614.08	20.4

∧ |--> note: for ϕ=90, b=0, then Na = Nmax = maximum for each specimen
solver in windows |
Prelim calc to obtain ϕc

	Nf	Zenner et.al. 1985 [45]																$\sigma_{eq;C\&S;Z\text{-}OP}$ [MPa]	
OP	1000000	137	286	286.00	0.00	286.00	90.00	0.00	38.69	38.69	51.31	174.22	-133.69	219.61	139.55	29.91	142.72	309.77	-22.2
IP	1000000	157	328	328.00	0.00	328.00	90.00	0.00	38.69	38.69	51.31	199.81	-153.21	251.79	160.04	34.28	163.67	355.21	-65.3
																		$\sigma_{eq;C\&S;Z\text{-}IP}$ [MPa]	

L3. Liu and Mahadevan 2005 – Critical Plane Criterion

Table L-3: Liu and Mahadevan 2005 criterion – equivalent multiaxial fatigue stress predictions

β 90.0 [°]
ϕ 90.0 [°] V enter after solver for specimen here onwards --> (N_a ; C_a) 90° Out-Of-Phase B&T

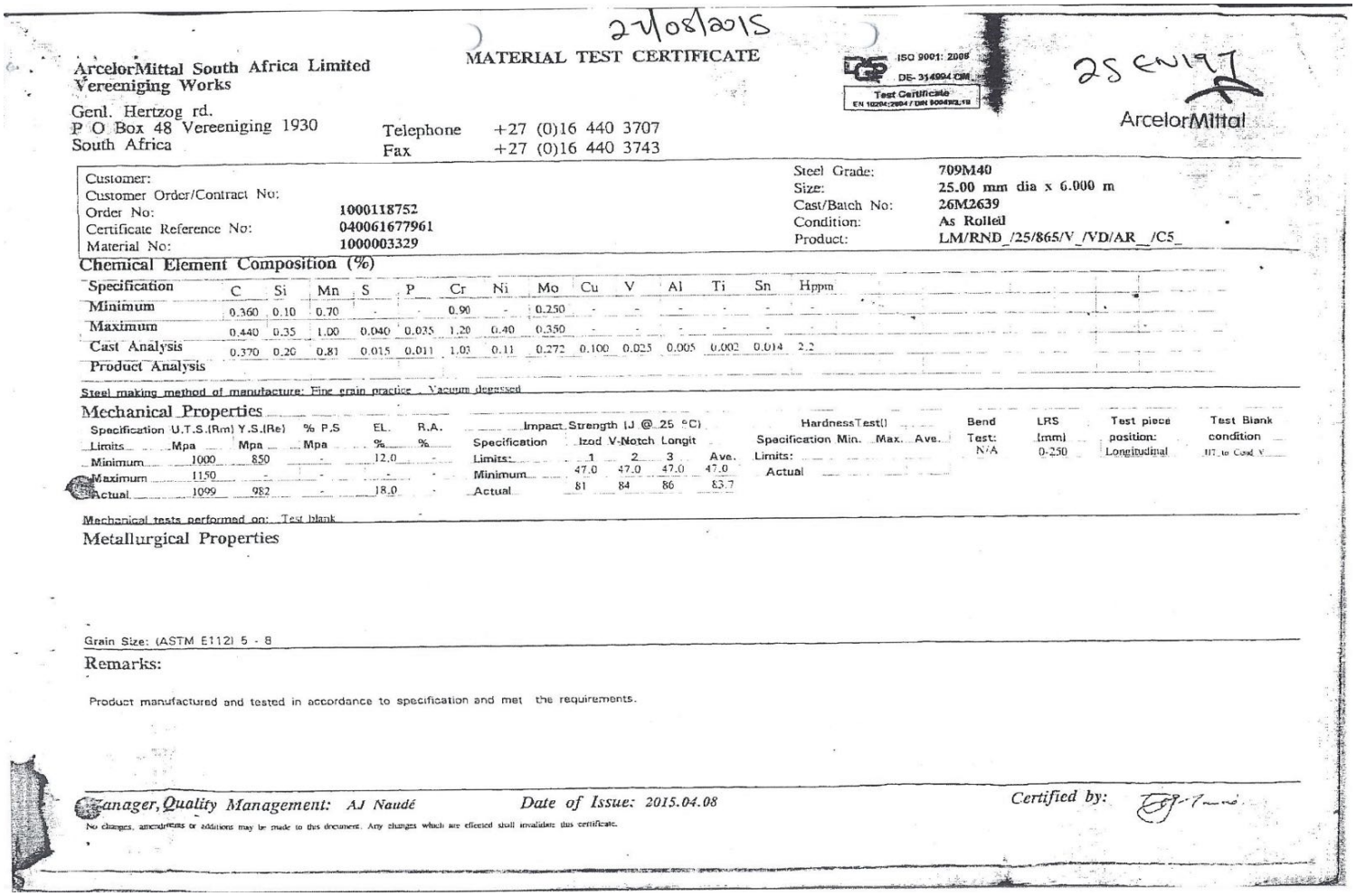
Specimen #	N_f [-]	λ [-]	Notes		τ_a [MPa]	σ_a [MPa]	a [MPa]	b [MPa]	$N_{max}=N_a$ [MPa]	ϕ_f [°]	ψ_f [°]	δ [°]	ψ_c [°]	ϕ_c [°]	a [MPa]	b [MPa]	N_a [MPa]	p [MPa]	q [MPa]	C_a [MPa]	λ [-]	$\sigma_{eq;L\&M}$ [-]	Err Indx I [%]
EN19T-BT-Spec-1	1532160	0.47	no fail	-	174.12	372.86	372.86	0.00	372.86	90.00	0.00	33.60	33.60	56.40	258.65	-160.52	304.42	171.87	67.45	184.64	0.96	0.79	-17.5
EN19T-BT-Spec-2	1504800	0.47	no fail	-	208.76	447.05	447.05	0.00	447.05	90.00	0.00	33.60	33.60	56.40	310.12	-192.46	364.99	206.07	80.87	221.37	0.96	0.95	-1.0
EN19T-BT-Spec-3	1561846	0.52	no fail	Dantec1 @195Hz	289.75	557.01	557.01	0.00	557.01	90.00	0.00	33.60	33.60	56.40	386.39	-267.13	469.74	256.76	112.25	280.22	0.96	1.21	26.5
EN19T-BT-Spec-4	27360	0.52	fail	-	387.49	745.29	745.29	0.00	745.29	90.00	0.00	33.60	33.60	56.40	517.01	-357.23	628.42	343.55	150.11	374.91	0.96	1.62	
EN19T-BT-Spec-5	223394	0.52	fail	-	339.10	652.24	652.24	0.00	652.24	90.00	0.00	33.60	33.60	56.40	452.46	-312.62	549.95	300.66	131.36	328.10	0.96	1.42	
EN19T-BT-Spec-6	346514	0.50	fail	-	279.37	562.72	562.72	0.00	562.72	90.00	0.00	33.60	33.60	56.40	390.35	-257.55	467.66	259.39	108.23	281.06	0.96	1.21	
EN19T-BT-Spec-7	193846	0.47	fail	-	255.20	546.52	546.52	0.00	546.52	90.00	0.00	33.60	33.60	56.40	379.12	-235.28	446.19	251.92	98.86	270.63	0.96	1.16	
EN19T-BT-Spec-8	1504800	0.47	no fail	repeats Spec7	254.83	545.72	545.72	0.00	545.72	90.00	0.00	33.60	33.60	56.40	378.56	-234.94	445.54	251.55	98.72	270.23	0.96	1.16	20.8
EN19T-BT-Spec-9	207526	0.50	fail	Dantec2 @195Hz - repeats Spec6	279.77	562.38	562.38	0.00	562.38	90.00	0.00	33.60	33.60	56.40	390.12	-257.92	467.68	259.23	108.38	280.98	0.96	1.21	
EN19T-BT-Spec-10	70726	0.52	fail	repeats Spec5	339.94	654.43	654.43	0.00	654.43	90.00	0.00	33.60	33.60	56.40	453.98	-313.39	551.64	301.67	131.69	329.16	0.96	1.43	
EN19T-BT-Spec-11	57046	0.52	fail	repeats Spec5	339.27	652.66	652.66	0.00	652.66	90.00	0.00	33.60	33.60	56.40	452.75	-312.78	550.28	300.85	131.43	328.31	0.96	1.42	
EN19T-BT-Spec-12	816286	0.50	fail	repeats Spec6	279.64	563.27	563.27	0.00	563.27	90.00	0.00	33.60	33.60	56.40	390.74	-257.80	468.12	259.64	108.33	281.33	0.96	1.21	
EN19T-BT-Spec-13	2804400	0.47	no fail	repeats spec7	254.83	545.72	545.72	0.00	545.72	90.00	0.00	33.60	33.60	56.40	378.56	-234.94	445.54	251.55	98.72	270.23	0.96	1.16	20.8
EN19T-BT-Spec-14	3182926	0.47	no fail	repeats spec7	255.41	546.96	546.96	0.00	546.96	90.00	0.00	33.60	33.60	56.40	379.42	-235.46	446.55	252.13	98.94	270.84	0.96	1.16	21.1
EN19T-BT-Spec-15	1527646	0.47	no fail	Dantec3 @195Hz - repeats Spec7	255.54	546.14	546.14	0.00	546.14	90.00	0.00	33.60	33.60	56.40	378.86	-235.58	446.13	251.75	98.99	270.51	0.96	1.16	21.0
EN19T-BT-Spec-16	118606	0.50	fail	repeats Spec6	279.68	563.36	563.36	0.00	563.36	90.00	0.00	33.60	33.60	56.40	390.80	-257.84	468.20	259.68	108.35	281.38	0.96	1.21	
EN19T-BT-Spec-17	3522600	0.50	no fail	repeats Spec6	279.91	563.82	563.82	0.00	563.82	90.00	0.00	33.60	33.60	56.40	391.12	-258.05	468.57	259.89	108.43	281.61	0.96	1.22	26.6

solver in windows ^ | --> note: for ϕ=90, b=0, then Na = Nmax = maximum for each specimen

Prelim calc to obtain ϕc

	Nf	Zenner et.al. 1985 [45]																	$\sigma_{eq;L\&M;Z-OP}$ [-]	
OP	1000000	137	286	286.00	0.00	286.00	90.00	0.00	36.61	36.61	53.39	184.29	-131.16	226.20	136.91	39.56	142.51	0.98	0.79	-19.1
IP	1000000	157	328	328.00	0.00	328.00	90.00	0.00	36.61	36.61	53.39	211.36	-150.31	259.36	157.01	45.34	163.43	0.98	0.91	-7.2
																			$\sigma_{eq;L\&M;Z-IP}$ [-]	

M. MATERIAL AND HEAT TREATMENT CERTIFICATE(S)



27/08/2015

MATERIAL TEST CERTIFICATE

ISO 9001: 2008
DE- 314994 CDN
Test Certificate
EN 10204:2004 / DIN 50049-3.1B

25 EN19T

ArcelorMittal South Africa Limited
Vereeniging Works

Genl. Hertzog rd.
P O Box 48 Vereeniging 1930
South Africa

Telephone +27 (0)16 440 3707
Fax +27 (0)16 440 3743

ArcelorMittal

Customer:		Steel Grade:	709M40
Customer Order/Contract No:		Size:	25.00 mm dia x 6.000 m
Order No:	1000118752	Cast/Batch No:	26M2639
Certificate Reference No:	040061677961	Condition:	As Rolled
Material No:	1000003329	Product:	LM/RND_/25/865/V_/VD/AR__/C5_

Chemical Element Composition (%)

Specification	C	Si	Mn	S	P	Cr	Ni	Mo	Cu	V	Al	Ti	Sn	Hppm
Minimum	0.360	0.10	0.70	-	-	0.90	-	0.250	-	-	-	-	-	-
Maximum	0.440	0.35	1.00	0.040	0.035	1.20	0.40	0.350	-	-	-	-	-	-
Cast Analysis	0.370	0.20	0.81	0.015	0.011	1.03	0.11	0.272	0.100	0.025	0.005	0.002	0.014	2.2
Product Analysis														

Steel making method of manufacture: Fine grain practice . Vacuum degassed

Mechanical Properties

Specification	U.T.S.(Rm)	Y.S.(Re)	% P.S	EL.	R.A.
Limits	Mpa	Mpa	Mpa	%	%
Minimum	1000	850	-	12.0	-
Maximum	1150	-	-	-	-
Actual	1099	982	-	18.0	-

Impact Strength (J @ 25 °C)				
Specification	Izod V-Notch Longit			
Limits:	1	2	3	Ave.
Minimum	47.0	47.0	47.0	47.0
Actual	81	84	86	83.7

HardnessTest()			Bend	LRS	Test piece	Test Blank
Specification	Min.	Max.	Ave.	Test:	(mm)	position:	condition
Limits:				N/A	0-250	Longitudinal	HT to Cond T
Actual							

Mechanical tests performed on: Test blank

Metallurgical Properties

Grain Size: (ASTM E112) 5 - 8

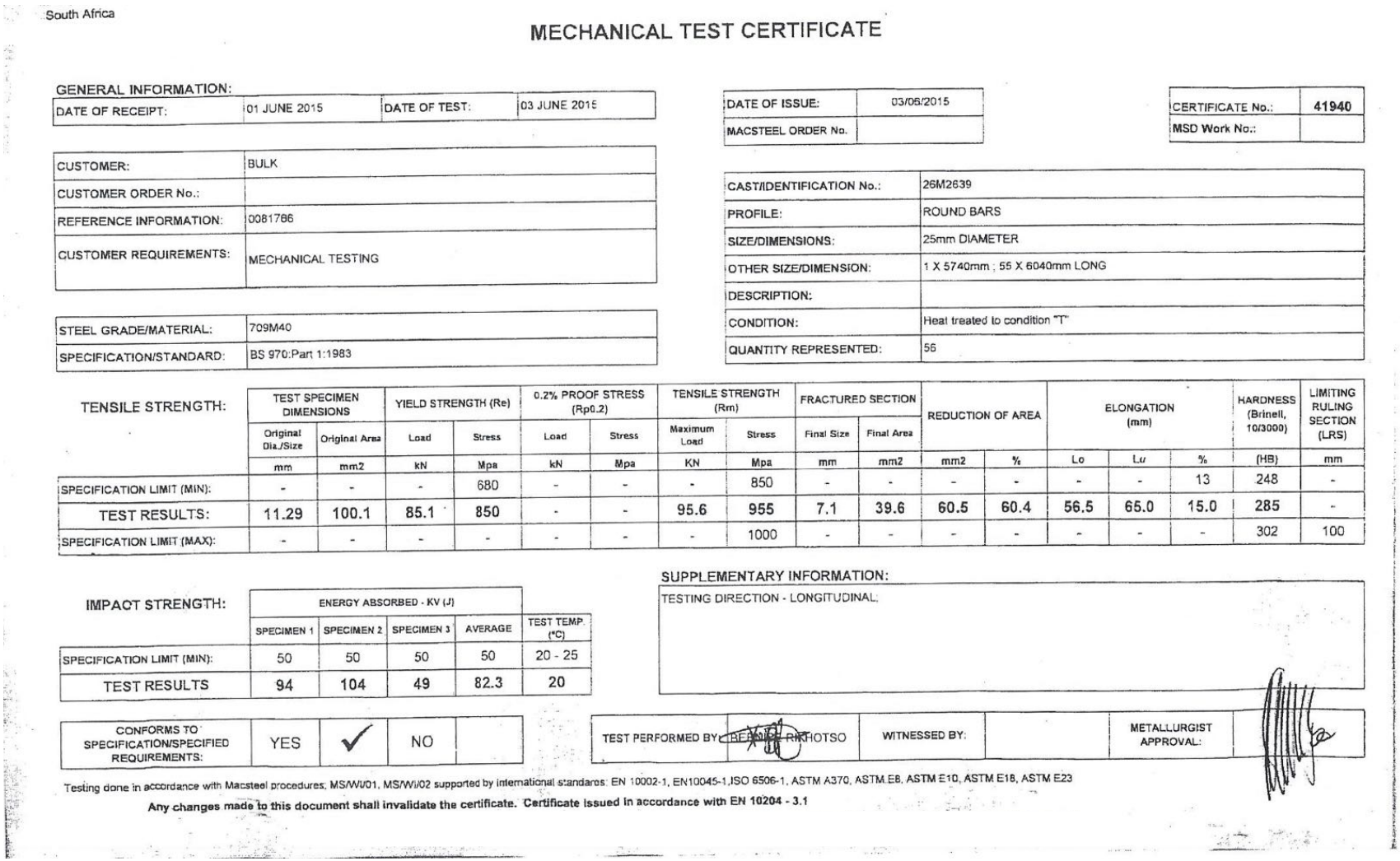
Remarks:

Product manufactured and tested in accordance to specification and met the requirements.

Manager, Quality Management: AJ Naudé *Date of Issue: 2015.04.08* *Certified by:*

No changes, amendments or additions may be made to this document. Any changes which are effected shall invalidate this certificate.

Figure M-1: EN19 (T-condition) alloy steel – material test certificate



South Africa

MECHANICAL TEST CERTIFICATE

GENERAL INFORMATION:

DATE OF RECEIPT:	01 JUNE 2015	DATE OF TEST:	03 JUNE 2015

DATE OF ISSUE:	03/06/2015
MACSTEEL ORDER No.	

CERTIFICATE No.:	41940
MSD Work No.:	

CUSTOMER:	BULK
CUSTOMER ORDER No.:	
REFERENCE INFORMATION:	0081786
CUSTOMER REQUIREMENTS:	MECHANICAL TESTING

CAST/IDENTIFICATION No.:	26M2639
PROFILE:	ROUND BARS
SIZE/DIMENSIONS:	25mm DIAMETER
OTHER SIZE/DIMENSION:	1 X 5740mm ; 55 X 6040mm LONG
DESCRIPTION:	
CONDITION:	Heat treated to condition "T"
QUANTITY REPRESENTED:	56

STEEL GRADE/MATERIAL:	709M40
SPECIFICATION/STANDARD:	BS 970:Part 1:1983

TENSILE STRENGTH:

	TEST SPECIMEN DIMENSIONS		YIELD STRENGTH (Re)		0.2% PROOF STRESS (Rp0.2)		TENSILE STRENGTH (Rm)		FRACTURED SECTION		REDUCTION OF AREA		ELONGATION (mm)			HARDNESS (Brinell, 10/3000)	LIMITING RULING SECTION (LRS)
	Original Dia./Size	Original Area	Load	Stress	Load	Stress	Maximum Load	Stress	Final Size	Final Area							
	mm	mm2	kN	Mpa	kN	Mpa	KN	Mpa	mm	mm2	mm2	%	Lo	Lu	%	(HB)	mm
SPECIFICATION LIMIT (MIN):	-	-	-	680	-	-	-	850	-	-	-	-	-	-	13	248	-
TEST RESULTS:	11.29	100.1	85.1	850	-	-	95.6	955	7.1	39.6	60.5	60.4	56.5	65.0	15.0	285	-
SPECIFICATION LIMIT (MAX):	-	-	-	-	-	-	-	1000	-	-	-	-	-	-	-	302	100

IMPACT STRENGTH:

	ENERGY ABSORBED - KV (J)				
	SPECIMEN 1	SPECIMEN 2	SPECIMEN 3	AVERAGE	TEST TEMP (°C)
SPECIFICATION LIMIT (MIN):	50	50	50	50	20 - 25
TEST RESULTS	94	104	49	82.3	20

SUPPLEMENTARY INFORMATION:

TESTING DIRECTION - LONGITUDINAL

CONFORMS TO SPECIFICATION/SPECIFIED REQUIREMENTS:	YES	✓	NO	

TEST PERFORMED BY:	[illegible]	WITNESSED BY:		METALLURGIST APPROVAL:

Testing done in accordance with Macsteel procedures; MS/WI/01, MS/WI/02 supported by international standards: EN 10002-1, EN10045-1,ISO 6506-1, ASTM A370, ASTM E8, ASTM E10, ASTM E18, ASTM E23

Any changes made to this document shall invalidate the certificate. Certificate issued in accordance with EN 10204 - 3.1

Figure M-2: EN19 (T-condition) alloy steel – mechanical test certificate

Heat Treatment Certificate

Customer:	
Material Spec:	**709M40**
Description:	**25 Dia**
Certificate No:	**81766**
Cast Number:	**26M2639**
Quantity:	**56 Off**

Process

Preheat	
Stress Relieve	
Full Anneal	
Sub-Critical Anneal	
High Temperature Normalize	
Normalize	
Oil Quench	x
Water Quench	
Air Quench	
Vacuum (Gas Quench)	
Vacuum (Oil Quench)	
Temper	x
Double Temper	
Carburize Only	
Case Hardening	
Neutral Harden (Retort)	
Neutral Harden (Salt Bath)	
Blackening	
Double Solution Anneal	
Sub-Zero	
Ageing	
Precipitation	
Shot Blast	
Glass Blast	
Stop Off Paint	
Case Depth/Micro	
Mechanical test certificate number	41940
Straightening	x
Gas Nitriding	
Hardness Requested:	I
Hardness Achieved:	277-293 HBW 10/3000

Note: Surface hardness alone does not guarantee mechanical properties.
Mechanical tests done on one test bar within Limiting Ruling Section is an indication of the batch mechanical properties. Mechanical results on material out of Limiting Ruling Section are for information only.
If no mechanical certificate number is printed on this certificate, mechanical tests were not requested.

Remarks:

Date of Issue	29-06-2015	Works Order No.	81766
In accordance with your verbal instructions/Order Number			
Certified as correct			

Figure M-3: EN19 (T-condition) alloy steel – heat treatment certificate